Shi, Patrick Chee Wai (2006) Single crystal fibres and their applications. PhD thesis

http://theses.gla.ac.uk/6741/

Copyright and moral rights for this thesis are retained by the author

A copy can be downloaded for personal non-commercial research or study, without prior permission or charge

This thesis cannot be reproduced or quoted extensively from without first obtaining permission in writing from the Author

The content must not be changed in any way or sold commercially in any format or medium without the formal permission of the Author

When referring to this work, full bibliographic details including the author, title, awarding institution and date of the thesis must be given.

Glasgow Theses Service
http://theses.gla.ac.uk/
theses@gla.ac.uk

SINGLE CRYSTAL FIBRES AND THEIR APPLICATIONS

Patrick Chee Wai Shi

Thesis is submitted for the degree of Doctor of Philosophy

Department of Mechanical Engineering

The University of Glasgow

July, 2006

© Patrick Chee Wai Shi 2006

Abstract

Single crystal fibres have been grown by the laser heated pedestal growth technique. Materials investigated in this work were Y_2O_3, $Y_3Al_5O_{12}$ and Al_2O_3. Doped with different rare earth concentration levels, these fibres were mainly grown from cold pressed powder mixtures. Each of the three materials exhibited different growth conditions. Al_2O_3 were the easiest to grow and has the highest shear strength of ~5MPa but has the least acceptance to rare earth doping. Y_2O_3 fibres displayed the lowest shear strength of ~0.71MPa but were able to accept dopant concentration up to 59mol%. All three SCFs experience diameter irregularity due to the power fluctuation in the CO_2 laser power. Detailed characterisations were carried out on YAG and Y_2O_3 SCFs in order to determine the suitable concentration levels to be used in thermometry applications. The rare earth ions in these materials experienced broadening of linewidths in absorption and fluorescence emission as the concentration levels increased. Upconversion emission in the green and red were also observed for both fibres. The red intensity increases with increasing concentration levels. Fluorescence decay increases also with increasing concentration level. For YAG:Er^{3+} doped 10mol% the lifetime was ~8ms and Y_2O_3:Er^{3+} doped at 6mol% it was ~12.4ms at the $^4I_{13/2} \rightarrow {}^4I_{15/2}$ transition. Fluorescence quenching was only evident for Y_2O_3:Er^{3+} at 59mol% with a τ = 1.7ms. YAG singly doped and co-doped Yb^{3+}, and Y_2O_3 SCFs were grown for sensing applications at starting concentration levels of 2mol%, 2 + 5mol% and 2 mol%, respectively. Methods such as fluorescence/upconversion intensity ratio and fluorescence lifetime decay were employed as a function of temperature. The temperature range studied was from ~293K to ~1473K. Both YAG singly doped and co-doped fibres displayed similar emission behaviour under thermal influence. The co-doped fibres provided an extra IR line in the transition $^2I_{11/2}$ for temperature sensing. The majority of the fluorescence intensity ratio (FIR) curves increased with increasing temperature. Curves that showed potential in sensing were selected and re-plotted with the theoretical formula. In the visible region, the YAG fibres saw that the co-doped fibre has a stronger red intensity. The green emission was shown to be more appropriate for temperature sensing due to the consistency in the respond to temperature. Lifetime decay showed that with Yb^{3+} co-doping the difference between low and

higher temperature was ~1.2ms. Y_2O_3 SCF sensors demonstrated that transition lines at 1530.5nm and 1550nm were the most ideal to be used for methods such as FIR and FD. In the visible region, the red emission was only effective up to ~673K whereas the green emission was able to measure temperature up to ~1473K. The fluorescence decay of $Y_2O_3:Er^{3+}$ at room temperature was ~9.5ms where its lifetime differences between 293K and 1273K was ~2.3ms which was the widest for all the materials studied.

Acknowledgements

I am grateful to these people for their invaluable contribution to my research and thesis.

Firstly, I would like to thank God for the blessings which He has so generously bestowed in the course of my studies. His faithfulness was ever evident through His provisions and in His Word, I found encouragement and strength which helped me overcome the impossible. My prayer is that this work would bring glory to His name.

I want to thank my principal supervisor, Dr. J. H. Sharp, for the immeasurable help which he has rendered: fighting for my scholarship; the inspiration which he has breathed into my research topic; the countless hours in enlightening and guiding me through the course of my studies; his readiness and openness to ideas which encouraged innovation; and last but not least, his commitment to seeing me through to the completion of my work.

My great appreciation to Ian Peden for providing me with technical support and advice: the many hours he spent with me in the laboratory engaging in problem-solving demonstrated his dedication to his work and the students assigned to his charge. Next on the list is Dr. Ian Watson who supported me by allowing me to use his equipment. Many thanks to the students placed under my care: Wei Chuan Lim, Chee Wai Ho, Melvin Tan and Leo Valentine. Without the help of whom, this work would not have come to past. Also remembered are all the technicians in the department of Mechanical Engineering for their help, favours and technical advice; and my colleague, Norizah, for the kindness she has shown through the sumptuous meals which she had kindly blessed.

I wish to acknowledge my friends at Calvary Charismatic Church. Their support and care have abundantly blessed me and the learning experience is incredible, unfathomable and beyond imagination. I pray that God will bless you in the same fashion.

To my lovely wife, Lynette, for her love, care and belief in me and my work, and whose influence on my writing and learning has been considerable—giving me the courage and confidence that I needed.

CONTENTS

Chapter 4 – Single Crystal Fibre Growth

Chapter 5 – Characterisation of SCF Experimental Methodologies

Section II – Characterisation of SCFs

Chapter 6 – $Y_3Al_5O_{12}$ – Single Crystal Fibre

Chapter 7 – Y_2O_3 – Single Crystal Fibre

Chapter 8 – Al_2O_3 – Single Crystal Fibre

Section III – SCFs Applications

Chapter 9 – Applications of SCF – Temperature Sensors

Chapter 10 – Conclusion and Future Works

Appendix

LIST OF FIGURES

Figures

Chapter 2

Chapter 3

Chapter 4

Chapter 5

Chapter 6

at 1528.5nm

[6.51] Spec YAl 20 – $Y_3Al_5O_{12}:Er^{3+}+Yb^{3+}$ (1+2mol%) Fluorescence lifetime (τ) at 1612nm

[6.52] $Y_3Al_5O_{12}:Er^{3+}+Yb^{3+}$ (1+2mol%) Fluorescence lifetime (τ) at 1027nm for different concentrations

[6.53] $Y_3Al_5O_{12}:Er^{3+}+Yb^{3+}$ Fluorescence lifetime (τ) at $^4I_{13/2}$ for different concentrations

[6.54] Spec YAl 08 – $Y_3Al_5O_{12}:Er^{3+}$ (0.5mol%) Fluorescence lifetime (τ) at 180mA

[6.55] Spec YAl 09 – $Y_3Al_5O_{12}:Er^{3+}$ (1mol%) Fluorescence lifetime (τ) at 180mA

[6.56] Spec YAl 10 – $Y_3Al_5O_{12}:Er^{3+}$ (5mol%) Fluorescence lifetime (τ) at 180mA

[6.57] Spec YAl 57 – $Y_3Al_5O_{12}:Er^{3+}$ (10mol%) Fluorescence lifetime (τ) at 180mA

[6.58] $Y_3Al_5O_{12}:Er^{3+}$ Fluorescence lifetime (τ) at 180mA at different concentrations

[6.59] $Y_3Al_5O_{12}:Er^{3+}$ Fluorescence lifetime (τ) at 180mA at different laser power settings

[6.60] Spec YAl 16 – $Y_3Al_5O_{12}:Er^{3+}+Yb^{3+}$ (1mol% each) Fluorescence lifetime (τ) at 180mA

[6.61] Spec YAl 20 – $Y_3Al_5O_{12}:Er^{3+}+Yb^{3+}$ (1+2mol%) Fluorescence lifetime (τ) at 180mA

[6.62] Spec YAl 19 – $Y_3Al_5O_{12}:Er^{3+}+Yb^{3+}$ (1+3mol%) Fluorescence lifetime (τ) at 180mA

[6.63] $Y_3Al_5O_{12}:Er^{3+}+Yb^{3+}$ Fluorescence lifetime (τ) at 180mA at different concentrations

[6.64] $Y_3Al_5O_{12}:Er^{3+}+Yb^{3+}$ Fluorescence lifetime (τ) at 180mA at different laser power settings

Chapter 7

[7.1] Spec 47 – Y_2O_3 fibre diameter measurement

[7.2] Spec 48 – Y_2O_3 fibre diameter measurement

[7.3] Spec 49 – Y_2O_3 fibre diameter measurement

[7.4] Three-point bending test on *Spec 47*

[7.5] Spec 42 – $Y_2O_3:Er^{3+}$ (0.03mol%) Absorption spectrum

[7.6] Spec 42 – $Y_2O_3:Er^{3+}$ (0.03mol%) Absorption spectrum ($^4I_{13/2}$)

[7.7] Spec 43 – $Y_2O_3:Er^{3+}$ (0.06mol%) Absorption spectrum

[7.8] Spec 43 – $Y_2O_3:Er^{3+}$ (0.06mol%) Absorption spectrum ($^4I_{13/2}$)

[7.9] Spec 44 – $Y_2O_3:Er^{3+}$ (0.3mol%) Absorption spectrum

[7.10] Spec 44 – $Y_2O_3:Er^{3+}$ (0.3mol%) Absorption spectrum ($^4I_{13/2}$)

[7.11] Spec 18 – $Y_2O_3:Er^{3+}$ (3.1mol%) Absorption spectrum

[7.12] Spec 18 – $Y_2O_3:Er^{3+}$ (3.1mol%) Absorption spectrum ($^4I_{13/2}$)

[7.13] Spec 20 – $Y_2O_3:Er^{3+}$ (6mol%) Absorption spectrum

[7.14] Spec 20 – $Y_2O_3:Er^{3+}$ (6mol%) Absorption spectrum ($^4I_{13/2}$)

[7.15] Spec 19 – $Y_2O_3:Er^{3+}$ (59mol%) Absorption spectrum

[7.16] Spec 19 – $Y_2O_3:Er^{3+}$ (59mol%) Absorption spectrum ($^4I_{13/2}$)

[7.17] Spec 42 – $Y_2O_3:Er^{3+}$ (0.03mol%) Fluorescence spectrum with excitation source at 965nm

[7.18] Spec 42 – $Y_2O_3:Er^{3+}$ (0.03mol%) Fluorescence spectrum with excitation

source at 965nm ($^4I_{13/2}$)

[7.19] Spec 42 – $Y_2O_3:Er^{3+}$ (0.03mol%) Fluorescence spectrum with excitation source at 975nm

[7.20] Spec 42 – $Y_2O_3:Er^{3+}$ (0.03mol%) Fluorescence spectrum with excitation source at 975nm ($^4I_{13/2}$)

[7.21] Spec 43 – $Y_2O_3:Er^{3+}$ (0.06mol%) Fluorescence spectrum with excitation source at 965nm

[7.22] Spec 43 – $Y_2O_3:Er^{3+}$ (0.06mol%) Fluorescence spectrum with excitation source at 965nm ($^4I_{13/2}$)

[7.23] Spec 43 – $Y_2O_3:Er^{3+}$ (0.06mol%) Fluorescence spectrum with excitation source at 975nm

[7.24] Spec 43 – $Y_2O_3:Er^{3+}$ (0.06mol%) Fluorescence spectrum with excitation source at 975nm ($^4I_{13/2}$)

[7.25] Spec 44 – $Y_2O_3:Er^{3+}$ (0.3mol%) Fluorescence spectrum with excitation source at 965nm

[7.26] Spec 44 – $Y_2O_3:Er^{3+}$ (0.3mol%) Fluorescence spectrum with excitation source at 965nm ($^4I_{13/2}$)

[7.27] Spec 44 – $Y_2O_3:Er^{3+}$ (0.3mol%) Fluorescence spectrum with excitation source at 975nm

[7.28] Spec 44 – $Y_2O_3:Er^{3+}$ (0.3mol%) Fluorescence spectrum with excitation source at 975nm ($^4I_{13/2}$)

[7.29] Spec 18 – $Y_2O_3:Er^{3+}$ (3.1mol%) Fluorescence spectrum with excitation source at 965nm

[7.30] Spec 18 – $Y_2O_3:Er^{3+}$ (3.1mol%) Fluorescence spectrum with excitation source at 965nm ($^4I_{13/2}$)

[7.31] Spec 20 – $Y_2O_3:Er^{3+}$ (6mol%) Fluorescence spectrum with excitation source at 965nm

[7.32] Spec 20 – $Y_2O_3:Er^{3+}$ (6mol%) Fluorescence spectrum with excitation source at 965nm ($^4I_{13/2}$)

[7.33] Spec 19 – $Y_2O_3:Er^{3+}$ (59mol%) Fluorescence spectrum with excitation source at 965nm

[7.34] Spec 19 – $Y_2O_3:Er^{3+}$ (59mol%) Fluorescence spectrum with excitation source at 965nm ($^4I_{13/2}$)

[7.35] Fluorescence intensity ratio (FIR) $I_{1530.5}/I_{1636.5}$

[7.36] Fluorescence intensity ratio (FIR) $I_{1010}/I_{1530.5}$

[7.37] Fluorescence intensity ratio (FIR) I_{1010}/I_{1650}

[7.38] Spec 42 – $Y_2O_3:Er^{3+}$ (0.03mol%) Upconversion spectrum

[7.39] Spec 43 – $Y_2O_3:Er^{3+}$ (0.06mol%) Upconversion spectrum

[7.40] Spec 44 – $Y_2O_3:Er^{3+}$ (0.3mol%) Upconversion spectrum

[7.41] Spec 18 – $Y_2O_3:Er^{3+}$ (3.1mol%) Upconversion spectrum

[7.42] Spec 20 – $Y_2O_3:Er^{3+}$ (6mol%) Upconversion spectrum

[7.43] Spec 19 – $Y_2O_3:Er^{3+}$ (59mol%) Upconversion spectrum

[7.44] Upconversion intensity ratio (UIR) R_{681}/G_{563}

[7.45] Spec 42 – $Y_2O_3:Er^{3+}$ (0.03mol%) SCF green emission

[7.46] Spec 19 – $Y_2O_3:Er^{3+}$ (0.03mol%) SCF green and red emission

[7.47] Spec 42 – $Y_2O_3:Er^{3+}$ (0.03mol%) Fluorescence lifetime (τ) at 1010nm

[7.48] Spec 43 – $Y_2O_3:Er^{3+}$ (0.06mol%) Fluorescence lifetime (τ) at 1010nm

[7.49] Spec 44 – $Y_2O_3:Er^{3+}$ (0.3mol%) Fluorescence lifetime (τ) at 1010nm

[7.50] Spec 18 – $Y_2O_3:Er^{3+}$ (3.1mol%) Fluorescence lifetime (τ) at 1010nm

[7.51] Spec 20 – $Y_2O_3:Er^{3+}$ (6mol%) Fluorescence lifetime (τ) at 1010nm

Chapter 8

Chapter 9

[9.15b] Spec YAl 26 $Y_3Al_5O_{12}:Er^{3+}$ FIR_{13}^{26} & FIR_{14}^{26} vs temperature

[9.15c] Spec YAl 26 $Y_3Al_5O_{12}:Er^{3+}$ FIR_{15}^{26} to FIR_{18}^{26} vs temperature

[9.15d] Spec YAl 26 $Y_3Al_5O_{12}:Er^{3+}$ FIR_{12}^{26} (fitted with Eq. 9.7) vs temperature

[9.15e] Spec YAl 26 $Y_3Al_5O_{12}:Er^{3+}$ FIR_{13}^{26} & FIR_{14}^{26} (fitted with Eq. 9.7)vs temperature

[9.15f] Spec YAl 26 $Y_3Al_5O_{12}:Er^{3+}$ FIR_{15}^{26} & FIR_{18}^{26} (fitted with Eq. 9.7) vs temperature

[9.15g] Spec YAl 26 $Y_3Al_5O_{12}:Er^{3+}$ FIR_{16}^{26} & FIR_{17}^{26} (fitted with Eq. 9.7) vs temperature

[9.16a] Spec YAl 26 $Y_3Al_5O_{12}:Er^{3+}$ FIR_{23}^{26} & FIR_{24}^{26} vs temperature

[9.16b] Spec YAl 26 $Y_3Al_5O_{12}:Er^{3+}$ FIR_{25}^{26} to FIR_{28}^{26} vs temperature

[9.16c] Spec YAl 26 $Y_3Al_5O_{12}:Er^{3+}$ FIR_{25}^{26} & FIR_{28}^{26} (fitted with Eq. 9.7) vs temperature

[9.16d] Spec YAl 26 $Y_3Al_5O_{12}:Er^{3+}$ FIR_{26}^{26} & FIR_{27}^{26} (fitted with Eq. 9.7) vs temperature

[9.17a] Spec YAl 26 $Y_3Al_5O_{12}:Er^{3+}$ FIR_{34}^{26} vs temperature

[9.17b] Spec YAl 26 $Y_3Al_5O_{12}:Er^{3+}$ FIR_{35}^{26} to FIR_{38}^{26} vs temperature

[9.17c] Spec YAl 26 $Y_3Al_5O_{12}:Er^{3+}$ FIR_{35}^{26} & FIR_{37}^{26} (fitted with Eq. 9.7) vs temperature

[9.17d] Spec YAl 26 $Y_3Al_5O_{12}:Er^{3+}$ FIR_{36}^{26} & FIR_{38}^{26} (fitted with Eq. 9.7) vs temperature

[9.18a] Spec YAl 26 $Y_3Al_5O_{12}:Er^{3+}$ FIR_{45}^{26} to FIR_{48}^{26} vs temperature

[9.18b] Spec YAl 26 $Y_3Al_5O_{12}:Er^{3+}$ FIR_{45}^{26} & FIR_{47}^{26} (fitted with Eq. 9.7) vs temperature

[9.18c] Spec YAl 26 $Y_3Al_5O_{12}:Er^{3+}$ FIR_{46}^{26} & FIR_{48}^{26} (fitted with Eq. 9.7) vs temperature

[9.19] Spec YAl 26 $Y_3Al_5O_{12}:Er^{3+}$ FIR_{56}^{26} to FIR_{58}^{26} vs temperature

[9.20a] Spec YAl 26 $Y_3Al_5O_{12}:Er^{3+}$ FIR_{67}^{26} & FIR_{68}^{26} vs temperature

[9.20b] Spec YAl 26 $Y_3Al_5O_{12}:Er^{3+}$ FIR_{68}^{26} (fitted with Eq. 9.7) vs temperature

[9.21] Spec YAl 26 $Y_3Al_5O_{12}:Er^{3+}$ FIR_{78}^{26} (actual and fitted with Eq. 9.7) vs temperature

[9.22a] Spec YAl 26 $Y_3Al_5O_{12}:Er^{3+}$ FIR_{AB}^{26}, FIR_{AC}^{26} & FIR_{BC}^{26} - integrated areas vs temperature

[9.22b] Spec YAl 26 $Y_3Al_5O_{12}:Er^{3+}$ FIR_{AC}^{26},& FIR_{BC}^{26} - integrated areas (fitted with Eq. 9.7) vs temperature

[9.23] Spec YAl 26 $Y_3Al_5O_{12}:Er^{3+}$ upconversion in room temperature, 293K

[9.24] Spec YAl 26 $Y_3Al_5O_{12}:Er^{3+}$ upconversion spectra from room temperature to 1473K

[9.25] Spec YAl 26 $Y_3Al_5O_{12}:Er^{3+}$ upconversion spectra from room temperature to 873K, $^2H_{11/2} + {}^4S_{3/2}$

[9.26] Spec YAl 26 $Y_3Al_5O_{12}:Er^{3+}$ upconversion spectra from 1173K to 873K, $^2H_{11/2} + {}^4S_{3/2}$

[9.27] Spec YAl 26 $Y_3Al_5O_{12}:Er^{3+}$ upconversion spectra from room temperature to 873K, $^2F_{9/2}$

[9.28] Spec YAl 26 $Y_3Al_5O_{12}:Er^{3+}$ upconversion spectra from 973 to 1473K & 273K, $^2F_{9/2}$

[9.29] Spec YAl 26 $Y_3Al_5O_{12}:Er^{3+}$ - Integrated intensity at $^2H_{11/2}$, $^4S_{3/2}$ and $^2F_{9/2}$

[9.30a] Spec YAl 26 $Y_3Al_5O_{12}:Er^{3+}$ intensity based sensing at 541nm (I_{541})

[9.30b] Spec YAl 26 $Y_3Al_5O_{12}:Er^{3+}$ integrated based sensing at 553.5nm & 560nm (I_{541} & I_{560})

[9.31] Spec YAl 26 $Y_3Al_5O_{12}:Er^{3+}$ integrated based sensing at 676nm (I_{676})

[9.32] Spec YAl 26 $Y_3Al_5O_{12}:Er^{3+}$ UIR_{12}^{26} & UIR_{13}^{26} (fitted with Eq. 9.7) vs temperature

[9.33] Spec YAl 26 $Y_3Al_5O_{12}:Er^{3+}$ UIR_{23}^{26} (actual and fitted with Eq. 9.7) vs temperature

[9.34] Spec YAl 26 $Y_3Al_5O_{12}:Er^{3+}$ UIR_{AB}^{26} (actual and fitted with Eq. 9.7) vs temperature

[9.35] Spec YAl 26 $Y_3Al_5O_{12}:Er^{3+}$ UIR_{ABC}^{26} (actual and fitted with Eq. 9.7) vs temperature

[9.36] Spec YAl 26 $Y_3Al_5O_{12}:Er^{3+}$ fluorescence decay at 1453nm

[9.37] Spec YAl 26 $Y_3Al_5O_{12}:Er^{3+}$ fluorescence decay at 1470nm

[9.38] Spec YAl 26 $Y_3Al_5O_{12}:Er^{3+}$ fluorescence decay at 1528.5nm

[9.39] Spec YAl 26 $Y_3Al_5O_{12}:Er^{3+}$ fluorescence decay at 1568nm

[9.40] Spec YAl 26 $Y_3Al_5O_{12}:Er^{3+}$ fluorescence decay at 1612nm

[9.41] Spec YAl 26 $Y_3Al_5O_{12}:Er^{3+}$ fluorescence decay at 1628.5nm

[9.42] Spec YAl 26 $Y_3Al_5O_{12}:Er^{3+}$ fluorescence decay at 1640.5nm

[9.43] Spec YAl 26 $Y_3Al_5O_{12}:Er^{3+}$ fluorescence decay at 1652.5nm

[9.44] Spec YAl 26 $Y_3Al_5O_{12}:Er^{3+}$ fluorescence decay at of different temperatures at varies wavelengths

[9.45] Spec YAl 32 $Y_3Al_5O_{12}:Er^{3+}$ + Yb^{3+} fluorescence in room temperature, 293K

[9.46] Spec YAl 32 $Y_3Al_5O_{12}:Er^{3+}$ + Yb^{3+} fluorescence spectra from room temperature to 1473K

[9.47] Spec YAl 32 $Y_3Al_5O_{12}:Er^{3+}$ + Yb^{3+} fluorescence spectra ($^4I_{11/2}$) – room temperature to 873K

[9.48] Spec YAl 32 $Y_3Al_5O_{12}:Er^{3+}$ + Yb^{3+} fluorescence spectra ($^4I_{11/2}$) – room temperature to 1473K

[9.49] Spec YAl 32 $Y_3Al_5O_{12}:Er^{3+}$ + Yb^{3+} fluorescence spectra ($^4I_{13/2}$) – room temperature to 873K

[9.50] Spec YAl 32 $Y_3Al_5O_{12}:Er^{3+}$ + Yb^{3+} fluorescence spectra ($^4I_{13/2}$) – room temperature to 1473K

[9.51] Spec YAl 32 $Y_3Al_5O_{12}:Er^{3+}$ + Yb^{3+} fluorescence spectra ($^4I_{13/2}$) – Integrated Intensity

[9.52a] Spec YAl 32 $Y_3Al_5O_{12}:Er^{3+}$ + Yb^{3+} FIR_{Y1}^{32} to FIR_{Y4}^{32} vs temperature

[9.52b] Spec YAl 32 $Y_3Al_5O_{12}:Er^{3+}$ + Yb^{3+} FIR_{Y5}^{32} to FIR_{Y8}^{32} vs temperature

[9.52c] Spec YAl 32 $Y_3Al_5O_{12}:Er^{3+}$ + Yb^{3+} FIR_{Y1}^{32} & FIR_{Y2}^{32} (fitted with Eq. 9.7) vs temperature

[9.52d] Spec YAl 32 $Y_3Al_5O_{12}:Er^{3+}$ + Yb^{3+} FIR_{Y3}^{32} to FIR_{Y4}^{32} (fitted with Eq. 9.7) vs temperature

[9.53a] Spec YAl 32 $Y_3Al_5O_{12}:Er^{3+} + Yb^{3+}$ FIR_{12}^{32} to FIR_{14}^{32} vs temperature

[9.53b] Spec YAl 32 $Y_3Al_5O_{12}:Er^{3+} + Yb^{3+}$ FIR_{15}^{32} to FIR_{18}^{32} vs temperature

[9.53c] Spec YAl 32 $Y_3Al_5O_{12}:Er^{3+} + Yb^{3+}$ FIR_{15}^{32} & FIR_{17}^{32} (fitted with Eq. 9.7) vs temperature

[9.53d] Spec YAl 32 $Y_3Al_5O_{12}:Er^{3+} + Yb^{3+}$ FIR_{18}^{32} (fitted with Eq. 9.7) vs temperature

[9.54a] Spec YAl 32 $Y_3Al_5O_{12}:Er^{3+} + Yb^{3+}$ FIR_{23}^{32} & FIR_{24}^{32} vs temperature

[9.54b] Spec YAl 32 $Y_3Al_5O_{12}:Er^{3+} + Yb^{3+}$ FIR_{25}^{32} to FIR_{28}^{32} vs temperature

[9.54c] Spec YAl 32 $Y_3Al_5O_{12}:Er^{3+} + Yb^{3+}$ FIR_{25}^{32} & FIR_{26}^{32} (fitted with Eq. 9.7) vs temperature

[9.54d] Spec YAl 32 $Y_3Al_5O_{12}:Er^{3+} + Yb^{3+}$ FIR_{28}^{32} (fitted with Eq. 9.7) vs temperature

[9.55a] Spec YAl 32 $Y_3Al_5O_{12}:Er^{3+} + Yb^{3+}$ FIR_{34}^{32} vs temperature

[9.55b] Spec YAl 32 $Y_3Al_5O_{12}:Er^{3+} + Yb^{3+}$ FIR_{35}^{32} to FIR_{38}^{32} vs temperature

[9.55c] Spec YAl 32 $Y_3Al_5O_{12}:Er^{3+} + Yb^{3+}$ FIR_{34}^{32} (fitted with Eq. 9.7) vs temperature

[9.55d] Spec YAl 32 $Y_3Al_5O_{12}:Er^{3+} + Yb^{3+}$ FIR_{35}^{32} & FIR_{37}^{32} (fitted with Eq. 9.7) vs temperature

[9.55e] Spec YAl 32 $Y_3Al_5O_{12}:Er^{3+} + Yb^{3+}$ FIR_{38}^{32} (fitted with Eq. 9.7) vs temperature

[9.56a] Spec YAl 32 $Y_3Al_5O_{12}:Er^{3+} + Yb^{3+}$ FIR_{45}^{32} to FIR_{48}^{32} vs temperature

[9.56b] Spec YAl 32 $Y_3Al_5O_{12}:Er^{3+} + Yb^{3+}$ FIR_{45}^{32} & FIR_{47}^{32} (fitted with Eq. 9.7) vs temperature

[9.56c] Spec YAl 32 $Y_3Al_5O_{12}:Er^{3+} + Yb^{3+}$ FIR_{48}^{32} (fitted with Eq. 9.7) vs temperature

[9.57] Spec YAl 32 $Y_3Al_5O_{12}:Er^{3+} + Yb^{3+}$ FIR_{56}^{32} to FIR_{58}^{32} vs temperature

[9.58a] Spec YAl 32 $Y_3Al_5O_{12}:Er^{3+} + Yb^{3+}$ FIR_{67}^{32} & FIR_{68}^{32} vs temperature

[9.58b] Spec YAl 32 $Y_3Al_5O_{12}:Er^{3+} + Yb^{3+}$ FIR_{67}^{32} & FIR_{68}^{32} (fitted with Eq. 9.7) vs temperature

[9.59] Spec YAl 32 $Y_3Al_5O_{12}:Er^{3+} + Yb^{3+}$ FIR_{78}^{32} (actual and fitted with Eq. 9.7) vs temperature

[9.60a] Spec YAl 32 $Y_3Al_5O_{12}:Er^{3+} + Yb^{3+}$ FIR_{YA}^{32} to FIR_{YC}^{32} - integrated intensity vs temperature

[9.60b] Spec YAl 32 $Y_3Al_5O_{12}:Er^{3+} + Yb^{3+}$ FIR_{AB}^{32}, FIR_{AC}^{32} & FIR_{BC}^{32} - integrated intensity vs temperature

[9.60c] Spec YAl 32 $Y_3Al_5O_{12}:Er^{3+} + Yb^{3+}$ FIR_{YA}^{32} - integrated intensity (fitted with Eq. 9.7) vs temperature

[9.60d] Spec YAl 32 $Y_3Al_5O_{12}:Er^{3+} + Yb^{3+}$ FIR_{AC}^{32} & FIR_{BC}^{32} - integrated intensity (fitted with Eq. 9.7) vs temperature

[9.61] Spec YAl 32 $Y_3Al_5O_{12}:Er^{3+} + Yb^{3+}$ upconversion in room temperature, 293K

[9.62] Spec YAl 32 $Y_3Al_5O_{12}:Er^{3+}$ + Yb^{3+} upconversion spectra from room temperature to 1473K

[9.63] Spec YAl 32 $Y_3Al_5O_{12}:Er^{3+}$ + Yb^{3+} upconversion spectra from room temperature to 873K, $^2H_{11/2}$ + $^4S_{3/2}$

[9.64] Spec YAl 32 $Y_3Al_5O_{12}:Er^{3+}$ + Yb^{3+} upconversion spectra from room 873K to 1473, $^2H_{11/2}$ + $^4S_{3/2}$

[9.65] Spec YAl 32 $Y_3Al_5O_{12}:Er^{3+}$ + Yb^{3+} upconversion spectra from room temperature to 873K, $^4F_{9/2}$

[9.66] Spec YAl 32 $Y_3Al_5O_{12}:Er^{3+}$ + Yb^{3+} upconversion spectra 873K to 1473K, $^4F_{9/2}$

[9.67] Spec YAl 32 $Y_3Al_5O_{12}:Er^{3+}$ + Yb^{3+}- Integrated intensity at $^2H_{11/2}$, $^4S_{3/2}$ and $^2F_{9/2}$

[9.68a] Spec YAl 32 $Y_3Al_5O_{12}:Er^{3+}$ + Yb^{3+} intensity based sensing at 541nm (I_{541})

[9.68b] Spec YAl 32 $Y_3Al_5O_{12}:Er^{3+}$ + Yb^{3+} intensity based sensing at 553.5nm & 560nm (I_{541} & I_{560})

[9.69] Spec YAl 32 $Y_3Al_5O_{12}:Er^{3+}$ + Yb^{3+} intensity based sensing at 676nm (I_{676})

[9.70] Spec YAl 32 $Y_3Al_5O_{12}:Er^{3+}$ + Yb^{3+} UIR_{12}^{32} & UIR_{13}^{32} (actual and polynomial fit) vs temperature

[9.71] Spec YAl 32 $Y_3Al_5O_{12}:Er^{3+}$ + Yb^{3+} UIR_{23}^{32} (actual and fitted with Eq. 9.7) vs temperature

[9.72] Spec YAl 32 $Y_3Al_5O_{12}:Er^{3+}$ + Yb^{3+} UIR_{AB}^{32} (actual and fitted with Eq. 9.7) vs temperature

[9.73] Spec YAl 32 $Y_3Al_5O_{12}:Er^{3+}$ + Yb^{3+} UIR_{ABC}^{32} (actual and fitted with Eq. 9.7) vs temperature

[9.74] Spec YAl 32 $Y_3Al_5O_{12}:Er^{3+}$ + Yb^{3+} fluorescence decay at 1027nm

[9.75] Spec YAl 32 $Y_3Al_5O_{12}:Er^{3+}$ + Yb^{3+} fluorescence decay at 1453nm

[9.76] Spec YAl 32 $Y_3Al_5O_{12}:Er^{3+}$ + Yb^{3+} fluorescence decay at 1470nm

[9.77] Spec YAl 32 $Y_3Al_5O_{12}:Er^{3+}$ + Yb^{3+} fluorescence decay at 1528.5nm

[9.78] Spec YAl 32 $Y_3Al_5O_{12}:Er^{3+}$ + Yb^{3+} fluorescence decay at 1568nm

[9.79] Spec YAl 32 $Y_3Al_5O_{12}:Er^{3+}$ + Yb^{3+} fluorescence decay at 1612nm

[9.80] Spec YAl 32 $Y_3Al_5O_{12}:Er^{3+}$ + Yb^{3+} fluorescence decay at 1628.5nm

[9.81] Spec YAl 32 $Y_3Al_5O_{12}:Er^{3+}$ + Yb^{3+} fluorescence decay at 1640.5nm

[9.82] Spec YAl 32 $Y_3Al_5O_{12}:Er^{3+}$ + Yb^{3+} fluorescence decay at 1652.5nm

[9.83] Spec YAl 32 $Y_3Al_5O_{12}:Er^{3+}$ + Yb^{3+} fluorescence decay at of different temperatures at varies wavelengths

[9.84] Spec 64 $Y_2O_3:Er^{3+}$ fluorescence in room temperature, 293K, $^4I_{11/2}$

[9.85] Spec 64 $Y_2O_3:Er^{3+}$ fluorescence in room temperature, 293K, $^4I_{13/2}$

[9.86] Spec 64 $Y_2O_3:Er^{3+}$ fluorescence spectra from room temperature to 1473K

[9.87] Spec 64 $Y_2O_3:Er^{3+}$ fluorescence spectra ($^4I_{11/2}$) – room temperature to 873K

[9.88] Spec 64 $Y_2O_3:Er^{3+}$ fluorescence spectra ($^4I_{11/2}$) – 873K to 1473K

[9.89] Spec 64 $Y_2O_3:Er^{3+}$ fluorescence spectra ($^4I_{13/2}$) – room temperature to 873K

[9.90] Spec 64 $Y_2O_3:Er^{3+}$ fluorescence spectra ($^4I_{13/2}$) – 873K to 1473K

[9.91] Spec 64 $Y_2O_3:Er^{3+}$ fluorescence spectra – Integrated intensity

[9.92a] Spec 64 $Y_2O_3:Er^{3+}$ FIR_{12}^{64} vs temperature

[9.92b] Spec 64 Y_2O_3:Er^{3+} FIR_{14}^{64} to FIR_{16}^{64} vs temperature

[9.92c] Spec 64 Y_2O_3:Er^{3+} FIR_{13}^{64}, FIR_{17}^{64} to FIR_{19}^{64} vs temperature

[9.92d] Spec 64 Y_2O_3:Er^{3+} FIR_{12}^{64} (fitted with Eq. 9.7) vs temperature

[9.92e] Spec 64 Y_2O_3:Er^{3+} FIR_{13}^{64} (fitted with Eq. 9.7) vs temperature

[9.92f] Spec 64 Y_2O_3:Er^{3+} FIR_{14}^{64} & FIR_{15}^{64} (fitted with Eq. 9.7) vs temperature

[9.93a] Spec 64 Y_2O_3:Er^{3+} FIR_{24}^{64} to FIR_{26}^{64} vs temperature

[9.93b] Spec 64 Y_2O_3:Er^{3+} FIR_{23}^{64}, FIR_{27}^{64} to FIR_{29}^{64} vs temperature

[9.93c] Spec 64 Y_2O_3:Er^{3+} FIR_{23}^{64} (fitted with Eq. 9.7) vs temperature

[9.93d] Spec 64 Y_2O_3:Er^{3+} FIR_{24}^{64} (fitted with Eq. 9.7) vs temperature

[9.94a] Spec 64 Y_2O_3:Er^{3+} FIR_{34}^{64} to FIR_{36}^{64} vs temperature

[9.94b] Spec 64 Y_2O_3:Er^{3+} FIR_{37}^{64} to FIR_{39}^{64} vs temperature

[9.94c] Spec 64 Y_2O_3:Er^{3+} FIR_{36}^{64} (fitted with Eq. 9.7) vs temperature

[9.94d] Spec 64 Y_2O_3:Er^{3+} FIR_{37}^{64} & FIR_{38}^{64} (fitted with Eq. 9.7) vs temperature

[9.95a] Spec 64 Y_2O_3:Er^{3+} FIR_{45}^{64} & FIR_{46}^{64} vs temperature

[9.95b] Spec 64 Y_2O_3:Er^{3+} FIR_{47}^{64} to FIR_{49}^{64} vs temperature

[9.95c] Spec 64 Y_2O_3:Er^{3+} FIR_{47}^{64} & FIR_{48}^{64} (fitted with Eq. 9.7) vs temperature

[9.95d] Spec 64 Y_2O_3:Er^{3+} FIR_{49}^{64} (fitted with Eq. 9.7) vs temperature

[9.96a] Spec 64 Y_2O_3:Er^{3+} FIR_{56}^{64} vs temperature

[9.96b] Spec 64 Y_2O_3:Er^{3+} FIR_{57}^{64} to FIR_{59}^{64} vs temperature

[9.96c] Spec 64 Y_2O_3:Er^{3+} FIR_{57}^{64} & FIR_{58}^{64} (fitted with Eq. 9.7) vs temperature

[9.96d] Spec 64 Y_2O_3:Er^{3+} FIR_{59}^{64} (fitted with Eq. 9.7) vs temperature

[9.97a] Spec 64 Y_2O_3:Er^{3+} FIR_{67}^{64} to FIR_{69}^{64} vs temperature

[9.97b] Spec 64 Y_2O_3:Er^{3+} FIR_{67}^{64} & FIR_{68}^{64} (fitted with Eq. 9.7) vs temperature

[9.97c] Spec 64 Y_2O_3:Er^{3+} FIR_{69}^{64} (fitted with Eq. 9.7) vs temperature

[9.98] Spec 64 Y_2O_3:Er^{3+} FIR_{78}^{64} & FIR_{79}^{64} vs temperature

[9.99] Spec 64 Y_2O_3:Er^{3+} FIR_{89}^{64} vs temperature

[9.100a] Spec 64 Y_2O_3:Er^{3+} FIR_{AB}^{64}, FIR_{AC}^{64} & FIR_{AD}^{64} vs temperature

[9.100b] Spec 64 Y_2O_3:Er^{3+} FIR_{BC}^{64}, FIR_{BD}^{64} & FIR_{CD}^{64} vs temperature

[9.100c] Spec 64 Y_2O_3:Er^{3+} FIR_{AC}^{64} (fitted with Eq. 9.7) vs temperature

[9.100d] Spec 64 Y_2O_3:Er^{3+} FIR_{CD}^{64} (fitted with Eq. 9.7) vs temperature

[9.101] Spec 64 Y_2O_3:Er^{3+} upconversion in room temperature, 293K

[9.102] Spec 64 Y_2O_3:Er^{3+} upconversion spectra from room temperature to 1473K

[9.103] Spec 64 Y_2O_3:Er^{3+} upconversion spectra from room temperature to 873K, $^2H_{11/2}$ + $^4S_{3/2}$

[9.104] Spec 64 Y_2O_3:Er^{3+} upconversion spectra from room temperature to 1473K, $^2H_{11/2}$ + $^4S_{3/2}$

[9.105] Spec 64 Y_2O_3:Er^{3+} upconversion spectra from room temperature to 773K, $^4H_{9/2}$

[9.106] Spec 64 $Y_2O_3:Er^{3+}$ - Integrated intensity at $^2H_{11/2}$, $^4S_{3/2}$ and $^2F_{9/2}$

[9.107] Spec 64 $Y_2O_3:Er^{3+}$ intensity based sensing at 538.5nm ($I_{538.5}$)

[9.108] Spec 64 $Y_2O_3:Er^{3+}$ intensity based sensing at 553nm and 563nm (I_{553} & I_{563})

[9.109] Spec 64 $Y_2O_3:Er^{3+}$ intensity based sensing at 681nm (I_{681})

[9.110] Spec 64 $Y_2O_3:Er^{3+}$ UIR_{12}^{64} & UIR_{13}^{64} (actual and fitted with Eq. 9.7) vs temperature

[9.111] Spec 64 $Y_2O_3:Er^{3+}$ UIR_{23}^{64} vs temperature

[9.112] Spec 64 $Y_2O_3:Er^{3+}$ UIR_{24}^{64} & UIR_{34}^{64} (actual and fitted with Eq. 9.7) vs temperature

[9.113] Spec 64 $Y_2O_3:Er^{3+}$ UIR_{AB}^{64} (actual and fitted with Eq. 9.7) vs temperature

[9.114] Spec 64 $Y_2O_3:Er^{3+}$ UIR_{ABC}^{64} vs temperature

[9.115] Spec 64 $Y_2O_3:Er^{3+}$ fluorescence decay at 1010nm

[9.116] Spec 64 $Y_2O_3:Er^{3+}$ fluorescence decay at 1028.5nm

[9.117] Spec 64 $Y_2O_3:Er^{3+}$ fluorescence decay at 1530.5nm

[9.118] Spec 64 $Y_2O_3:Er^{3+}$ fluorescence decay at 1550nm

LIST OF TABLES

Tables

1 Introduction

The growth of good quality single crystals for the purpose of material investigation has always been a challenge for many researchers. With the development of the Laser Heated Pedestal Growth (LHPG) technique, high quality single crystal samples could be produced quickly and cost effectively. Extremely versatile, this technique can also grow a wide variety of materials and lends itself well to the field of developing novel crystalline materials, particularly in optical applications.

In the present optical fibre industry, dominating glass-based optical fibres have shown that there are limitations due to their material properties while single crystal fibres have proven to be able to eradicate these limitations. Probably the single most important optical application to emerge in the last 30 years is that of optical fibre communication. In terms of technological and economic impact no other field in optics comes close. As new and more challenging applications are found for this technology there are instances where material limitations begin to restrict and constrain development.

An example of this is in the fibre sensor applications, where glass-based fibres are not suitable for certain hostile environments. Crystalline fibres offer a new range of materials to address these problems. The LHPG technique makes it easy and quick to grow high quality crystalline fibres that are of similar sizes as conventional fibres. This increases the ease of integration with present optical technology. The many advantages that single crystal fibres have will, in the future, open many doors to a broader scope of applications.

The aim of this work is to employ the LHPG technique to grow single crystal fibres of various oxide materials with a range of dopant concentrations and to characterise them. To identify and choose the best concentrations, through the characterisation processes, and exploit them in application in thermometry. This thesis is divided into three sections. Section I – Literature and Theoretical Reviews comprises Chapter 2 to 5. Section II – Characterisation of SCFs comprises Chapter 6 to 8 and Section III – SCFs Applications comprises Chapter 9.

Chapter 2 comprises a brief historical background of Single Crystal Fibres (SCFs). A review is also made on the different techniques used to grow SCFs. The applications of SCFs are discussed.

Chapter 3 is divided into two sections. In the first section, a review is made on the basic knowledge that is required when growing SCFs using the LHPG technique. The fundamentals of achieving steady state growth are discussed and the types of defects that might occur during the growth process are also mentioned. In the second section of this chapter, a theoretical review on the spectroscopic characterisation of the Er^{3+} and Yb^{3+} ions is made. Different energy transfer processes are also examined.

Chapter 4 presents the overview of the LHPG technique. A description of each subsystem within the LHPG system is given in this chapter. The preparation stages before the growth of the SCF are described and discussed. The growth conditions of the three materials ($Y_3Al_5O_{12}$, Y_2O_3 and Al_2O_3) are evaluated and examined.

In Chapter 5, the characterisation experiments are explained. This chapter is divided into two sections. In the first section, the physical characterisation comprising diameter and strength measurements are explained. Layouts and equipment used in these experiments are also discussed. The second section consists of the discussion of the spectroscopic characterisation experiments. Absorption, fluorescence/ upconversion and lifetime decay experimental layouts are presented.

Chapter 6 comprises the characterisation of $Y_3Al_5O_{12}$ SCFs. Physical properties of the SCF fibres were investigated. Spectroscopy characterisation of the Er^{3+} singly and Er^{3+}+Yb^{3+} co-doped YAG SCFs were investigated. The spectroscopy results of absorption, fluorescence, upconversion and lifetime decay are presented and discussions on the findings are made.

Chapter 7 presents the findings of the Y_2O_3 SCFs. Physical and spectroscopic characterisations were carried out on these singly doped Er^{3+} SCFs. Results from the experiments are reported and discussions on the findings are made.

In Chapter 8, transition metal ions doped Al_2O_3 SCFs were investigated. Cr^{3+}:Al_2O_3 fibres were grown and both physical and spectroscopic investigations were carried

out on these fibres. Absorption and fluorescence measurements were conducted on these fibres and results from these experiments are presented.

Chapter 9, the application chapter, investigates $Y_3Al_5O_{12}:Er^{3+}$, $Y_3Al_5O_{12}:Er^{3+}+Yb^{3+}$ and $Y_2O_3:Er^{3+}$ as temperature sensors in extreme conditions. The emission (both visible and infrared spectrums) from the rare earths within these fibres were assessed as a function of temperature. Methods such as fluorescence intensity ratio (FIR), upconversion intensity ratio (UIR) and fluorescence decay lifetime were correlated with temperature.

Chapter 10 conclude the thesis. New approaches in the improvement of the LHPG systems are recommended for the enhancement of fibre quality. Future work that is required in the investigation of SCFs in other areas of application are also discussed.

Section I

Literature and Theoretical Reviews

2 Literature Review

2.1 Introduction

The study of Single Crystal Fibres (SCF) has intensified in the last three decades. In the 1950s, work done on SCFs was motivated by their mechanical properties for structural applications but this gradually subsided. Slow growth rates and difficulties in diameter and length control were some of the limitations for these SCFs. The renewal of interest in this field of study can in some measure be attributed to its main rival, glass or silica fibre. In the 1970s, silica fibres were in great demand because of their flexibility in production and ability to be used in long distance optical transmission. The main area of use was in telecommunications; however, fibres were not able to transmit effectively in mid to high infrared regions. Research was then directed to the SCF's. Many other advantages came with the use of SCF. Fibres were found to have high crystalline perfection, near-theoretical strength, low optical losses, high melting temperatures, and excellent chemical inertness. To date, SCFs have been used for optical amplifiers, modulators, beam delivery, machining and welding, solid state laser devices, linear and non-linear optics and sensors. SCF at present may not be able to replace the silica fibre as a passive device but as an active device, SCF shows much potential. Integrating the two maybe an area also worth investigating, for each has its own unique features.

Another promising application of SCF is in the area of crystal growth research. In solid state laser or amplifier applications, instead of fabricating bulk material, SCFs can be used so that cost and time of development of novel materials is greatly minimised. Due to their small sample diameters, crystalline fibres are quickly and easily prepared and minimal material is required. Small crystal dimensions also reduce the possible defect rate that can occur in bulk crystal. These factors increase efficiency and also accelerate the development of crystals knowledge. The primary impetus of the present work is to grow SCFs by Laser Heated Pedestal Growth method and to characterise them.

2.2 Historical Background of Single Crystal Fibre (SCF)

The first documented case of a fibre being produced in an optical material was in the year 1887 by *Sir Charles Vernon Boys* [2.1, 2]. Fibres were drawn with a crossbow and straw arrow [2.1]. Firstly, the quartz rod was attached to the tail of the straw arrow with sealing-wax and the other end was held by hand. Secondly, the middle of the quartz was heated with an oxyhydrogen flame. Thirdly, the crossbow was fired by a leg pedal, the arrow then shot off creating fibres. With this method, Boys was able to make fibres from quartz as fine as 0.25 μm in diameter. When Boys used these fine fibres as torsion-threads, they were shown to be near prefect in their elasticity and extremely strong [2.1].

In 1967, a group from Massachusetts (Tyco Laboratories, Inc), *LaBelle* and *Mlavsky* [2.3] reported the melt growth of sapphire that had diameters ranging from 0.05 to 0.50mm. These sapphire filaments were pulled at rates as high as 1.5cm/min. The equipment used—a modification from the Czochralski crystal puller—had a RF heating element and molybdenum crucible. Despite the melt looking greyish in the crucible, the grown filament remained transparent. These fibres possessed a high tensile strength of 300000 lb/in^2 (1 lb/in^2 = 6894.757 N/m^2), and the strength increasing when the diameter fell in the range of 0.1 – 0.13 mm to 500000 lb/in^2. Understanding how to control the thermal gradient of the material permitted them to grow continuous c-axis sapphire filaments. In their later work in 1971, *LaBelle* and *Mlavsky* [2.4] were able to develop a technique—the edge-defined film growth (EFG) method [2.5]—to grow continuous sapphire fibres, several hundreds of feet long. In this method, a capillary tube made from molybdenum was affixed to the bottom of a crucible, allowing molten alumina to ascend the capillary. Using a c-axis filament as seed, a continuous fibre was grown by pulling at a growth rate as fast as 20cm/min where it was then taken up by a wheel drum. One key motivation in this work was to use the fibres in structural composites; the idea was to develop a method to grow sapphire crystals in different shapes such as tubes and ribbons.

Using the floating zone method, *D.B. Gasson* and *B. Cockayne* [2.6], in 1970, were the first to use a laser as a heat source to grow large single crystals of high melting materials in the temperature range from 2000°C to 2400°C. Two AC-energised CO_2-N_2-He lasers, with an output power ranging from 50 to 400W, were used as heat sources to grow oxide materials such as Al_2O_3, $CaZrO_3$, $MgAl_2O_3$, NdO_3 and Y_2O_3.

These oxides were initially in powder form, then pressed and sintered into a rod with diameters as small as 0.5 cm to as big as 10 cm. In their experiments, Y_2O_3 and $CaZrO_3$ posed a problem due to the large temperature differences between the surrounding temperature in the furnace and their melting temperatures. The result was the appearance of cracks in the crystal. As for the other materials, growth was crack-free because of their lower melting temperature. The use of lasers as a heat source reduced the thermal gradients in the material which in turn reduced the strain that was evident in growth methods such as Czochralski. *Haggerty et al* [2.7] built a floating zone technique which used four CO_2 lasers instead of two. The primary role of this research was to study the growth procedures of different materials and to test their mechanical properties. With this knowledge, improvement could be made to the growth process and apparatus. It was found that chromium-doped Al_2O_3 exhibited a flexural strength of 9.64×10^9 N/m^2 which was the highest among the materials investigated. Although Y_2O_3 exhibited no surface or internal cracks, this material did not prove to be a good choice to use for fibre reinforcement of metal matrices due to its relatively low elastic modulus (1.03×10^{11} to 1.10×10^{11} N/m^2). Its highly susceptibility to water in the environment was suggested as the reason for its poor strength.

The focus of research into SCF's in the early 1970s was their potential use as structural materials. *Haggerty* and *Levitt* [2.8] reviewed work on material composites of SCFs which were at that time commonly known as 'whiskers'. Different methods were reviewed in the investigation of strength, growth behaviour and crystalline perfection. Interest then was to use these whiskers as reinforcement agents, in particular in fibre matrix composites. This interest gradually subsided as alternative materials with better strength performance were discovered. However, this did not stop others from researching the use of SCFs in other applications. In 1975, *Burrus and Stone* [2.9] were the first to use SCFs as fibre lasers. They grew a Nd: YAG fibre with a diameter of 50μm and a length of 0.5 to 1cm. The method adopted by the group was similar to that of *Poplawsky* [2.10] in 1962 which, instead of using a crucible, an iron pedestal was used where materials like magnetite, manganese ferrite and nickel ferrite boules shaped in a cylindrical form were placed on it. This reduced contamination since the melt would not come into contact with any containment materials. This technique, pedestal growth (modified zone melting), was the

inspiration for the work of *Burrus and Stone*. In their work a square source rod of 2mm, 1% Nd-doped YAG, was cut. Using a beam from a single CO_2 laser to melt the tip of the source rod, a platinum wire (20-25μm) was then used to pull from the melt to form a new crystal fibre. The fibres grown, with a diameter less than 250μm, were free from cracks or inhomogeneities. The absorption and fluorescence spectra of these fibres remained consistent to the original fibre even after a five-time regrowth. In order to improve the growth system, *Stone and Burrus* in their work in 1976 [2.11] used two CO_2 lasers instead of one. This improved the uniformity and straightness of the Nd:YAG fibre. This fibre laser gave an output of 0.8mW, operating about 10% above threshold and had a relaxation period about 50μs. Using a similar method of growth, *Burrus and Coldren* [2.12], demonstrated the growth of sapphire-clad ruby fibres. Firstly, the ruby fibre was grown from a homogenously doped Cr sapphire source rod. Secondly, the surface of the ruby fibre was melted and regrown using the same CO_2 laser. The Cr concentration was reduced by an approximated factor of 100 or more through evaporation. The end result of this additional process created a new fibre of a smaller diameter, with a core and cladding comprising different Cr concentrations. These fibres could then be used as waveguides for optical or acoustical energy.

Y_2O_3 crystals, grown conventionally by flame fusion or Verneuil method, were also investigated and grown by *Stone* and *Burrus* [2.13] using the modified zone melting method mentioned above. Nd:Y_2O_3 fibres were grown to be used as lasers operating in 1.07 and 1.35μm. Highly pure Y_2O_3 and Nd_2O_3 powders were packed into cylindrical tubes of about 5-cm long and were used as source materials for the growth. Fibres of diameter ranging from 50-100μm were achieved after three to four times of growth reduction. Y_2O_3 SCFs were found to be relatively brittle and had a rough surface and, unlike sapphire and YAG, were easily broken if not handled properly. One similarity among the three materials was that the increase in dopant level resulted in the melt being unstable and caused crystalline imperfection. The number of growth reductions for higher dopant fibres had to be reduced and had slower pull rates as compared to undoped fibres. The fibres grown were free from strain and appeared to have high optical quality. Based on the fluorescence lifetime versus concentration measurement, Nd_2O_3 (1.5 wt%) doped Y_2O_3 gave the best fit requirement of a laser as compared to the other dopant levels. At 1.5 wt%, the fibre

had a fluorescence lifetime of 340μs when it was excited with a Kr laser at 0.7525μm. It was found that the lifetime decreased as the Nd concentration increased. At 3wt%, it had a decay of approximately of 200μs. Due to their small diameter, Y_2O_3 fibres did not suffer from cracks either in the growth process nor exhibited any spontaneous cracks after 24 hours of storage at room temperature.

Although a very active area of research, it did not attract much attention at that time. One reason was that there was no obvious suitable application at that time for SCFs which gave a significant performance advantage. Another reason was that the crystal growth community was preoccupied with other areas such as thin film development and the improvement of bulk crystals. These are fields that are still greatly researched to this day. In 1978, *Goodman* [2.14] investigated the potential of using SCFs as optical devices in the 4μm band. Interest began to grow again in the 1980s when a group from Stanford University, motivated by the many potential applications of SCFs, produced a range of optical devices. A major step that contributed to this was when *Fejer* and *Nightingale* [2.15] introduced a novel method called the Laser Heated Pedestal Miniature Growth (LHMPG) which was able to grow SCFs with high optical quality. One key concern was to grow fibres for their assessment in developing new optical materials. Previously, diameter instabilities and surface irregularities led to relatively high losses in optical transmission. It was found that diameter fluctuations arose not only from growth instability, but a large portion also came from the mechanical and optical abnormalities. Thus, solving this problem would solve the problem of having uneven diameters on the SCF. The team found that in a 5-cm long, 25μm diameter fibre for every 1% random diameter fluctuations, the loss was of the order of 25%. Part of the new design of the LHPG was the reproduction of modified zone melting by *Burrus* and *Stone* [2.9], but major changes were made to it. The concept of having two lasers and a rotating periscope or ellipsoidal focusing system were removed and replaced. In previous designs, there would always be cold spots on the growth zone. Therefore, a symmetrical irradiance would be ideal. The group redesigned the system by having a one-laser system, but with a reflaxicon and a paraboloidal mirror to direct the CO_2 laser beam to the tip of the source material. This approach provided a symmetrical heat source during the growth. A diameter monitoring system was also set up. The monitoring system was able to control the fluctuation of the diameter to less than 0.1%. Opportunities of

using SCFs as optical devices were further investigated by *Feigelson* [2.16] in 1988. His team from Stanford University had successfully demonstrated the possibility of growing many different SCF materials and utilising them in different areas of application. The LHPG method has been shown to be effective in producing fibres of uniform diameter; it is fast and easy-to-prepare materials for growth; and it is cost effective when it comes to single crystal property analysis. For these reasons, many around the globe have adopted this method of growing SCF.

2.3 Rare Earth Doped SCF

Rare earth elements, also known as lanthanides, consist of a series of elements ranging from lanthanum to lutetium in the Periodic Table. Luminescence produced by rare earth ions have been extensively investigated by many researchers since the start of the 20th century. The use of rare earth ions as phosphor activators is a common and mature technology. Cathode-Ray Tube (CRT) phosphors are an example of exploiting triply charged ions of the rare earths producing transitions in the red, green and blue. In the 1960s, rare earth ions were predominantly used in solid-state lasers because the energy levels in these ions are largely insensitive to a variety of host materials.

The use of rare earth doped fibre was first reported in 1964 by a team from the American Optical Company in Massachusetts. *Koester* and *Snitzer* [2.17] from the team successfully developed a neodymium-doped glass amplifier. The fibre, which amplified at 1.06μm, had a core diameter of 10μm, a cladding of 0.75 to 1.5mm and a total length of 1m. For convenient pumping from a flashtube, the fibre was wound into the form of a helix and the ends of the fibre were polished at an angle which prevented laser oscillation. The gain from the system was a strong function of the pump power where it achieved a net pass gain as high as 47dB. The same team in 1965, *Snitzer* and *Woodcock* [2.18] were the first to demonstrate the use of rare earths, ytterbium and erbium, incorporated into glass as a laser material. Transferring energy from Yb^{3+} to Er^{3+} in the silicate glass, a laser emission at 1.5426μm was attained at room temperature.

In 1973, neodymium doped silica was investigated by *Burrus* and *Stone* [2.19]. Pumped by an argon ion laser at wavelengths of 0.5145 and 0.590μm, the fibre laser operated at wavelengths of 1.06 and 1.08μm and had a low threshold of 1 to 2mW of absorbed pump power. *Burrus* and *Stone* [2.9] were also the pioneers of rare earth doped SCF. Nd doped YAG fibres were investigated because of their compatibility with other optical devices. These doped crystal fibres, grown in small diameters, were shown to be good lasing materials. The development of Nd:YAG lasers had been the most outstanding success of its time. The basic role for rare earth doped silica fibres in the 1970s was in the area of fibre transmission systems. However, the findings on these fibres were not immediately appreciated.

A decade later, interest in this field was once again raised when there was an increasing need to fulfil the great demand in the telecommunication arena. In 1985, *Poole* and *Payne* [2.20] from University of Southampton reported a novel technique of fabricating single mode rare earth doped fibres by modifying the existing chemical vapour deposition technique. Doped fibres produced from this new technique, known as the Modified Chemical Vapour Deposition (MCVD), are low in losses, achieved high gain, have narrow bandwidth, and are compact and stable. This new development brought about a whole new recognition toward rare earth doped fibres. A large research effort was focused on this area, mainly driven by optical communication applications which require rare earth doped silica fibres. Rare earth doped crystal fibres meanwhile found themselves being used more in laser physics applications and research.

In the 1980s, *Snitzer* and co-workers [2.21] used rare earth (europium and neodymium) doped glass fibre in the area of thermometry. The absorption/transmission behaviour of the rare earths was found to be dependent on temperature. Absorption occurred in both the visible and infrared regions. Investigations showed that for neodymium doped fibres, there was an increase in transmission in the region nearer to the infrared wavelengths when the temperature increased. As for the europium sensor, transmission through the glass fibre reduced as the temperature increased. *Grattan* and *Palmer* [2.22] also developed an inexpensive neodymium rod as a temperature sensor. More recently, instead of using conventional fibres for thermometry, SCF doped rare earth has been used in thermometric measurement. This work was carried out by *Seat* and *Sharp* [2.23].

Er^{3+}+Yb^{3+}-codoped single crystal sapphire fibres fabricated using LHPG were investigated as sensors for high temperature environments. Employing an upconversion intensity-based sensing scheme, the thermal behaviour in a harsh environment was monitored by the relative emission in the red and green spectral regions. The strong upconverted emission in those regions was partially contributed by the high dopant concentration and the unique transitions known as the 4f-4f interaction in the rare earth ions.

In the late 1980s and early 1990s, a new interest grew in the development of diode pumped rare earth doped lasers that were able to emit in the visible spectrum, especially in the green and blue regions. These frequency doubled, tripled or upconversion lasers were developed based on rare earth ions that are doped in bulk crystals, glasses or fibres. Compact in size, these short-wavelength lasers offered many attractions in technical applications such as full-colour display, data storage, laser printing, etc. One of the successful materials studied for upconversion lasers is $LiYF_4:Er^{3+}$ [2.24, 25]. The reason for its success is that it has a long decay time of 3 and 14 ms at the intermediate levels of $^4I_{11/2}$ and $^4I_{13/2}$. These levels become good holding reservoirs and permit excited ions to be produced for a reasonable excitation level. The work done by *McFarlane* [2.24] on upconversion lasers demonstrated the ability to achieve a laser output power of 0.5W at a visible wavelength of 551nm and with an efficiency of 14%.

Single crystal Er:$YAlO_3$, used as a cw upconversion laser, was first reported by *Silversmith* [2.26] in 1987. *Silversmith* was possibly the first to use a bulk crystal to demonstrate cw upconversion laser action at wavelengths of 550nm. With a pump power of 200mW from two infrared dye lasers, a cw output power of approximately of 1mW of the green was achieved. More recent work done by *Shur* [2.27] has studied, Er doped in $LiNbO_3$ SCF. Er_2O_3 was doped in $LiNbO_3$ (congruent and stoichiometric) both kinds of crystal fibres show an upconversion in the green region at the maximum peak of 550nm. These emission dominant peaks in both the crystal fibres were the result of $^4S_{3/2} \rightarrow {}^4I_{15/2}$ transitions and the other less intense peaks at 530nm were the result of $^2H_{11/2} \rightarrow {}^4I_{15/2}$ transitions. Rare earths such as erbium have dominated work on the upconversion, mainly because they were the first ions to demonstrate efficient upconversion and studies in these ions continue presently.

2.4 SCF Fabrication Methods

According to *H. Scheel* [2.28], the first crystal growth method was possibly developed as early as 2500 BC where salt was purified through crystallisation. Therefore, the subject of crystal growth is not novel. However, the different methods used are something worth investigating. In this section, six different methods of SCF growth are discussed. They include: Capillary Shaping From Melt (similar to Stepanov's), Bridgman, Micro-Czochralski (μ-CZ), Drawing Down and Pulling Down (μ-PD), Floating Zone (FZ) and Laser Heated Pedestal Growth Methods (LHPG). Four out of the six methods require a crucible during the growth. A brief account of the techniques employed by each method is presented. The choice of which method one wishes to employ—to a large extent—depends on the material needed to be grown.

2.4.1 Capillary Shaping From Melt Method

This method [2.29] is similar to Stepanov's method and edge-defined film-fed growth which are very successful in the commercial arena. A shaper—in this case the capillary tube—is placed in the melt with one of its ends protruding from the melt. The crystal is pulled from this end. See figure 2.1 for schematic. The crystal cross section is shaped by the edges and walls of the capillary tube. It is important that the material of both the crystal and the capillary tube match well; this ensures the prevention of contamination. Therefore, the material of the capillary tube must be well chosen. The shape and diameter of the crystal is dependent on four areas: the capillary tube's geometry; the crystallisation surface position and shape; the pressure feeding the melt to the capillary tube; and lastly, the shape of the seed used. Sapphire [2.30], KRS-5 (thallium bromoiodide), $LiNbO_3$ (lithium niobate) and YAG (yttrium aluminium garnet) [2.31] are some materials grown using such a method.

2.4.2 Bridgman Method

There are two configurations for this method: the Vertical Bridgman method and the Horizontal Bridgman method [2.32]. In both methods, a crucible is used to contain the melt.

One of the main advantages for the use of the Vertical Bridgman method is from the mechanical perspective, the system can be manufactured more easily. Lowering the crucible through the heating elements is easier than moving it horizontally across. When vibration is of concern during the growth, the crucible will then be held stationary while the heating element is moved. Another advantage of the system is that the heating element and crucible are axially symmetric. This enhances the homogeneity of the crystal growth.

There are also some advantages to using Horizontal Bridgman method. In this arrangement, GaAs can be grown more easily. The vapour distance to the growth is relatively constant over the entire length of the crystal whereas in a vertical arrangement, the distance travelled by the crystal varies with the fraction of the melt solidification. Figure 2.2 shows the vertical arrangement. In the growth of single crystal fibres using the Bridgman method, capillary tubes are employed. The capillary, acting as a form of shaper, is submerged in the melt and the crucible is then lowered into the heating coils which have a temperature gradient. The melt will then encounter a liquid and solid interface. The capillary tubes define the shape and diameter of the single crystal fibre so its material must match the melt to ensure chemical inertness. This method is used to fabricate low melting point organic fibres [2.33] and fluoride fibres [2.34].

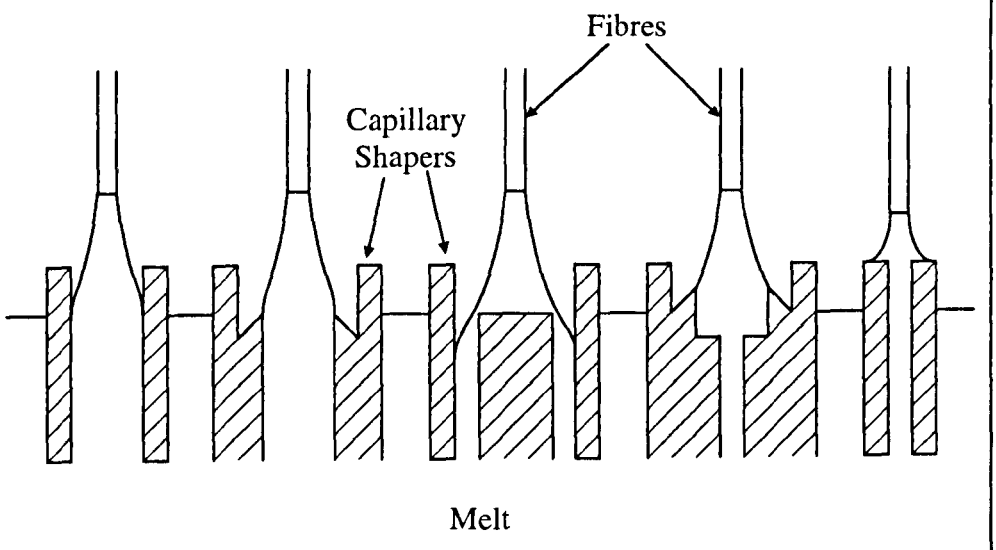

Figure 2.1 – Schematic of Capillary Shaping method

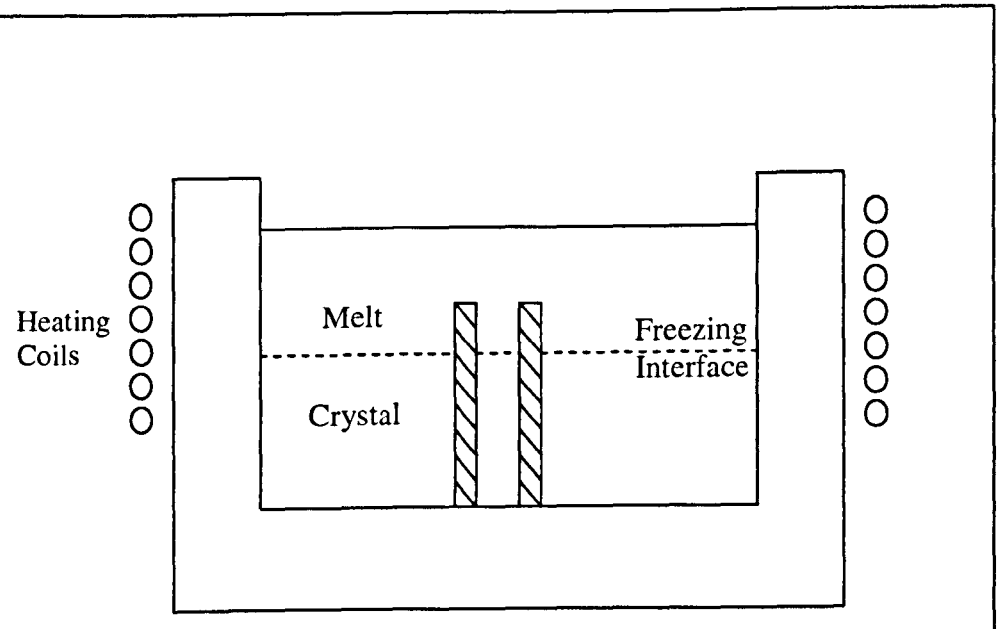

Figure 2.2 – Schematic of Bridgman method

2.4.3 Micro Czochralski (μ-CZ) Method

The conventional Czochralski method could not support the growth of small-diameter single crystal fibres due to thermal convention. For such fibres, the temperature in the melt has to be precisely controlled and the melt volume must be small in order to reduce convection. μ-CZ [2.35] method was developed to overcome this problem. Figure 2.3 shows the schematic of the μ-CZ method. From the figure, a platinum heater with a small protrusion is seen embedded in the crucible. Due to the miniaturisation of the system, the volume of the melt is greatly reduced to a size whereby thermal convection is no longer a problem for crystal growth. The melt's close contact with the heater also enables controllability of the melting temperature. A seed crystal is lowered to the small protrusion, and once it comes into contact with the melt, the seed is pulled up at a speed of 0.4-1 mm/min. Fibres with diameters ranging from 70 – 130 μm with lengths up to 70 mm have been successfully grown.

The advantages of this method are the orientation of the crystal can be controlled by the seed crystal and a shaper is not required as with the Capillary Shaping from Melt method. Limitations, on the other hand, are also evident in this system. A chemical mismatch between the melt and the crucible can cause contamination during growth of fibres and the maximum temperature is restricted by the heating element. In the first mention of μ-CZ method, $LiNbO_3$ single crystal fibres were grown. In subsequent work, the method has been employed to grow crystalline Bi-Sr-Ca-Cu-O fibres [2.36].

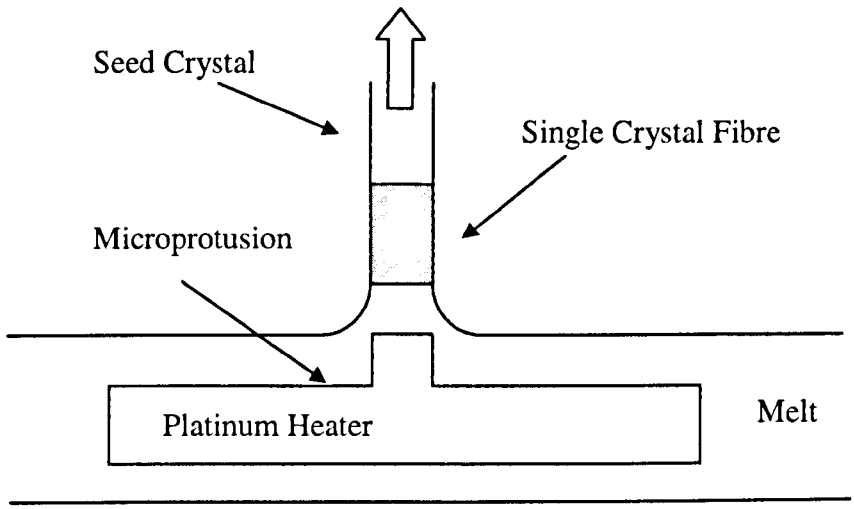

Figure 2.3 – Schematic of μ-CZ method

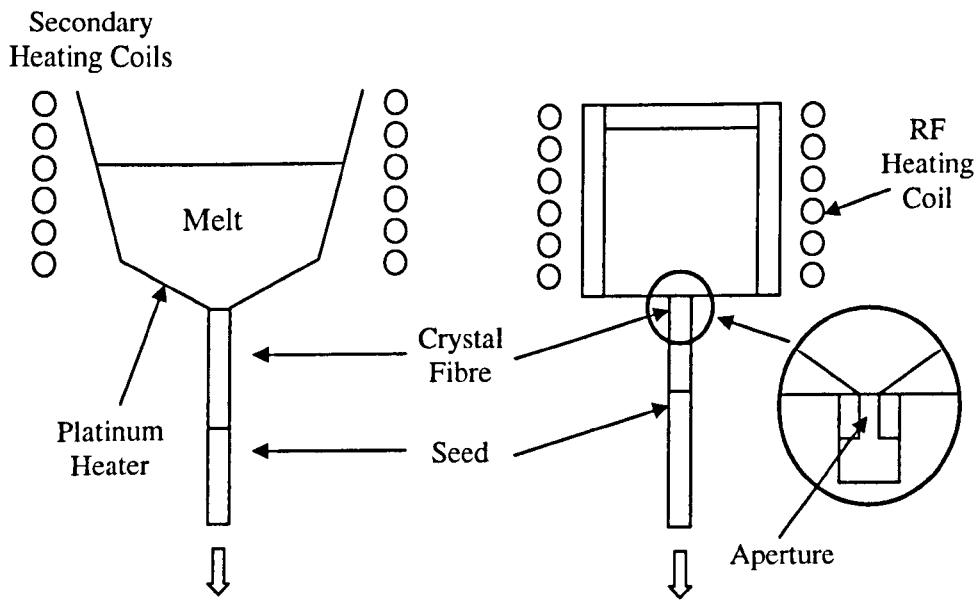

Figure 2.4 – Schematic of Drawing Down (left) and μ-Pull Down (right) methods

2.4.4 Drawing Down and Micro Pull Down (μ-PD) Methods

Drawing Down and μ-PD methods employ similar techniques, but are named differently by individual research groups [2.37, 2.38]. These methods were initially designed to grow MgO-doped $LiNbO_3$ fibres [2.37] and were developed for thin single crystal fibres. *Oguri* managed to achieve fibres with diameters as small as 10 μm with fluctuations of ± 0.2 μm. See Figure 2.4 for schematics. Comprising a crucible and a platinum heater as the primary heat source, it is surrounded by a RF (radio frequency) coil which acts as the system's secondary heater. The melt in the crucible flows through the aperture. A seed fibre with the desired crystallographic orientation is attached to the pull mechanism, and is raised to make contact with the melt and then pulled at a constant speed in a downward direction to form the grown crystal.

To achieve a fibre of a consistent diameter, the molten zone's volume and shape must be constant throughout the growth process. Since a crucible is used, one major disadvantage of this method is the occurrence of contamination. Residue from the previous growth material may not have been properly removed. Another setback in the use of a crucible is that the material of the crucible and the melt must be chemically compatible. The diameter of the fibre is restricted to the choice of the aperture/orifice and the wetting conditions. However, an advantage in the use of a small aperture is that there will be uniformity across the fibre. Various materials are grown by this method: lithium niobate ($LiNbO_3$) [2.37, 38, 40] used in nonlinear- and electro-optical devices, silicon [2.38] for device applications like solar cell, yttrium-lithium tetrafluoride ($LiYF_4$) [2.41] as a laser material application, $Al_2O_3/Y_3Al_5O_{12}$ [2.42] for eutectic fibres, and strontium barium niobate (SBN) [2.43] for photorefractive applications.

2.4.5 Floating Zone (FZ) Method

Since the Floating Zone (FZ) method was first developed [2.44], many researchers have used it to grow a wide range of crystalline materials. Its crucible-free technique is one of the many reasons for its popularity. Without the use of a crucible, the limitations of crucible materials are eradicated. See Figure 2.5 for schematic. In the growth chamber, the melting rod which is in a free-standing position is clamped at the top end of the system. The heating elements will melt the tip of the melting rod, creating a suspended molten zone. A known crystalline seed is then raised to the molten zone where it is then lowered to form a single crystal fibre. In some FZ systems, the melting rod can be rotated at different rotation rates to achieve the desired growth condition. This method employs various heat sources, the most commonly used is RF coils [2.45], which are frequently used in industry. Other heat sources include high-powered lamp [2.44, 2.46], electric arc, electron bombardment method [2.47] and laser [2.48, 2.49]. This system has some limitations. For successful growth, there needs to be a stable melting zone which can pose a difficult task for FZ and with this instability. Convection can cause degradation in the fibres grown. Another problem for this growth method is its high thermal gradient found along its free surface which can lead to crystal cracking.

2.4.6 Laser Heated Pedestal Growth (LHPG)

LHPG was developed by a group from Stanford University [2.50] for growing crystal fibres. See Figure 2.6 for schematic. There are some similarity between FZ and LHPG. The major difference is that in FZ the crystal fibre grows in the downward direction whereas in LHPG fibres are grown by pulling in the upper direction and the melt is heated symmetrically. For the latter, its heating source is solely laser radiation. As shown schematically, a CO_2 laser emitting at 10.6 μm is used to focus down to melt the tip of the source material, until a hemispherical molten zone is formed. Single crystals, polycrystals and pressed powers can be used as the source material. A seed crystal of known crystallographic orientation is then lowered into the molten zone to initiate the growth. The seed crystal is then withdrawn from the molten zone at a rate faster than the feed rate of the source material. The shape of the molten zone and growing fibre's consequent reduction in diameter are due to the

conservation of mass. This technique does not require the use of a crucible. The crystal can be easily doped with a large variety of transition metal and rare earth ions. Thus far, fibres with diameters as small as 3 μm [2.50] have been grown. The advantage of using a laser and focusing optics in LHPG is that a large range of materials can be grown. Materials like refractory oxides, fluorides, semiconductors, perovskites, garnets, niobates, eutectics and high temperature superconductors. See Appendix A for different types of materials grown using this technique. This technique is adopted in the current study and a further discussion will be presented in Chapter 4.

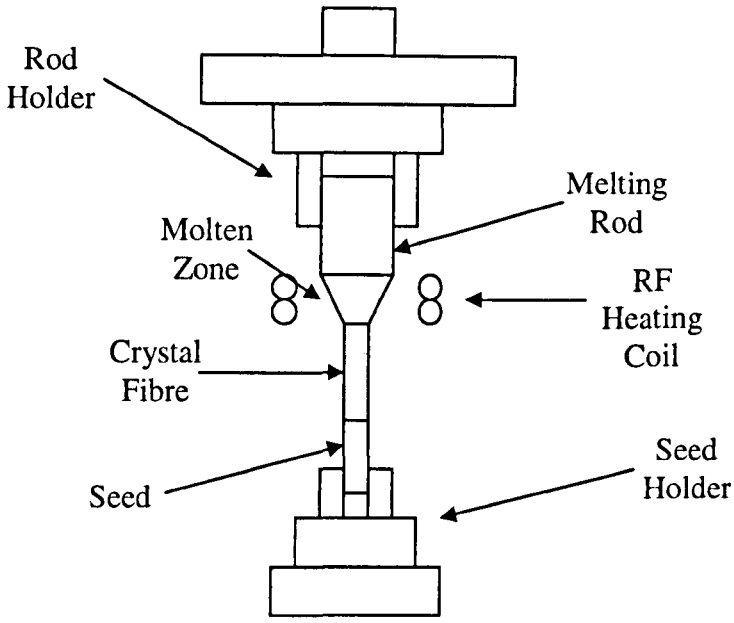

Figure 2.5 – Schematic of Floating Zone (FZ) method

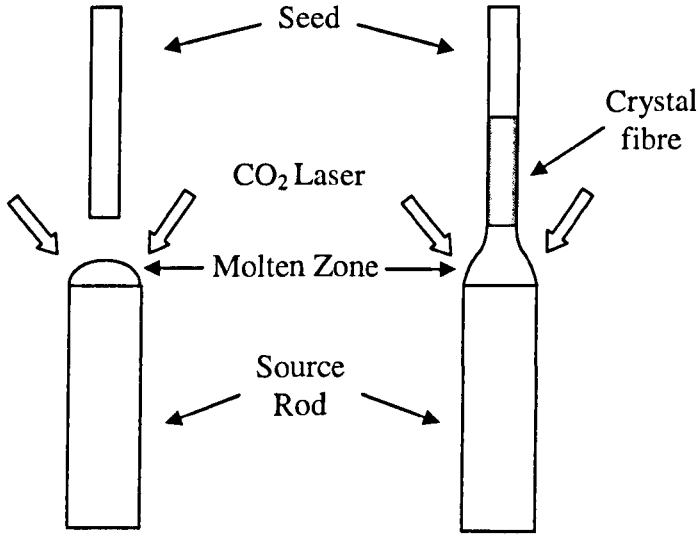

Figure 2.6 – Schematic of Laser Heated Pedestal Growth (LHPG) method

2.5 SCF Applications

In the area of telecommunication, signal processing depends greatly on electronic processing, whereby electronic signals are converted to optical signals and vice versa. Research on having all signals processed in optical form has been a driving force behind the intense growth of silica based fibre lasers, optical fibre amplifiers and associated optics. Due to the relatively slow growth rate when compared to glass fibre production and no significant advantage in wavelength for telecommunication applications, SCF's were not the number one choice in this field as it developed. However, SCF's have many other attractive attributes that have become interesting areas of research in the past few decades.

One of the most attractive usages of SCF's is in the area of the SCF laser. After *Burrus and Stone* [2.9], who were the first to employ SCF as a laser device, many others have contributed to this field. SCF lasers can exhibit higher optical damage thresholds, high emission cross-sections and, due to its intrinsic qualities, most crystals have good mechanical strength. In addition, SCF laser efficiency is generally better than its equivalent glass based devices. The ability to operate in the high infrared region also gives SCF a clear advantage as a wave-guide delivering high power laser beams. Although fluoride glass fibres can cover a range from the visible to about 4.5μm, it has its constraints [2.51]. Having wide transparency, it has limited mechanical strength and a very low operating temperature of 150°C, whereas sapphire crystalline fibre can operate as high as 2000°C, it is biologically inert and able to transmit up to ~3μm.

Sapphire SCF's [2.51] have been used in medical laser beam delivery for Er:YAG lasers with an operating wavelength of 2.94μm. Having a high melting point, being biologically inert and its resistance against degradation under a high power transmission beam, sapphire is indeed an excellent choice to be used in operating theatres. Nd doped YAG SCF is of late being used in laser thermotherapy [2.52]. A Ti:Sapphire laser, operating at more than a few hundred mW, is used as a excitation source for the Nd-tip doped YAG SCF. The laser energy that propagates through the fibre is absorbed by the Nd ions and converted to heat due to phonon relaxation. The temperature generated is easily controlled by the optical power. This system not only achieves linearity between temperatures and pump powers, it also has high

mechanical strength and physical and chemical permanence, making it a good and promising laser thermotherapy device.

In recent years, the use of SCF has taken on a new direction. Due to its high melting point and robust nature, SCF's have been employed as temperature sensors in extreme or hostile environments which ordinary sensors cannot withstand. Conventional optical fibre sensors are mainly silica-glass-based. They have been widely investigated and have been successfully used in many areas. These fibres are restricted to operating at temperatures up to 1000°C exceeding these results in a degradation of their mechanical and optical integrity. Therefore, silica-glass-based sensors are only suited to operate at relatively low temperatures.

A wide range of crystalline materials, however, can function at temperatures exceeding 1000°C. Many industrial applications require sensors that can detect temperatures higher then 1000°C. Examples include the aerospace industries for the monitoring of engines, process industries and nuclear plants, where temperatures concerned are higher than 1000°C. Using techniques such as blackbody radiation [2.53], a thin film is coated at the tip of a single crystal aluminium oxide (sapphire) fibre 0.05 to 0.3m long and the fibre is used as a temperature sensor. The high temperature sensor is then connected to a low temperature fibre where the radiation signal emits from the blackbody cavity and is collected by a detector at the end of the latter fibre. Although the melting point of sapphire is 2045°C, the effective operating temperature for this system ranges from 600°C to 1300°C. Other SCF materials such as YAG [2.54] which has a melting point of 1900°C is able to operate as a sensor close to its melting point. This probe is grown as an all-crystalline fibre with the tip of this fibre doped with Erbium. Since the sensor tip and the waveguide are made of the same material, it can therefore be used in extreme conditions without having the consideration of adhesives or mechanical coupling to the waveguide.

The search for higher temperature sensing capabilities is one of the driving forces for researchers in this field. Zirconia (Y_2O_3-stablized ZrO_2) [2.55], with a melting temperature as high 2700°C, is potentially ideal for such applications. The sensing tip and the fibre—both of the same material and grown using LHPG—are used as an ultra-high temperature fibre optic sensor that operates up to 2300°C. Due to the large residual thermal stress in this material, it is neither efficient nor accurate to make a

fair comparison with sapphire temperature sensors. To improve accuracy, a good control over the material's temperature gradient during growth is extremely important [2.56]. Good control of the temperature gradient will improve its transmission and therefore reduce the optical losses within the fibre. In any case, with its high melting temperature, zirconia will be the likely material used if the required operating temperature surpasses the melting point of sapphire.

Strain and stress measurements are important in the areas of material science and structural engineering. Conventional strain gauges or strain rosettes have their constraints. It is desirable to study the internal strain in certain structures and this is what traditional methods have difficulty in achieving this. Conventional gauges are only able to monitor the external behaviour of the structure where optic fibre sensors can be embedded in the structure to fully determine the strain state inside the composition. Other advantages of using fibres as strain gauges are that they are light in weight, small in size, highly resistant to chemical corrosion, immune to electromagnetic interference, and able to be embedded in composites. The physical properties of SCF's imply they can make good strain or stress gauges. An example of using sapphire as a sensor in stress or strain measurement is demonstrated by *Seat* [2.57]. The work was based on the polarimetric interference in the fibre. The above discussion only touches on the list of potential application areas. SCF's are also employed as waveguides, filters, polarisers, isolators, couplers, electro-optics modulators, etc.

2.6 References

[2.1] C.V. Boys, *On the Production, Properties, and some suggested Uses of the Finest Threads,* Proc. Phys. Soc. **9**, 8, 1887

[2.2] C.V. Boys, *Quartz Fibres,* Nature **40**, 247, 1889

[2.3] H. E. LaBelle and A. I. Mlavsky, *Growth of Sapphire Filaments from Melt* Nature, **216**, 574, 1967

[2.4] H. E. LaBelle and A. I. Mlavsky, *Growth of Controlled Profile Crystals from the Melt: Part 1 – Sapphire Filaments*, Mat. Res. Bull. **6**, 571, 1971

[2.5] H. E. LaBelle, *Growth of Controlled Profile Crystals from the Melt, Part II – Edge-Defined, Film-Fed Growth (EFG)*, Mat. Res. Bull. **6**, 581, 1971

[2.6] D.B. Gasson and B. Cockayne, *Oxide Crystal Growth using Gas Lasers*, J. Cryst Growth **5**, 100, 1970

[2.7] J. S. Haggerty, *Production of Fibers by a Floating Zone Fiber Drawing Techniques*, Final Report NASA-CR-120948, 65, 1972

[2.8] A. P. Levitt, *Whisker Technology*, Wiley-Interscience, 1970

[2.9] C. A. Burrus and J. Stone, *Single-Crystal Fiber Optical Devices: A Nd: YAG Fiber Laser*, App. Phys. Let., **26**, 6, 318, 1975

[2.10] R. P. Poplawsky, *Ferrite Crystal Using as Arc Image Furnace*, J. App Phys **33**, 4, 1616, 1962

[2.11] J. Stone, C. A. Burrus and A. G. Dentai, *Nd:YAG Single-Crystal Fiber Laser: Room-Temperature CW Operation Using a Single LED as an pump*, App. Phys. Let., **29**, 1, 37, 1976

[2.12] C. A. Burrus and L. A. Coldren, *Growth of Single-Crystal Sapphire-Clad Fibers*, App. Phys. Let., **31**, 6, 383, 1977

[2.13] C. A. Burrus and J. Stone, *Nd:Y_2O_3 Single-Crystal Fiber Laser: Room Temperature CW Operation at 1.07- and 1.35-μm Wavelength*, J. App. Phys., **49**, 4, 2281, 1978

[2.14] C. H. L. Goodman, *Devices and Materials for 4 μm Band Fibre-Optical Communication*, Solid State Electron Devices, **2**, 5,129, 1978

[2.15] M. M. Fejer, J. L. Nightingale, G. A. Magel, and R. L. Byer, *Laser-Heated Miniature Pedestal Growth Apparatus for Single-Crystal Optical Fibers*, Rev. Sci. Instrum., **55**, 11, 1791, 1984

[2.16] R. S. Feigelson, *Opportunities for Research on Single-Crystal Fibers*, Mat. Sci. Eng. B1, **1**, 1, 67, 1988

[2.17] C. J. Koester and E. Snitzer, *Amplification in Fibre Laser*, App. Opt. **3**,10, 1182, 1964

[2.18] E. Snitzer and R. Woodcock, Yb^{3+}- Er^{3+} *Glass Laser*, App. Phys. Let., **6**, 3, 45, 1965

[2.19] J. Stone and C. A. Burrus, *Neodymium-Doped Silica Lasers in End-Pumped Fibre Geometry*, App. Phys. Let., **23**, 7, 388, 1973

[2.20] S. B. Poole, D. N. Payne and M. E. Fermann, *Fabrication of Low-Loss Optical Fibres Containing Rare-Earth Ions*, Elect. Let., **21**, 17, 737, 1985

[2.21] E. Snitzer, W. W. Morey and W. H. Glenn, *Fiber Optic Rare Earth Temperature Sensors*, Proc. 1st Inter. Conf. Optical Fiber Sensors, London, **79**, 1983

[2.22] K. T. V. Grattan and A. W. Palmer, *A Simple, Inexpensive Neodymium Rod Fibre Optic Temperature Sensor*, Proc. 3rd Inter. Conf. Optical Fibre Sensors, San Diego, **142**, 1985

[2.23] H. C. Seat and J. H. Sharp, Er^{3+}+ Yb^{3+} - *codoped* Al_2O_3 *Crystal Fibres for High Temperature Sensing*, Meas. Sci. Tech. **14**, 3, 279, 2002

[2.24] R. A. McFarlane, *High-Power Visible Upconversion Laser*, Opt. Let., **16**, 18, 1397, 1991

[2.25] P. Xie, and S. C. Rand, *Visible Cooperative Upconversion Laser in Er:*$LiYF_4$, Opt. Let., **17**, 17, 1198, 1992

[2.26] A. J. Silversmith, W. Lenth and R. M Macfarlane, *Green Infrared-Pumped Erbium Upconversion Laser*, App. Phys. Let., **55**, 24, 1977, 1987

[2.27] J. W. Shur, W. S. Yang, S. J. Suh, J. H. Lee, T. Fukuda and D. J. Yoon, *Optical Properties of Er Doped Congruent and Stoichiometric $LiNbO_3$ Single Crystal*, Cryst. Res. Tech., **37**, 4, 353, 2002

[2.28] H. J. Scheel, *Handbook of Crystal Growth Vol. 1, Chapter 1 Historical Introduction*, 3, 1993

[2.29] V. A. Tatarchenko, *Capllary Shaping in Crystal Growth From Melt*, J. Cryst. Growth, **37**, 3, 272, 1977

[2.30] P. I. Antonov and V. N. Kurlov, *A Review of Developments in Shaped Crystal Growth of Sapphire by the Stepanov and Related Techniques*, Prog. Cryst. Growth. and Char. Mat., **44**, 2, 63, 2002

[2.31] P. Rudolph and T. Fukuda, *Fiber Crystal Growth from the Melt*, Cryst. Res. Tech., **34**, 1, 3, 1999

[2.32] D. T Hurle, *Handbook of Crystal Growth 2 – Bulk Crystal Growth Part A: Basic Techniques*, 55, 1994

[2.33] P. V. Vidakovic, M. Coquillay and F. Salin, *N-(4-Nitrophenyl)-N-Methylamino-Aceto-Nitrile: A new Organic Material for a Efficient Second-Harmonic Generation in Bulk and Waveguide Configurations. I Growth, Crystal Structure, and Characterization of Organic Crystal-Cored Fibers*, J. Opt. Soc. Am. B, **4**, 6, 998, 1987

[2.34] V. M. Orera and A. Larrea, *NaCl-Assisted Growth of Micrometer-Wide Long Single Crystalline Fluoride Fibres*, Opt. Mat. **27**, 11, 1726, 2005

[2.35] N. Ohnishi and T. Yao, *A Novel Growth Technique for Single-Crystal Fibres: The Micro-Czochralski (μ-CZ) Method*, Jpn. J. App. Phys., **28**, 2, L278, 1989

[2.36] A. Kurosaka, M. Aoyagi, H. Tominaga, O. Fukuda and H. Osanai, *Superconducting Bi-Sr-Ca-Cu-O Crystalline Fibers Prepared by the Micro-Czochralski Method*, App. Phys. Let., **55**, 4, 390, 1989

[2.37] H. Oguri, H. Yamanmura and T. Orito, *Growth of MgO Doped $LiNbO_3$ Single Crystal Fibers by Novel Drawing Down Method*, J. Cryst. Growth, **110**, 4, 669, 1991

[2.38] K. Shimamura, S. Uda, T. Yamada, S. Sakaguchi and T. Fukuda, *Silicon Single Crystal Fibre Growth by Micro Pulling Down Method*, Jpn. J. App. Phys., **35**, 2,6B, L793, 1996

[2.39] D. Yoon, I. Yonenaga, T. Fukuda and N. Ohnishi, *Crystal Growth of Dislocation-Free $LiNbO_3$ Single Crystals by Micro Pulling Down Method*, J. Cryst. Growth, **142**, 3-4, 339, 1994

[2.40] D. Yoon and T. Fukuda, *Characterisation of $LiNbO_3$ Micro Single Crystals Grown by the Micro Pulling Down Method*, J. Cryst. Growth, **144**, 3-4, 201, 1994

[2.41] A. M. E. Santo, I. M. Ranieri, G. E. S. Brito, B. M. Epelbaum, S. P. Morato, N. D. Vieira Jr and S. L. Baldochi, *Growth of $LiYF_4$ Single Crystalline Fibres by Micro-Pulling-Down Technique*, J. Cryst. Growth, **275**, 3-4, 528, 2005

[2.42] M. Nakai, H. Kaiden, J. H. Lee, A. Yoshikawa, K. Sugiyama and T. Fukuda, *Eutectic $Al_2O_3/Y_3Al_5O_{12}$ Fibers Modified by the Substitution of Sc_2O_3, Fe_2O_3 or Cr_rO_3*, J. Euro. Cerm. Soc., **25**, 8, 1405, 2005

[2.43] A. E. Hassouni, K. Lebbou, C. Goutaudier, G. Boulonm, A. Yoshikawa and T. Fukuda, *SBN Single Crystal fibers Grown by Micro-Pulling Down Technique*, Opt. Mat., **24**, 1-2, 419, 2003

[2.44] P. H. Keck and M. J. E. Golay, *Crystalline of Silicon from a Floating Liquid Zone*, Phys. Rev., **89**, 6, 1297, 1953

[2.45] P. Dold, *Analysis of Microsegregation in RF-Heated Float Zone Growth of Silicon-Comparison to the Radiation-Heated Process*, J. Crys. Growth, **261**, 1, 1, 2004

[2.46] C. Kloc, S. W. Cheng and P. Malt, *Floating-Zone Crystal Growth of Perovskite Manganites with Colossal Magnetoresistance*, J. Crys. Growth, **191**, 1-2, 294, 1998

[2.47] C. M. Chen, L. T. Zhang and W. C. Zhou, *Characterization of LaB_6–ZrB_2 Eutectric Composite Grown by the Floating Zone Method*, J. Crys. Growth, **191**, 4, 873, 1998

[2.48] K. M. Kim, A. B. Dreeben and A. Schujko, *Maximum Stable Zone Length in Floating-Zone Growth of Small-Diameter Sapphire and Silicon Crystals*, J. App. Phys., **50**, 6, 4472, 1979

[2.49] T. Sekijima, H. Satoh, K. Tahara, T. Fujii, K. Wakino and M. Okada, *Growth of Fibrous YIG Single Crystals by the Self-Adjusting Solvent FZ Method*, J. Crys. Growth, **193**, 3, 446, 1998

[2.50] R. S. Feigelson, W. L. Kway and R. K. Route, *Single Crystal Fibers by the Laser-Heated Pedestal Growth Method*, Opt. Eng., **24**, 6, 1102, 1985

[2.51] G. N. Merberg, *Current Status of Infrared Fiber Optics for Medical Laser Power Delivery*, Lasers Surg. Med., **13**, 5, 572 1993

[2.52] L. Tong, D. Zhu, Q. Luo and D. Hong, *A Laser Pumped Nd^{+3}-doped YAG Fiber-Optic Thermal Tip for Laser Thermotherapy*, Lasers Surg. Med., **30**, 1, 67, 2002

[2.53] R. R. Dils, *High-Temperature Optical Fiber Thermometer*, J. Appl. Phys., **54**, 3, 1983

[2.54] Z. Zhang, J. H. Herringer, and N. Djeu, *Monolithic Crystalline fibre Optic Temperature Sensor*, Rev. Sci. Instrum. **68**, 5, 2068, 1997

[2.55] L. Tong, Y. Shen, L. Ye and Z. Ding, *A Zirconia Single-Crystal Fibre-Optic Sensor for Contact Measurement of Temperature Above 2000°C*, Meas. Sci. Technol., **10**, 7, 607, 1999

[2.56] L. Tong, *Growth of High-Quality Y_2O_3 – ZrO_2 Single-Crystal optical fibres for Ultra-High-Temperature Fiber-Optic Sensors*, J. Cryst. Growth, **217**, 3, 281, 2000

[2.57] H. C. Seat, *Single Crystal Fibre Sensors*, PhD Thesis University of Glasgow, 2001

3 Crystal Growth and its Characterisation

3.1 Introduction

The first part of this chapter gives a brief account of the basic considerations for the growth of single crystal fibres using the Laser Heated Pedestal Growth (LHPG) method. Extensive research work has been carried out in the area of crystal growth from the melt and it is obviously vital that the melt zone remains stable during growth. Likewise in LHPG, the melt stability is crucial in the growth of high quality fibres. The second part of this chapter gives an account of the ion-ion interactions in rare earths between Er^{3+}- Er^{3+} and Er^{3+}-Yb^{3+}. A short introduction to the kind of rare earths used in the work is followed by a discussion on the possible ion-ion interactions that may occur in the fibres. The discussion includes an account of the use of rare earths at present. In the last part of this chapter, processes involving upconversion are further expounded.

3.2 Crystal Growth

A range of methods are available to grow SCF's from the melt. The objective in any growth system is to produce SCFs that are of good optical quality. To achieve a steady state growth in SCFs, a few considerations are necessary. *Feigelson's* [3.1] work on pulling optical fibres stated a few fundamentals for steady state growth of SCFs and work by *Rudolph* and *Fukuda* [2.31] placed further emphasis on the fundamentals drawn by *Feigelson.* These fundamentals will be revisited in this section and also short discussions will be made on areas specific to segregation and crystal defects.

3.2.1 Fundamentals for Steady State Growth

Melting temperature, also known as equilibrium temperature, is the temperature at which a liquid phase (melt) and a solid phase (crystal) coexist. These two states must be at equilibrium for growth to take place [3.2]. Both phases can exist above and below the equilibrium temperature. The basic difference between the melt and the

crystal is that the latter is in an environment where its atoms are in a crystalline symmetry whereas the former is in an environment where the atoms are in a random arrangement. Figure 3.1 illustrates schematically the molten zone in pedestal growth, where the crystal and the melt coexist. For growth to occur, physical aspects such as the molten zone length and volume are to be kept constant [3.1]. *Feigelson* classified the fundamental considerations for the LHPG method into three areas: (1) conservation of mass, (2) conservation of energy, and (3) shape stability.

(1) Conservation of Mass

To achieve a stable growth of a SCF, the growth length and volume must be kept constant. Therefore, steady state growth of fibre with a constant diameter is:

$$\frac{r_p}{R_s} = \left(\frac{v_p}{V_s}\right)^2 \tag{3.1}$$

r_p and R_s are radii of the pull fibre and source rod respectively, and v_p and V_s are the pull and feed rate of the fibre and source rod respectively.

(2) Conservation of Energy

A stable molten zone results when the steady state heat flow at the solid and the melt interfaces shares a relationship. It is as follows:

$$Q_s = Q_f + Q_m$$

$$AK_s\left(\frac{\delta T}{\delta x}\right)_s = A\rho_s \Delta H_f \left(\frac{dx}{dt}\right) + AK_l\left(\frac{dT}{\delta x}\right)_l = constant \tag{3.2}$$

Q_s and Q_m are both heat flux. The former is present in the crystal away from the growth interface while the latter, from the melt going into the interface. Q_f represents the latent heat of crystallisation while the two constants, K_s and K_l, are the thermal conductivity of solid and liquid phase respectively. A is the area of the interface, ρ_s is the density of the solid, and ΔH_f is the latent heat of fusion. The remaining two terms, $(dT/\delta x)_s$ and $(dT/\delta x)_l$, are the thermal gradients of the solid phase and the liquid phase respectively.

The temperature that is distributed from the melting zone into the SCF is taken into account and formulated by *Korpela* [3.3]. Temperature is known to decay over a length of time and this is characterised as a length z = z_d (decay length) where

$$z_d = r_p\left[-\frac{1}{2}Pe+\left(\frac{1}{4}(Pe)^2+2Bi+\frac{16\sigma n^2 T_s^3 k_p r_p^2}{k}\right)^{\frac{1}{2}}\right]^{-1} \qquad (3.3)$$

In equation 3.3, T_s is the surrounding temperature, k_p is the Planck mean absorption coefficient, σ is the Stefan-Boltzmann constant, and n is the refractive index. The findings by *Korpela* shows that as z_d increases, temperature will eventually fall to that of the surrounding environment, as the Biot number ($Bi = {}^{hr_p}/_{k}$ where h is convective heat, r_p is the radius of pulled fibre, and k is thermal conductivity) and the Péclet number ($Pe = {}^{rcv_p r_p}/_{k}$ where r is the reflectivity, c is specific heat, and v_p pulling velocity) reduce. Likewise, the absorptivity of the fibre will be reduced. A low absorptivity (oxides) [2.31] of the fibre lowers its cooling rate by radiation. This does not mean materials such as silicon and metals with higher absorptivity will have a smaller decay. Instead, it is greatly dependent on the high thermal conductivity, k, which will determine the value of z_d [3.3].

(3) Shape Stability

In achieving a consistent diameter for the SCF, two essential areas need to be observed during the growth process. Firstly,

$$\Phi = \Phi_o \qquad (3.4)$$

From Figure 3.1, Φ is the angle between the crystal and the melt, which has a relationship with the surface tension and its ability to wet the SCF. Φ_o is the material constant that defines the crystallographic orientation which is neither dependent on fibre growth rate nor zone length. *Feigelson* stated that the optimum steady state interfacial wetting angle is:

$$\cos\Phi_o = \sigma_{sg}^2 + \sigma_{lg}^2 - \frac{\sigma_{sl}^2}{2\sigma_{sg}\sigma_{lg}} \tag{3.5}$$

The interfacial free energy is represented by σ (where *sg* –solid to gas, *lg* – liquid to gas and *sl* – solid to liquid). For example, Si has a Φ_o of 11° with an orientation of {111} [3.4], sapphire – 12° with orientation of {0001} [3.5], and YAG – 8° with an orientation of {100} [3.6].

Thirdly, deviation from steady state by perturbation of L or r_p of the growing SCF causes variation in diameter given by:

$$\frac{dr}{dt} = v_p \tan(\Phi - \Phi_o) \neq 0 \tag{3.6}$$

The forth consideration in maintaining a stable molten zone is the length, L. For L to be consistent, a relationship with the radius has to be established. The relationship is as follows:

$$L = \frac{3}{2}(R_s + r_p) \tag{3.7}$$

Investigation by *Feigelson* [3.1] shows that the reduction ratio in fluorides and oxides grown by the LHPG method usually falls within the range of 1:2 to 1:3 while fibres with a small diameter ranging from ~5 to 10μm has a reduction ratio of 1:10. Detailed study done by *Fejer* [3.6] in the area of stability and the dynamics of the molten zone of SCF in LHPG showed that gravity has a negligible effect on the molten zone for small diameter SCFs. The shape stability is mostly determined by the surface tension. From his work, he showed that Bond number ($Bo = \rho g R_s^2 / 4\gamma$ where ρ is the melt density, g is the gravitational pull, and γ is the surface tension), which is related to gravitational effect, is relatively low. For SCFs of sapphire, *Bo* is $3\text{x}10^{-3}$, which is less than 1 and is therefore negligible. From this, it is concluded that surface tension forces have the dominant effects on the molten zone shape and stability.

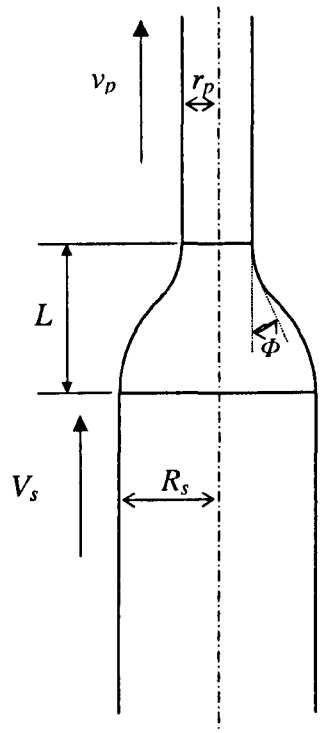

Figure 3.1 – Molten zone for pedestal growth

3.2.2 Segregation

All SCFs in this work are doped with rare earth ions to act as active ions. It would be desirable to be able to control the level of concentration and distribution of the dopant across the fibre as much as one can. A simple phase diagram, see Figure 3.2, representing a solid solution (interfaces between the melt and the fibre) between *A* and *B*. During fibre growth, it will start at the liquid state, point 1, and then crystallises to the solid state, point 2. As this growth process proceeds, the composition of the liquid may move from point 1 to 3 and likewise for the solid, it may travel from point 2 to 4. From Figure 3.2, the liquid and the solid do not have similar compositions and they vary from point to point in the crystal. The separation of solids and liquids can be simply expressed by a coefficient, k which is called the distribution or segregation coefficient and is defined as C_f/C_m, where C_f and C_m are the concentration of the pulled crystal and the melt respectively. The k valve determines the ease of pulling of the SCF. Thus, when k differs from unity, greater separation results and this also adds difficulties in the growth process.

For SCF growth using the LHPG method, *Sharp* [3.7] has developed a theoretical model in the investigation of dopant being transferred from the source rod to the growing fibre. The developed theoretical model matches well with experiment and the evaporation time could also be established. Similar models can be employed to determine the dopant transfer into the fibres grown in this work. The assumption made is that the dopant in the melt only comes from the source rod and losses of dopant from the melt are only through evaporation and to the growth fibre. In this case, evaporation is characterised by the evaporation time constant, τ. If evaporation in the melt is incongruent, crystals using the LHPG method will be difficult to grow. On the other hand, fibres with good optical quality have a rate of evaporation that is moderate and source material can be made containing excess of the volatile component [3.1]. τ is defined as the time at which concentration in the melt, C_m, decreases by a factor of e^{-1} at zero growth rate.

$$\frac{C_f(z)}{C_{s0}} = k\left[C'e^{\frac{-\beta z}{v}} + \frac{\alpha}{\beta}\left(1-e^{\frac{-\beta z}{v}}\right) + \frac{\alpha(C'-1)}{\beta-\gamma}\left(e^{\frac{-\gamma z}{v}} - e^{\frac{-\beta z}{v}}\right)\right] \qquad (3.8)$$

C_f is the concentration in the fibre, C_s is concentration in the source rod, $C^{'} = C_{si} / C_{s0}$ (C_{si} is the initial concentration of the source rod and C_{s0} is the concentration at equilibrium as time, $t \rightarrow 0$), $\alpha = {\pi r_p^2 v_p}/{V}$ (V is the volume of melt), $\beta = {\alpha k + 1}/{\tau}$ and reduction ratio, $\gamma = {R_s}/{r_p}$. From the equation above, a general prediction of the growth fibre can be made. The above examples, although not the principal focus of this work, set the theoretical parameters and establish the SCF growth concepts surrounding the subsequent chapters.

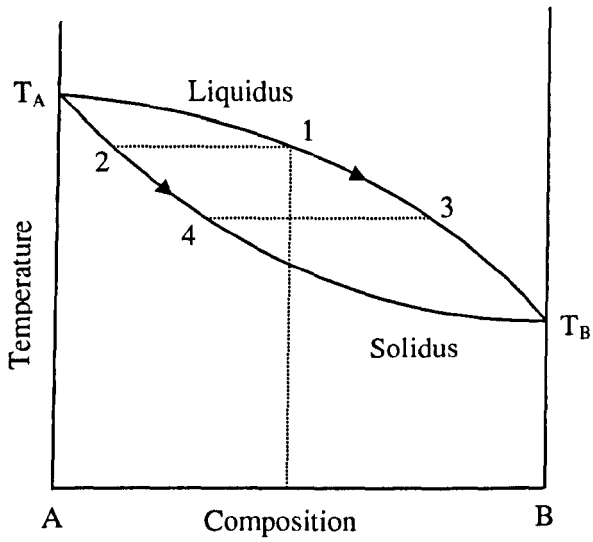

Figure 3.2 – Simple phase diagram

3.2.3 Crystal Defects

It is impossible to grow crystals that are free from defects. Identifying the defects and understanding them will help the crystal grower to minimise possible occurrences of defects. Common defects encountered in SCFs are point and line defects.

Point defects are classified as atoms missing (vacant) from the lattice and these vacancies are occupied by either interstitial atoms or impurities atoms. A study done by *Kim* [3.8] describes microdefects, which result from the out diffusion of the point as defects. Silicon fibres grown by the pedestal technique witnesses no defects around the outer rims of the fibres but micro-defects appear uniformly in the centre of the fibres. Investigation by *Takagi* [3.9] on sapphire fibres shows that the number of microvoids in the fibre is proportional to the pull rate of the fibre. The fibre turned opaque at a high pull rate of 29cm/h. When pulled at 4.7cm/h, there was no sign of voids in the fibre. A measurement was made and the size of each void was about 5μm. Reducing the gas pressure within the growth chamber gave no signs of improvement. Defects were still appearing when the crystal was being grown at high pull rates. The investigation demonstrated that microvoid formation is greatly dependent of the temperature gradient of the melt.

Line defects are classified as edge dislocations and screw dislocations. Dislocations are the misalignment of atoms in the lattice. An edge dislocation results when there is an extra partial sheet in the structure at the edge. A screw dislocation results when a cut is made through part of a crystal and the edge is displaced upward. Both edge and screw dislocations can take place concurrently. This is also known as mixed dislocations. One major contributing factor of dislocations is the elastic shear strain. If the shear strain is below its critical amount, dislocation will not happen [3.10]. Non-homogeneous temperature distributions from the melt to the fibre, step changes in lattices constants, and the presence of strain gradients and inclusions are the sources of shear strain. Work by *Tang* [3.11] on Barium Metaborate (BaB_2O_4) SCF grown using the LHPG method, showed inclusions in the fibres. The major cause of inclusions in fibres is the process of supercooling ahead of the interface. A number of reasons can attribute to the process of supercooling, e.g. inconsistent laser power, and mechanical discontinuity within the system.

3.3 Spectroscopy Characterisation of Rare Earth Ions

3.3.1 Rare Earth Characteristics

The demand for rare earth ion based optical materials has been increasing through the years, the bulk of which is for optical communication. The great attraction of rare earth research is largely due to erbium which has an emission band around 1500nm to 1600nm; this region of wavelengths corresponds very well with the optical communication sectors. Larger bandwidth and long optical storage time make erbium favourable for optical communication devices. Telecommunications is not the only field interested in rare earth luminescence. Other areas such as fibre sensors, laser materials, display, data storage and many more also employ rare earths as their mediators.

Rare earth ions are mainly divided into two groups: lanthanides and actinides. Lanthanide ions are the main focus in this work. Having an atomic number 58 (Cerium), through 71 (Lutetium), lanthanides are commonly used as activators in crystalline hosts. Erbium (Er) [3.12], Holmium (Ho) [3.12, 13], Neodymium (Nd) [3.14] and Thulium (Tm) [3.15], are some example of lanthanide ions that are common in the research field. These lanthanides, when incorporated into crystalline hosts, will either exist as bivalent (2+) or trivalent (3+) ions. Samarium (Sm) and Europium (Eu), are the only reported bivalent ions that exhibit luminescence. However, it is the trivalent ions that are the most stable and are widely suitable for optical devices. They are also most interesting. They are characterised by a basic electron configuration of $6s^2$ and $5d^1$ and a progressive filling of the $4f$ shell. The two that are in the rare earths' list which are not held by this rule are Europium (Eu) and Ytterbium (Yb) which do not have a 5d shell. Transitions between the $4f$ energy levels are where most devices such as lasers doped with trivalent rare earth ions operate. The partial shielding of the $4f$ electrons by its surrounding 5s and 5p electrons explains the richness of the rare earths' optical spectrum. The result of this effect causes the $4f - 4f$ transitions of the rare earth ions to be relatively sharp, narrow and the emission highly efficient. Other consequences from this shielding effect are that the $4f - 4f$ transitions become free ion-like; electron to phonon coupling becomes weak in relation to different types of host, and has small host-

induced splitting. The small splitting effect is due to the positions of the rare earth electronic levels which are greatly influenced by the spin-orbit interaction rather than by the applied host. Although the rare earth ions are relatively independent to the hosts, stark splitting and broadening are affected by the host material [3.16]. These rare earth ions produce emissions from the visible to the infrared region.

3.3.2 Spectroscopy Characteristics of Er^{3+} and Yb^{3+} Ion

Having an atomic number of 68, an atomic weight 167.3 and an electron configuration [Xe] $4f^{12}6s^2$, [Xe] is the closed shell electronic configuration of xenon. Erbium on its own is a metal, but when doped into different hosts, will usually take the trivalent charge state of [Xe] $4f^{11}$. Er^{3+} has been extensively researched; due to its popularity in the area of optical amplification. This attraction comes from the $^4I_{13/2} \leftrightarrow {}^4I_{15/2}$ transition (ΔE = 6500 cm^{-1}, at λ = 1.54μm) which is in the third telecommunications window (termed as the ultra low-loss window) ranging from 1450nm to 1600nm. Therefore, Er^{3+} doping can produce the optical amplification in this region, leading to devices with high gain, low insertion loss and a board bandwidth [3.17, 18] which is highly desirable in all amplification systems. Another critical factor for Er^{3+} dominating in optical communications is its $^4I_{13/2}$ amplifying transition level. Due to the large energy gap from the next lower level (therefore permitting high population inversions within steady-state conditions and under the influence of a reasonable pump source) this state has a long emission lifetime. For Ge/P-silica and Silicate L22 fibres, when doped with Er^{3+}, a gain as high as 20dB is attainable for the former and the latter has a lifetime of 14.5ms [3.19]. Erbium-doped fibre amplifiers (EDFA) have revolutionised the optical amplification industry making it possible to have long-haul optical communication. Er^{3+} is an important material used in the optoelectronics and this area of technology has been growing rapidly. Semiconductors like silicon and gallium nitride have also been used to host rare earth ions, particularly Er^{3+} ions. Er^{3+} doped crystalline silicon is able to produce emission at 1.5μm but the time constant of the non-radiative energy back-transfer (microseconds) is much shorter than the Er^{3+} luminescence (milliseconds) [3.20]. This is due to the insolubility of the erbium ions in the silicon host. When Er^{3+} is doped in amorphous silicon, solubility is no longer an issue [3.21] and that greatly improves the luminescence. Gallium nitride doped with Er^{3+} is optically active in the

third telecommunication window [3.22]. The popularity of Er^{3+} led to the development of Er^{3+} doped fibre lasers at low-loss windows and it was reported that lasers doped with Er^{3+} have low-threshold, high-power and narrow-linewidth [3.23, 24, 25]. Er^{3+}-doped materials for high intensity sources (~ 3μm) is applicable to by the medical field because the strong absorption at this wavelength by water. These lasers are able to penetrate skin tissue to just few micrometers, allowing precision incisions in the operating theatre [3.26]. Being an effective laser in the IR region, Er^{3+} and many other trivalent rare earth ions also show great potential to operate as upconversion lasers in the visible regions (red, blue and green) due to their energy level systems. Using the upconversion process in rare earth ions to generate coherent visible light has been investigated by many. When $YAlO_3$ is doped with Er^{3+} [2.26], it is able to produce lasing at 550nm on the $^4S_{3/2} \rightarrow {}^4I_{15/2}$ transition which is in the green region. Similar lasing action at 550nm is observed in Er^{3+} doped $YLiF_4$ [3.27] pumped with an 800nm dye laser. The output power produced from these upconversion lasers consist of semi-random pulses of 80-150ns duration and is able to achieve average output lasing powers of 0.5 to 5mW. Having a fluorescent lifetime in the millisecond range, Er^{3+} doped silica composites or crystalline hosts are commonly used as temperature sensors. Excited by an infrared source, doped sensor probes are used to measure temperature changes by employing techniques such as fluorescence decay [3.28, 29]. The range of temperature measured greatly depends on the host material. Silica composites have a lower melting point (~1000K) as compared to many crystalline hosts (for YAG ~2200K). Significant changes in lifetime decay are observed when Er^{3+} of different concentrations is doped into silica. High content (4370ppm) doping produces a decay time of ~4ms where lower content (200ppm) has a much longer decay time of ~10ms [3.28]. Er^{3+} has shown to be a good transducer in the area of temperature sensing and more could be explored in the area of thermometry. Figure 3.3 shows the schematic of the 4*f* erbium energy level, of the free ion and in a solid host.

Yb has an atomic number of 70, an atomic weight of 173, and an electron configuration of [Xe] $4f^{14}6s^2$. Yb has a cubic structure, does not exhibit anisotropic optical properties and behaves a little like a transition metal. Yb^{3+} is found to be the smallest of the trivalent lanthanides. It has a simple energy level diagram of only one excited state manifold $^2F_{5/2}$ and a ground state manifold $^2F_{7/2}$. These two manifolds

are the only two states in the 4*f* transitions. The energy level of Yb^{3+} consists of three crystal field levels in the excited state manifold, and four at the ground state manifold. When Yb^{3+} (0.006 mol%) was first incorporated into silicate glass for application as a rare earth doped laser, absorption bands in the ultraviolet and infrared regions were observed: in the ultraviolet region, a weak peak at 310nm and a strong peak at 220nm are seen; and in the infrared regions, peaks appear at 914nm, 946nm and 976nm. The 976nm peak in the absorption band was the strongest and had an absorption coefficient of 8 cm^{-1}. The emission band measurement shows that luminescence takes place at 1015nm when excited in the ultraviolet region [3.30]. When Yb^{3+} was doped into a crystal material such as YAG, the fluorescence emission fell at ~1030nm [3.31]. Yb^{3+} is commonly used as sensitiser for other rare earth ions. Typically an Er^{3+} laser has relatively low output efficiency ~0.1% [3.32] and power output in the region of μW [3.33]. The solution to this is to co-dope with Yb^{3+}. The first report of Yb^{3+} sensitized Er^{3+} was in a glass silicate laser. 15 wt% of Yb_2O_3 and 0.25 wt% of Er_2O_3 were doped in silicate glass which resulted in an increased upper laser population [2.18]. Since Yb^{3+} does not introduce additional absorption bands at 1.5μm when co-doped with Er^{3+} in silica fibres, it permits a healthy absorption at pump power wavelengths. Moreover, there will be inhomogeneous broadening of the Yb^{3+} $^2F_{5/2}$ multiplet resulting in a wide absorption band, typically ±200nm centred around 930nm [3.34], which in turn allows for a wider range of pump excitation sources to be used [3.35]. Based on the fluorescence intensity ratio method, Yb^{3+} doped silica fibre temperature sensors proved to be reliable and were able to attain an accuracy of ±1°C, with an average standard deviation of 0.6°C, in the 20°C to 600°C temperature range [3.36]. It was observed that the $^4F_{5/2} \rightarrow {}^4F_{7/2}$ manifolds have three emission peaks at 916nm, 976nm and 1030nm when a laser diode pump source at 810nm was used. When silica fibre sensors with dopant concentrations of Yb^{3+}: 2500ppm were investigated in terms of the fluorescence lifetime decay, the work showed that the two $^2F_{5/2}$ levels at 916nm and 976nm had a lifetime decay of 357μs and 873μs respectively [3.37]. After an annealing process of 100hrs at 700°C, it was shown that there was an increase in lifetime decay to 548μs for the former and the latter to 914μs. The advantages of using Yb^{3+} as a sensitiser also created an interest in co-doping it with Er^{3+} for optical sensors [3.38]. Er^{3+}+Yb^{3+} co-doped fibre sensors which had undergone thermal annealing demonstrate that the lifetime drift was lower when compared to fibres such

as Er^{3+}, Nd^{3+}, Tm^{3+} and Yb^{3+}. Er^{3+}+Yb^{3+} co-doped Al_2O_3 crystal fibres were used as thermometry sensors at high temperatures. Co-doping Yb^{3+} increased the energy transfer for Er^{3+} and this resulted in stronger intensity upconversion in the visible region of the blue, green and red [2.23]. Upconversion processes were observed when these rare earth ions were doped in Al_2O_3 and were exploited an the intensity based temperature process [2.23]. This system witnessed a strong red emission, $^4F_{9/2}$, of the Er^{3+} ion which would be suitable for temperatures up to ~1423K and for the green, $^4S_{3/2}$, which was weaker would be suitable for temperatures up to ~1323K. Figure 3.4 shows the schematic of the 4*f* ytterbium energy level, as a free ion and in a solid host.

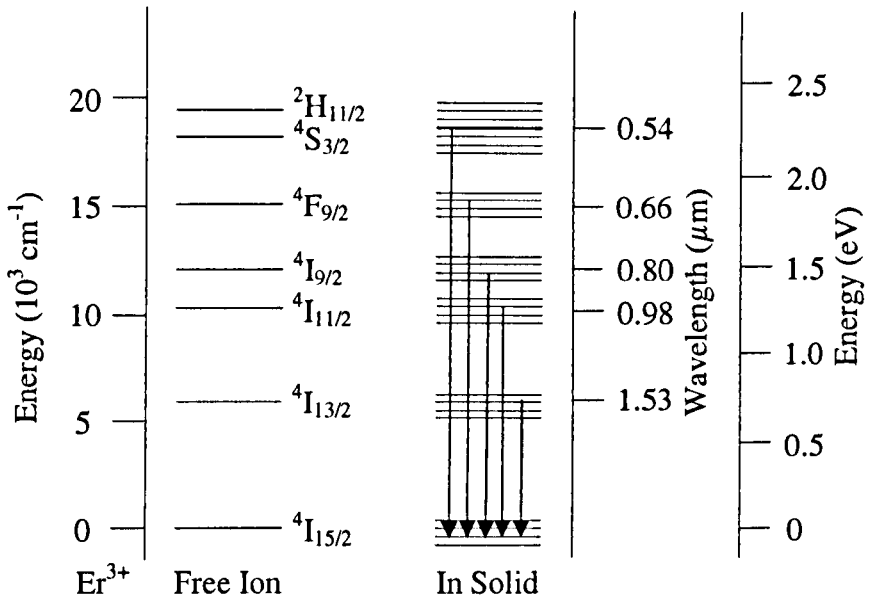

Figure 3.3 – Energy level of Er^{3+} ion, free and solid host

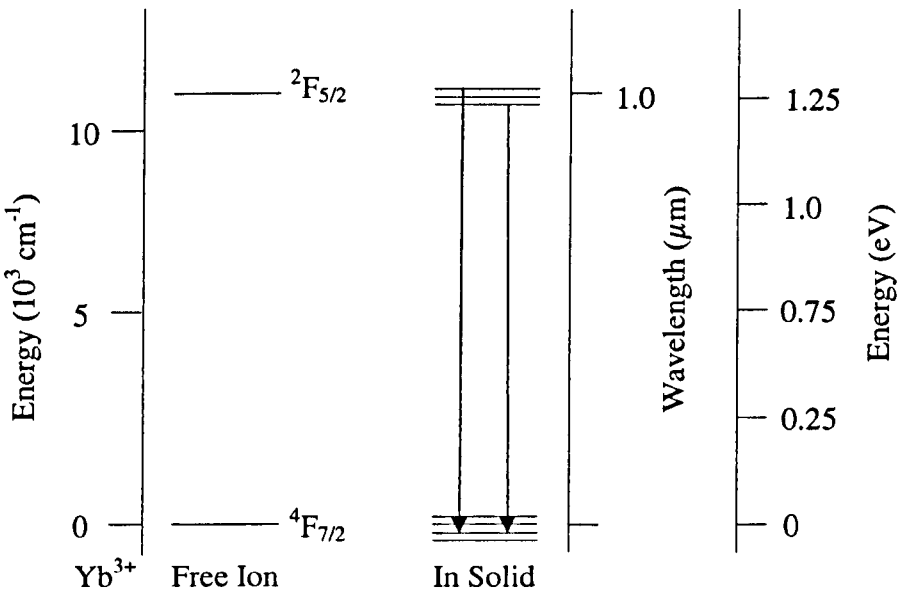

Figure 3.4 – Energy level of Yb^{3+} ion, free and solid host

3.3.3 Energy Transfer Between Ions

Energy transfer between rare earth ions may occur in a fibre under the influence of an external source applied to it, for example a laser source. In some cases, more than one ion could be involved in this process contributing to either the absorption or emission of a photon. Considering first single ion processes, a simple description of this process is that absorption occurs when a photon is absorbed promoting an ion from its ground state to one of its excited states. When more than one ion is involved, this process changes. The level of concentration in the host naturally affects the probability of ion-ion interaction. Under low dopant levels, the ions are evenly distributed and the separation between each ion is relatively large in the host material. Increased concentration levels may result in clustering of the ion distribution and the distance between each ion is then greatly reduced. The smaller separation distance will encourage an increase in the ion-ion interactions and this may result in energy transfer.

Sensitised luminescence is one of the common ion-ion interactions. This process involves a donor ion (sensitizer) and an acceptor ion (activator). When excited, the sensitizer transfers its energy to the activator followed by the emission of fluorescence. This process is common when Er^{3+} is co-doped with Yb^{3+}. In this case, the Yb^{3+} is the sensitizer and Er^{3+} the activator. See Figure 3.5. In the case of a silica fibre laser, the absorption bandwidth of Er^{3+} at $^4I_{13/2}$ – $^4I_{15/2}$ is relatively narrow [3.34]. Co-doping with Yb^{3+} improves the performance by increasing the absorption cross-section. It then has a broad absorption band from 875 – 1000nm which overlaps the Er^{3+} absorption band [3.34, 3.39]. When Yb^{3+} is excited with a pump source within its absorption band, it is promoted from the ground state level $^2F_{7/2}$ to the $^2F_{5/2}$ manifold, this energy can be then be transferred to the $^4I_{11/2}$ manifold of the Er^{3+} and followed by a non-radiative decay to the $^4I_{13/2}$ lasing level of the Er^{3+}, resulting in emission.

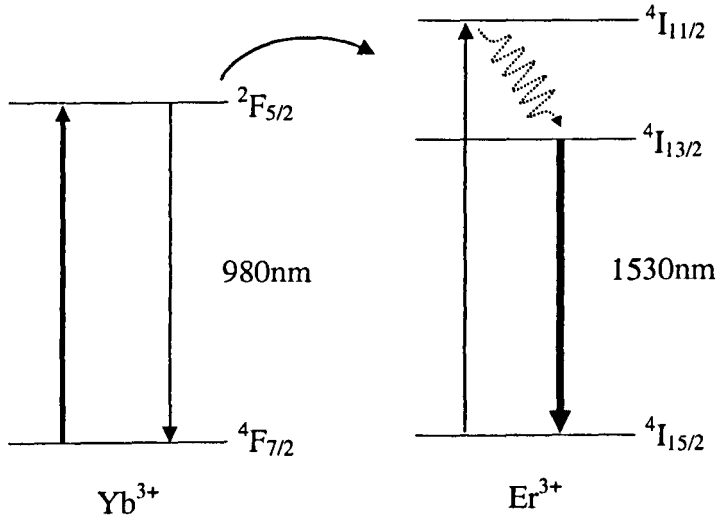

Figure 3.5 – Energy transfer between Er^{3+} and Yb^{3+} ions

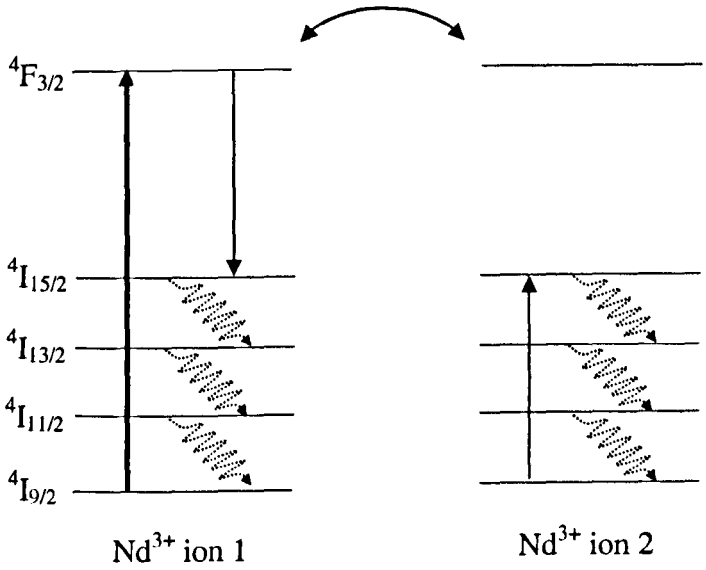

Figure 3.6 – Cross relaxation in Nd^{3+} ions. Interactions between the two ions

When an ion is excited, part of its energy can be transferred to a neighbouring ion. This process is known as cross relaxation. Such a process is common in Nd^{3+} doped materials [3.19, 40]. When an ion from the ground level $^4I_{9/2}$ of Nd^{3+} is excited to the $^4F_{3/2}$ level, part of its energy is transferred to a nearby ion when both of the ions have a similar energy gap. See Figure 3.6. A quick non-radiative decay to the ground state takes place for both ions from the $^4I_{15/2}$ state since the energy levels near the ground state are very close [3.19].

Upconversion processes are another form of ion-ion interactions. These processes can be classified into cooperative energy transfer upconversion, sequential two-photon absorption upconversion, and photon avalanche upconversion. Upconversion is form of energy transfer in which the emission wavelength is shorter than the absorption wavelength. A brief account of the three upconversion processes will be illustrated in the section below. For simplicity, a basic three-level scheme will be used to describe each process. Two extra metastable levels, 2a and 3a, are added into the three-level system for a more accurate representation of a typical rare earth energy level.

In cooperative energy transfer upconversion, the mechanism of the energy transfer in a singly doped crystal and co-doping with another ion is slightly different. As mentioned in the earlier section, Yb^{3+} is commonly used as the sensitiser because of its simple energy level configurations which only has one excited state with its large absorption cross section at about $1\mu m$. Singly doped rare earths, other than Yb^{3+}, have an intermediate metastable state. That is where a photon is absorbed, followed by non-radiative relaxation. When excited by a pump source, the donor ion and acceptor ion, responding to the photon wavelength, each absorb a photon and is then promoted to the intermediate metastable level (level 2a). See Figure 3.7. For the donor ion, the population in level 2a will experience a rapid non-radiative decay to its metastable level (level 2). At level 2, the donor ion can either decay radiatively to the ground state (level 1) or its energy will be transferred to the acceptor ion. For the acceptor, the energy transfer will aid the ion in level 2 to be promoted to the next intermediate metastable level (level 3a). The population accumulated in level 3a quickly decays to level 3, followed by a radiative transition in the visible. In the case of YAG:Er^{3+} [3.41] (see Figure 3.8a for schematic) strong absorption is observed for the $^4I_{15/2} \rightarrow {}^4I_{9/2}$ transition and emission from the level $^4S_{3/2}$ (green region) is evident

when an excitation source of the infrared region is used corresponding to its absorption band. The upconversion is initiated by promoting the donor ion (Er^{3+}-1) and the acceptor ion (Er^{3+}-2) from $^4I_{15/2}$ (level 1) to the intermediate metastable level, $^4I_{9/2}$ (level 2a), followed by a rapid non-radiative decay to $^4I_{11/2}$. Interaction between the two causes the acceptor ion to be further promoted to the next state, $^4F_{7/2}$ (level 3a). The metastable state $^4S_{3/2}$ (level 3) is quickly populated by non-radiative transitions from the $^4F_{7/2}$ state and upconversion fluorescence then takes place at a wavelength of 560nm. The cooperative energy transfer upconversion mentioned in YAG:Er^{3+} can repeat several times with the same acceptor, where the number of repetitions is dependent on the number of intermediate metastable states and metastable states in the acceptor. $BaYF_5$:Er^{3+} [3.42] has shown very efficient upconversion of 1.5μm radiation into visible wavelengths. This multi-step cooperative energy transfer upconversion process involves two Er^{3+} ions as a donor and an acceptor. Under the radiation source of 1.5μm at room temperature, $BaYF_5$:Er^{3+} produces upconversion fluorescence from the near infrared to the visible regions. See Figure 3.9. Energy transfer steps at 1-2-3-5-6 are observed. When the two Er^{3+} ions are excited, both the donor and acceptor ions are promoted simultaneously to the $^4I_{13/2}$ level. The acceptor is then excited to $^4I_{9/2}$, followed by a non-radiative decay to $^4I_{11/2}$ by energy transfer from the donor ion which results in an emission at 990nm. Subsequent emissions in the system are of similar manner. Er^{3+} doped phosphors exhibit similar multi-step cooperative energy transfer upconversion and the energy transfer steps are at 1-2-4-6 [3.43]. See Figure 3.9.

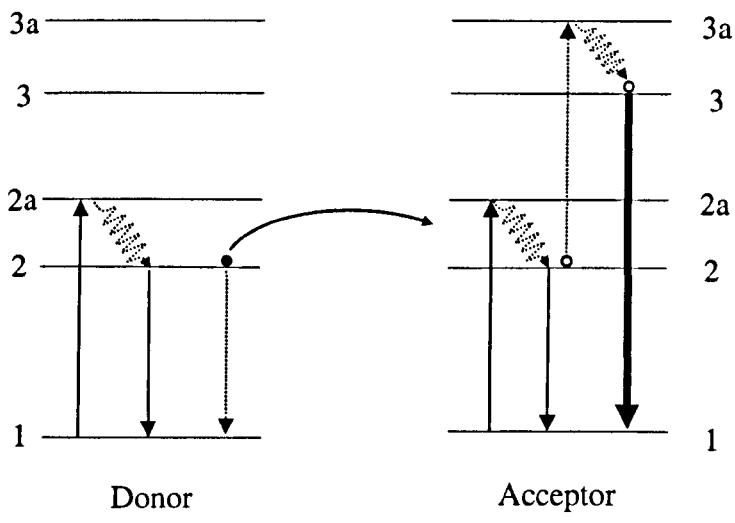

Figure 3.7 – Cooperative energy transfer upconversion

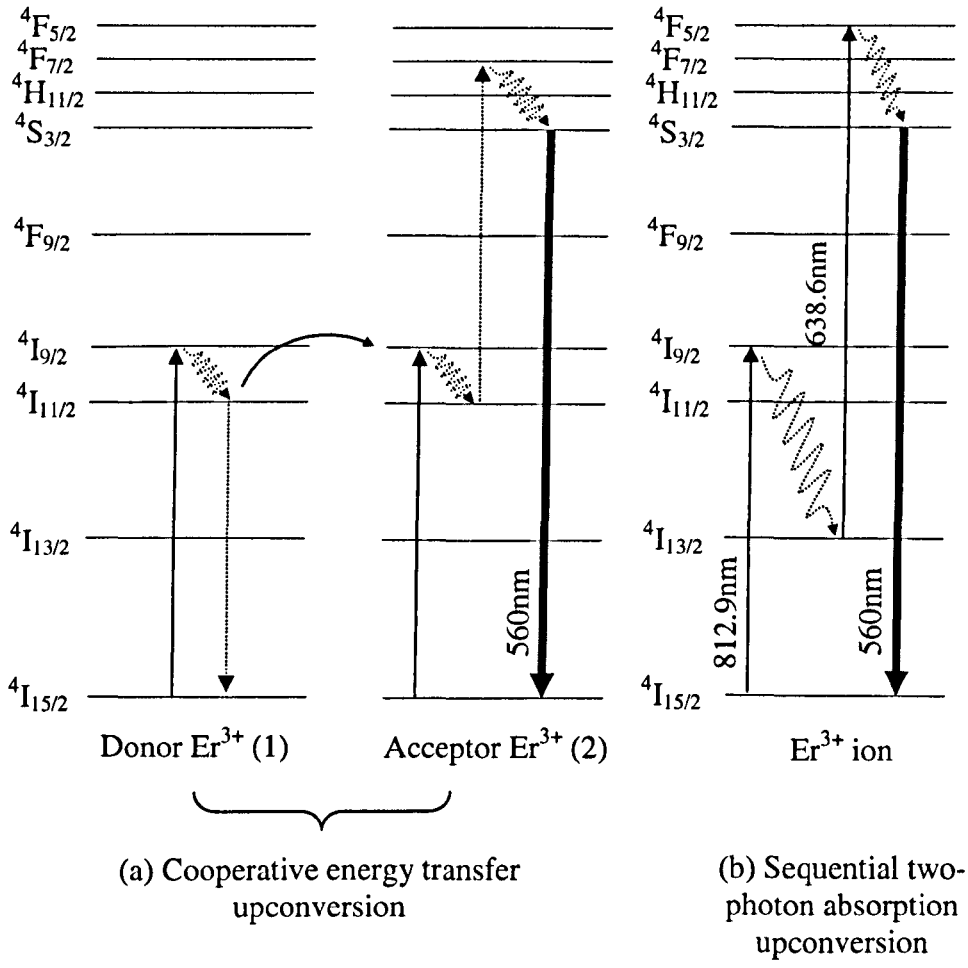

Figure 3.8 – (a) Cooperative energy transfer upconversion in Er^{3+}:$Y_3Al_5O_{12}$, Donor – Er^{3+} (1) and Acceptor – Er^{3+} (2) (b) Sequential two-photon absorption upconversion with 812.9nm – 'a' and 638.6nm – 'b' pumps

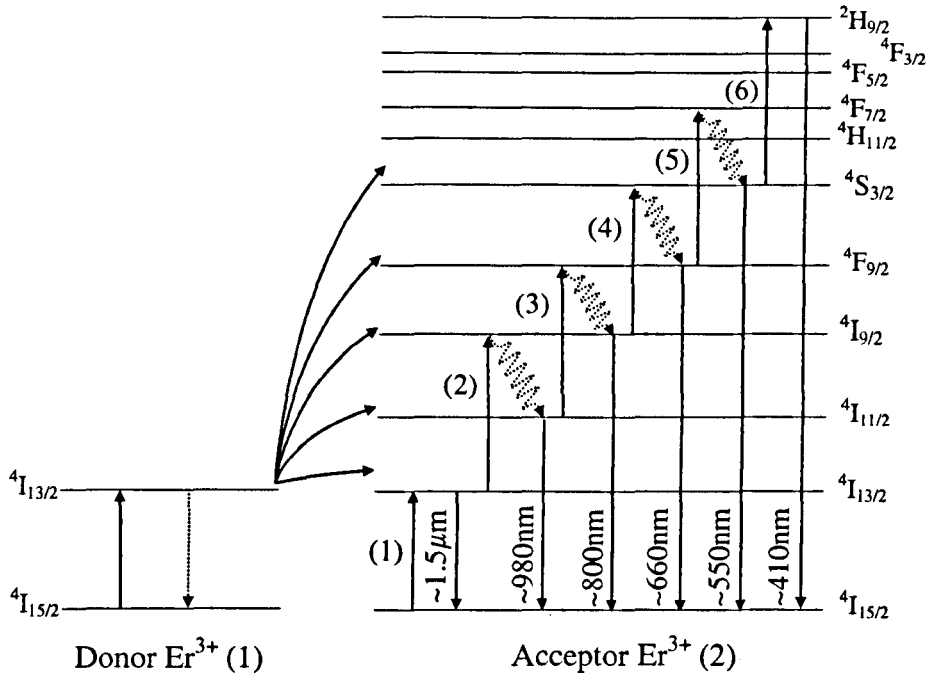

Figure 3.9 – Multi-step cooperative energy transfer upconversion Er^{3+}-Er^{3+} resulting near infrared to visible emission

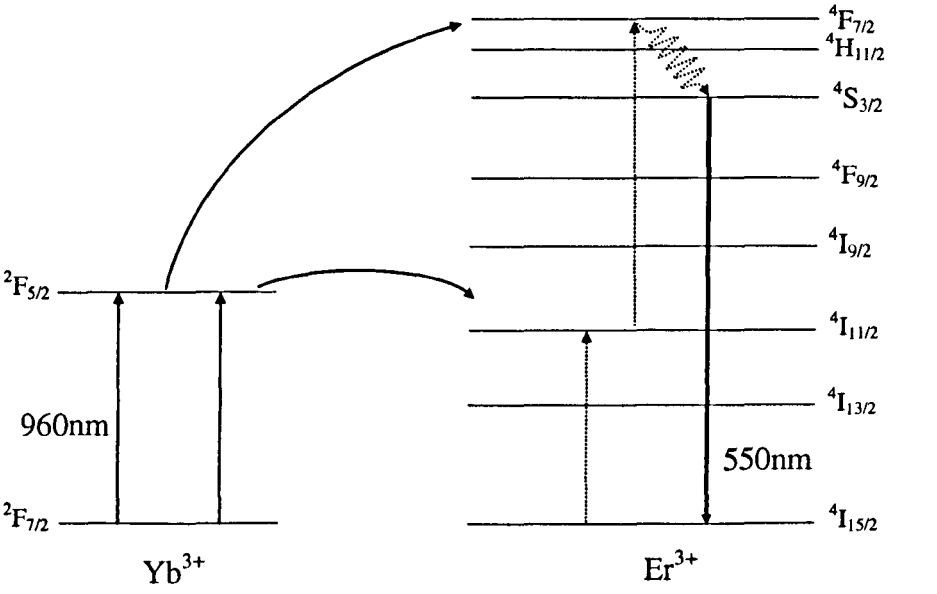

Figure 3.10 – Yb^{3+}+Er^{3+} doped in BaY_2F_8. Cooperative energy transfer upconversion was observed with emission at the green region 550nm

Co-doping upconversion has being extensively investigated through the years. Much of it was done with Yb^{3+} as a 'sensitiser' or donor. The excited state, $^2F_{5/2}$, matches the energy level $^4I_{11/2}$ in Er^{3+} making it a desirable sensitiser for Er^{3+}. When excited with a pump source the ions from the $^2F_{7/2}$ ground state are excited to the $^2F_{5/2}$ state and by cooperative energy transfer, the energy of the ions from the $^2F_{5/2}$ state are transferred to the Er^{3+}. Another of the Yb^{3+} ions promotes the Er^{3+} from its first excited level to its metastable state, $^4I_{11/2}$. Both the second Yb^{3+} ion from the $^2F_{5/2}$ state and Er^{3+} ion in the metastable state through cooperative energy transfer, further promotes the Er^{3+} ion to the $^4F_{7/2}$ state. The emitting state, $^4S_{3/2,}$ is rapidly populated by non-radiative decay from the short lived $^4F_{7/2}$ state. See Figure 3.10. Upconversion fluorescence in the green region (550nm) is observed when Yb^{3+} + Er^{3+} are doped in BaY_2F_8 [3.44]. The process of cooperative energy transfer observed in BaY_2F_8 doped with the sensitiser and the acceptor is as mentioned above.

A few main factors affect the efficiency of cooperative energy transfer upconversion between ions. Firstly, the dipole to dipole interaction strength varies as $1/r^6$, where r is the distance between the two ions. Ion-to-ion separation must be extremely small before energy can be effectively transferred, thereby enhancing the efficiency of the upconversion. Secondly, this small separation distance between ions suggests the need for a high concentration of rare earth dopant. The third factor is that high intensity pumping is essential for energy transfer within the system. This is where energy migrates between donor ions within the crystal lattice before locating an acceptor [3.44, 45]. The resulting effect may lead to energy migration where the excited ion would transfer its energy to the ground state by non-radiative decay. In most cases regarding rare earths in crystals, exponential decay in the transition $3 \rightarrow 1$ is apparent, but when non-exponential decay occurs, it signifies that the donor-acceptor pairs density distribution across the crystal are not consistent [3.44].

The next upconversion process is sequential two-photon absorption upconversion. In this process, two excitation sources are required. See Figure 3.11. Photon 'a' excites the ion from level 1 to level 2a. It experiences a rapid relaxation occurring through multi-phonon non-radiative decay from the intermediate metastable level 2a to the next lower level 2. In this level, there is a possibility of multi-phonon non-radiative decay to level 1. However, the occurrence of non-radiative transitions is unlikely

because of the large energy gap between levels 1 and 2 [3.44]. Before the ion, decays to level 1, photon 'b' is absorbed and the ion is excited to level 3a. Non-radiative decay from this level then populates level 3. Visible emission with wavelengths much smaller than the two pump wavelengths are observed from transition 3 → 1. In most rare earths the storage time at level 3 is ~100μs which also has a high emission cross-section from this level to the ground level [3.44]. In experiments with $Y_3Al_5O_{12}:Er^{3+}$ [3.41], two lasers at 812.9nm and 638.6nm can be employed to produce upconversion fluorescence at 560nm. See Figure 3.8b for energy diagram of $Y_3Al_5O_{12}:Er^{3+}$. Tuning the first laser to its optimum wavelength (812.9nm), excites the first ion from the $^4I_{15/2}$ to $^4I_{9/2}$ state, rapid non-radiative relaxation to $^4I_{13/2}$ is observed. Before decaying into $^4I_{15/2}$, photon 'b' is absorbed (638.6nm) promoting the ion to a high lying excited state, $^4I_{9/2}$. The ion is then induced to $^4F_{5/2}$ which quickly experiences a non-radiative decay to the $^4S_{3/2}$ state. Transition from this state to the $^4I_{15/2}$ exhibits a fairly strong emission at 560nm. When the red laser is blocked, green emission is still evident due to cooperative energy transfer upconversion. However, the intensity of the transition at 560nm drops by a factor of 20.

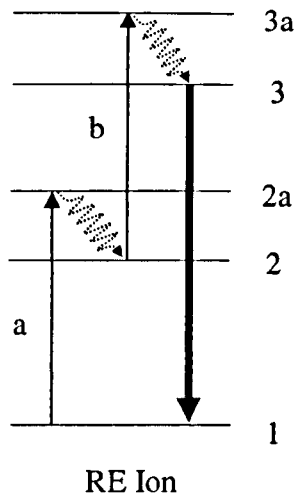

Figure 3.11 – Two sequential two-photon absorption upconversion. 'a' and 'b' photons are excited by two pump sources

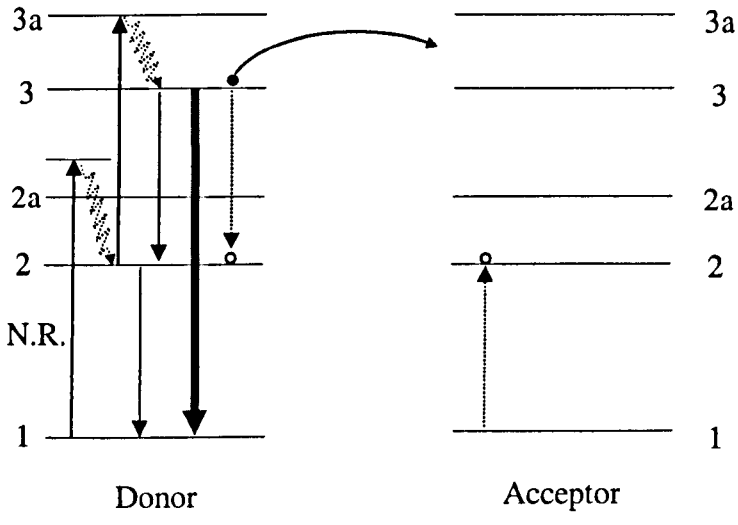

Figure 3.12 – Photon avalanche upconversion. N.R. represents non-radiative absorption

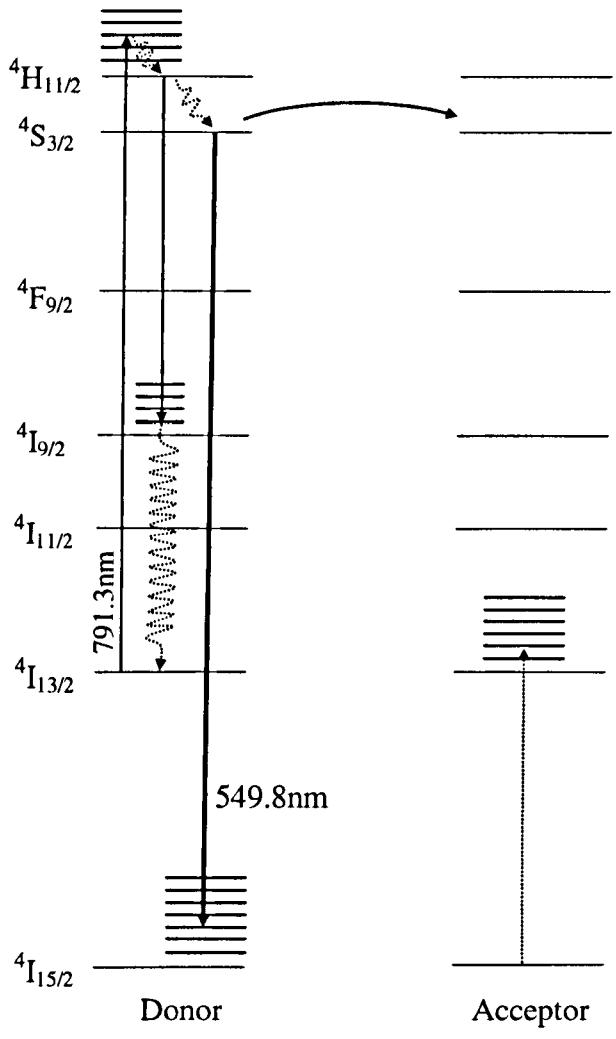

Figure 3.13 – Er^{3+}:$YAlO_3$ Photon avalanche upconversion energy diagram

The most efficient amongst the three upconversion processes discussed in this work is photon avalanche upconversion. There are three prominent characteristics that are found in this process, the first being a well-defined intensity threshold. Secondly, rapidly increasing absorption and an increase in fluorescence from the upper excited state by many orders-of-magnitude is evident when the pump power is increased above threshold. Thirdly, this process is strongly dependant on pump intensity: response time is longest for pump intensities just slightly above threshold [3.46]. The process in this system starts off by absorption from an excited state. Prior to applying any excitation source to the system, an assumption is made that the donor ion is at the level 2 metastable level, and the acceptor ion is at level 1 (ground state). See Figure 3.12. For the donor ion to be in level 2 it is assumed to be due to non-resonant absorption by a pump photon. A pump photon is then resonant with the transition between the 2 and 3a states and, in this case, not with the 1→2a transition. Upon excitation, donor ions in level 2 will be promoted to level 3a followed by rapid non-radiation relaxation to level 3. In the last two processes, radiative transitions 3→1 will occur in the form of visible emission. At the same time a non-radiative decay from 3→2 can occur where part of the energy is transferred to a neighbouring acceptor ion. Such energy transfer is commonly known as cross relaxation. The acceptor ion is then promoted into level 2. The sharing of energy between the two results in having a pair of ions in the metastable level. At this point, the two ions are ready for further absorption of the pump source. This increasing process, from one to two ions, is due to absorption and subsequent energy transfer at the metastable state, level 2, and is the foundation of the photon avalanche upconversion process. More ions can start to populate this level under a sufficiently strong pump, with the initial one to two ions, it can increase geometrically from 1 to 4, 4 to 8, and so on. In the case of Er^{3+}:$YAlO_3$ lasers [3.47], non-resonant absorption promotes ions from the donor ion metastable state $^4I_{15/2}$ to $^4I_{13/2}$, which has a radiative lifetime of 7.2ms. In this work [3.47], optical excitation wavelengths between 787nm and 796nm were used to resonate with the transition between the $^4I_{13/2}$ and $^4F_{9/2}$ states. Through absorption, the ion in the metastable state can then be promoted to the $^2H_{11/2}$ state, where relaxation to the $^4S_{3/2}$ is rapid and upconversion fluorescence is emitted at 549.8nm. Figure 3.13 shows the avalanche process, where energy transfer takes place between the $^2H_{11/2}$ state of donor ions and the acceptor ion in the ground state. Part of the energy from the donor ion is then transferred to the acceptor ion through cross

relaxation, in turn promoting it from the ground state to the $^4I_{13/2}$ state. Donor ions will then relax to $^4I_{9/2}$. From this state, it will subsequently relax to its metastable state, $^4I_{13/2}$. The process repeats itself again, now having two ions in the metastable level, and absorption from the optical excitation will then promote them to the $^2H_{11/2}$ state where rapid non-radiative relaxation to $^4S_{3/2}$ is followed by upconversion emission in the green. The number of ions in the metastable state, because of absorption and subsequent energy transfers, will continue to increase geometrically. However, the photon avalanche upconversion process will only occur when it is above the pump threshold power. The requirement for this process to occur is when the rate of population is faster then the metastable state lifetime.

Considering the various processes, a few issues need to be considered while working with these processes. One of which is loss in the system. Excited state absorption (ESA) is not desirable, especially in an amplification system. This happens when an ion in the excited state is promoted to an even higher state by resonant absorption. Both in amplification and upconversion processes, Er^{3+} ions are usually promoted to intermediate metastable states, and usually these states are populated before amplifying or lasing transitions. One way to reduce ESA is to choose the correct pump source. Using a pump source at 800nm [3.19, 29] weakens the ESA process. Although two photons are produced first by ground state excitation (GSE) and ESA, only one ion is excited to $^4I_{9/2}$. In contrast, when pumping at about 980nm in a region that is free from the pump ESA, no ESA is observed in Er^{3+} doped glass [3.19, 29]. In any system, unwanted radiative transition/decays are not desirable, and non-radiative relaxation is another mechanism that will reduce the efficiency of the system. For example, the metastable $^4I_{13/2}$ level could experience rapid non-radiative multi-phonon decay to the ground state which greatly reduces the intensity and decreases its fluorescence. The process is caused by the interaction between the electrons and the lattice of the crystal [3.48]. Concentration quenching is also detrimental. It reduces the quantum efficiency in the ion. This happens when the dopant concentration is high and a clear signature that concentration quenching is present is when the lifetime at the excited states shortens. When calcium metaphosphate $Ca(PO_3)_2$ glass is doped at 10mol% Er^{3+}, its decay time is as low as ~ 200μs from the $^4I_{13/2}$ level whereas at 0.1mol%, its decay time is ~ 4ms [3.49].

The general considerations when working with Er^{3+} ions are briefly mentioned above. The concentration level chosen greatly depends on the application. In the area of telecommunication systems, high dopant levels are never desirable because it greatly reduces efficiency. $^4I_{13/2}$ is the metastable state in which Er^{3+} is at the transition level producing gain around 1500nm which is the optimum telecommunication wavelength. Therefore, any processes other than the stimulated emission into the optical signal will reduce the efficiency of the amplification system. Its pump wavelength, host, as well as dopant concentration have a significant role in this system. Although upconversion processes are never desirable in the telecommunication industry, they have been found to be of great interest in other areas. Er^{3+} doped laser emissions in the visible regions through upconversion processes are one of the many that have drawn great interest. The section above has succinctly demonstrated that there is great potential in Er^{3+} and investigation in this field has yet to come to a state of exhaustion.

3.4 References

[3.1] R. S. Feigelson, *Pulling Optical Fibers*, J. Cryst. Growth, **79**, 1-3, 669, 1986

[3.2] K. A. Jackson, *Theory of Melt Growth – Crystal Growth and Characterization*, R. Ueda and J. B. Mullin (Eds), 1975

[3.3] S. A. Kprela, J. Ni, A. Chait and M. Kassemi, *Radiative Heat Transfer in Fiber Drawing and Crystal Pulling*, **165**, 4, 455, 1996

[3.4] T. Surek and B. Chalmers, *The Direction of Growth of the Surface of a Crystal with its Melt*, J. Cryst. Growth, **29**, 1, 1, 1975

[3.5] A. B. Dreeben, K. M. Kim and A. Schujko, *Measurement of Meniscus Angle in Laser Heated Float Zone Growth of Constant Diameter Sapphire Crystal*, J. Cryst. Growth, **50**, 1, 126, 1980

[3.6] M. M. Fejer, *Single Crystal Fibers: Growth Dynamics and Nonlinear Optical Interactions*, PhD Thesis Stanford University, 1986

[3.7] J. H. Sharp, T. P. J. Han, B. Henderson, R. Illingworth and I. S. Ruddock, *Dopant Incorporation in Single-Crystal Fibre Growth by the Laser-Heated Miniature Pedestal Growth Technique*, J. Cryst. Growth, **131**, 3-4, 457, 1993

[3.8] K. M. Kim, *Microdefects in Small-Diameter Silicon Crystal Grown by the Pedestal Technique*, J. App. Phys., **50**, 2, 1135, 1979

[3.9] K. Takagi and M. Ishii, *Crystal Growth of Sapphire Filaments by a Laser-Heated Floating Zone Technique*, J. Mat. Sci., **12**, 3, 517, 1977

[3.10] J. C. Brice, *Crystal Growth Processes*, John Wiley and Sons New York, 1986

[3.11] D. Y. Tang, R. K. Route and R. S. Feigelson, *Growth of Barium Metaborate (BaB_2O_4) Single Crystal Fibres by the Laser-Heated Pedestal Growth Method*, J. Crys. Growth, **91**, 1-2, 81, 1988

[3.12] L. F. Johnson, H. J. Guggenheim, T. C. Rich and F. W. Ostermayer, *Infrared-to-Visible Conversion by Rare-Earth Ions in Crystals*, J. App. Phys., **43**, 3, 1125, 1972

[3.13] M. Malinowski, Z. Frukacz, M. Szuflinska, A. Wnuk and M. Kaczkan, *Optical Transitions Ho^{3+} in YAG*, J. Alloy and Comp., **300-301**, 389, 2000

[3.14] H. G. Danielmeyer, *Progress in Nd:YAG Lasers, in Lasers*, Vol.4., 1976

[3.15] L. Esterowitz, R. Allen and R. Eckardt, *Cascade Laser Action in Tm:YLF*, Rare Earth Mod. Sci. Tech., 3, 1982

[3.16] A. J. Kenyon, *Recent Developments in Rare-Earth Doped Materials for Optoelectronics*, Prog. Quant. Elect., **26**, 4-5, 225, 2002

[3.17] E. Desurvire, J. R. Simpson and P. C. Becker, *High-Gain Erbium-Doped Traveling-Wave Fiber Amplifier*, Opt. Lett, **12**, 11, 888, 1987

[3.18] R. J. Mears, L. Reekie, I. M. Jauncey and D. N. Payne, *Low-Noise Erbium-Doped Fibre Amplifier Operating at 1.54μ*, Elect. Let, **23**, 19, 1026, 1987

[3.19] W. J. Miniscalco, *Erbium-Doped Glasses for Fiber Amplifiers at 1500nm*, J. Light. Tech., **9**, 2, 234, 1991

[3.20] J. Palm, F. Gan, B. Zheng, J. Michel and L. C. Kimerling, *Electroluminescence of Erbium-Doped Silicon*, Phy. Rev. B, **54**, 24, 17603, 1996

[3.21] T. Oestereich, C. Swiatkowski and I. Broser, *Erbium Luminescence in Doped Amorphous Silicon*, App. Phy. Lett., **56**, 5, 446, 1990

[3.22] T. M. Levin, A. P. Young, J. Schäfer, L. J. Brillson, J. D. Mackenzie and C. R. Abernathy, *Low-Energy Cathodoluminescence Spectroscopy of Erbium Gallium Nitride Surface*, J. Vac. Sci. Tech., **17**, 6, 3437, 1999

[3.23] L. M. Jauncey, J. T. Lin, L Reekie and R. J. Mears, *Efficient Diode-Pumped CW and Q-Switch Single-Mode Fibre Laser*, Elect. Lett., **22**, 4, 198, 1986

[3.24] R. J. Mears, L. Reekie, S. B. Poole and D. N. Payne, *Low-Threshold Tunable CW and Q-Switch Fibre Laser Operating at 1.55μm*, Elect. Lett., **22**, 3, 159, 1986

[3.25] L. M. Jauncey, L. Reekie, R. J. Mears and C. J. Rowe, *Narrow Linewidth Fibre Laser Operating at 1.55μm*, Elect. Lett., **12**, 3, 164, 1987

[3.26] D. Heifer, M. Frenz, V. Romano and H. P. Weber, *Fibre-End Micro-Lens System for Endoscopic Erdium-Laser Surgery Applications*, App. Phy. B, **58**, 4, 309, 1993

[3.27] W. Lenth, A. J. Silversmith and R. M. Macfarlane, *Green Infrared-Pumped Erbium Upconversion Lasers*, Adv. Laser Sci. 3, Proceeding of the Third International Laser Science Conference, **172**, 8, 1988

[3.28] Z. Y. Zhang, K. T. V. Grattan, A. W. Palmer, B. T. Meggitt and T. Sun, *Fluorescence Decay-Time Characteristics of Erbium-Doped Optical Fiber at Elevated Temperature*, Rev. Sci. Instrum., **68**, 7, 2764, 1997

[3.29] D. M. Henry, J. H. Herringer and N. Djeu, *Response of 1.6μm Er:$Y_3Al_5O_{12}$ Fibre-Optic Temperature Sensor up to 1520K*, App. Phy. Let., **74**, 23, 3447, 1999

[3.30] H. W. Etzel, H. W. Gandy and R. J. Ginther, *Stimulated Emission of Infrared Radiation from Ytterbium Activated Silicate Glass*, App. Opt., **1**, 4, 534, 1962

[3.31] L. F. Johnson, J. E. Geusic and L. G. Van Uitert, *Coherent Oscillations from Tm^{3+}, Ho^{3+}, Yb^{3+} and Er^{3+} ions in Yttrium Aluminum Garnet*, App. Phy. Let., **7**, 5, 127, 1965

[3.32] G. A. Ball and W. W. Morey, *Continuously Tunable Single-Mode Erbium Fiber Laser*, Opt. Let., **17**, 6, 420, 1992

[3.33] J. L. Zyskind, V. Mizrahi, D. J. DiGiovanni and J. W. Sulhoff, *Short Single Frequency Erbium-Doped Fibre Laser*, Elect. Let., **28**, 15, 1385, 1992

[3.34] W. L. Barnes, S. B. Poole, J. E. Townsend, L. Reekie, D. J. Taylor and D. N. Payne, *Er^{3+} -Yb^{3+} and Er^{3+} Doped Fiber Lasers*, J. Light. Tech., **7**, 10, 1461, 1989

[3.35] M. E. Fermann, D. C. Hanna, D. P. Shepherd, P. J. Suni and J. E, Townsend, *Efficient Operation of an Yb-Sensitised Er Fibre Laser at 1.56μm*, Elect. Let., **24**, 18, 1135, 1988

[3.36] E. Maurice, S. A. Wade, S. F. Collins, G. Monnom and G. W. Baxter, *Self-Reference Point Temperature Sensor Based on a Fluorescence Intensity Ratio in Yb^{3+}-doped Silica Fiber*, App. Opt., **36**, 31, 8264, 1997

[3.37] T. Sun, Z. Y. Zhang, K. T. V. Grattan and A. W. Palmer, *Ytterbium-Based Fluorescence Decay Time Fibre Optic Temperature Sensor Systems*, Rev. Sci. Instrum., **69**, 12, 4179, 1998

[3.38] T. Sun, Z. Y. Zhang and K. T. V. Grattan, *Erbium/Ytterbium Fluorescence Based Fiber Optic Temperature Sensor System*, Rev. Sci. Instrum., **71**, 11, 4017, 2000

[3.39] E. Cantelar, J. A. Muñoz, J. A. Sanz-García and F. Cusso, *Yb^{3+} to Er^{3+} Energy Transfer in $LiNbO_3$*, J. Condens. Matter., **10**, 39, 8893, 1998

[3.40] M. J. Weber, *Handbook of Laser Science and Technology Vol. 1 Laser and Masers*, CRC Press Inc, 1986

[3.41] A. Silversmith, *Upconversion Excitation of Green Fluorescence in Er:YAG*, J. Lumin., **60&61**, 636, 1994

[3.42] L. F. Johnson, H. J. Guggenheim, T. C. Rich and F. W. Ostermayer, *Infrared-to-Visible Conversion by Rare-Earth Ions in Crystals*, J. App. Phy., **43**, 3, 1972

[3.43] J. P. van der Ziel, L. G. Van Uitert, W. H. Grodkiewicz and R. M. Mikulyak, *1.5μm Infrared Excitation of Visible Luminescence in $Y_{1-x}Er_xF_3$ and $Y_{1-x-y}Er_xTm_xF_3$ via Resonant-Energy Transfer*, J. App. Phy., **60**, 12, 4262, 1986

[3.44] R. Scheps, *Upconversion Laser Processes*, Prog. Quant. Elect., **20**, 4, 271, 1996

[3.45] G. N. van den Hoven, E. Snoeks, A. Polman, C. van Dam, J. W. M. van Uffelen and M. K. Smit, *Upconversion in Er-Implanted Al_2O_3 Waveguides*, J. App. Phy., **79**, 3, 1258, 1995

[3.46] M. E. Koch, A. W. Kueny and W. E. Case, *Photon Avalanche Upconversion Laser 644nm*, App. Phy. Let., **56**, 12, 1083, 1990

[3.47] R. Scheps, *Photon Avalanche Upconversion in Er^{3+}:$YAlO_3$*, J. Quant. Elect. IEEE, **31**, 2, 309, 1995

[3.48] R. I. Laming, S. B. Poole and E. J. Tarbox, *Pump Excited-State Absorption in Erbium-Doped Fibers*, Opt. Let., **13**, 12, 1084, 1988

[3.49] Y. Mita, T. Yoshida, T. Yagami and S. Shionoya, *Luminescence and Relaxation Processes in Er^{3+}-Doped Glass Fibre*, J. App. Phy., **71**, 2, 938, 1991

4 Single Crystal Fibre Growth

4.1 Introduction

In Chapter 2, a short discussion was made on the existing techniques available for growing SCFs. As mentioned, the choice of technique employed greatly depends on the physical and chemical properties of the material that is required to be grown. One might reasonably consider that perhaps the most versatile growth technique is Laser Heated Pedestal Growth (LHPG). The advantages of this technique make it suitable for the current work where small, quick and low cost fibres are required for characterisation and applications studies. In this chapter, discussions will be made on the overview of the LHPG method, preparation procedures, growth processes of different materials, polishing of grown fibres and lastly, the 'finished' fibres.

4.2 Laser Heated Pedestal Growth (LHPG) – The Technique

One of the reasons for the extensive range of materials that can grown using this method is its ease in material preparation. Source materials can be in various forms. There are two common methods in the preparation of source materials. The more convenient way to grow SCFs is from bulk or poly-crystal materials [2.57]. They are usually cut or ground into either cylindrical or square rods. Since this method of preparation is quick and easy, it is good for rapid investigation and development of novel devices. The second form of preparing source materials is from a stoichiometric mixture of constituent powders [3.7]. These powders are pressed into pellets by either hot or cold pressing and after which, are cut into the required dimensions for growth. The only setback of the latter preparation method is that the pressed powder might not be sufficiently dense. This can result in bubble formation in the melt during the growth. The advantages are that dopant can be incorporated into the source material easily and evenly, provided the powder is thoroughly mixed. Vapour deposition, painting or dip coating can be used to apply dopant on the surface of undoped crystalline rods. However these methods of doping do not allow for good control over the dopant concentration because it is difficult to correlate the thickness of coating on the rod or the number of dip coatings to a specific dopant concentration level.

LHPG employs a laser as its heat source. The arrangement of laser heating can have various configurations. Different forms of beam-shaping optics are used to either create two or more opposing beams which can be adjusted independently, or an annular symmetric beam which is used in this work (see Figure 4.1). Multi-beam heating can be employed for LHPG but for better thermal uniformity, an annular beam is recommended [4.2]. Using a laser as a heat source can provide a clean radiation and the great availability of appropriate lasers makes it possible to grow materials with high melting temperatures. Due to the large temperature gradient between the solid and liquid interface, it is possible to pull fibres at high rates. *Phomsakha* [4.3] was able to pull sapphire fibres of good optical quantity at speed as high as 20mm/min, much faster than the typical growth rate of 1mm/min. The ability to achieve such speed was attributed to the beam shaping optics and growth SCFs under an inert gas environment. It was further reported by *Feigelson* [2.50] that sapphire using LHPG can be pulled at a rate of 40mm/min. However, due to supercooling internal scattering defects were evident in fibres grown at this rate. Since *Nightingale* [4.4] pulled sapphire at 8mm/min, compared to *Feigelson* at 40mm/min, the speed of growth has been a factor of concern for the purpose of high turn over and the one major advantage of LHPG in material development is that it is able to produce fibres at high pull rates.

Another advantage of LHPG is the capability to grow fibres of very small diameters. Fibres with small diameters minimise the possibility of internal crystal defects [2.16]. *Feigelson* [3.1] explained that the dislocation density of crystals with small diameters best fitted the *Tsivinsky* relationship [4.5] of

$$N = \left[\frac{\alpha}{b}\nabla T\right] - \left[\frac{2\tau_{cr}}{Gb}\frac{1}{D}\right] \tag{4.1}$$

where N is the dislocation density per unit area, α and b are the coefficients of linear thermal expansion and Burgers vector of dislocation respectively, ∇T is the temperature gradient in the melt, τ_{cr} is the critical shear stress, G is the shear modulus and D is the crystal diameter. From the equation, as D becomes smaller, the second term becomes larger hence reducing the dislocation density or defects present in the fibre. Since the diameters throughout the growth process in LHPG remain constantly small, applying the *Tsivinsky* relationship would indicate that there will be a very low

defect density in the fibres. LHPG should therefore be able to produce good quality fibres. In the area of material research, the cost of materials can be a setback. However, LHPG requires a very small amounts of source material. The fibres produced are small and that can reduce excessive cost incurred in the research programme.

There are, however, some problems associated with this technique. Firstly, it is extremely difficult to grow materials with highly volatile melts or melts that exhibit excessively high vapour pressure. An example of such material with high vapour pressure is $Gd_3Ga_5O_{12}$ (GGG) garnet. During growth under atmospheric conditions, gallium (Ga) evaporates from the melt [4.6]. A solution to this problem is to increase Ga content excessively in the source rod [4.7]. In all growth mechanisms, the heat source plays a vital role. When a laser is used as the heat source, two elements must be looked into. Firstly, the melting temperature of the materials dictates the required power of the laser and secondly, the laser's emission wavelength must be observed. This is another limitation of this technique. In order to produce a stable molten zone for the material to be grown, its absorption of the laser radiation is essential. Fortunately, in this work, the materials that were grown have a good absorption at 10.6μm [2.16]. LHPG is capable of growing fibres of diameter ranging from 10-2000μm [4.1]. However, fibres with large diameters grown using the LHPG proved difficult due to the steep temperature gradients $(dT/\delta x)$ that generate large amounts of thermal stresses. The results of these stresses are strains and cracks in the fibres. Small diameter fibres have few defects, but characterising them proves to be difficult. Therefore, the recommended fibre diameter should fall in the range of 500-2000μm for desirable characterisation measurements [4.1].

The most challenging problems of this technique is to maintain a consistent fibre diameter throughout the growth process. For the use of fibres in optical applications, diameter uniformity is crucial in minimising transmission losses. Scattering losses are mainly due to diameter variation [4.8]. Therefore, a closed loop system based on monitoring the constancy of the diameter of the fibre during the growth is an added advantage. The development of this closed loop system for diameter monitoring could be incorporated into the present LHPG method used in this work in the near future. A good model for this system can be found in reference [2.15].

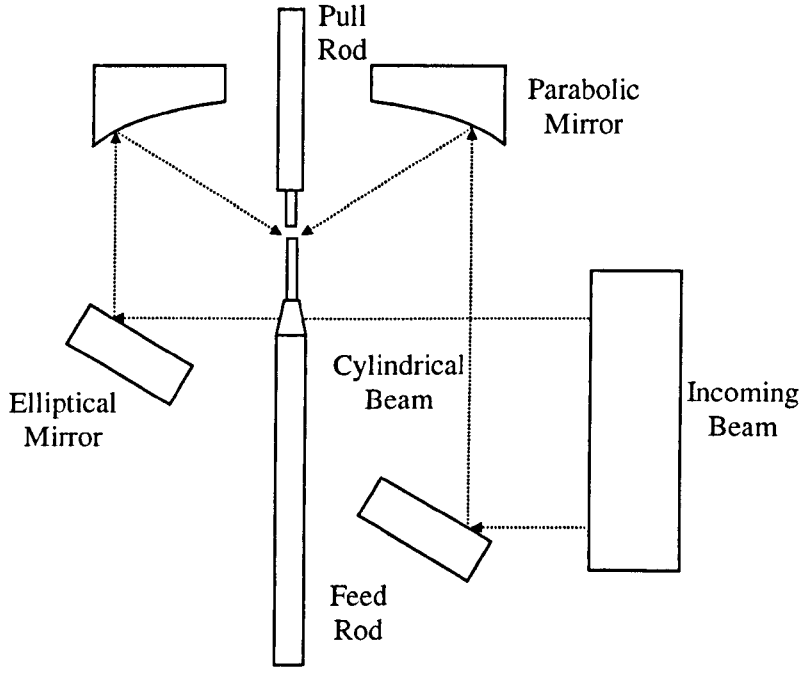

Figure 4.1 – Annular symmetric beam of the LHPG

4.3 Laser Heated Pedestal Growth (LHPG) – The System

The LHPG system in this work is modelled after Stanford University [2.15]. It consists of a CO_2 laser, gold plated elliptical mirror at 45°, a reflaxicon, a parabolic mirror and pull/feed mechanisms. The beam from the laser is generally expanded by 4 gold coated mirrors before being directed into the other optics on the optical table. See Figure 4.2 for a schematic of the LHPG system. The section below is a brief introduction of the apparatus used in the LHPG method.

4.3.1 Heat Source – CO_2 Laser

The heat source in any growth system plays an important role. The shape of the melt is greatly determined by the stability of the heat source supplied to the melt zone. It is therefore important to ensure the stability of the heat source during the growth process. The diameter of SCF grown is greatly influenced by the molten zone shape and this shape is determined by the temperature distribution throughout the molten zone where the temperature stability is established by the laser's power stability. Therefore, to achieve fibres with consistent diameters throughout the fibre length, laser power fluctuation should be kept to a minimum. Figure 4.3 shows the CO_2 laser used in the system from *Synrad, Inc* Series 48. It has a maximum output power of 33W. See Figure 4.4. The output power from the laser is controlled by *Synrad, Inc* UC-1000 laser output controller. Its closed loop operation is able to stabilise the output power to approximately ±2%. The output power is controlled by a thermopile detector mounted at the side of the CO_2 laser and approximately 8% of the output power is directed to the detector. One of the reasons this laser was chosen is because the laser, unlike conventional CO_2 lasers, is a sealed gas waveguide laser. Therefore, it is free from any jitter which is commonly caused by irregular gas flow. To further prevent power fluctuation, the laser was allowed to warm up for half an hour before the growth process. Experiments were carried out to determine the stability of the laser's output power at different input voltages over a period of 3 hours. From Figure 4.5, it was observed that at higher power, the laser was not as stable compared to the lower power. It can also be seen that the fluctuation at high power took a longer time to stabilise. These fluctuations observed were still within the ±2% of the laser power output controller specification.

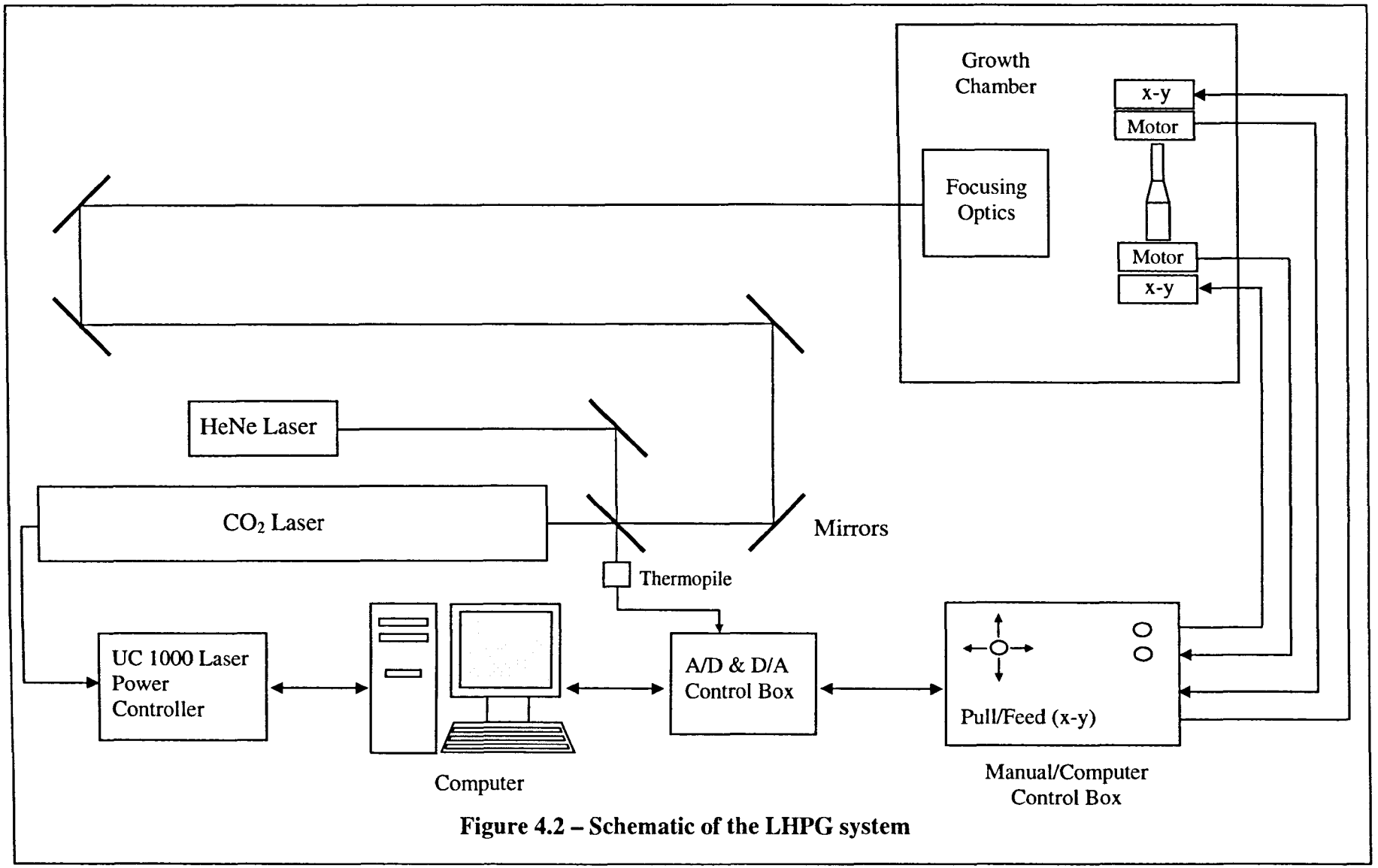

Figure 4.2 – Schematic of the LHPG system

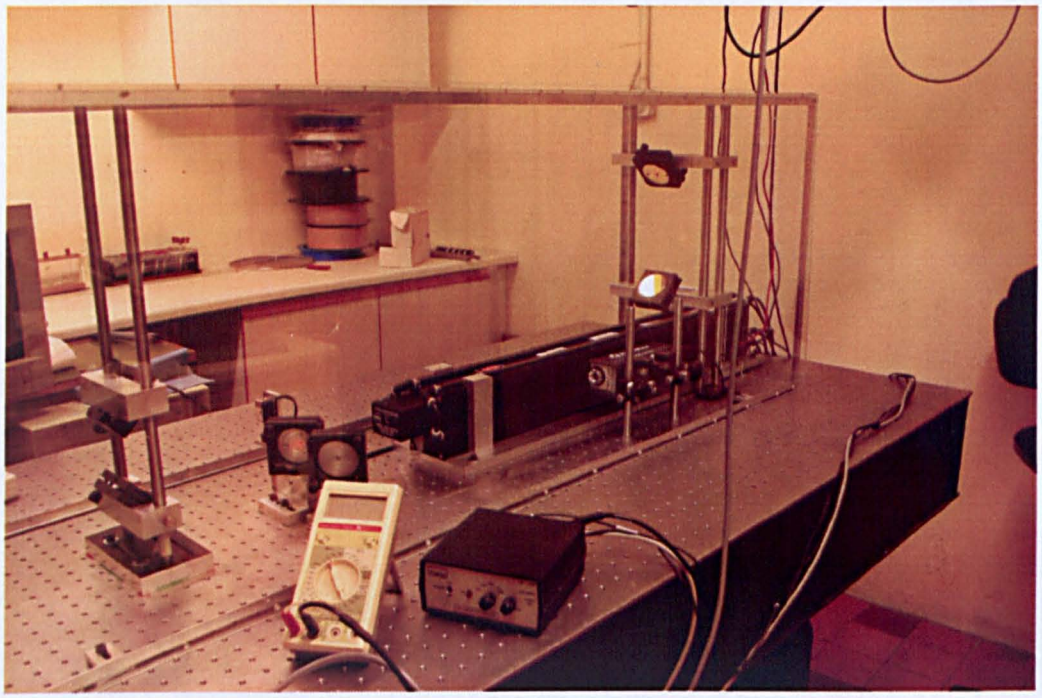

Figure 4.3 – CO_2 laser and optical mirrors

Figure 4.4 – CO_2 laser power

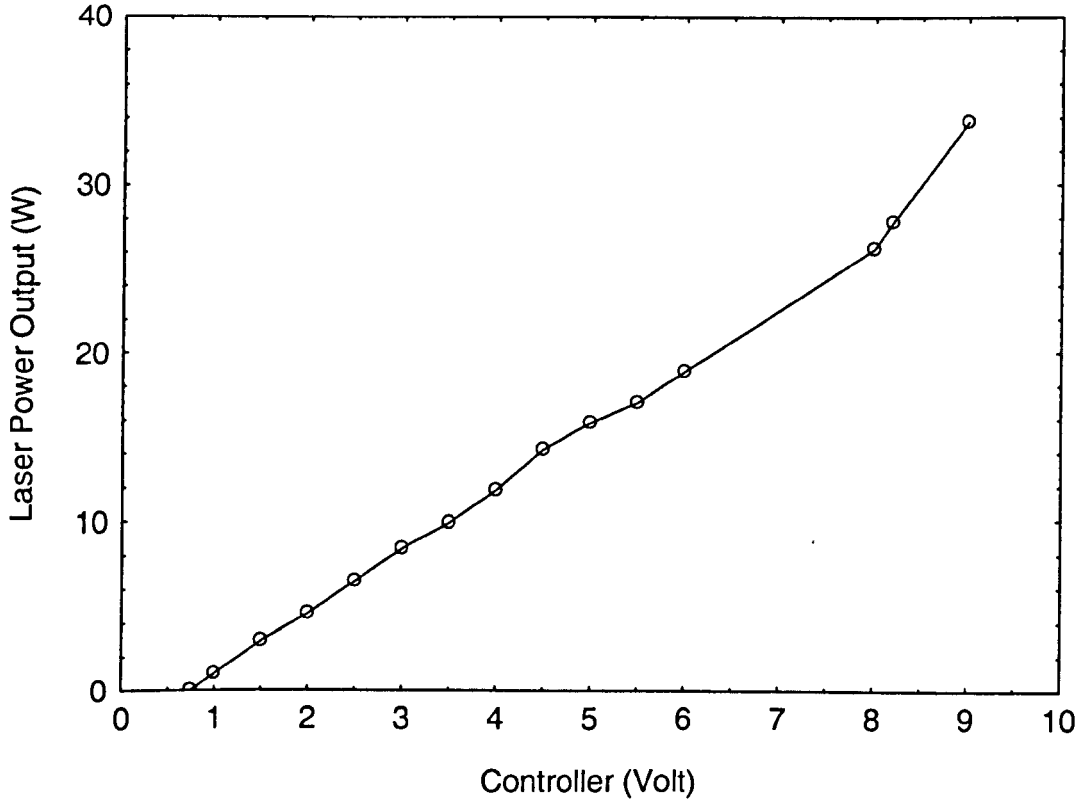

Figure 4.5 – CO_2 laser output power over a period of time

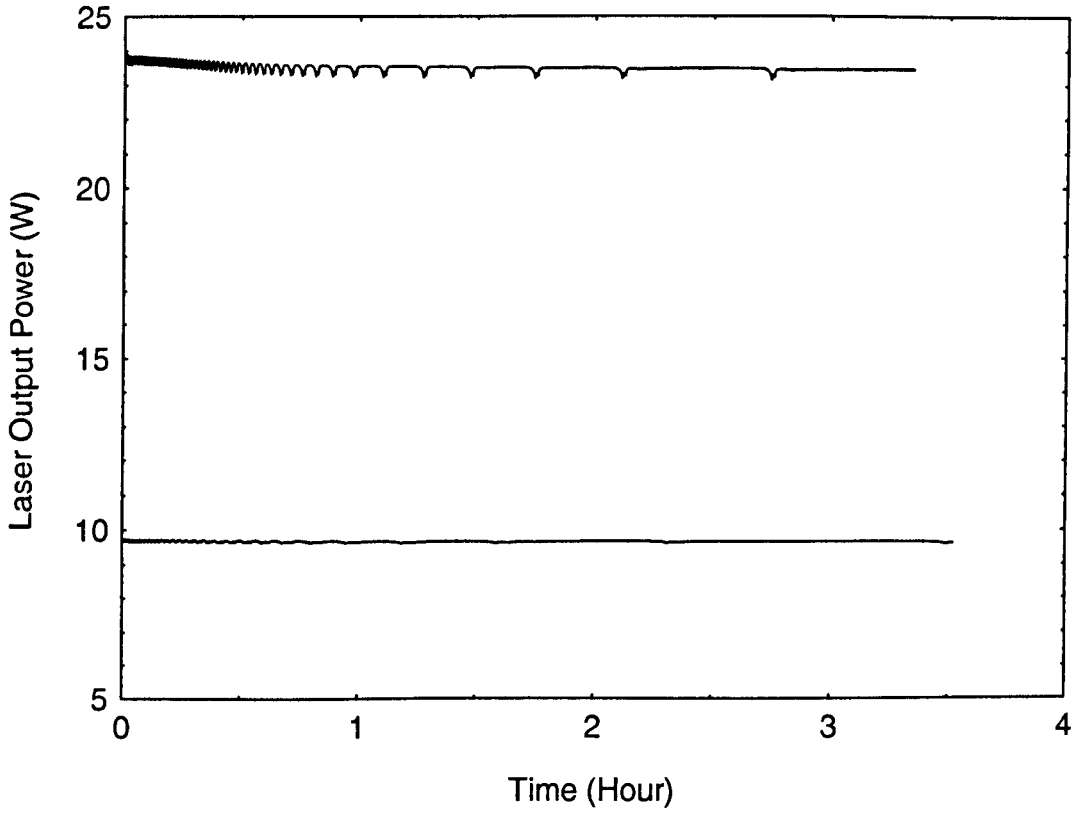

4.3.2 Optics

In this system, the optics used can be classified into two sections. One is the viewing optics and the second is the CO_2 and helium-neon laser focusing optics. In the order to position the source rod/fibre with respect to the fixed CO_2 laser focal point, proper viewing optics are required. See Figure 4.6. Two 1x microscope objectives (MO) are placed in the growth chamber and two microscope eyepieces, to view the growth process, are placed on the outside of the chamber. A mirror is mounted behind the y-axis MO to reflect the light into the y-axis viewer. With these, the x-y positions can be easily controlled. Two adjustable polarisers are attached to the front of the eyepieces to reduce the viewing intensity during growth.

The CO_2 laser focusing optics consists of four mirrors, a reflaxicon, an elliptical mirror and a parabolic mirror in which all of the optics used are gold coated. The four mirrors are to direct the beam from the CO_2 laser through a ZnSe window and into the reflaxicon. These mirrors are used to expand the beam size from the CO_2 laser by allowing the beam to travel over a distance. This beam is then delivered into the reflaxicon where there are two axi-centric spherical cones. The smaller cone is used to split the incoming beam into a larger circular ray and the larger cone is used to deliver the 'hollow' Gaussian beam (see Figure 4.7), onto the elliptical mirror. The annular ray is focused to a small spot (~22μm) by the parabolic mirror. Fibres with diameters as small as ~130μm have been grown. Figure 4.3, 4.7 to 10 shows the laser focusing optics. As for the guiding He-Ne laser, a beam combiner is used just before the CO_2 laser, see Figure 4.3. This channels the visible beam onto the path of the CO_2 laser beam.

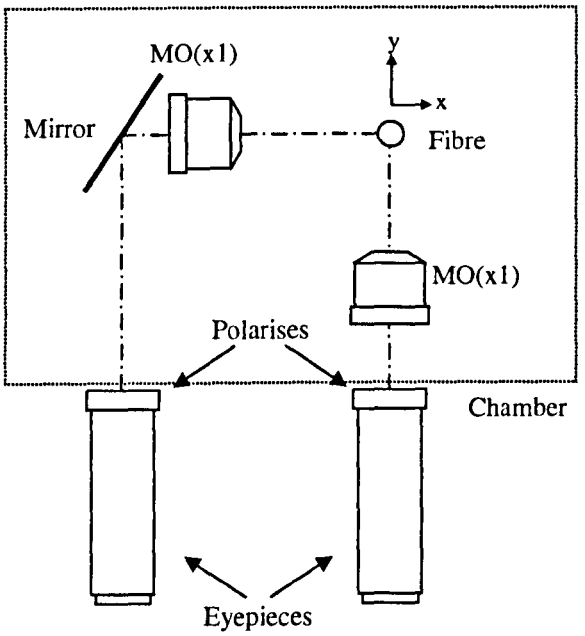

Figure 4.6 – LHPG viewing optics – plan view

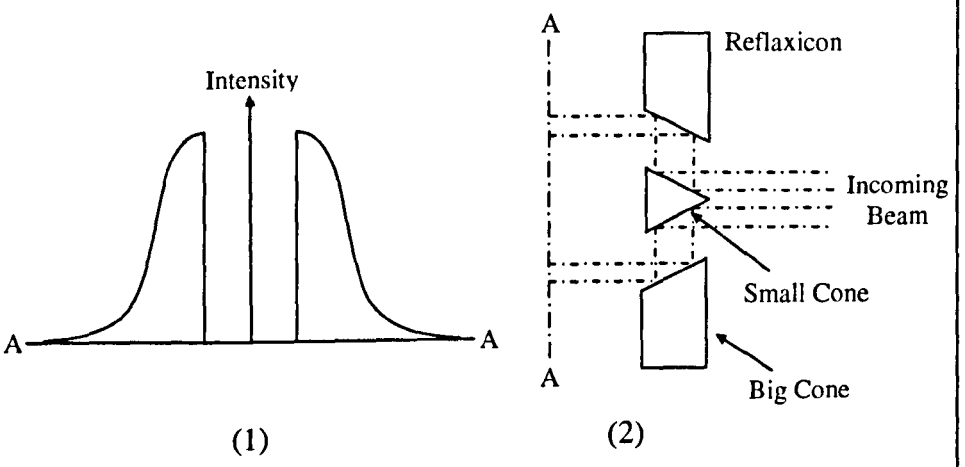

Figure 4.7 – Reflaxicon (2) used in producing a 'hollow' beam – Gaussian beam (1)

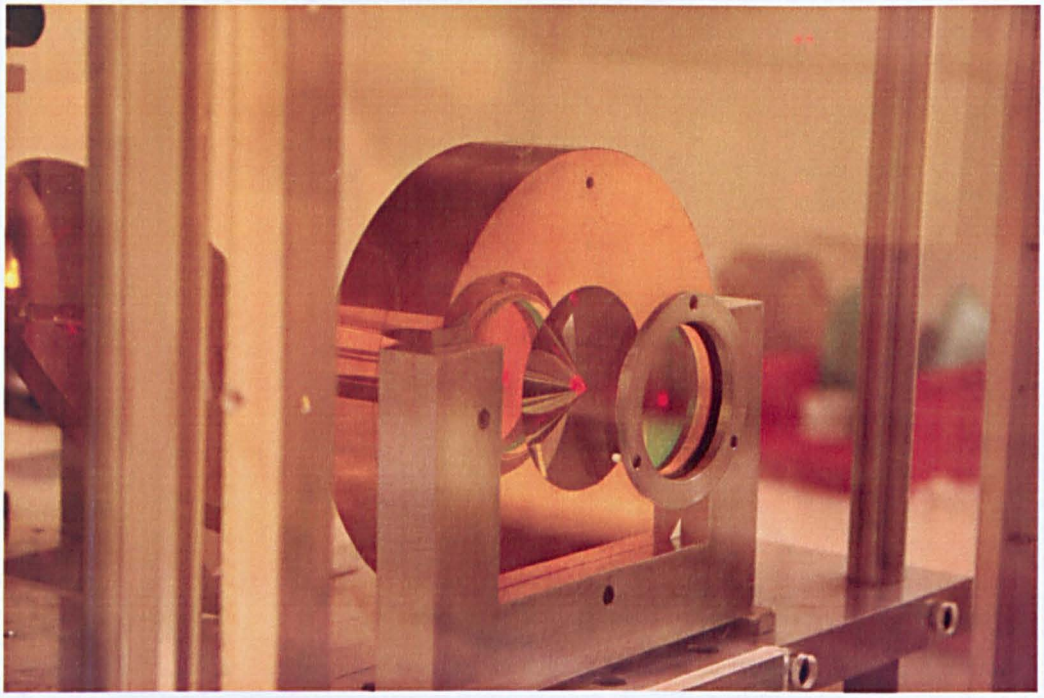

Figure 4.8 – Reflaxicon used in LHPG

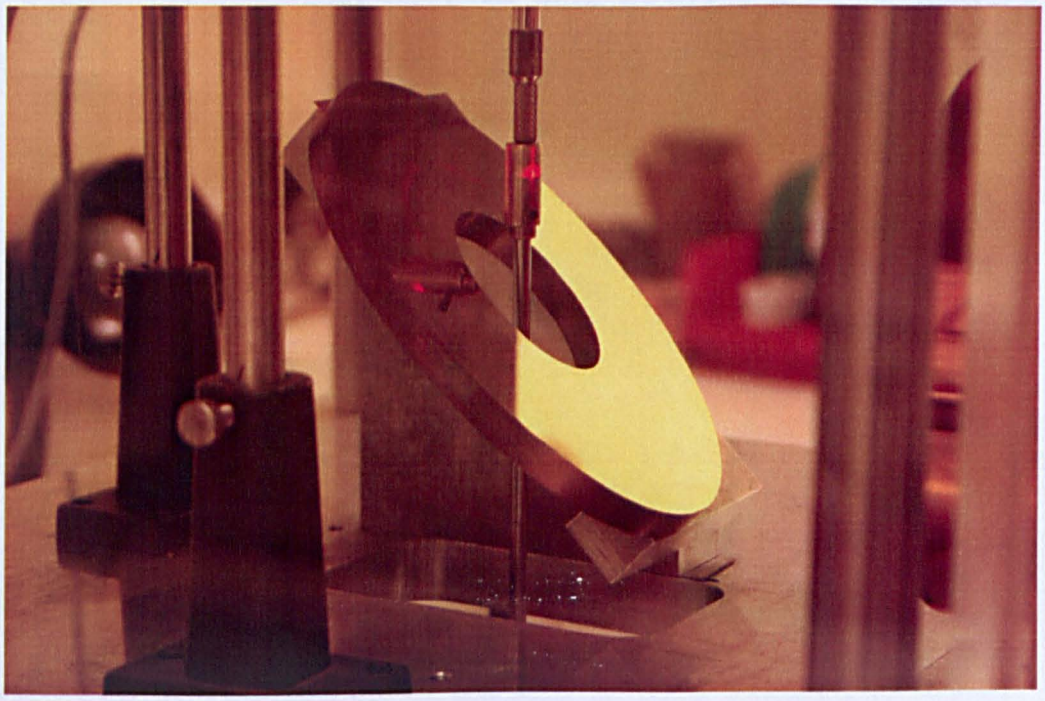

Figure 4.9 – Elliptical mirror used in LHPG

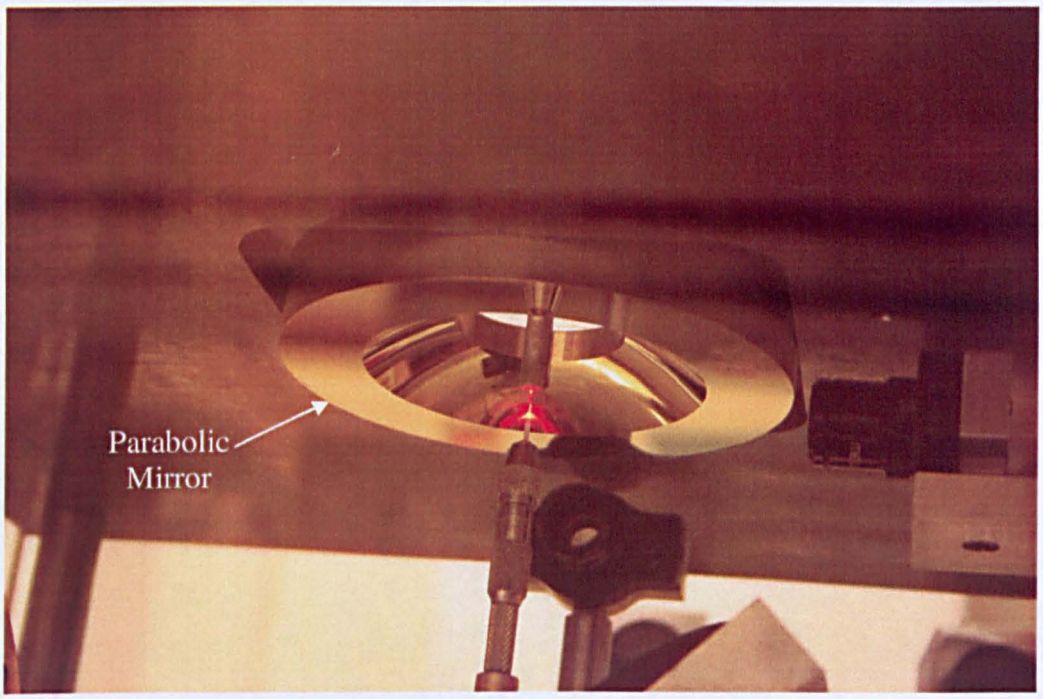

Figure 4.10 – Parabolic mirror used in LHPG

4.3.3 Fibre Feed and Pull Mechanism

A large portion of the molten zone stability depends on the feed and pull mechanisms. Fluctuation occurring in the growth velocities will lead to an unstable molten zone and the fibres grown will contain striations. In order to maintain a stable molten zone shape, velocities of the pull and the feed mechanisms must be free from fluctuation. Therefore, the above concerns are taken into careful consideration when designing and building this system.

The feed mechanism comprises of a miniature pin chuck, a 5mm diameter stainless steel rod, a unislide, a gearbox and a DC motor. The miniature pin chuck, with four retaining jaws, was used to hold the source rods. The source materials were firmly held in the chuck by rotating the cylindrical catch at the end of it clockwise. See Figure 4.11. Care was taken to ensure that the materials were aligned parallel to the feed/pull directions. The pin chuck was then attached to one end of a stainless steel rod. This rod was attached to carriage slider of the unislide where its movement is restricted to vertical motion by two precision machined holes located at the top and bottom of the unislide. See Figure 4.12. The unislide, (*Time & Precision* model A1506V), has an effective stroke of 114mm and a leadscrew of pitch 0.5mm. The vertical translation of the unislide was controlled by a precision gearbox of 320:1 reduction ratio from *RS Components* and a high precision DC motor from *Physik Instrumente* model C136.10. The DC motor operates at its mid-operating speed and the reason for this was to minimise velocity error [2.57]. Investigation by *Seat* [2.57] on this system shows that the effective useful range of the unislide was approximately 70mm. Within this stated range problems associated with friction, generated by the moving carriage slide, will be avoided.

The pull mechanism does not have a miniature pin chuck. It was removed and replaced with a single 5mm diameter stainless steel rod. In the previous design, the pull mechanism consisted of only a miniature pin chuck which was attached to the carriage slider of the pull mechanism's unislide. One problem encountered was ensuring parallel alignment during the growth process. The present modified design reduces the problems encountered. One end of the stainless steel rod has a v-groove cut for holding the seed fibre. The fibre is clamped in place and the v-groove allows the fibre to sit parallel to the growth direction. The two precision machine holes were

made at the end of unislide to improve the parallel translation during the growth process. The unislide, (*Time & Precision* model A1512K), had a length of 266mm and leadscrew of pitch 1mm. The effective usable length was found to be approximately 236mm. The vertical movement was generated by a gearbox with a reduction ratio of 80:1 from *RS Components* and had a similar dc motor as the feed mechanism from *Physik Instrumente* model C136.10. The motor was also run at mid-operating speed for the reason of reduction in velocity error. See Figure 4.13.

Commonly stepper motors are chosen for use with computer control. However, for this work it is inappropriate because it would not provide a smooth translation during the growth process. The two dc motors employed for this work have blacklash-free gearboxes and have a maximum speed of 3.3 revolutions per second with a stated resolution of 0.006 degrees per pulse. A two channel dc motor controller card from *Physik Instrumente* model C842.2 was used so that the motors can be controlled from the computer. The motors attached to differential encoder drives registered a maximum speed of 195600 pulses per second and when operating at mid-range, had a speed of approximately 90000 pulses per second. In this range, the pull rate could go as high as 3mm/min. A frequency counter (*RS Component* model 5001 Universal Counter Timer) was used to observe the velocity reduction in the pull/feed motors. The final pulled fibre diameter was governed by equation 3.1 which is the mass conservation equation. From the computer software, the user can specify the required diameter reduction ratio between the source and fibre, and also the pull rate velocities. Using equation 3.1, the computer then calculates the feed rate. Finally, both the feed and pull mechanisms are sat on two cross-stacked, side driven linear positioners to control its x-y translation. With this, alignment of the seed/source materials to the laser was made possible.

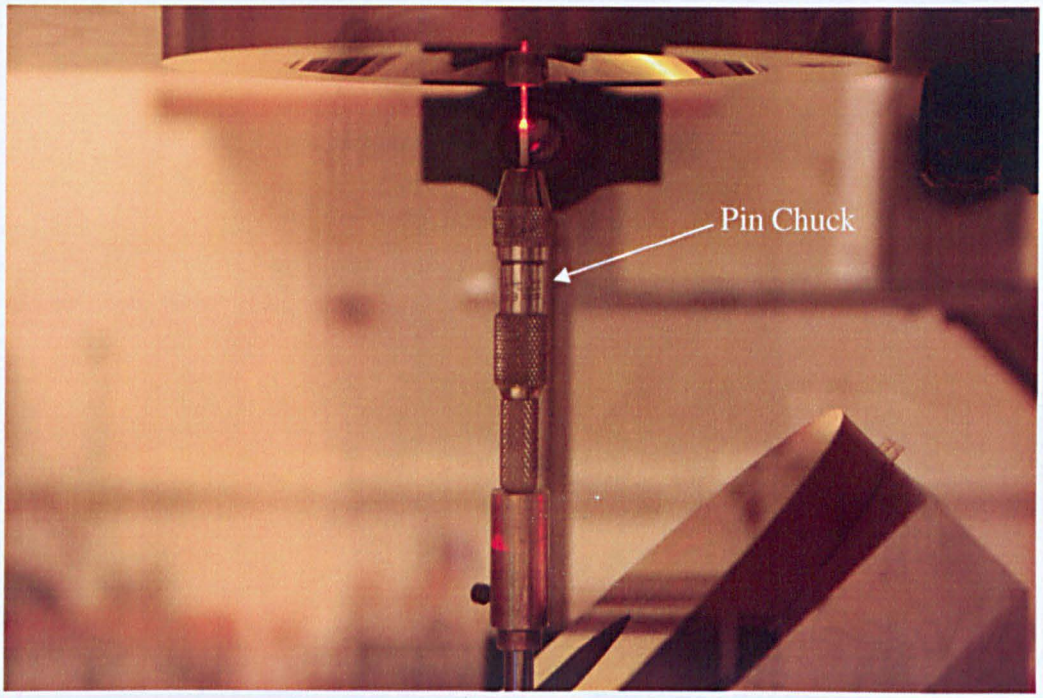

Figure 4.11 – Miniature pin chuck

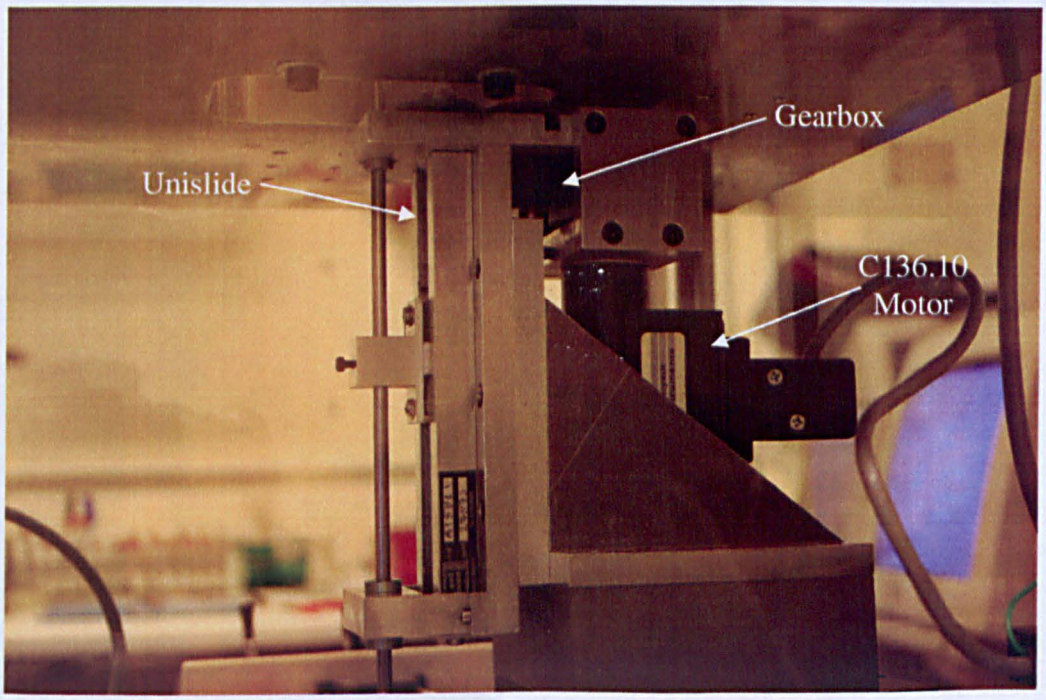

Figure 4.12 – Feed mechanism

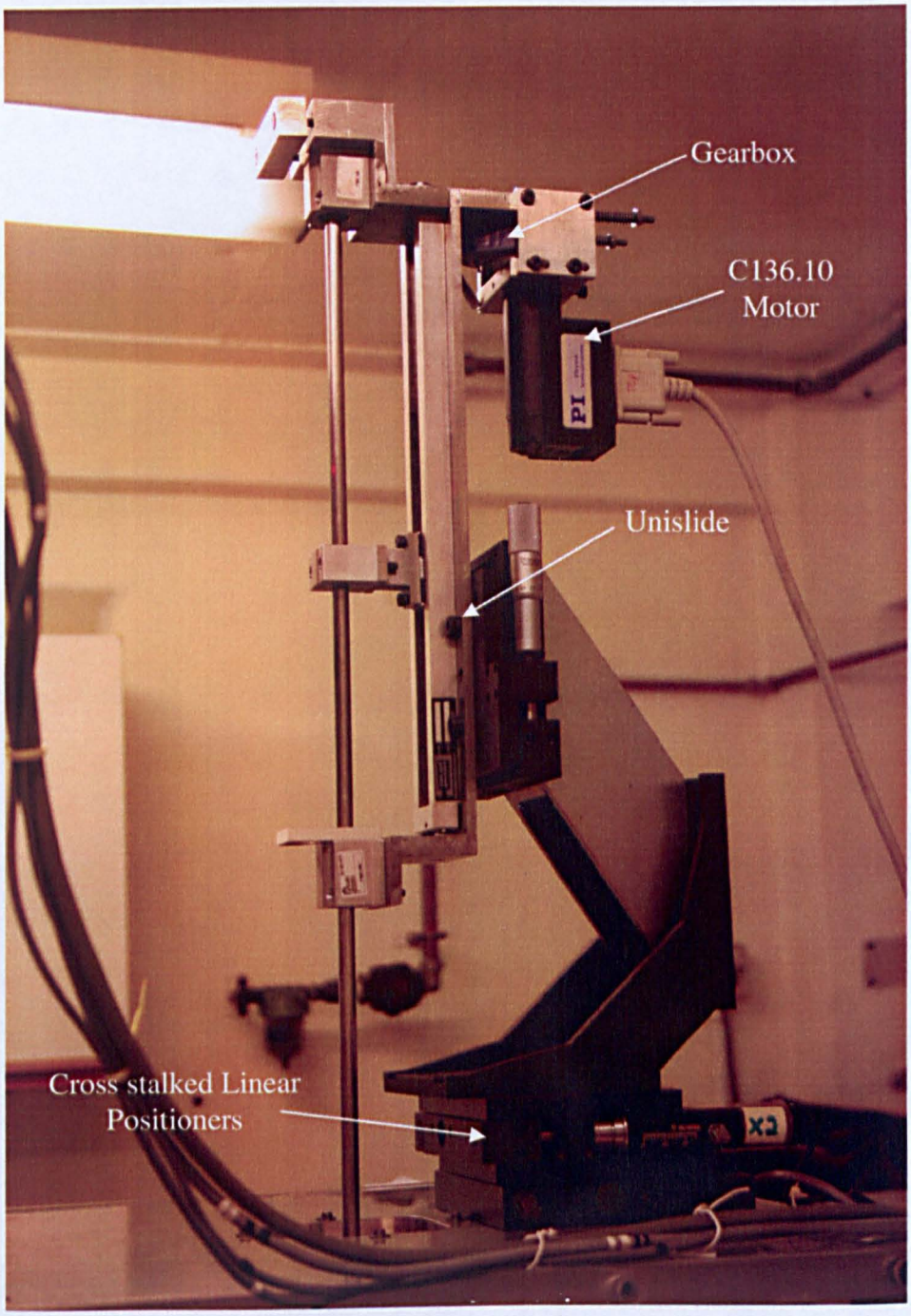

Figure 4.13 – Pull mechanism

4.3.4 Fibre Growth Chamber

The chamber is made up of transparent polycarbonate in the shape of a rectangular box, approximately 530 x 425 x 425mm, with an aluminium cover. Within, the chamber it is divided into two levels. The top level is where the two viewing lenses, the parabolic mirror, plane elliptical mirror and reflaxicon are located and on the lower level sits the feed mechanism. The pull mechanism is mounted on the top of the Growth Chamber. See Figure 4.14. The growth process of the crystal takes place within the confines of the chamber. Its acrylic walls prevent stray CO_2 radiation that might be present during the growth process. The chamber not only provides a contamination free environment for growth, it also prevents unwanted cooling air currents from the surroundings that will affect the uniformity of the fibre diameter in the growth system. The design allows the partial evacuation of the air in the chamber and could be back filled with inert gases which aid the growth of materials with melts that behaves incongruently. All crystals that are mentioned in this work are grown under normal conditions, which is without the introduction of any inert gas and are grown under atmospheric pressure.

4.3.5 Optical Table

All the equipment used in the LHPG are fixed onto an optical table (*Newport model RS3000TM*). The table itself is mounted onto four vibration isolators since it is impossible to create a totally rigid body which does not change in shape and size under the introduction of a force contribution through vibration. Therefore, isolators are used to limit all possible vibrations that might be introduced from the surrounding environment. If this high frequency noise is not prevented, it will be translated into the melt of the crystal. Although all the external vibrations can be limited or likely removed with these isolators, the vibration from the pull and feed mechanism can not be eliminated. Very small amounts of vibration are produced from these two mechanisms, with each have a high gearing ratio gearbox attached to them. With the gearboxes, vibration is further reduced to a reasonable amount. The re-circulating cooling system of the CO_2 laser is placed outside of the growth lab so that its vibration would not adversely affect the growth process. The circulating

water from the chiller to the laser through the cooling tubes may also contribute a tiny amount of vibration.

4.3.6 Growth System's Control Software

The choice of implementing computer software control over hardware control was due to its flexibility in integration and manipulation of growth parameters with ease and also the ability to incorporate a feedback control system. In the area of crystal growth, be it from melt, bulk or fibre, there are many parameters of consideration. Therefore, monitoring these parameters is extremely important. These parameters include melt shape, melt volume, growth rate of the crystal and the heat source. Constant melt shape and volume are greatly dependent on the feed rate, pull rate and the heat source. To achieve high quality fibres, it is important to monitor and control these three parameters closely. Another advantage of using computer control is that it caters for future expansion. If the need arises for additional components or features, it can be easily and quickly modified. At the present, the software for the growth system is written in Delphi and the computer used has Microsoft Windows NT as its operating system. The software allows the user to control parameters such as the pull/feed rate and diameter reduction ratio which are the most important in the growth process. The user is able to key in the pull rate and the reduction ratio and the last parameter is automatically calculated by the programme. The programme was also written to monitor the fibre length grown and time taken for growth. Other monitoring features include the pull and feed rate where the speed of both is recorded for future analysis. The positioning of x-y axes could be controlled manually by the x-y control box or can be controlled by the computer. Laser power monitoring is also integrated into the system. The system is also able to vary the diameter of the fibre, for example producing tapers at the end of the fibre for sensing application and sinusoidal variation which can be used in either Bragg reflector or long period gratings. The pull and feed motors are in closed loop control. Diameter monitoring is an open loop system.

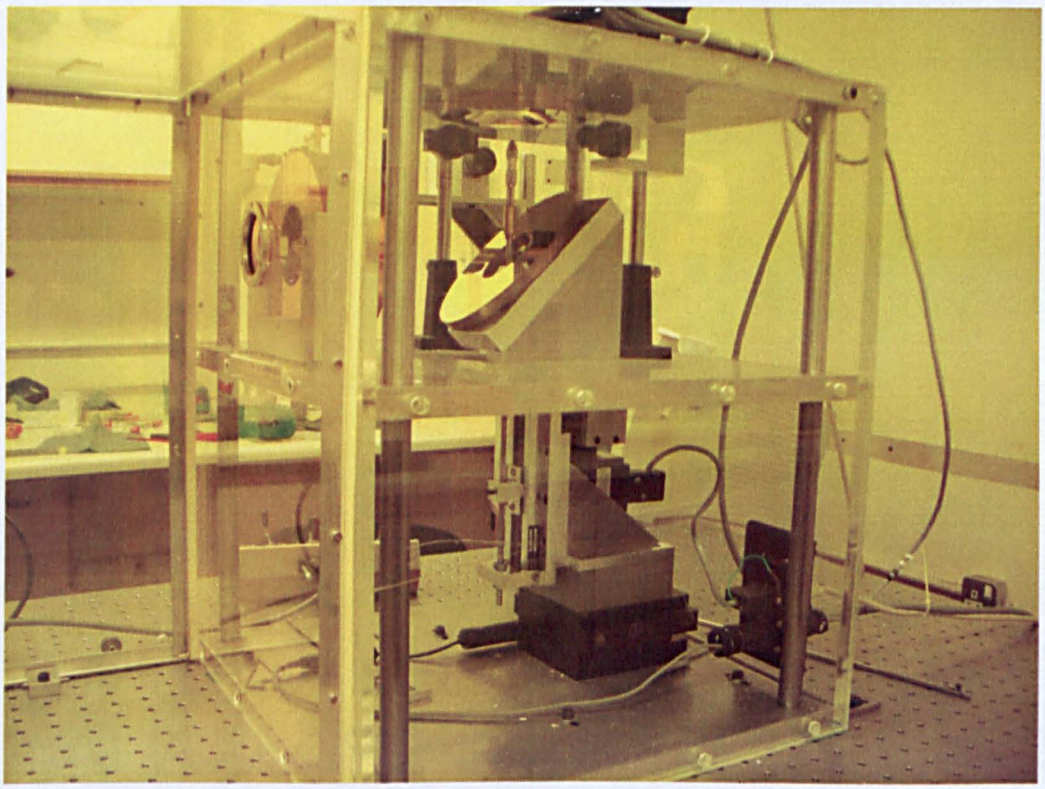

Figure 4.14 – Fibre growth chamber

4.4 Growth Processes

The objective in this work is to grow fibres of sufficient length to be characterised and with the knowledge from the characterisation thereby use the fibres for different applications. The reason why SCFs were chosen in this work was because of the high temperature resistance of certain crystalline materials. SCFs produced with high crystalline perfection have a tensile strength that is close to the theoretical maximum [4.1]. Since SCFs have a minimal chemical segregation, grain boundaries therefore are eliminated and this in turn reduces the dislocation densities. The three materials that have been grown for this work are $Y_3Al_5O_{12}$, Y_2O_3 and Al_2O_3. Each material has unique features. More in-depth discussions on each material will be made in subsequent chapters. In this section, the discussion consists of preparation processes of the materials, the growth of the different materials, polishing of the materials and discussion on the final products.

4.4.1 Preparation of Source Rods

In any growth process, starting materials are required in order that the crystal can be produced. In the case of LHPG, source materials usually come from cut bulk single crystal or cold pressed powder. In this work, both of these are employed. The former is the easier to prepare compared to the latter. Few fibres were produced from the former because it is expensive.

Cr^{3+}:Al_2O_3 fibres are the only fibres that were produced from the bulk material. Two processes were required in order to produce the source rod required for the growth. The first process was cutting from the bulk crystal. The bulk ruby was mounted onto a ceramic tile secured with wax and then this assembly was screwed to an X-Y attachment table of the Ultraslice 2000 Precision Saw (*Ultra Tec Manufacturing, Inc.*). A diamond metal bond sintered blade was used to cut the bulk ruby to a manageable size. One problem encountered was that it was very difficult to cut the crystal to the shape of a rod. The source rod that was required should approximately be 0.9 x 0.9 x 15 mm. The reason for this size was because the miniature pin chuck was not able to clamp anything larger than this dimension. The specified dimension was too small for the Ultraslice to produce since during the cut, the bulk ruby would

fracture into small pieces impossible to be used for growth. Therefore a grinding (second) process was introduced. The rod of 5 x 5 x 15 was cut with Ultraslice and then was mounted onto Ultrapol (*Ultra Tec Manufacturing, Inc.*) to be ground. The source rod was ground to the approximate dimension with a silicon carbide grinding paper grit size 1200 (*Ultra Tec Manufacturing, Inc.*)

The second method of producing source materials was from cold pressing. The required amount of oxide materials and rare earth dopants were weighed and thoroughly mixed. Table 4.1 shows the mixed content of the oxide materials and rare earth dopants used in this work. Both the oxide and the rare earth dopant(s) were weighed in a 60ml glass cap bottle and a metal stirrer was used to mix the two compounds that were in glass bottle homogenously. The 'stirrer process' lasted for no less than 10min. The mixed oxide and dopant(s) were then placed into a 15mm diameter die from *Medway Optics Ltd.* The die is then subjected to a cold pressing loading of 15 ton by a manual hydraulic press (*Fluxama model PR-25*). 15mm pellets of thickness of ~1mm were produced. The conditions of the pellets produced depended on the material. Y_2O_3 produced the most robust pellets and the was easiest to handle. Second was $Y_3Al_5O_{12}$ followed by Al_2O_3. The last was the most fragile, therefore binder (*Fluxana – Lico Wax*) was added to the mixture to aid in holding the powers together. The ratio of Al_2O_3 to binder was 4:1. Table 4.2 shows the amount of binder used in the mixture. See Figure 4.15 for pellet. $Y_3Al_3O_{12}$ pellets were formed from the mixture of Y_2O_3 (0.342g) and Al_2O_3 (0.258g). One of the applications of interest in this work is in the area of optical sensors. For this kind of SCF, only the tip is doped with rare earth(s). In order to prepare the source rod for such fibres, the pellet produced would be different from that described above. See Figure 4.16. One half of the pellet is white while the other is pinkish. The half that is white was without any dopant whereas the other half was doped with rare earth(s). To produce this kind of pellet, first the die was separated into half by a thin metal brass plate of 15 x 40 x 0.5mm. One half was filled with oxide without dopant while the other was with dopant(s). The brass plate was removed and was then pressed as before producing pellets that have dopant(s) on only one side. See Table 4.3 for pellet contents.

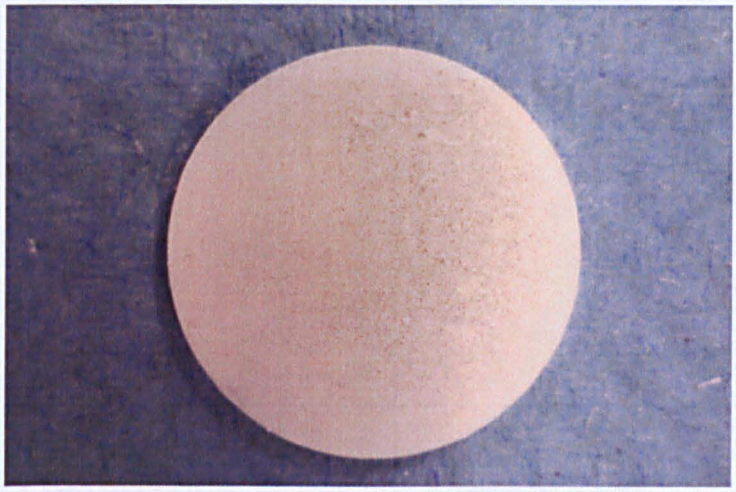

Figure 4.15 – Pellet pressed from 15mm die

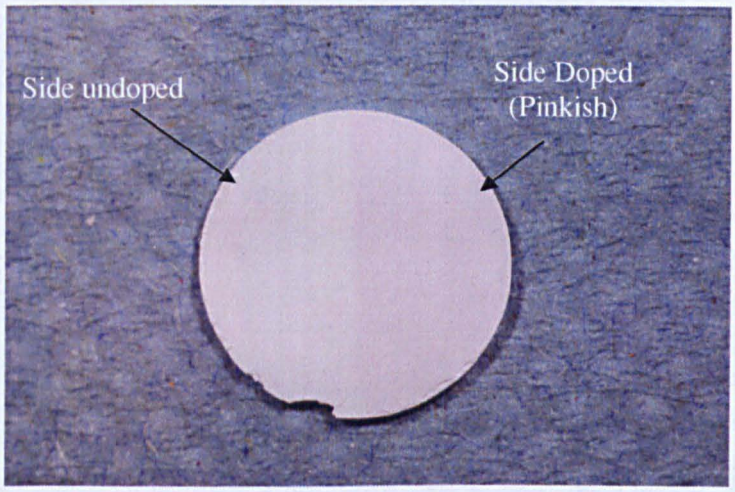

Figure 4.16 – Pellet ($Y_3Al_5O_{12}:Er^{3+}$) used for sensory application with one side doped (pinkish) with rare earth and the other without doping (left)

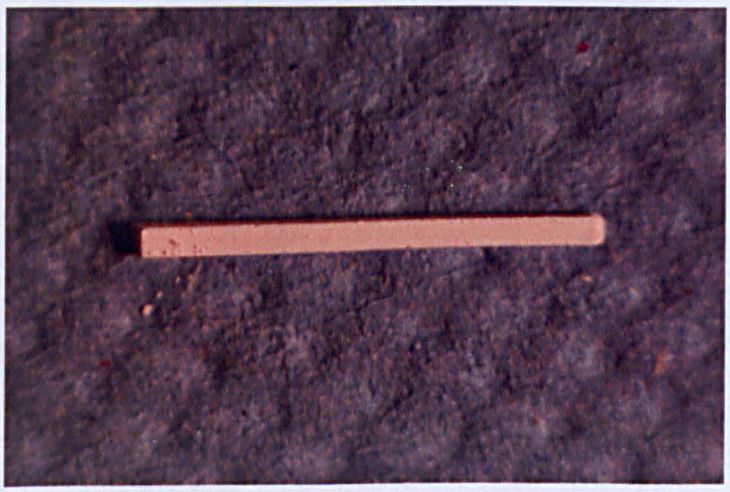

Figure 4.17 – Square rod cut from pellet.

Table 4.1 – Rare earth content in each material

Materials Oxide : Dopant	Rare Earth Content mol%
$Y_2O_3 : Er^{3+}$	59, 6, 3.1, 0.3, 0.06, 0.03
$Y_3Al_5O_{12} : Er^{3+}$	15, 10, 5, 1, 0.5
$Y_3Al_5O_{12} : Er^{3+} + Yb^{3+}$	1+1, 1+2, 1+3
$Al_2O_3 : Er^{3+}$	5, 4, 3, 2, 1, 0.5, 0.1

Table 4.2 – Binder amount used in Al_2O_3

$Al_2O_3 : Er^{3+}$ (mol%)	Pellet Weight (g)	Binder (g)
5, 4, 3, 2, 1, 0.5, 0.1	6	1.5

Table 4.3 – Pellets for sensor applications

Materials Oxide : Dopant(s)	Rare Earth Content (mol%) (on the side of with dopant)
$Y_2O_3 : Er^{3+}$	2
$Y_3Al_5O_{12} : Er^{3+}$	2
$Y_3Al_5O_{12} : Er^{3+} + Yb^{3+}$	2 + 5

In the initial stage, pellets pressed were sintered at 1100°C for a period of 24hrs in a horizontal furnace (*Carbolite Eurotherm model MTF12/25/25*) but this process did not significantly improve the strength of the pellet, hence all pellets subseqeuently pressed did not go through this process. These pellets were then cut into square rods of 1 x 1 x 15mm with the Ultraslice. It was impossible to cut it smaller than this because the rod would break into small pieces or return to it powder form. In order to have smaller rods, the cut rods were ground down by hand using a silicon carbide grinding paper grit size 1200. The smallest rod that can be achieved without destroying it was ~0.8mm. It was difficult to produce rods with both sides similar in width because the process was done manually. So the range of the size of the side of square rods was approximately between 0.9 and 0.8mm and the length was about 13 to 15mm. See Figure 4.17. Circular rods would be most desirable but the pressed material was too fragile to be rounded.

4.4.2 Growth Process

Three materials (Y_2O_3, $Y_3Al_5O_{12}$ and Al_2O_3) had been grown using the LHPG method in this work. Each of these materials responded differently during the growth process but the basic process is similar for the three materials. The CO_2 laser is focused onto the tip of the source rod which is seated in the feed mechanism. It is important to align the source rod tip to the focused CO_2 laser beam to maintain a stable melt zone during the growth process. The HeNe laser was used as a guide to bring the source material in line with the CO_2 laser. When a 'half spherical' shape appears on the tip of the source rod this indicates growth is ready to commence. The half spherical shape's diameter must be approximately the width of the source rod. See Figure 4.18. If its diameter is bigger then the laser power is too high and when it is smaller the power is too low for growth to take place. To initiate the growth, a seed fibre is lowered into the melt and is then withdrawn from the molten zone as shown in Figure 4.19. Pure sapphire fibres of diameters 130μm and 325μm were used as seed fibres in this work depending on the size of source rod. The growth speed ranged from 0.2 – 1mm/min and this was greatly dependant on how dense the cold pressed square rods were. In the remaining sections, discussions are made on the growth characteristics observed for each material.

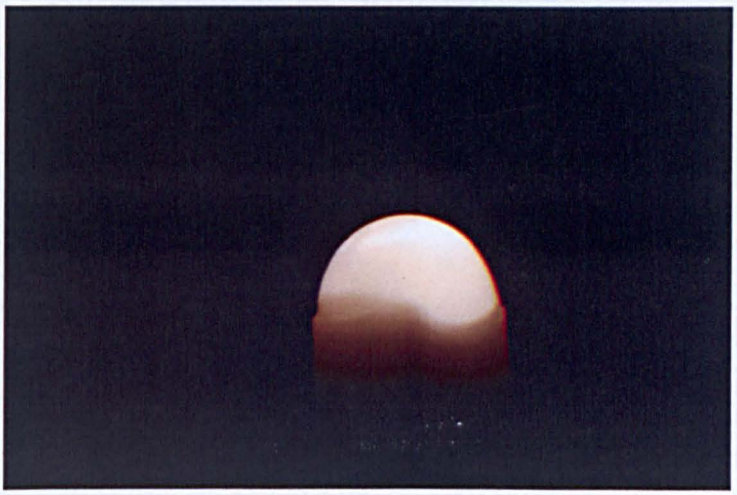

Figure 4.18 – Melt in spherical shape ready for growth

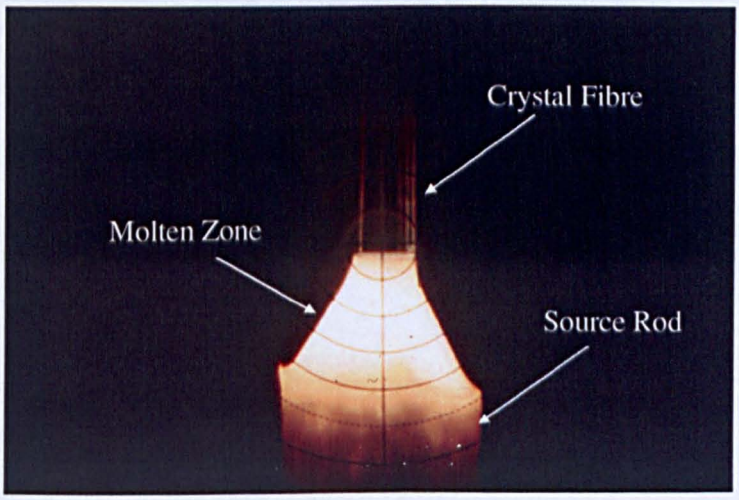

Figure 4.19 – Redrawing of SCF from melt

4.4.2.1 Al_2O_3 SCFs

Cr^{3+}:Al_2O_3 fibres were grown from a bulk ruby laser rod. To achieve a smaller diameter, the diameter reduction by repeated growth was required. Starting with the bulk ruby crystal, the power required to melt the source was approximately 25W and the pull rate was at 0.7mm/min. The average diameter of this fibre was 440μm. This newly produced fibre was then used as a source rod for the second growth. The final ruby fibre was grown at a pull rate of 0.7mm/min and with laser a power of ~11W. The diameter of the new fibre was ~200μm. There were no observed complications in the melts which remained very stable for the consecutive growths. The quality of these fibres was the best among all the fibres that were grown in this work. Figure 4.20 shows the typical fibre surface condition. The second re-growth fibres were free from any visible defects within the fibre. This observation was carried out during the growth process, through the viewing optics in the LHPG. The reduction in diameter increases the flexibility of the fibre and larger diameter fibres are more rigid. Therefore, when growing thin fibres, slight movements can cause misalignment with the laser beam and result in disruption of the melt. Therefore, for better control, a slow pull rate is advised when fibres with small diameters are grown. A pure sapphire fibre c-axis feed rod was used and the fibres grown as a result were c-axis.

The fibres of Er^{3+}:Al_2O_3 grown from cold pressing were more difficult to grow. Firstly, under the high temperature from the laser the wax binder melts away producing soot. Fine particles in smoke form evaporate from the source rod and leave a black soot mark on the source rod. The fine particles tend to settle onto the focusing optics and after every growth, cleaning of the focusing optics was required. Secondly, bubbles appeared in the melt. This was a clear sign that the powder was not dense enough. It was noted by *Sharp* [4.9] that under stable melt, the bubbles remained static and were on the surface near the growing crystal/melt interface. Under unstable conditions, the bubbles start circulating around the melt. As the concentration of Er^{3+} increased the frequency of instability in the melt also increased. When the fibre has dopant at low concentration of 0.1mol%, bubbles were present but stable but when concentration increases to 1mol% the melt becomes unstable more frequently. Figure 4.21 shows that as the concentration of Er^{3+} increases the transparency of the fibre reduces. The fibre with 1mol% is the only fibre that is clear throughout its length and the fibre with 2mol% started off clear but become opaque

as it proceeded in its growth. As for the last three fibres, they were pink because of the high Er^{3+} concentrations. All Al_2O_3 fibres were grown at a pull rate of 0.7mm/min. The slower pull rate shows no effect of reducing the opacity of the fibres with high concentration. The diameters of the fibres grown were approximately 400μm. Laser power used to grow the fibres was between 11– 15W, and this was greatly dependent on the dimensions of the source rods.

4.4.2.2 $Y_3Al_5O_{12}$ SCFs

All $Y_3Al_5O_{12}$ source rods were prepared by cold pressing. Care had to be taken when handling the sources rods. They were fragile and could be easily broken during grinding down to the dimensions required for the growth. Bubbles were evident in the melt for $Y_3Al_5O_{12}$. See Figure 4.22. As mentioned in the previous section, the pressed powder was not compact enough. A way to solve this problem is to use a hot iso-static press or sinter the pellets at very high temperature (~2100K). The pull rate for this material can be as high as 1mm/min. When pulled at a rate higher than 1mm/min, periodic striations were seen on the surface of the fibres. The laser power used for this material was between 11-17W, and it is dependent on the size of the source rod. Diameters of the fibres were approximately 400μm. Fibres doped with Er^{3+} at levels below 10mol% did not have any problems during the growth process. But for fibres grown at 15mol% and above, the melt became unstable. From Figure 4.23, it can be seem that the fibres started to cloud up with microvoids appearing in the fibre. At a high concentration, at the beginning of growth, small amounts of scattered microvoids appeared in the fibre and eventually filled the whole fibre as seen in Figure 4.23. After a period of time, the microvoids reduced and disappeared and clarity was restored to the fibre. This happened periodically. When grown at 20 and 30 mol%, this happened more frequently and from Figure 4.24, it is seen that the unstable melt caused the change of shape of the fibre and it became opaque. One possible explanation would be that the built up of rare earth dopant in the melt caused the changes in the freezing and melting interfaces. The lowering of the freezing point of the melt caused the high dopant concentration to freeze out and become crystal. Cloudiness appearing in the fibre was likely due to dopant build up at high concentration [4.9]. The characterisation was only done on fibres of lower

concentrations (10mol% and below). At 10mol%, the fibre appeared to have a slight pinkish colour. When fibres were doped with Er^{3+} and Yb^{3+}, investigation was only done at low concentrations. See Table 4.1. The conditions of the melt were similar to Er^{3+} doped at low concentration.

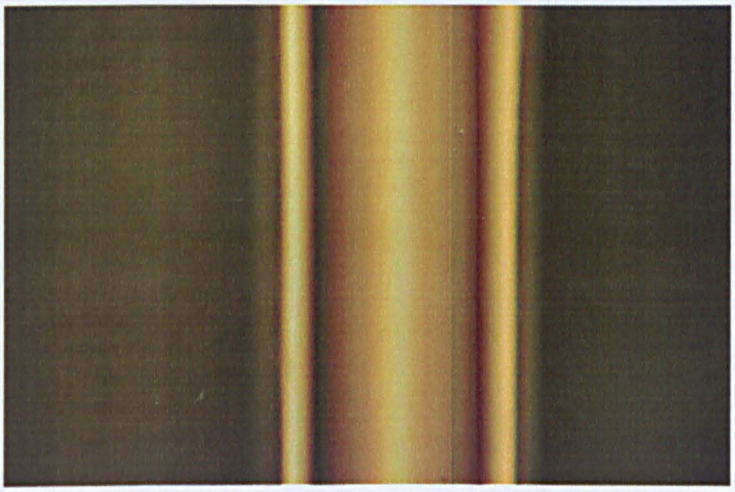

Figure 4.20 – $Al_2O_3:Cr^{3+}$ (Ruby) fibre

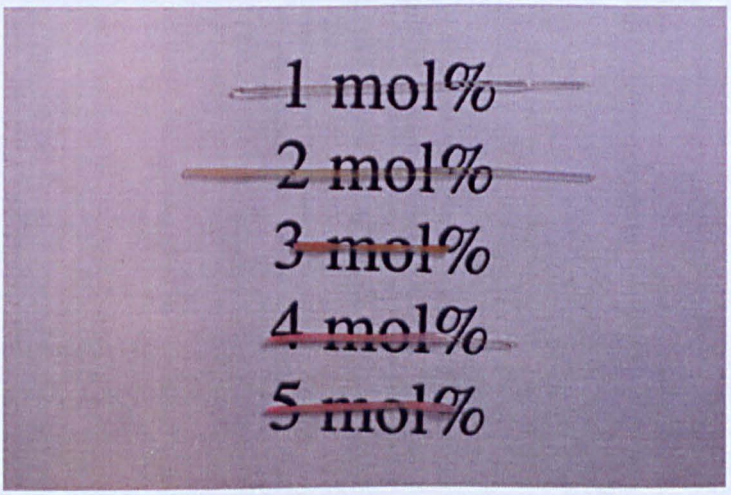

Figure 4.21 – $Al_2O_3:Er^{3+}$ fibres with different concentrations

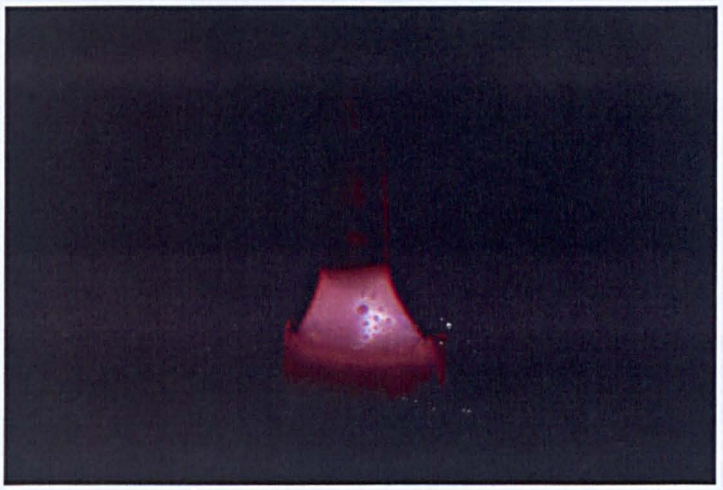

Figure 4.22 – Bubbles in melt during growth

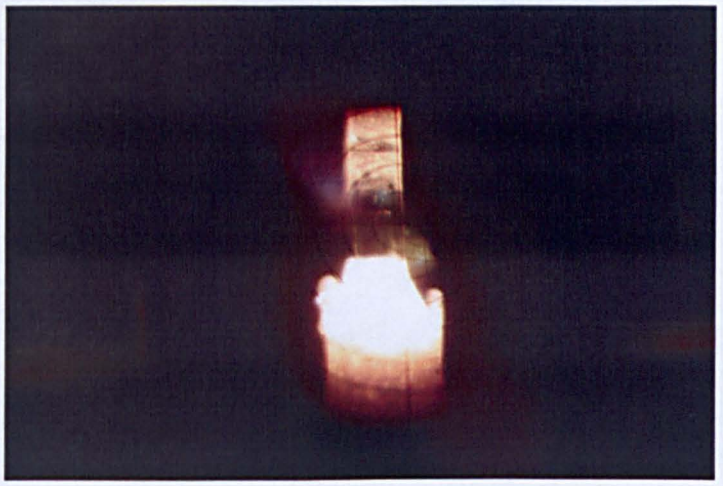

Figure 4.23 – $Y_3Al_5O_{12}:Er^{3+}$ (15mol%) unstable melt causes microvoids in fibre

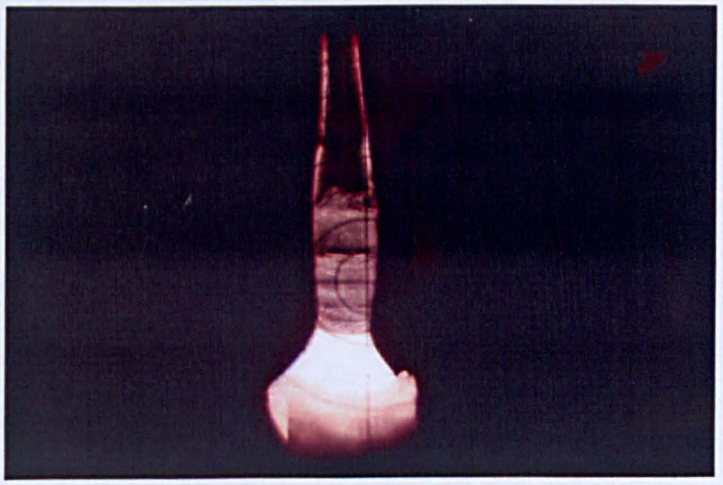

Figure 4.24 – $Y_3Al_5O_{12}:Er^{3+}$ (20mol%) unstable melt causes cloudiness in fibre

4.4.2.3 Y_2O_3 SCFs

All Y_2O_3 source rods were cold pressed and were cut into the required dimension. Among the three, Y_2O_3 was the easiest to handle and even though it was fragile, it was the most robust. Yttrium oxide was densely packed when pressed within a 15 ton load. No bubbles were seen in the melt during the growth processes. The diameters of the fibres grown were approximately 400μm. The pull rate used to grow this material was 1mm/min. The laser power used for this material fell in the range of 18-22W and again, is greatly dependent on the size of the source rod. There were no complications during the growth process even when dopant was at high concentration. The fibres at high concentrations of Er^{3+} were pinkish in colour and becoming a deeper pink as the concentration increased. See Figure 4.25. No visible cracks were observed in the fibres during the growth process.

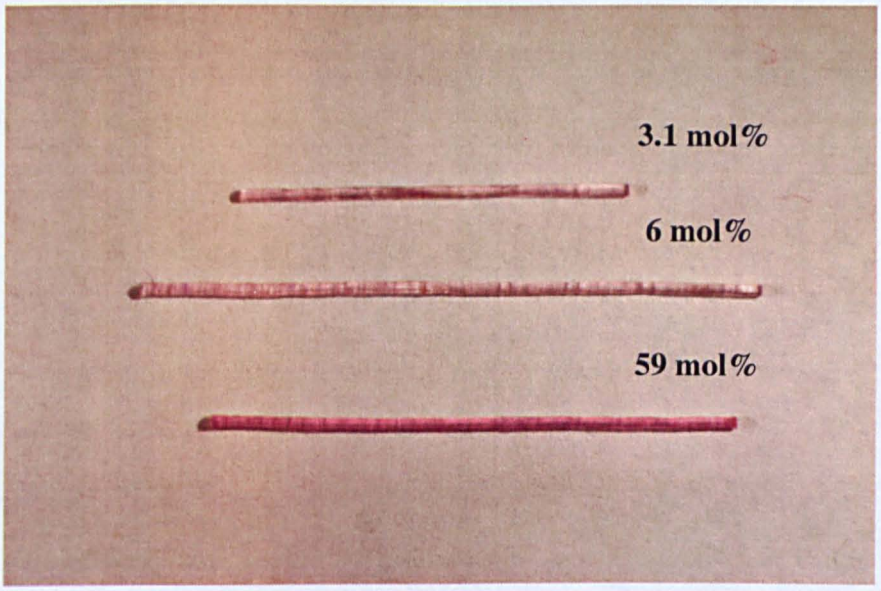

Figure 4.25 – $Y_2O_3:Er^{3+}$ fibres of different dopant concentrations

4.4.3 Polishing Processes

For fibres to be effective for characterisation and applications, the fibres have to be polished. In this work, a PM 2 Polishing Machine from *Logitech* was used to polish the fibres. The fibres were first mounted in capillary tubes. The fibres are aligned to the wall of the capillary tube and quartz wax used to secure it. Y_2O_3 fibres were extremely brittle, therefore to prevent them from breaking during polishing and characterisation, these fibres were placed in the capillary tube as shown in Figure 4.26. A hole was drilled in the middle of the capillary tube with an ultra-sonic drill, creating an opening that allowed the capillary effect to take place, since wax was required to be at both ends of the capillary tube. All other oxide fibres were mounted in the capillary tubes seen in Figure 4.26 throughout the polishing and characterisation processes. Polishing Y_2O_3 and $Y_3Al_5O_{12}$ required two stages in the polishing process. One is coarse polishing and the other is fine polishing. The capillary tubes, with the fibres, were mounted onto the PP5 polishing jig from *Logitech*. For coarse polishing, the jig was placed on a cast iron polishing plate and silicon carbide powder of 600μm (from *Buehler – Grit 600*) was used. Once the outline of the fibre ends appear and was relatively flat, the jig is then removed and placed onto a PM 2 polishing machine with a polyurethane pad. In this second stage, colloidal silica (from *Morrisons – Summer Grade Morisol W30*) was used to provide a fine polish. At this stage, the fibres were being polished below 1μm. Figure 4.27 and 28 show the ends of the fibres Y_2O_3 and $Y_3Al_5O_{12}$ respectively. It was noticed that cracks started appearing in Y_2O_3 fibres. These cracks were attributed to a moisture-related phenomenon which was mentioned in [2.7] and [2.13]. In the case of polishing Al_2O_3 fibres, which is the hardest material of the three, an extra stage was required before fine polishing. After the coarse polishing was done, the fibre was then polished on a brass polishing plate with 6μm diamond compound. Figure 4.29 shows the polished fibre end of Al_2O_3:Cr^{3+}. A reddish colour was observed and this showed that Cr^{3+} is present in the fibre. The orientations of the fibres grown were c-axis for Al_2O_3, <111> for $Y_3Al_5O_{12}$ and c-axis for Y_2O_3.

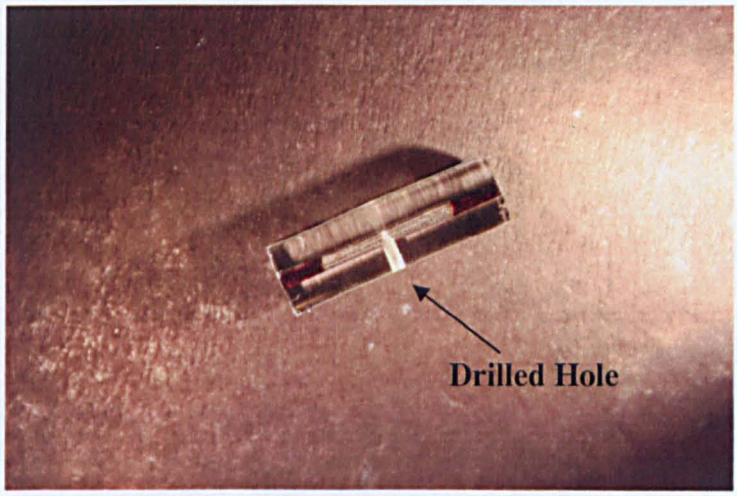

Figure 4.26 – Capillary tube with fibre mounted within

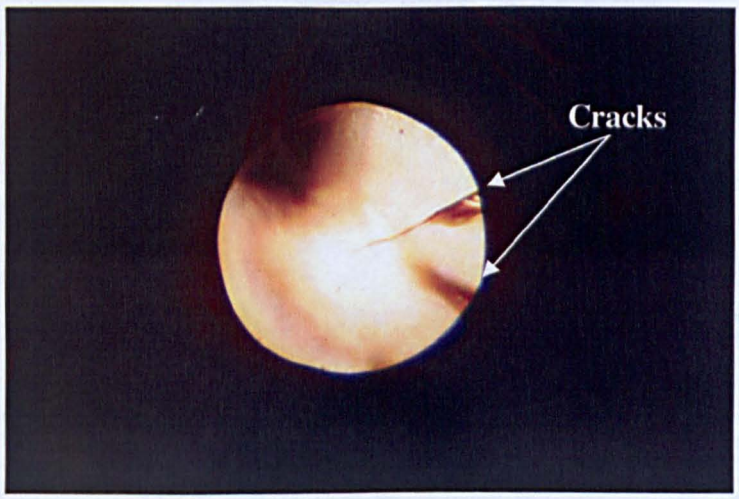

Figure 4.27 – Y_2O_3 fibre end

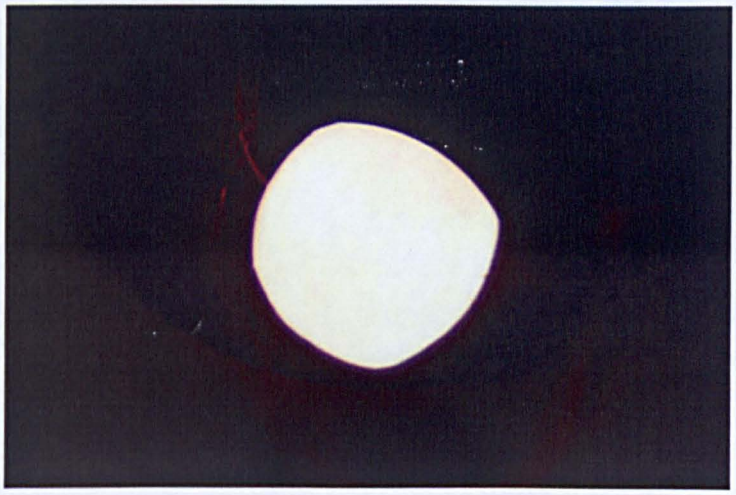

Figure 4.28 – $Y_3Al_5O_{12}$ fibre end

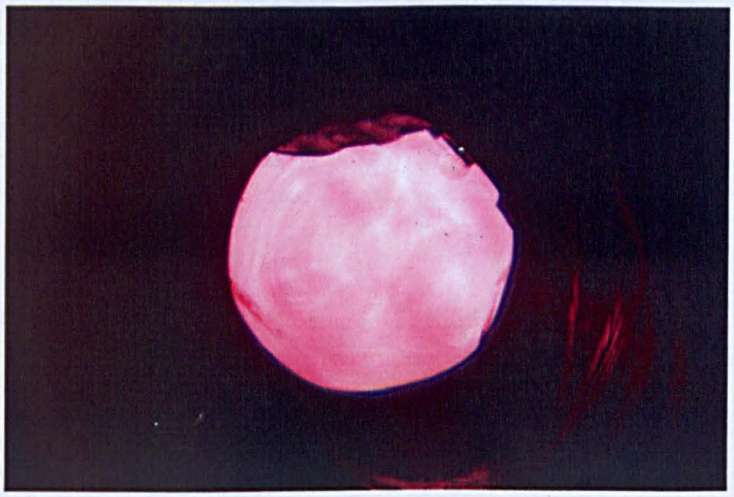

Figure 4.29 – $Al_2O_3:Cr^{3+}$ fibre end

4.4.4 SCFs Defects

As mentioned in the previous section, $Al_2O_3:Cr^{3+}$ (ruby) fibres gave the best quality and were the easiest to grow. *Seat* had mentioned also that pure sapphire and ruby fibres are easier to grow when there are from polycrystalline and monocrystalline source rods [2.57]. Besides it being easy to grow which minimises defects, another reason is that the diameter of the fibre is relatively small as compared to the other fibres grown. There were no observable irregularities in the diameter of the ruby fibres. Equation 4.1 states that the reduction in diameter, D reduces the dislocation density or defects present in the fibre. In Figure 4.30 a ruby fibre has a uniform diameter without visible defects on the surface. The other fibres grown in this work have diameters in the range of 300μm to 440μm. It was observed that all fibres in this range had irregular diameters and, when viewed under a microscope, had inclusions and rough growth ridges on the surface of the fibres. See Figure 4.31 to 33 for defects. These defects were tell-tale signs of poor temperature and zone stability [3.1]. *Tang's* [3.11] observation of SCF BaB_2O_4 showed similar inclusions to those found in the SCFs is in this work. Formation of inclusions occurs when supercooling takes place before the growth interface. Fibre growth rate plays an important role in constitutional supercooling because high growth rate and shallow temperature gradient leads to supercooling. Therefore, in this work the growth rate was reduced to eliminate inclusions. However, this problem persisted. The cause of these defects can be due to either the laser power instability or mechanical problems from the pull and feed mechanisms that introduced discontinuity. If it is mechanical defects, then the ruby fibre should share the same condition as the rest of the fibres. Therefore mechanical problems are ruled out. Then laser power instabilities would be the likely cause of the defects. From the Figure 4.5, it is observed that at high wattage, the laser power fluctuates more compared to when it is used at lower power. This can explain why ruby fibres with a small diameter do not have the defects whereas larger diameter fibres do. Reducing the diameter size of the fibre would then minimise the defect observed in this work and this would correspond to the equation 4.1. The focus of this work was to produce fibres of reasonable quality for simple characterisation and the fibres grown were good enough for this work as the fibres used in sensor applications have diameters ~300μm. Defects were still evident but a reduction of diameter did reduce the defects too.

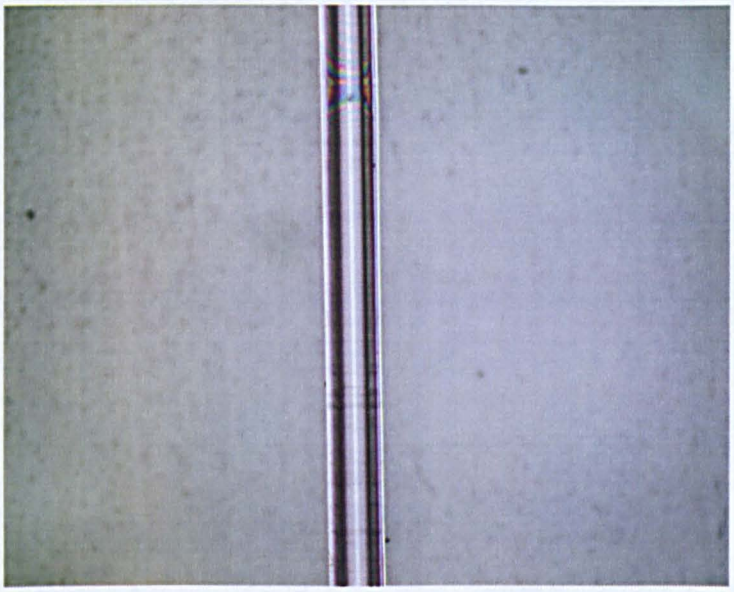

Figure 4.30 – Ruby fibre with uniform diameter

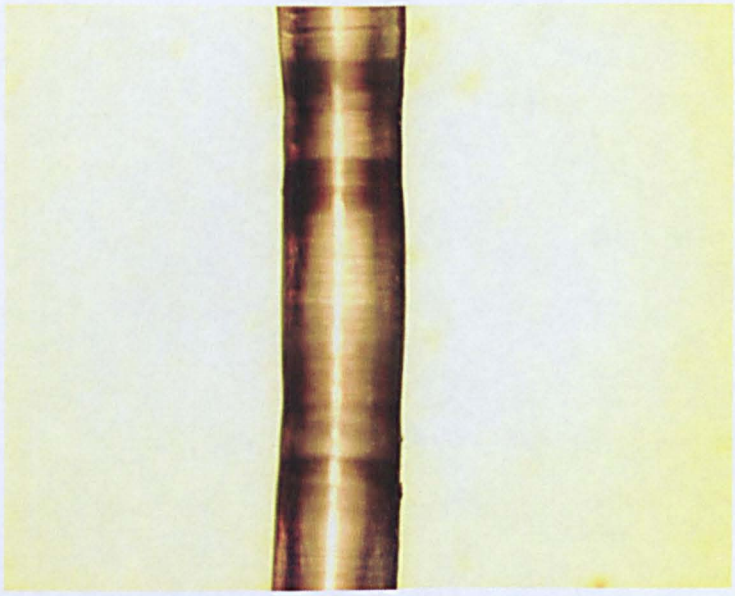

Figure 4.31 – Y_2O_3 fibre with irregularity in diameter

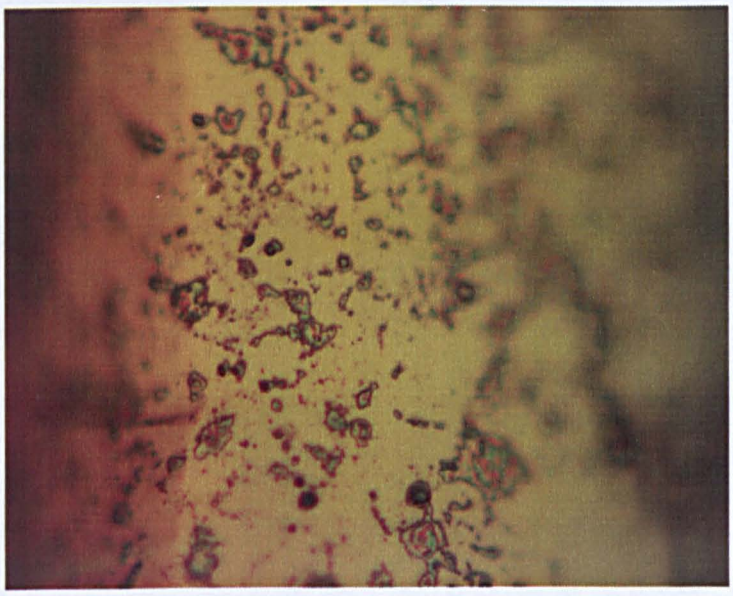

Figure 4.32 – $Y_3Al_5O_{12}$ fibre with inclusion defects (Magnification x100)

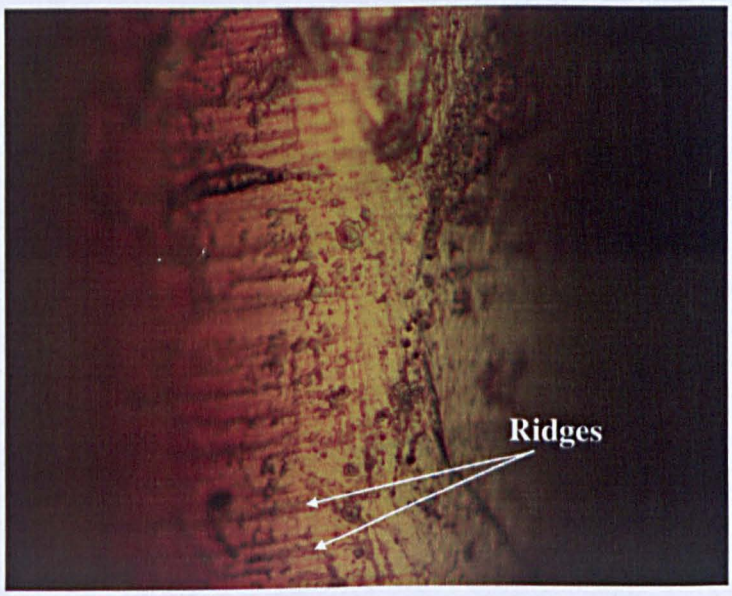

Figure 4.33 – $Y_3Al_5O_{12}$ fibre with inclusion defects and rough ridges (Magnification x100)

4.5 References

[4.1] K. Eickhoff and K. Gürs, *Crucible Free Zone Melting of Ruby Crystals by Heating Up the Melting Zone via Laser*, J. Cryst. Growth, **6**, 1, 21, 1969

[4.2] R. S. Feigelson, *Growth of Single Crystal Fibers*, MRS Bull., **13**, 10, 47, 1988

[4.3] V. Phomsakha, R. S. F. Chang and N. Djeu, *Novel Implementation of Laser Heated Pedestal Growth for Rapid Drawing of Sapphire Fibers*, Rev. Sci. Instrum., **65**, 12, 3860, 1994

[4.4] J. L. Nightingale, *The Growth and Optical Applications of Single-Crystal Fibres*, PhD Thesis, Stanford University, 1986

[4.5] S. V. Tsivinsky, *Factors Governing the Dislocations Density in the Czochralski Method of Growing Crystals*, Fiz. Met. Metalloved., **25**, 6,1013, 1968

[4.6] L. M. Thomas, D. M. Andrauskas and H. R. Verdún, *Growth and Characterization of Nickel-Doped Garnets by the Laser-Heated Pedestal Growth Method*, Pro. SPIE, **1104**, 87, 1989

[4.7] C. R. Black, D. M. Andrauskas, G. F. de la Fuente and H. R. Verdún, *Laser Heated Pedestal Growth of Nd-Doped Oxide Crystals for Diode Pumping*, Proc. SPIE, **1104**, 175, 1989

[4.8] M. J. F. Digonnet, C. J. Gaeta, D. O'Meara and H. J. Shaw, *Clad Nd:YAG Fibers for Laser Applications*, J. Light. Tech., **LT-5**, 5, 642, 1987

[4.9] J. H. Sharp, *The Growth and Optical Characterisation of Single-Crystal Fibres*, PhD Thesis, University of Strathclyde, 1992

5 Characterisation of SCF Experimental Methodologies

5.1 Introduction

Chapter 3 has briefly introduced the background theory of the trivalent rare earth ions Er^{3+} and Yb^{3+} and the behaviour of these ions in both crystals and glasses. In Chapter 4, description of the growth of SCFs and characteristics of the fibres was discussed. This chapter will discuss the characterisation experiments carried out on the grown fibres. Investigations are made to develop a deeper understanding to both the physical and spectroscopic characteristics of the doped fibres produced by the LHPG technique.

Chapter 5 is divided into two sections. The first section deals with the physical characterisation and the second the spectroscopic characterisation. The first section consists of diameter measurements of the growth fibre (Section 5.2.1) and strength measurements of each host material (Section 5.2.2). In the latter section, the absorption (5.3.1), fluorescence and upconversion spectra (Section 5.3.2) and lifetime emission (Section 5.3.3) are investigated. From these experiments, we can determine the fundamental advantages and limitations of the fibres that have been produced and analysis made based on the findings from these experiments for future applications.

5.2 Section One – Physical Characterisation

5.2.1 SCF Diameter Measurement

It is crucial that the diameter of optical fibres produced is uniform. Consistency in diameter is required in order to reduce radiation losses and to maintain a good optical transmission. Various methods are available to determine the diameter of fibres. It is desirable to have a feedback system that is able to monitor the diameter of fibre as it is being grown. In situations like these, a non-contact based method would be extremely suitable.

Most non-contact diameter measurement methods involve the use of a laser. The fibre Image Projection method [5.1] is one of them. An oscillating mirror is used to traverse a laser beam from one side of the fibre to the other. This sweeping motion projects an image onto a photo-detector which is placed just after the laser beam passing through the fibre. The fibre diameter is approximately proportional to the interception time interval. Another non-contact method is Forward Light Scattering [5.2]. A laser beam is directed at fibre at an angular range of ± (5 – 90°) in the plane perpendicular to its axis and the beam is collected by a diode array detector. The intensity of the diffraction fringes that are produced is determined by the angle of the incident beam. The change in diameter of the fibre not only changes the number of fringes produced but also the separation of these fringes. The fringe spacing is directly proportional to the diameter.

In the present LHPG growth system, (an open loop system) such monitoring arrangements are not yet available. Therefore a quick method is needed to establish the diameter of the fibre. Understanding the geometrical qualities could aid in the improvement of the present LHPG system.

5.2.1.1 Experiment Layout and Settings

All fibres grown were measured post-growth with the Filar Eyepieces technique [5.3]. This is a quick and effective method to determine the diameter of the SCF. In this technique, a Filar microscope eyepiece (*Nikon Filar Microscope Eyepiece 10 x N*) is mounted as the right side eye piece of a microscope (*Nikon Eclipse ME 600*). A 10x microscope objective was selected for all the diameter experiments. See Figure 5.1 and 5.2 for the Filar microscope eyepiece and experimental set up. Before the start of any measurements, calibration is needed between the Filar microscope and a graticule. The Filar microscope and the graticule have a scale of 1mm and are divided into 100 smaller divisions of 0.01mm. In order to calibrate the system, the two scales must coincide with each other. This is done by moving one end of the graticule scale to the 0 (zero) position of the Filar Microscope and after which turning the Magnification adjustment ring until the two scales overlaps. The set up must be repeated if a different microscope objective is used.

The graticule is then removed and is replaced with the fibre that requires measurement. Before any measurement is taken the 0 (zero) positions of the main and vernier scales must be aligned. Once that is completed the fibre on the traversing stage of the microscope is then moved until the fiducial line in the Filar microscope is aligned at one edge of the diameter, see Figure 5.2. By rotating the Filar Microscope knob, the fiducial line is then moved to the other edge of the fibre. From the main and the vernier scale, a length L is then recorded. The actual length L_{actual} is obtained with the following:

$$L_{actual} = \frac{L}{MOP} \tag{5.1}$$

MOP is the magnification power of the objective used. To obtain the average diameter of the fibre, the measurement mentioned above is taken throughout the entire length of the fibre at intervals of 0.5mm. This also determines the uniformity of the fibre. To prevent errors which could occur due to focusing of the edges of the fibre and variation in the intensity of the light from the microscope, each point along the fibre is taken three times. The average of the three readings is then substituted into the formula 5.1.

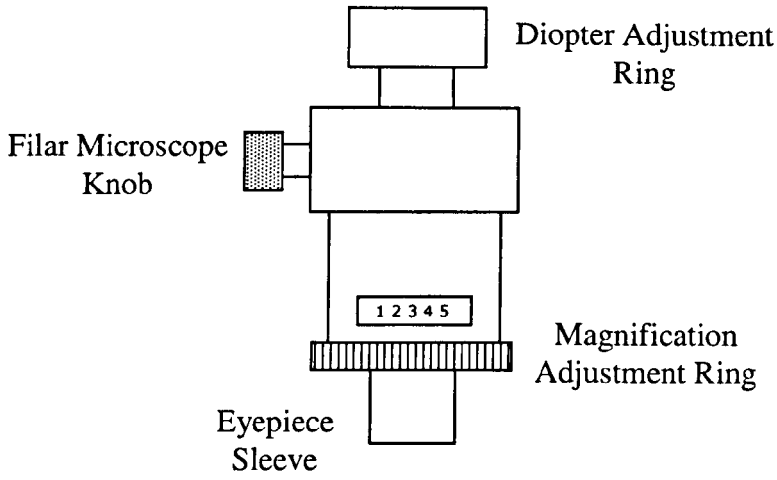

Figure 5.1 – Filar microscope eyepiece

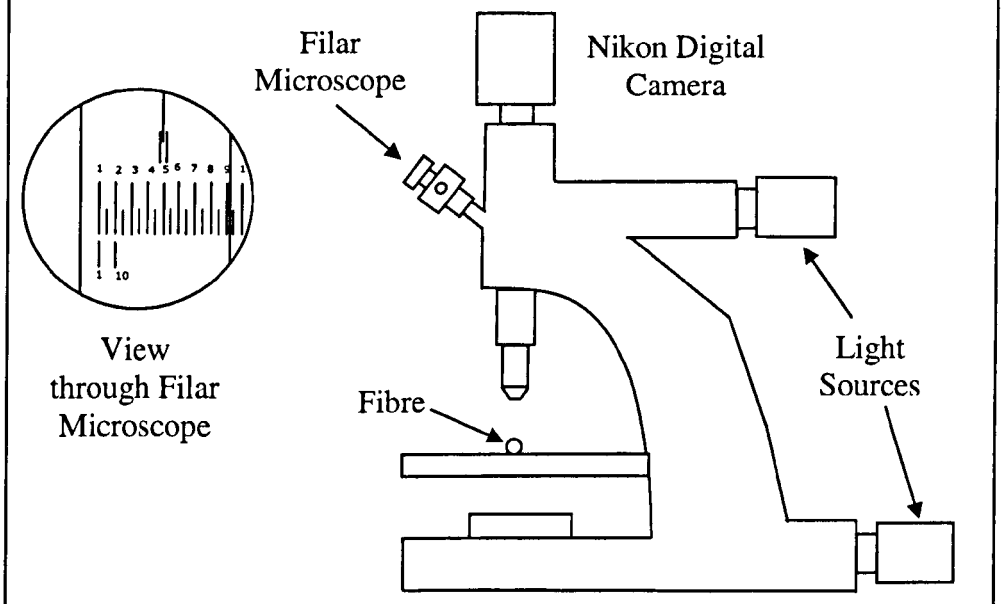

Figure 5.2 – Diameter measurement setup

5.2.2 Mechanical Testing Measurement

The shear strength of the fibres was measured using a simple three-point bending test on the fibres that were growth by LHPG. All tests were preformed under room temperature conditions. This test was done to demonstrate the difference in strength of the three different fibre materials that were grown in this work. The principle of the three-point bending test was to place a specimen, in this case a fibre, on two supports and a force is applied at the centre of the fibre until it is fractured, (sometimes known as the strain to failure (STF) test).

5.2.2.1 Experimental Layout and Settings

A simple jig was constructed for this experiment. See Figure 5.3. The jig consists of two supporting legs on which the fibre can be placed on. The distance between the supports is adjusted by micrometer head at the side of one of the supporting legs. The loading bar is fabricated from clear acrylic. The radii of the supporting legs and the loading bar are similar. A *Llyod Instrument 10000* Material Testing Machine was used to carry out this three-point bending test. Firstly, the jig was placed at the base of the Material Testing Machine, where a 50N load cell was attached to the depression arm. The acrylic loading bar was then attached to the end of the load cell. The distance between the two supporting legs was 19mm. This dimension was chosen because most of the fibres grown for these experiments were approximately 24mm in length. The fibres were then placed at the centre of the two supporting legs as shown in Figure 5.3. The acrylic loading bar was then brought near to the fibre, ~1mm above the fibre, and further adjustment was made to ensure that the loading bar was at the centre of supporting arms and the force to be applied at a 90° angle to the fibre being tested. After which the acrylic loading bar was lowered at a speed of 0.5mm/min. When in contact with the acrylic loading arm, the fibre is bent until it breaks. The instrument is linked to a computer and the force required to strain the fibre until it breaks recorded. The recorded force, F in Newtons is then substituted into the formula below:

$$S = \frac{Fl}{4M} \times 10^{-6} \tag{5.2}$$

S is the bending/shear strength in MPa, l is the distance, in mm, between the two supporting legs and M is the moment of resistance, in mm^3, of the test fibre and can be calculated by $M = \pi d^3/32$, where d is the diameter in mm. See Figure 5.4. All forces required to strain the fibres to failure were recorded and comparisons made between different materials.

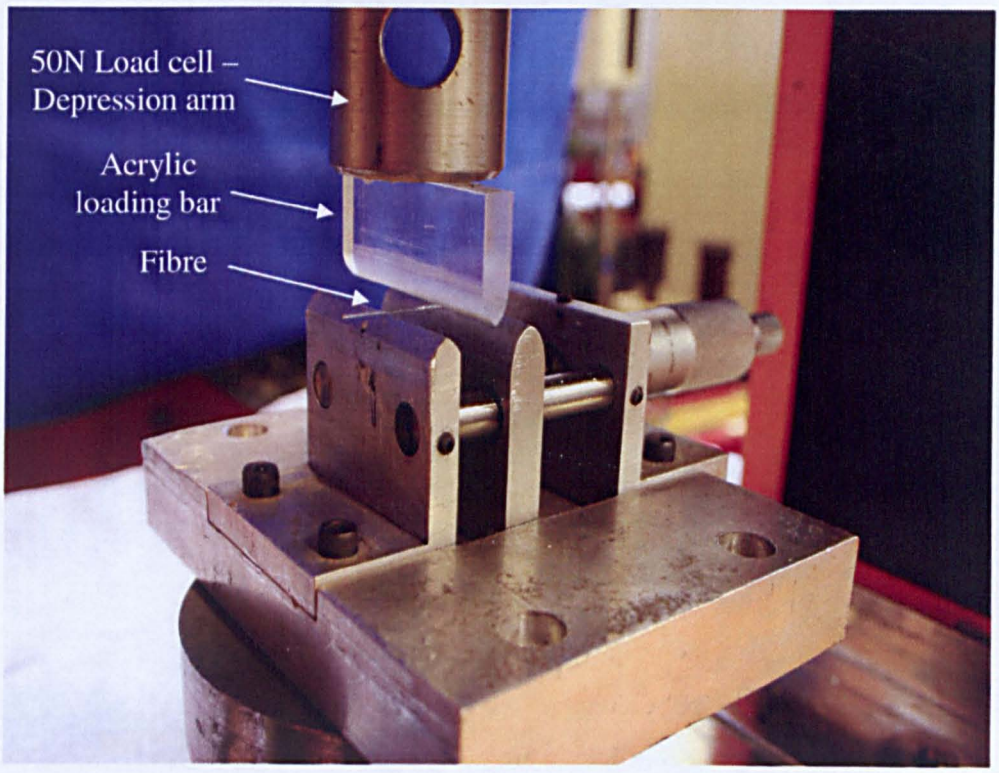

Figure 5.3 – Three point bending jig

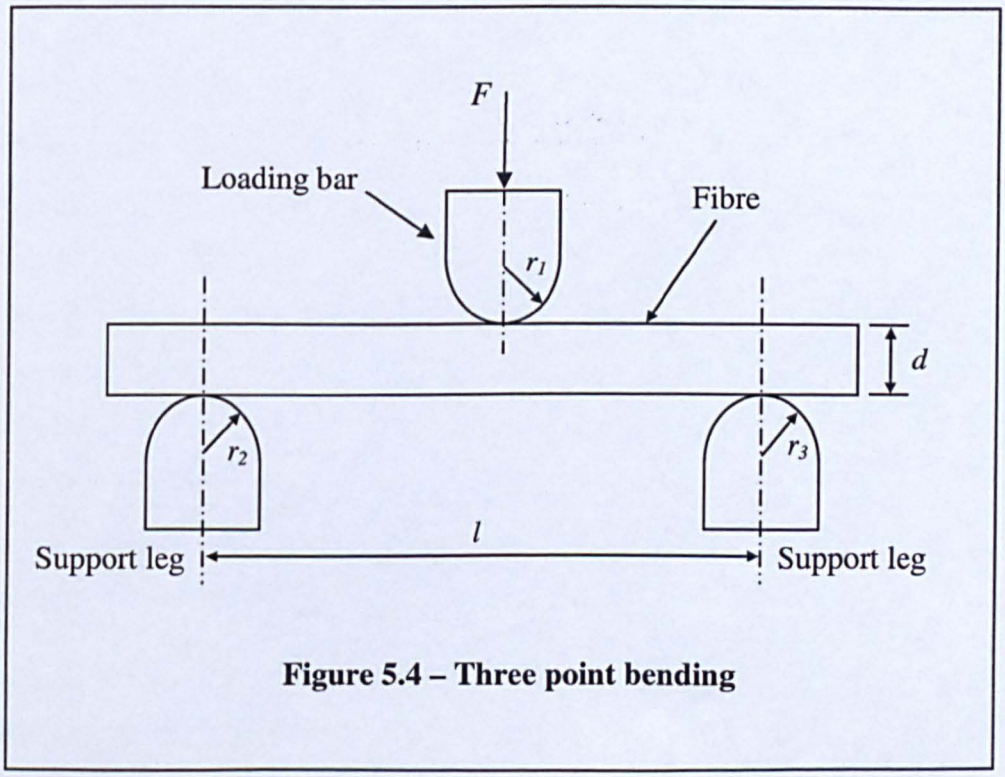

Figure 5.4 – Three point bending

5.3 Section Two – Spectroscopy Characterisation

5.3.1 Absorption Spectrum Measurement

YAG and Yttria fibres have been grown doped with either Er^{3+} alone or Er^{3+} co-doped with Yb^{3+} and Al_2O_3 fibres containing the transition metal Cr^{3+} (ruby). The absorption spectra were recorded from the 400nm to 1700nm. The spectra collected reveal the strength of each individual absorption band of the different doping levels of rare earths used in the fibres. This measurement helps to determine the appropriate choice of the excitation source.

5.3.1.1 Experimental Layout and Settings

The single-beam method, see Figure 5.5, is a simple and quick way to determine the absorption spectrum for an extensive range of wavelengths. A Quartz Halogen lamp (*Bentham IL4*), having an output wavelength range of >400nm, was used as the light source. The source was collimated using two collimating lenses. The parallel beam is then directed into a 20x microscope objective where it is then focussed onto the end of the fibre. The light exiting the other end of the fibre is collected by a second 20x microscope objective. A third lens after last microscope objective is then used to focus the light into the entrance slit of the monochromator (*1/2m DIGIKRÖM DK480 – CVI Laser Corporation*). At the exit slit, either a PIN silicon photodetector (*Hamamsutsu*) for the visible region or a InGaAs/PIN photodetector (*IR Femto Watt Photoreceiver – New Focus Inc.*) for the near infrared region is used. An optical chopper was placed in between the last lens and the entrance slit of the monochromator. The entrance and exit slit widths for the monochromator used for this experiments ranged from 30μm to 150μm, depending on the desired bandpass. Scanning was done at 0.5nm/step from 400nm to 1800nm. The signals from the detectors were processed by a lock-in amplifier (*500MC – Sci Tech*) to facilitate a high signal to noise ratio. Labview software was used to control the monochromator remotely and also used to process the data collected.

Absorption bands are apparent when there is a significant reduction in the intensity of the light transmitted through the sample. They are generally in the form of dips in

the spectrum collected. Therefore, the lamp spectrum from the visible to the infrared region is required as a reference to determine the absorption spectra of the doped fibre. This is obtained by directing the lamp source into the monochromator by placing the two microscope objectives together. The absorption spectrum is determined by dividing the reference light (lamp spectrum) by the spectrum from the doped fibre. The lamp spectrum from the Quartz Halogen lamp for both the visible and the infrared regions is shown in Figure 5.6 and 5.7. Figure 5.8 an image of the end of a Y_2O_3 fibre as it is collected from the second microscope objective.

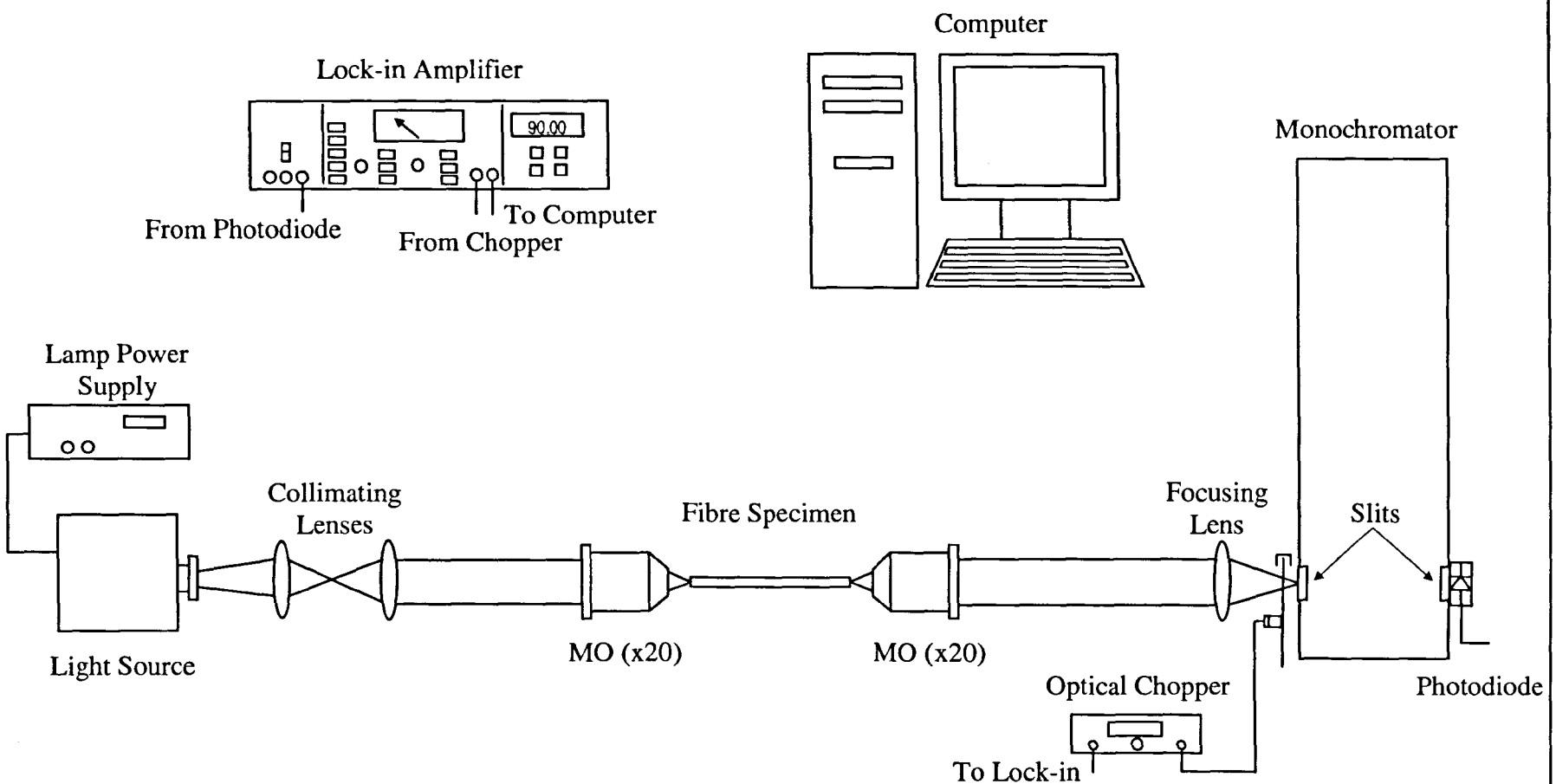

Figure 5.5 – Absorption spectrum experimental setup

Figure 5.6: Visible spectrum of Quartz Halogen lamp (Bentham IL4)

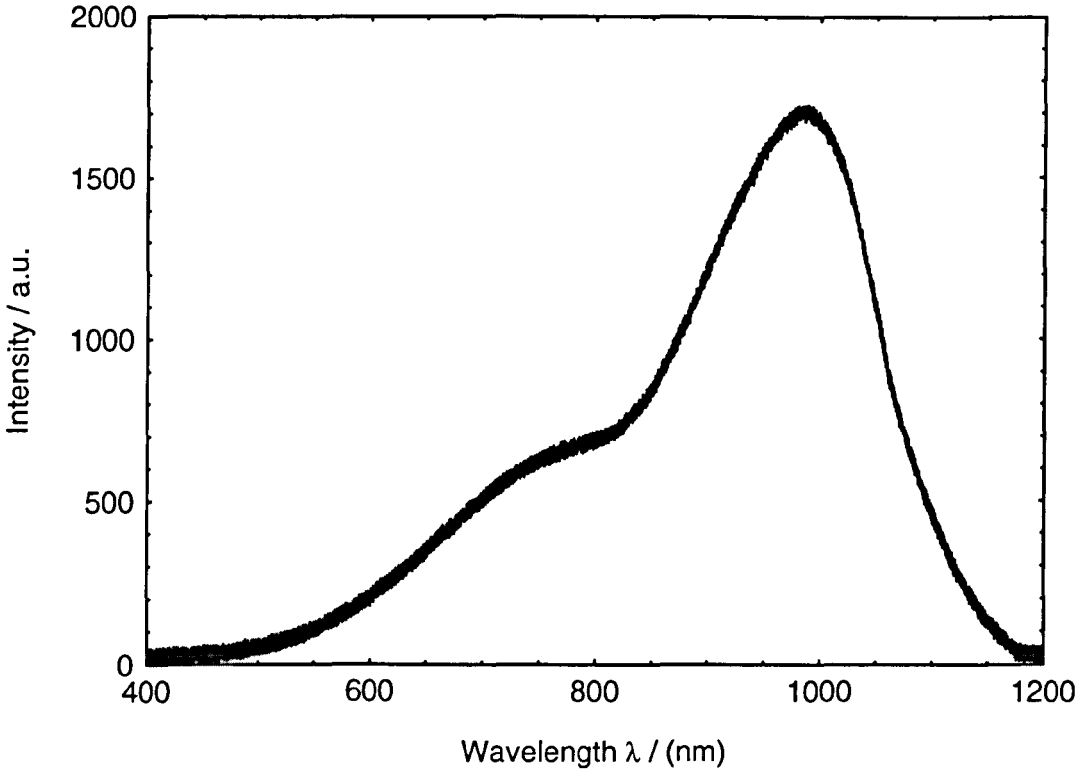

Figure 5.7: Infrared spectrum of Quartz Halogen lamp (Bentham IL4)

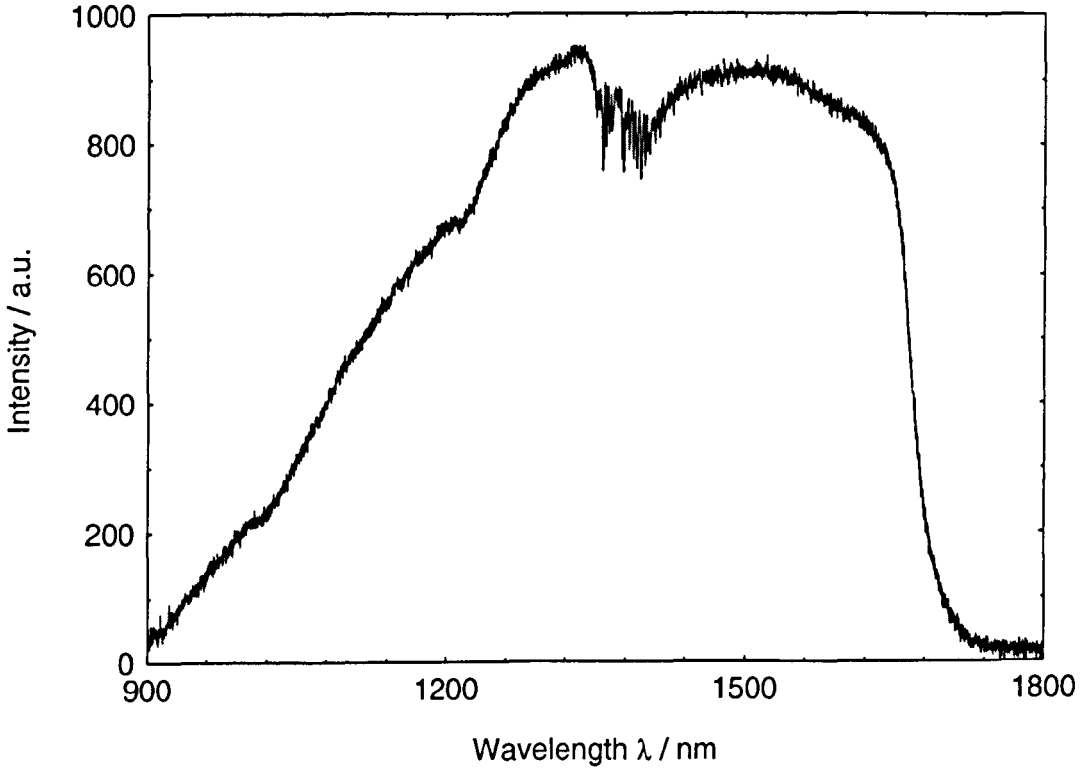

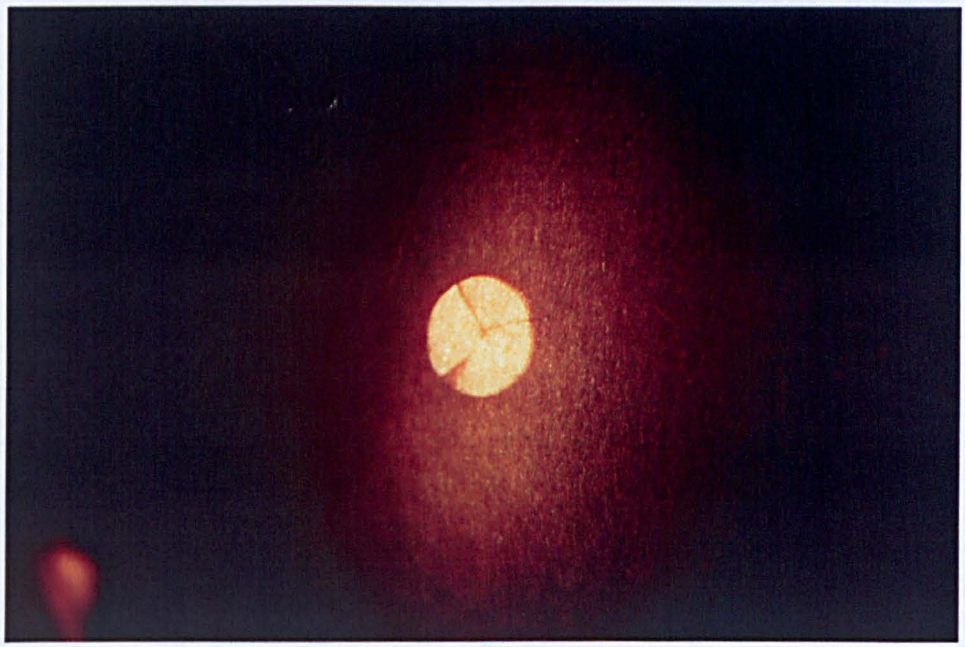

Figure 5.8 – Light from end of Y_2O_3 fibre

5.3.2 Fluorescence and Upconversion Measurement

From the absorption spectrum, one can determine the laser source needed to excite the doped fibre. It was observed that all SCFs doped with Er^{3+} has an absorption band at $^4I_{15/2} \rightarrow {}^4I_{11/2}$ transition similar to the work in Er^{3+} doped glass fibers [5.4]. Therefore an excitation source in this region was selected. Throughout the process of the fluorescence experiments, it was observed that light was emitted from the fibres not only in the infrared region but also at wavelengths shorter than that of the excitation source, in the visible region. All excited fibres produce a visible green emission. This is the tell tail sign of the process known as anti-Stokes fluorescence or upconversion. This process only occurs when the dopant level is high and all fibres in this work are relatively highly doped with erbium.

As for ruby, the absorption bands are in the $^4T_1$ and $^4T_2$ energy levels which fall in the regions of 400nm to 600nm [5.5]. Only the absorption in the 500nm region was used for excitation in this work. A laser of this region was selected to excite the fibre.

5.3.2.1 Experimental Layout and Settings

Both the fluorescence and the upconversion experimental setup are similar. Different excitation sources were used during the experiments. Lasers selected were according to the appropriate absorption bands. For both YAG and Yttria SCF, 965nm and 975nm laser diodes were used. See Figure 5.9 and Figure 5.10. For the pump source at 965nm (*LACRYS – model 402*), collimating lenses were placed in front of the laser. The collimated laser beam is directed into a 20x microscope objective and is then focused into the fibre. The emission from the fibre is collected by the second 20x microscope objective. The collected beam is then focussed, by the third lens, into the entrance slit of the monochromator and an optical chopper is located at the entrance slit. The slits for both entrance and exit of the monochromator were no larger then 250μm. The InGaAs/PIN photodetector was used for fluorescence experiments and as for the upconversion experiment a Photomultiplier tube (PMT – *Hamamsutsu model R928*) was used for data acquisation. When the pigtail laser diode at 975nm (Avanex *model A1998PLM*) was used, the collimating lenses and the first microscope objective are removed. Since this laser diode is a pigtail laser a fibre

optic cable is attached, it is directly butt coupled to the end of the fibres. For the ruby fibres, a 532nm (*Frequency Doubled Nd:YAG laser – Excellence Optoelectronics Inc.*) was employed to excite the fibre. The setup of this experiment is similar to that when using the 965nm diode laser. A PIN silicon photodetector was place at the exit slit of the monochromator to collect the fluorescence light. All data for the experiments are collected and stored in the computer. Fluorescence measurements performed for fibres doped with Er^{3+} and Yb^{3+} was measured over the wavelength range of 400nm to 1700nm. For ruby fibres the fluorescence performed was from 500nm to 600nm. The laser lines for 532nm, 965nm and 975nm are shown in Figure 5.11, 5.12 and 5.13.

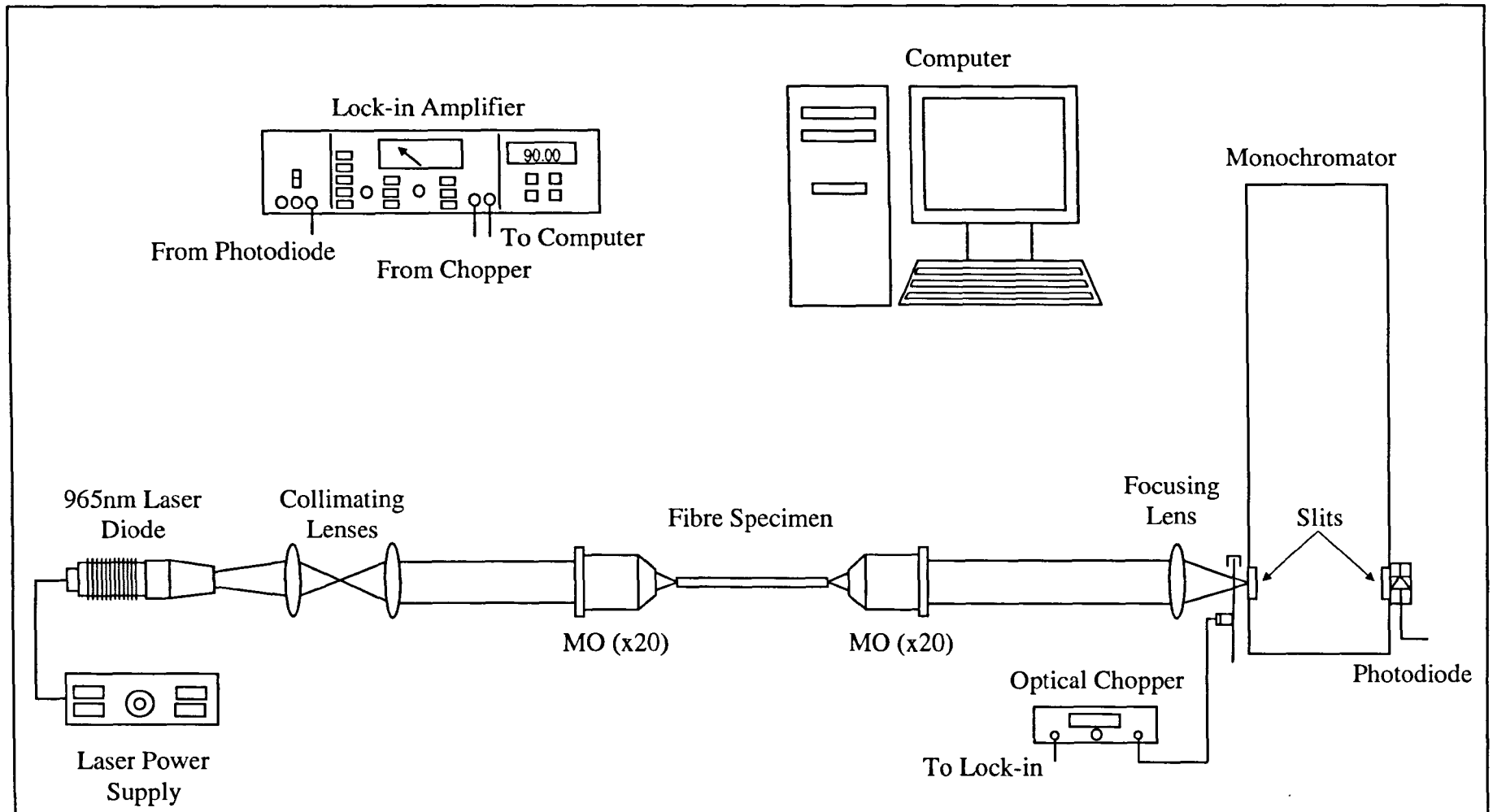

Figure 5.9 – Fluorescence spectrum experiment setup with 965nm laser diode

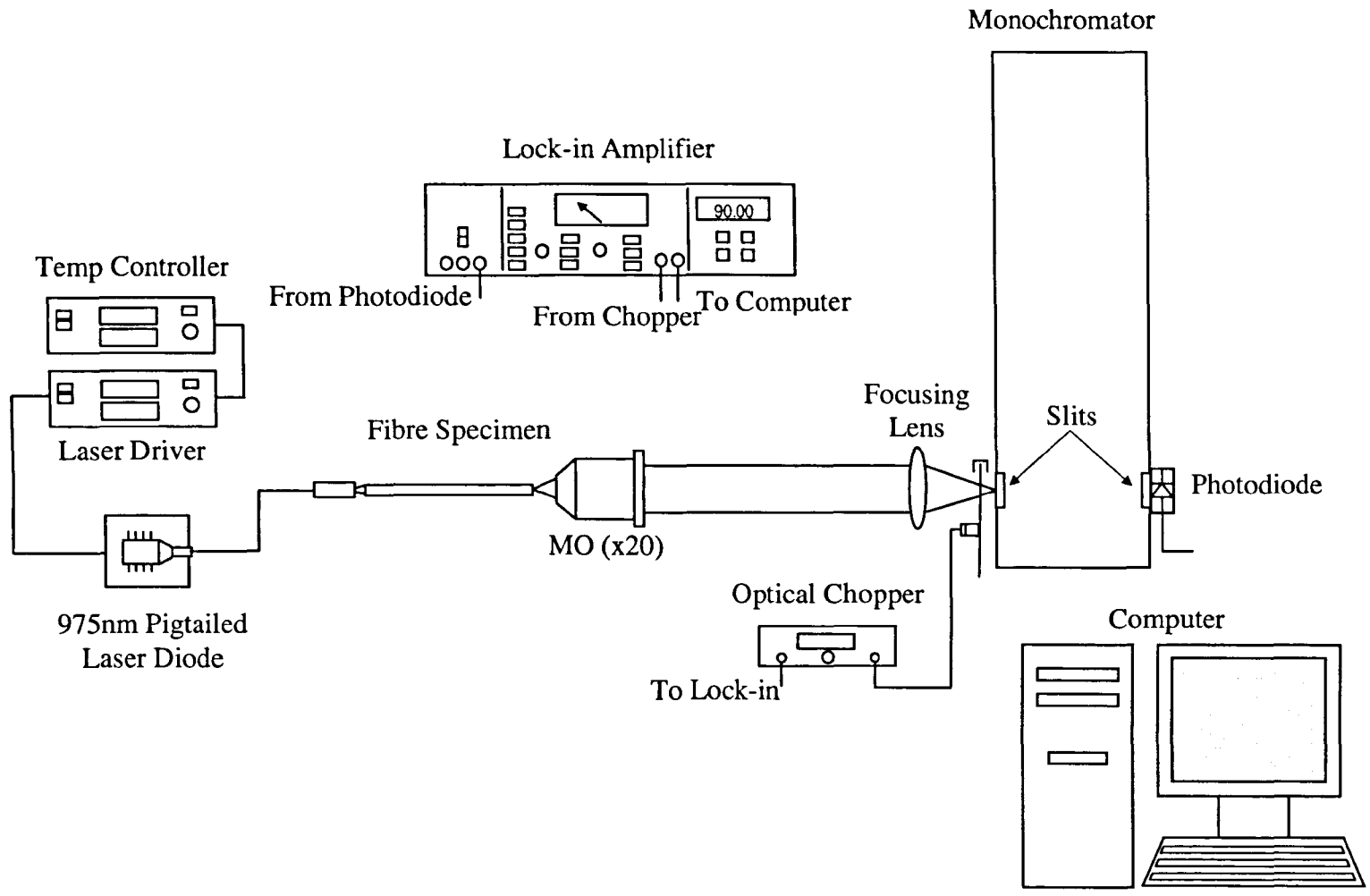

Figure 5.10 – Fluorescence spectrum experiment setup with 975nm pigtail laser diode

Figure 5.11: Laser line for 532nm laser diode

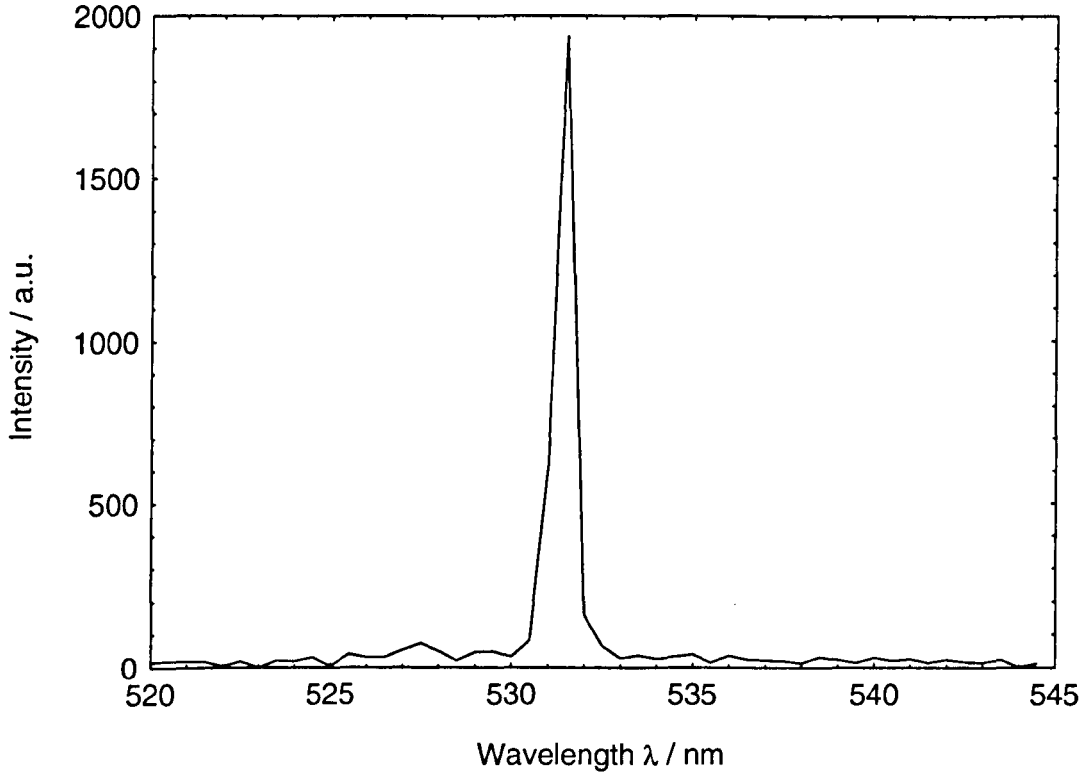

Figure 5.12: Laser line for 965nm laser diode

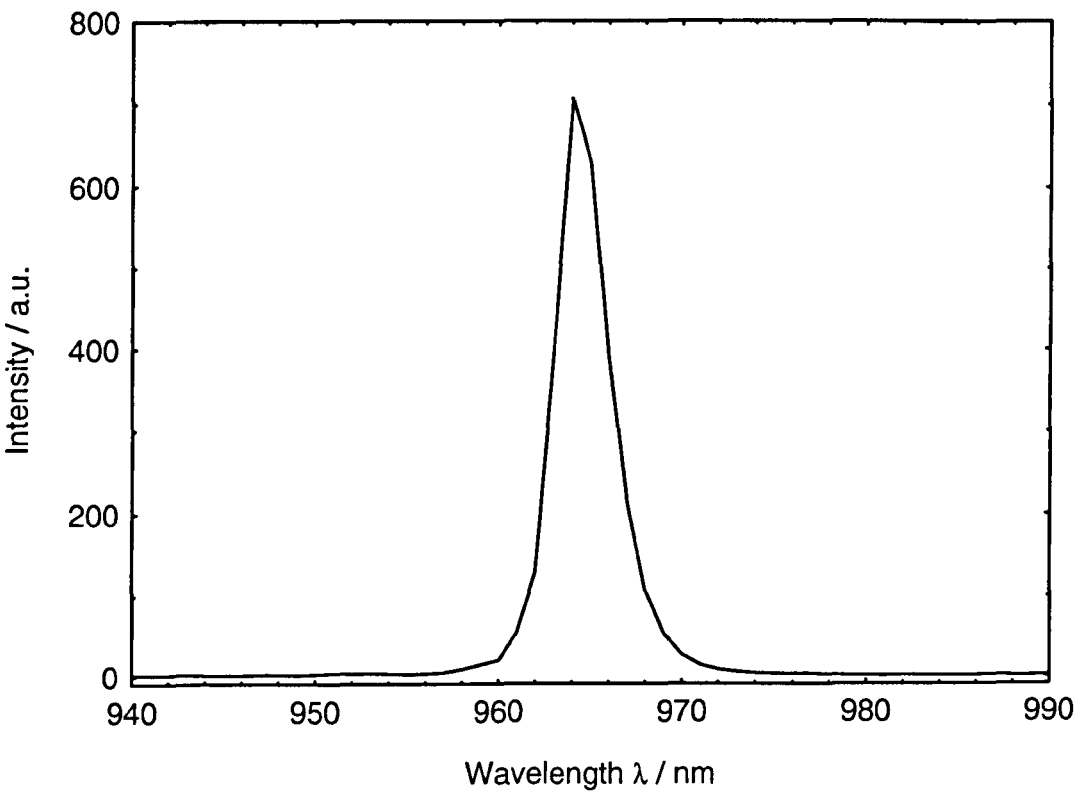

Figure 5.13: Laser line for 975nm pigtailed laser diode

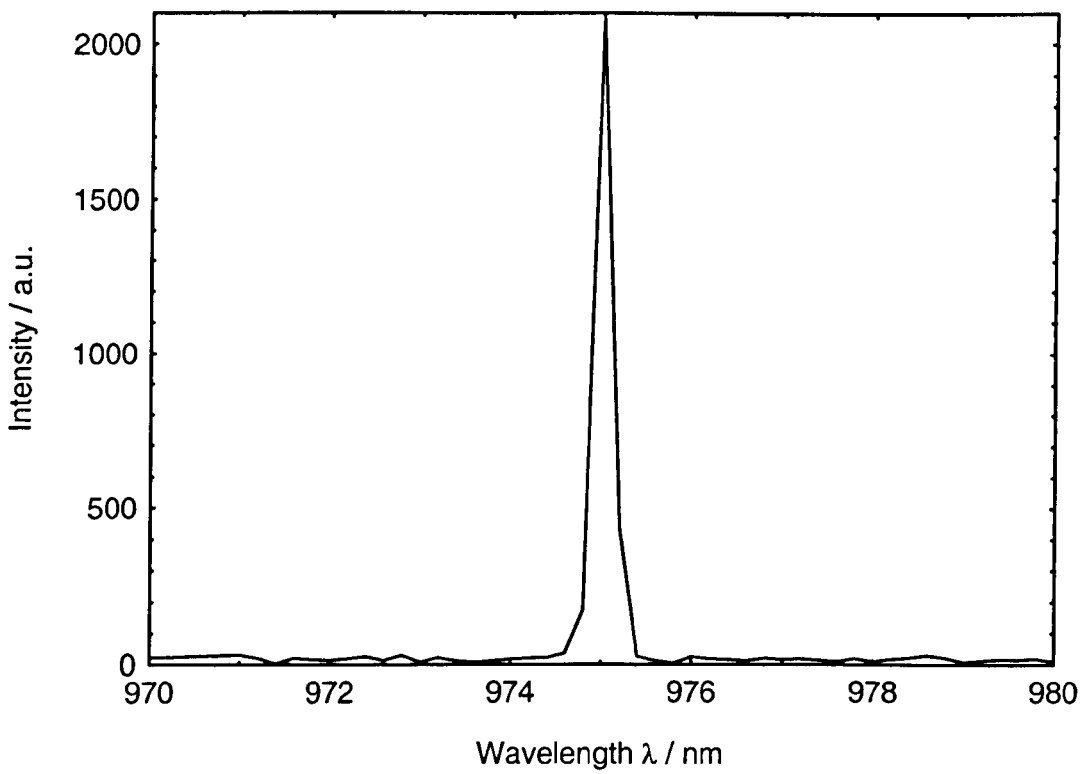

5.3.3 Fluorescence Lifetime Measurement

One way to study the interaction between the host material and the rare earth is to know its lifetime, τ. The lifetime of Er^{3+} varies with different hosts. Much work has already been done for Erbium doped glass composition materials which can have lifetimes as low as 4ms [5.6] for tellurite to as high as 14ms [5.7] for Na-K-Ba-silicate at transition $^4I_{13/2} \rightarrow {}^4I_{15/2}$. In this work, it is our interest to look at the lifetime decay of Er^{3+} and Er^{3+} co-doped with Yb^{3+} in the $^4I_{13/2} \rightarrow {}^4I_{15/2}$ levels under different concentration levels for different host SCFs. The level of concentration of rare earth incorporated into the host fibre will determine the difference in τ [5.8, 9]. Fibres that are doped with higher amounts will have the possibility of rare earth clustering or concentration quenching.

5.3.3.1 Experimental Layout and Settings

Figure 5.14 shows the schematic of the experiment for fluorescence lifetime measurements. Two excitation sources, at 965nm and 975nm, were used in these experiments. For the diode laser at 965nm, its beam is collimated using a telescope arrangement and an optical chopper is placed in between the two lenses at the confocal point. The output beam is focused onto the fibre by a 20x microscope objective. When the 975nm, pigtailed laser, was used the collimating lenses and the first microscope objectives were removed. The fibre optic cable from the laser is placed at the entrance of the fibre. An optical chopper was placed in between the two. The fluorescence from the fibre is collected by the second microscope objective and focussed onto the InGaAs/PIN photodetector. Optical filters were placed in front the detector to observe decay at specific wavelength/band. A long pass filter was used to eliminate all wavelengths below 1250nm, firstly to prevent the detector from saturation and secondly the interest was to look at the decay at wavelengths in 1400nm to 1700nm region. A bandpass filter at 1550nm (centre wavelength tolerance ±2.4nm) was used to determine the decay just at this wavelength. The monochromator could also be used as a bandpass filter. The grating of the monochromator was rotated to the specific wavelength of interest and the detector was placed at the exit slit. The signal is then processed by a digital oscilloscope (*Hewlett Packard – model 54520A*) and data stored on disk. In order to observe an

exponential curve that represents the fluorescence decay, the modulation of the signal must be done at a low frequency. In this experiment, the signal is modulated by an optical chopper and the frequency used was ranging from 5Hz to 8Hz (the setup system has a decay of 0.4ms and was taken into account in all decay experiments). Data collected is then curve fitted using the EASYPLOT software package to obtain the decay. It was demonstrated that the data followed the first order exponential decay function (graphs not shown). Due to the relatively weak upconversion signal from the fibre, upconversion decay is not investigated in this work.

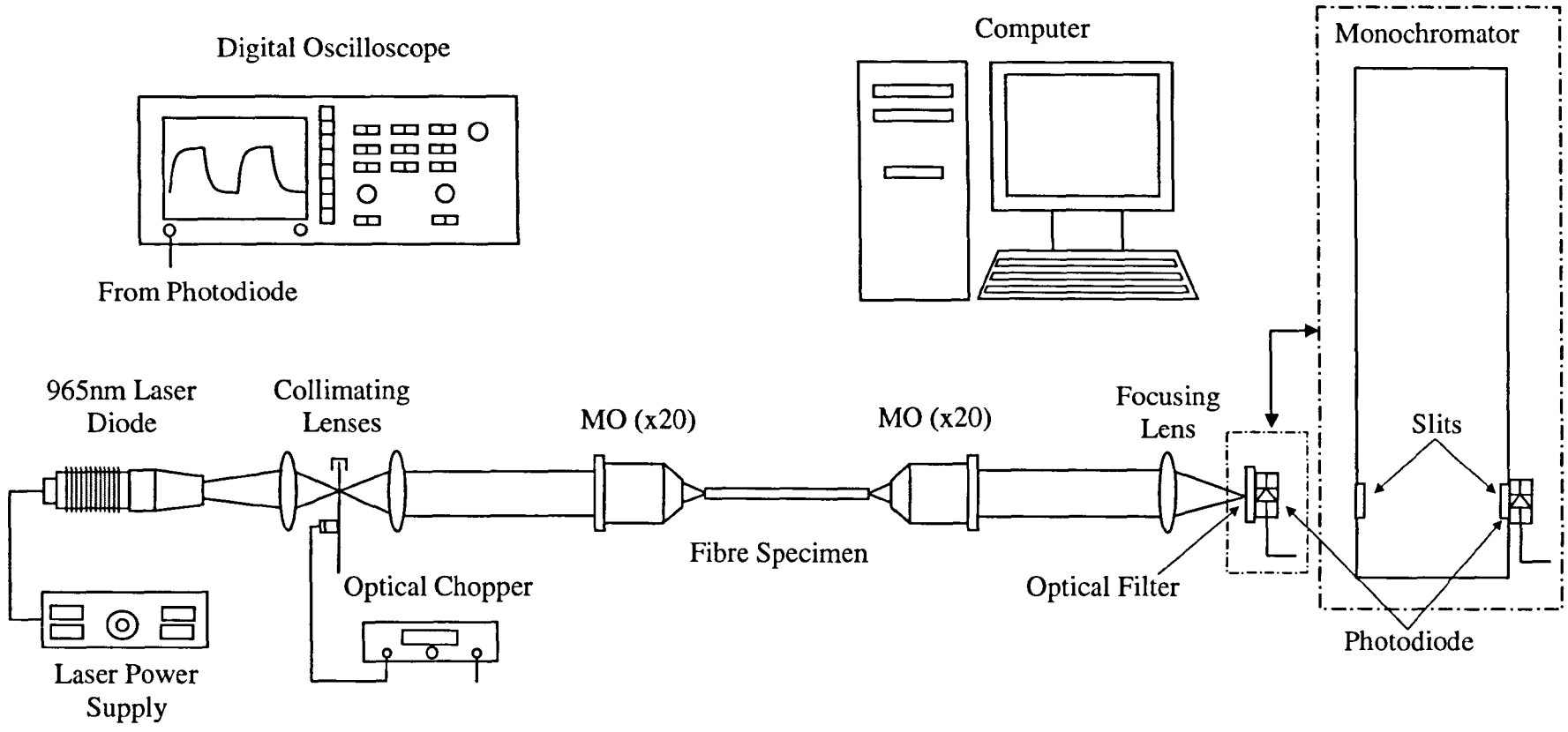

Figure 5.14 – Lifetime experimental layout with 965nm laser diode

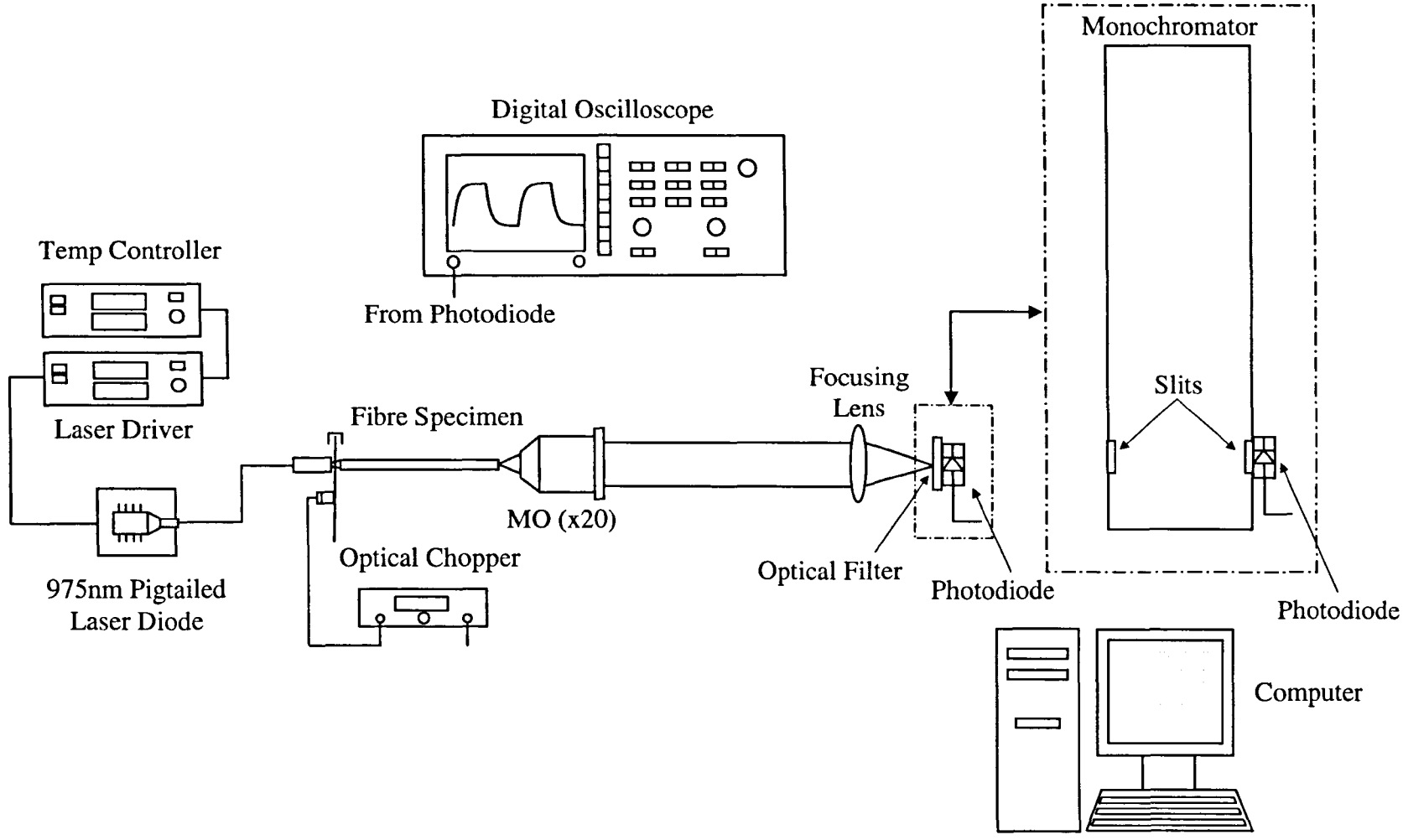

Figure 5.15 – Lifetime experimental layout with 975nm pigtail laser diode

5.4 Reference

[5.1] L. G. Cohen and P. Glynn, *Dynamic Measurement of Optical Fiber Diameter*, Rev. Sci. Instrum., **44**, 12, 1749, 1973

[5.2] D. H. Smithgall, L. S. Watkins and R. E. Frazee Jr., *High-Speed Noncontact Fiber-Diameter Measurement Using Forward Light Scattering*, App. Optics, **16**, 9, 2395, 1977

[5.3] J. G. N. Baines, A. G. Hallam, K. W. Raine and N. P. Tuner, *Fiber Diameter Measurements and Their Calibration*, J. Lightwave Tech, **8**, 9, 1259, 1990

[5.4] W. J. Miniscalco, L. J. Andrews, B. A. Thompson, T. Wei and B. T. Hall, *The Effect of Glass Composition on the Performance of Er^{3+} Fibre Amplifier*, Fiber Laser Sources and Amplifier, Proc. SPIE, **1171**, 93, 1989

[5.5] R. C. Powell, *Physics of Solid-State Laser Materials – Chap. 6 Al_2O_3:Cr^{3+} Laser Crystal*, 239, 1998

[5.6] A. Mori, Y. Ohishi, M. Yamada, H. Ono, Y. Nishida, K. Oikawa and S. Sudo, *1.5μm Broadband Amplification by Tellurite-Based EDFAs*, Optical Fibre Communication Conference, Opt. Soc. America, Technical. Digest Series, Washington D.C., **6**, 371, 1997

[5.7] V. P Gapontsev, S. M. Matitsin, A. A. Isinev and V. B. Kravchenko, *Erbium Glass Lasers and their Applications* , Opt. & Laser Tech. **14**, 4, 189, 1982

[5.8] L. Laversenne, C. Goutaudier, Y. Gyot, M. Th. Cohen-Adad and G. Boulon, *Growth of Rare Earth (RE) Doped Concentration Gradient Crystal Fibres and Analysis of Dynamical Processes of Laser Resonant Transitions in RE-Doped Y_2O_3 (RE=Yb^{3+}, Er^{3+}, Ho^{3+})*, J. Alloys and Comp., **341**, 1-2, 214, 2002

[5.9] G. N. van den Hoven, E. Snoeks, A. Polman, J. W. M. van Uffelen, Y. S. Oei and M. K. Smit, *Photoluminescence Characterization of E-implanted Al_2O_3 Films*, App. Phys. Lett., **62**, 24, 3065, 1993

Section II

Characterisation of SCFs

6 $Y_3Al_5O_{12}$ – Single Crystal Fibre

6.1 Introduction

Commonly known as YAG (Yttrium Aluminium Garnet) and having a chemical notation of $Y_3Al_5O_{12}$ or $Y_3Al_2(AlO_4)_3$, YAG is extensively used as a host medium for rare earth solid state lasers. Having a garnet like structure, this synthetic crystal has many advantages as a host material for laser applications. These include high thermal conductivity to dissipate excess energy, the ability to incorporate a wide range of rare earth ions, and the ease of growth of large, high quality crystals. *Burrus* and *Stone* [2.9] were the first to demonstrate the a Nd:YAG fibre laser (grown by LHPG). The fibres grown, pulled at 5mm/min, were free from micro cracks. *Burrus* and *Stone* were also the first to operate these YAG fibre lasers without a heat sink while pumping with a single LED. Although Nd is the most common rare earth ion doped in YAG, other rare earths such as Ho [6.1], Tm [6.1], Yb [6.2] and Er [6.3] can also be found in YAG. In recent years, YAG SCFs have been used in the medical field for laser thermotherapy [2.52]. Having a high chemical resistance, good mechanical strength and high temperature tolerance makes them very attractive in the medical field. Having a high temperature resistance, YAG fibres have been employed as temperature sensors [6.4]. YAG has a high melting temperature of 1900°C and as a temperature sensor, it can operate close to its melting point without any problems [2.54]. Work carried out on Yb:YAG sensors exploiting fluorescent decay proved to have excellent sensitivity in the temperature range of 1300°C and 1600°C, with an accuracy of ±1°C within this range. They also demonstrated good durability in oxidising environments at elevated temperatures [6.4]. The purpose of this section is to study the concentration effects of Er^{3+} and Er^{3+}+Yb^{3+} doped in $Y_3Al_5O_{12}$ fibres, grown by LHPG. Investigations were carried out to discover the spectral parameters in the visible and the near infrared regions, and the fluorescence lifetime of each fibre. Physical aspects of the fibres were also examined to obtain a clearer understanding of the conditions of the fibres grown. The results present the physical and optical status of the different dopant concentrations of singly and co-doped YAG SCF.

6.2 Diameter Measurement

The fibres grown in this work were either for physical or spectroscopic characterisation. Three fibres were specially grown for diameter measurements and the same three fibres were then used for mechanical testing measurements which will be discussed in the next section. The conditions of growth for the three fibres were kept the same. They were grown from source rods prepared from cold pressed powder. Refer to Chapter 5.2.1 for experimental set-ups.

6.2.1 Results and Discussion

Acquiring the diameter for the fibres was achieved using the Filar Eyepieces technique. Each fibre was measured with the same technique three times. This was done to reduce possible measurement errors. Repeated measurement of the same fibre showed a diameter variation error of not more than 3%. The lengths of the fibres measured were in the range of 20mm and 30mm. Measurement intervals of 0.5mm were taken across the length of the fibres. The average diameter of the three fibres fell within the range of 390 to 425μm. The variation in diameters from sample to sample was due to the variation in size of the square source rod. Table 6.1 shows the average diameter and the standard deviation. From the results, deviations from the mean diameters were very large for all the three fibres. Figures 6.1 to 3 show the diameters across the length of the fibre. The variation across each fibre was likely caused by unstable melt zone contributed by the heat source, and hence, the large variation of the diameters. The variation of the diameters of the fibre coincides with the pattern of the laser plot as seen in Figure 6.4. Lastly, one possible error source in this experiment of diameter measurement was that the fibres grown were not circular in cross-section. See Figure 4.26. Generally, the scope of this work did not require first-class quality fibres. The fibres grown were good enough for the experiments required.

Table 6.1 – $Y_3Al_5O_{12}$ fibre diameter measurements

Specimen Name	Average Diameter (μm)	Standard Deviation (μm)
Spec YAl21	399.80	27.73
Spec YAl22	423.30	23.93
Spec YAl23	391.95	16.67

Figure 6.1: Spec YAl 21 – $Y_3Al_5O_{12}$ fibre diameter measurement

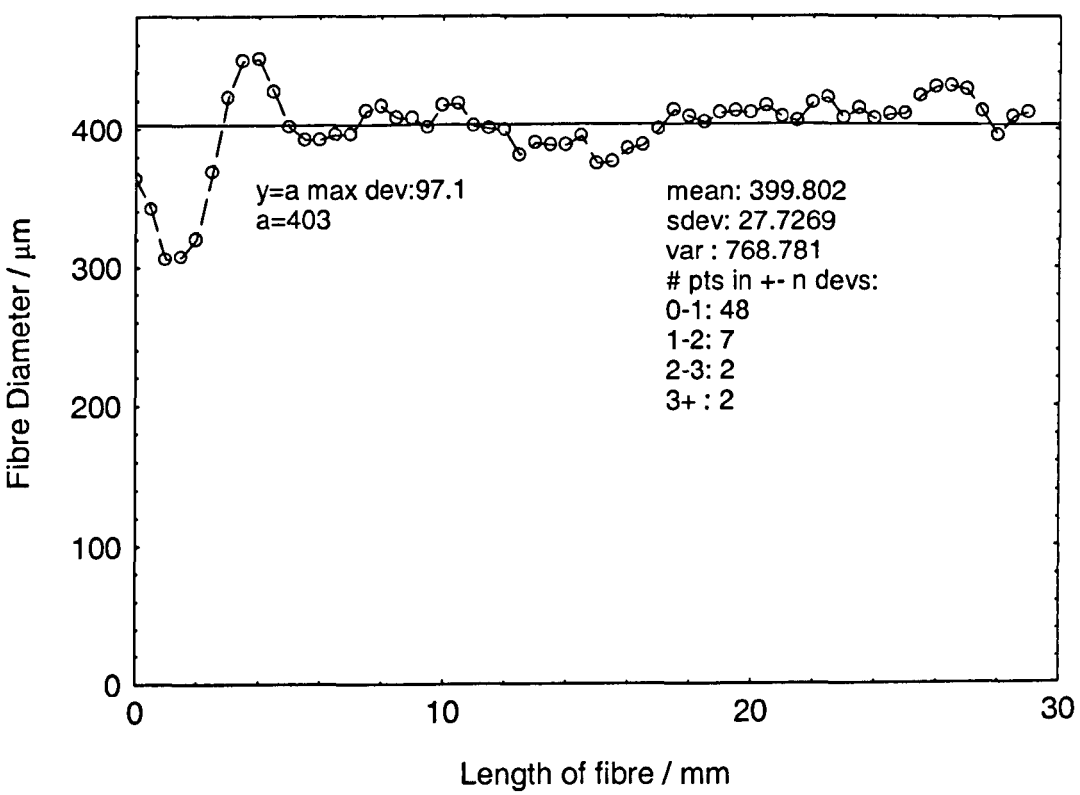

Figure 6.2: Spec YAl 22 – $Y_3Al_5O_{12}$ fibre diameter measurement

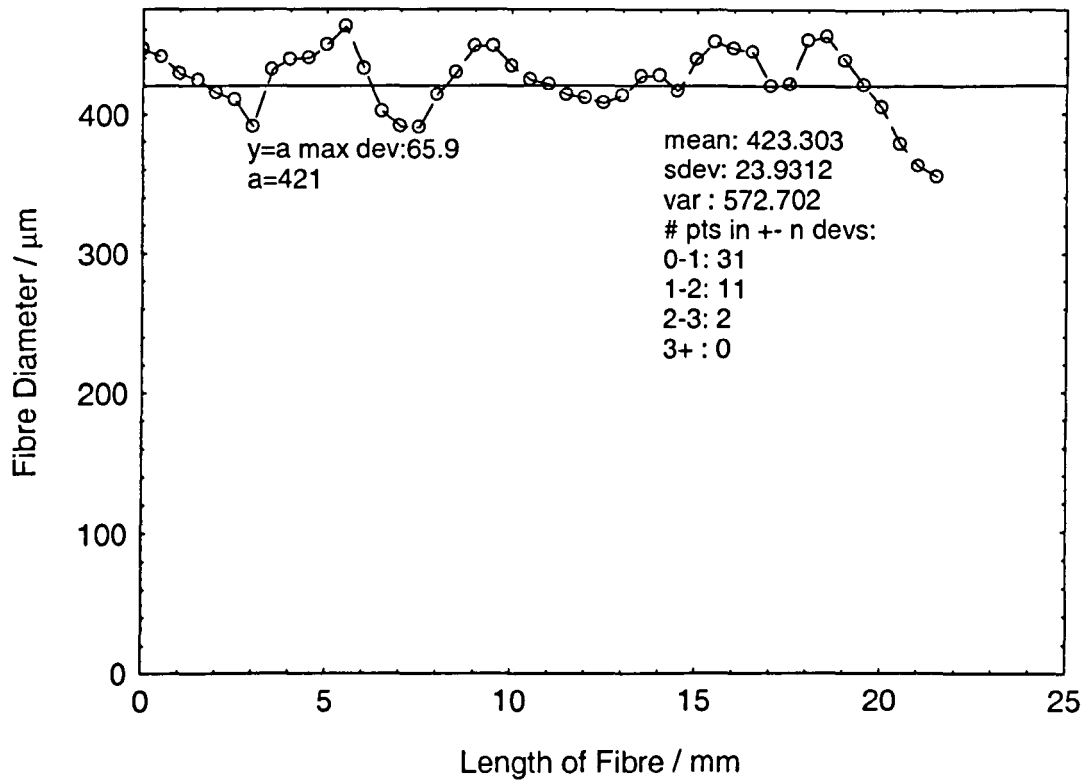

Figure 6.3: Spec YAl 23 – $Y_3Al_5O_{12}$ fibre diameter measurement

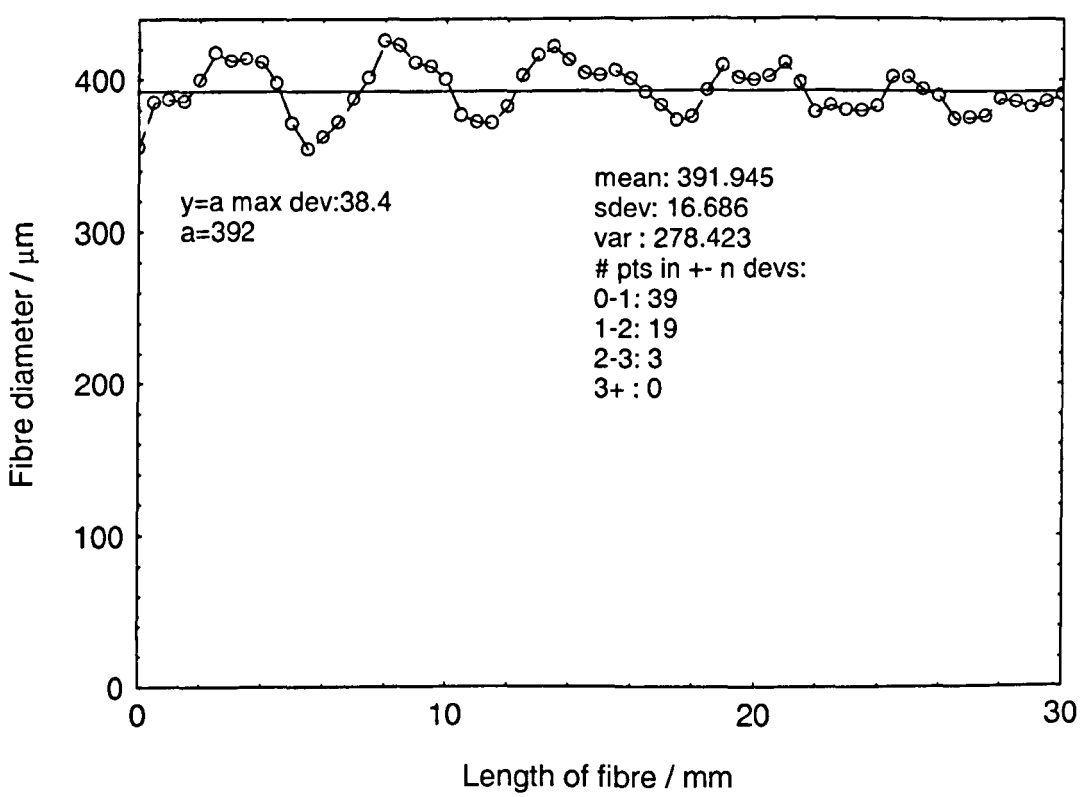

Figure 6.4: CO_2 laser power fluctuation

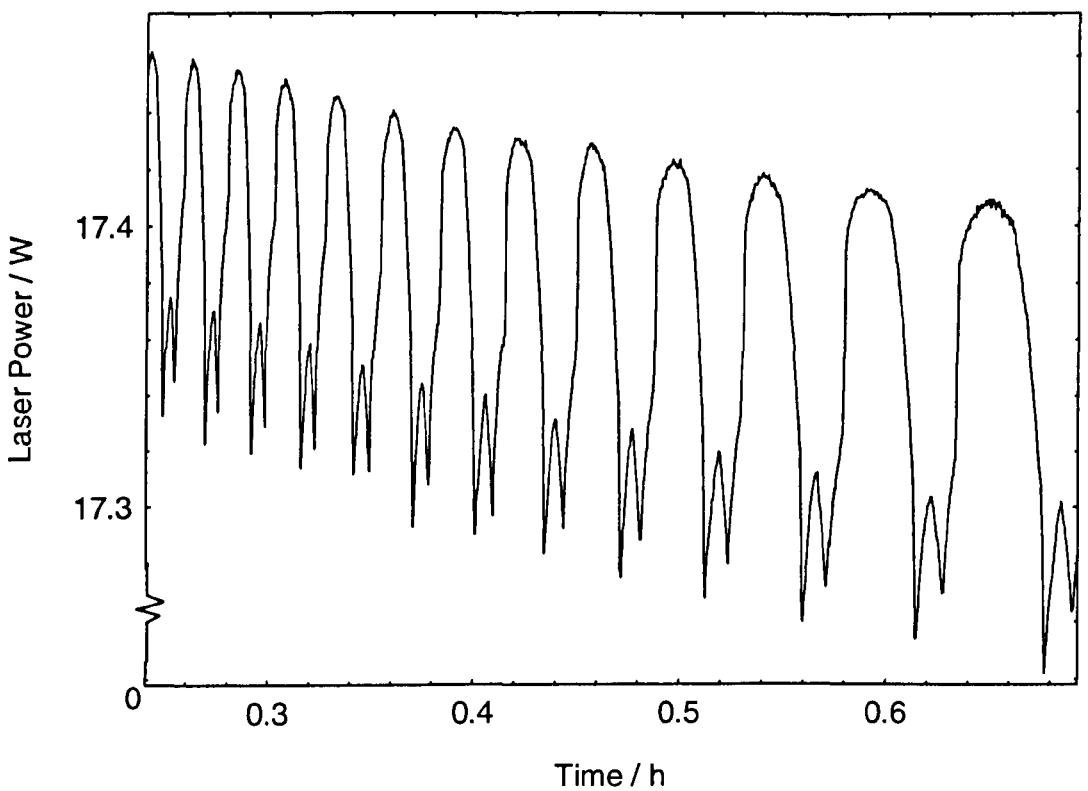

6.3 Mechanical Testing Measurement

A simple three-point mechanical bending/shear strength test was carried out on the fibres grown. The test was conducted under room temperature conditions. The purpose of this test was to get the basic characteristics of the mechanical properties of the fibres grown. Reference for the layout of experiment can be made in Chapter 5.2.2.

6.3.1 Results and Discussion

All three fibres that were used in this test were grown under similar conditions. From Table 6.2, the results attained from the test show inconsistency. It is logical to expect that the fibre with the largest diameter would require with the greatest force when it is bent. However, that was not the case during the test. In fact, it required the lowest force compared with the other two fibres. A larger sample size and more fibres would be helpful to verify this inconsistency. The length of the fibres were kept short to prevent internal micro-cracks from occurring during the growth process and there were no visible traces of micro-cracks observed during the growth process. A likely cause of this inconsistency could be the mixture of the source material. Two different compounds (Y_2O_3 and Al_2O_3) were required to form YAG fibres and the ratio of the two may have varied between the three fibres. This was an initial assumption made to explain the possible inconsistency shown in the results. Confirmation of this could be made by using a larger fibre sample size for the experiments and EMPA (electron microprobe analysis) could be conducted on the fibres before the mechanical testing. This would reveal the relative concentration levels of the two compounds. Figure 6.5 shows the force (N) against the deformation (mm) of *Spec YAl23*. The force started at zero and increased with the deformation. The falling of the force back to zero signified that the fibre had broken and the maximum force required to strain the fibre to breaking point was the value before the plot falls to zero.

Table 6.2 – $Y_3Al_5O_{12}$ fibre mechanical testing measurements

Specimen Name	Diameter (μm)	Force, F (N)	$M = \pi d^3/32$ ($\times 10^{-12}$)	Shear/Bending Strength, S (MPa)
Spec YAl21	399.80	3.029	6.273	2.29
Spec YAl22	423.30	1.541	7.447	0.983
Spec YAl23	391.95	2.457	5.923	1.97

Figure 6.5: Three-point bending test on *Spec YAl 23*

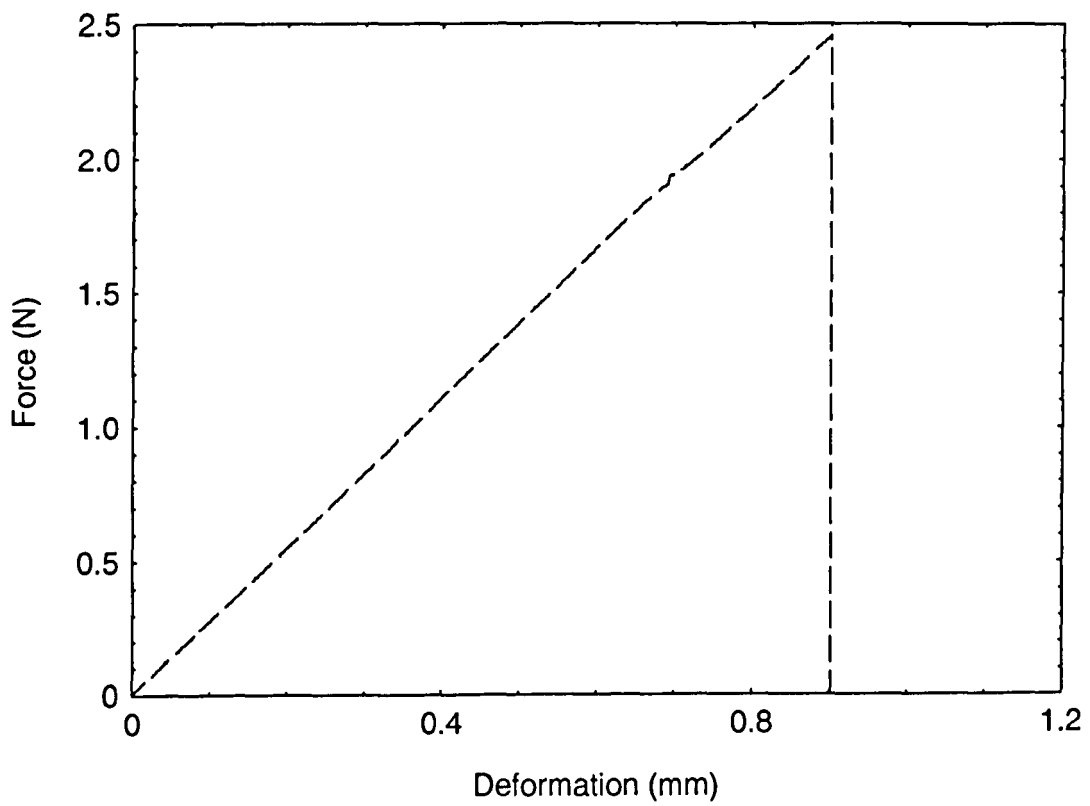

6.4 Absorption Spectrum Measurement

The experimental layout and equipment used in this measurement were discussed in Chapter 5.3.1. $Y_3Al_5O_{12}$ fibres doped with Er^{3+} of content 0.5, 1, 5 and 10mol%, and fibres doped with Er^{3+}+Yb^{3+} of content 1+1, 1+2 and 1+3mol%, were prepared using the cold pressed method and grown by LHPG. This section presents the results of the absorption spectra of these YAG fibres.

6.4.1 Results and Discussion

Figures 6.6 to 19 show the absorption spectra of the different content of Er^{3+} and Er^{3+}+Yb^{3+} doped YAG fibres. The results are presented in the range 400 to 1200nm, and 900nm to 1700nm. This was done due to the different photodetectors that were employed in the experiments. The absorption bands for singly doped and co-doped YAG fibres spread across the visible and infrared region and are relatively sharp and narrow. The absorption peaks for Er^{3+} doped YAG in this work are relatively similar to work done by *Cornacchia* [6.5] and in [3.40]. The quartz halogen lamp used in these experiments was not ideal because the intensity in the blue region was extremely low, see Figure 5.6. Several peaks appeared throughout the spectrum and the intensity of the absorption spectra was strongly influence by the Er^{3+} and Yb^{3+} content. The peaks observed in this work for singly doped and co-doped occur in the manifolds $^4F_{7/2}$, $^2H_{11/2}$, $^4S_{3/2}$, $^4F_{9/2}$, $^4I_{9/2}$, $^4I_{11/2}$ and $^4I_{13/2}$. The two strongest peaks in the singly doped YAG fibres for the region of the $^4F_{7/2}$ transition were at 485nm and 486nm. These two peaks were observed only for content of 1mol% above. At 0.5mol%, there was no peak observed in this work. See Figure 6.6. The noise level was high for 0.5mol% samples and the presence of the absorption peaks in this blue region might have been obscured by the noise. Due to the limitation of the light source employed in this experiment, no firm conclusion could be made with regards to the present absorption in this region. To verify the possibility, a light source that gives out higher UV emission should be employed for future investigations. The two peaks observed in $^4F_{7/2}$ were present and remained consistent for all the other higher Er^{3+} doped YAG fibres. In the manifold $^2H_{11/2}$, two narrow sharp lines at 523nm and 524nm were observed at 0.5mol%. As the Er^{3+} content increased, more peaks at 517nm and 518nm appeared beside the two already mentioned. The sharp peak at

523nm had the highest intensity among all the peaks in the range 400 to 1200nm. However, its relative intensity reduced as the dopant level increased. The only peak observed in the manifold $^4S_{3/2}$ was at 540nm. This peak was relatively weak and reasonably similar at all dopant levels. As for manifold $^4F_{9/2}$, strong peaks were at 645nm, 646nm, 650nm and 652nm. At dopant levels of 0.5 and 1mol%, the peak at 650nm was the highest among the others at this manifold. Figure 6.8 shows clearly that the peak at 650nm was the highest among its manifold and all other peaks. When doped with 5 and 10mol% of Er^{3+}, the peak at 646nm became the strongest, overtaking 650nm. Increments in dopant level changed the intensity of peaks. The $^4F_{9/2}$ manifold has the highest intensity from 1 to 10mol%. Smaller peaks at 661nm, 668nm and 677nm were also observed in this manifold which remained fairly similar at all dopant levels. In $^4I_{9/2}$ transition, several peaks were observed at 785nm, 797nm and 811nm. These peaks were relative weak at 0.5mol% of Er^{3+} but became stronger as the dopant level increased. The peak at 785nm was the strongest among the three. See Figure 6.12. For $^4I_{11/2}$ transition, there were nine narrow peaks observed. See Figure 6.6. For all the four Er^{3+} doped YAG fibres, these remained consistent. The strongest of these was at 963nm, but was replaced by the peak at 959nm at doping level of 10mol%. The basic profile of the absorption spectrum at in this region remained the same for all singly doped YAG fibres. Lastly, in transition to the $^4I_{13/2}$ levels, there were at least 16 prominent peaks observed. See Figures 6.7 and 6.9 for the peaks. The narrow and sharp peaks were very distinctive at dopant levels of 0.5 and 1mol%. The intensity between 1400 and 1500nm increased as the concentration of the Er^{3+} increased. The distinctive peaks that were observed at the lower concentrations merged together at the high dopant levels, forming a spectrum with a board linewidth. See Figures 6.11 and 6.13. At 10mol%, the width of the profile of the absorption band was 45nm. The small peaks at 1565nm and 1612nm were also observed at this concentration. Therefore, at a higher Er^{3+} concentration, the narrow absorption lines of the $^4I_{13/2}$ manifold broadened and the peaks merged to form a broader absorption linewidth.

YAG fibres with Er^{3+} concentration of 1mol% were co-doped with Yb^{3+} of 1, 2 and 3mol%. Figures 6.14 to 19 show the absorption spectrum of these fibres. When co-doped with Yb^{3+}, this sensitiser ion broadened the absorption band around 930nm [3.34], as discussed in Chapter 3.3.2. Previous workers had observed that Er^{3+}+Yb^{3+}

doped in a poly-crystalline YAG matrix had shown a broadening effect with the range of 900nm and 1050nm [6.6]. The spectral region of $^2F_{7/2} \rightarrow {}^2F_{5/2}$ transition present in the Yb^{3+} ions overlapped the Er^{3+} ion transition at $^4I_{15/2} \rightarrow {}^4I_{11/2,}$ therefore causes an increase in linewidth at the transition $^4I_{11/2}$ and resulting in an increase in its optical pumping efficiency [6.6,7]. In this work, it was observed that additional peaks appeared at 911nm, 938nm, 966nm and 1027nm when co-doped Yb^{3+} ion. See Figure 6.14. The absorption spectrum was also broadened approximately from across the range 900 to 1030nm. Comparing with 1mol% Er^{3+} (Figure 6.8) singly doped which had a linewidth from 956 to 965nm, Yb^{3+} had indeed increased the linewidth. Increasing the Yb^{3+} concentration level from 1 to 3 mol% also increased the intensity of the peaks in the range of 900nm and 1030nm. 3mol% Yb^{3+} had the highest absorption strength among the co-doped fibres. The absorption spectrum in the range of 1400nm and 1700nm of the co-doped fibres was similar to the singly doped fibres at 1mol% Er^{3+} concentration level. No additional absorption peaks were observed in this range. See Figures 6.15, 17 and 19 for absorption spectra.

From the results mentioned above, it can be concluded that singly and co-doped fibres can be excited at several wavelengths. In this work, the $^4I_{11/2}$ manifold was selected for two reasons: firstly, the ease of diode pumping at this wavelength and, secondly, to prevent any ESA.

Figure 6.6: Spec YAl 08 – $Y_3Al_5O_{12}:Er^{3+}$ (0.5mol%)
Absorption spectrum

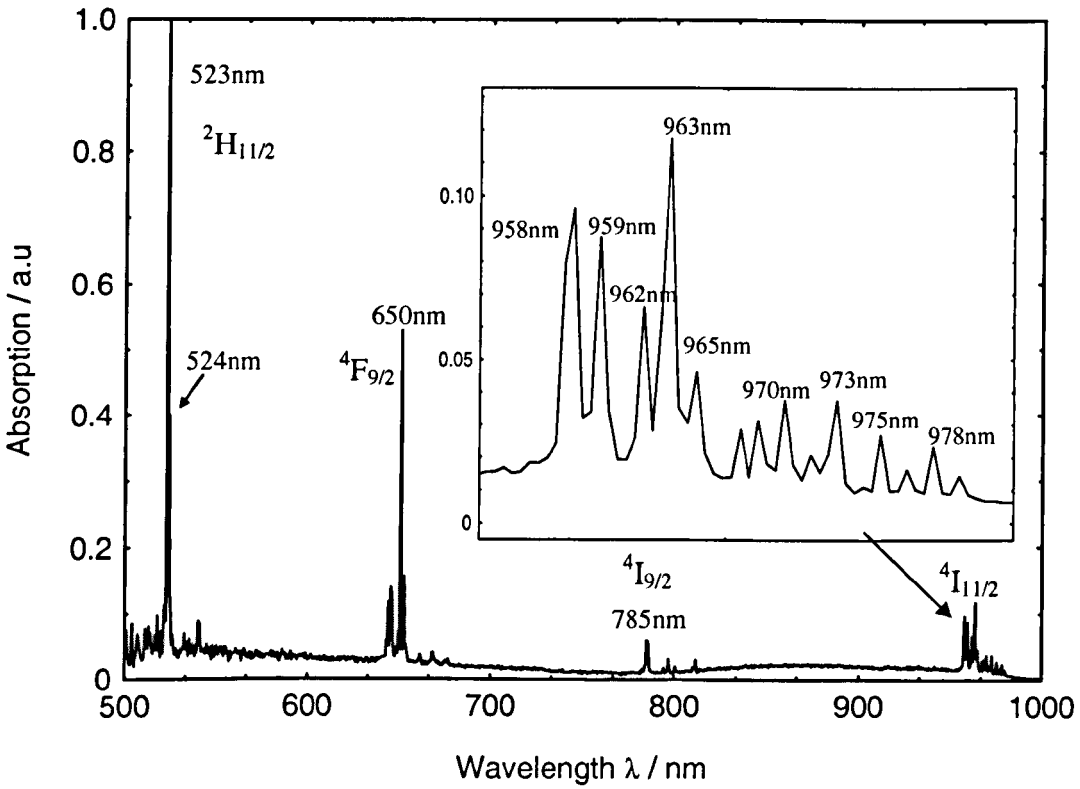

Figure 6.7: Spec YAl 08 $Y_3Al_5O_{12}:Er^{3+}$ (0.5mol%)
Absorption spectrum ($^4I_{13/2}$)

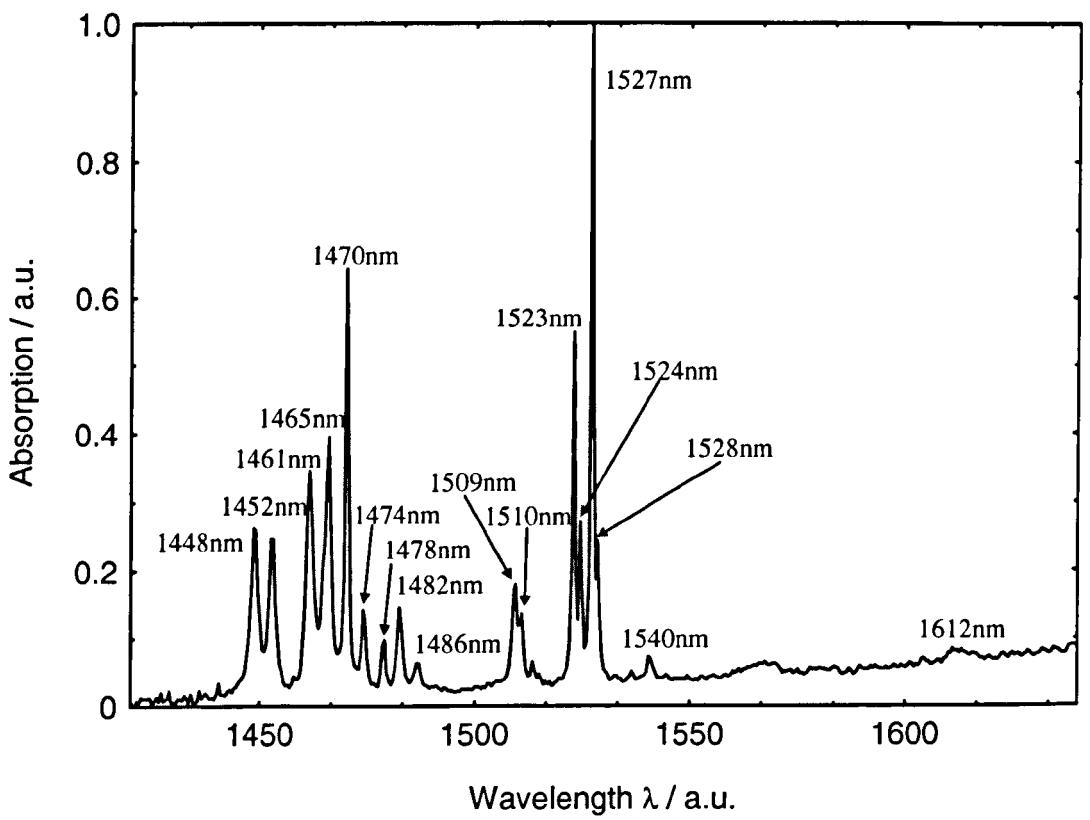

Figure 6.8: Spec YAl 09 $Y_3Al_5O_{12}:Er^{3+}$ (1mol%)
Absorption spectrum

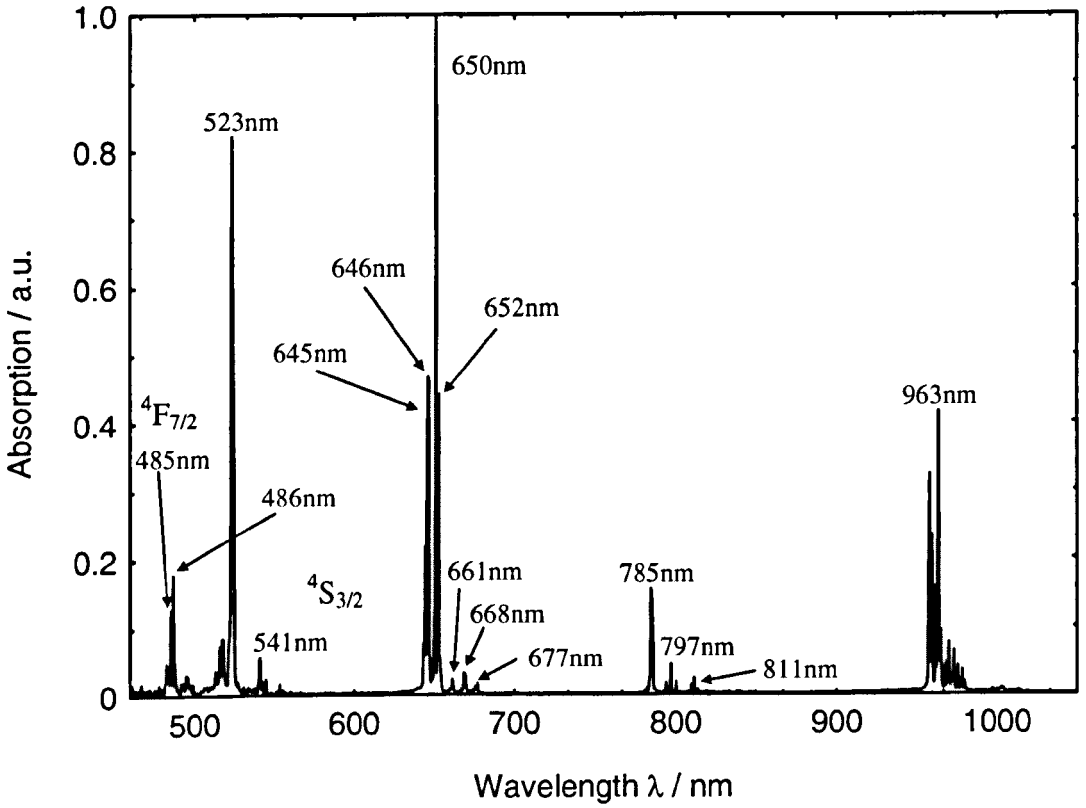

Figure 6.9: Spec YAl 09 $Y_3Al_5O_{12}:Er^{3+}$ (1mol%)
Absorption spectrum ($^4I_{13/2}$)

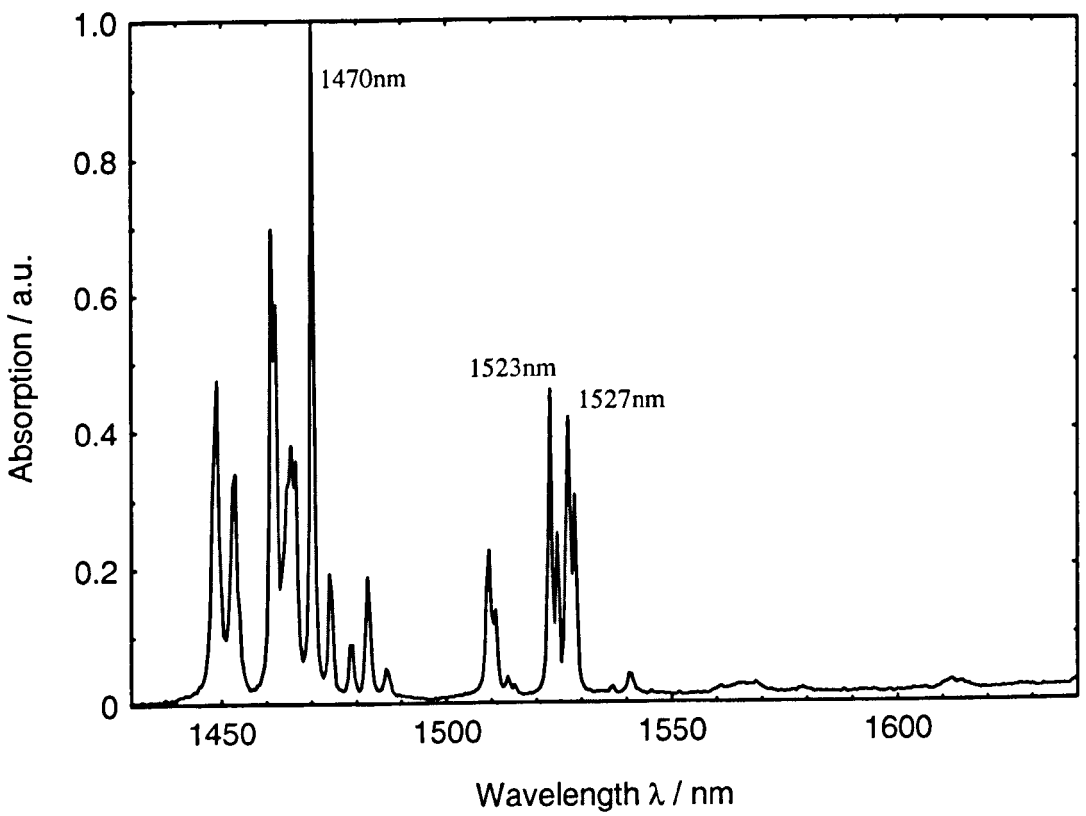

Figure 6.10: Spec YAl 10 $Y_3Al_5O_{12}:Er^{3+}$ (5mol%)
Absorption spectrum

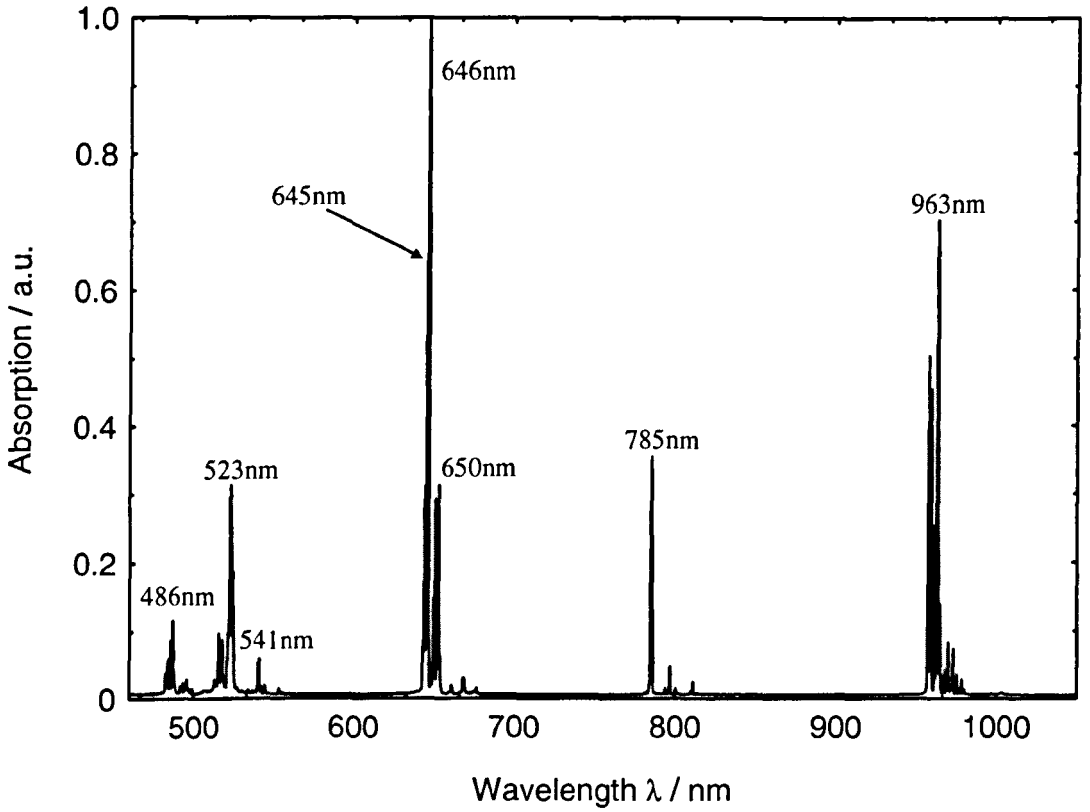

Figure 6.11: Spec YAl 10 $Y_3Al_5O_{12}:Er^{3+}$ (5mol%)
Absorption spectrum ($^4I_{13/2}$)

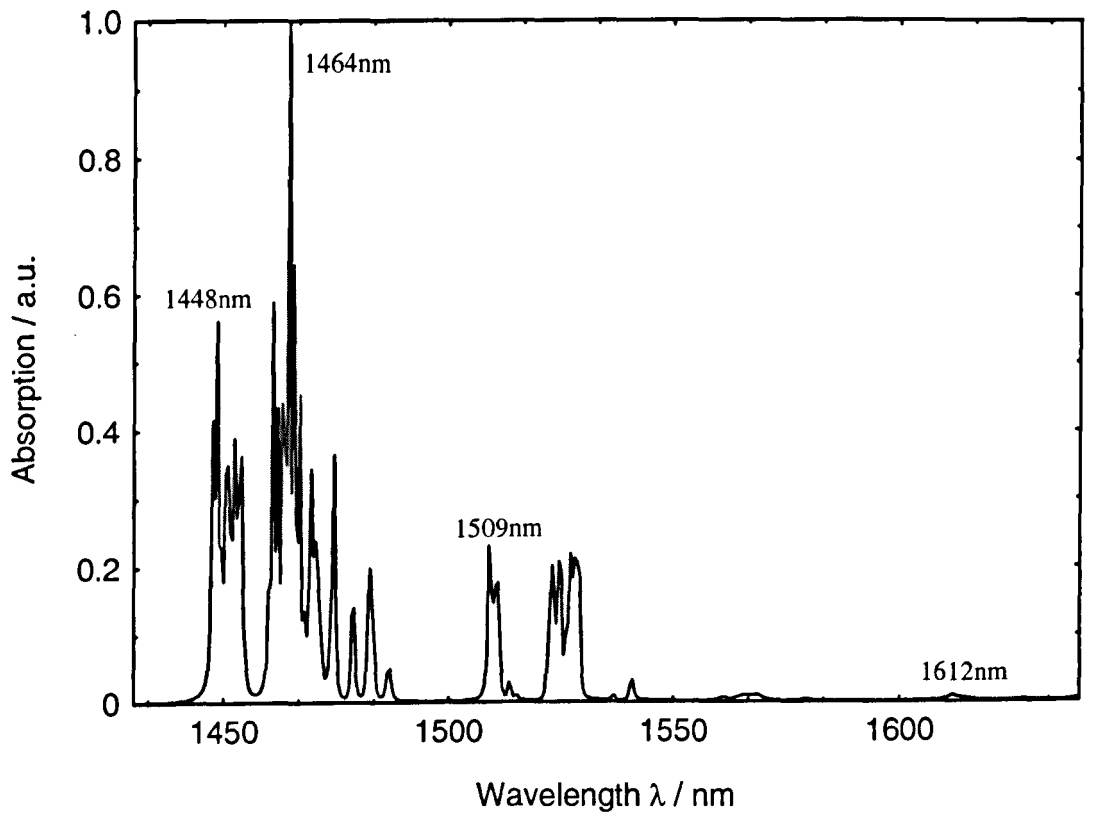

Figure 6.12: Spec YAl 13 $Y_3Al_5O_{12}:Er^{3+}$ (10mol%)
Absorption spectrum

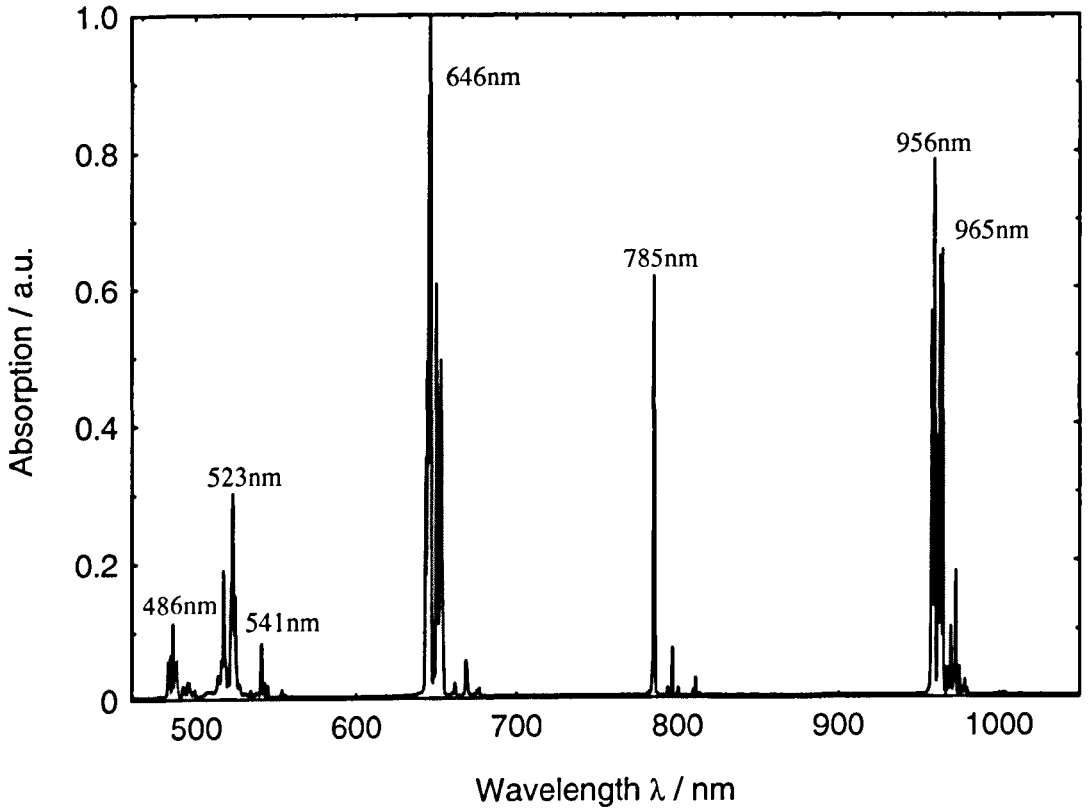

Figure 6.13: Spec YAl 13 $Y_3Al_5O_{12}:Er^{3+}$ (10mol%)
Absorption spectrum ($^4I_{13/2}$)

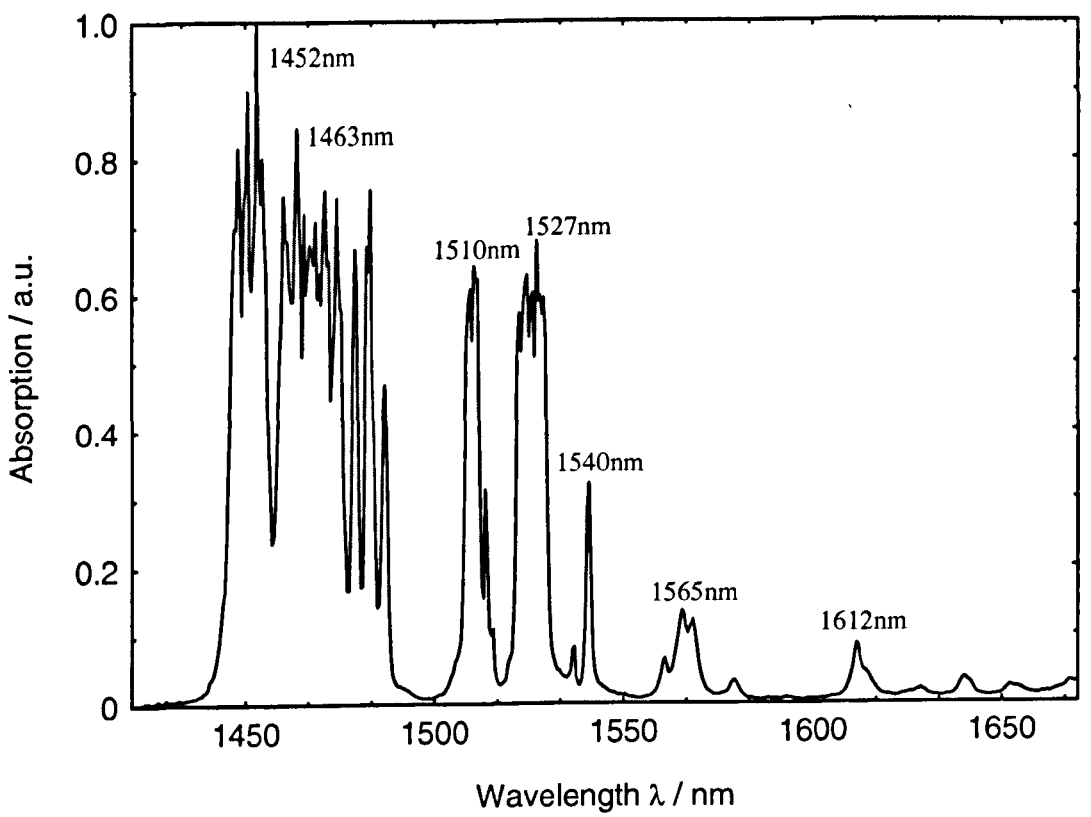

Figure 6.14: Spec YAl 16 $Y_3Al_5O_{12}$:Er^{3+}+Yb^{3+} (1mol% each) Absorption spectrum

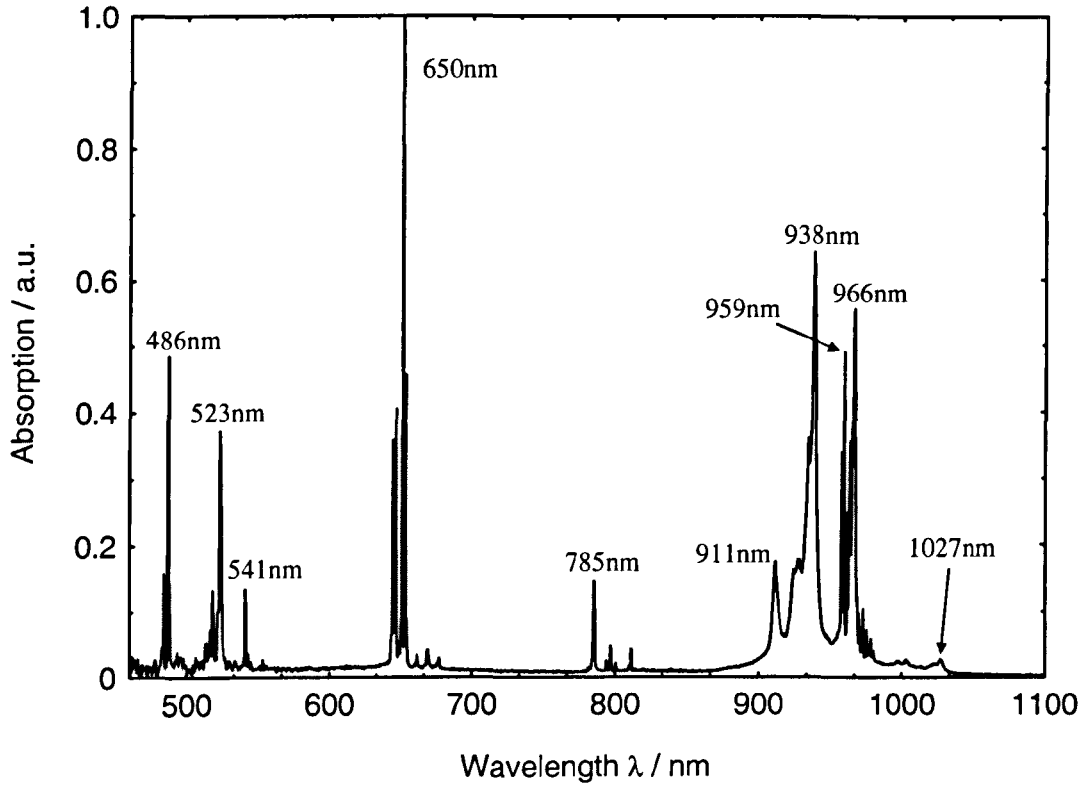

Figure 6.15: Spec YAl 16 $Y_3Al_5O_{12}$:Er^{3+}+Yb^{3+} (1mol% each) Absorption spectrum ($^4I_{13/2}$)

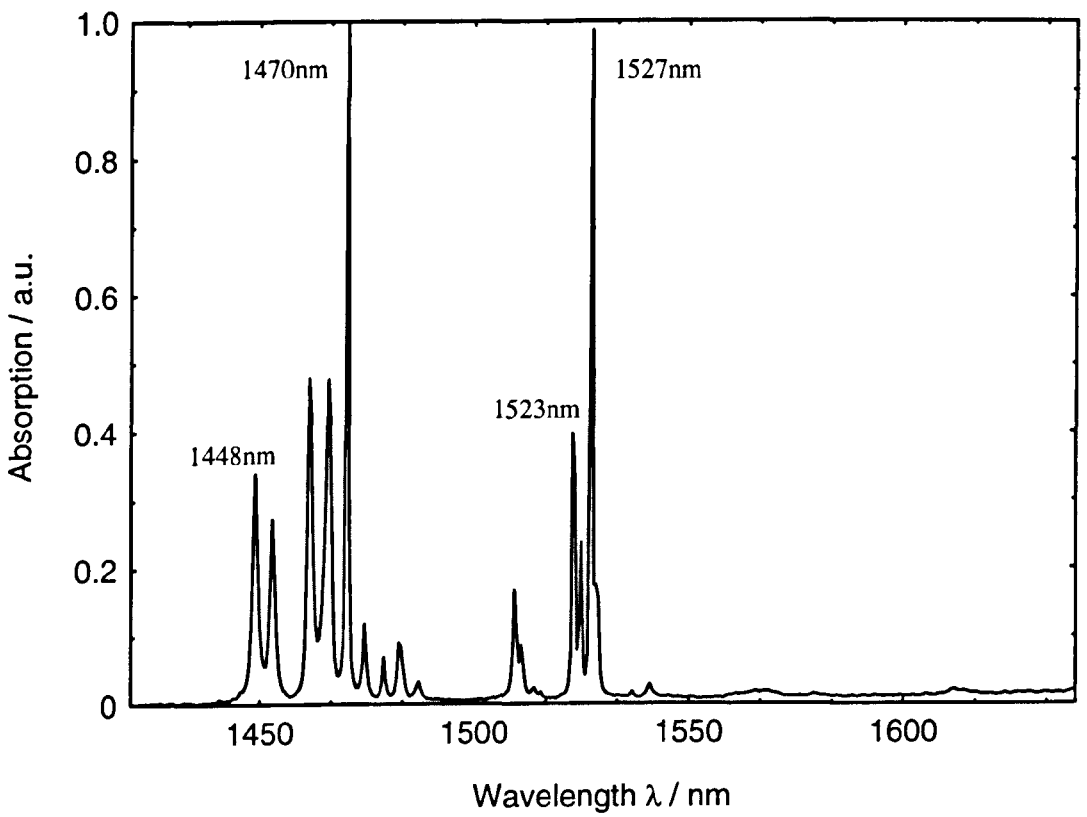

Figure 6.16: Spec YAl 20 $Y_3Al_5O_{12}:Er^{3+}+Yb^{3+}$ (1+2mol%) Absorption spectrum

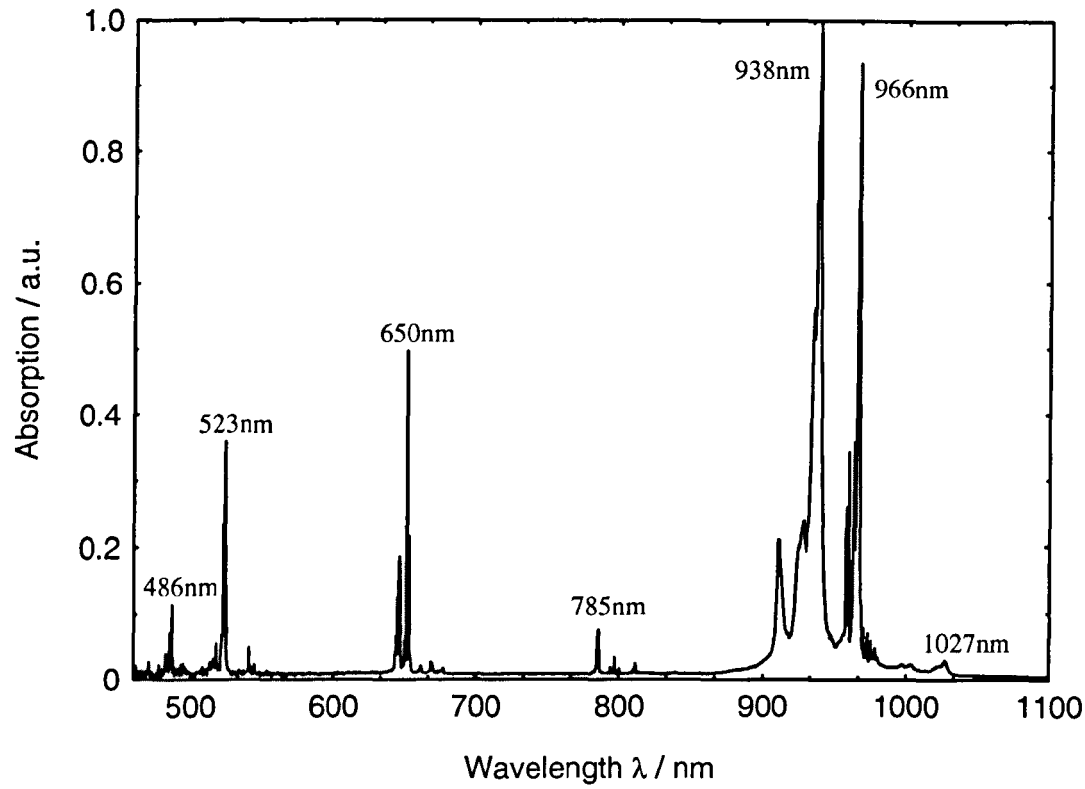

Figure 6.17: Spec YAl 20 $Y_3Al_5O_{12}:Er^{3+}+Yb^{3+}$ (1+2mol%) Absorption spectrum ($^4I_{13/2}$)

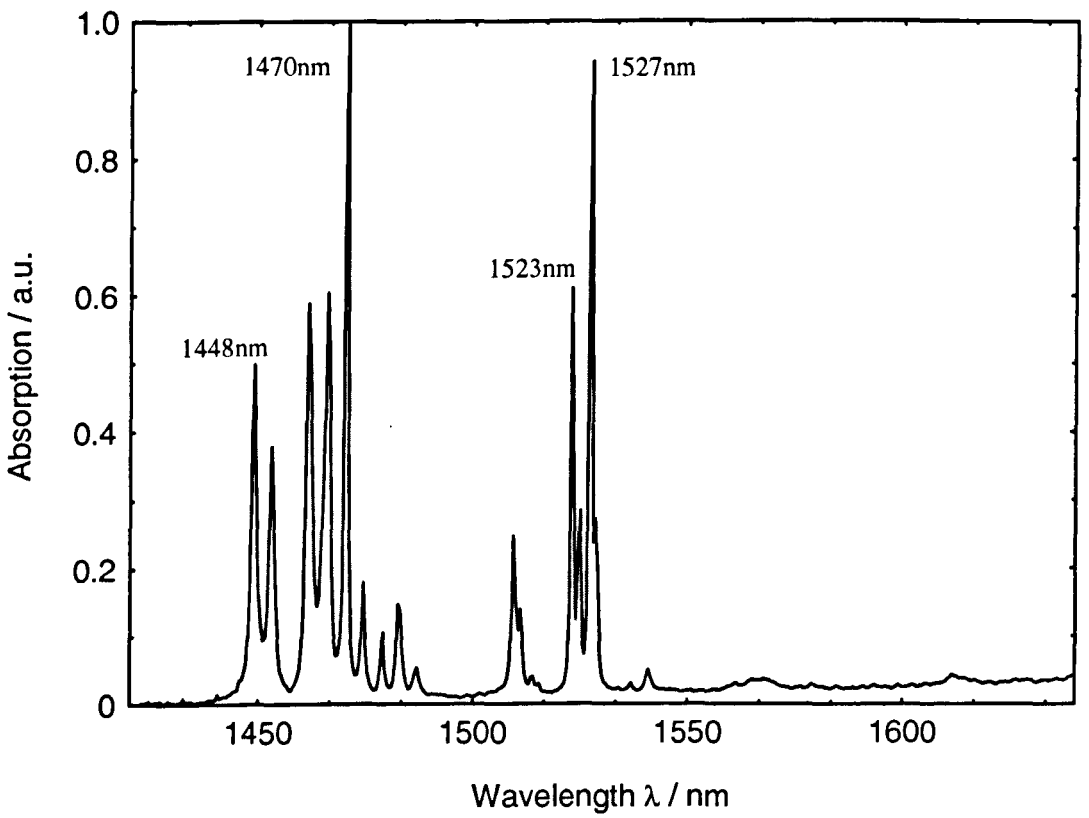

Figure 6.18: Spec YAl 19 $Y_3Al_5O_{12}:Er^{3+}+Yb^{3+}$ (1+3mol%) Absorption spectrum

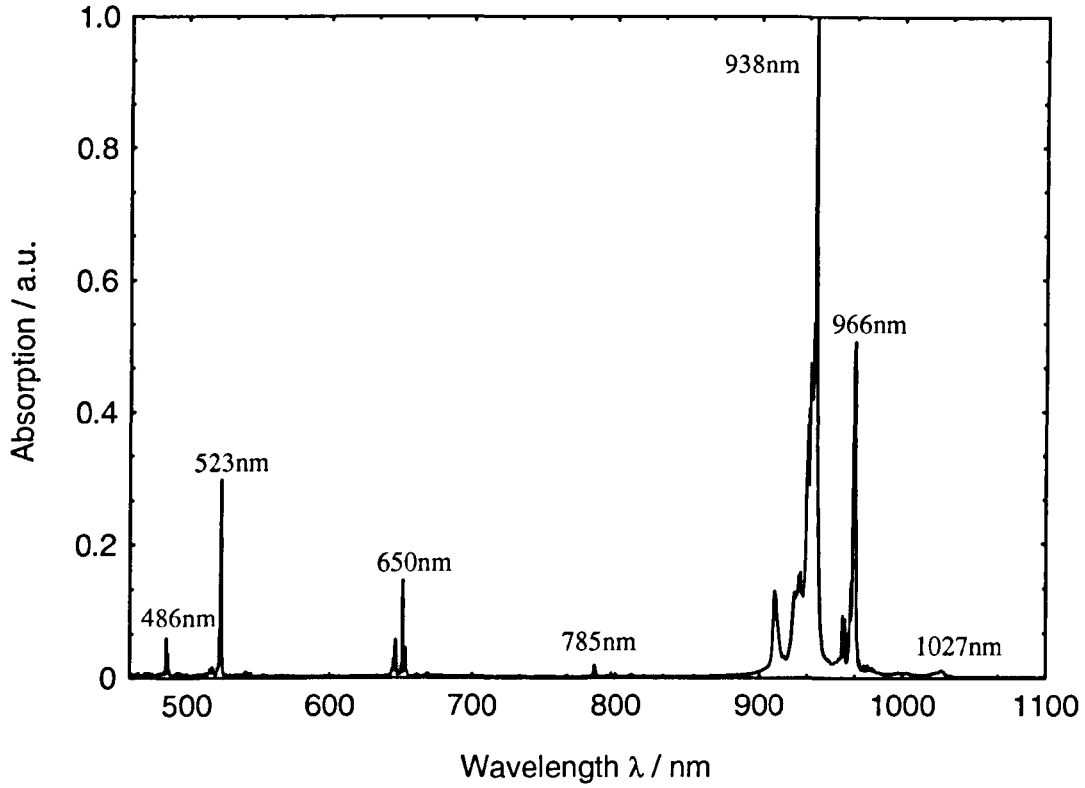

Figure 6.19: Spec YAl 19 $Y_3Al_5O_{12}:Er^{3+}+Yb^{3+}$ (1+3mol%) Absorption spectrum ($^4I_{13/2}$)

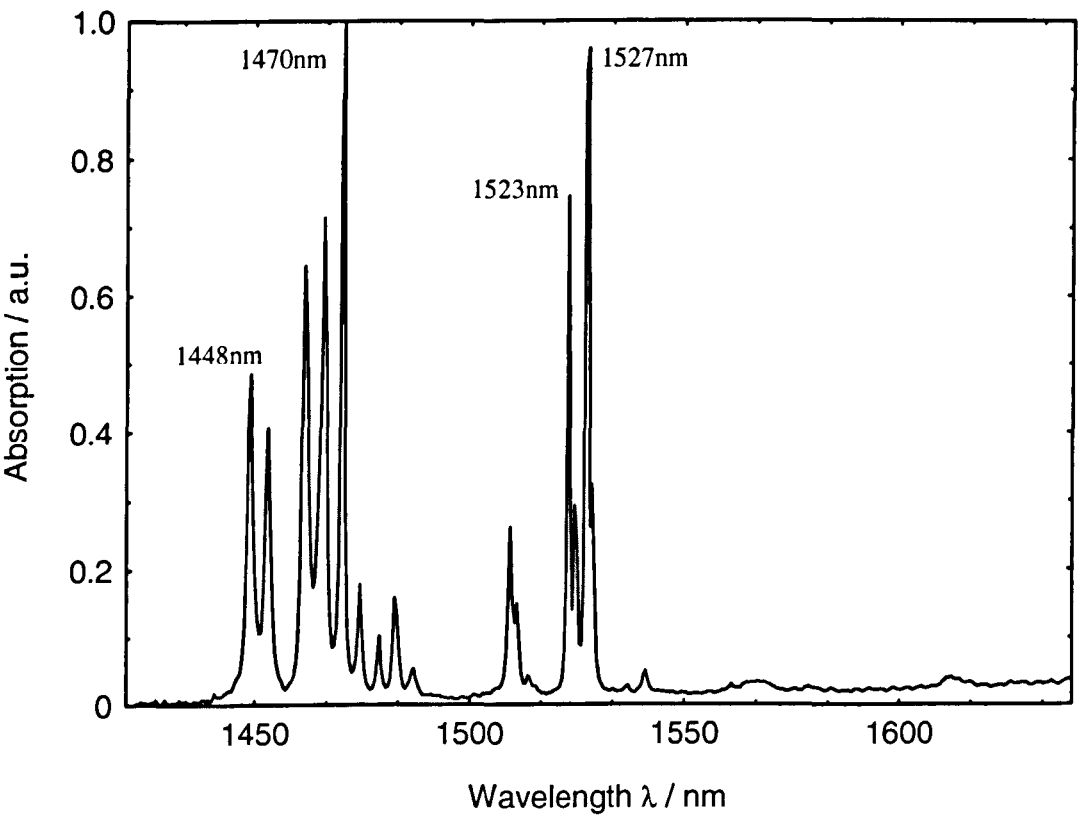

6.5 Fluorescence Measurement

From the section above, the absorption spectrum revealed that there was absorption at 975nm for all the YAG fibres. A laser diode at this wavelength was used to excite the fibres. Although the absorption spectrum showed that the absorption intensity at this wavelength was relatively low, good results could be obtained from the fluorescence measurement using a 975nm pigtailed laser diode. In the telecommunication applications, laser diodes at this wavelength are commonly used. A detailed discussion on experimental layout was made in Chapter 5.3.2.

6.5.1 Results and Discussion

When the YAG fibres were excited at 975nm, a weak green emission was observed. This is the telltale sign of upconversion emission. An investigation on upconversion emission will be discussed in the following section. Figures 6.20 to 23 and 6.26 to 31 show the fluorescence spectra from the $^4I_{13/2}$ manifold of all the six YAG fibres. For the singly doped Er^{3+}:YAG fibres, absorption from $^4I_{15/2} \rightarrow {}^4I_{11/2}$ manifolds due to the excitation source at 975nm, promoted the ions to $^4I_{11/2}$ metastable level which then experienced a non-radiative relaxation to the $^4I_{13/2}$ manifold and resulting in fluorescence emissions from $^4I_{13/2}$ manifold to the $^4I_{15/2}$ ground state. Several peaks observed. At lower concentrations of 0.5 and 1mol%, peaks were seen at 1470nm, 1528.5nm, 1568nm, 1612nm, 1628.5nm, 1640.5nm, 1652.5nm and 1668nm. These wavelengths denote the Stark splitting of the level in the $^4I_{13/2}$ and $^4I_{15/2}$ manifold. The fluorescence emissions at these concentrations were in agreement with previous work carried out on YAG crystals or SCFs [6.5, 8, 9]. The distinctive 'five fingers' emission profile in the 1600nm region was also observed in this work which is to be expected when dealing with Er^{3+} doped YAG. It was also observed that there were four additional strong peaks at 1441nm, 1481nm, 1601nm and 1680nm. Occurrences of these peaks were likely caused by either contamination present in the constituent powder of the hosts' material or contamination present in equipment used at the preparation stage before the growth of the fibres. At 0.5mol% Er^{3+} concentration, the 1500nm region was the highest in fluorescence intensity. See Figure 6.20. As the concentration of Er^{3+} increased, the 1600nm region intensity became more prominent with the peak at 1640nm the strongest at a concentration of 10mol%. See Figure

6.23. Broadening effects were also observed at high concentrations. In the 1400nm region, broadening of the Stark lines were seen at 1mol% concentration. At 5 and 10mol%, the broadening effect of the linewidth had overlapped each other completely to form a broad bandwidth across the 1400nm region. At the 1500nm region, a similar effect was seen at 5 and 10mol%. Broadening of the linewidth caused overlapping of the Stark lines, therefore the narrow peaks were no longer seen and a broad bandwidth was formed across the region. As the dopant level increased, the relative fluorescence intensity in this region decreased. See Figures 6.22 and 23. For the region around 1600nm, the sharp Stark levels remained distinguishable. Broadening of these lines mostly took place at the base of these peaks and also at high dopant concentration the relative intensity of this region increased. Emission linewidth broadening has also been seen in glass fibres. The processes that were responsible for these effects were homogeneous and inhomogeneous broadening. Another possible reason for this broadening effect could be due to the increase in dopant concentration which then disturbed the lattice in the crystalline structure [6.10]. Distortion of the lattice, producing dislocation or interstitial defects could be expected in the crystal which would result in linewidth broadening. One of the advantages of this phenomenon is that it can be useful for the gain flatness at the 1500nm region optical telecommunication wavelengths [6.10]. To have a clearer view of the change caused by an increment of dopant concentrations, the fluorescence intensity ratio (FIR) was used to compare the difference between fibres at different concentration levels. This technique is commonly used in the thermometry in determining temperature. Detailed discussion of this technique will be done in Chapter 9. A peak from the 1500nm region, 1528.5nm ($I_{1528.5}$) and a peak from the 1600nm region, 1612nm (I_{1612}) were chosen. Dividing $I_{1528.5}$ by I_{1612} and plotting the values against the dopant concentration, a decrease in FIR is observed. See Figure 6.24.

When YAG fibres were co-doped with Yb^{3+}, a new emission band was observed at ~980 to 1100nm. In this band, a strong peak at 1027nm became evident. The Yb^{3+} emission peak in this work was extremely close to that of reference [3.31] which was at ~1030nm. Three Yb^{3+} concentrations of 1, 2 and 3mol% were investigated. See Figures 6.25 to 30 for fluorescence spectra. The $^4I_{13/2}$ emission profiles of the three co-doped fibres looked similar to that of the singly doped 1 mol% Er^{3+} fibre. Peaks

in the co-doped emission spectra were also similar. As the Yb^{3+} concentration increased, the peak at 1027nm increased in intensity. See Figure 6.31. When dividing the intensity peak at $I_{1528.5}$ and I_{1612} by 1027nm (I_{1027}) intensity peak, the FIR decreases. From Figure 6.29, it was observed that the intensity strength at 1027nm was as strong as the other two peaks at 1528.5nm and 1612nm. Co-doping with Yb^{3+} did not only broaden the absorption band as shown in the previous section, see Figure 6.14 to 19, but this large spectral overlap between the Yb^{3+} emission at $^2F_{7/2} \rightarrow {}^2F_{5/2}$ and Er^{3+} absorption at $^4I_{15/2} \rightarrow {}^4I_{11/2}$ also increased the rate of energy transfer between the two rare earth ions. Figure 6.32 shows the results of the FIR between the singly doped and the co-doped fibres. When dividing $I_{1528.5}$ by I_{1612}, an increasing FIR was observed. It could also be seen that the FIR values of the co-doped fibres were higher than the singly doped Er^{3+} 1mol%. The increasing FIR values were relatively small as compared to the other singly doped fibres. The result presented in Figure 6.32 was insufficient to determine if there was an increase in energy transfer when Yb^{3+} was added. This result did, however, show that there was possible energy transfer between the Stark levels at the $^4I_{13/2}$ manifold since the intensity of the 1528.5nm and 1612nm multiplets intensity ratios increased when Yb^{3+} dopant level increased.

Figure 6.20: Spec YAl 08 – $Y_3Al_5O_{12}:Er^{3+}$ (0.5mol%)
Fluorescence spectrum ($^4I_{13/2}$)

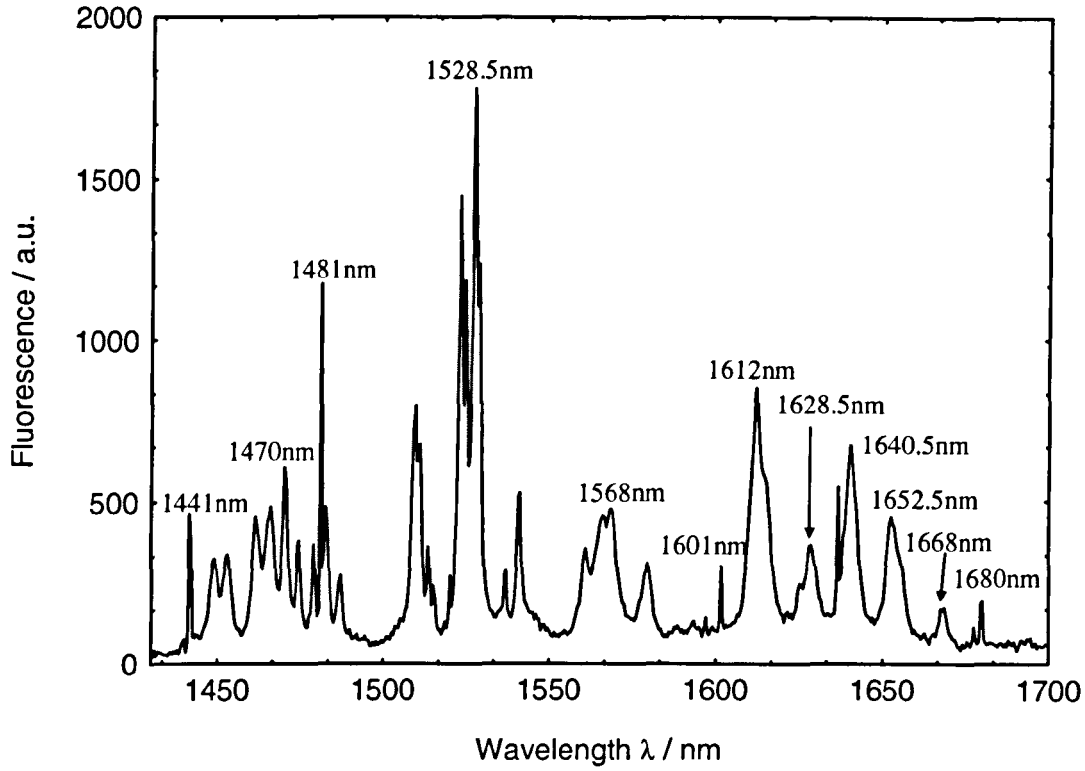

Figure 6.21: Spec YAl 09 – $Y_3Al_5O_{12}:Er^{3+}$ (1mol%)
Fluorescence spectrum ($^4I_{13/2}$)

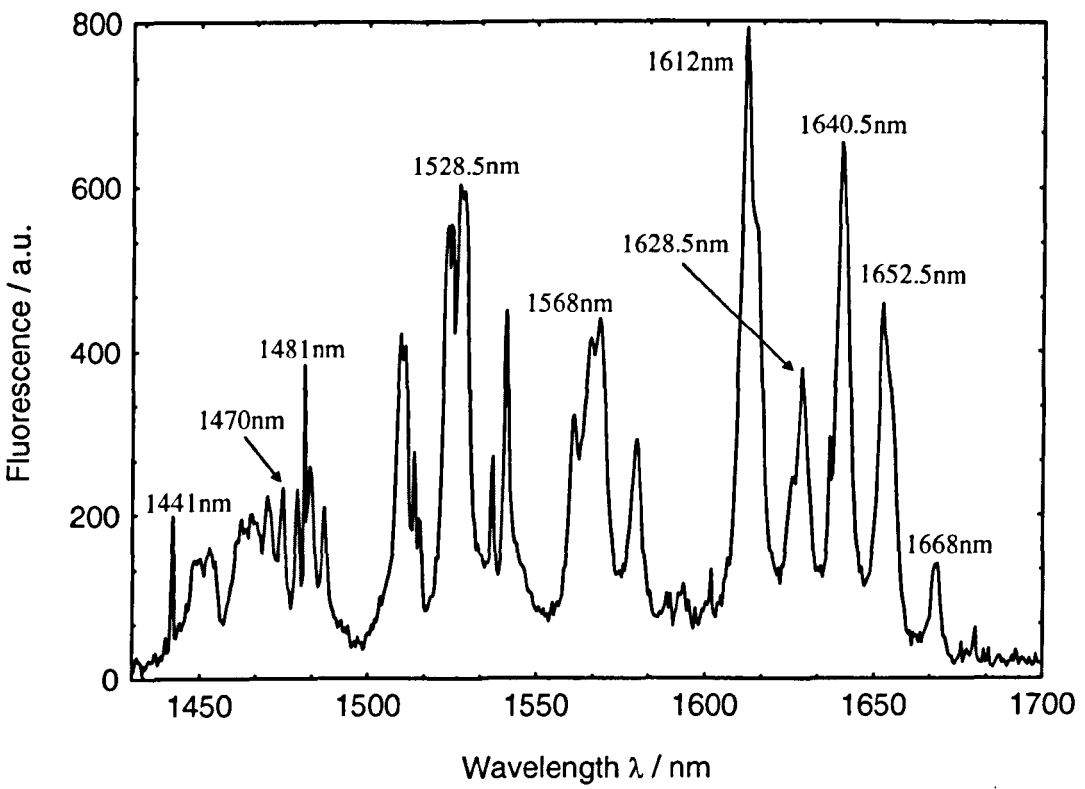

Figure 6.22: Spec YAl 10 – $Y_3Al_5O_{12}:Er^{3+}$ (5mol%)
Fluorescence spectrum ($^4I_{13/2}$)

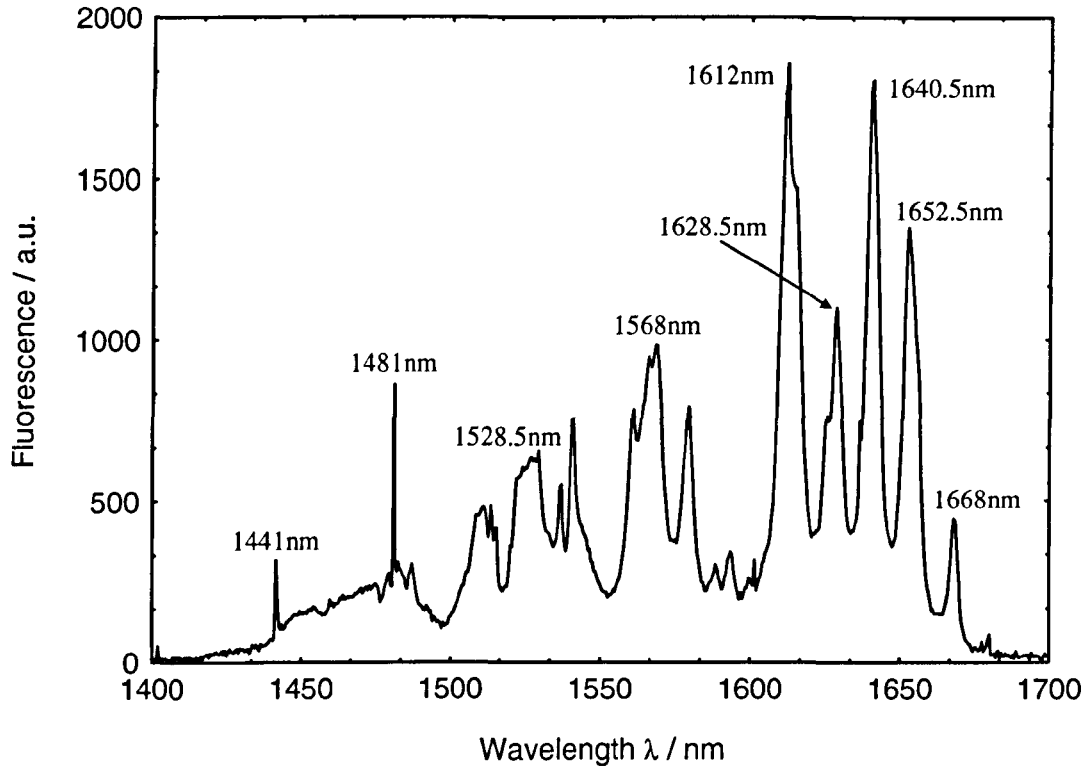

Figure 6.23: Spec YAl 13 – $Y_3Al_5O_{12}:Er^{3+}$ (10mol%)
Fluorescence spectrum ($^4I_{13/2}$)

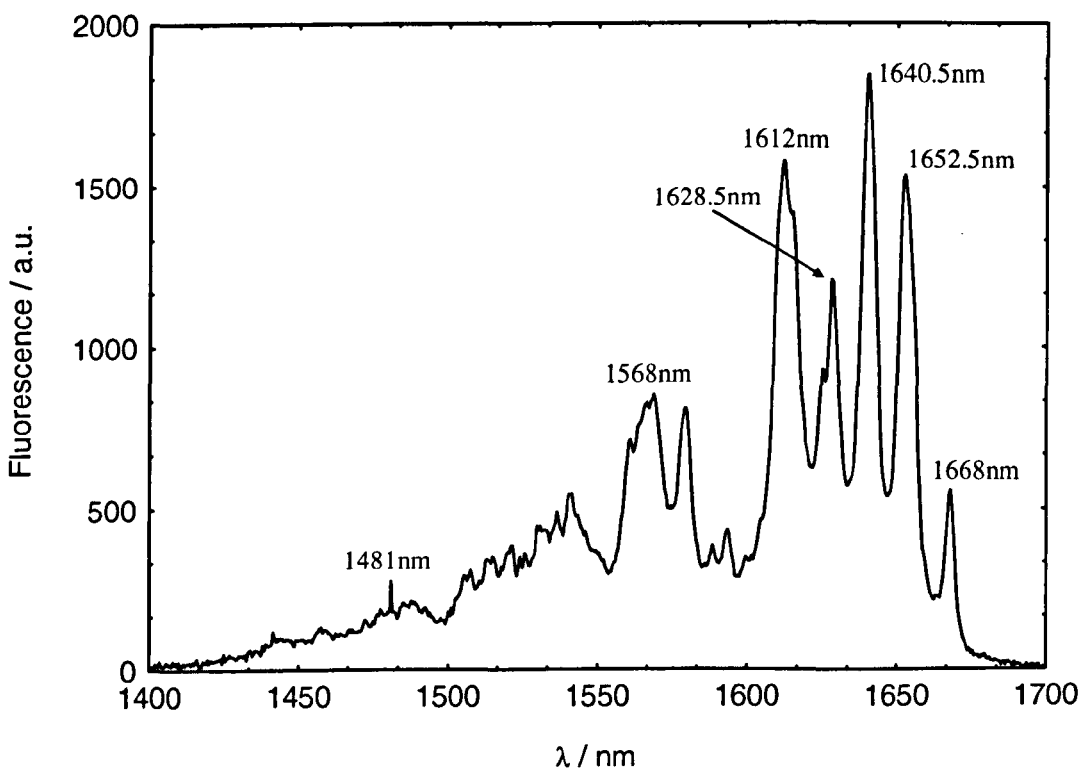

Figure 6.24: $Y_3Al_5O_{12}:Er^{3+}$ Fluorescence intensity ratio (FIR) ($I_{1528.5}/I_{1612}$)

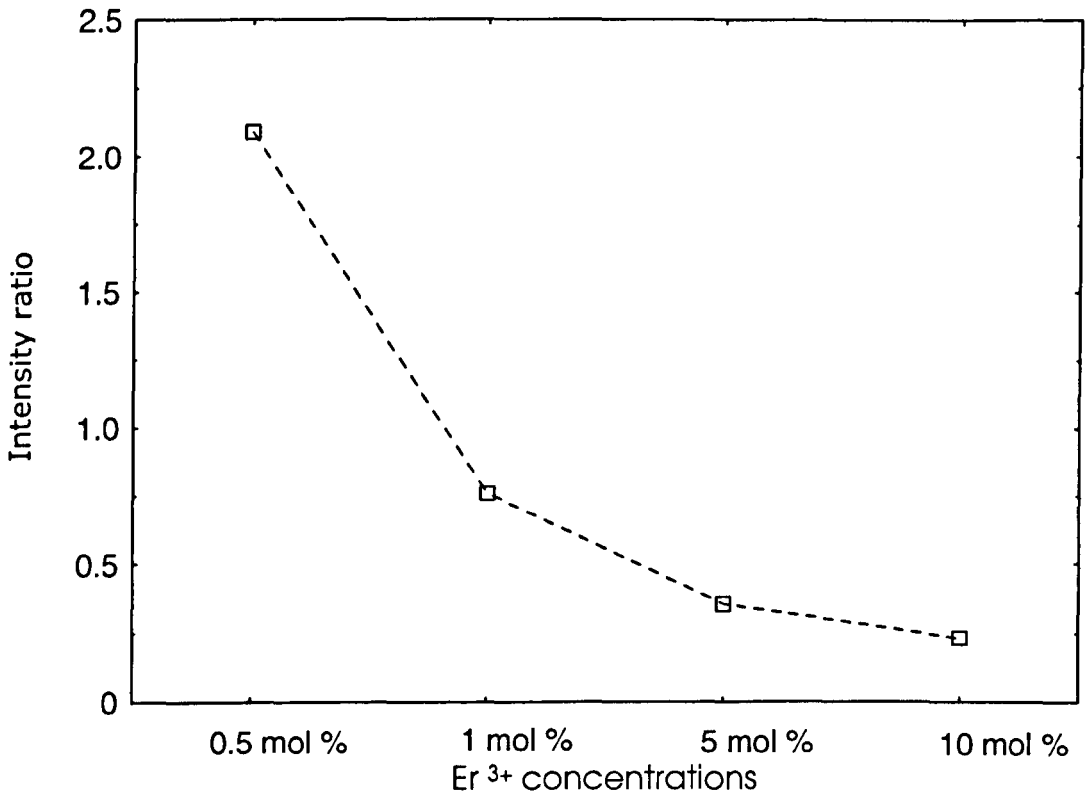

Figure 6.25: Spec YAl 16 – $Y_3Al_5O_{12}:Er^{3+}+Yb^{3+}$ (1mol% ea) Fluorescence spectrum

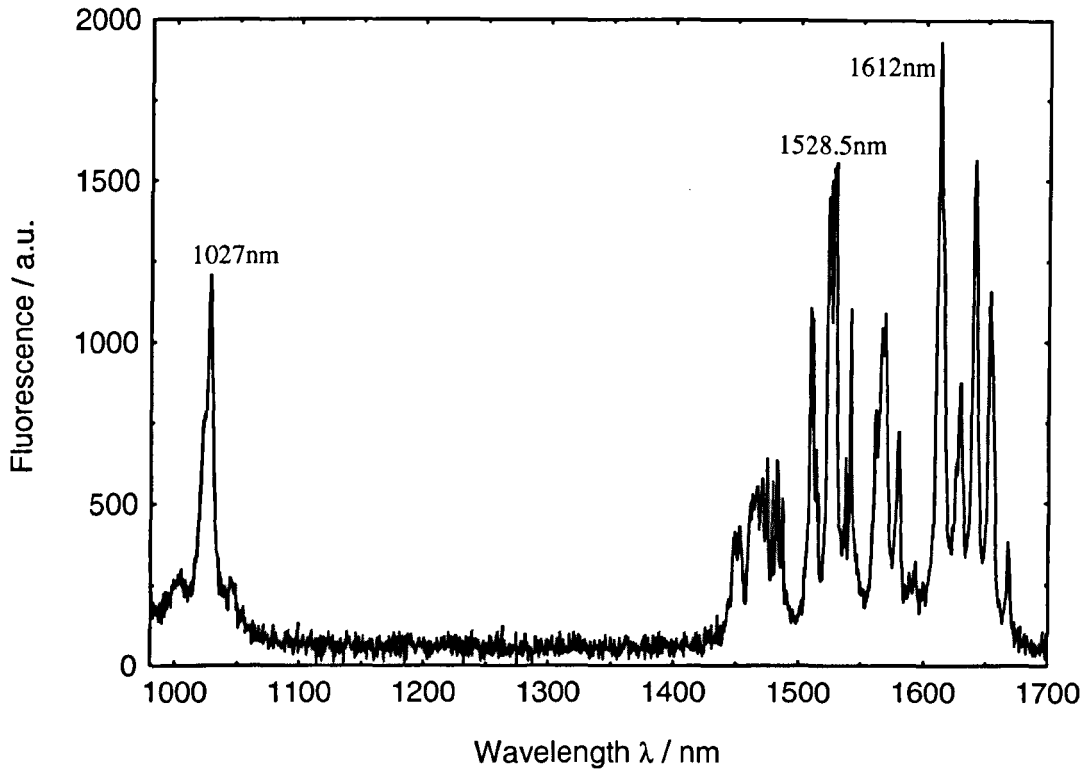

Figure 6.26: Spec YAl 16 – $Y_3Al_5O_{12}:Er^{3+}+Yb^{3+}$ (1mol% ea) Fluorescence spectrum ($^4I_{13/2}$)

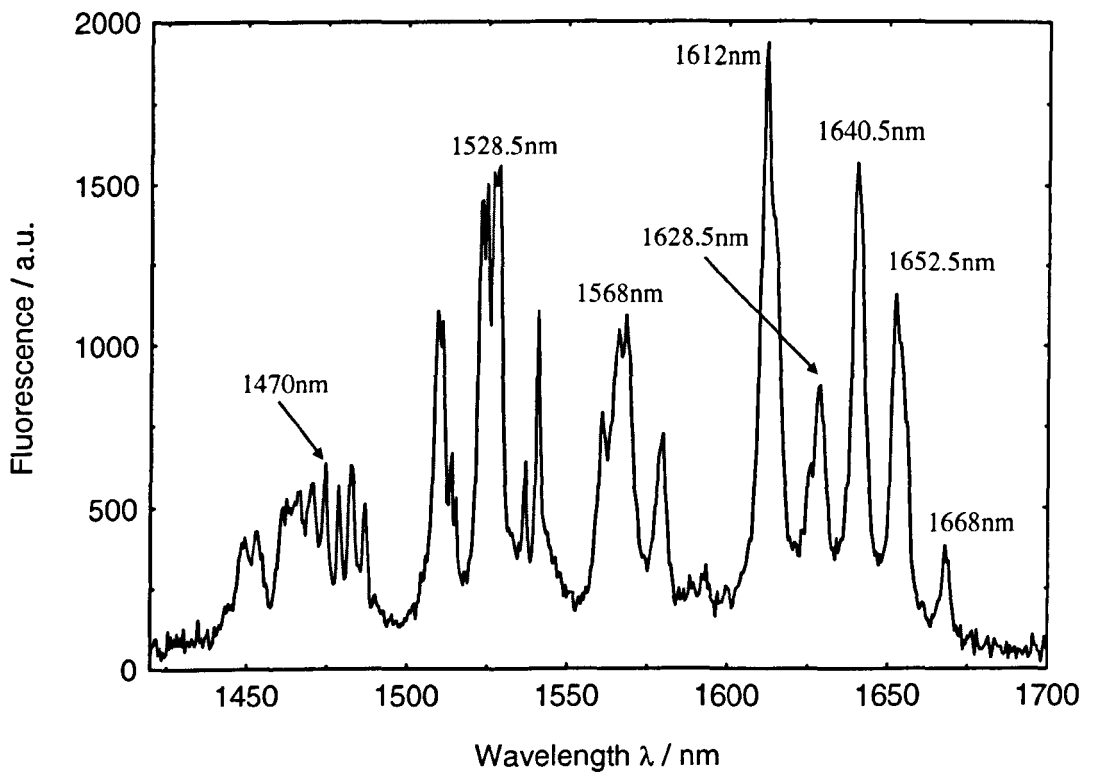

Figure 6.27: Spec YAl 20 – $Y_3Al_5O_{12}:Er^{3+}+Yb^{3+}$ (1+2mol%) Fluorescence spectrum

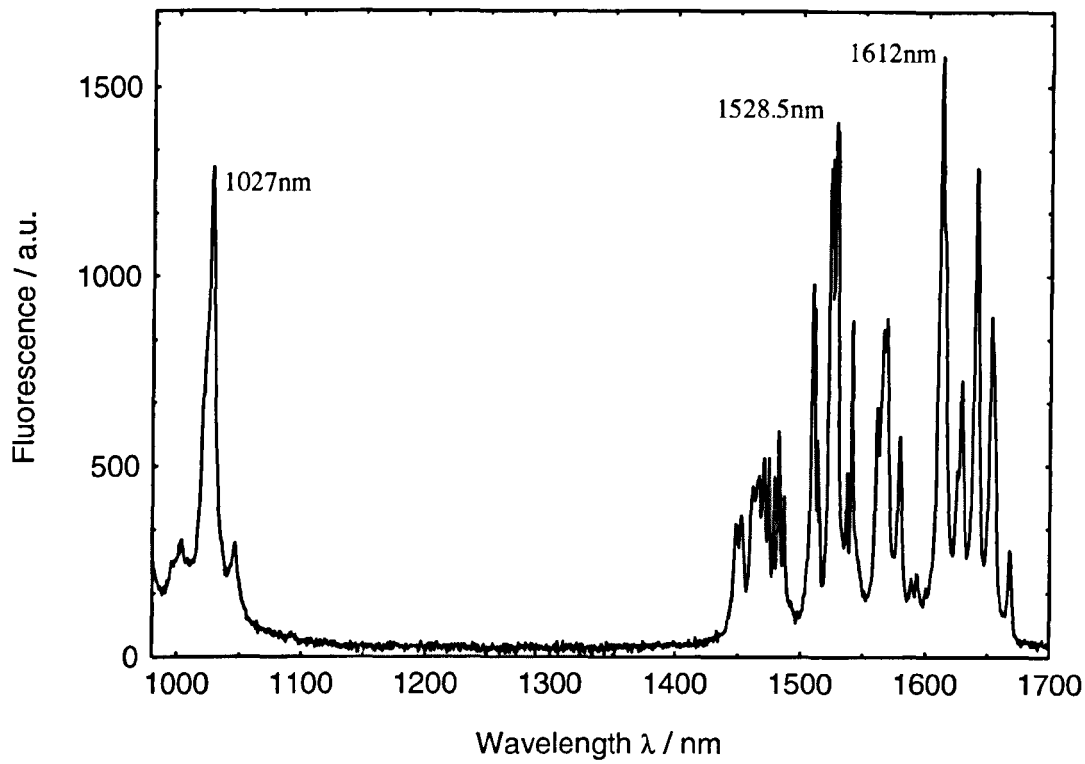

Figure 6.28: Spec YAl 20 – $Y_3Al_5O_{12}:Er^{3+}+Yb^{3+}$ (1+2mol%) Fluorescence spectrum ($^4I_{13/2}$)

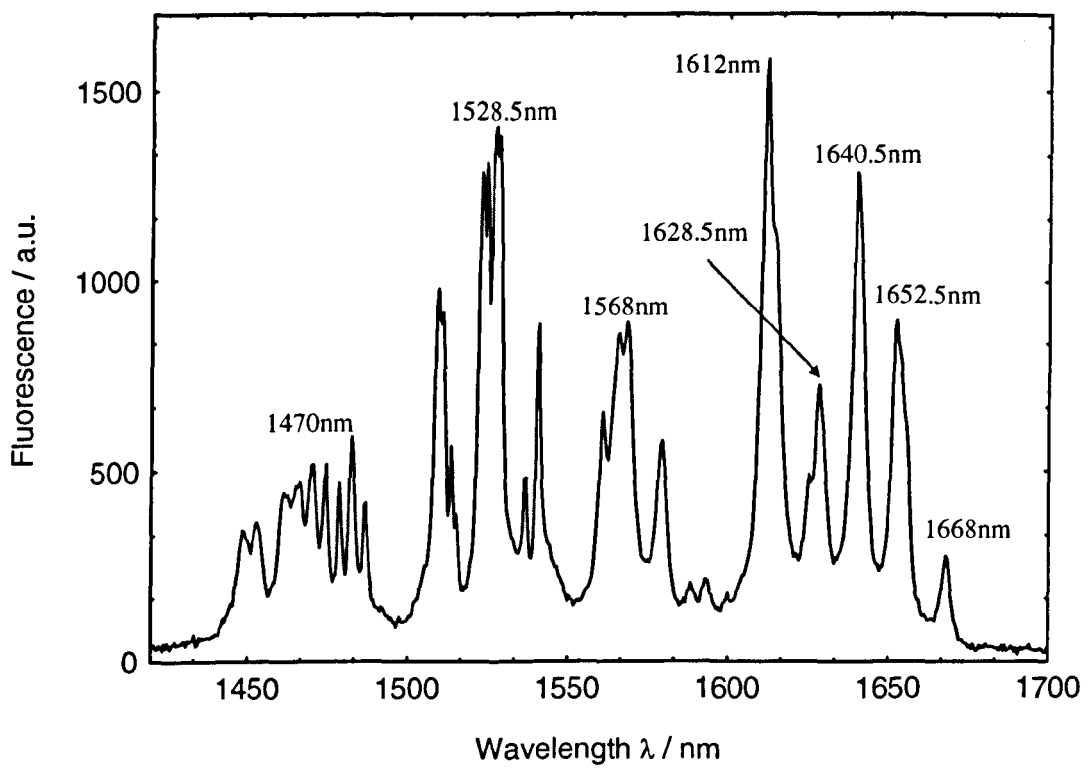

Figure 6.29: Spec YAl 19 – $Y_3Al_5O_{12}:Er^{3+}+Yb^{3+}$ (1+3mol%) Fluorescence spectrum

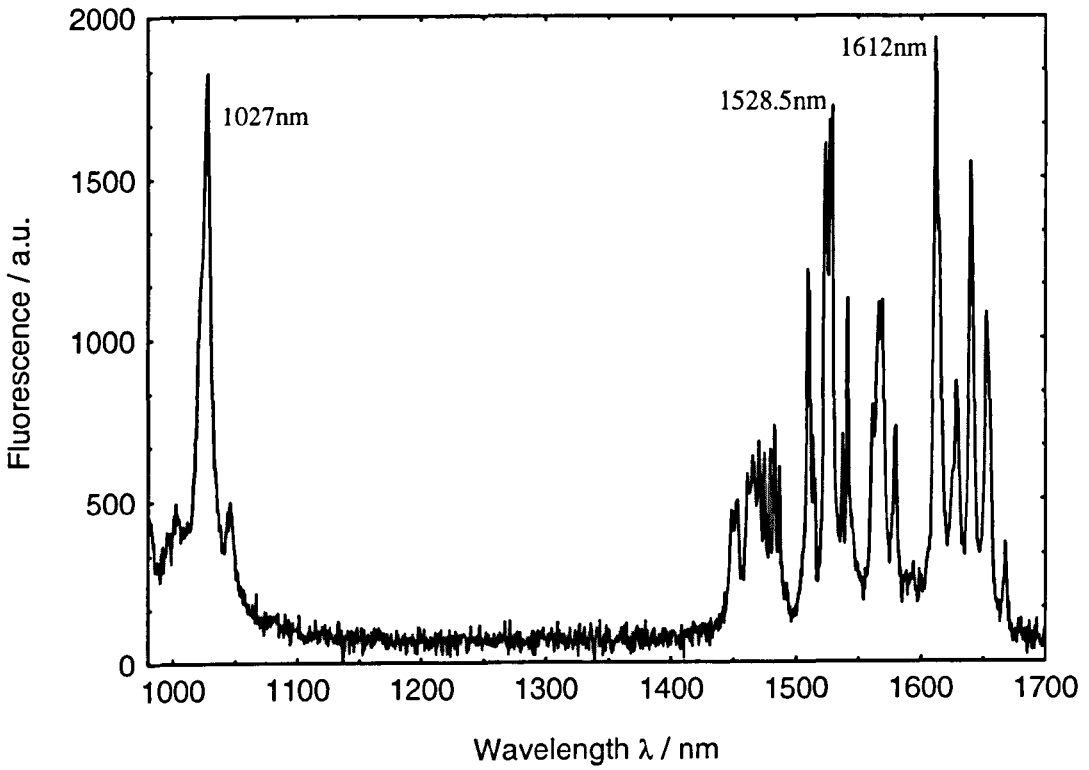

Figure 6.30: Spec YAl 19 – $Y_3Al_5O_{12}:Er^{3+}+Yb^{3+}$ (1+3mol%) Fluorescence spectrum ($^4I_{13/2}$)

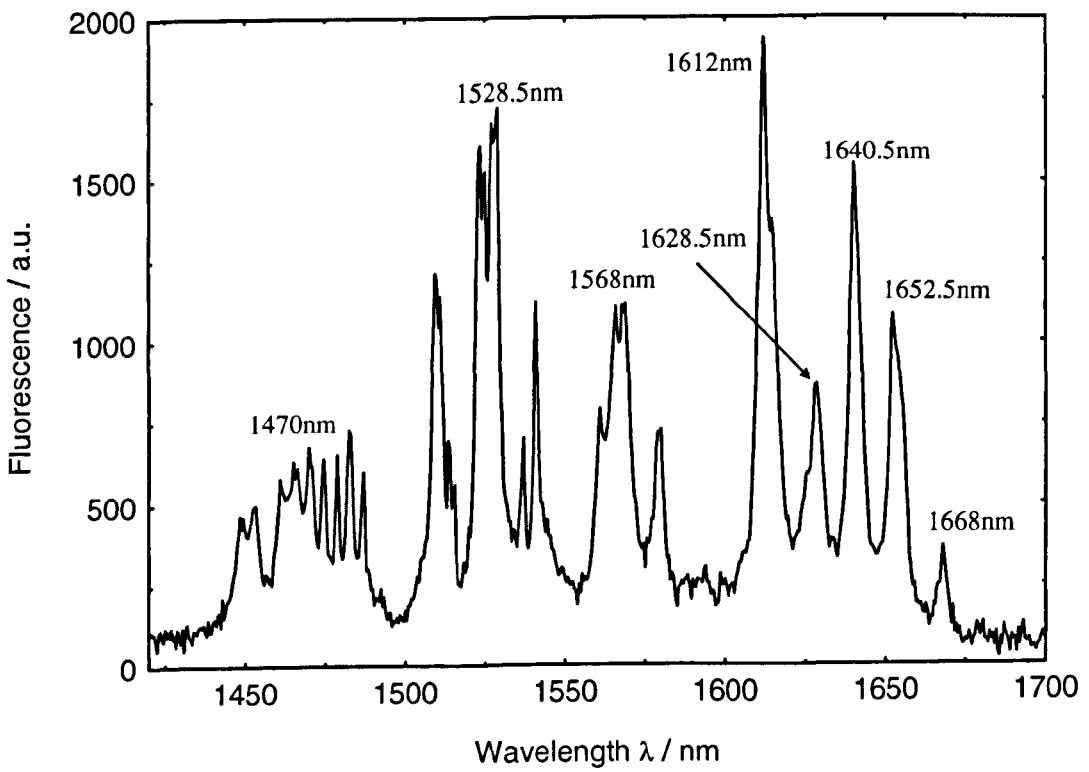

Figure 6.31: $Y_3Al_5O_{12}:Er^{3+}+Yb^{3+}$ Fluorescence intensity ratio (FIR) ($I_{1528.5\ \&\ 1612}/I_{1027}$)

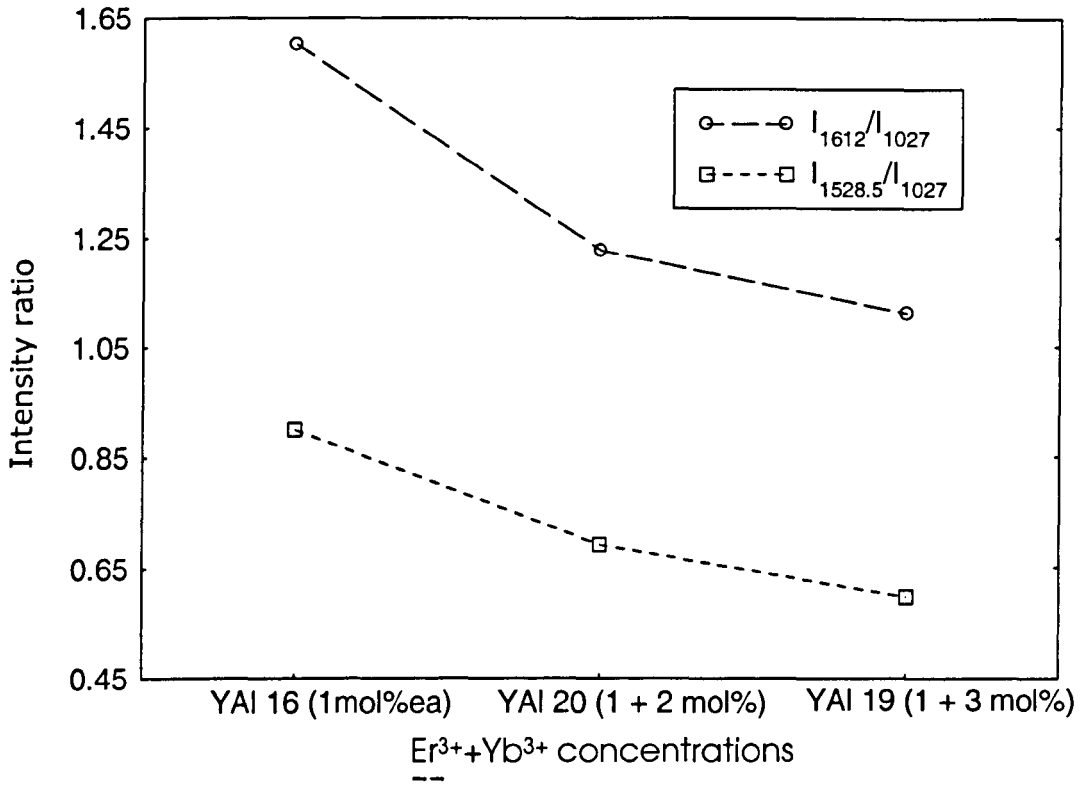

Figure 6.32: $Y_3Al_5O_{12}:Er^{3+}$& $Er^{3+}+Yb^{3+}$ Fluorescence intensity ratio (FIR) ($I_{1612}/I_{1528.5}$)

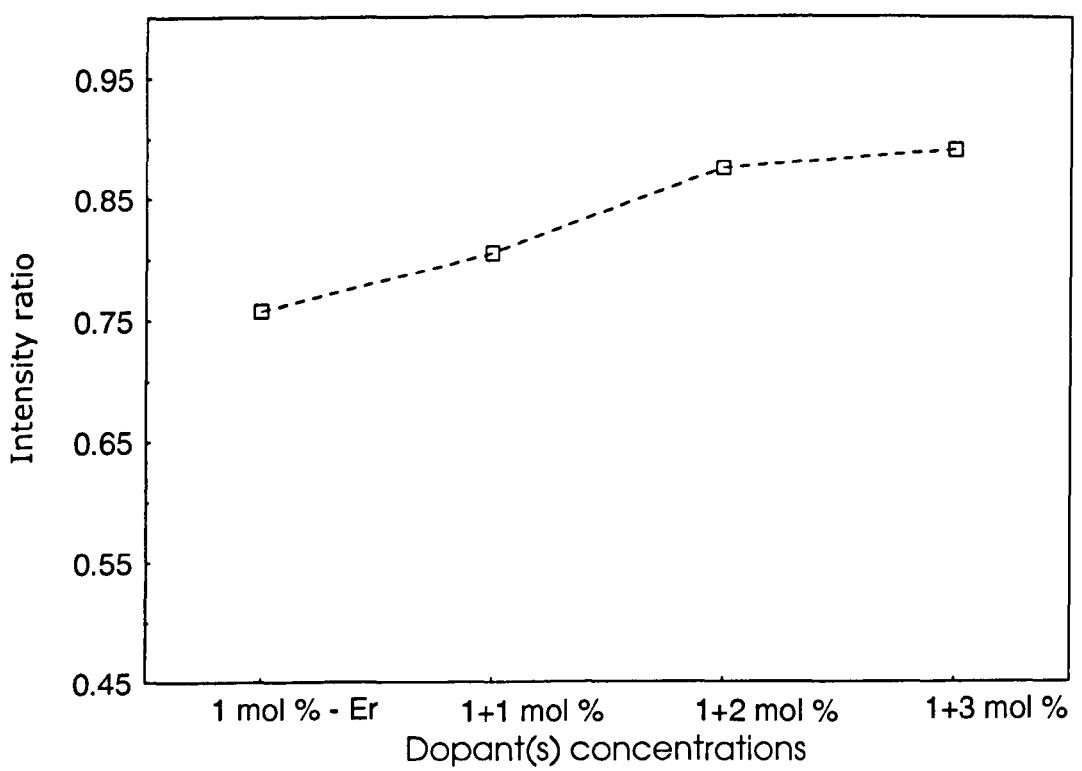

6.6 Upconversion Measurement

Green emission was observed from all the YAG fibres when a 975nm laser diode was used to excite fibres during the fluorescence spectra measurements. Therefore, further experiments were conducted on these fibres to investigate the transition lines in the visible spectrum. The visible emission indicated that a cooperative energy transfer upconversion process was present within the system and the theoretical background on this process was discussed in Chapter 3.3.3. Refer to Chapter 5.3.2 for details on experimental setting and layout.

6.6.1 Results and Discussion

The visible emission produced by excitation with the 975nm laser diode was too weak for the photomultiplier tube (PMT) to sense even at maximum power (120mW). This was due to the great losses through the monochromator. Therefore, a 965nm laser diode array (maximum power 5W) was used in this experiment. In order for cooperative energy transfer upconversion to occur, a minimum of two Er^{3+} ions are involved. More power, thus, was required to promote the ion to the higher metastable state, $^4F_{7/2}$, to facilitate transitions to the visible regions. From the absorption spectra, it was observed that the absorption had very narrow and sharp peaks scattered across the ~950 to ~980nm. Weak absorption was observed at 975nm. Therefore, when a laser at this wavelength was employed, it was not efficient enough to promote a strong upconversion emission within the system to overcome the losses caused by optics in experimental settings. From Figure 5.12, it was observed that the 965nm laser had a broader linewidth compared to the 975nm device and 965nm was very near to an absorption peak. The quality of the grown fibres also produced large scattering losses which could also add to the inefficiency of pumping with the 975nm laser diode. For the singly doped YAG fibres, $^2H_{11/2}+^4S_{3/2}\rightarrow{}^4I_{15/2}$ and $^4F_{9/2}\rightarrow{}^4I_{15/2,}$ transitions were observed in the upconversion spectra. The green emission, seen in Figures 6.33 to 36 was much stronger than the red emission. At the lowest concentration of 0.5mol%, see Figure 6.33, the red emission was the also at it's lowest. The emission ranged from 530nm to 570nm and had a number of peaks. At this concentration, the peak at 553.5nm was the most intense. Although the red emission was extremely weak, several peaks can be

observed after multiplying a factor of 15 to the red emission intensity. At 1mol% Er^{3+} concentration, the general green emission spectrum looked similar to that of the lowest concentration. See Figure 6.34. The maximum peak at this concentration was in agreement with work done by *Silversmith* [3.41]. The red emission was stronger as compared to 0.5mol%. After multiplying the red emission by a factor of 5 increases the emission profile. When doped with 5mol% of Er^{3+}, see Figure 6.35, broadening effects were observed at the base of the green emission spectrum's profile. The red upconversion emission profile was more prominent and was more intense. Slight broadening of the linewidths at the red emission profile was also observed. At 10mol% concentration, see Figure 6.36, the maximum peak at 560nm increased with respect to the other peaks within the green emission. Broadening of the transition lines in this region was also observed. The lines at the 530nm to 550nm region were no longer discernable due to the broadening and overlapping of the transition lines. The red emission at this concentration became more intense as compared to the other concentrations. From this work, increasing the Er^{3+} resulted in a relative increase in the red emission intensity, similar observations have been made by *Capobianco* [6.11] when nanocrystalline Er^{3+} was added to bulk and cubic Y_2O_3 crystals. To further illustrate the increment of intensities in red and green emissions with respect to the dopant concentration, an upconversion intensity ratio (UIR) was calculated with the peaks at 553.5nm ($G_{553.5}$), 560nm (G_{560}) and 676nm (R_{676}). Taking these peaks for each concentration and dividing one by the other and plotting the ratio versus the dopant concentration gives Figure 6.37. An increased intensity ratio is seen as the dopant concentration increases. Figure 6.38 shows the relationship between the red and the green emissions.

Figures 6.39 to 41 present the upconversion spectra of the co-doped YAG fibres. The emission profile of the various co-doped fibres appears similar to that of the 1mol% Er^{3+} singly doped YAG fibre. The differences are that the red emission is much more intense and this intensity increases with dopant concentration. Figure 6.42 shows UIR of the peaks G_{560}/G_{553} for the co-doped fibres where the change between the peaks is seen to be minimal or possibly not at all. This was also observed by *Balda* [6.7] with Er^{3+}+Yb^{3+} doped lead-niobium-germanante glasses: that the green emission stayed consistent and only the red emission spectrum increased with the increase in Yb^{3+} concentration. Work done by *Matsuura* [6.12] stated that in

Er^{3+}+Yb^{3+} doped Y_2O_3 nanocrystals at 2mol% of Yb^{3+} concentration, the intensity of the $^2H_{11/2}$+$^4S_{3/2}$→$^4I_{15/2}$ transitions reached a maximum. Figure 6.42 shows the current work is in agreement with [6.7] and [6.12]. The influence of Yb^{3+} has improved the mechanism of the energy transfer within the system and Figure 6.43 shows that Yb^{3+} had increased the efficiency of the upconversion process.

Figure 6.33: Spec YAl 08 – $Y_3Al_5O_{12}:Er^{3+}$ (0.5mol%) Upconversion spectrum

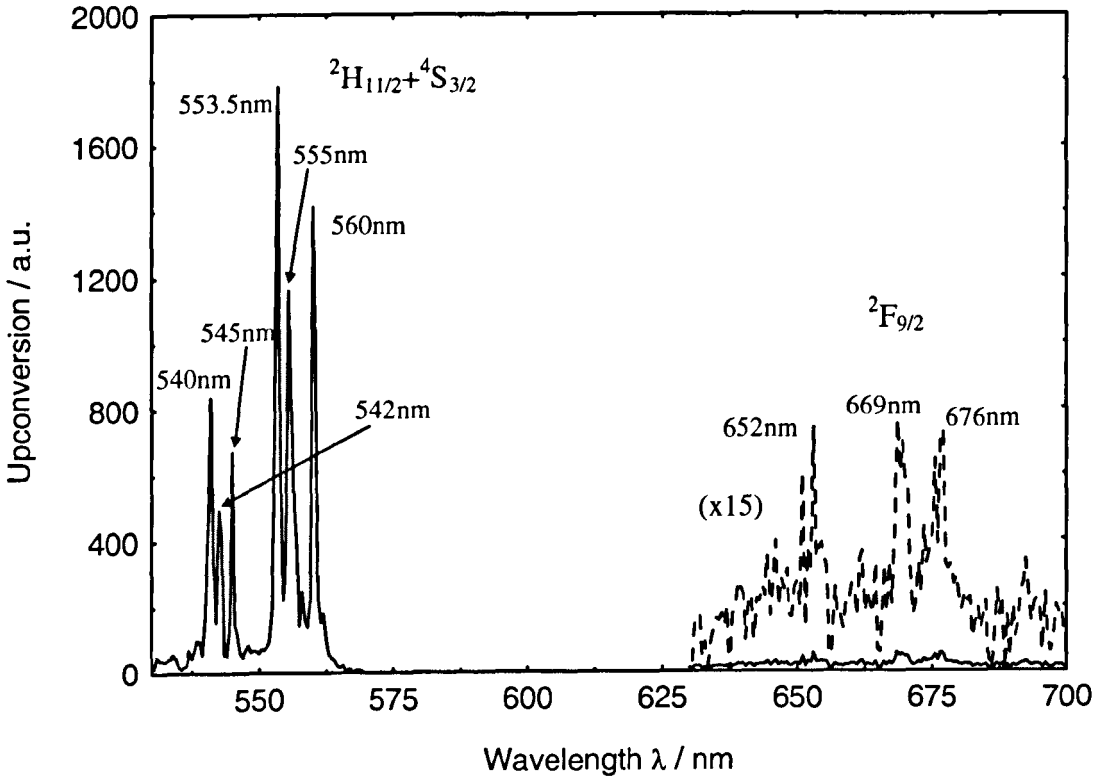

Figure 6.34: Spec YAl 09 – $Y_3Al_5O_{12}:Er^{3+}$ (1mol%) Upconversion spectrum

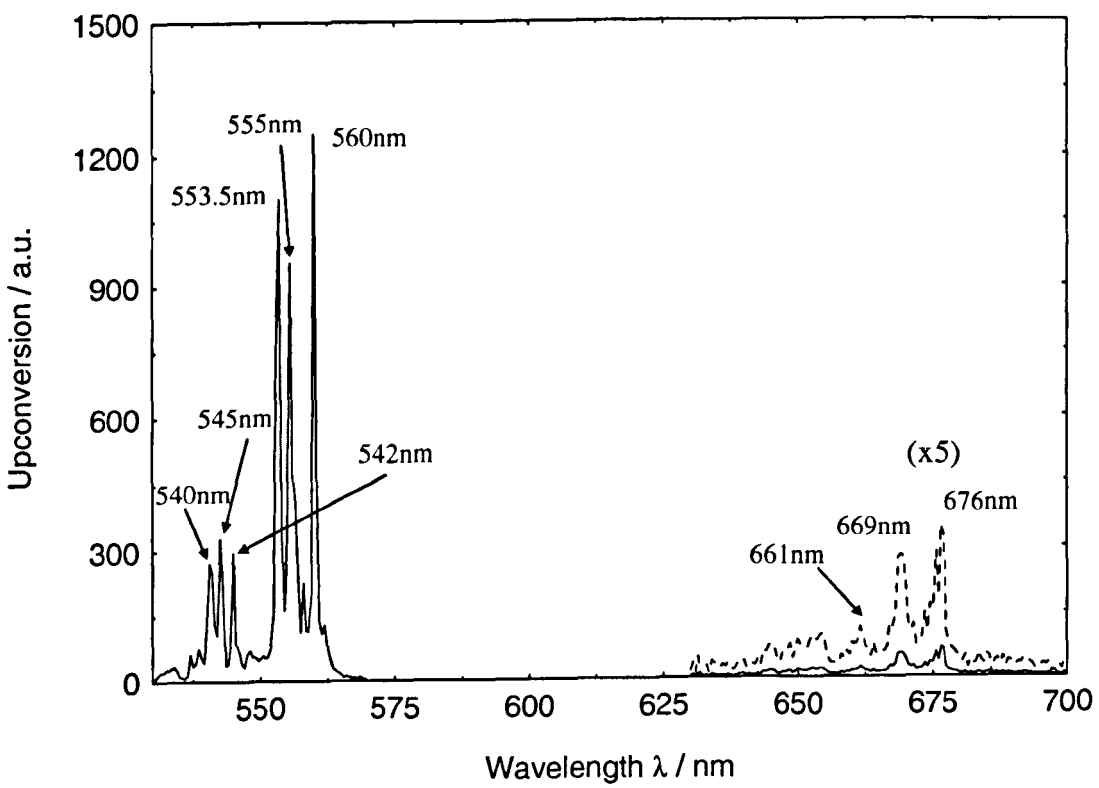

Figure 6.35: Spec YAl 10 – $Y_3Al_5O_{12}:Er^{3+}$ (5mol%)
Upconversion spectrum

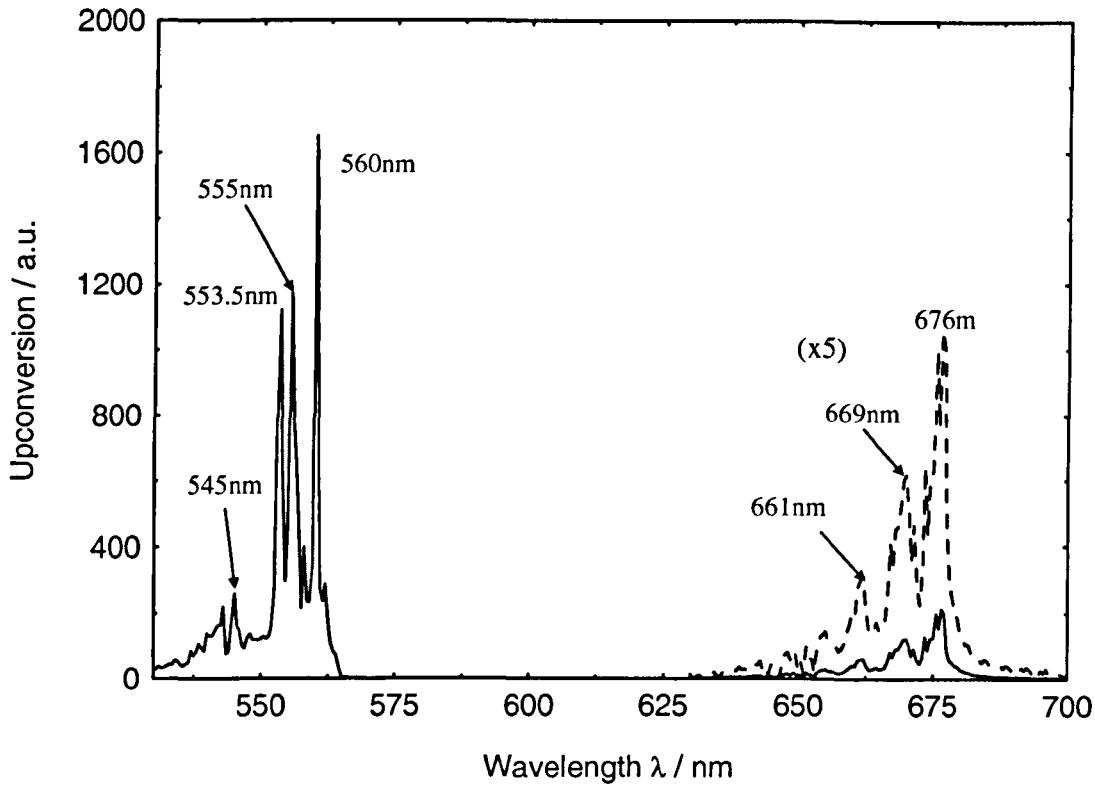

Figure 6.36: Spec YAl 13 – $Y_3Al_5O_{12}:Er^{3+}$ (10mol%)
Upconversion spectrum

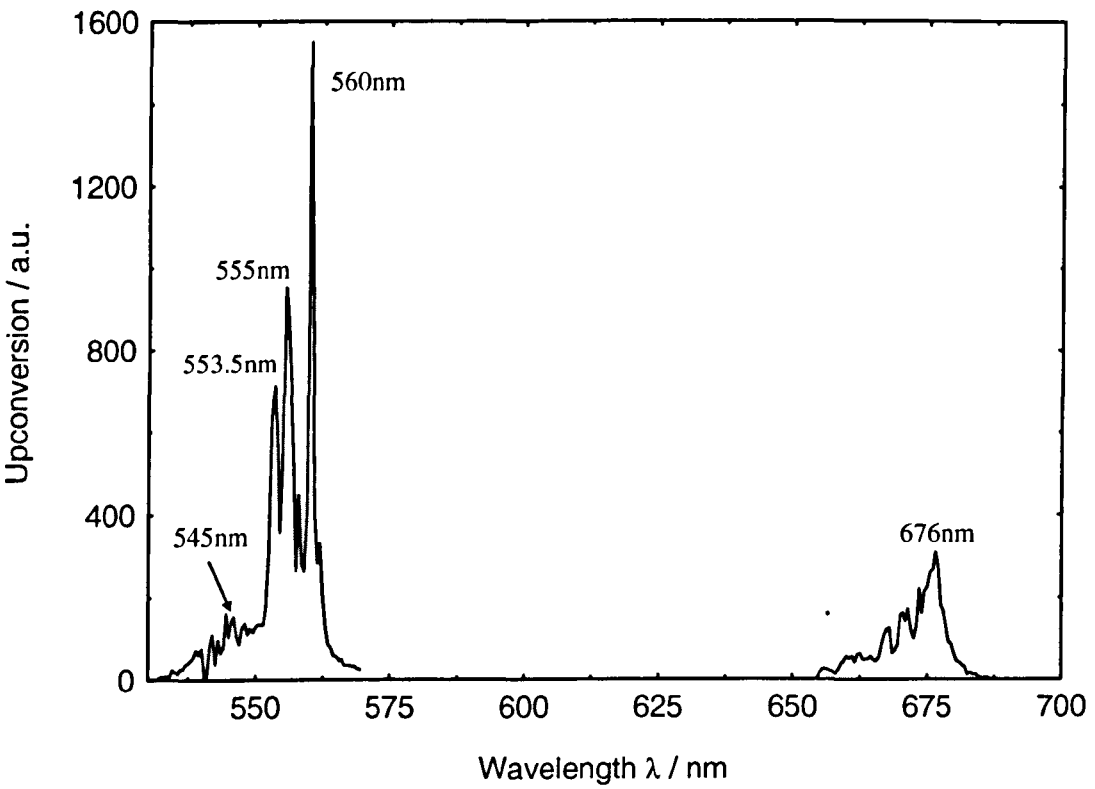

Figure 6.37: $Y_3Al_5O_{12}:Er^{3+}$ Upconversion intensity ratio (UIR) ($G_{560}/G_{553.5}$)

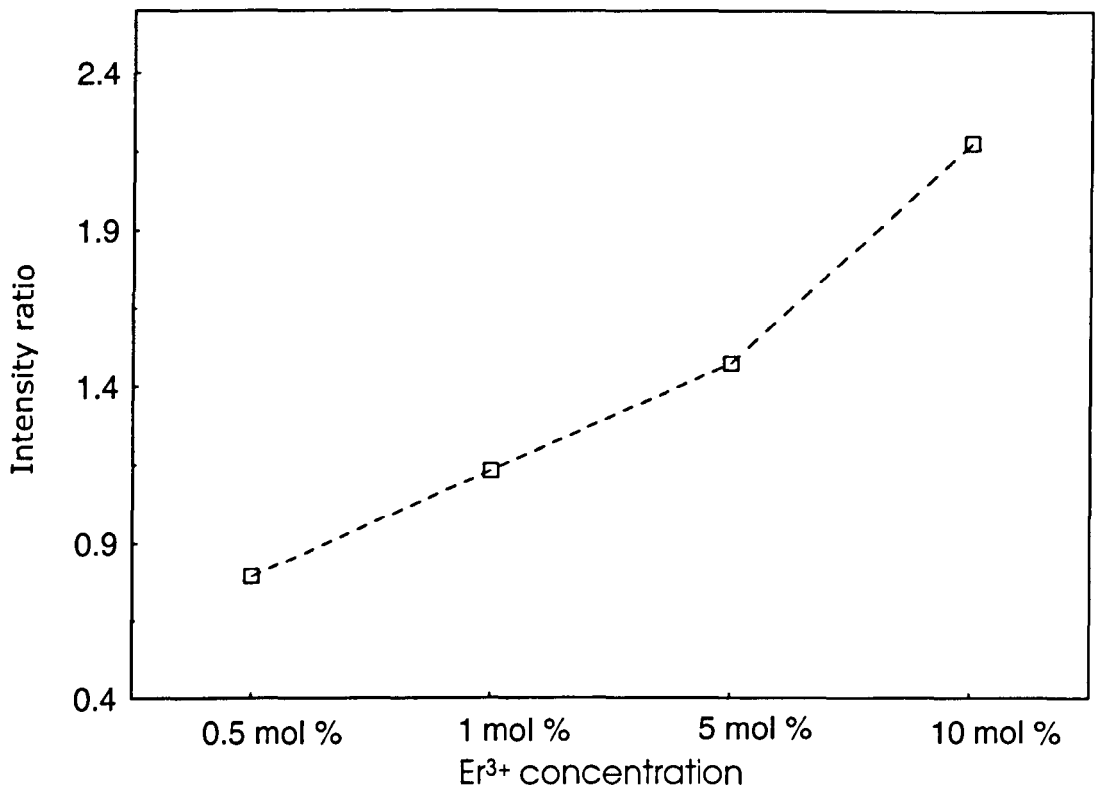

Figure 6.38: $Y_3Al_5O_{12}:Er^{3+}$ UIR at green and red emission ($R_{676}/G_{553.5\ \&\ 560}$)

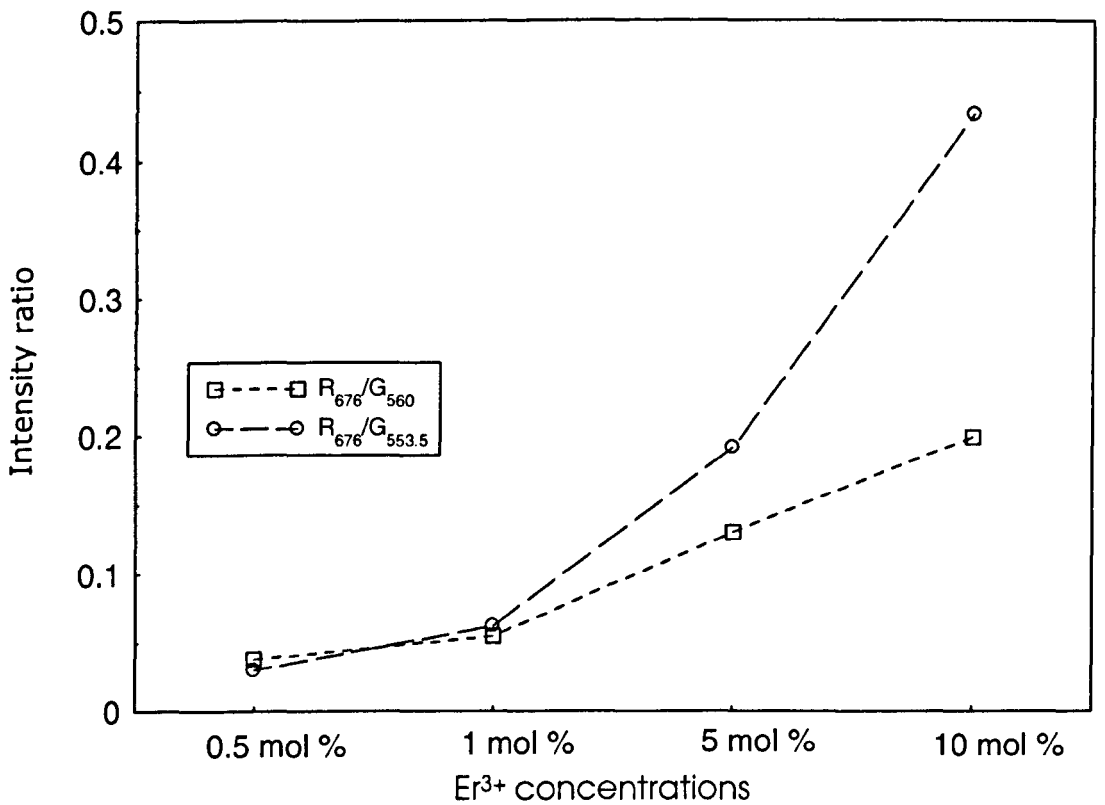

Figure 6.39: Spec YAl 16 – $Y_3Al_5O_{12}:Er^{3+}+Yb^{3+}$ (1mol% ea) Upconversion spectrum

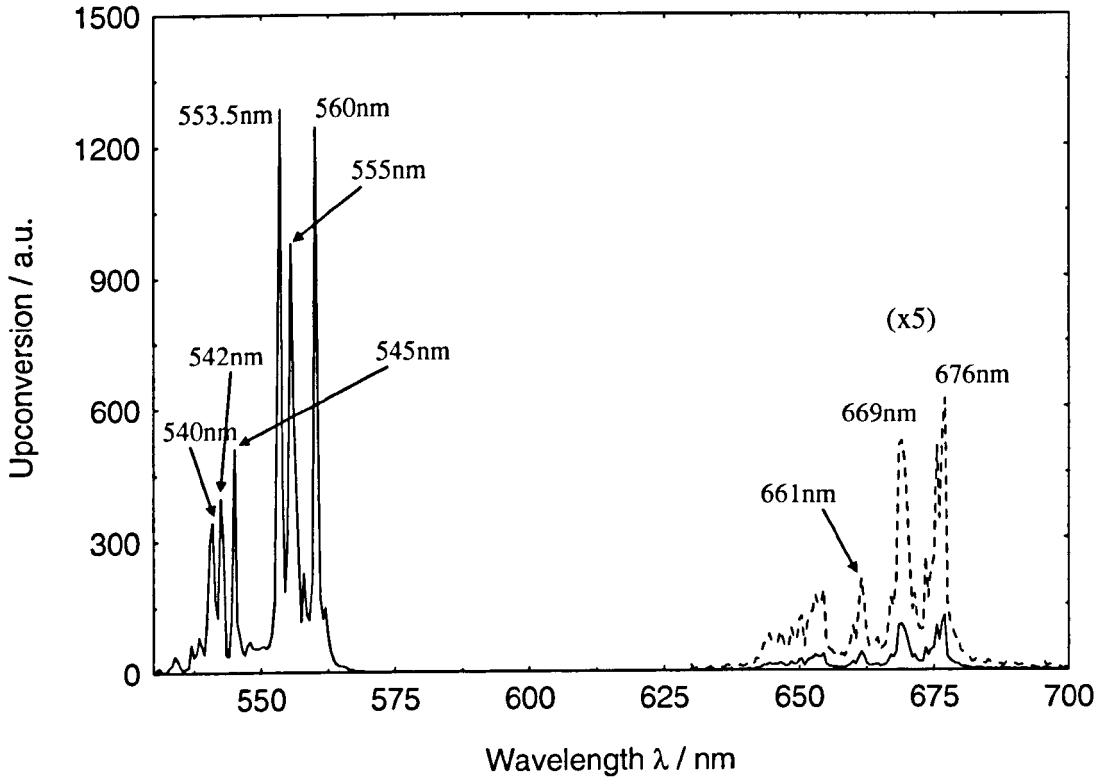

Figure 6.40: Spec YAl 20 – $Y_3Al_5O_{12}:Er^{3+}+Yb^{3+}$ (1+2mol%) Upconversion spectrum

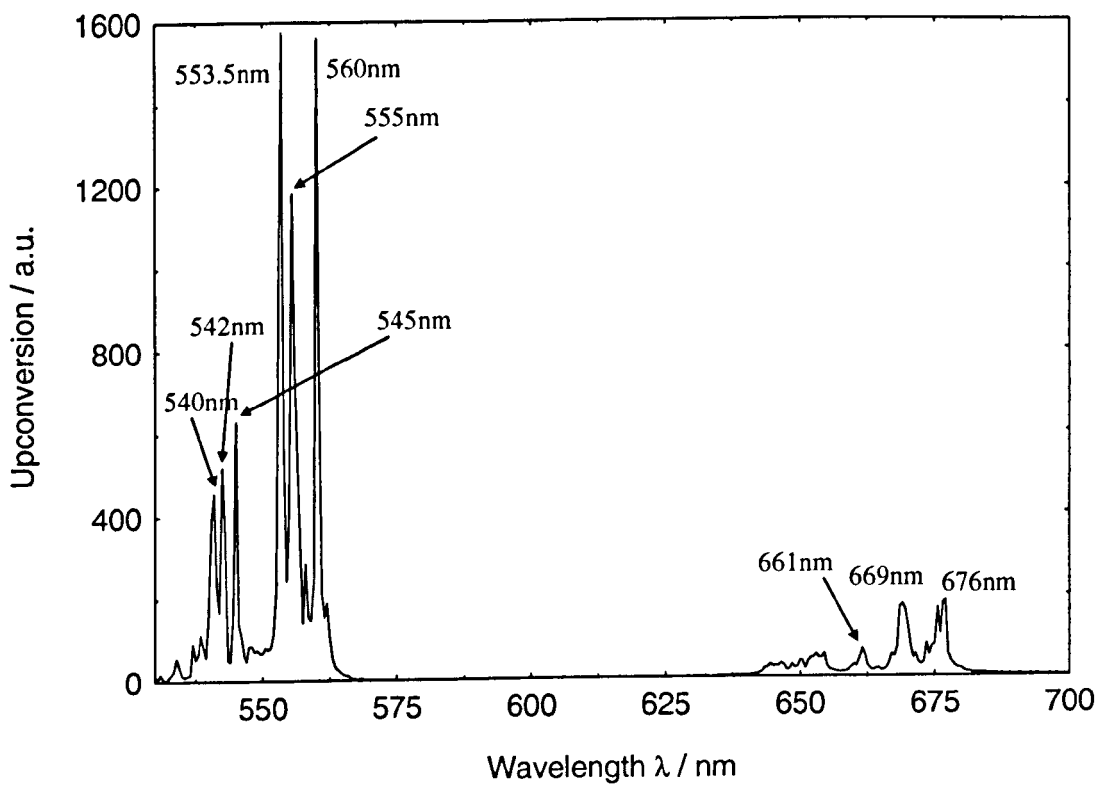

Figure 6.41: Spec YAl 19 – $Y_3Al_5O_{12}:Er^{3+}+Yb^{3+}$ (1+3mol%) Upconversion spectrum

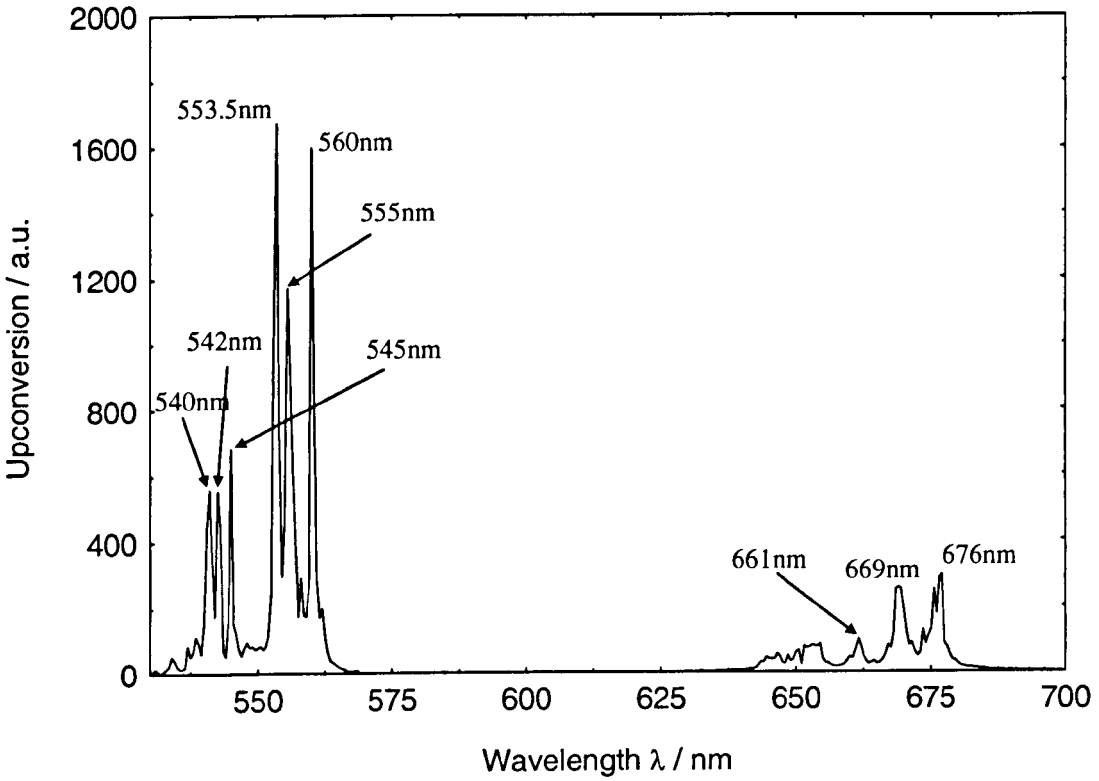

Figure 6.42: $Y_3Al_5O_{12}:Er^{3+}+ Yb^{3+}$ Upconversion intensity ratio (UIR) ($G_{560}/G_{553.5}$)

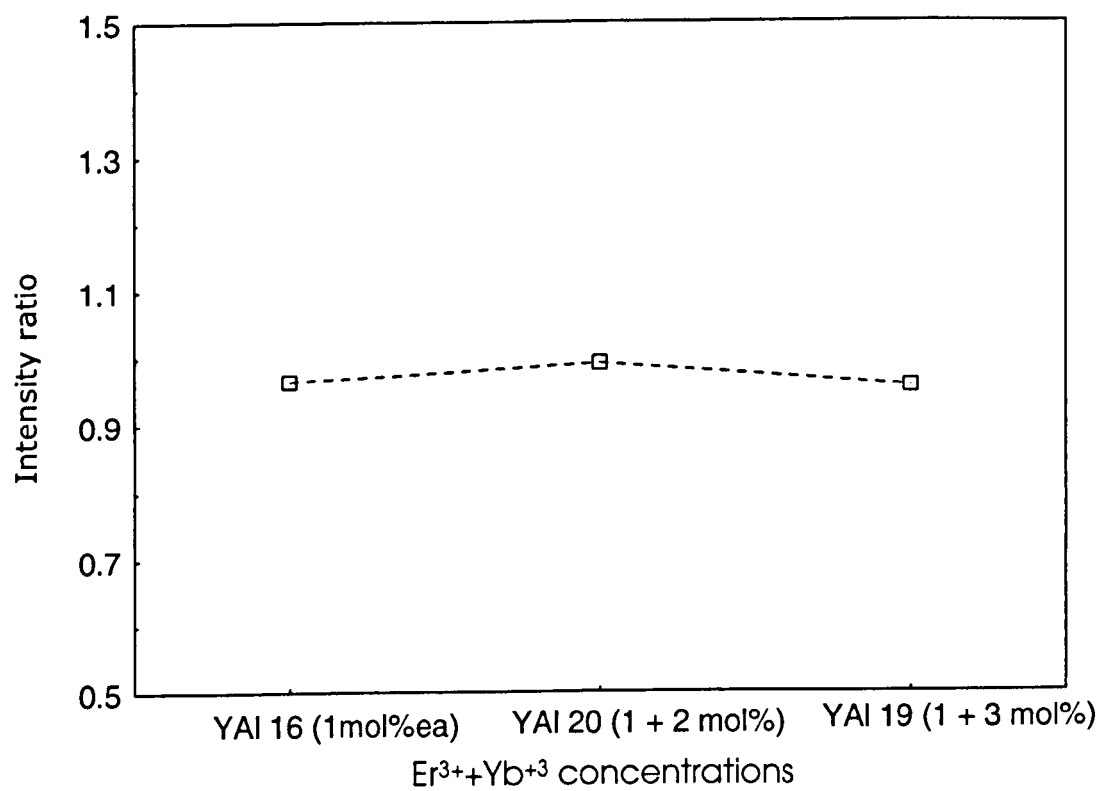

Figure 6.43: $Y_3Al_5O_{12}:Er^{3+}+Yb^{3+}$ UIR at green and red emission

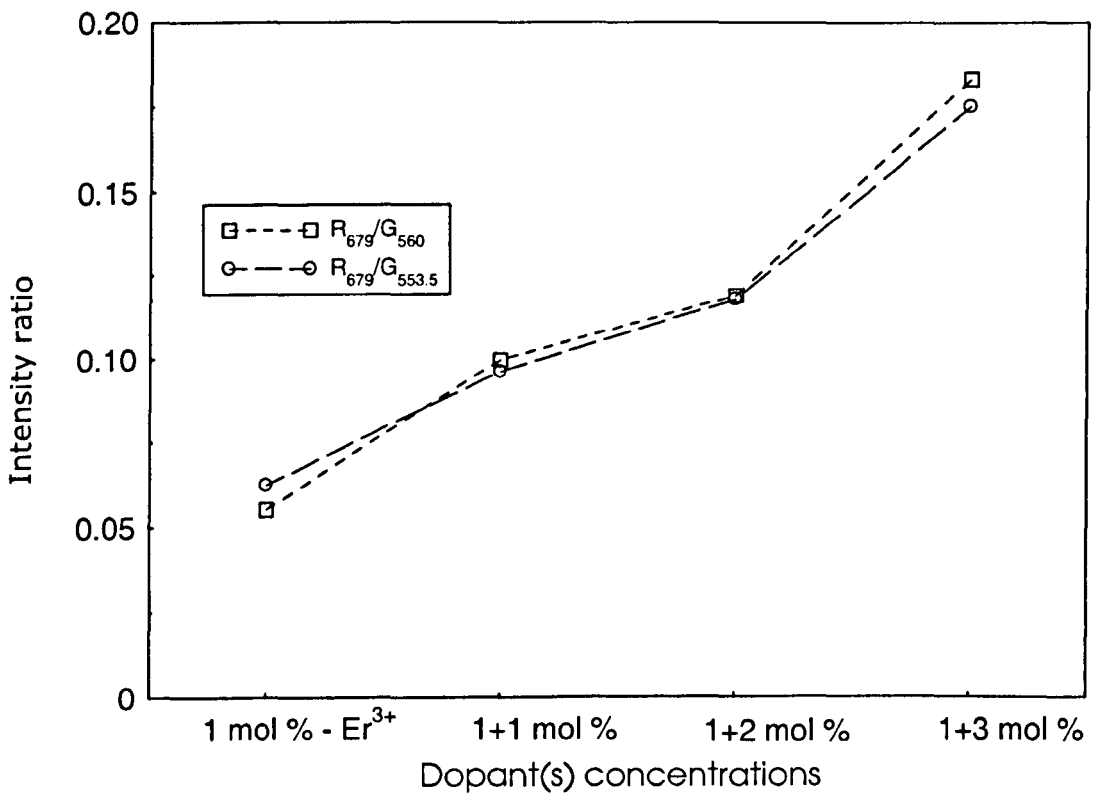

6.7 Fluorescence Lifetime Measurement

In this section, investigations were carried out under room temperature conditions to determine the fluorescence lifetime from the $^4I_{13/2} \rightarrow {}^4I_{15/2}$ and $^4I_{11/2} \rightarrow {}^4I_{15/2}$ transitions for the YAG fibres with different dopant concentrations. The lifetime decay of individual peaks located in the $^4I_{13/2}$ manifold was investigated, along with analysis of the influence of laser power on the lifetime decay. Results from these findings are presented in this section. Experimental layout on this was earlier discussed in Chapter 5.3.3.

6.7.1 Results and Discussion

Fluorescence lifetime experiments were carried firstly on the singly doped Er^{3+}:YAG fibres. From the fluorescence spectra in Section 6.5, several peaks were observed at 1528.5nm, 1568nm, 1612nm, 1628.5nm, 1640.5nm, 1652.5nm and 1668nm when excited with the 975nm laser diode. The fluorescence lifetime of each of these peaks was taken using a monochromator acting as a bandpass filter. Figures 6.44 and 45 show the typical fluorescence lifetime curves at 1528.5nm and 1612nm. The experimental lifetime results are denoted by the boxes seen in the two figures. Using the EASYPLOT curve fitting function, a curve (solid line exponential curves seen in the figures) was fitted to the experimental results and the decay, τ, was calculated. Figures 6.46 and 47 show that the fluorescence lifetime increased as the dopant level increased. Figure 6.48 shows the lifetime of the individual peaks taken for the singly doped fibres from 0.5 to 10mol%. It can be seen for the different dopant concentrations that as the mol% increased, the τ value increased. The results also show that all peaks (for all the fibres) that fell in the $^4I_{13/2} \rightarrow {}^4I_{15/2}$ transition had approximately the same decay time. The fluorescence lifetime of the singly doped fibres ranged from ~6ms to ~8ms, see Table 6.3. There was no evidence of fluorescence quenching even at 10mol% since the decay time increased rather than decreased. As for the co-doped fibres, Figures 6.49 to 51 show the typical fluorescence decay curves. From Figure 6.49, it is observed that the lifetime at wavelength 1027nm was faster than compared to Er^{3+} wavelengths at $^4I_{13/2} \rightarrow {}^4I_{15/2}$ transitions. At 1027nm, the decay time of the co-doped fibres remained similar even though the Yb^{3+} dopant concentration had increased. No significant change in τ was

observed when the fibres were co-doped with Yb^{3+}, see Figure 6.52. From Figure 6.53, it is observed that there is no significant difference in decay lifetimes for peaks from the $^4I_{13/2}$ transition between the singly doped Er^{3+} (1mol%) and co-doped fibres. The addition of Yb^{3+} ions did not influence the lifetime of the $^4I_{13/2}$ emission. Table 6.4 shows the average fluorescence lifetime of the co-doped fibres. For $^4I_{13/2}$ transition lines, the fluorescence decay is ~6ms and at the peak 1027nm, ~1ms. This lifetime is close to the work done by *Shi* [6.13].

Investigations were also conducted to determine the influence of laser power to the fluorescence lifetime at $^4I_{13/2} \rightarrow {}^4I_{15/2}$ transitions. A long pass filter was used to eliminate wavelengths under 1250nm. Figures 6.54 to 57 show the usual fluorescence lifetime curves for the singly doped YAG fibres. The r^2 values in all the curves were close to 1 which indicated that the curves were well fitted. Figure 6.58 shows that at a laser power of 180mA (~95mW) the fluorescence lifetime increased with the dopant concentration. This result was similar to that done on the individual peaks with a fluorescence decay lifetime in the range of ~6ms to ~8ms. Figure 6.59 shows the fluorescence decay lifetime for each fibre at different laser powers (drive currents ranging from 40mA to 200mA). The results show that the lifetime remained consistent with the different pump powers. The lifetime at 0.5mol% Er^{3+} was 6.2ms, which was in agreement with *Cornacchia* [6.5] and for the high concentration of 10mol%, the lifetime was at 7.9ms, similar to the work done by *Pollack* [6.14]. Table 6.5 shows the lifetime decay at different laser powers. When similar experiments were done on the co-doped fibres, the results again showed that laser power did not affect the lifetime. Figures 6.60 to 62 show the typical fluorescence curves were well fitted as the r^2 valves were closed to unity. It is seen from Figure 6.63 that lifetime for three co-doped fibres pumped at 180mA were ~6.9ms. No change was observed when Yb^{3+} was added to the fibres and fluorescence decay of the co-doped fibres showed no change from the singly doped Er^{3+} (1mol%) fibre, see Figure 6.64. Table 6.6 shows the average fluorescence decay of co-doped fibres at different laser powers.

Figure 6.44: Spec YAl 09 – $Y_3Al_5O_{12}:Er^{3+}$ (1mol%)
Fluorescence lifetime (τ) at 1528.5nm

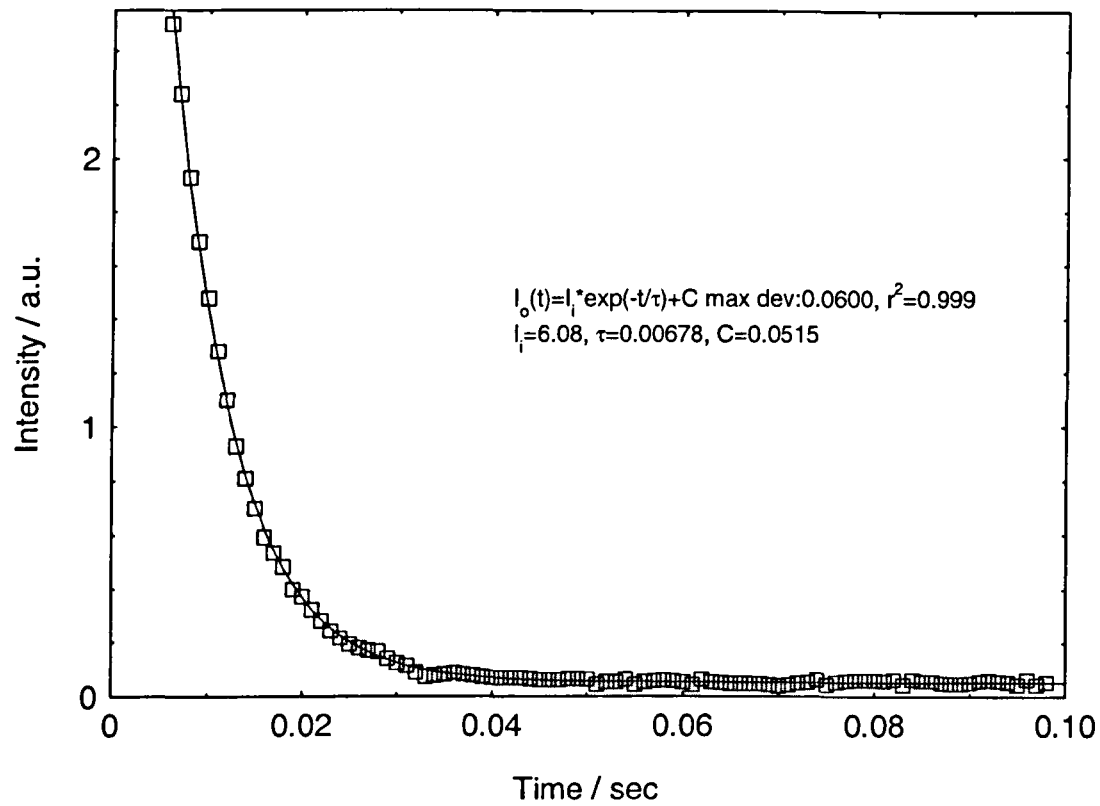

Figure 6.45: Spec YAl 09 – $Y_3Al_5O_{12}:Er^{3+}$ (1mol%)
Fluorescence lifetime (τ) at 1612nm

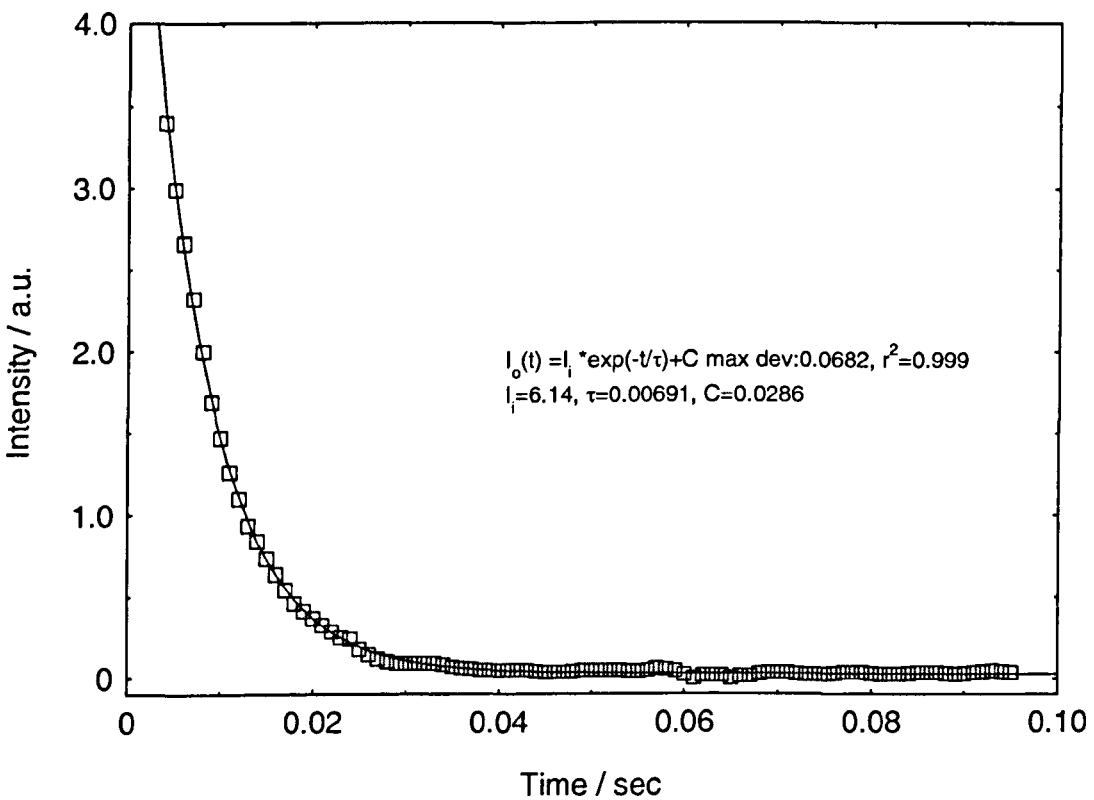

Figure 6.46: $Y_3Al_5O_{12}:Er^{3+}$ Fluorescence lifetime (τ) at 1528.5nm for different concentrations

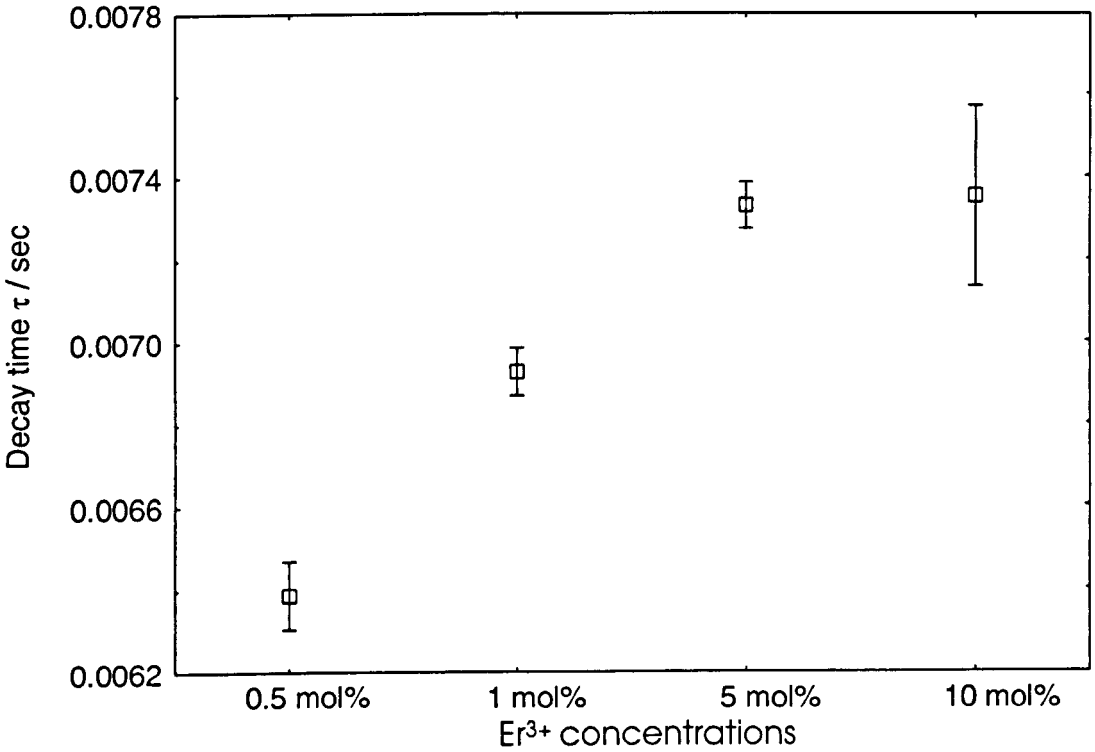

Figure 6.47: $Y_3Al_5O_{12}:Er^{3+}$ Fluorescence lifetime (τ) at 1612nm at different concentrations

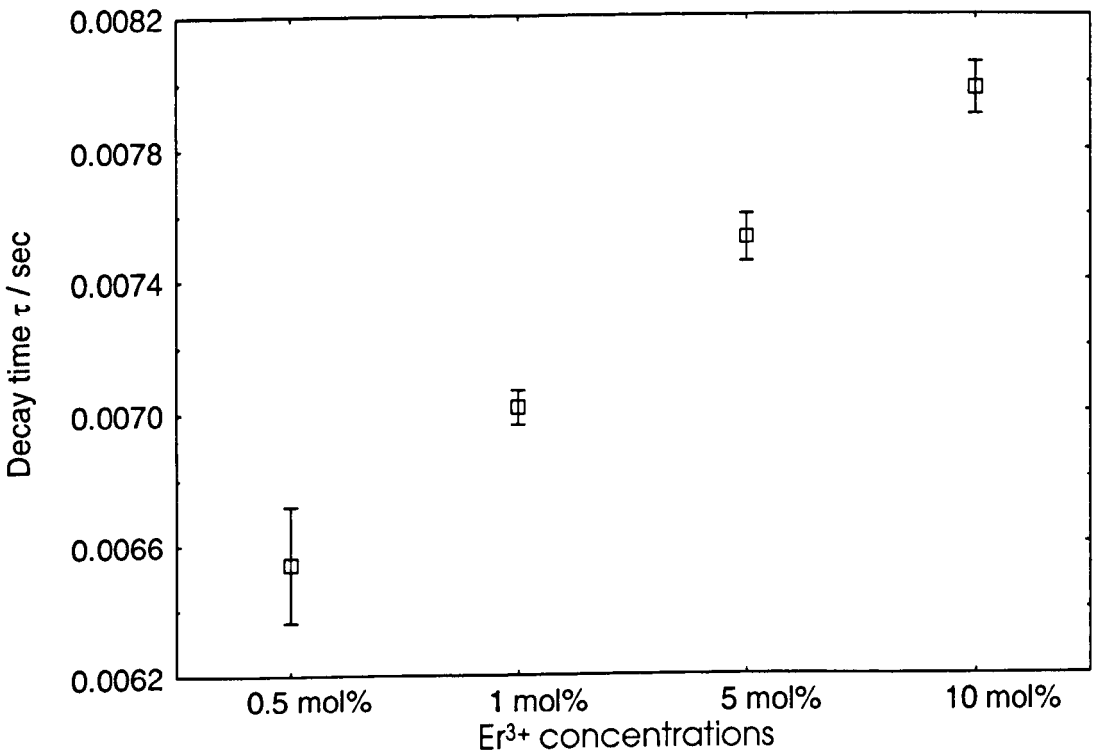

Figure 6.48: $Y_3Al_5O_{12}:Er^{3+}$ Fluorescence lifetime (τ) at $^4I_{13/2}$ at different concentrations

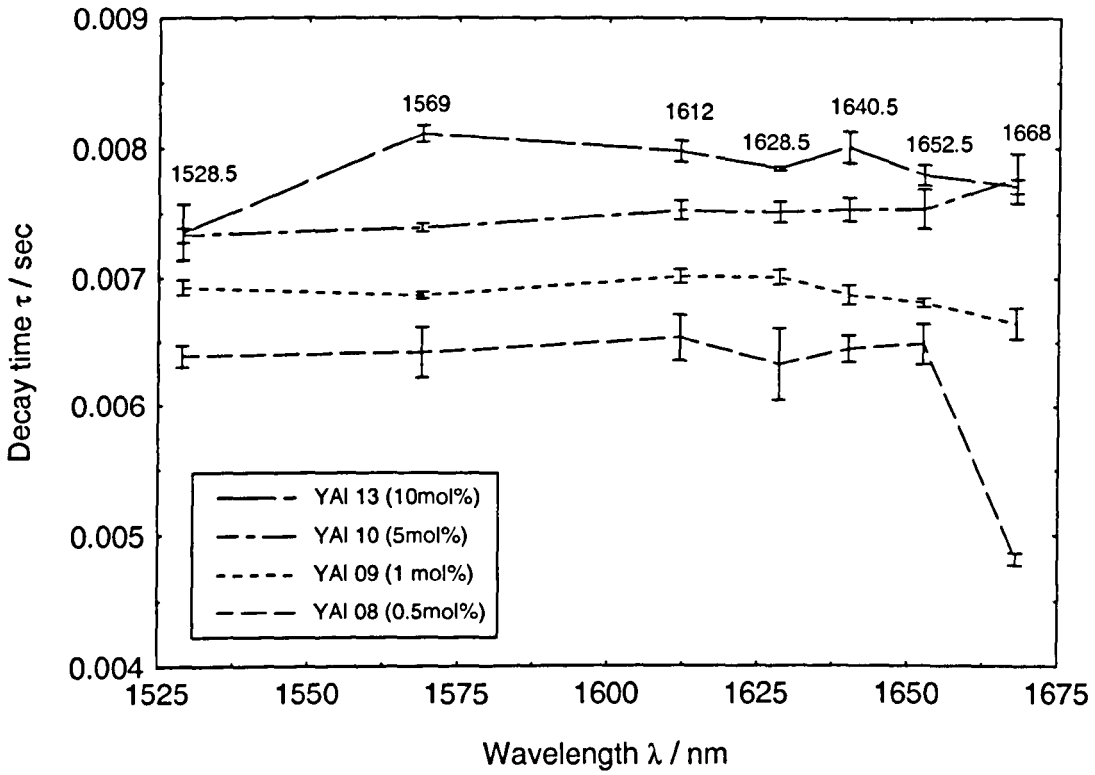

Table 6.3 – $Y_3Al_5O_{12}:Er^{3+}$ Fluorescence lifetime (τ) at $^4I_{13/2}$

Wavelength (nm)	0.5 mol% (τ) ms	1 mol% (τ) ms	5 mol% (τ) ms	10 mol% (τ) ms
1528.5	6.3	6.9	7.3	7.4
1569	6.4	6.9	7.4	8.1
1612	6.5	7.0	7.5	8.0
1628.5	6.3	7.0	7.5	7.9
1640	6.5	6.9	7.5	8.0
1652.5	6.5	6.8	7.5	7.8
1668	4.8	6.7	7.8	7.7

Figure 6.49: Spec YAl 20 – $Y_3Al_5O_{12}:Er^{3+}+Yb^{3+}$ (1+2mol%) Fluorescence lifetime (τ) at 1027nm

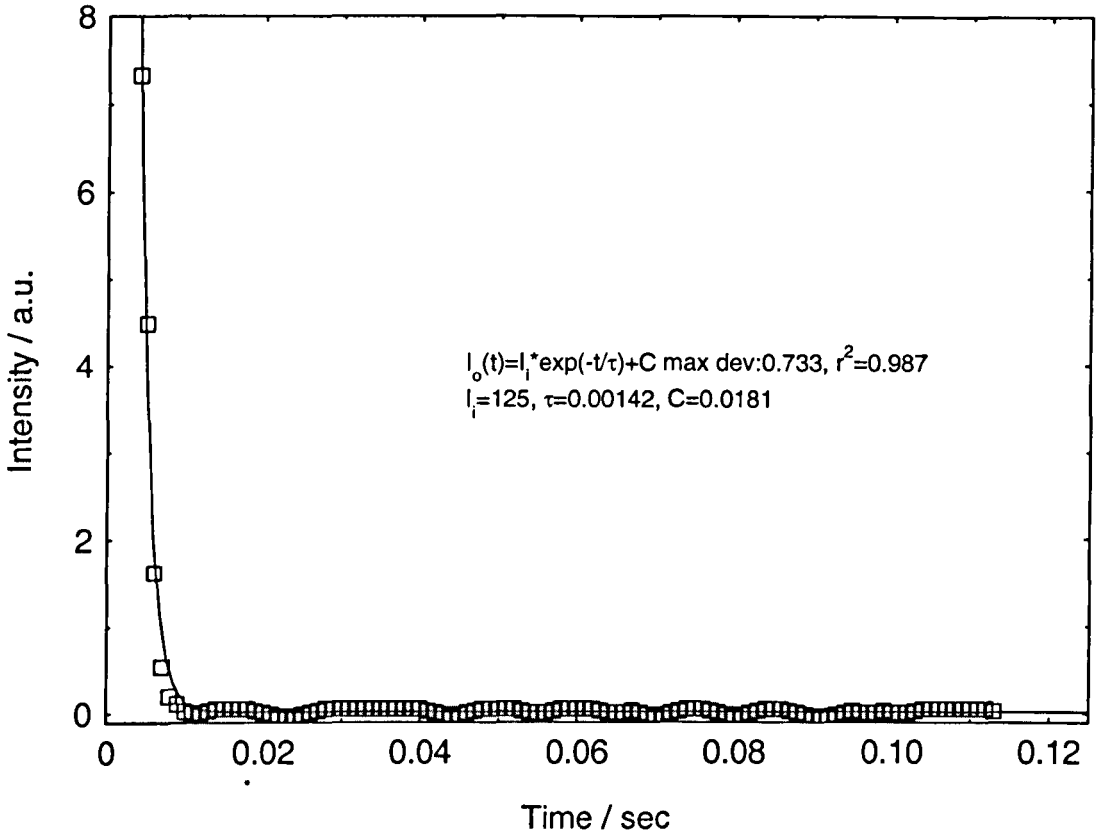

Figure 6.50: Spec YAl 20 – $Y_3Al_5O_{12}:Er^{3+}+Yb^{3+}$ (1+2mol%) Fluorescence lifetime (τ) at 1528.5nm

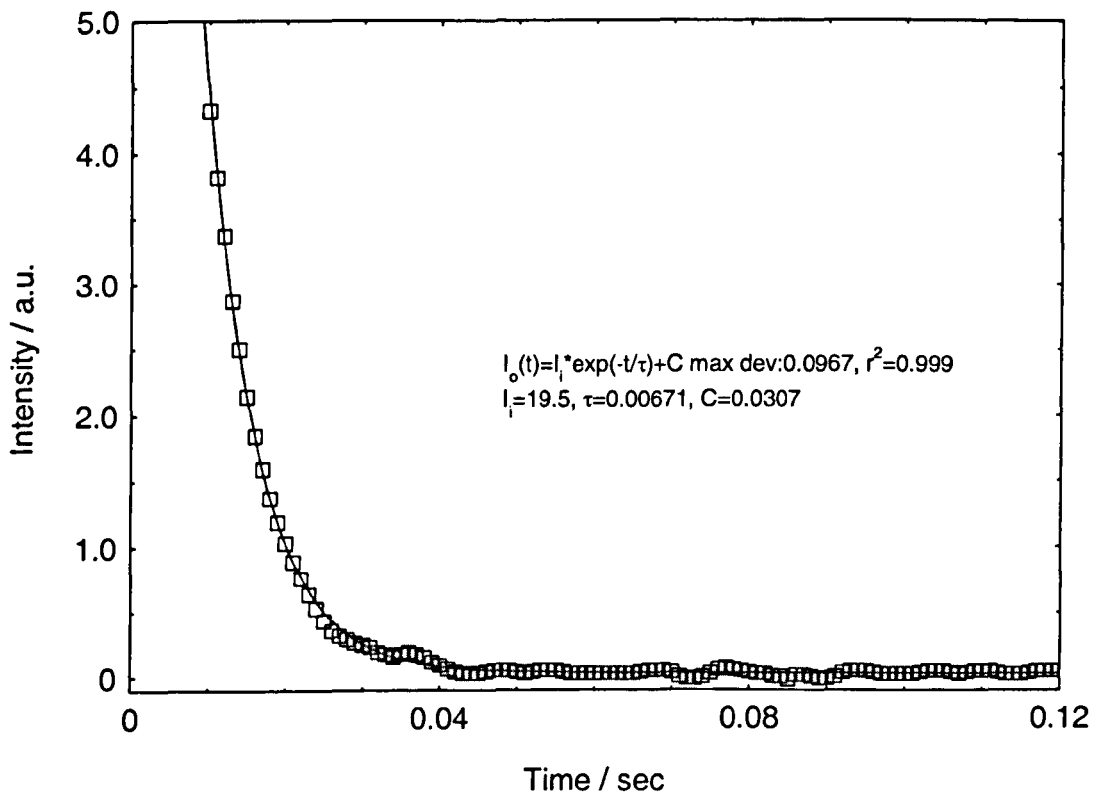

Figure 6.51: Spec YAl 20 – $Y_3Al_5O_{12}:Er^{3+}+Yb^{3+}$ (1+2mol%)
Fluorescence lifetime (τ) at 1612nm

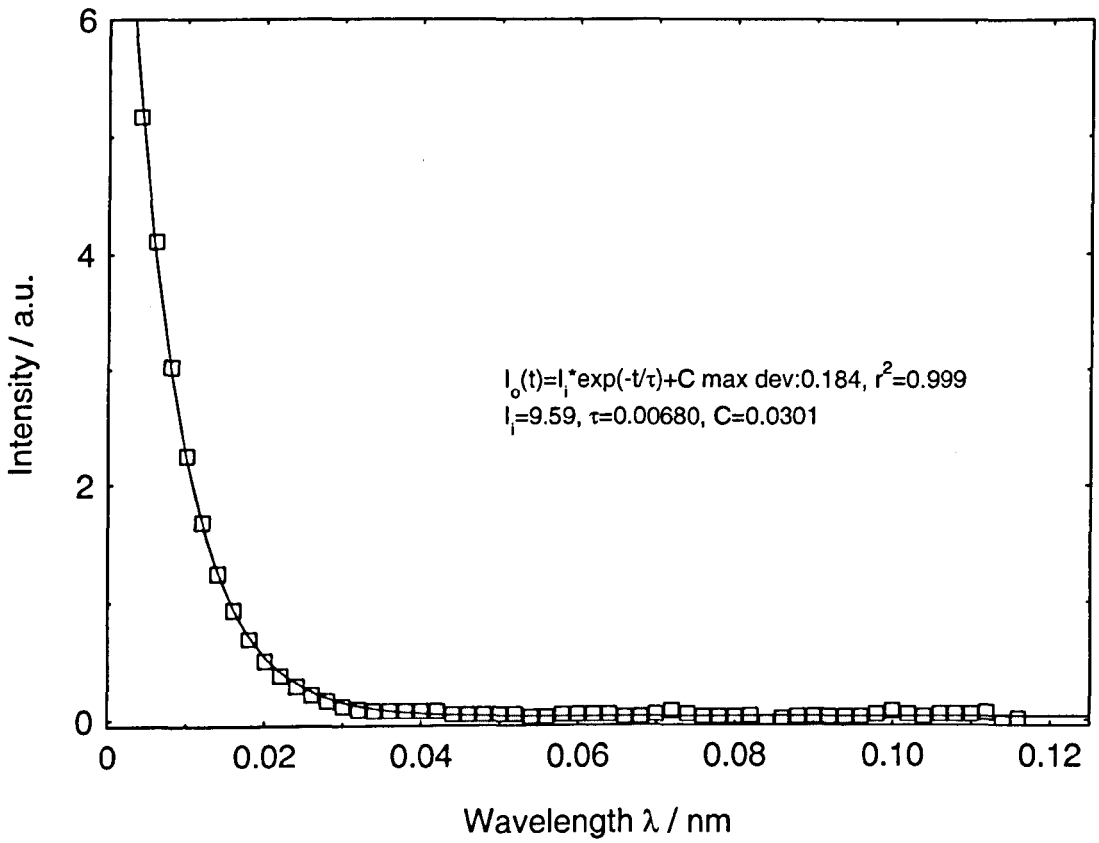

Figure 6.52: $Y_3Al_5O_{12}:Er^{3+}+Yb^{3+}$ Fluorescence lifetime (τ) at 1027nm for different concentrations

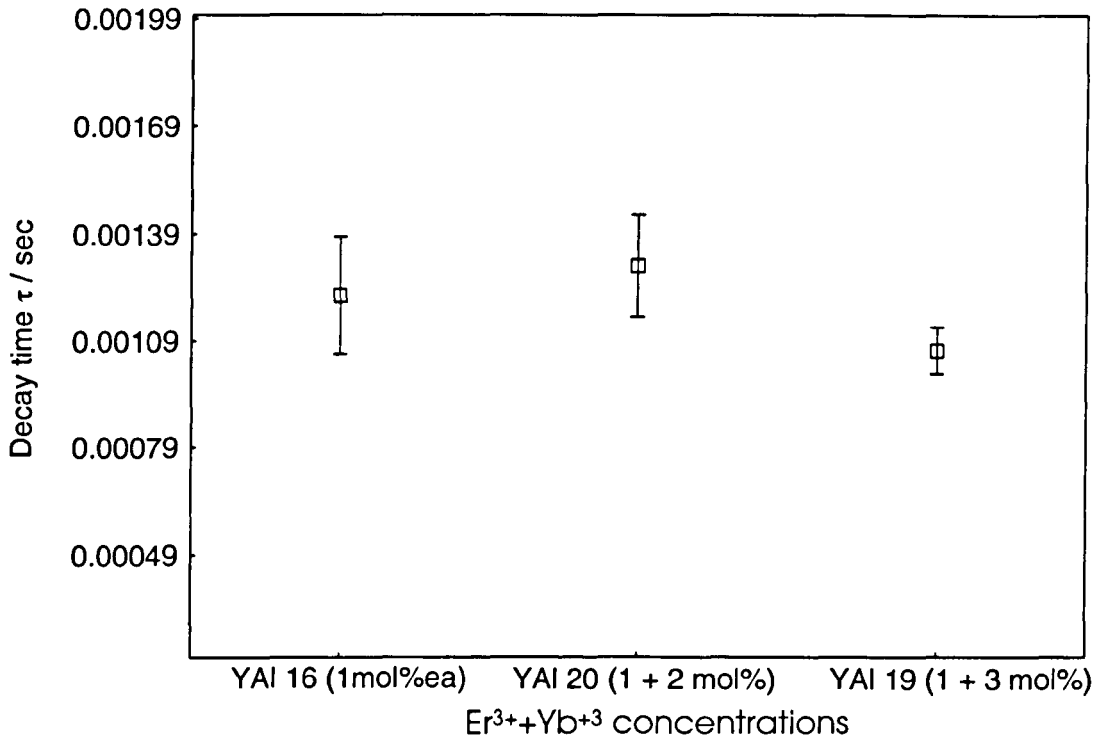

Figure 6.53: $Y_3Al_5O_{12}:Er^{3+}+Yb^{3+}$ Fluorescence lifetime (τ) at $^4I_{13/2}$ for different concentrations

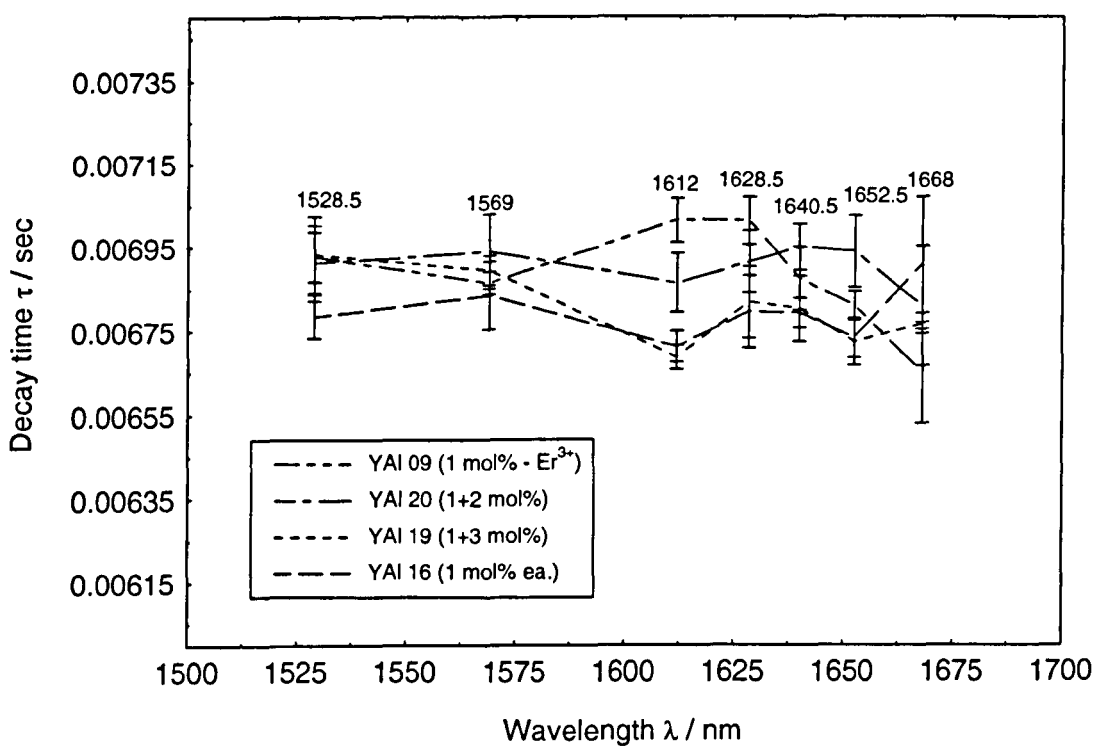

Table 6.4 – $Y_3Al_5O_{12}:Er^{3+}+Yb^{3+}$ Fluorescence lifetime (τ) at different peaks

Wavelength (nm)	1 mol% (ea) (τ) ms	1 + 2 mol% (τ) ms	1+ 3 mol% (τ) ms
1027	1.2	1.3	1.1
1528.5	6.8	6.9	6.9
1569	6.8	6.9	6.9
1612	6.7	6.8	6.7
1628.5	6.8	6.9	6.8
1640	6.8	7.0	6.8
1652.5	6.7	6.9	6.7
1668	6.9	6.8	6.8

Figure 6.54: Spec YAl 08 – $Y_3Al_5O_{12}:Er^{3+}$ (0.5mol%)
Fluorescence lifetime (τ) at 180mA

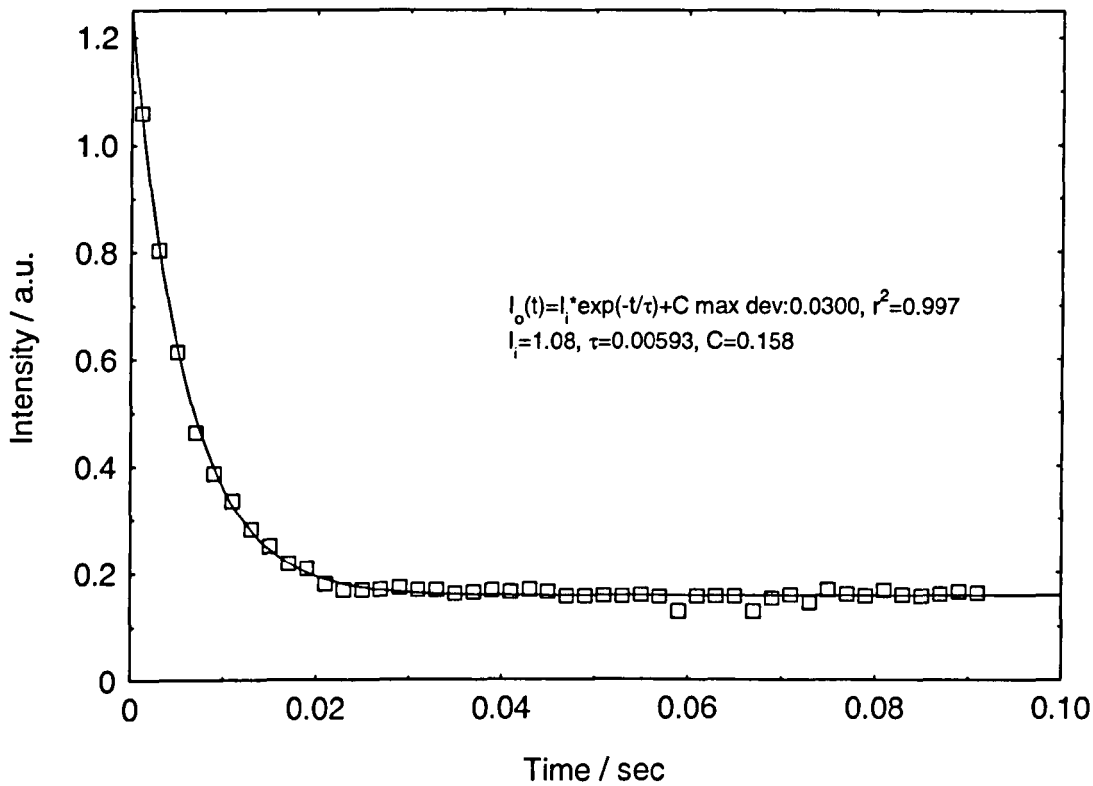

Figure 6.55: Spec YAl 09 – $Y_3Al_5O_{12}:Er^{3+}$ (1mol%)
Fluorescence lifetime (τ) at 180mA

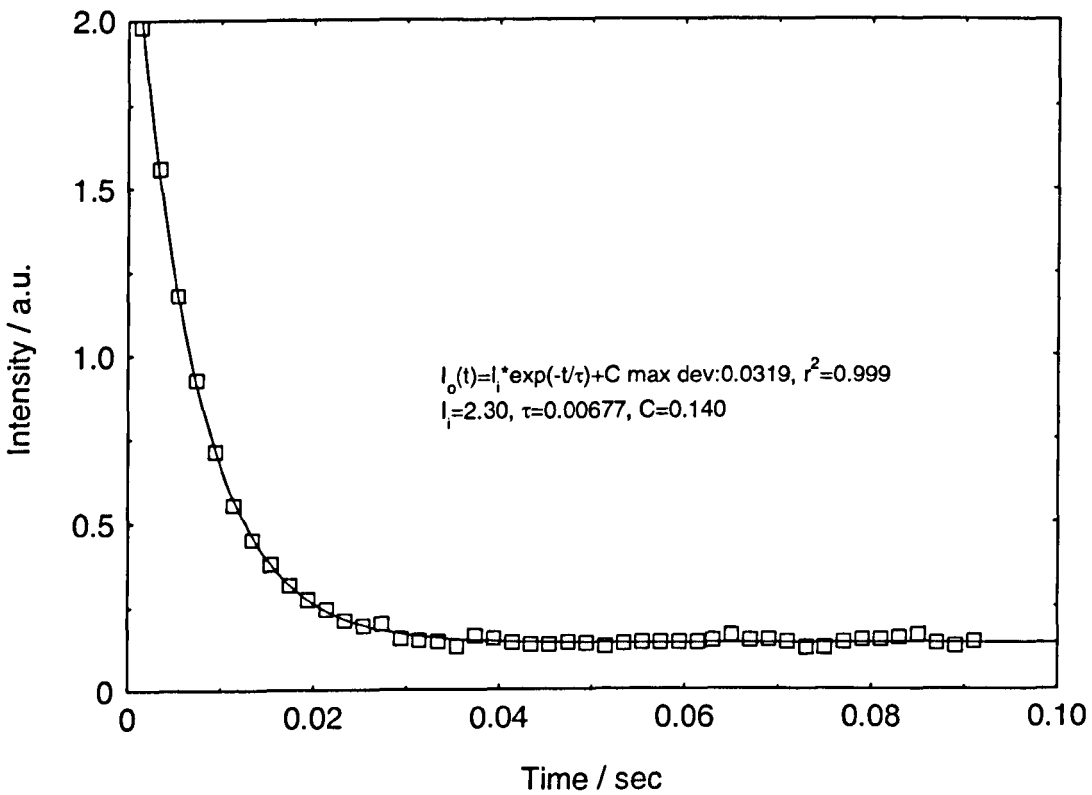

Figure 6.56: Spec YAl 10 – $Y_3Al_5O_{12}:Er^{3+}$ (5mol%)
Fluorescence lifetime (τ) at 180mA

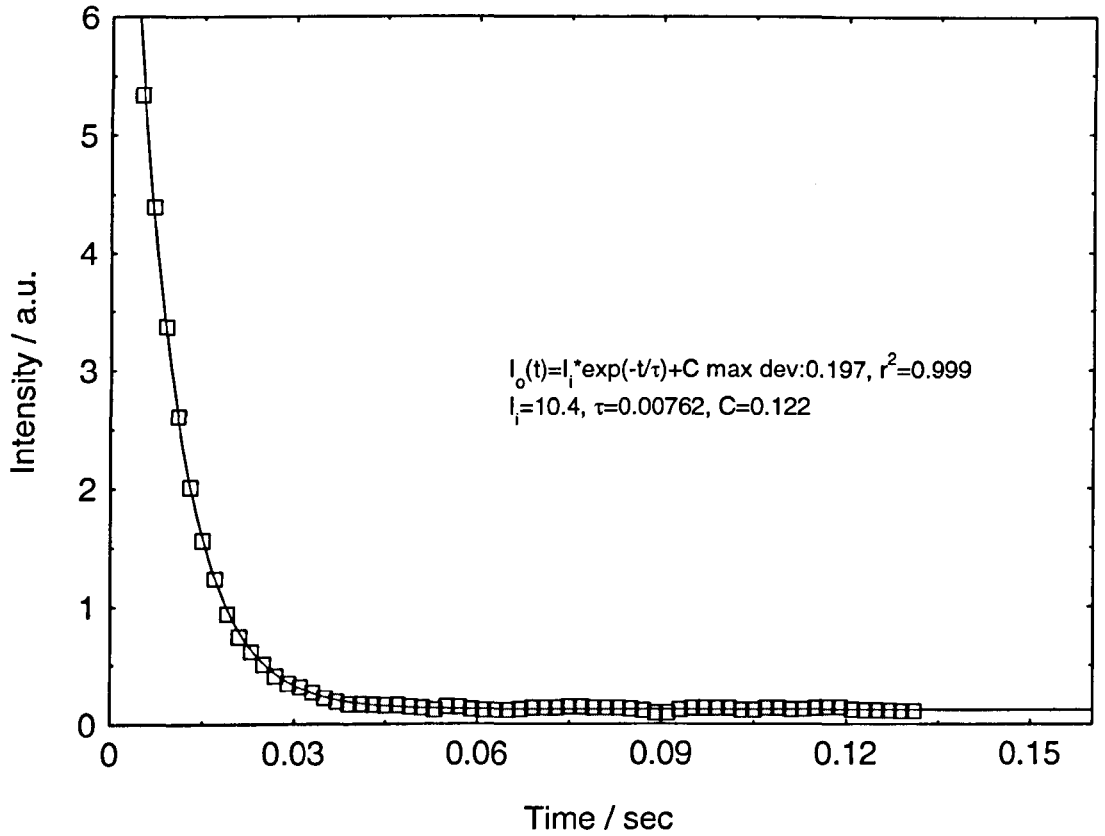

Figure 6.57: Spec YAl 13 – $Y_3Al_5O_{12}:Er^{3+}$ (10mol%)
Fluorescence lifetime (τ) at 180mA

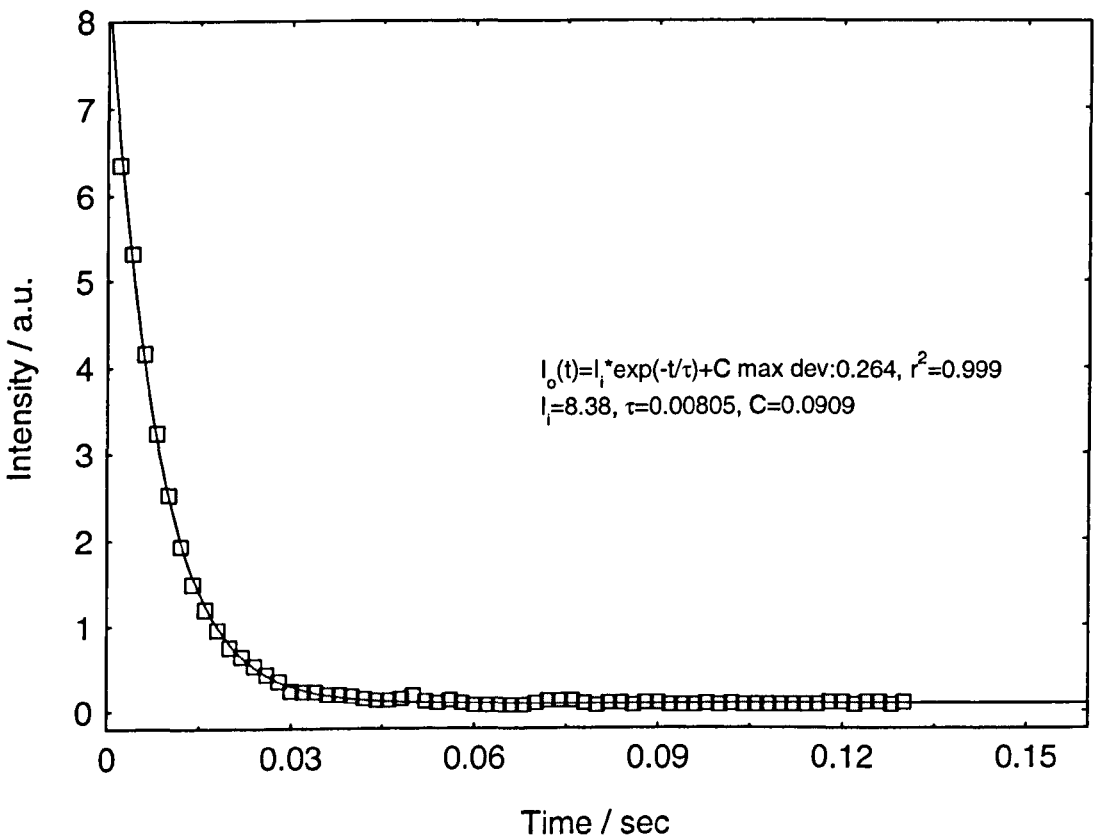

Figure 6.58: $Y_3Al_5O_{12}:Er^{3+}$ Fluorescence lifetime (τ) at 180mA at different concentrations

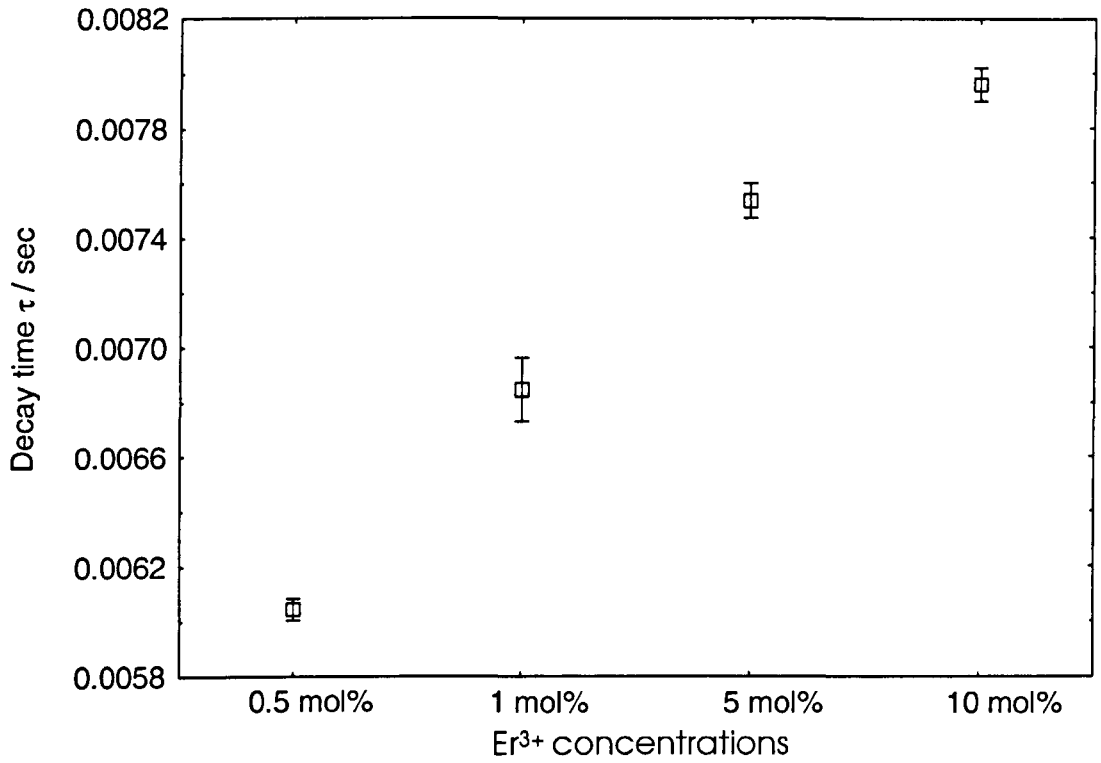

Figure 6.59: $Y_3Al_5O_{12}:Er^{3+}$ Fluorescence lifetime (τ) at different laser power settings

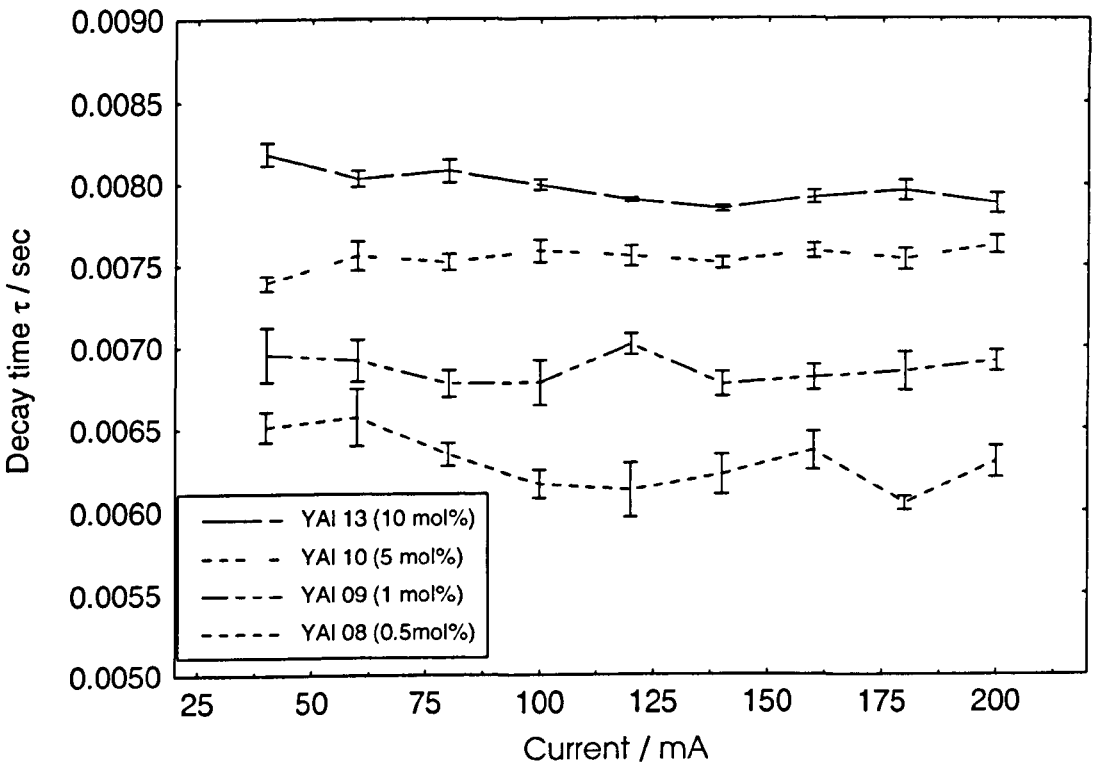

Table 6.5 – $Y_3Al_5O_{12}:Er^{3+}$ Fluorescence lifetime (τ) at different laser current setting

Laser Current (mA)	0.5 mol% (τ) ms	1 mol% (τ) ms	5 mol% (τ) ms	10 mol% (τ) ms
40	6.5	7.0	7.3	8.2
60	6.6	6.9	7.6	8.0
80	6.3	6.8	7.5	8.0
100	6.2	6.8	7.6	8.0
120	6.1	7.0	7.5	7.9
140	6.2	6.8	7.5	7.8
160	6.4	6.8	7.6	7.9
180	6.0	6.8	7.5	8.0
200	6.2	6.9	7.6	7.9

Figure 6.60: Spec YAl 16 – $Y_3Al_5O_{12}:Er^{3+}+Yb^{3+}$ (1mol%ea)
Fluorescence lifetime (τ) at 180mA

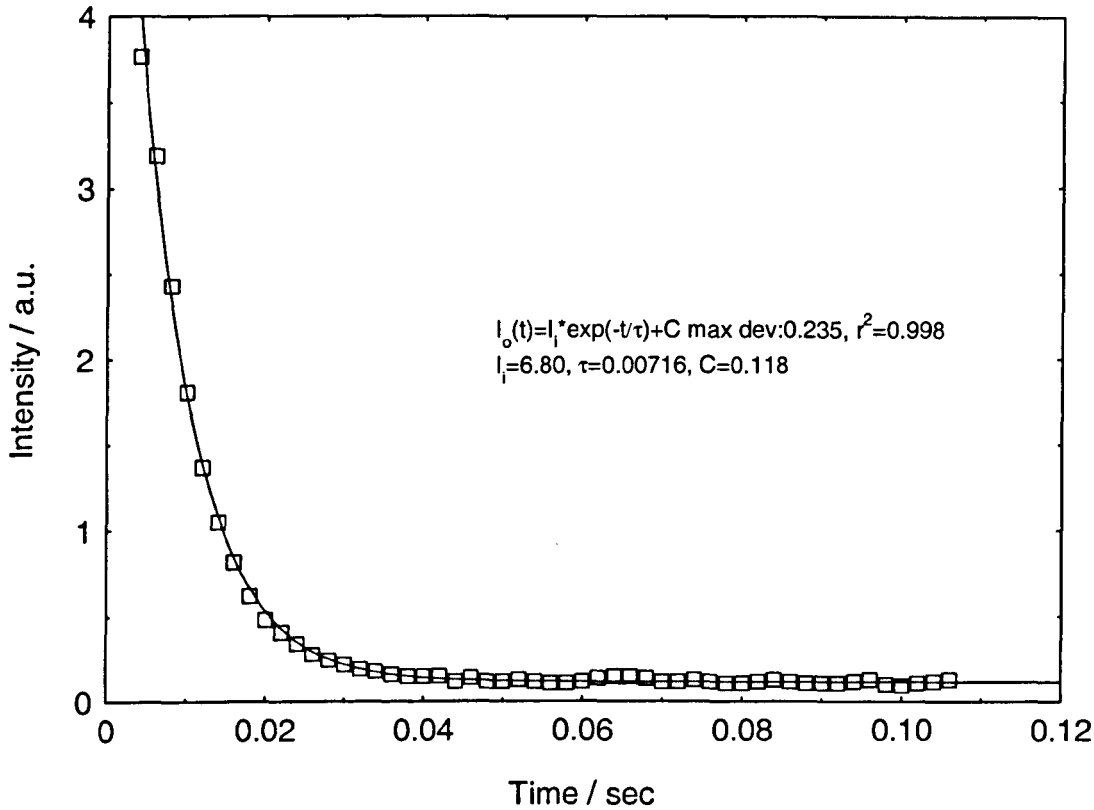

Figure 6.61: Spec YAl 20 – $Y_3Al_5O_{12}:Er^{3+}+Yb^{3+}$ (1+2mol%)
Fluorescence lifetime (τ) at 180mA

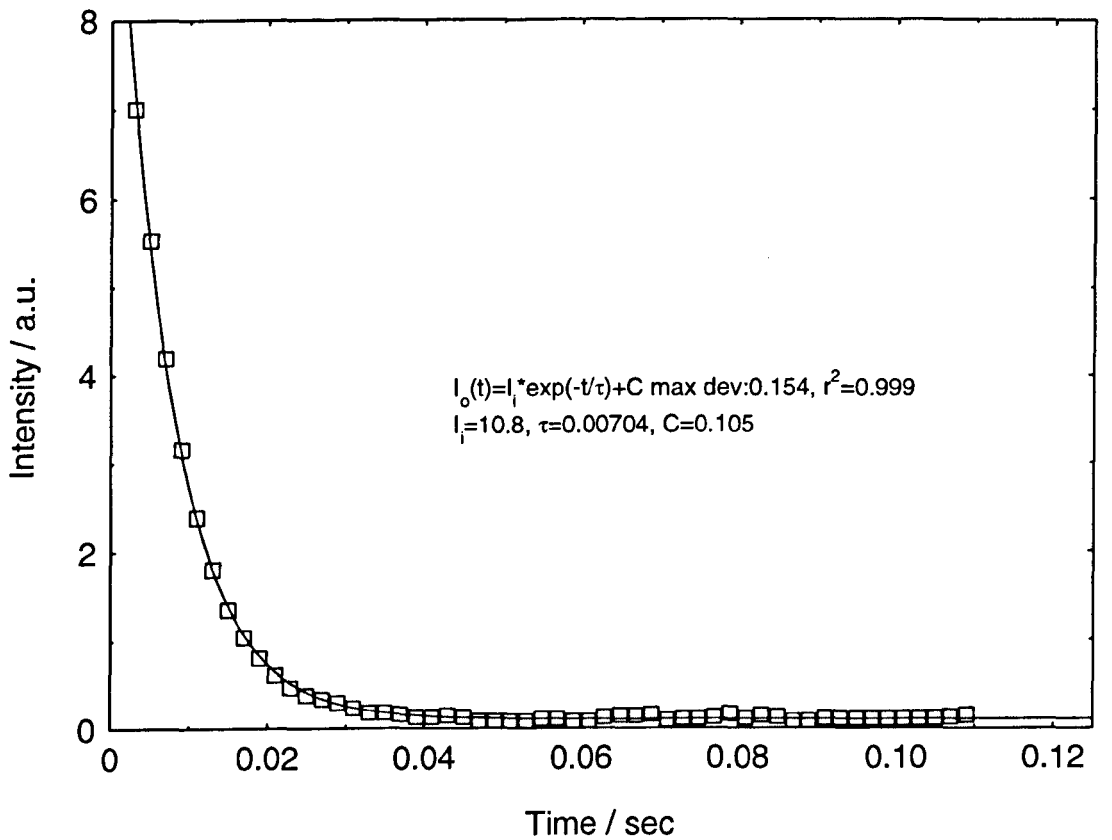

Figure 6.62: Spec YAl 19 – $Y_3Al_5O_{12}:Er^{3+}+Yb^{3+}$ (1+3mol%) Fluorescence lifetime (τ) at 180mA

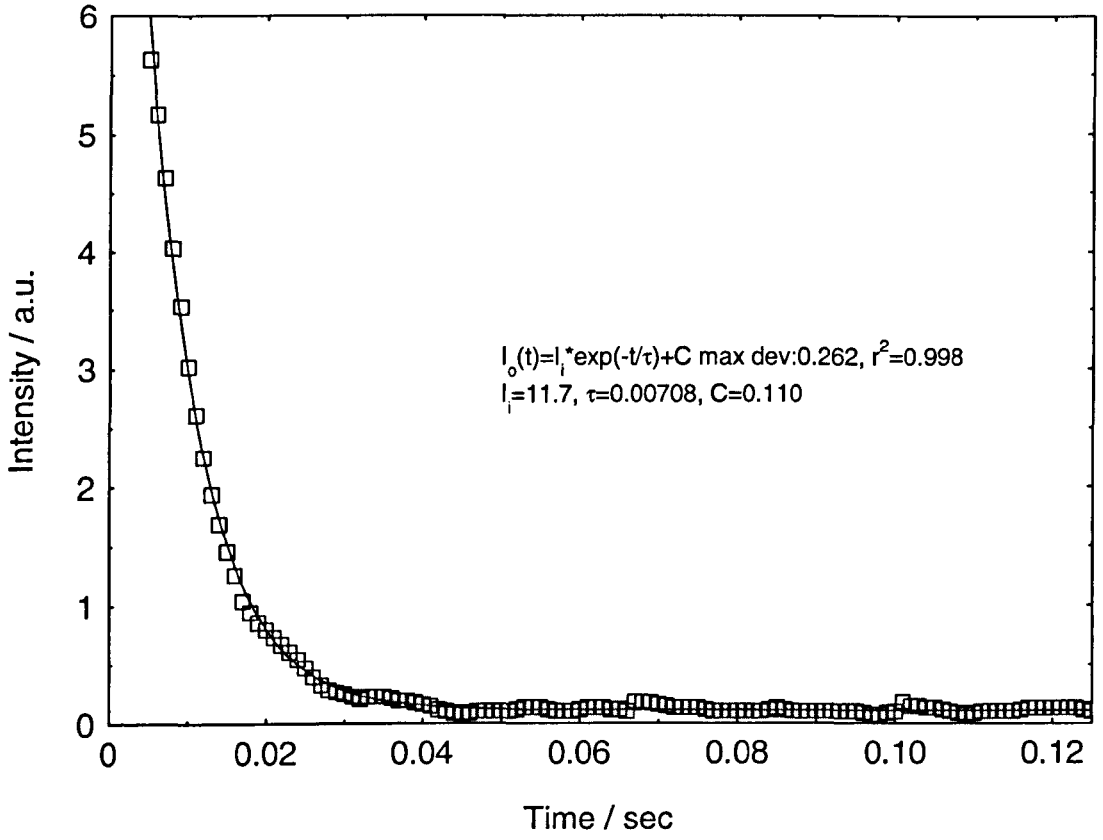

Figure 6.63: $Y_3Al_5O_{12}:Er^{3+}+Yb^{3+}$ Fluorescence lifetime (τ) at 180mA at different concentrations

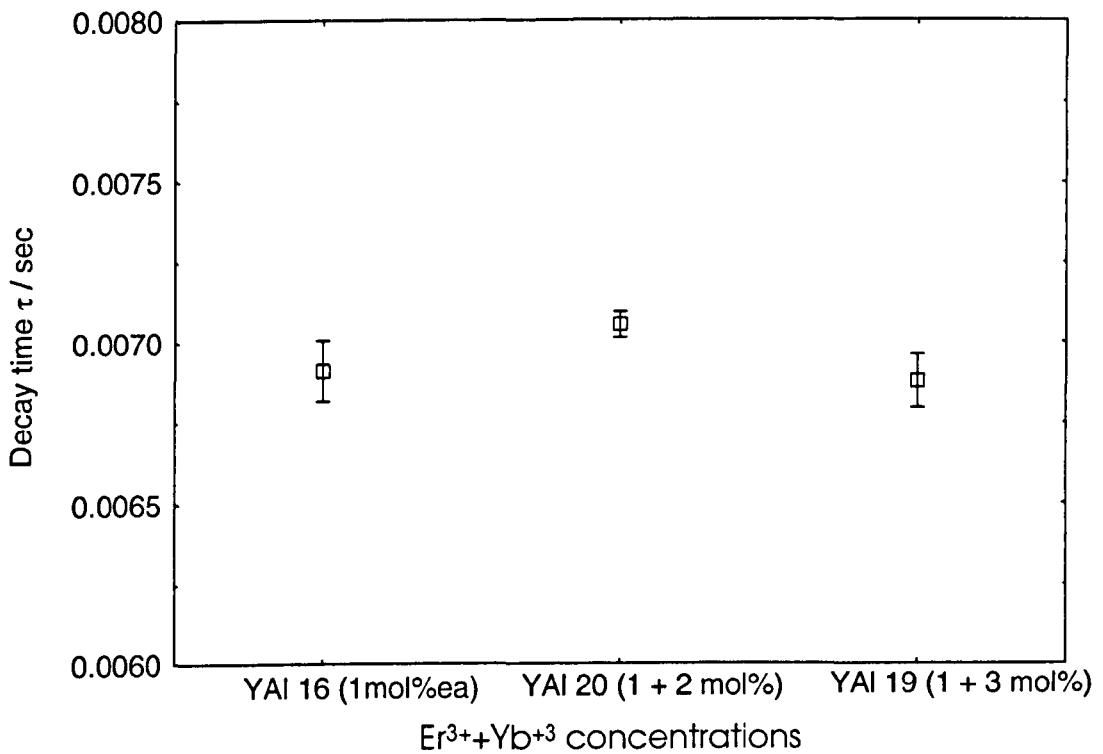

Figure 6.64: $Y_3Al_5O_{12}:Er^{3+}+Yb^{3+}$ Fluorescence lifetime (τ) at different laser current settings

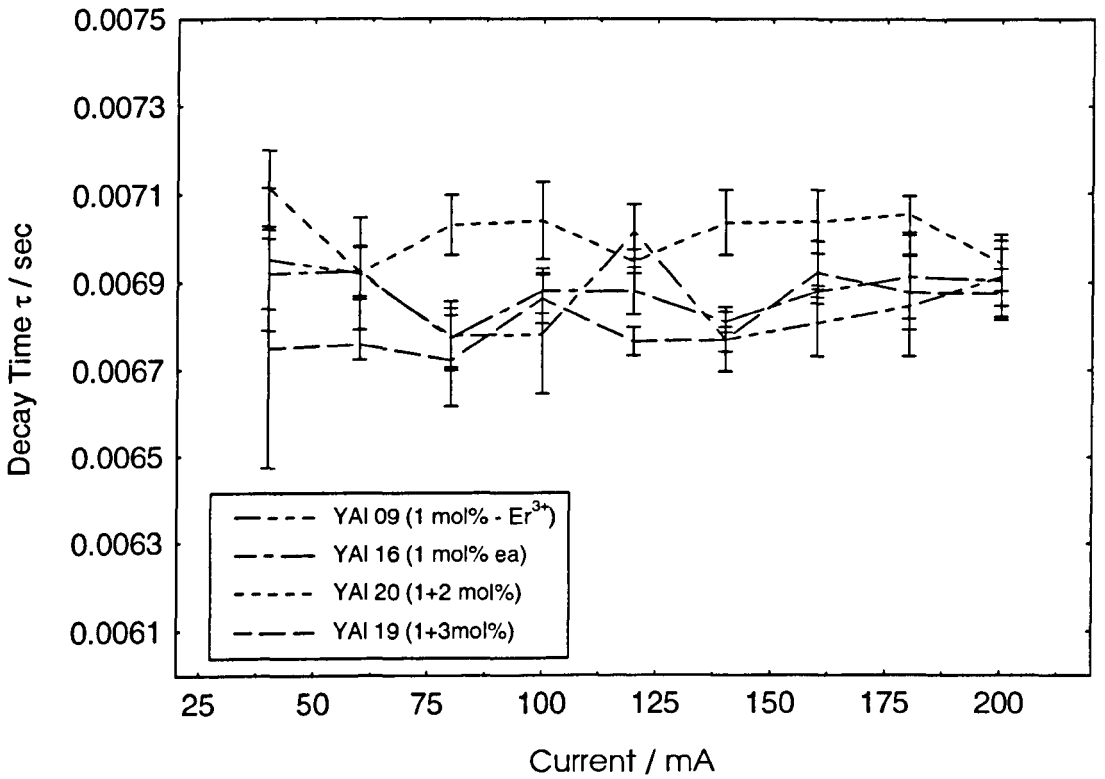

Table 6.6: $Y_3Al_5O_{12}:Er^{3+}+Yb^{3+}$ Fluorescence Lifetime (τ) at different laser current settings

Laser Current (mA)	1 mol% (ea) (τ) ms	1 + 2 mol% (τ) ms	1+ 3 mol% (τ) ms
40	6.9	7.1	6.7
60	6.9	6.9	6.8
80	6.8	7.0	6.7
100	6.9	6.9	6.9
120	6.9	7.0	6.8
140	6.8	7.0	6.8
160	6.9	7.0	6.9
180	6.9	7.1	6.9
200	6.9	6.9	6.9

6.8 Reference

[6.1] L. B. Shaw, R. S. F. Chang and N. Djeu, *Measurement of Up-Conversion Energy-Transfer Probabilities in Ho:$Y_3Al_5O_{12}$ and Tm: $Y_3Al_5O_{12}$*, Phy. Rev. B, **50**, 10, 6609, 1994

[6.2] V. I. Chani, A. Yoshikawa, Y. Kuwano, K. Inaba, K. Omote and T. Fukuda, *Preparation and Characterization of Yb: $Y_3Al_5O_{12}$ Fiber Crystals*, Mat. Res. Bull., **35**, 10, 1615, 2000

[6.3] Y. Yu, Z. Wu and S. Zhang, *Concentration Effects of Er^{3+} ion in YAG:Er Laser Crystals*, J. Alloys and Comp., **302**, 1-2, 204, 2000

[6.4] J. L. Kennedy, N. Djeu, *Operation of Yb:YAG Fiber-Optic Temperature Sensor Up to 1600°C*, Sen. and Act., **100**, 2-3, 187, 2002

[6.5] F. Cornacchia, M. Alshourbagy, A. Toncelli, M. Tonelli, H. Ogino, A. Yoshikawa and T. Fukuda, *Growth and Spectroscopic Properties of Er:YAG Crystalline Fibres*, J. Cryst. Growth, **275**, 3-4, 534, 2004

[6.6] S. Hinojosa, O. Bardosa-García, M. A. Meneses-Nava, J. L. Maldonado E. de la Rosa-Cruz and G. Ramos-Ortiz, *Luminescent Properties and Energy Transfer Processes of Co-Doped Yb-Er Poly-Crystalline YAG Matrix*, Opt. Mat., **27**, 12, 1839, 2005

[6.7] R. Balda, J. Fernández, M. A. Arriandiaga and J. M. Fdez-Navarro, *Infrared to Visible Upconversion of Er^{3+} and Er^{3+}/Yb^{3+} Codoped Lead-Niobium-Germanate Glasses*, Opt. Mat., 25, **2**, 157, 2004

[6.8] J. Koetke, G. Huber, *Infrared Excited-State Absorption and Stimulated-Emission Cross Sections of Er^{3+}-Doped Crystal*, App. Phy. B, **61**, 2, 151, 1995

[6.9] S. A. Payne, L. L. Chase, L. K. Smith, W. L. Kway and W. F. Krupke, *Infrared Cross-Section Measurements for Crystals Doped with Er^{3+}, Tm^{3+} and Ho^{3+}*, IEEE J. Quant. Elect., **28**, 11, 2619, 1992

[6.10] M. Nishi, S. Tanabe, M. Inoue, M. Takahashi, K. Fujita and K. Hirao, *Optical-Telecommunication-Band Fluorescence Properties of Er^{3+}-*

Doped YAG Nanocrystals Synthesized by Glycothermal Method, Opt. Mat., **27**, 4, 655, 2005

[6.11] J. A. Capobianco, F. Vetrone, J. C. Boyer, A. Speghini and M. Bettinelli, *Enhancement of Red Emission ($^4F_{9/2} \rightarrow {}^4I_{15/2}$) via Upconversion in Bulk and Nanocrystalline Cubic $Y_2O_3:Er^{3+}$*, J. Phy. Chem. B, **106**, 6, 1181, 2002

[6.12] D. Matsuura, H. Hattori and A. Takano, *Upconversion Luminescence Properties of Y_2O_3 Nanocrystals Doped with Trivalent Rare-Earth Ions*, J. Elect-chem, Soc., **152**, 3, H39, 2005

[6.13] W. Q. Shi, M. Bass, and M. Birnbaum, *Effects of Energy Transfer Among Er^{3+} Ions on the Fluorescence Decay and Lasing Properties of Heavily Doped Er:$Y_3Al_5O_{12}$*, J. Opt. Soc. Am. B, **7**, 8, 1456, 1990

[6.14] S. A. Pollack, D. B. Chang, M. Birnbaum and M. Kokta, *Upconversion-Pumped 2.8-2.9μm Lasing of Er^{3+} ion in Garnets*, J. App. Phy., **70**, 12, 7227, 1991

7 Y_2O_3 – Single Crystal Fibre

7.1 Introduction

Yttrium oxide, Y_2O_3, makes a very attractive laser medium due its very high thermal conductivity, κ. It is has a κ = 27 W/mK whereas YAG has a κ = 13 W/mK [5.8]. Y_2O_3 has a very close ionic radius with rare earth ions (for example Y^{3+} = 0.892 Å and Er^{3+} = 0.881 Å) with two sites, C_2 and C_{3i} of a body centred cubic structure. Therefore rare earth ions can easily be doped in Y_2O_3, even large amounts can be incorporated without distorting the lattice [7.1]. In the 1970s, *Haggerty* [2.7] was the first to grow Y_2O_3 SCF's, the method used was the floating zone technique. *Stone* and *Burrus* [2.13] were the first to grow Y_2O_3 SCF using the LHPG method and these doped fibres were employed as fibre lasers. The fibres grown were of good optical quantity but under storage cracks appeared due to moisture in the environment. Previously, growing Y_2O_3 fibres had not been easy because of its high melting temperature, 2450°C. Moreover, the fibres had very poor mechanical properties. Extra care was required when handling these fibres because they were brittle and were easily broken. *Goutaudier* [7.2] had demonstrated the possibility of growing high quality pure Y_2O_3 fibres using LHPG technique and had introduced a post growth thermal treatment. This increased the homogeneity of the thermal gradient between the molten zone and the crystallization interface. Y_2O_3-ZrO_2 SCF [2.56] grown by the LHPG method have been employed an ultra-high temperature sensors. The combination of the two materials greatly increases the melting point to 2700°C. However, these fibre sensors do not have ideal optical and mechanical properties. Y_2O_3 is also commonly investigated in the area of optical waveguides due to the long fluorescence lifetime of Er^{3+} at 1.53μm, it's broad transparency range from 200nm to 8μm, high refractive index and low phonon energy [7.3]. In this work, Er^{3+} ions of different concentration levels were doped in Y_2O_3 powder and then grown by LHPG into fibres. Since it can be easily doped with rare earths, high Er^{3+} concentrations of 59mol% were doped into crystal. The two aspects of characterisations that were carried out on the fibres were physical and optical. Physical characterisation comprised diameter and strength measurements while optical characterisation comprised absorption, fluorescence, upconversion and

lifetime measurements. Results and discussion for these experiments are presented in this chapter.

7.2 Diameter Measurement

Experimental set-ups were discussed in Chapter 5.2.1. Specimens 47, 48 and 49 were grown specifically for diameter measurements. Subsequently, they were also used for mechanical testing measurements. The three fibres were grown under similar conditions, as with the YAG fibres discussed in the previous chapter. The Y_2O_3 fibres were grown from cold pressed source rod.

7.2.1 Results and Discussion

Data collected from the Filar Eyepiece Technique indicated that the average diameter of the Y_2O_3 fibres fell in the range of 390 to 430μm. The diameter of the each fibre was measured three times and the measurements were made with an interval of 0.5mm along the length. The diameter variation error was not more than 3μm. The source rod for Y_2O_3 were the easiest to handle as compared with YAG and Al_2O_3, but in order to fabricate it with the dimensions for it to be held in the miniature pin chuck, the source rod had to be roughed down and this process was done manually. This resulted in some inconsistency of diameters from fibre to fibre. The average diameters and standard deviations are presented in Table 7.1. Similar to the YAG fibres in the previous chapter, it was observed that the deviation from the mean for all fibres was large. Figures 7.1 to 3 show variations of diameter along the length of the three fibres. These fluctuations arise due to the instability of the molten zone during the growth process. The laser power required to grow Y_2O_3 was ~22W, see Figure 4.5. The output power was prone to fluctuating and this could be the likely reason for the instability in the melt. The fibres were not circular but were hexagonal, and this could contribute to some measurement errors. As mentioned before, the scope of the work for this section does not require optical quality fibres or fibres with high circularity. The diameter measurement gives a general indication of the physical property of the grown fibre.

Table 7.1 – Y_2O_3 fibre diameter measurements

Specimen Name	Average Diameter (μm)	Standard Deviation (μm)
Spec 47	394.24	19.31
Spec 48	430.16	13.53
Spec 49	392.52	20.86

Figure 7.1 : Spec 47 – Y_2O_3 fibre diameter measurement

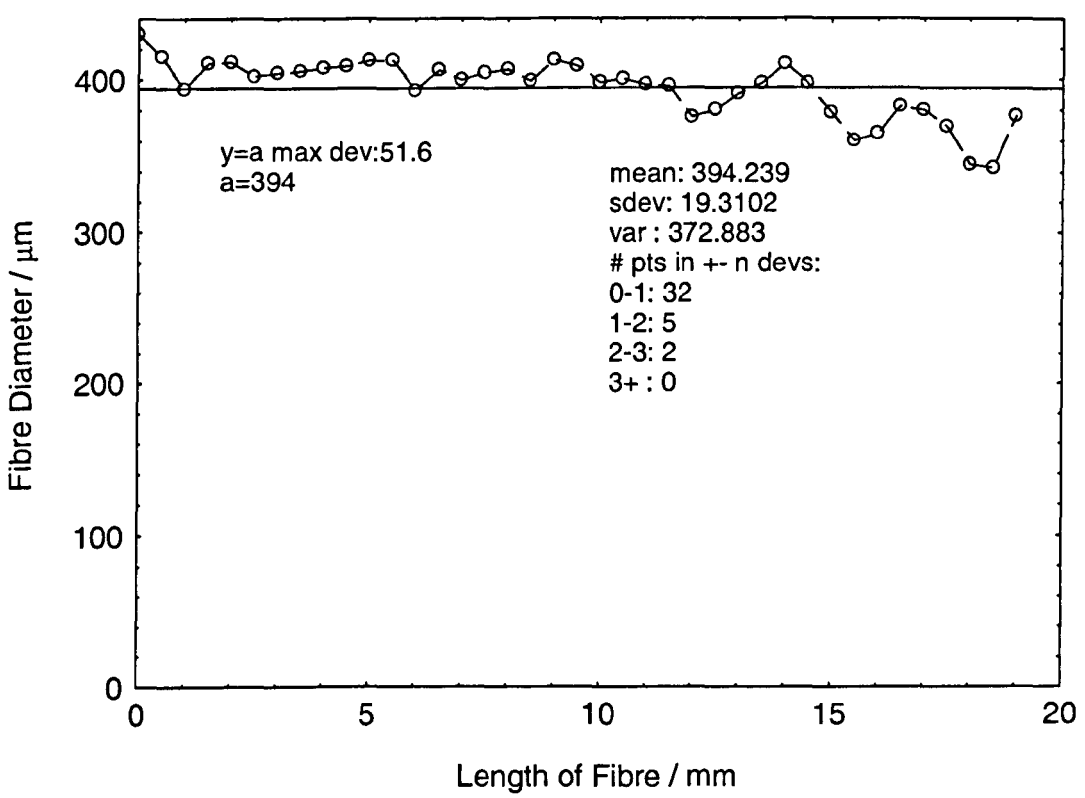

Figure 7.2 : Spec 48 – Y_2O_3 fibre diameter measurement

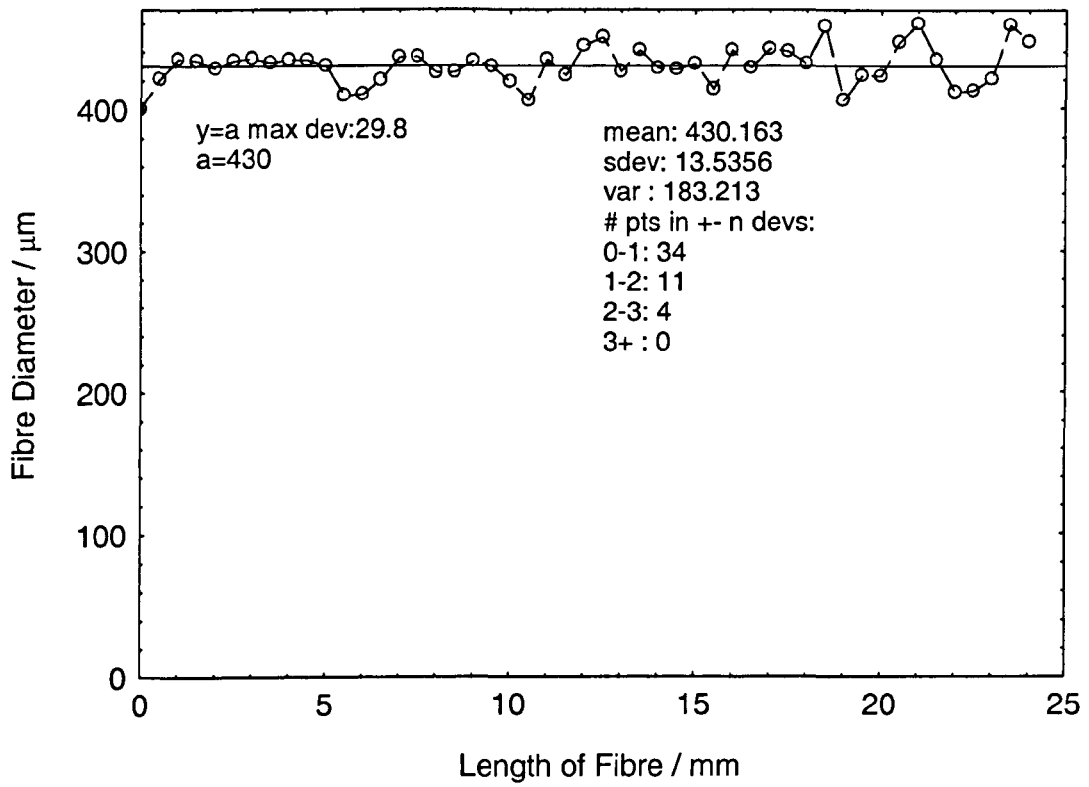

Figure 7.3 : Spec 49 – Y_2O_3 fibre diameter measurement

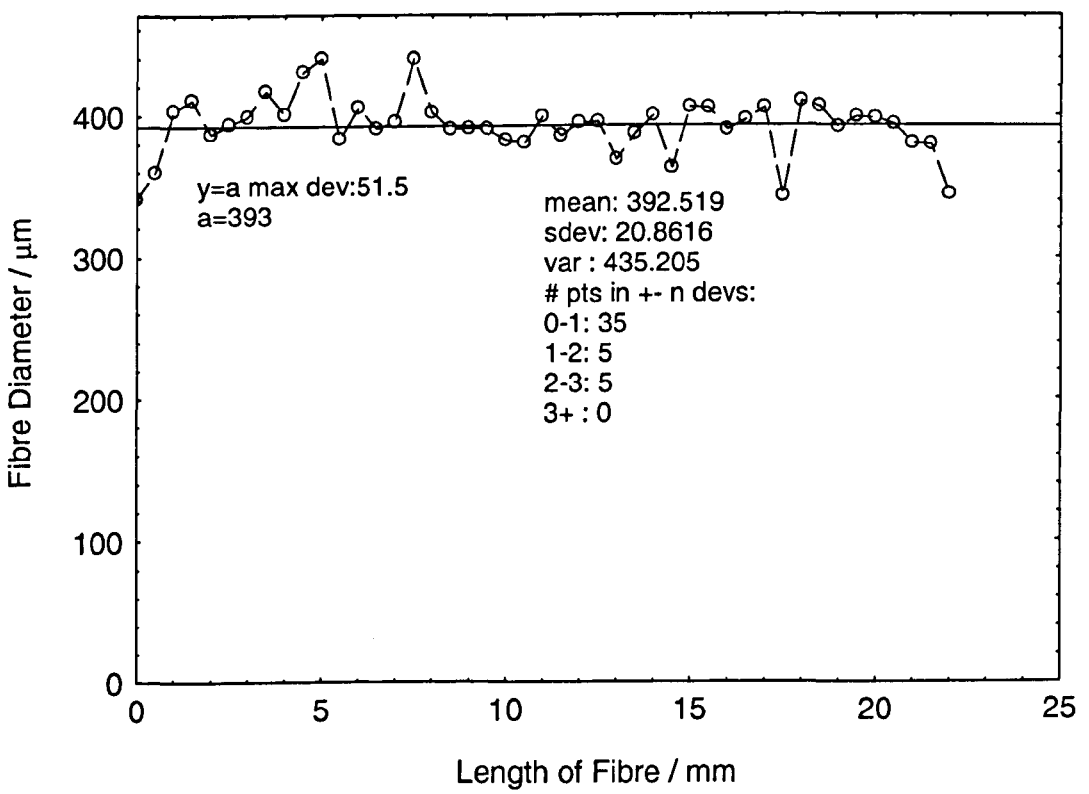

7.3 Mechanical Testing Measurement

Among the three oxide materials in this work, Y_2O_3 is the weakest in its mechanical strength. Fibres grown in this work were grown under the same condition and the experiments were conducted at room temperature. To reduce the number of inner micro-cracks, fibres were grown in short lengths [2.56].

7.3.1 Results and Discussion

The three-point bending test was carried out on the three fibres and Table 7.2 shows the result of the experiments. Refer to Chapter 5.2.2 for experiment layout. The forces, *F*, recorded show that as the fibre diameter increased, the forces for deformation increased with it. The overall length of *Spec 47* was too short for testing. Therefore, the length, *l*, between the two supporting legs was reduced to 18mm from 19mm. The forces measured from the experiments were then substituted into equation 5.2 and the bending/shear strength, *S*, calculated. Table 7.2 shows that, in this case, *S* was the highest when the diameter was the smallest. There was no significant difference in *S* between *Spec 47* and *Spec 48* even though the diameter difference was large. The calculated mean, S_m, among the three fibres is 0.66MPa and has a standard deviation of 0.08MPa. Figure 7.4 shows the force (N) and deformation (mm) for *Spec 47*. The forces required to strain the Y_2O_3 fibres to failure were the lowest of the three oxides examined. From [2.7] and [2.13], Y_2O_3 was reported as brittle and cracks were also observed over a period of time due to moisture in the air. Micro-cracks in the fibres, see Figure 4.27, were observed in this work too and the fibres produced were extremely brittle. It can be observed that the maximum deformation was 0.69mm, followed by breakage of the fibre. The results collected show that diameter was an indirect factor that would affect the *S* value. In order for a more in-depth study, a larger sample size and more fibres would be required so that the accuracy of *S* could be improved. The purpose of this experiment was to give a quick and simple analysis of the strength of the fibre produced by the LHPG method.

Table 7.2 – Y_2O_3 fibre mechanical testing measurement

Specimen Name	Diameter (μm)	Force, F (N)	$M = \pi d^3/32$ ($\times 10^{-12}$)	Shear/Bending Strength, S (MPa)
Spec 47	394.24	0.94	6.02	0.70
Spec 48	430.16	1.17	7.82	0.71
Spec 49	392.52	0.71	5.94	0.57

Figure 7.4 : Three-point bending test on *Spec 47*

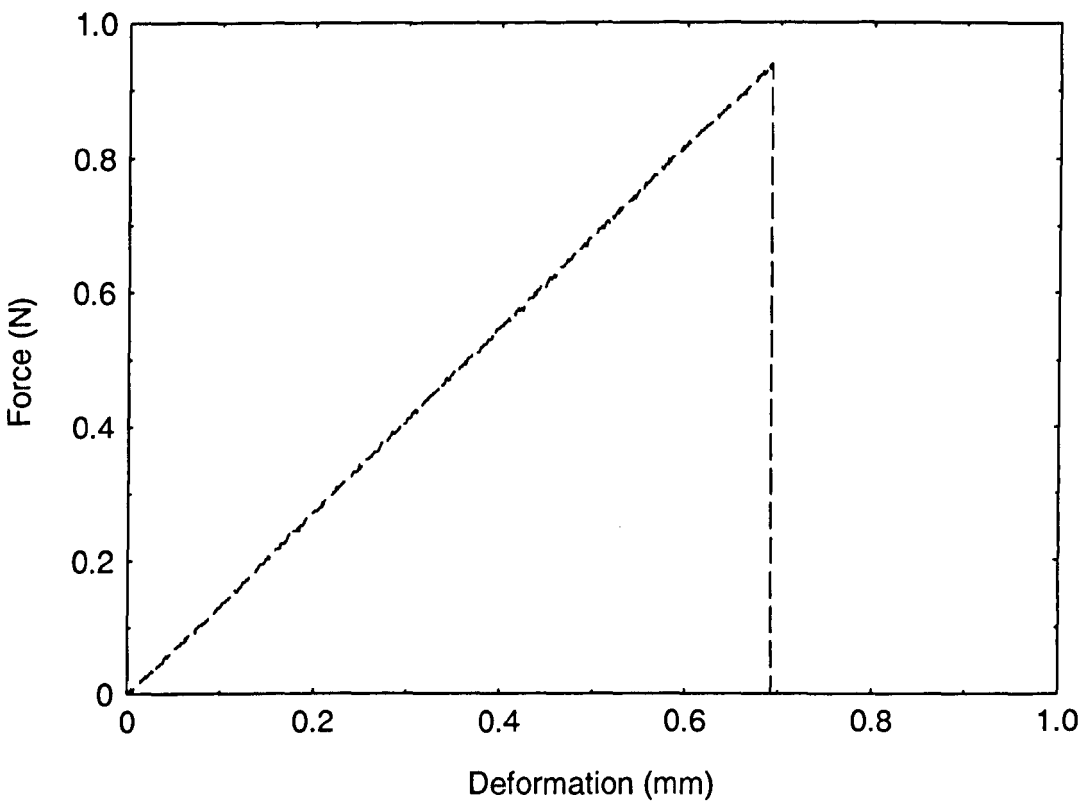

7.4 Absorption Spectrum Measurement

Investigations were carried out on Y_2O_3 fibres singly doped with Er^{3+} ions to identify their absorption spectrum from 400 to 1700nm for six different dopant concentrations. The fibres were doped with Er^{3+} content of 0.03, 0.06, 0.3, 3.1, 6 and 59mol%. All SCF fibres were prepared by cold pressing and grown by the LHPG method. Discussions on the experimental set-up and equipment were made in Chapter 5.3.1. This section presents the results of the absorption spectra of the Y_2O_3 fibres.

7.4.1 Results and Discussion

The results presented are in the range of 400 to 1200nm, and 1400 to 1800nm. Two photodiodes were required for the absorption spectrum experiments: one for the visible region to low infrared while the other was employed for the absorption bands in the higher infrared range. Sharp and narrow linewidths were only prominent at low Er^{3+} concentrations (0.03, 0.06 and 0.3mol%) and at higher concentrations (3.1, 6 and 59mol%) these linewidths broadened to form wider bands. Figures 7.5 to 16 show the absorption spectrum of the Y_2O_3 fibres investigated. Absorption peaks were observed in the $^2H_{11/2}$, $^4F_{9/2}$, $^4I_{9/2}$, $^4I_{11/2}$ and $^4I_{13/2}$ manifolds. No absorption was observed for the manifold $^4F_{7/2}$. In the $^2H_{11/2}$ manifold, several narrow peaks at 519nm, 521nm and 525nm were seen at low concentrations. See Figure 7.5. At a low dopant level, the $^2H_{11/2}$ manifold had the strongest absorption intensity. However, as the dopant level was increased, this manifold became the weakest, see Figure 7.15. The $^4F_{9/2}$ manifold exhibited noticeable peaks at lower concentration levels. Peaks were consistent throughout the low concentrations fibres. Among these the prominent peak at 653nm was the strongest in this manifold at low dopant concentrations. When doped at high dopant concentrations, these peaks broadened as before. See Figure 7.11. At 3.1mol%, the $^4F_{9/2}$ manifold had a 17.5nm linewidth which centred at ~655nm. The linewidth at this manifold increased with dopant concentration. When doped at 6mol%, the linewidth was 21nm centred at ~655nm and at 59mol%, the linewidth was 50nm, centred at ~655nm. Table 7.3 shows the summary of the linewidth at different dopant concentration levels. Peaks appearing in the $^4I_{9/2}$ manifold for low dopant concentrations were situated at 791nm, 797nm

and 801nm. Although there were peaks at 789nm and 804nm at 0.03mol%, these peaks were no longer distinguishable as the dopant level increased. See Figures 7.11,13 and 15. The absorption of the $^4I_{11/2}$ manifold at 0.03mol% was very weak, the signal being only slightly above the background noise, see Figure 7.5. The highest peak at this concentration was at 974nm but the absorption profile changed at the next higher concentration level. The absorption linewidth became wider as concentration increased. In the $^4I_{13/2}$ manifold, a distinctive peak was observed at 1530mn. This peak was observed in dopant concentrations of 0.03, 0.06, 0.3 and 3.1mol%. At 0.03 and 0.06mol%, the absorption at this manifold had relatively weak and narrow absorption lines. See Figures 7.6 and 7.8. Absorption fell within the 1550 to 1570nm region at these concentration levels. This absorption spectrum extended to the 1450nm region as the concentration increased. More peaks emerged at higher dopant levels, see Figure 7.10. These narrow absorption lines started broadening at 6mol%. At 59mol% concentration, see Figure 7.16 a plateau at the top of the absorption band was evident in spectrum. This signified that in the region ~1450 to ~1575nm, full absorption which did not permit any light to pass through was experienced. Peaks at 1637nm, 1650nm and 1658nm in the 1600nm region also become apparant. From Figure 7.15 (insert) when the halogen lamp shape was superimposed onto the absorption spectrum, it was observed that the absorption spectrum had several points where we experienced complete absorption. A combination of low lamp power and detector insensitivity meant that no signal could be measured at these points.

From these spectra, it was observed that at high concentrations the narrow lines broadened and formed wider linewidths. The broadening effects resembled that seen in rare earth doped glasses where the absorption spectrum can stretch over a continuous range of wavelengths instead of narrow discrete lines. The high rare earth concentrations doped in the crystals could have influenced the crystal field splitting and instead of narrow lines appearing, a broad continuous range of wavelengths emerged in the spectrum. Homogeneous and inhomogeneous processes were also the possible causes of such effects in changing the structure of the Er^{3+} doped Y_2O_3 fibres into that similar to Er^{3+} doped glass fibres [7.4]. Another possible reason for the broadening effect could be contributed to the distorting of the crystal lattice under high concentration levels [6.10].

Table 7.3 – $Y_2O_3:Er^{3+}$ linewidth at different regions under different concentrations

Dopant Concentrations (mol%)	Linewidth (nm)			
	$^4F_{9/2}$	$^4I_{9/2}$	$^4I_{11/2}$	$^4I_{13/2}$
3.1	17.5	14	20	15.6
6	21	25	30	128.5
59	50	59	82	174

Figure 7.5: Spec 42 – $Y_2O_3:Er^{3+}$ (0.03mol%)
Absorption spectrum

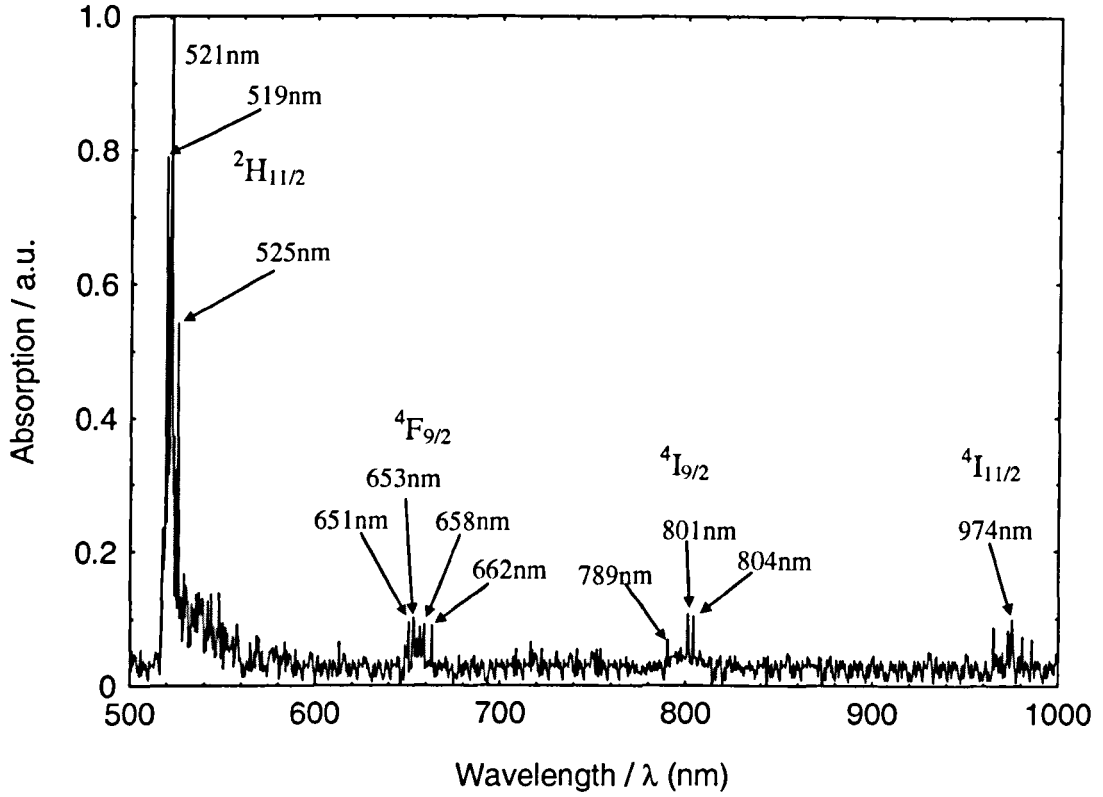

Figure 7.6: Spec 42 – $Y_2O_3:Er^{3+}$ (0.03mol%)
Absorption spectrum ($^4I_{13/2}$)

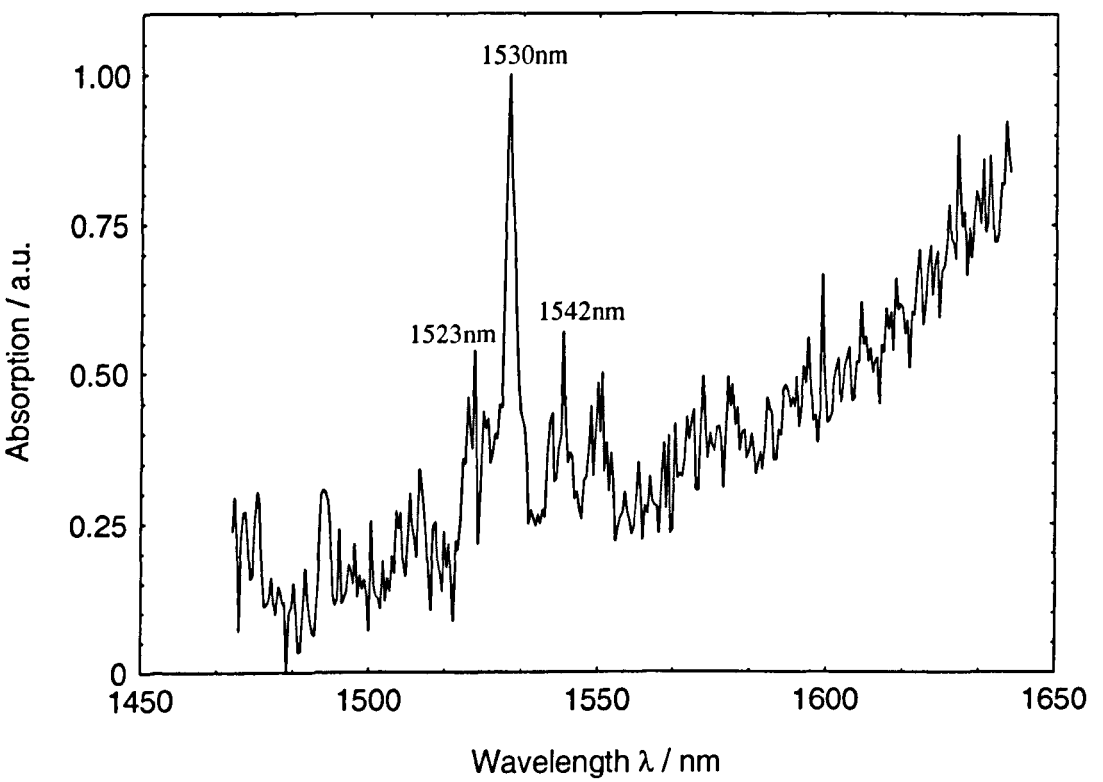

Figure 7.7: Spec 43 – $Y_2O_3:Er^{3+}$ (0.06mol%)
Absorption spectrum

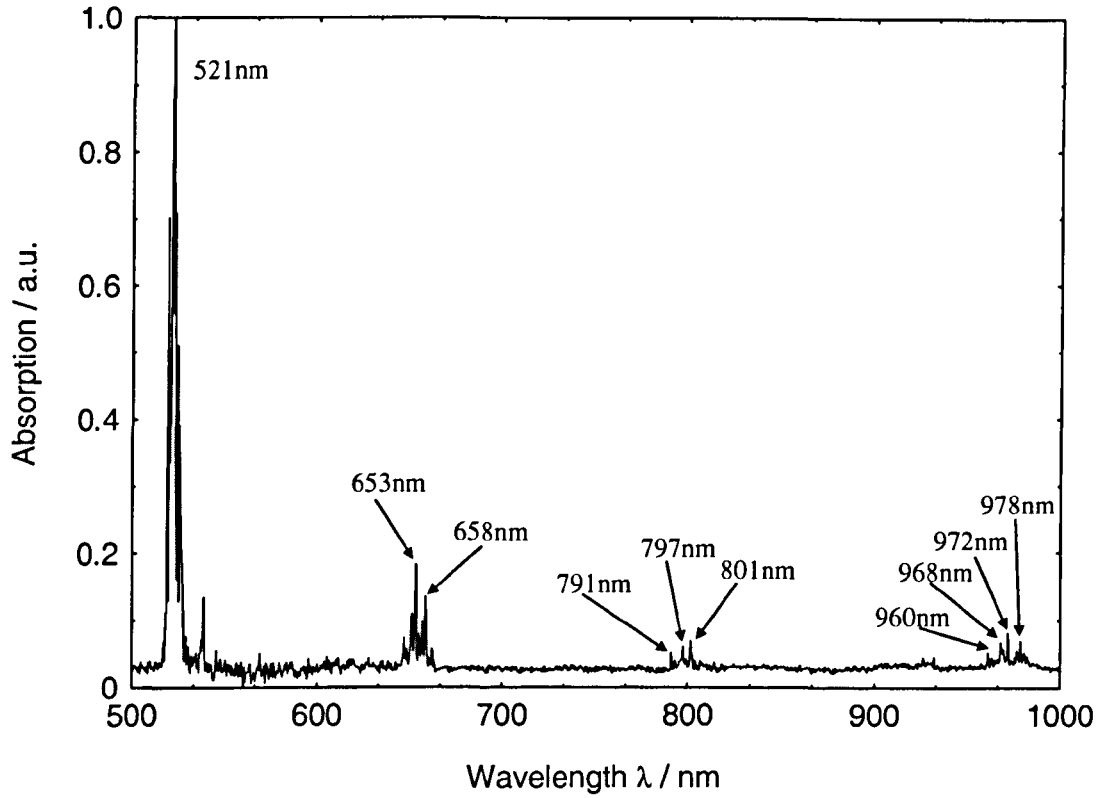

Figure 7.8: Spec 43 – $Y_2O_3:Er^{3+}$ (0.06mol%)
Absorption spectrum ($^4I_{13/2}$)

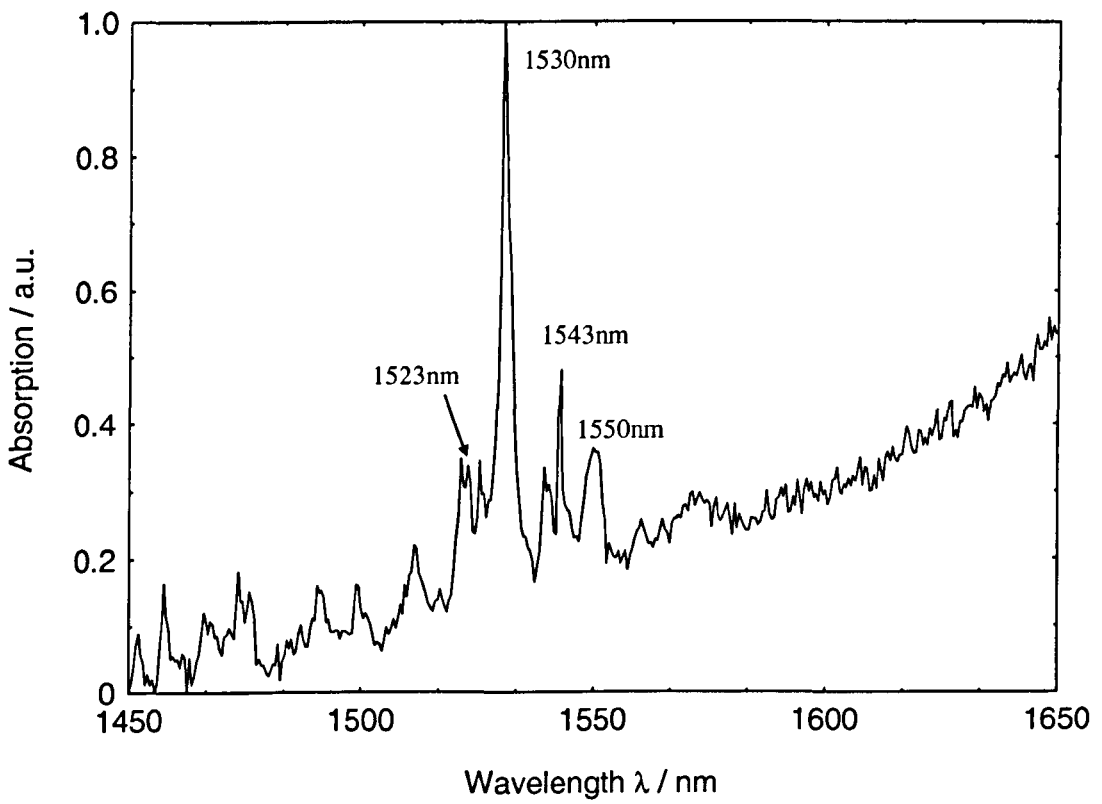

Figure 7.9: Spec 44 – $Y_2O_3:Er^{3+}$ (0.3mol%)
Absorption spectrum

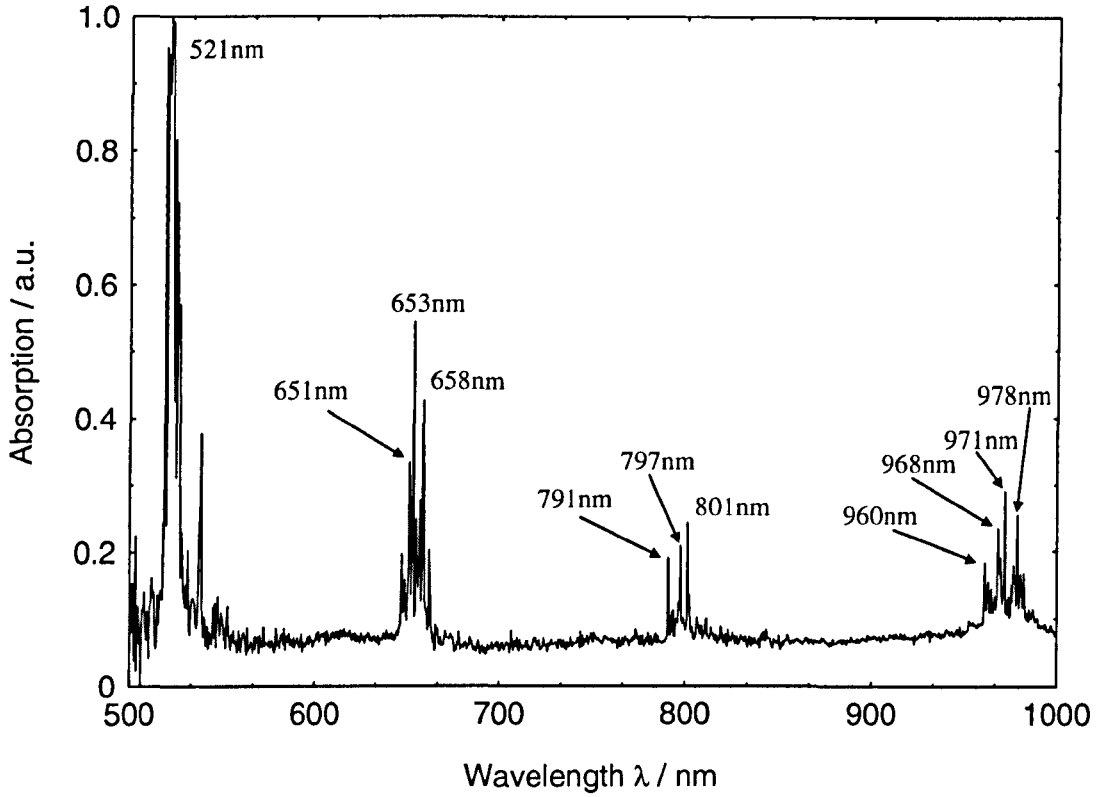

Figure 7.10: Spec 44 – $Y_2O_3:Er^{3+}$ (0.3mol%)
Absorption spectrum ($^4I_{13/2}$)

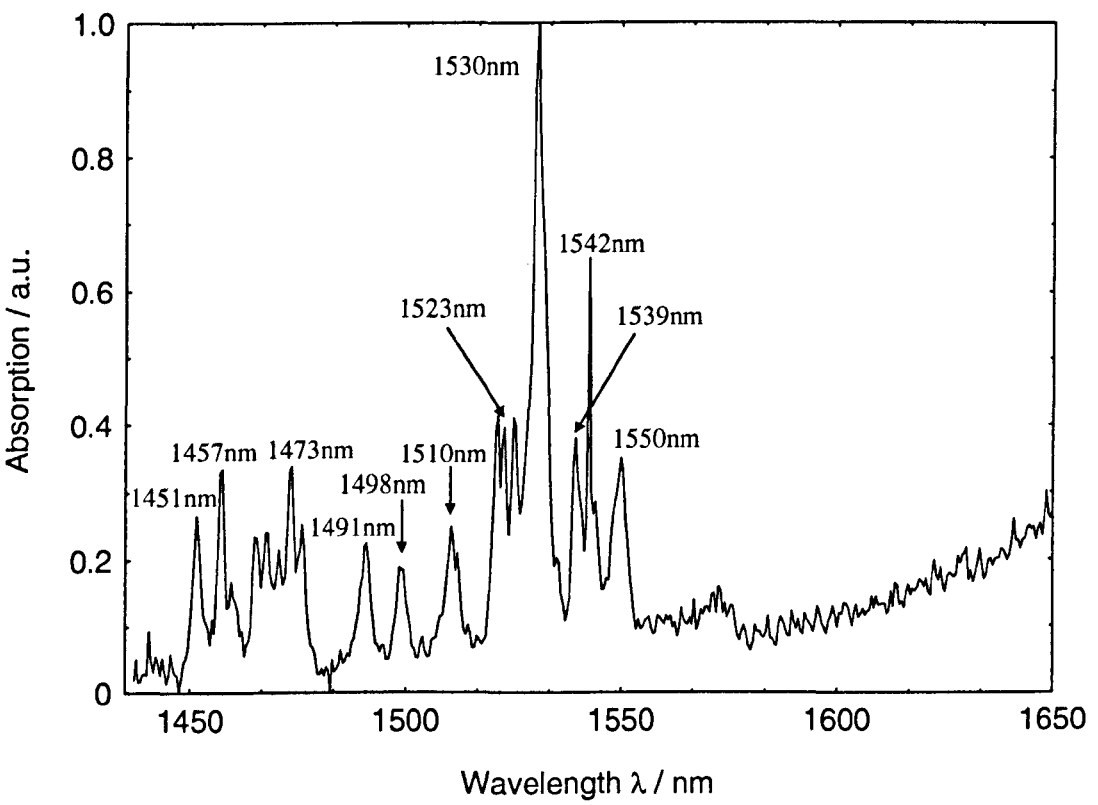

Figure 7.11: Spec 18 – $Y_2O_3:Er^{3+}$ (3.1mol%)
Absorption spectrum

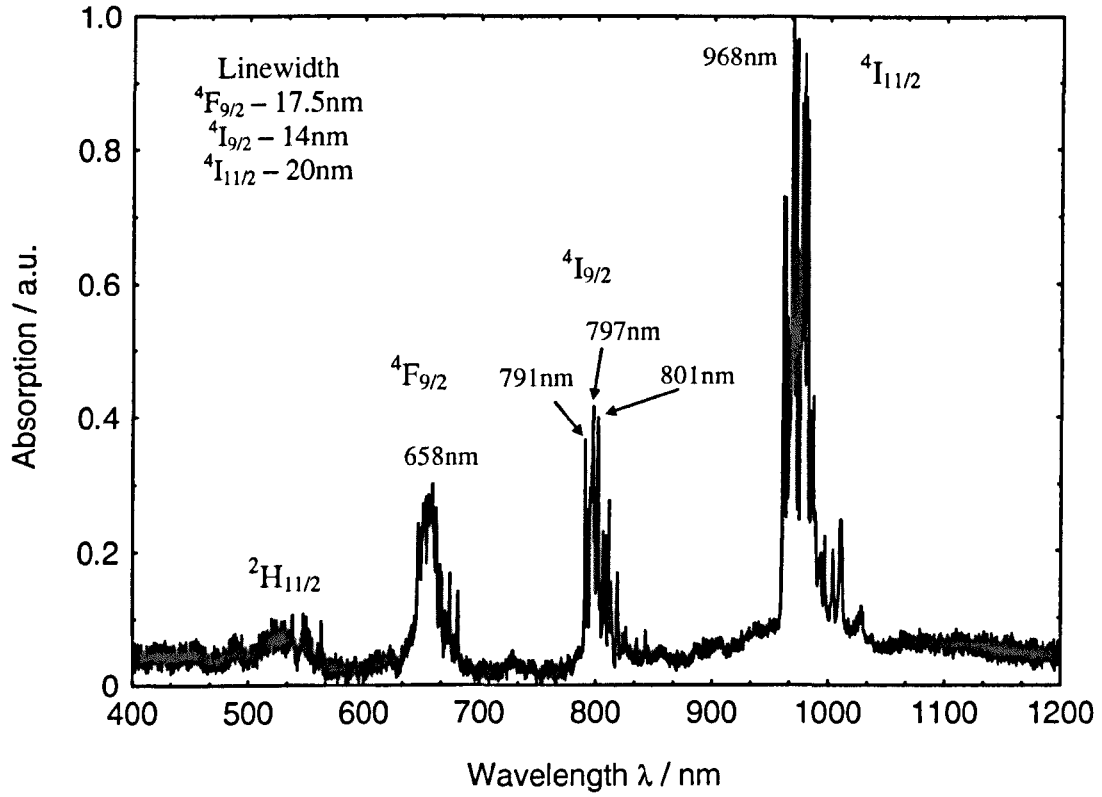

Figure 7.12: Spec 18 – $Y_2O_3:Er^{3+}$ (3.1mol%)
Absorption spectrum ($^4I_{13/2}$)

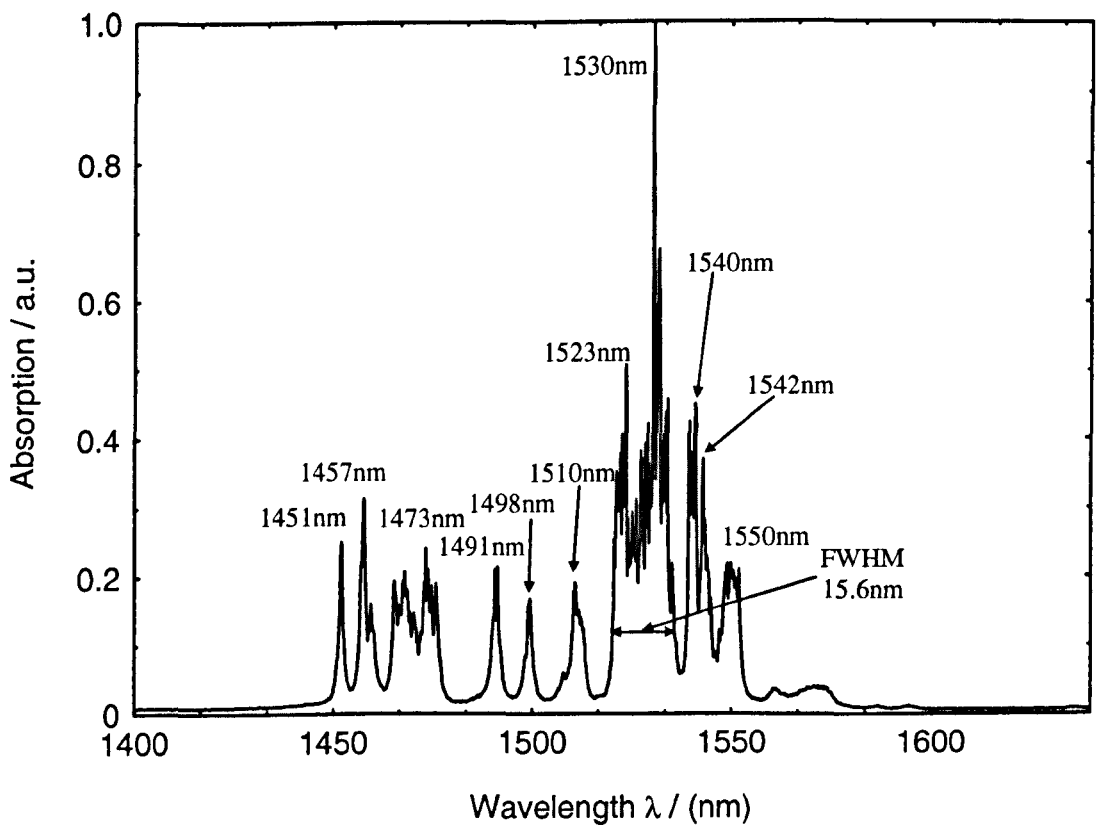

Figure 7.13: Spec 20 – $Y_2O_3:Er^{3+}$ (6mol%)
Absorption spectrum

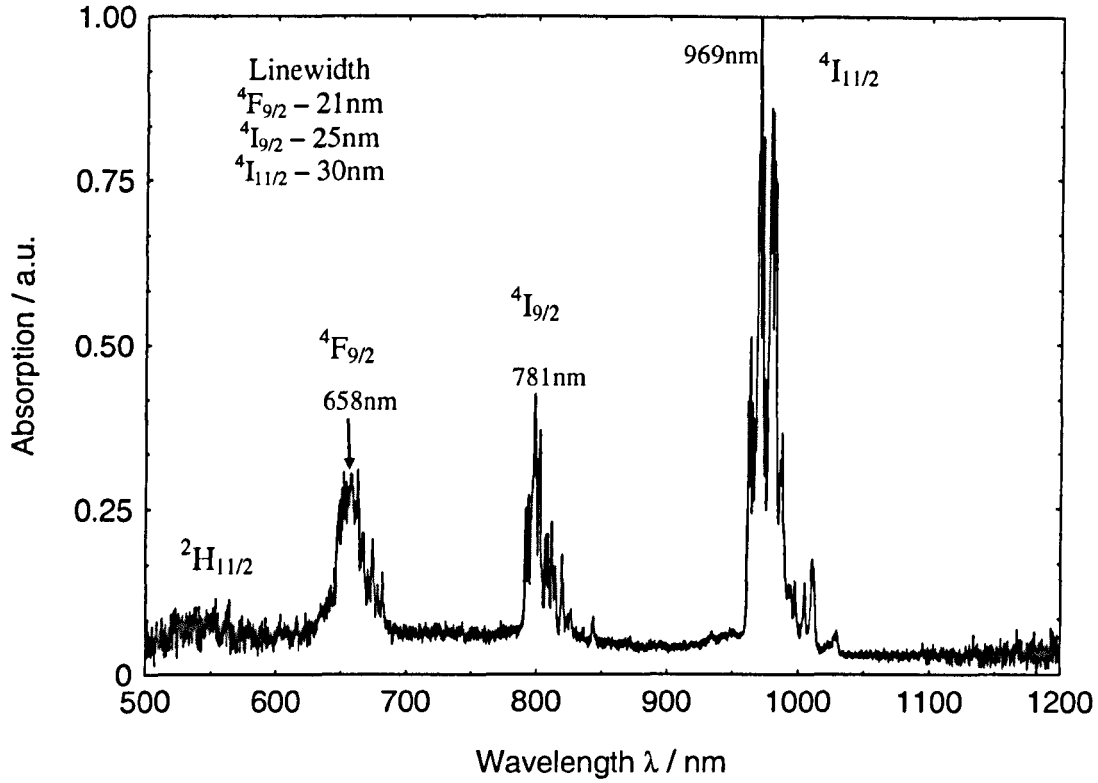

Figure 7.14: Spec 20 – $Y_2O_3:Er^{3+}$ (6mol%)
Absorption spectrum ($^4I_{13/2}$)

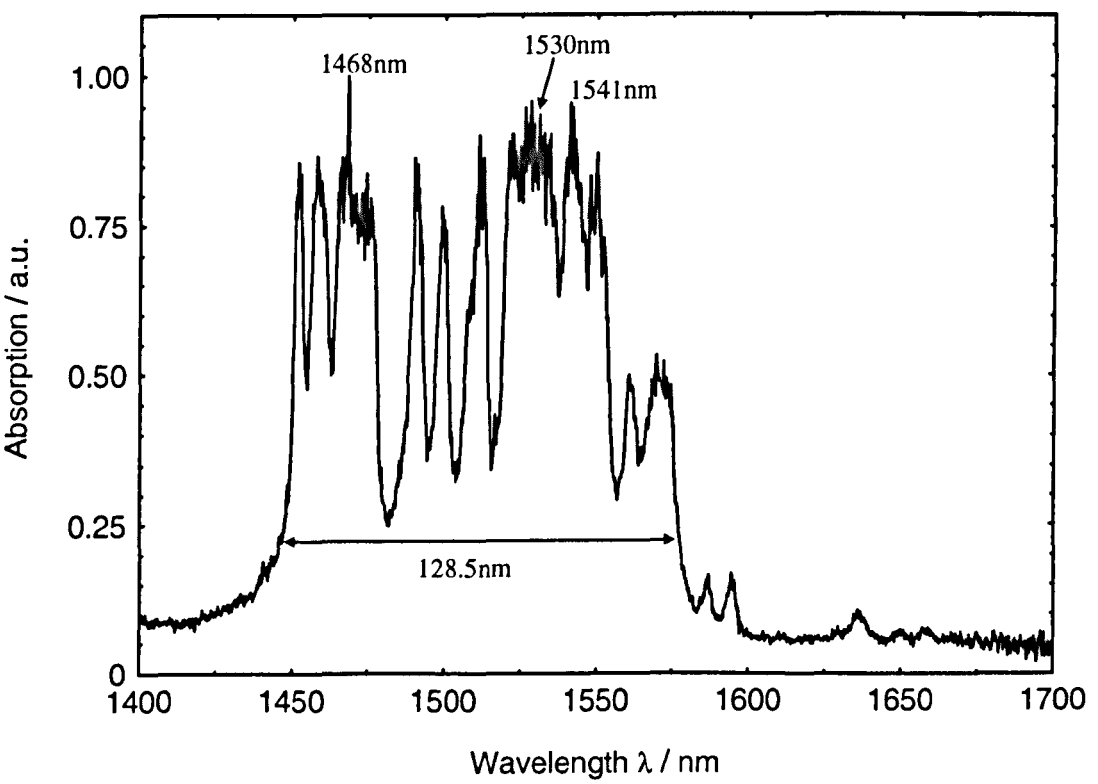

Figure 7.15: Spec 19 – $Y_2O_3:Er^{3+}$ (59mol%) Absorption spectrum

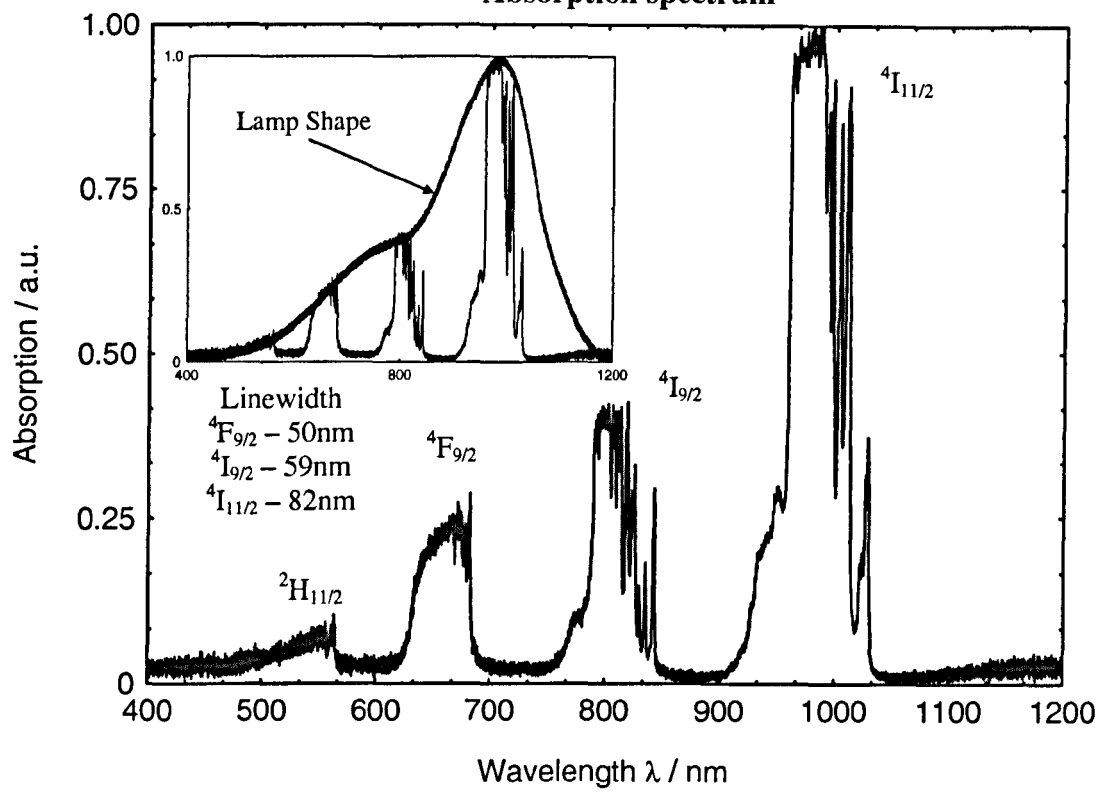

Figure 7.16: Spec 19 – $Y_2O_3:Er^{3+}$ (59mol%) Absorption spectrum ($^4I_{13/2}$)

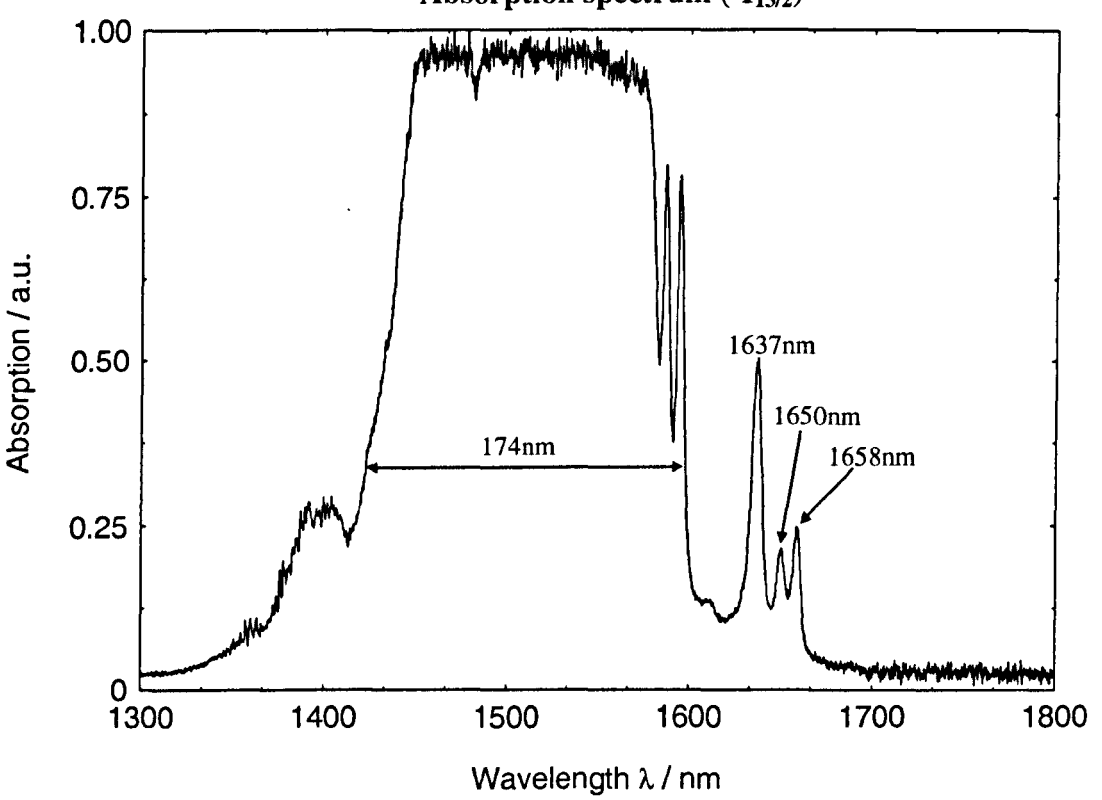

7.5 Fluorescence Measurement

Y_2O_3:Er^{3+} fibres were excited with 965nm and 975nm laser diodes; the results for these fluorescence spectra are presented in this section. From the absorption spectra, the low Er^{3+} concentrations had a weaker absorption at the $^4I_{13/2}$. Comparisons between the two laser diodes were made to verify which would be more appropriate for exciting these fibres. Detailed experimental layout has been discussed in Chapter 5.3.2.

7.5.1 Results and Discussion

When the fibres were excited with the 965nm and 975nm laser diode, a weak green emission was observed for all the fibres except the fibre with 59mol% where red emission was seen. Visible emission from the fibres indicated that an upconversion process had taken place. Further discussion on this process will be made in the following section. Figures 7.17 to 28 show the fluorescence emission spectrums of the fibres by the two laser diodes at the low concentrations. Emissions were observed at $^4I_{11/2} \rightarrow {}^4I_{15/2}$ and $^4I_{13/2} \rightarrow {}^4I_{15/2}$ in the experiments for both the high and low concentration fibres. In the $^4I_{11/2} \rightarrow {}^4I_{15/2}$ transition, three strong peaks at 1003.5nm, 1010nm and 1028.5nm were observed when excited by both the diodes. Transitions at the $^4I_{11/2}$ manifold were also observed by *Polman* [7.1] when Er^{3+} was doped in a Y_2O_3 thin film. The emission profiles in this work were similar to *Polman* at the ~1000nm region. The strongest peak at the $^4I_{11/2}$ transition was at 1009.5nm, the intensity being relatively weak for all three low concentration (0.03, 0.06 and 0.3mol%) fibres as compared to the $^4I_{13/2} \rightarrow {}^4I_{15/2}$ transitions. When excited with the 975nm laser diode, the $^4I_{13/2}$ transition manifold peaked at 1441nm, 1448nm, 1601nm and 1680nm. See Figure 7.19. These peaks were similar to those in the YAG fibres mentioned in Chapter 6.5.1. A possible cause of these peaks could be the presence of impurities in the host material or contamination in the apparatus. These peaks were only observed when excited with the 975nm laser but not when the 965nm laser was used. One way to determine if impurities were present in the fibres would be to conduct an electron micro-probe analysis (EMPA). For low concentration Er^{3+} doped Y_2O_3 fibres, the common transitions from the $^4I_{15/2}$ manifold when excited by either laser diode were at 1530.5nm, 1550nm 1573nm and 1636.5nm. When excited

at 965nm, the ~1450nm region had broader linewidths and the intensity in this region was stronger, see Figures 7.18, 22 and 26. Compare this to using an excitation source at 975nm, see Figures 7.20, 24 and 28. From these figures, one can observe, two additional peaks at 1650nm and 1658nm. These peaks were not prominent when the 975nm laser was used. One possible reason for this was because the absorption band at the $^4I_{11/2}$ manifold had several weak and narrow absorption lines and the 975nm laser produces a relatively narrow emission line, see Figure 5.13. This reduced the excitation efficiency of the Er^{3+} ions. The 965nm laser had a broader linewidth which ranged from 960nm to 970nm, see Figure 5.12. This range covered approximately half of the absorption band at the $^4I_{11/2}$ manifold which promoted a more effective energy transfer within the system and therefore explained the stronger emission in the 1600nm region. The general fluorescence emission profiles produced by the two laser diodes at the low concentrations were in agreement with work done by *Laversenne* and *Georgobiani* [7.5, 6]. Narrow peaks were observed at low concentrations (0.03, 0.06 and 0.3mol%) while at higher concentrations (3.1, 6 and 59mol%) these narrow peaks merged and formed a wider linewidth. From this work, it was found that the fluorescence spectra at high concentrations were similar when excited by both laser diodes. The reason for this similarity could be explained by the wide absorption linewidth of the $^4I_{11/2}$ manifold. The absorption linewidths for the high concentration fibres were at ~950 to 1000nm which was sufficiently wide to cover the emission lines of the two laser diodes. In this section, only the fluorescence emission results from the 965nm laser diode are presented, see Figures 7.29 to 34. Stark line broadening at the $^4I_{13/2}$ manifold was observed in all the high concentration fibres. At 3.1mol%, see Figures 7.29 and 30, the 1400nm region seemingly merged with the 1500nm region. The narrow peaks, for example the 1530.5nm and 1550nm, seen at the low concentrations overlapped and formed a broader bandwidth which had a linewidth of 47nm. Again these broadened fluorescence emission profiles were similar to that seen in Er^{3+} doped glass fibres. The peaks in the 1600nm region had a stronger intensity where 1636.5nm was the strongest peak in this region. The $^4I_{11/2}$ transition manifold also increased its intensity. At this dopant level, the peak at 1010nm was the strongest peak among the two manifolds. When doped with 6mol%, the broadening effect became more evident. The linewidth at this concentration was 64.5nm, which was wider than that seen for the 3.1mol%. See Figure 7.32. From Figure 7.31, one can observe that at 6mol%, the intensity at transition $^4I_{11/2}$ has

increased. Peaks in the 1600nm region have become more intense. At a 59mol% dopant level, the fluorescence emission was only observed from ~1575nm to 1675nm, see Figure 7.33. The 1400nm to 1575nm region was no longer seen. It is likely that high Er^{3+} dopant concentration had distributed the crystal field to the point where some of the Stark lines were no longer apparent. Broadening of the existing lines also created a wide bandwidth ranging from ~1575nm to 1675nm. At this dopant level, the linewidth was 72nm. Peaks at 1650nm, 1656nm and few others were observed, see Figure 7.34. It was clear that the broadening of the fluorescence emission spectra were due to the increase in the Er^{3+} ion concentration. The changes in the crystal structure due to the introduction of Er^{3+} ions distorted the lattice probably leading to dislocation and interstitial defects possibly contributing to the broadening effects [6.10]. In this reference, under low dopant level conditions, discrete lines were observed in crystals. Also, continuous emission bands, similar to those seen in this work, were observed in glass hosts. A broad emission band leads to a low stimulated emission cross section with a reduction in amplified spontaneous emission generation. This would raise the threshold for laser action, but permit storage of energy for pulsed lasers and low noise for amplifiers, advantages for the telecommunication arena [7.7, 6.10].

The change in the peak intensities with respect to the dopant concentrations were further illustrated by examining the fluorescence intensity ratio (FIR). Peaks 1010nm (I_{1010}), 1530.5nm ($I_{1530.5}$), 1636.5nm ($I_{1636.5}$) and 1650nm (I_{1650}) were chosen to demonstrate the relationship between the changes. From Figures 7.35 and 36, the intensity ratio started with a gradual increase until, at high concentrations a dramatic increase is seen producing a very steep gradient. There was no discernable peak at 1530.5nm for 59mol% fibres. In order to have a comparison for all doped Y_2O_3 fibres, the intensities at 1010nm and 1636.5nm were used. See Figure 7.37. From this figure, it is observed that for all concentrations except 59mol%, the ratio intensity (between 1010nm and 1636.5nm) was constant as the concentration increased.

Figure 7.17: Spec 42 – Y_2O_3:Er^{3+} (0.03mol%) Fluorescence spectrum with excitation source at 965nm

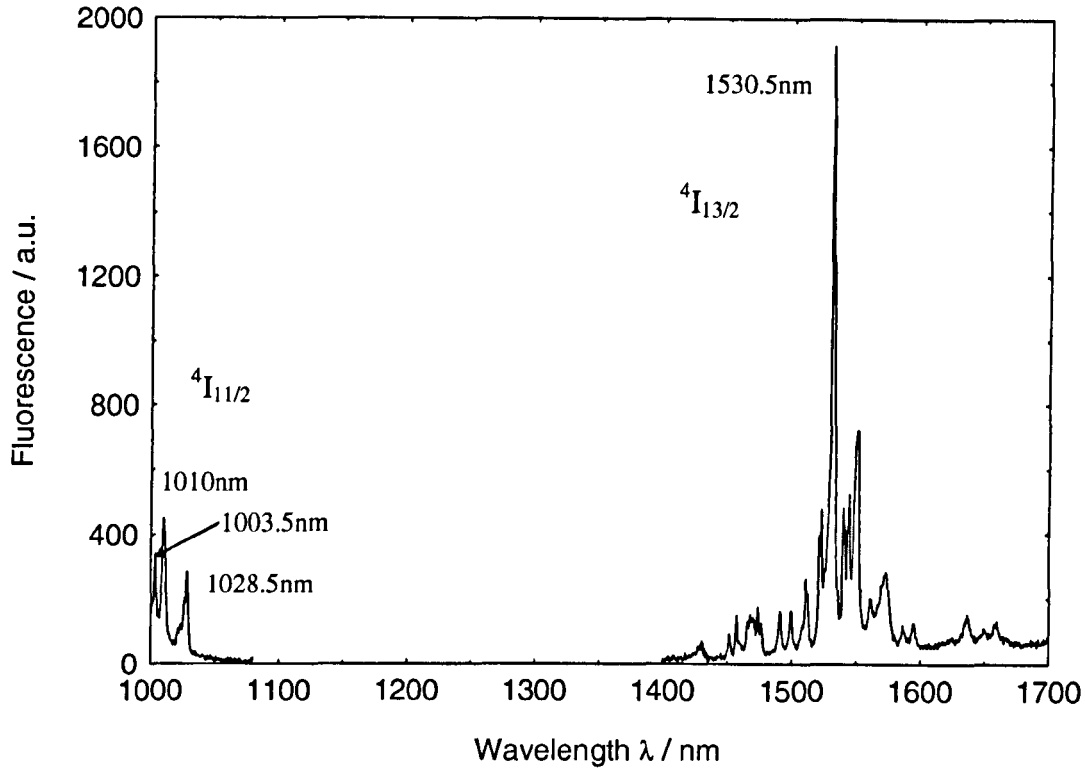

Figure 7.18: Spec 42 – Y_2O_3:Er^{3+} (0.03mol%) Fluorescence spectrum with excitation source at 965nm ($^4I_{13/2}$)

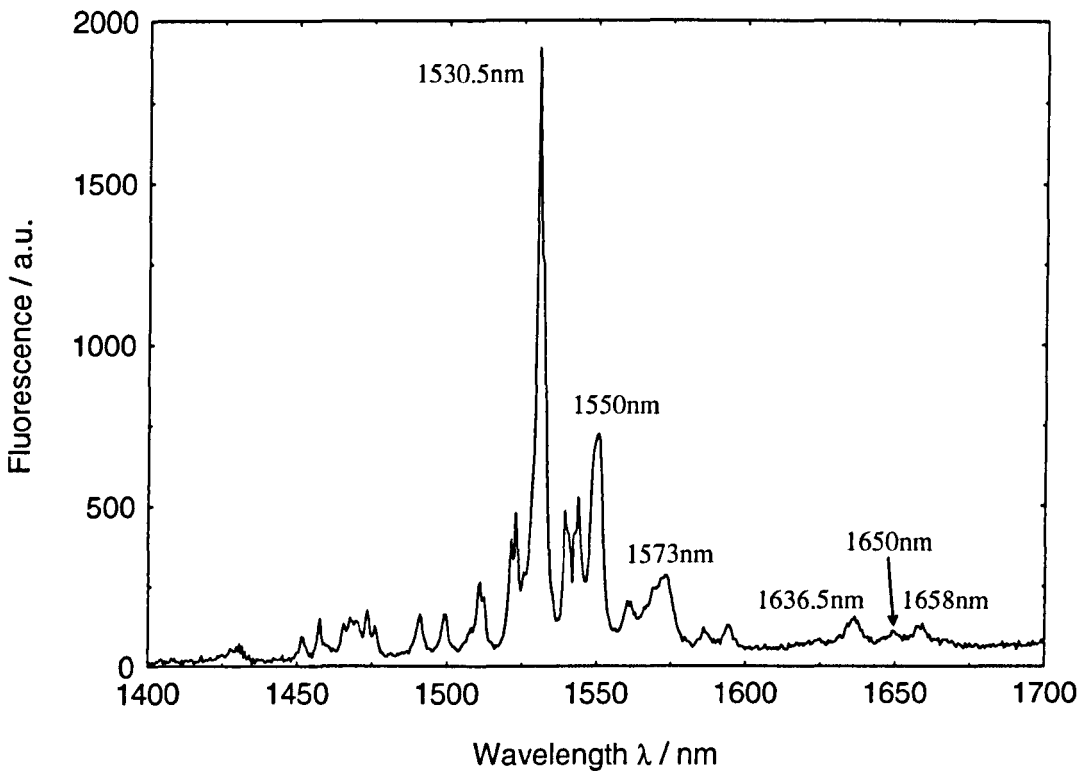

Figure 7.19: Spec 42 – Y_2O_3:Er^{3+} (0.03mol%) Fluorescence spectrum with excitation source at 975nm

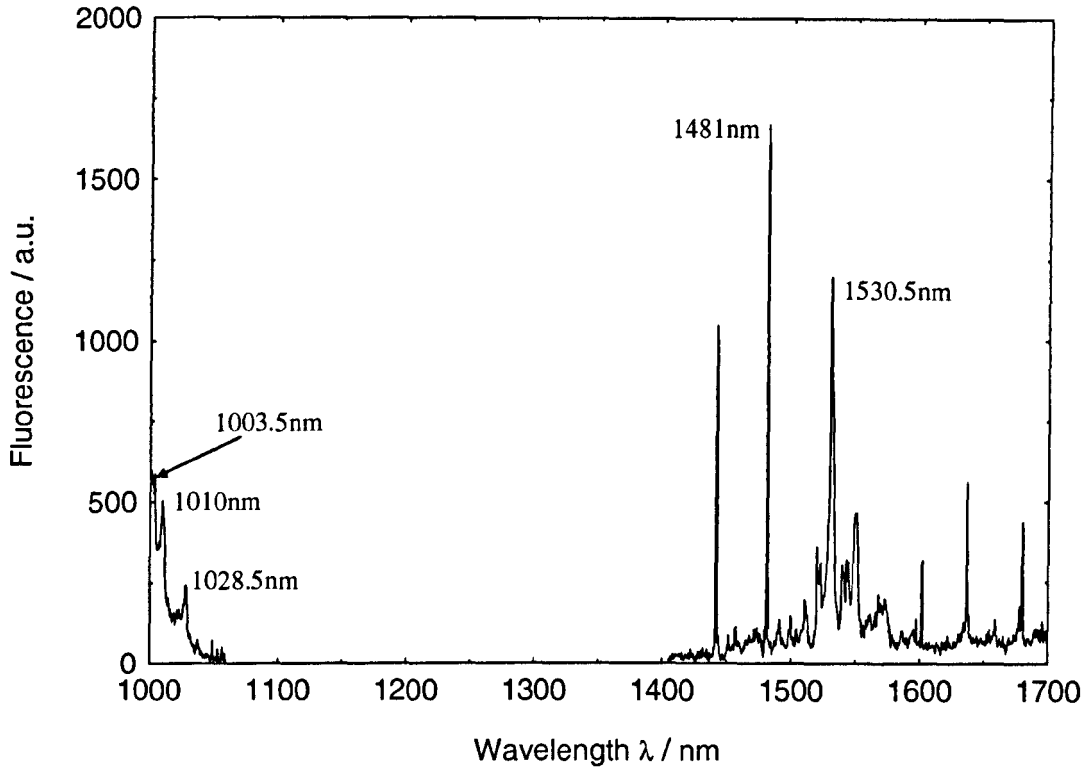

Figure 7.20: Spec 42 – Y_2O_3:Er^{3+} (0.03mol%) Fluorescence spectrum with excitation source at 975nm ($^4I_{13/2}$)

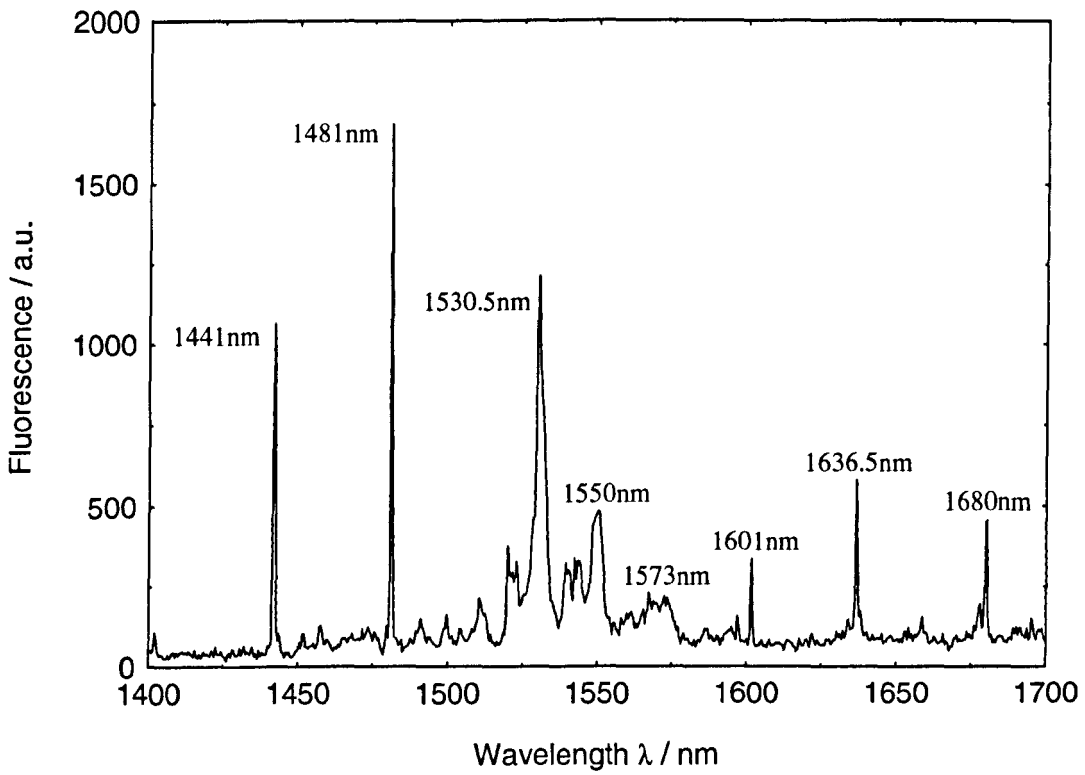

Figure 7.21: Spec 43 – $Y_2O_3:Er^{3+}$ (0.06mol%) Fluorescence spectrum with excitation source at 965nm

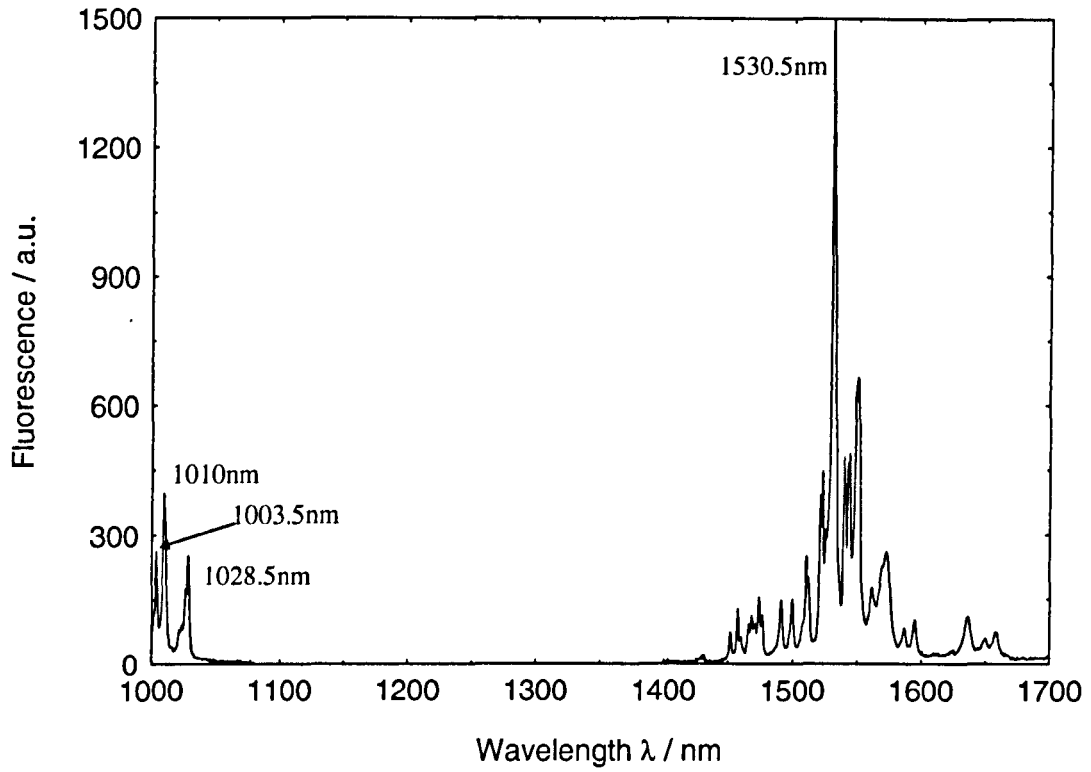

Figure 7.22: Spec 43 – $Y_2O_3:Er^{3+}$ (0.06mol%) Fluorescence spectrum with excitation source at 965nm ($^4I_{13/2}$)

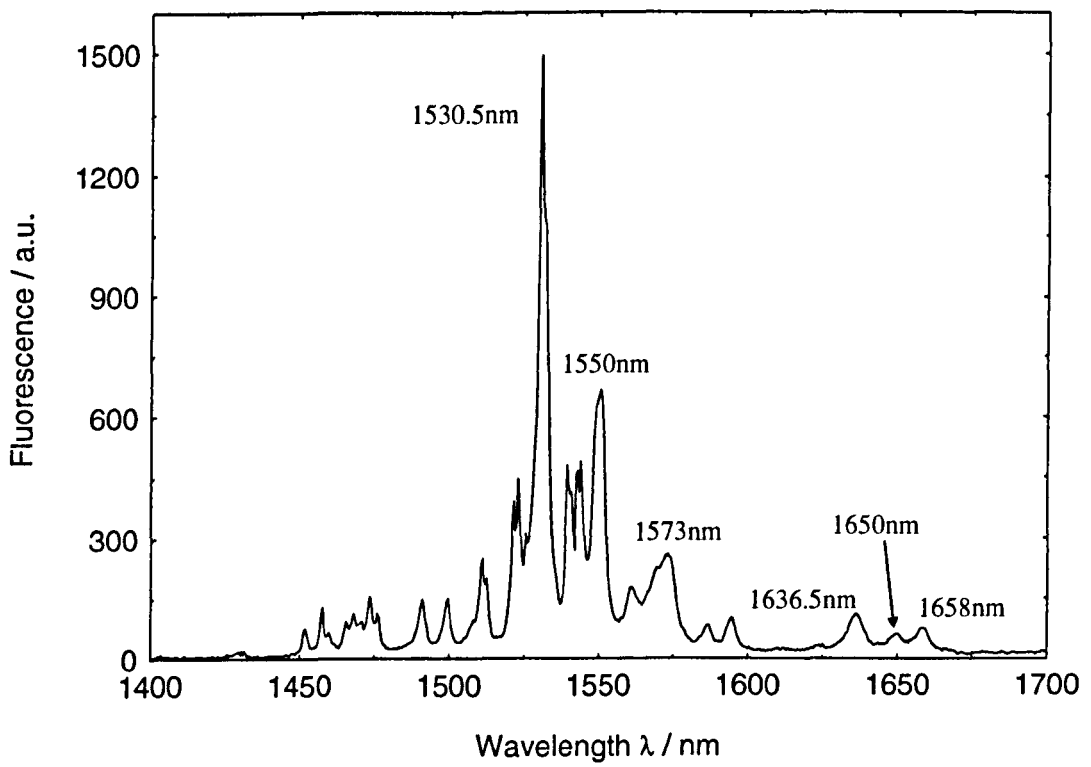

Figure 7.23: Spec 43 –Y_2O_3:Er^{3+} (0.06mol%) Fluorescence spectrum with excitation source at 975nm

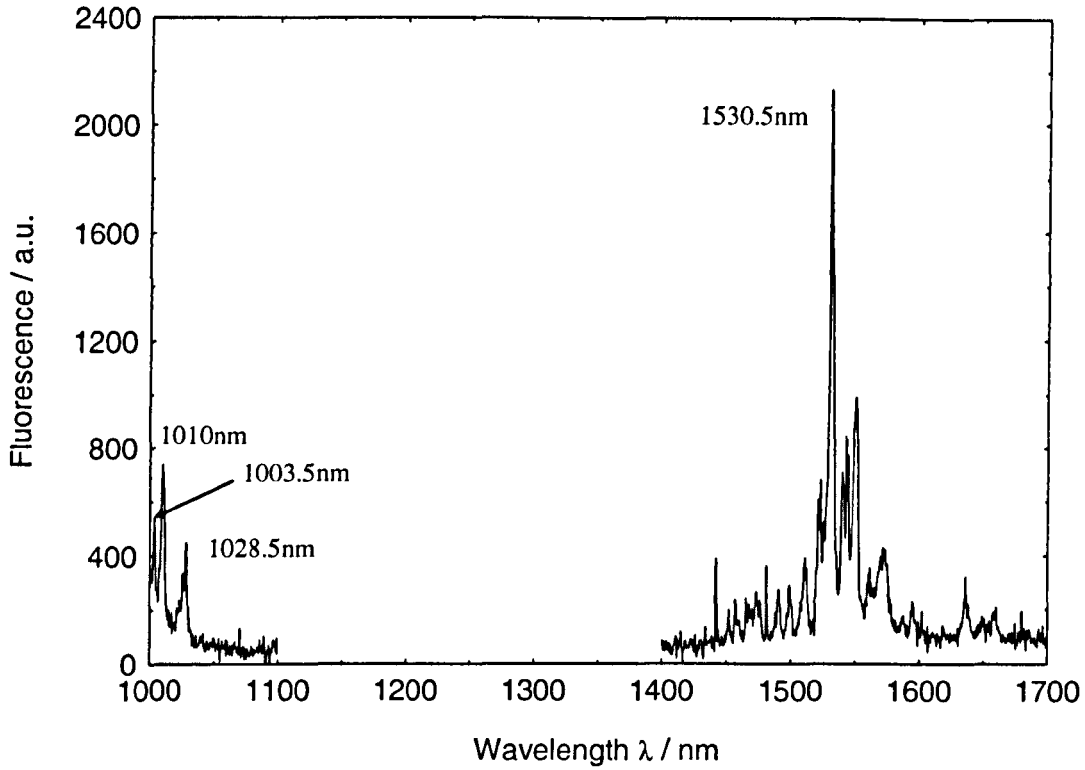

Figure 7.24: Spec 43 – Y_2O_3:Er^{3+} (0.06mol%) Fluorescence spectrum with excitation source at 975nm ($^4I_{13/2}$)

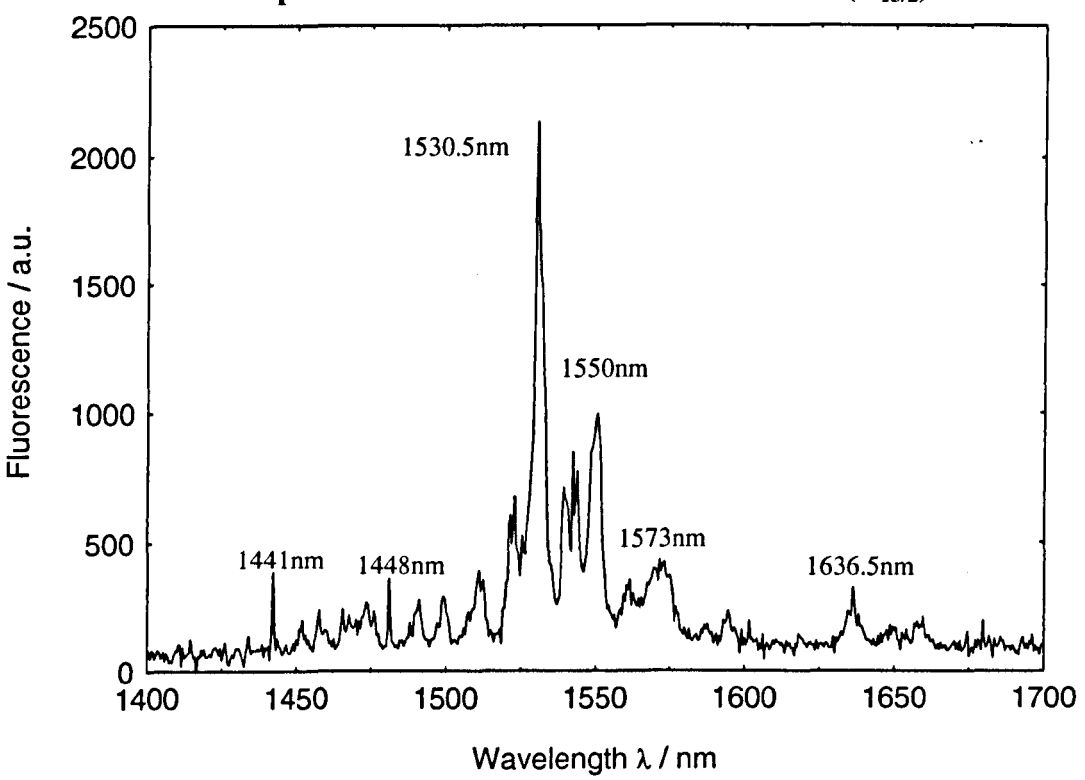

Figure 7.25: Spec 44 – Y_2O_3:Er^{3+} (0.3mol%) Fluorescence spectrum with excitation source at 965nm

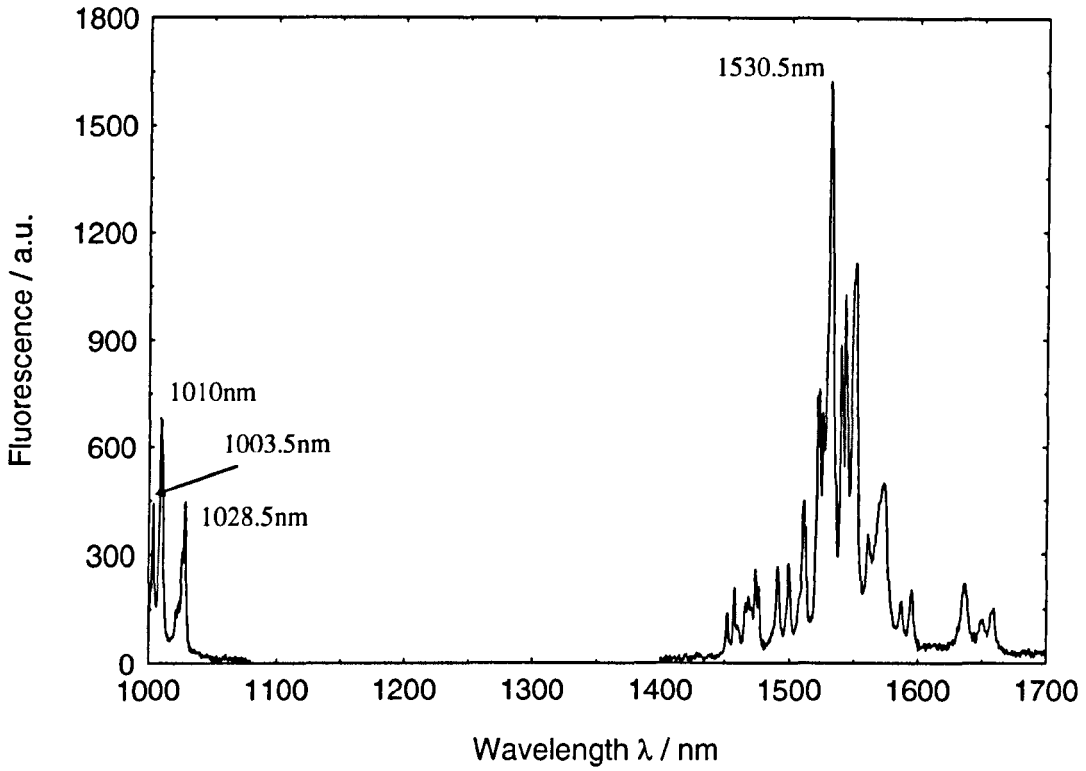

Figure 7.26: Spec 44 – Y_2O_3:Er^{3+} (0.3mol%) Fluorescence spectrum with excitation source at 965nm ($^4I_{13/2}$)

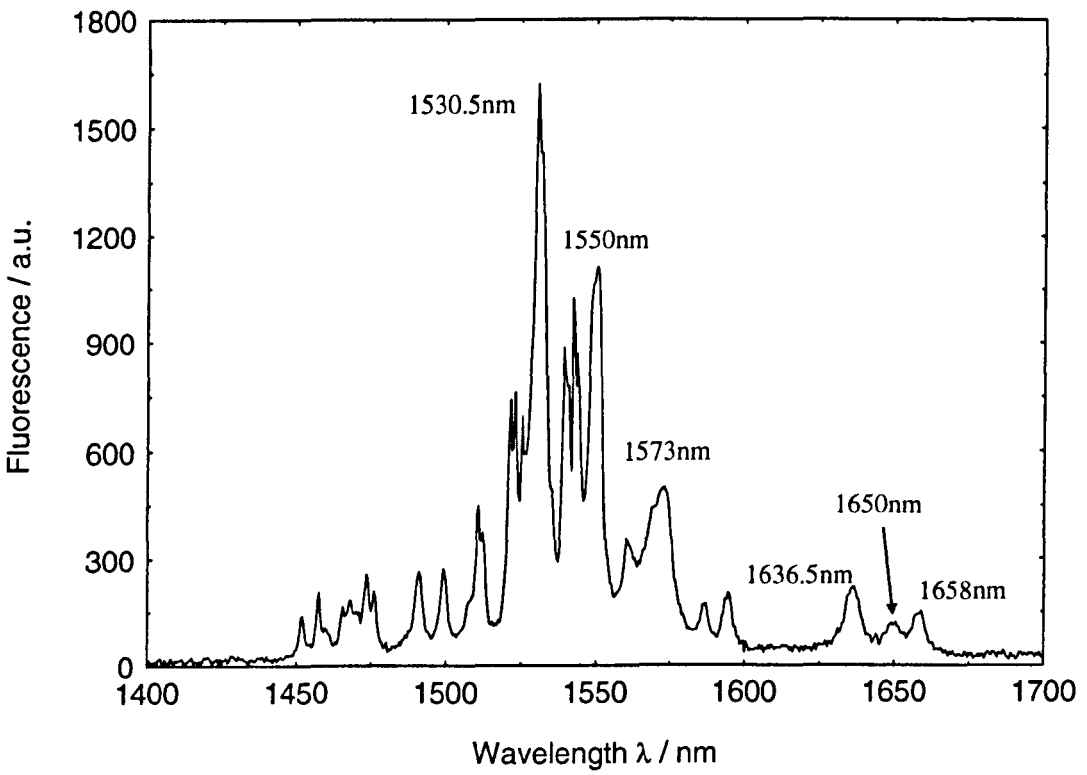

Figure 7.27: Spec 44 – $Y_2O_3:Er^{3+}$ (0.3mol%) Fluorescence spectrum with excitation Source at 975nm

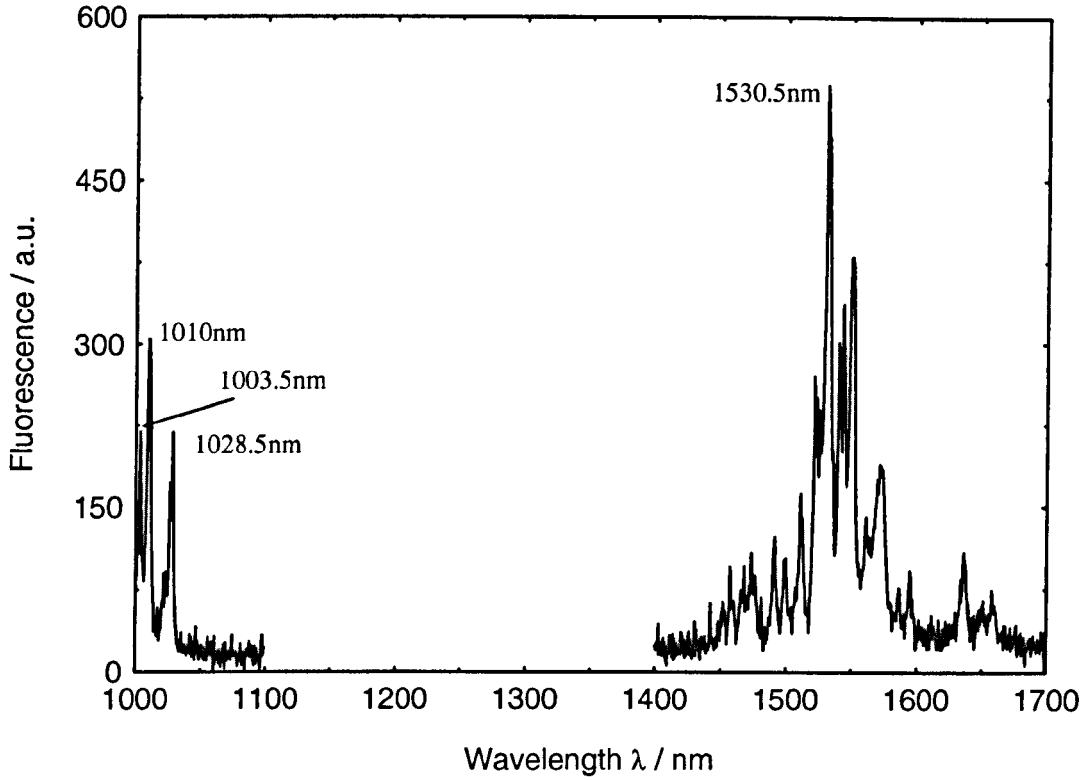

Figure 7.28: Spec 44 – $Y_2O_3:Er^{3+}$ (0.3mol%) Fluorescence spectrum with excitation source at 975nm ($^4I_{13/2}$)

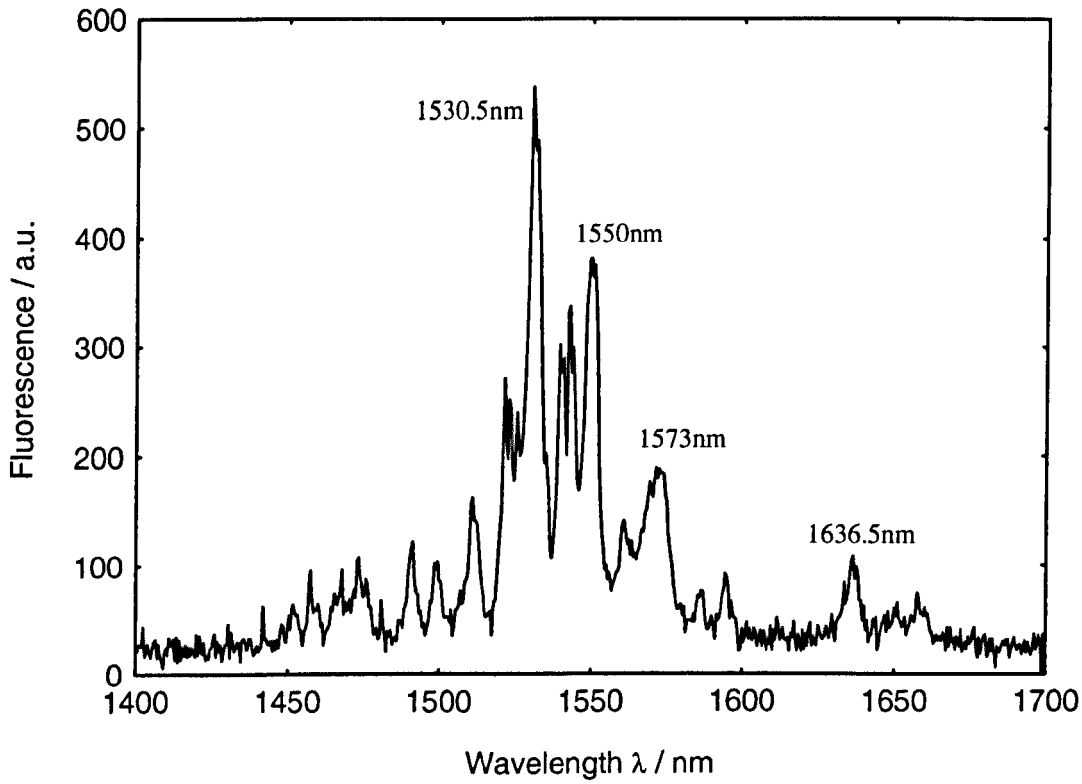

Figure 7.29: Spec 18 – $Y_2O_3:Er^{3+}$ (3.1mol%) Fluorescence spectrum with excitation source at 965nm

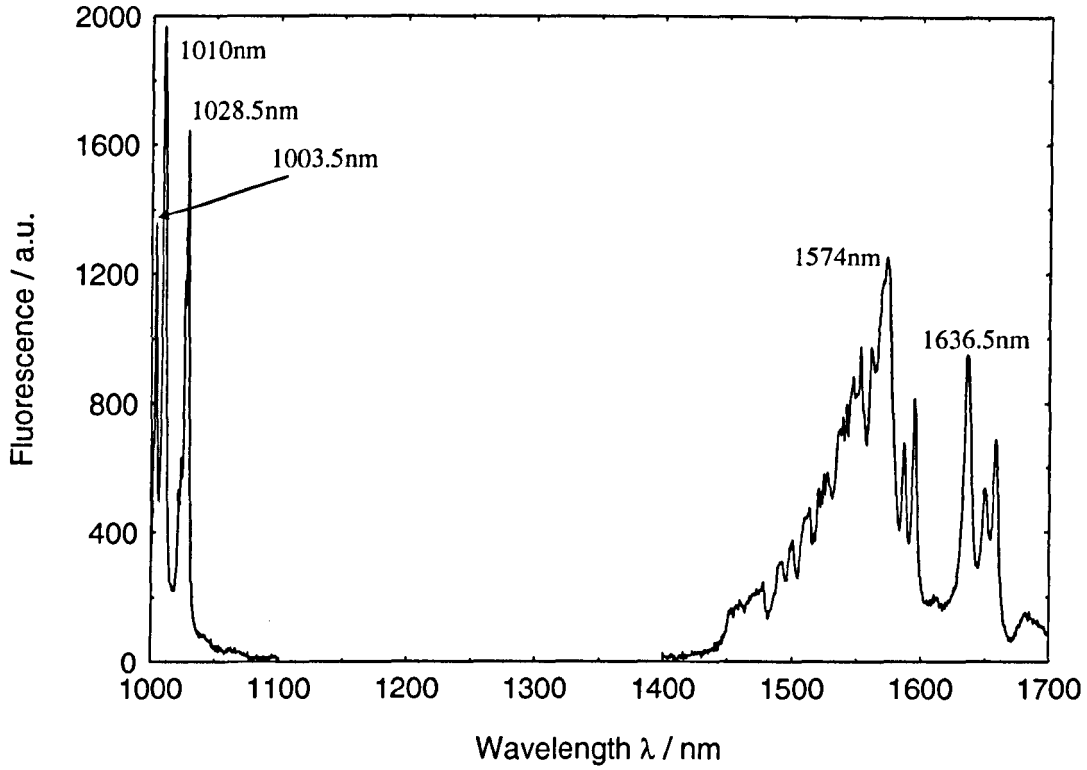

Figure 7.30: Spec 18 – $Y_2O_3:Er^{3+}$ (3.1mol%) Fluorescence spectrum with excitation source at 965nm ($^4I_{13/2}$)

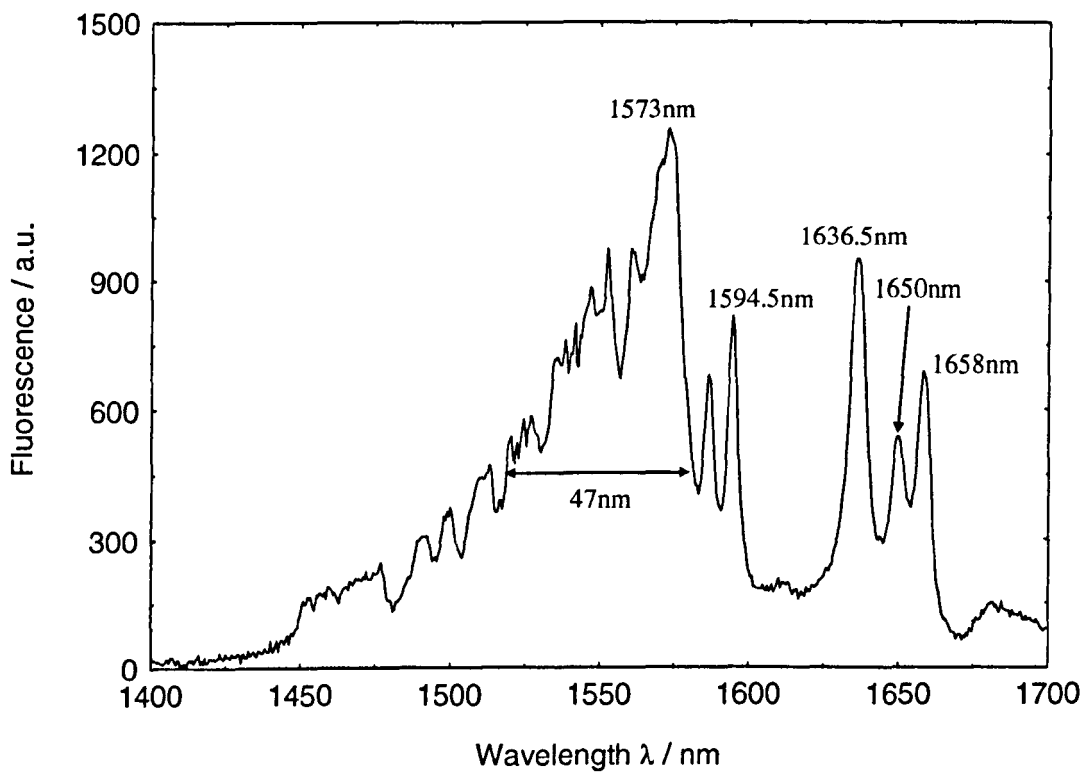

Figure 7.31: Spec 20 – $Y_2O_3:Er^{3+}$ (6mol%) Fluorescence spectrum with excitation source at 965nm

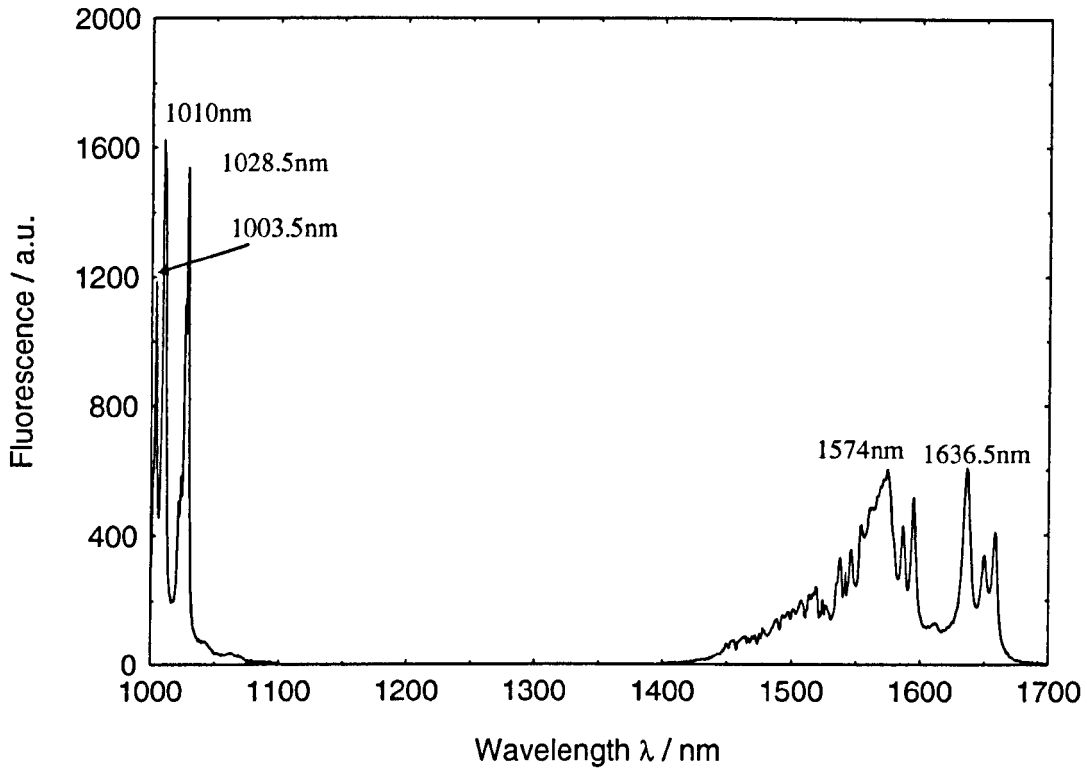

Figure 7.32: Spec 20 – $Y_2O_3:Er^{3+}$ (6mol%) Fluorescence spectrum with excitation source at 965nm ($^4I_{13/2}$)

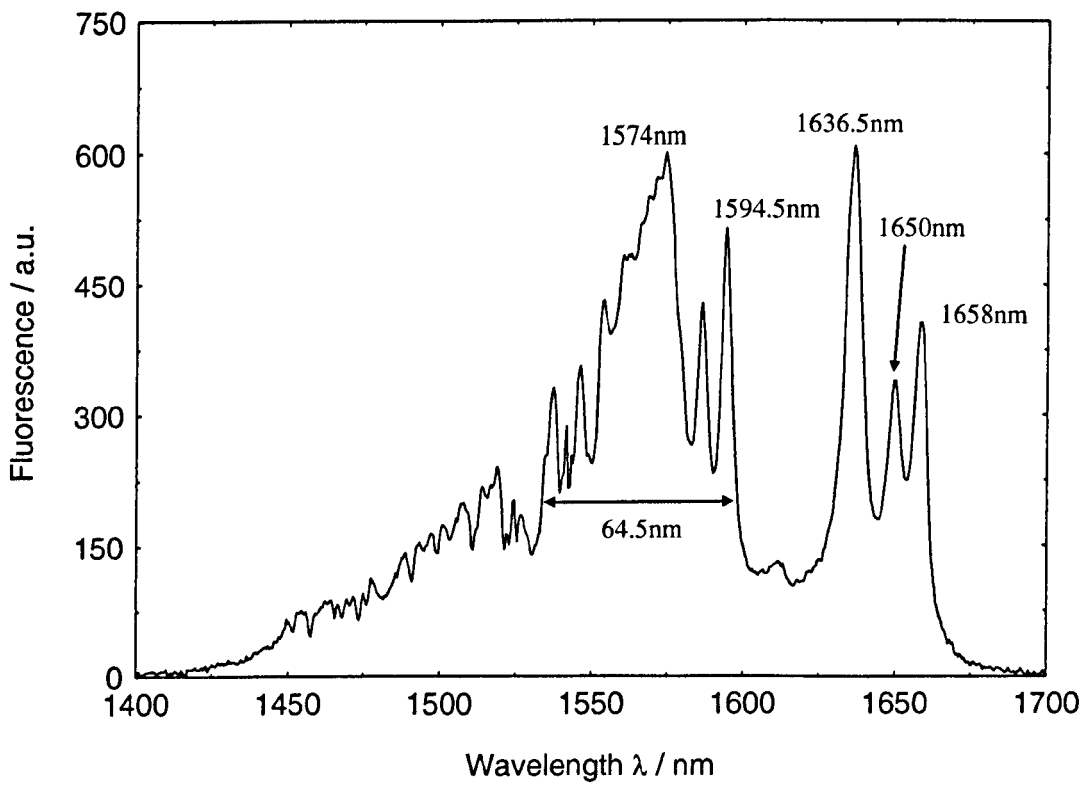

Figure 7.33: Spec 19 –Y_2O_3:Er^{3+} (59mol%) Fluorescence spectrum with excitation Source at 965nm

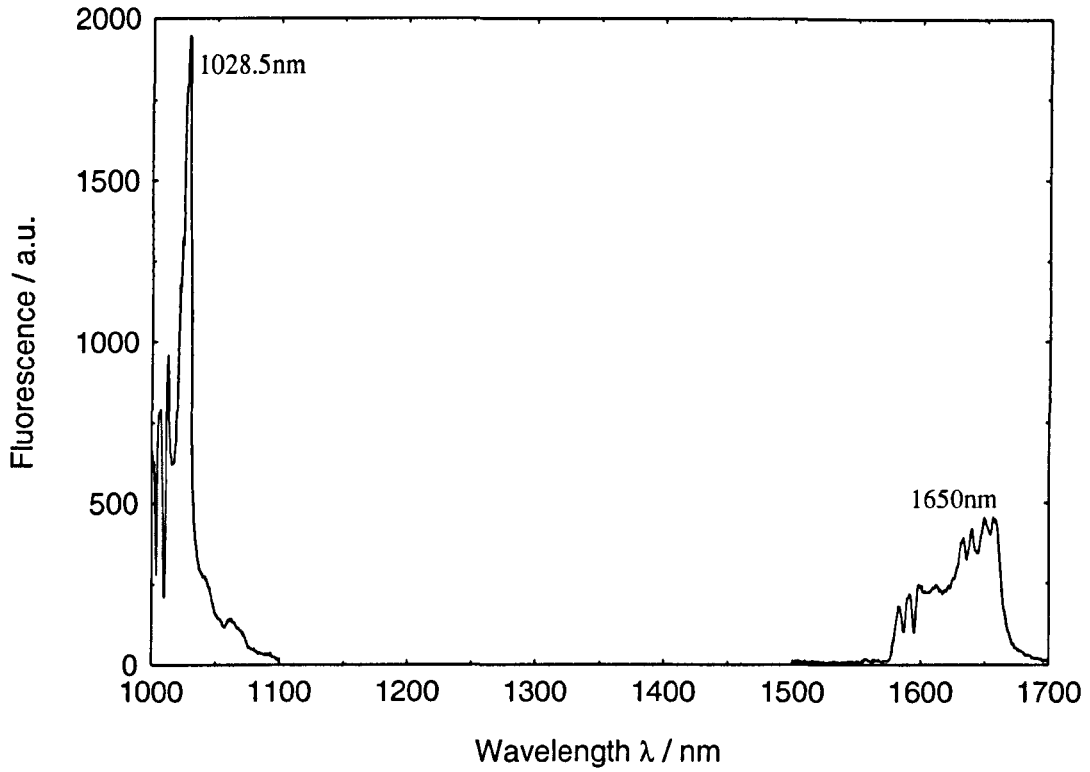

Figure 7.34: Spec 19 – Y_2O_3:Er^{3+} (59mol%) Fluorescence spectrum with excitation source at 965nm ($^4I_{13/2}$)

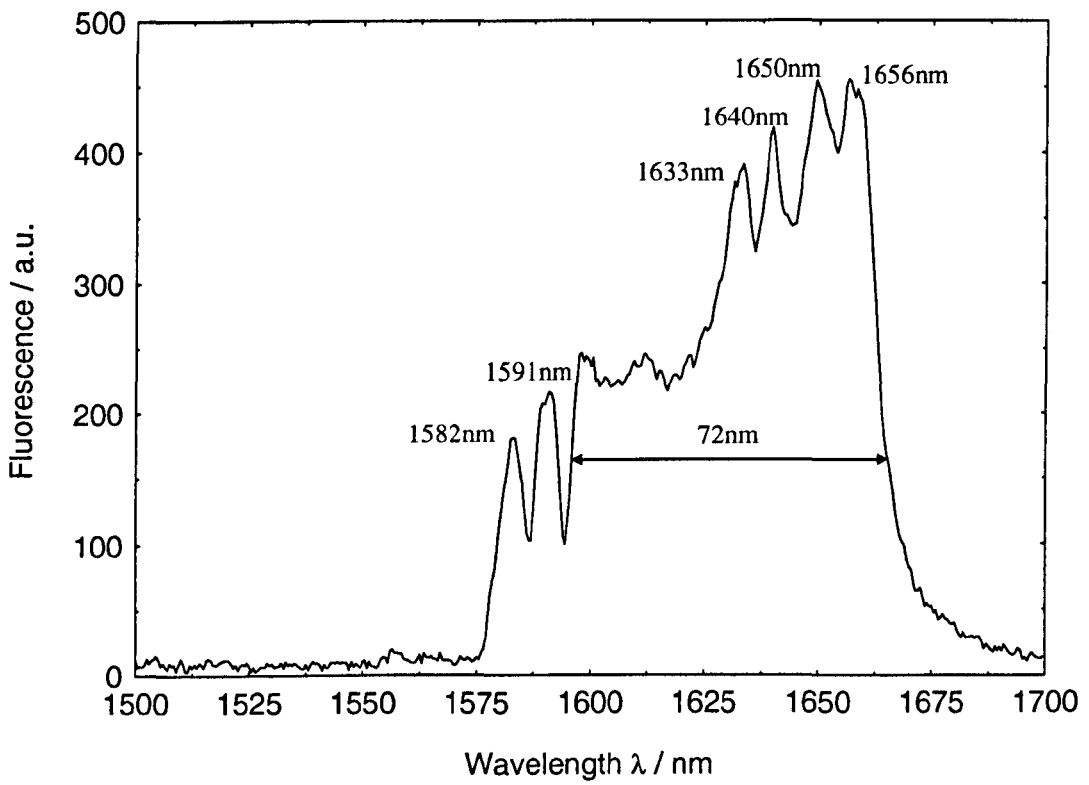

Figure 7.35: Fluorescence intensity ratio (FIR) $I_{1530.5}/I_{1636.5}$

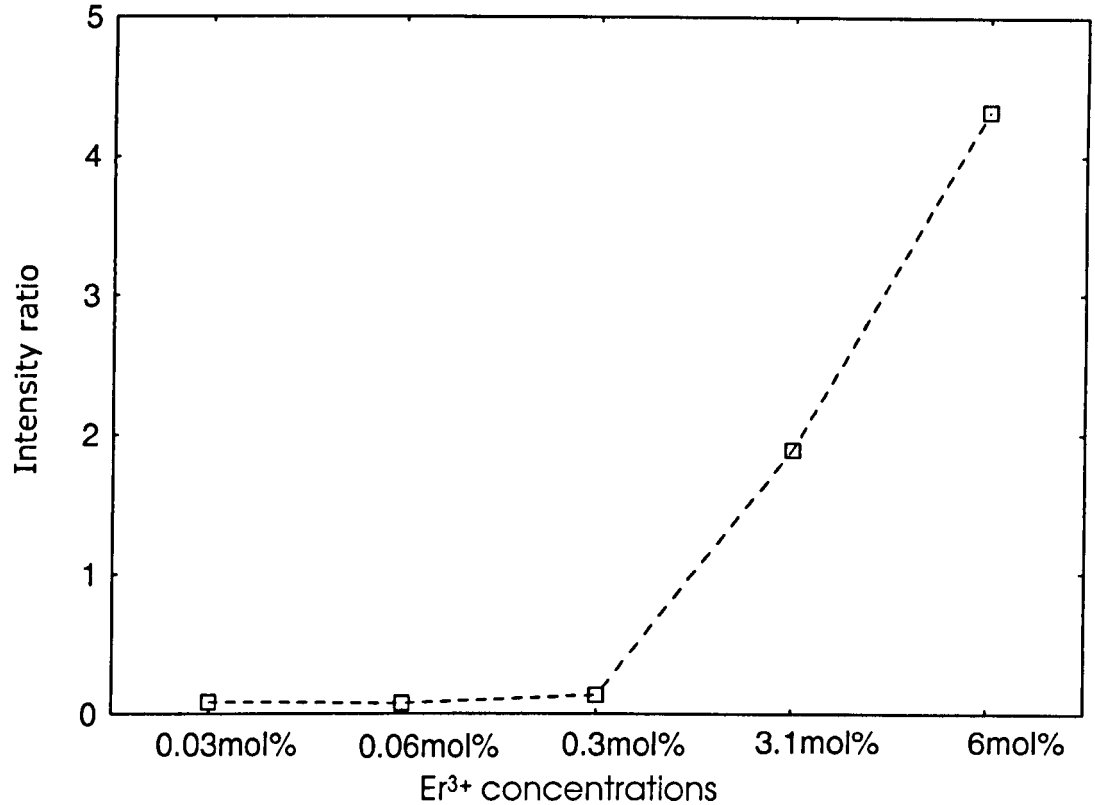

Figure 7.36: Fluorescence intensity ratio (FIR) $I_{1010}/I_{1530.5}$

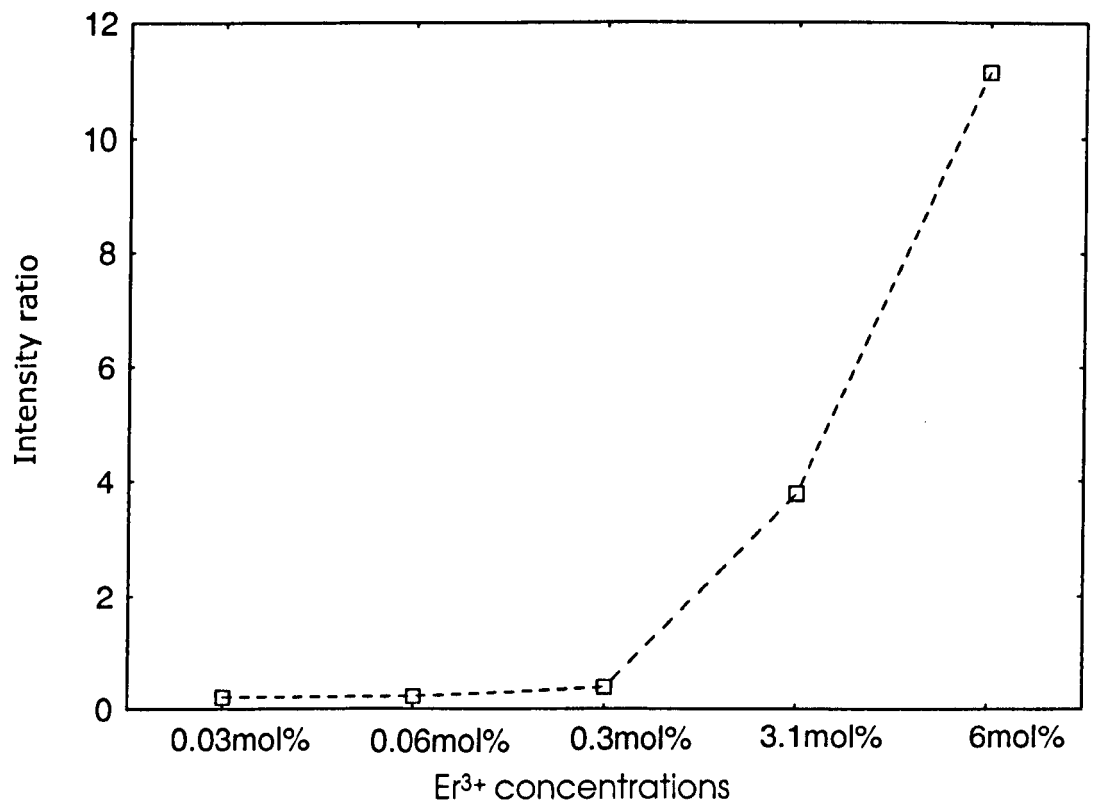

Figure 7.37: Fluorescence intensity ratio (FIR) I_{1010}/I_{1650}

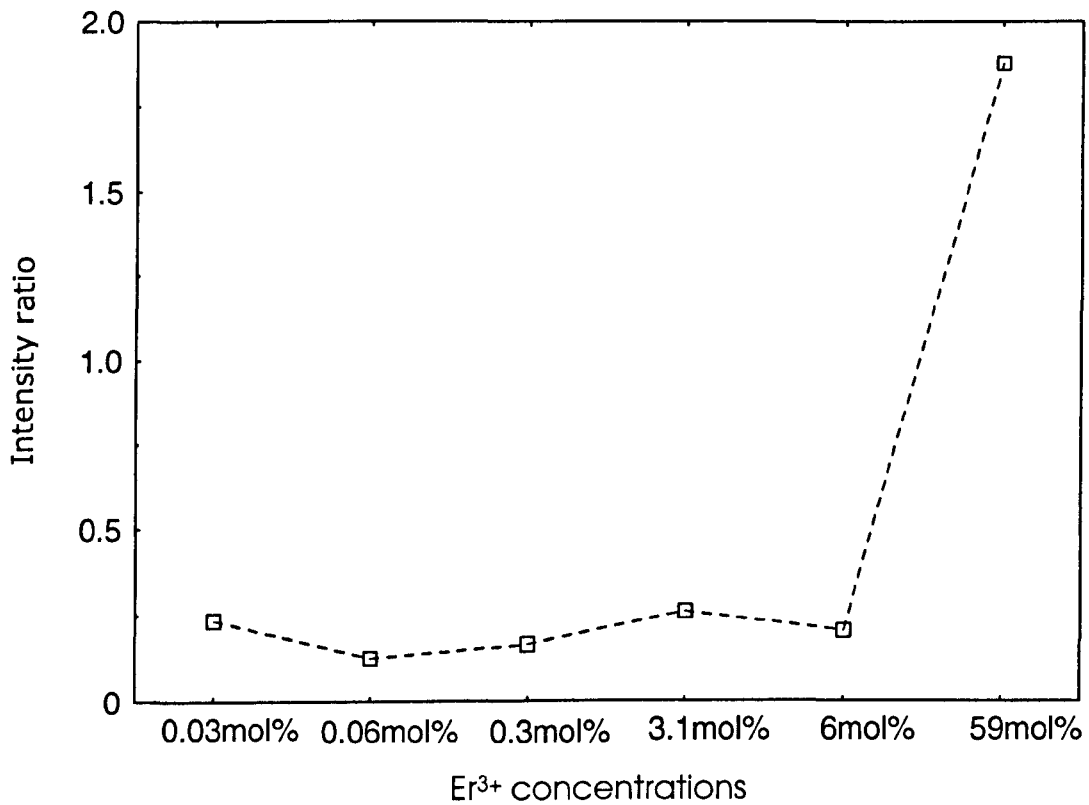

7.6 Upconversion Measurement

In the previous section, it was observed that there were emissions in the visible regions and these are the telltale signs of upconversion processes taking place within the Er^{3+} ions. Refer to Chapter 3.3.3 for a discussion on the theoretical background on cooperative energy transfer upconversion. Experimental investigations were carried out to determine the emission behaviour of these transitions. Experimental layouts were discussed in Chapter 5.3.2.

7.6.1 Results and Discussion

The use of the 975nm laser diode at maximum power (120mW) was not able to provide a strong enough excitation source for detection with the photomultiplier tube (PMT) even through a visible green emission could be seen coming from the fibre. This possibly was due to the great loss of signal through the monochromator. However, there was not a problem for the PMT to pick up the visible light from the Y_2O_3:Er^{3+} fibres when the 965nm laser diode was employed. Figures 7.38 to 43 show the upconversion spectra measured in this work. At low concentrations (0.03, 0.06 and 0.3mol%), a strong green emission was observed. However, from the upconversion spectra, it can be seen that red emission was present but very weak. From the figures, it was observed that upconversion emission at the green were $^2H_{11/2}$+$^4S_{3/2}$→$^4I_{15/2}$ transitions ranging from 515nm to 575nm and the red was $^4F_{9/2}$→$^4I_{15/2}$ transition ranging from 630nm to 700nm. At low concentrations, for the green emission, several peaks were observed, 553nm and 563nm being the strongest among them, see Figures 7.38 to 40. The green upconversion profile at these low concentrations was in agreement with the work done by *Korzenski* [7.8]. For this work, at low concentration, seemingly nothing was observed in the red emission. The reason for $^4F_{9/2}$→$^4I_{15/2}$ transitions not being detected was because the $^2H_{11/2}$+$^4S_{3/2}$→$^4I_{15/2}$ transitions intensities were too strong. In order to attain a decent upconversion spectrum of the red emission, sensitivity on the lock-in amplifier had to be increased and the slits of the monochromator opened to ~300μm. The inserts in Figures 7.38 to 40 show the red emission. The relative intensities of the red emission transitions increased with increased Er^{3+} concentrations. Figure 7.40 showed that within the same scale of the green emission, the red emission was visible when the

Er^{3+} dopant level increased to 0.3mol%. The sharp lines seen at the low dopant concentrations signified that broadening was small, implying that the crystal lattices in the Y_2O_3 SCF were not unduly disrupted by the Er^{3+} ions and that these ions were located in the well defined positions in the crystal [7.1]. At high concentrations (3.1, 6, 59mol%), the narrow sharp lines started overlapping and formed broader bandwidths. Figures 7.41 to 43 show the upconversion emission spectra for high dopant concentrations. Visible green emission was seen for all these fibres. The green emission was strong enough that the red emission could not be seen by eye. See Figure 7.45. When doped at 59mol% of Er^{3+} concentration, see Figure 7.43, both the green and red emission spectrums were equally intense. From the fibre, a strong orange/reddish colour was seen from the fibre at this concentration. See Figure 7.46. Most of the green emission seen at this dopant level was only from the $^4S_{3/2} \rightarrow {}^4I_{15/2}$ transition. It is speculated that these equally intense emissions from both the green and red were a result of strong the Er^{3+}- Er^{3+} ion interaction. It is assumed that the neighbouring Er^{3+} ions were promoted to $^4F_{7/2}$ and $^4F_{9/2}$ from the $^4I_{11/2}$ manifold (excitation wavelength at 965nm) due to cooperative energy transfer upconversion. Broadening effects were observed for both the green and the red. These linewidth broadening effects were likely caused by dislocations or interstitial defects within the crystalline structure that distorted the crystal lattice [6.10]. Homogeneous and inhomogeneous process could be possible contributions to the broadening of linewidths. Due to the broadening effects, the peaks shifted to 564nm and 682nm at the green and red emissions respectively. The increase in peak red emission with increasing Er^{3+} concentration was also observed by *Capobianco* [6.11] when nanocrystalline Er_2O_3 was doped in bulk and cubic Y_2O_3 crystal.

To obtain a better understanding of the changes of the green and red intensities at different dopant concentrations, the upconversion intensity ratio (UIR) of the green over the red emission versus the dopant concentrations were plotted. The peak at 563nm (G_{563}) in the green emission and at 681nm (R_{681}) were chosen. Dividing the peak intensity at I_{681} by peak intensity at I_{563}, these ratios were then used to form a relationship with the dopant level, see Figure 7.44. It was observed that as the concentration level increased, the intensity ratio between the two peaks increased correspondingly. At low concentrations, virtually no increment was seen. Intensity

ratios only increased at the high concentrations. 59mol% was not included due to the change in peaks wavelengths.

Figure 7.38: Spec 42 – Y_2O_3:Er^{3+} (0.03mol%)
Upconversion spectrum

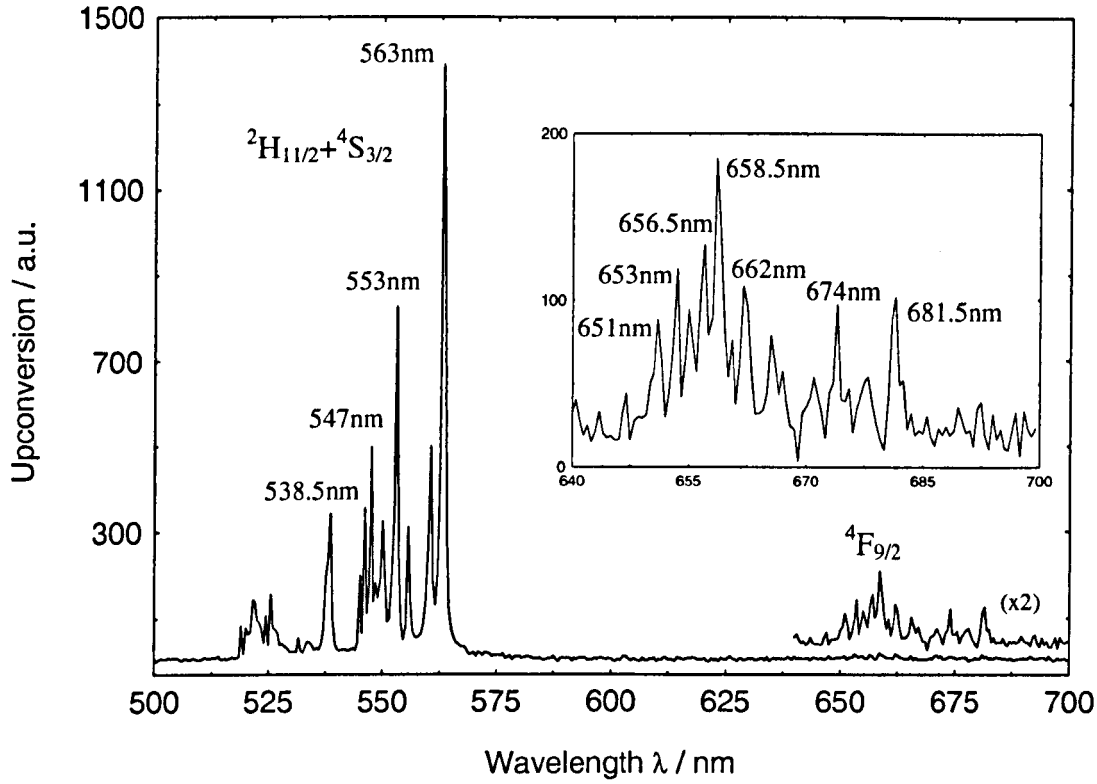

Figure 7.39: Spec 43 – Y_2O_3:Er^{3+} (0.06mol%)
Upconversion spectrum

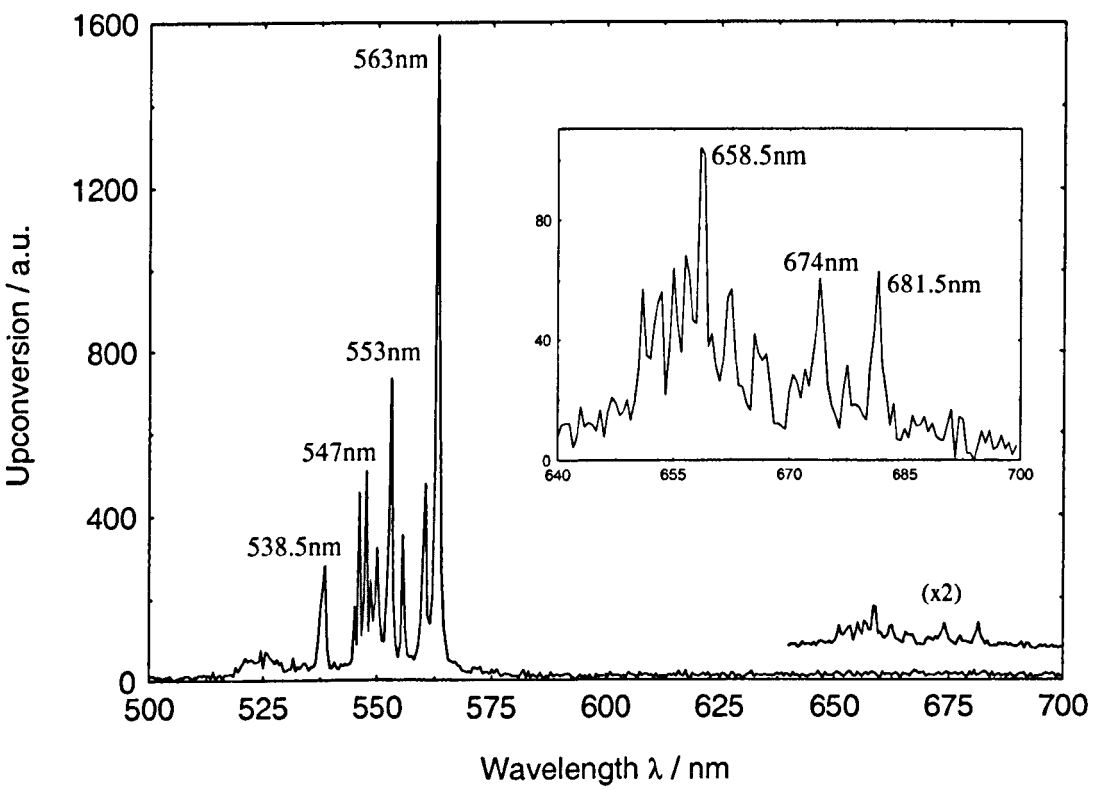

Figure 7.40: Spec 44 – $Y_2O_3:Er^{3+}$ (0.3mol%)
Upconversion spectrum

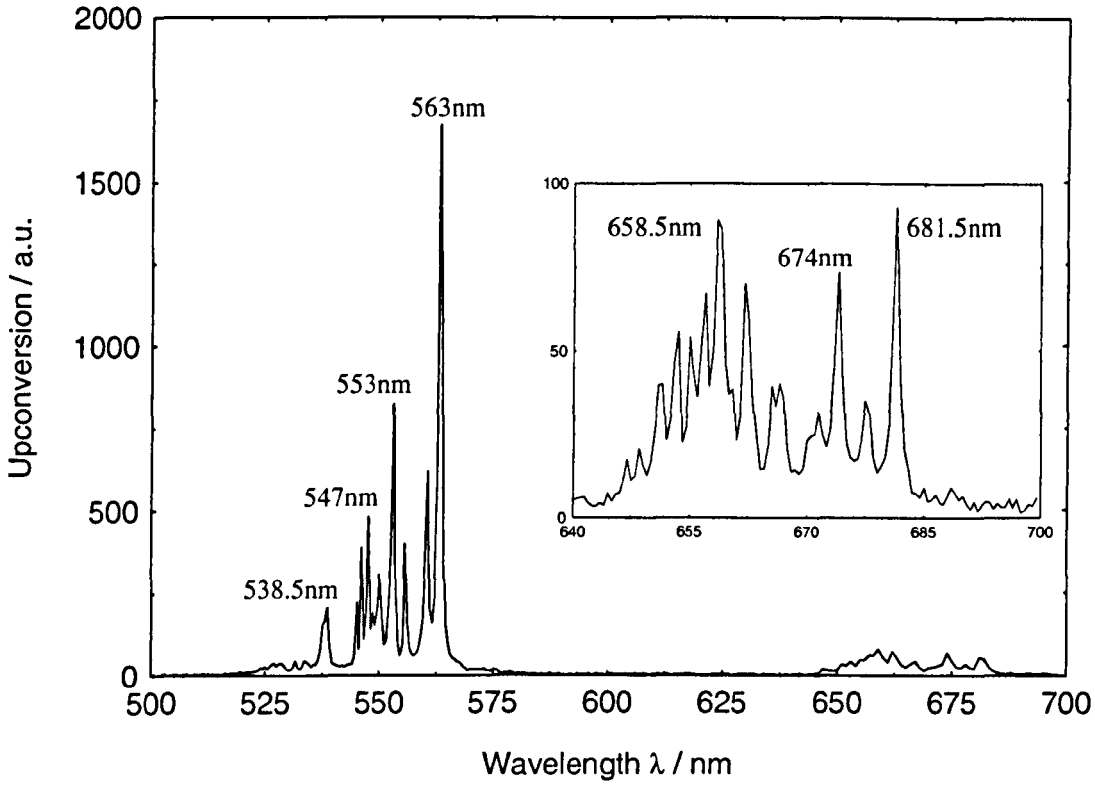

Figure 7.41: Spec 18 – $Y_2O_3:Er^{3+}$ (3.1mol%)
Upconversion spectrum

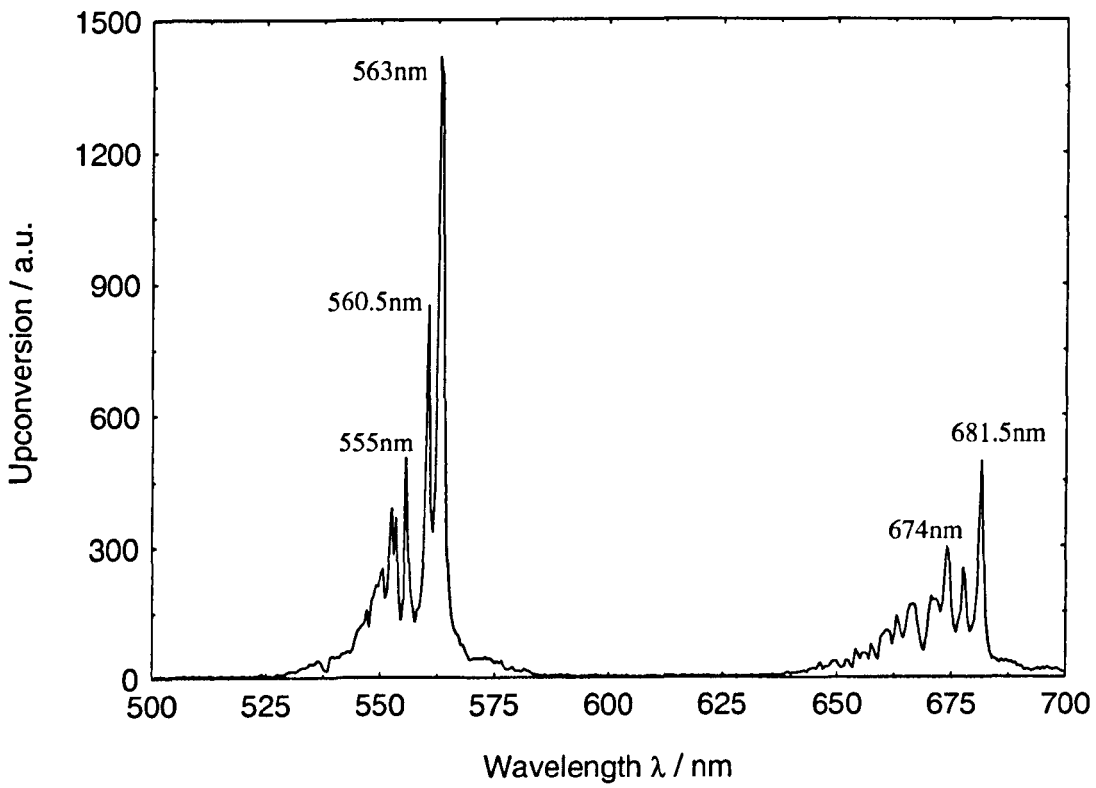

Figure 7.42: Spec 20 – $Y_2O_3:Er^{3+}$ (6mol%)
Upconversion spectrum

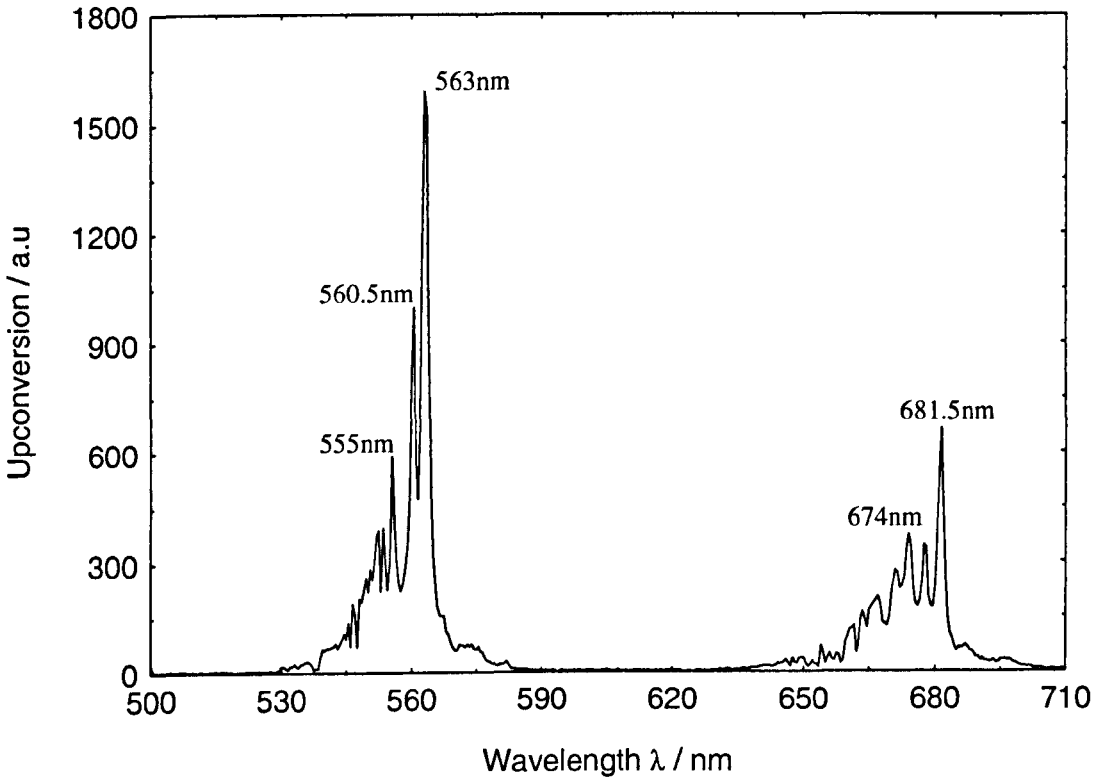

Figure 7.43: Spec 19 – $Y_2O_3:Er^{3+}$ (59mol%)
Upconversion spectrum

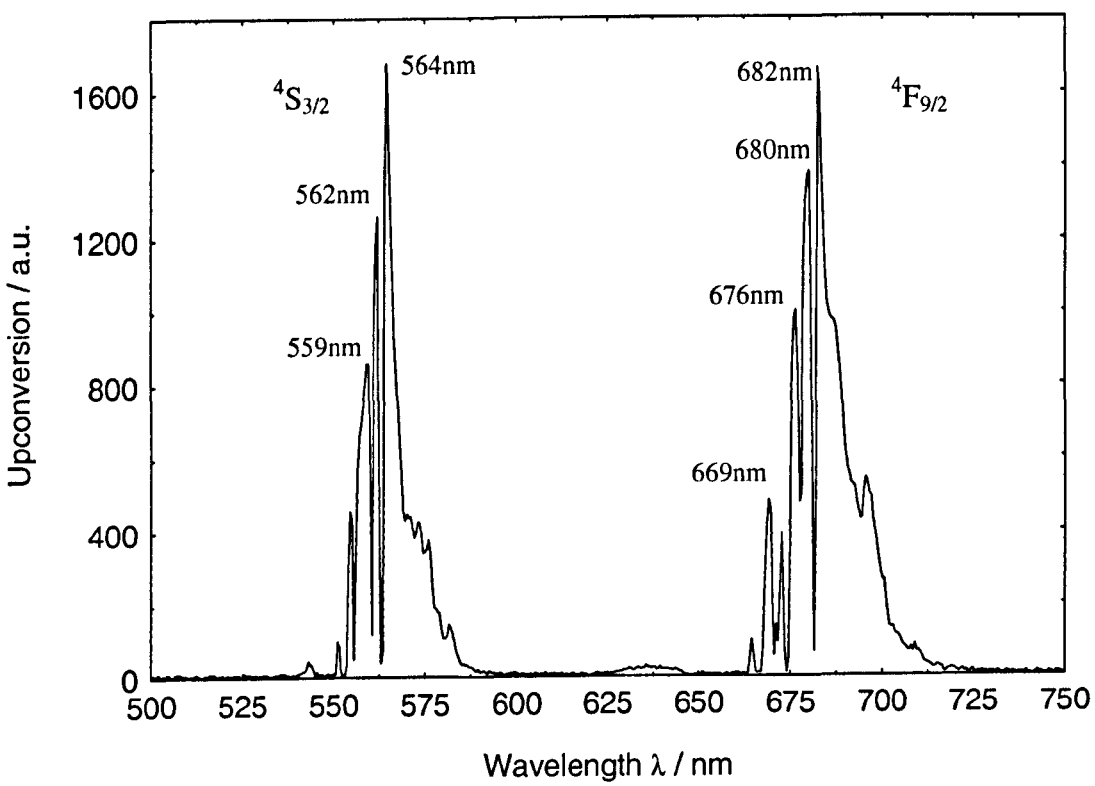

Figure 7.44: Upconversion intensity ratio (UIR) R_{681}/G_{563}

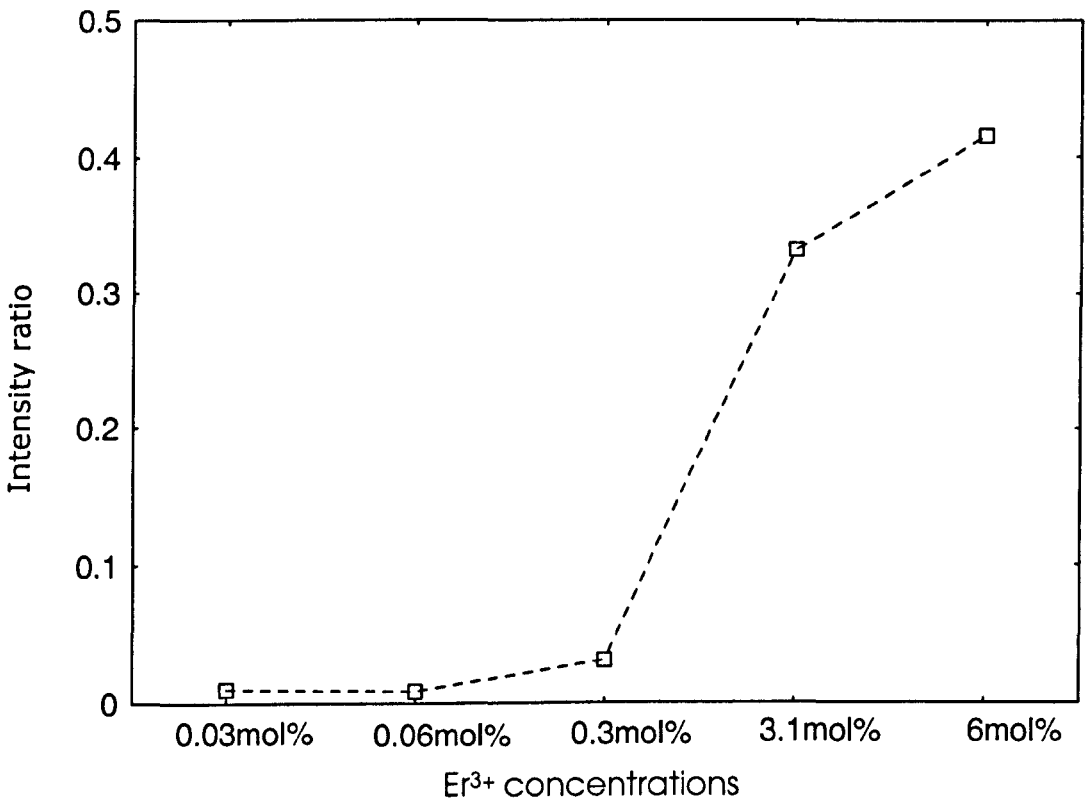

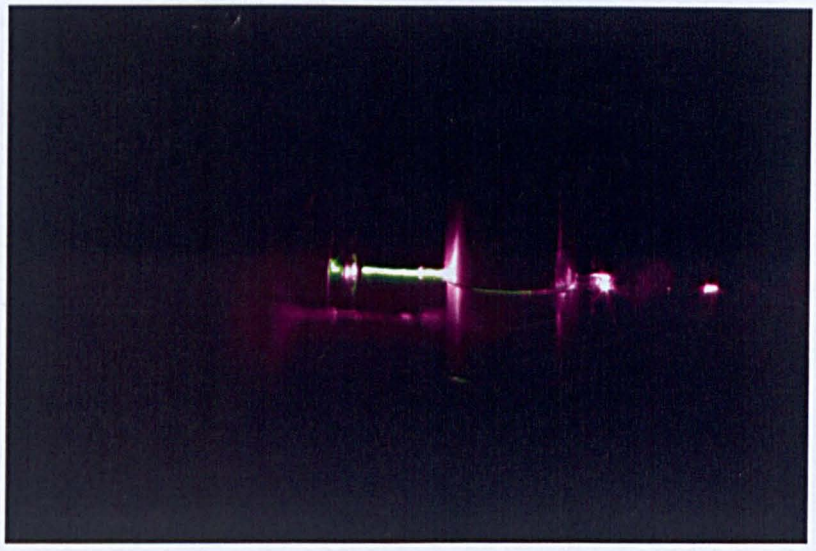

Figure 7.45 – Spec 42 $Y_2O_3:Er^{3+}$ (0.03mol%) SCF green emission

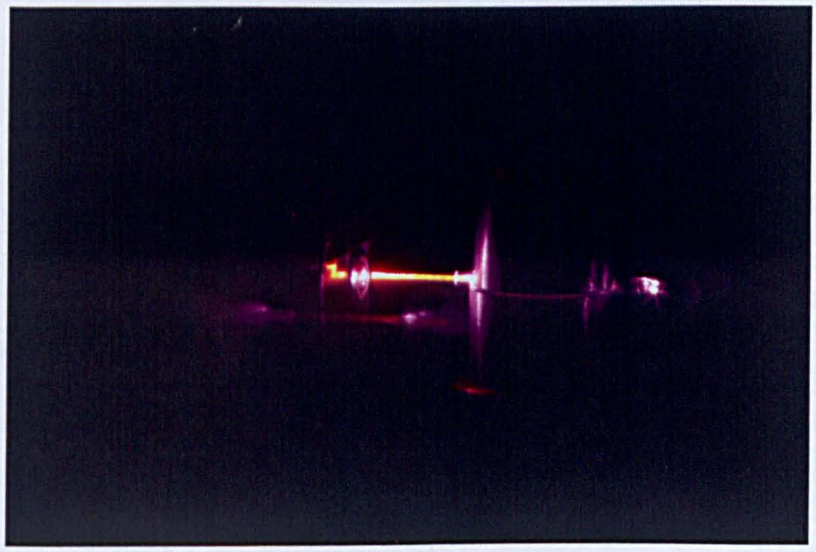

Figure 7.46 – Spec 19 $Y_2O_3:Er^{3+}$ (59mol%) SCF green and red Emission

7.7 Fluorescence Lifetime Measurement

The measurement of the fluorescence lifetime was carried out for the Er^{3+} doped Y_2O_3 fibres at the $^4I_{11/2} \rightarrow {}^4I_{15/2}$ and $^4I_{13/2} \rightarrow {}^4I_{15/2}$ transitions. The peak at 1010nm in the $^4I_{11/2}$ manifold and the two peaks at 1530nm and 1550nm in the $^4I_{13/2}$ manifold were the strongest, and the lifetimes at these wavelengths were studied in detail. The overall decay within the $^4I_{13/2}$ manifold was also investigated. These results were recorded in this section. Refer to Chapter 5.3.3 for experimental layouts.

7.7.1 Results and Discussion

From the fluorescence spectra in section 7.5, it was observed that there were several strong emission peaks from the $^4I_{11/2}$ and $^4I_{13/2}$ manifolds. Fluorescence lifetime measurements were taken for peaks at 1010nm, 1530nm and 1550nm, and integrated over the transition $^4I_{13/2} \rightarrow {}^4I_{15/2}$. Figures 7.47 to 51 show a single exponential profile of the fluorescence lifetime for the variously doped fibres at 1010nm. The squares in the figures indicate the experimental data whereas the solid lines were fitted by EASYPLOT. At a concentration of 59mol%, the 1010nm peak was replaced by measurements at 1028.5nm. See Figure 7.33. Therefore, this fibre was not included in the subsequent comparisons. The r^2 values for the low dopant concentrations of 0.03, 0.06 and 0.3mol% were further away from 1 as compared to the higher concentration levels. 0.03mol% was the furthest from unity as compared with the other fibres investigated for this peak. See Figure 7.47.

The signals received by the photodetector were relatively weak for the low concentration fibres. As shown previously as concentration levels increased, the intensity of the transition at the $^4I_{11/2} \rightarrow {}^4I_{15/2}$ transition also increased improving signal quality and signal-to-noise ratio. The increasing intensity can be seen the decay profile in Figures 7.48 to 51 where the r^2 values were closer to unity. The use of the monochromator as a bandpass filter also further weakened the signal as the radiation from the fibres had to travel through the monochromator before reaching the photodetector. Employing a proper bandpass filter at this wavelength would further enhance the signal-to-noise ratio. Figure 7.52 shows the fluorescence lifetime of the fibres versus dopant concentration and it is observed that at 0.03mol%, the average fluorescence lifetime, τ, was significantly lower than the rest. There is an

increase in τ at 0.06mol% to 3.3ms and it remained in the 3ms region for other dopant concentrations. For these fibres, it is observed that there is no significant increase or decrease in lifetime but it remains consistently within the 3ms region from 0.06mol% to 6mol% of Er^{3+} doped in Y_2O_3. To see a more distinct trend line, additional ranges of concentrations would be are required. Table 7.3 shows the average fluorescence lifetime of the fibres at 1010nm.

The next fluorescence lifetime was investigated at 1530nm. The fibre dopant at 59mol% did not exhibit any emission in the 1500nm region. Therefore, comparison was only done for the other five concentration levels. Figures 7.53 to 57 show the typical fluorescence lifetime profile. Since the peak at 1530nm was the strongest for the low concentration fibres, it accounted for the increase in signal-to-noise ratio for these fibres. The increase in r^2 value (closer to 1) for these fibres signified that the emission at peak 1530nm was stronger. See Figures 7.53 to 55. Figure 7.58 shows that increased concentration leads to increase in the fluorescence lifetime, τ. Table 7.3 lists the average τ, at 1530nm. Again, when measuring τ at 1550nm, Er^{3+}:Y_2O_3 at 59mol% did not show any emission. Therefore, it was again excluded from this comparison. Figures 7.59 to 63 show the decay profile at 1550nm. Since the peak at 1550nm was the weaker as compared with 1530nm, therefore the noise level also decreased. The r^2 values at low concentrations were once again the furthest from unity. Figure 7.64 shows τ against the dopant concentration. An increase in dopant concentration increased the value of τ. Table 7.3 shows the fluorescence lifetime of the fibres at 1550nm.

The last fluorescence lifetime measurement was done across the entire transition $^4I_{13/2} \rightarrow {}^4I_{15/2}$. Figures 7.65 to 70 show the exponential lifetime profiles of all the fibres at this transition. It was observed that in all the experiments, at 0.03mol% concentration the signal-to-noise ratio was the weakest and the possible reason was the low dopant level within the fibre. From Figure 7.71, increasing dopant levels again increased the value of τ. However at high concentrations (59mol%), the decay lifetime decreased. The results in this work are in agreement with the work done by *Laversenne* [5.8] and *Auzel* [7.9]. As the dopant concentration increased, the τ value increased with it. τ would then reach a plateau and would subsequently decrease if the more Er^{3+} was included in the fibre. *Auzel* showed in his work that at approximately 6mol%, τ began to decrease and at 60mol%, it fell to the 1ms region –

a result in agreement with this work. The decrease in lifetime at high concentration dopant levels is likely due to concentration quenching and de-excitation of the emitting level of Er^{3+} by cooperative energy transfer or/and excited state absorption [5.8]. Table 7.4 shows the fluorescence lifetime, τ, of all the fibres at this transition.

Figure 7.47: Spec 42 – $Y_2O_3:Er^{3+}$ (0.03mol%)
Fluorescence lifetime (τ) at 1010nm

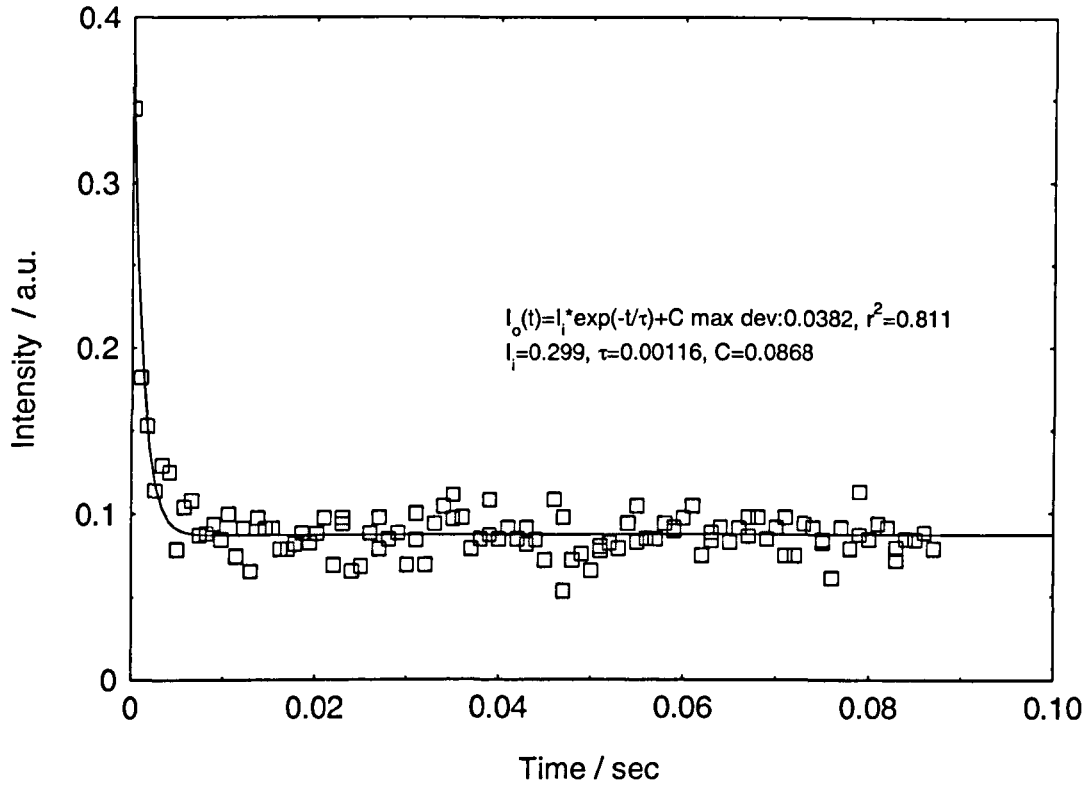

Figure 7.48: Spec 43 – $Y_2O_3:Er^{3+}$ (0.06mol%)
Fluorescence lifetime (τ) at 1010nm

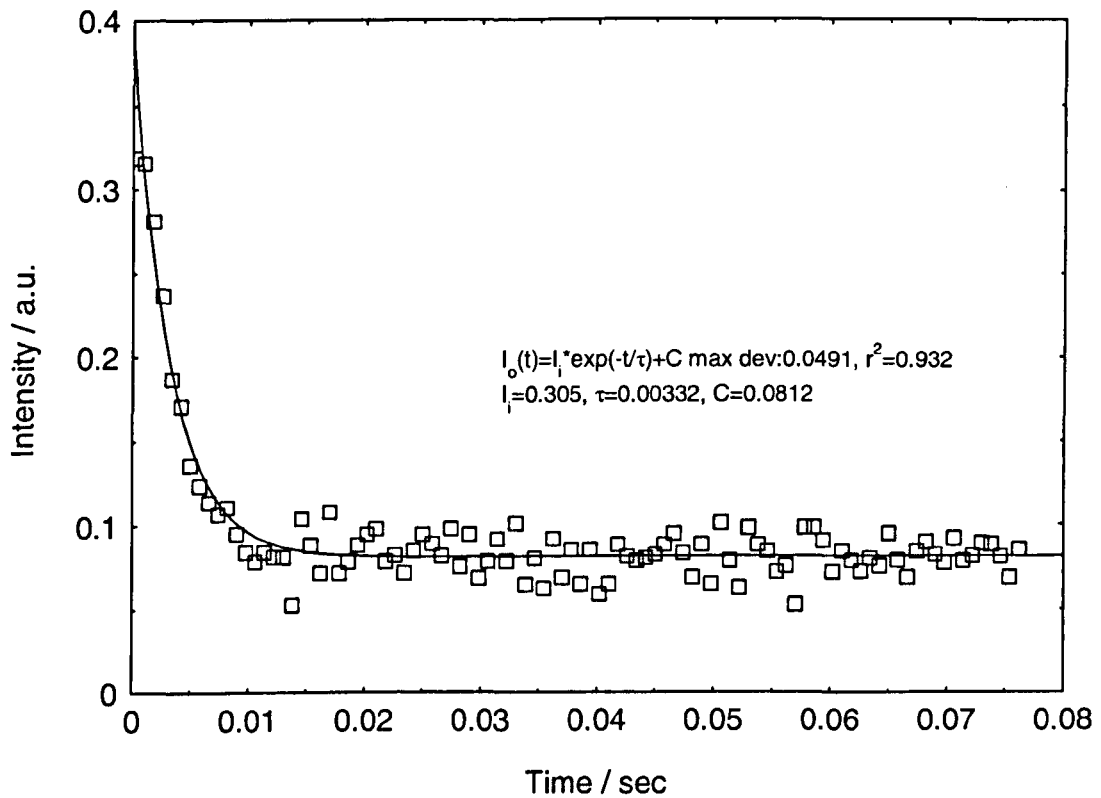

Figure 7.49: Spec 44 – $Y_2O_3:Er^{3+}$ (0.3mol%)
Fluorescence lifetime (τ) at 1010nm

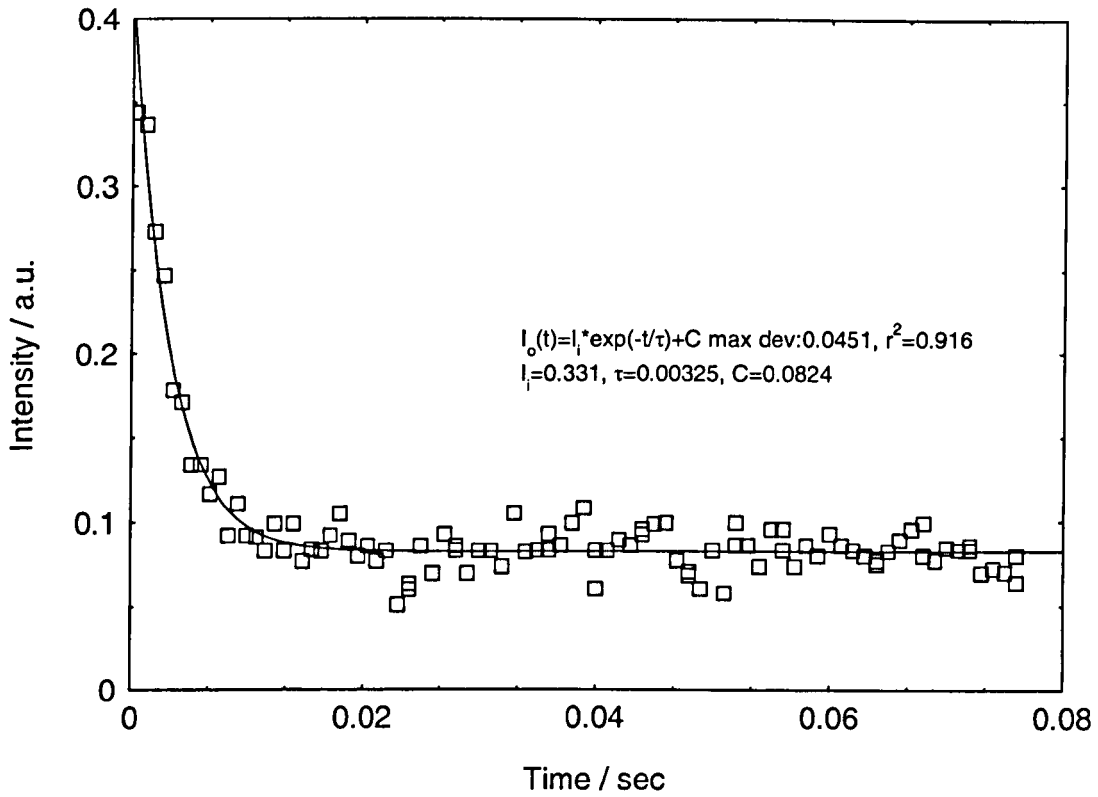

Figure 7.50: Spec 18 – $Y_2O_3:Er^{3+}$ (3.1mol%)
Fluorescence lifetime (τ) at 1010nm

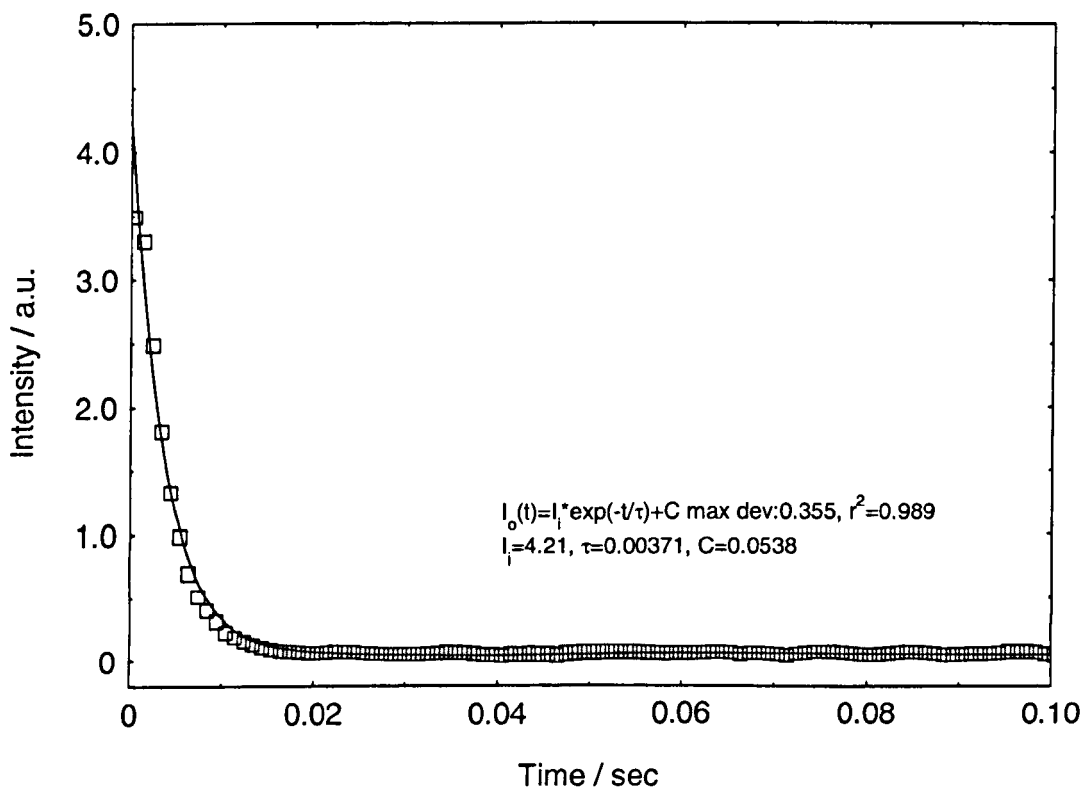

Figure 7.51: Spec 20 – $Y_2O_3:Er^{3+}$ (6mol%) Fluorescence lifetime (τ) at 1010nm

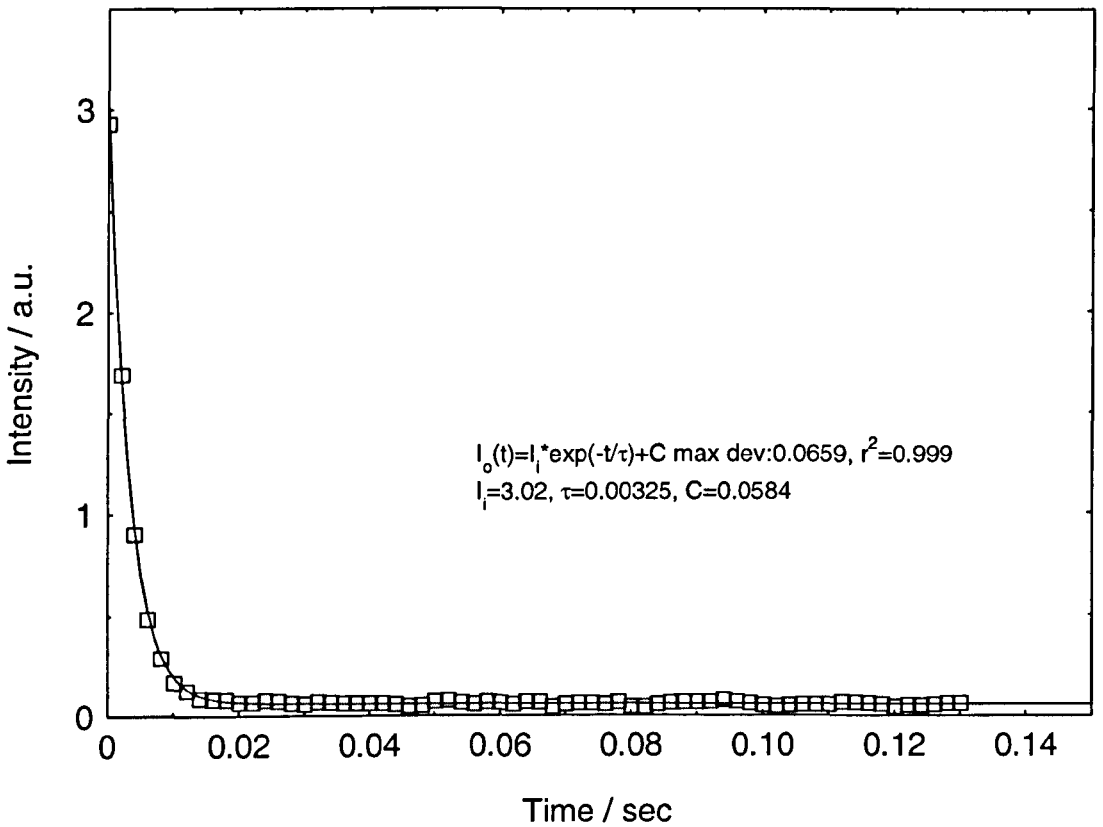

Figure 7.52: $Y_2O_3:Er^{3+}$ Fluorescence lifetime (τ) at 1010nm

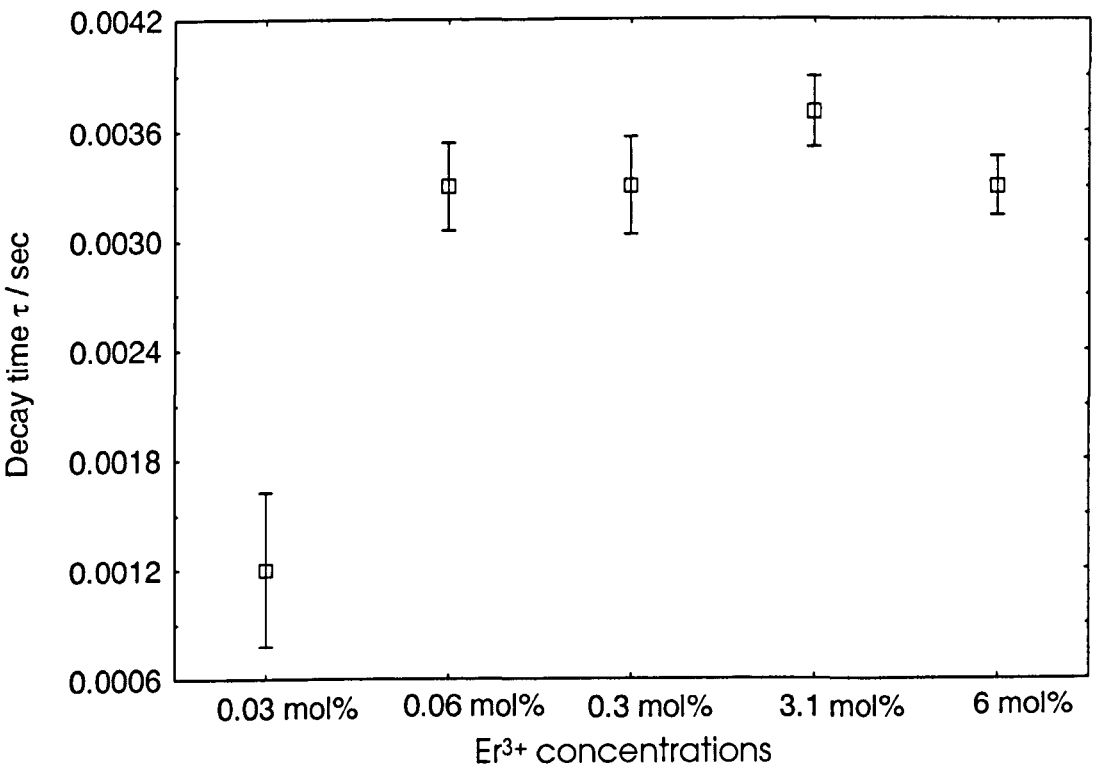

Table 7.4 - $Y_2O_3:Er^{3+}$ Fluorescence lifetime (τ) at different wavelength

Dopant level (mol%)	1010nm (τ) ms	1530nm (τ) ms	1550nm (τ) ms	$^4I_{13/2}$ (τ) ms
0.03	1.2	8.2	8.1	7.4
0.06	3.3	8.9	8.3	8.5
0.3	3.7	9.1	8.8	9.2
3.1	3.3	10.4	10.7	10.8
6	2.9	12.6	10.8	12.4
59	-	-	-	1.7

Figure 7.53: Spec 42 – $Y_2O_3:Er^{3+}$ (0.03mol%)
Fluorescence lifetime (τ) at 1530nm

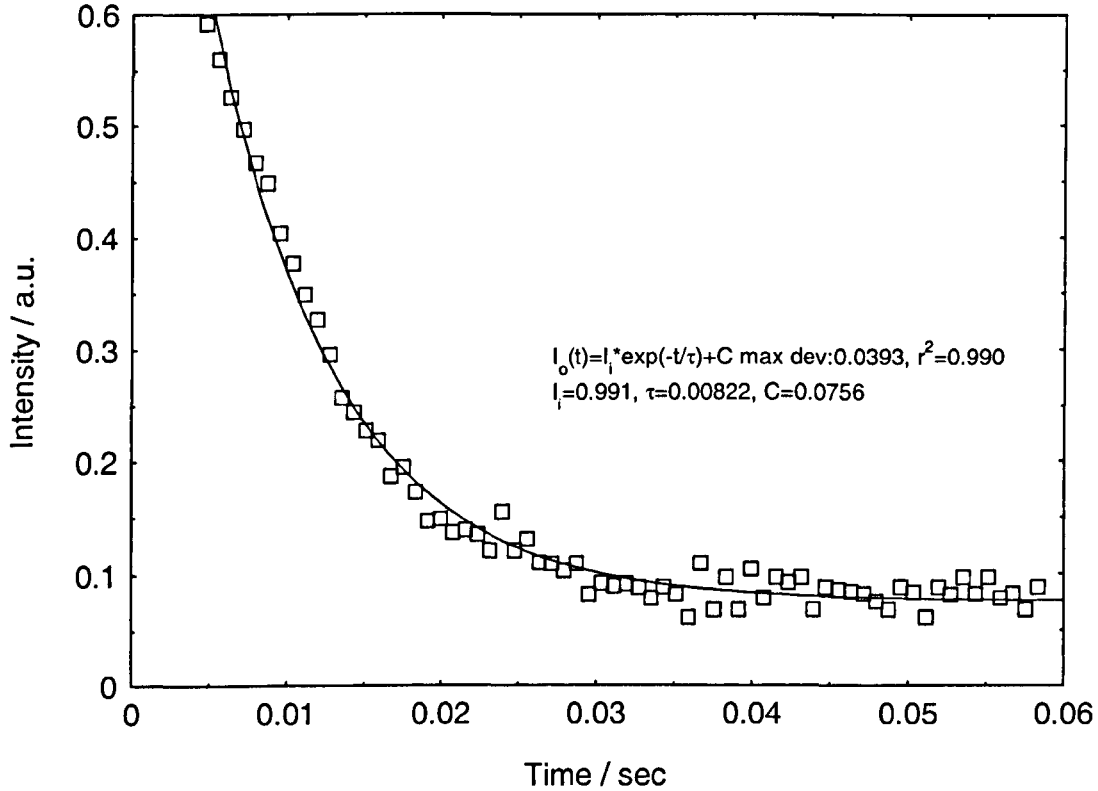

Figure 7.54: Spec 43 – $Y_2O_3:Er^{3+}$ (0.06mol%)
Fluorescence lifetime (τ) at 1530nm

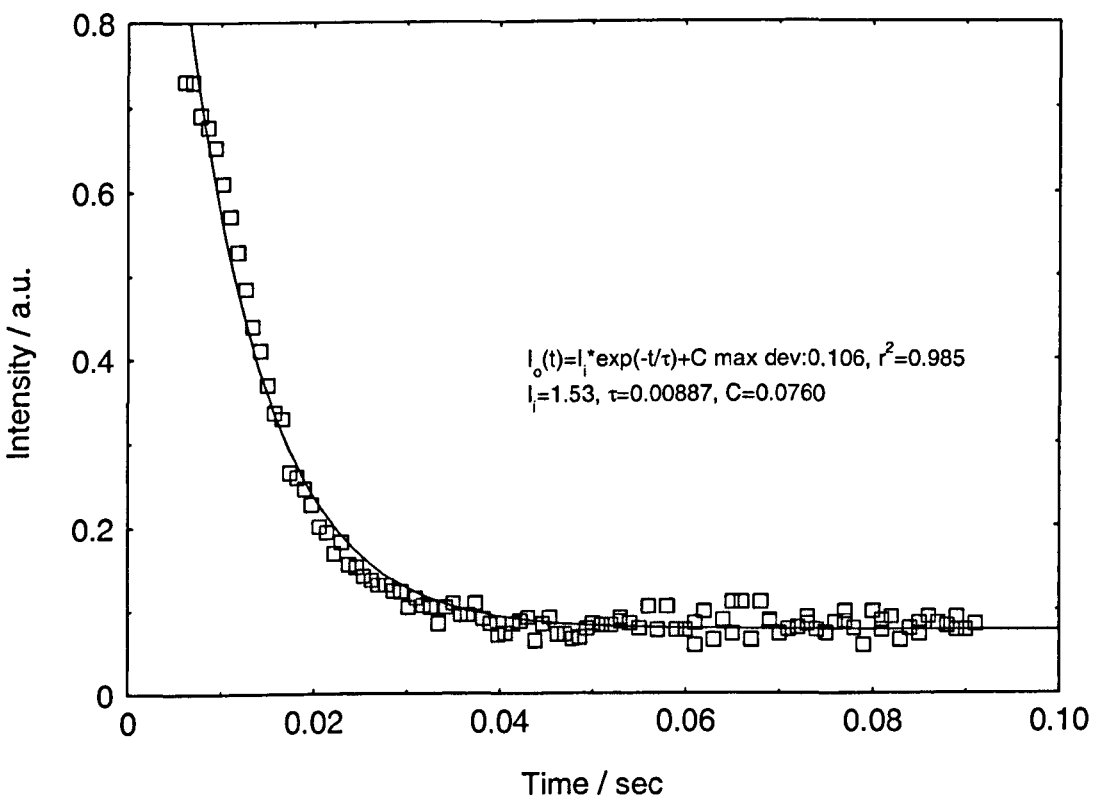

Figure 7.55: Spec 44 – $Y_2O_3:Er^{3+}$ (0.3mol%)
Fluorescence lifetime (τ) at 1530nm

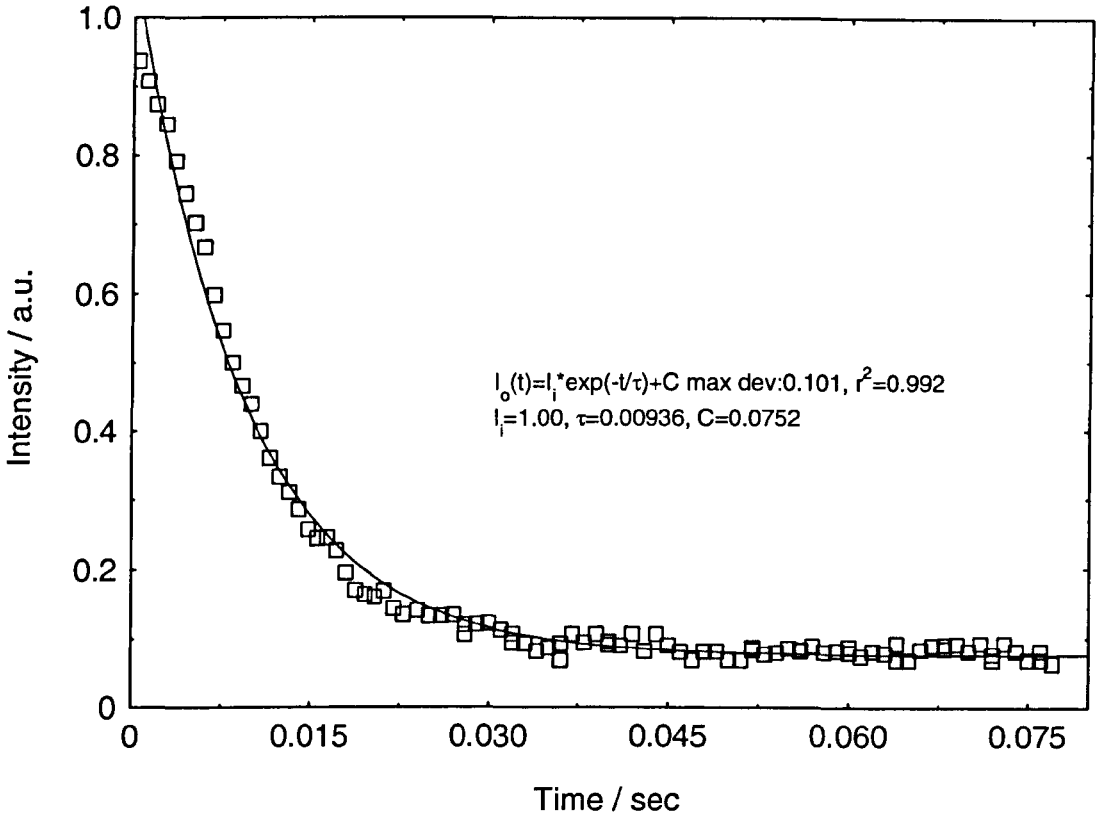

Figure 7.56: Spec 18 – $Y_2O_3:Er^{3+}$ (3.1mol%)
Fluorescence lifetime (τ) at 1530nm

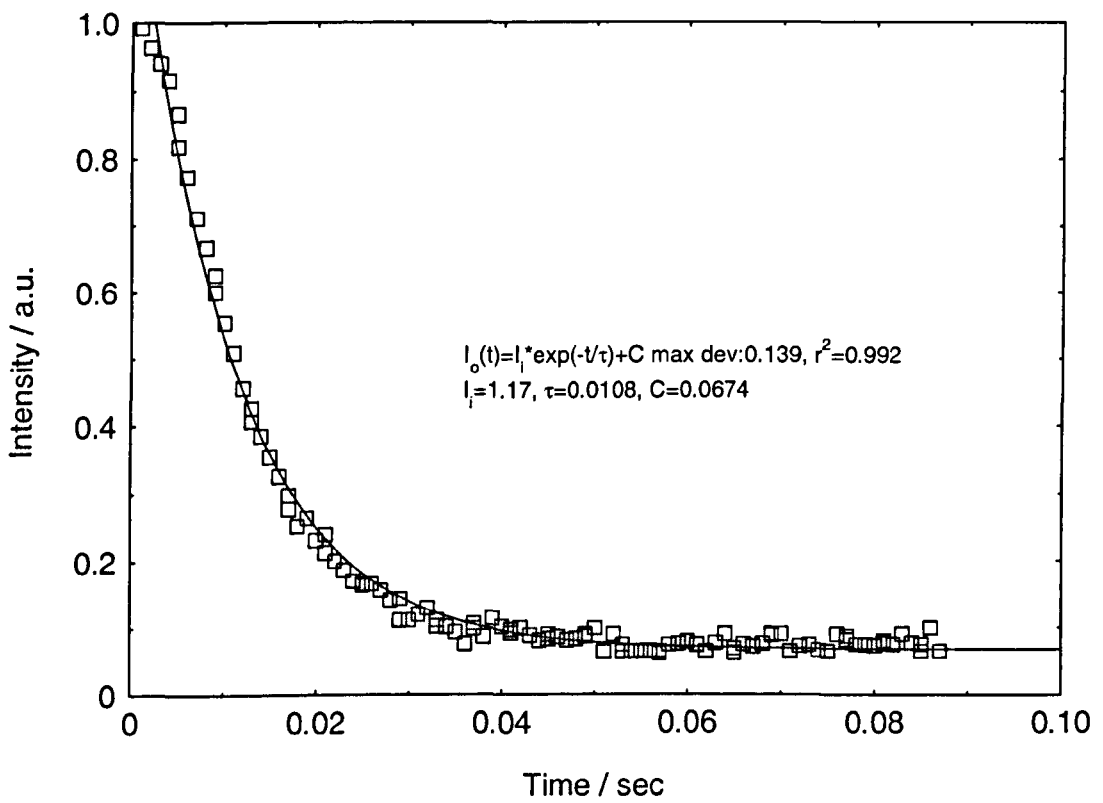

Figure 7.57: Spec 20 – $Y_2O_3:Er^{3+}$ (6mol%) Fluorescence lifetime (τ) at 1530nm

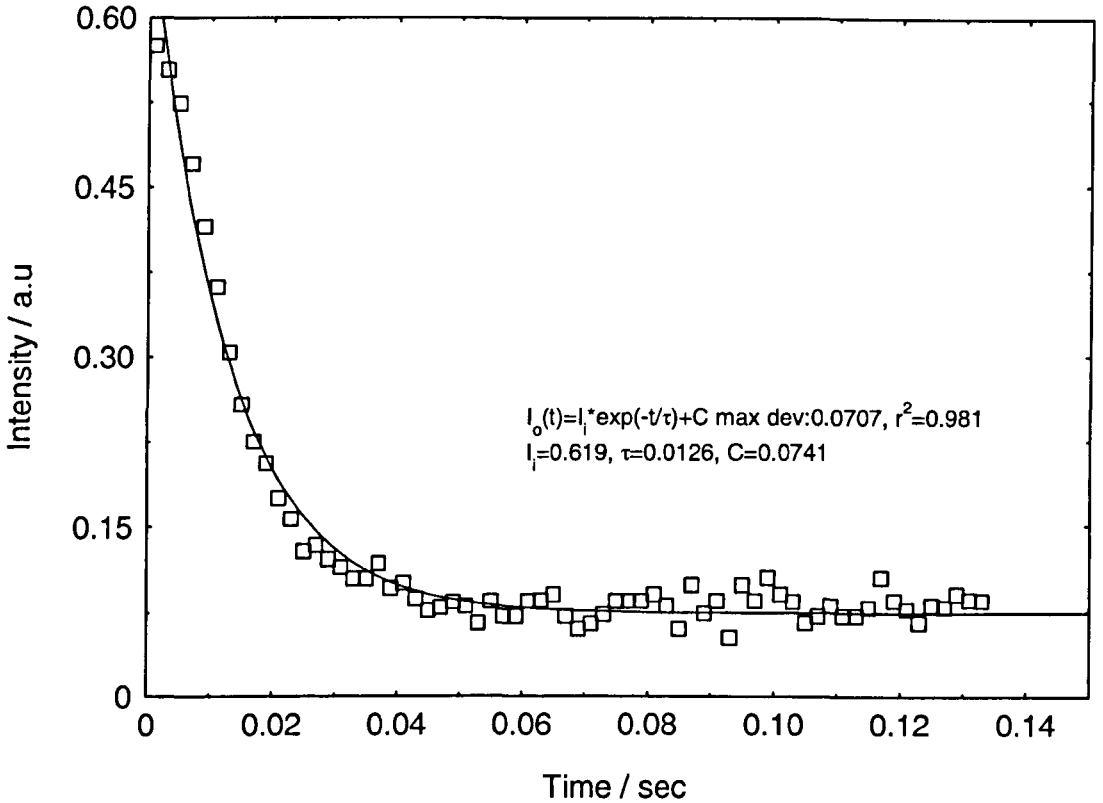

Figure 7.58: $Y_2O_3:Er^{3+}$ Fluorescence lifetime (τ) at 1530nm

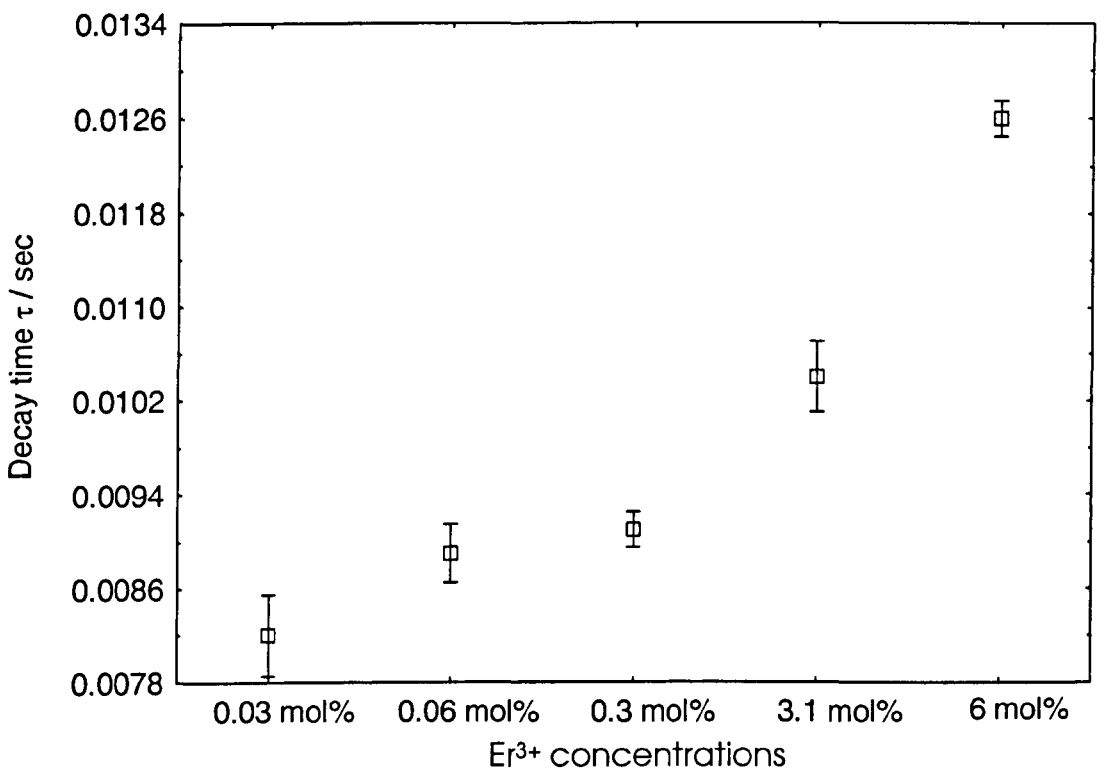

Figure 7.59: Spec 42 – $Y_2O_3:Er^{3+}$ (0.03mol%)
Fluorescence lifetime (τ) at 1550nm

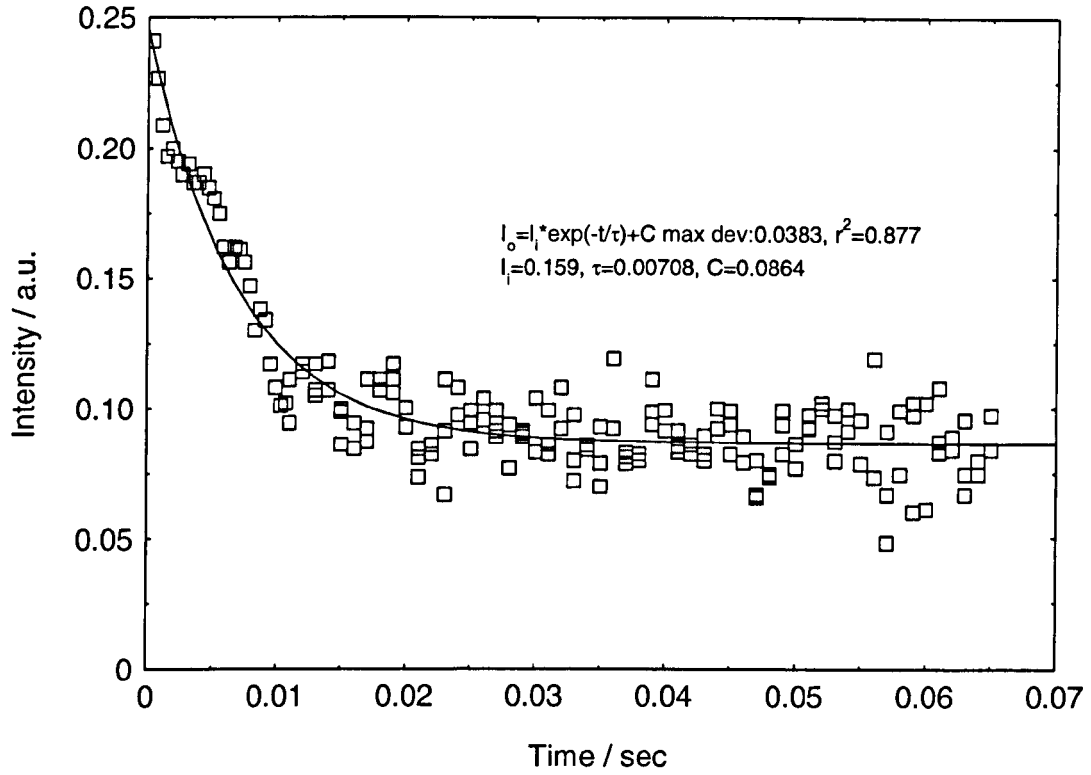

Figure 7.60: Spec 43 – $Y_2O_3:Er^{3+}$ (0.06mol%)
Fluorescence lifetime (τ) at 1550nm

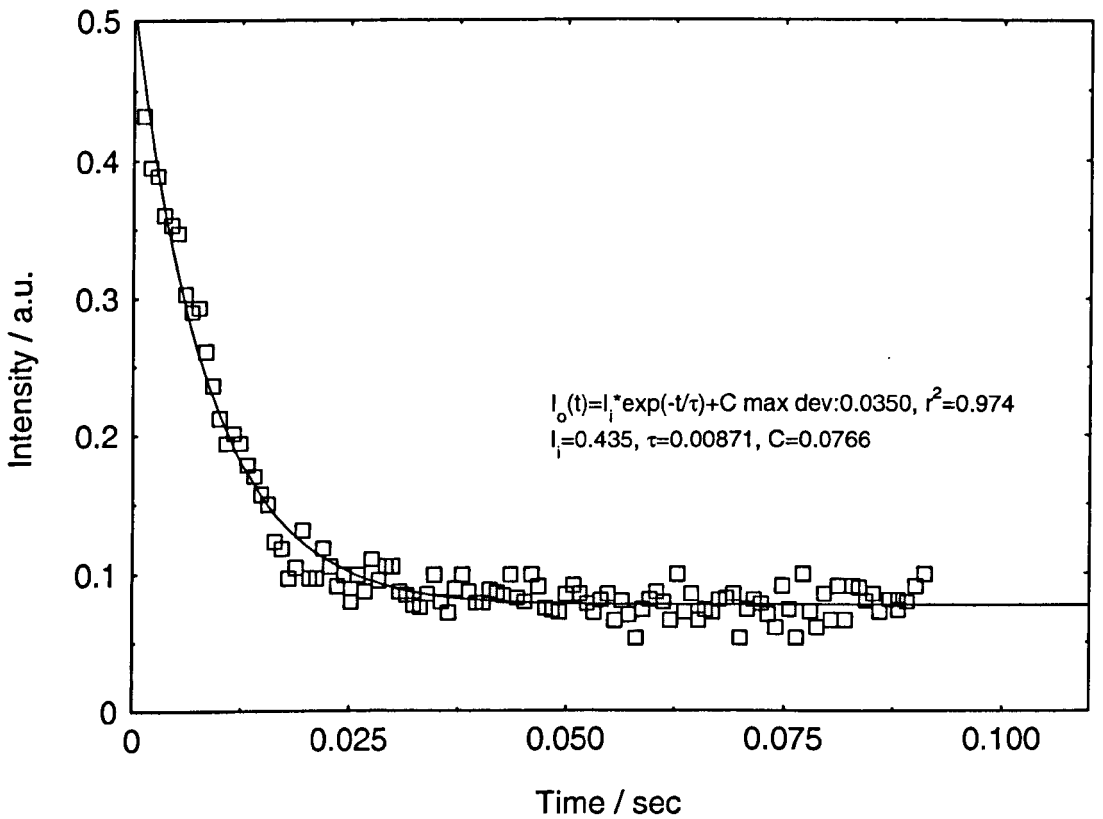

Figure 7.61: Spec 44 – $Y_2O_3:Er^{3+}$ (0.3mol%)
Fluorescence lifetime (τ) at 1550nm

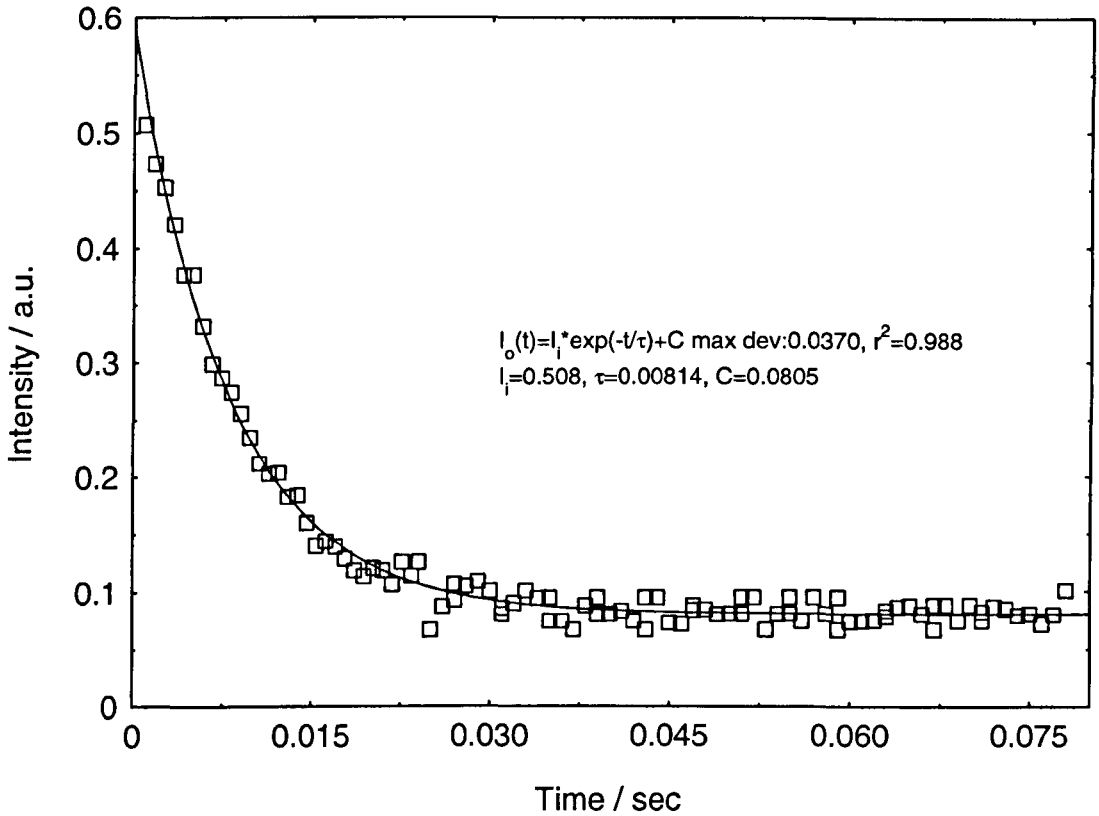

Figure 7.62: Spec 18 – $Y_2O_3:Er^{3+}$ (3.1mol%)
Fluorescence lifetime (τ) at 1550nm

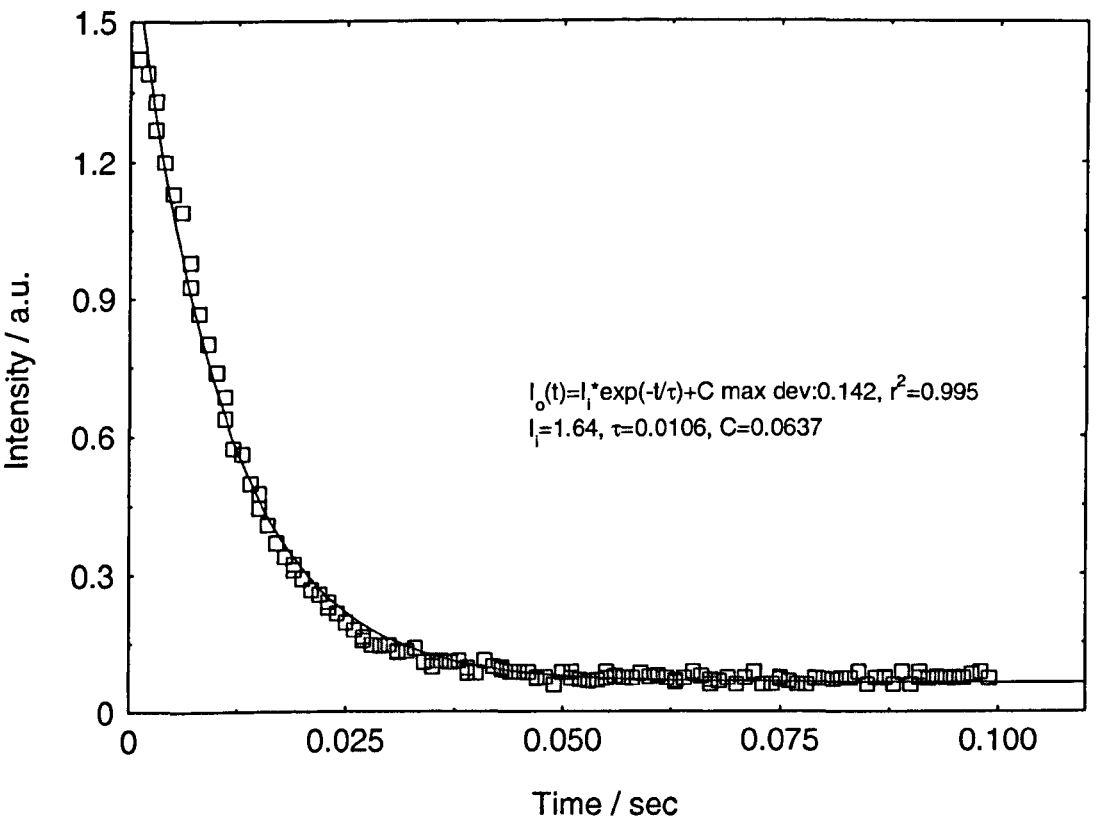

Figure 7.63: Spec 20 – $Y_2O_3:Er^{3+}$ (6mol%) Fluorescence lifetime (τ) at 1550nm

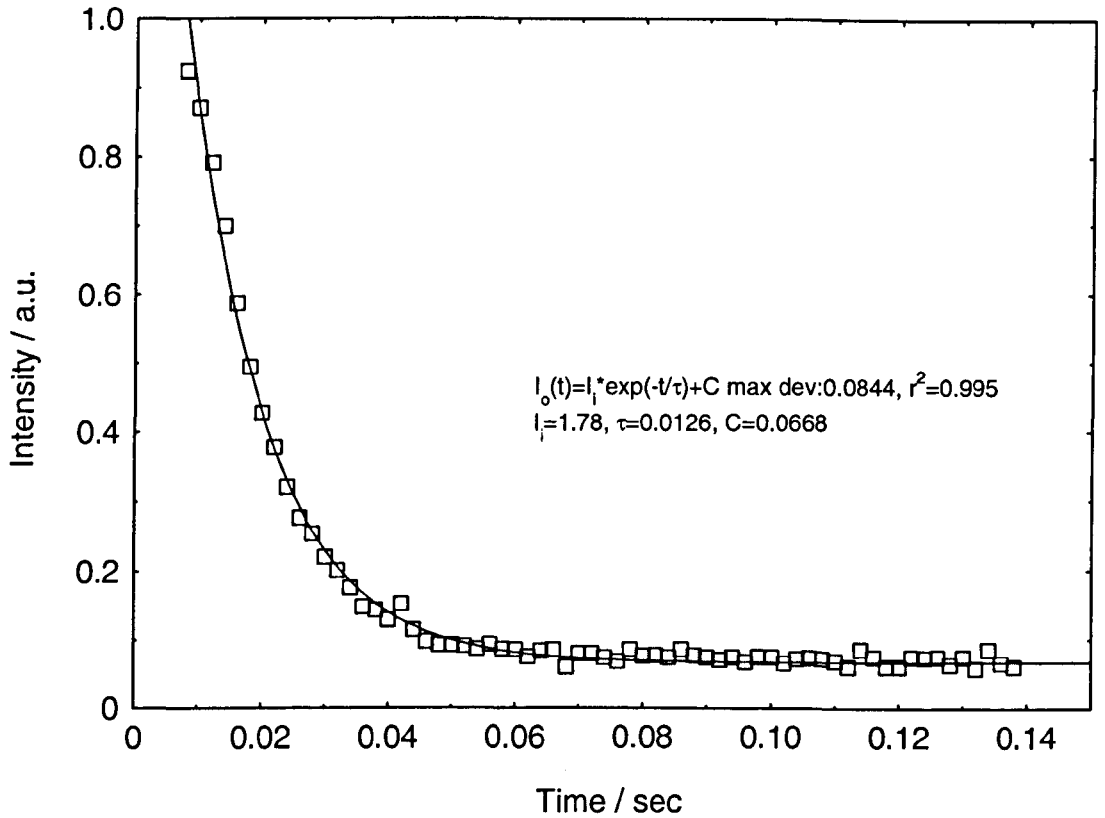

Figure 7.64: $Y_2O_3:Er^{3+}$ Fluorescence lifetime (τ) at 1550nm

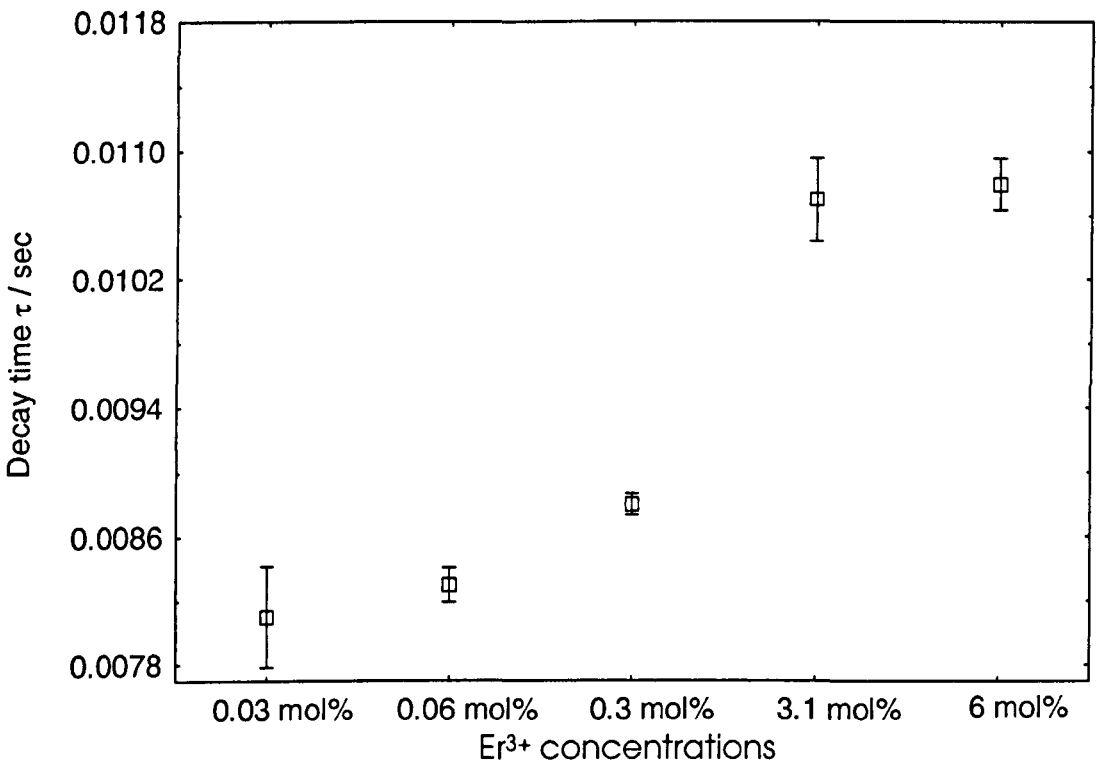

Figure 7.65: Spec 42 – $Y_2O_3:Er^{3+}$ (0.03mol%)
Fluorescence lifetime (τ) at $^4I_{13/2}$

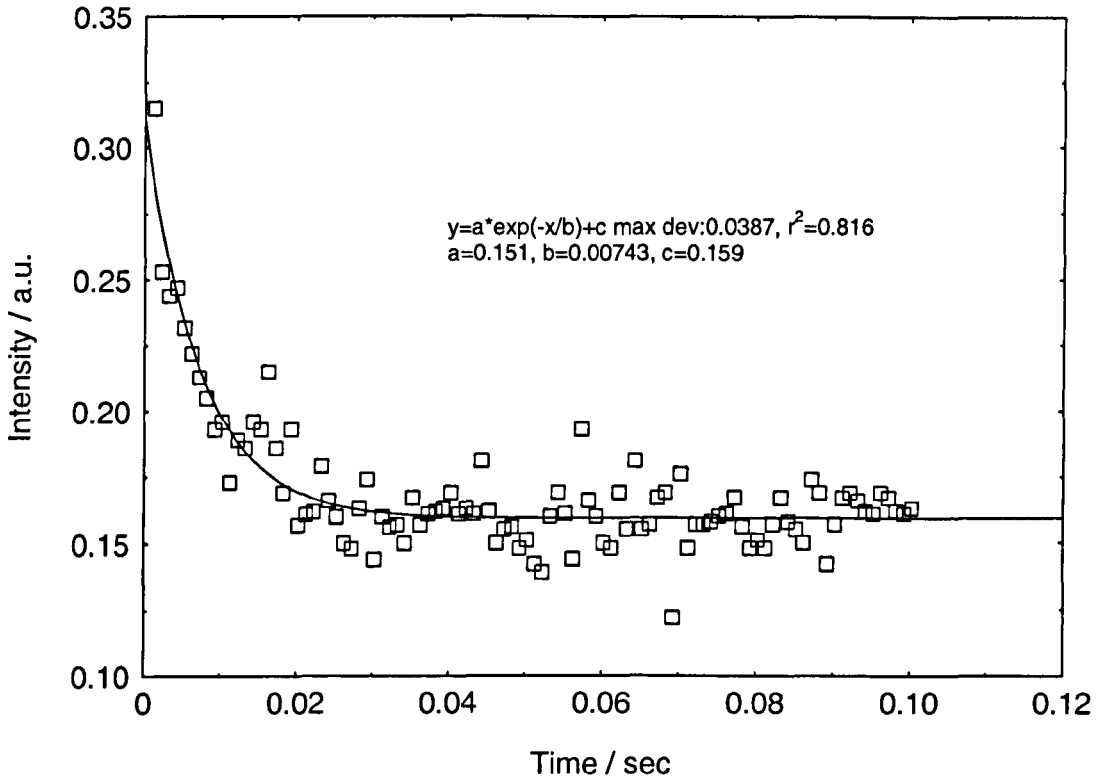

Figure 7.66: Spec 43 – $Y_2O_3:Er^{3+}$ (0.06mol%)
Fluorescence lifetime (τ) at $^4I_{13/2}$

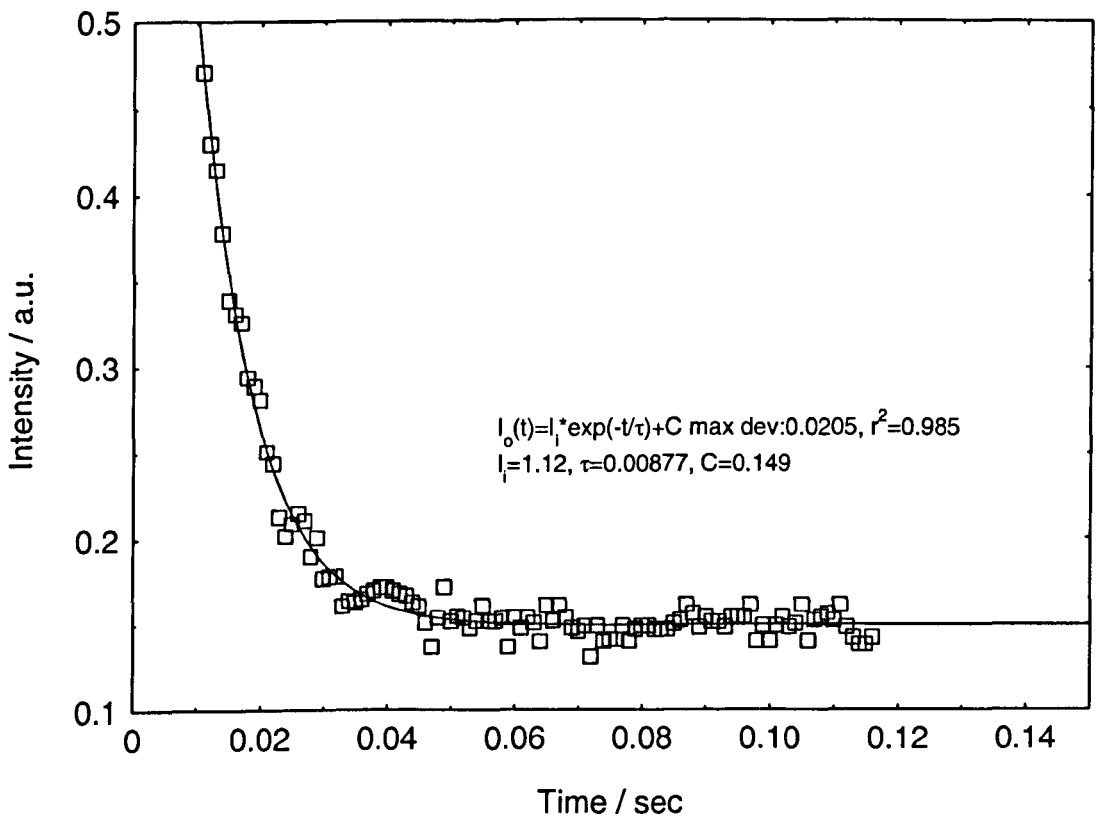

Figure 7.67: Spec 44 – $Y_2O_3:Er^{3+}$ (0.3mol%)
Fluorescence lifetime (τ) at $^4I_{13/2}$

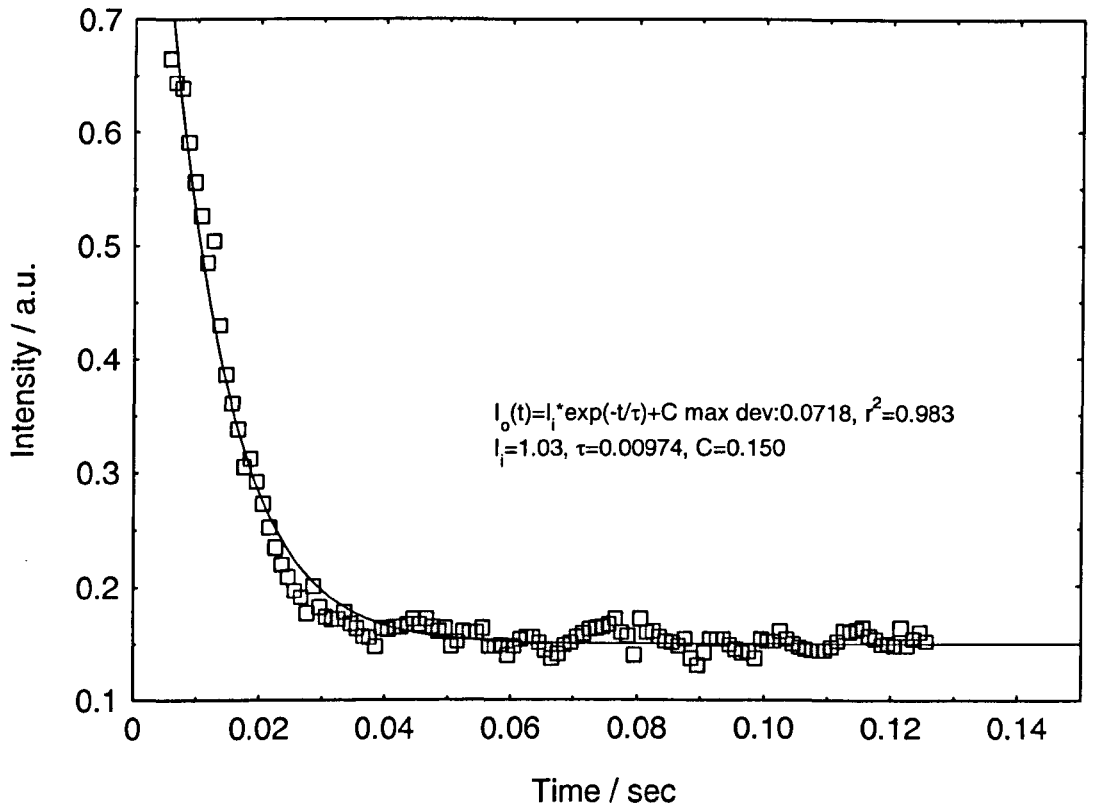

Figure 7.68: Spec 18 – $Y_2O_3:Er^{3+}$ (3.1mol%)
Fluorescence lifetime (τ) at $^4I_{13/2}$

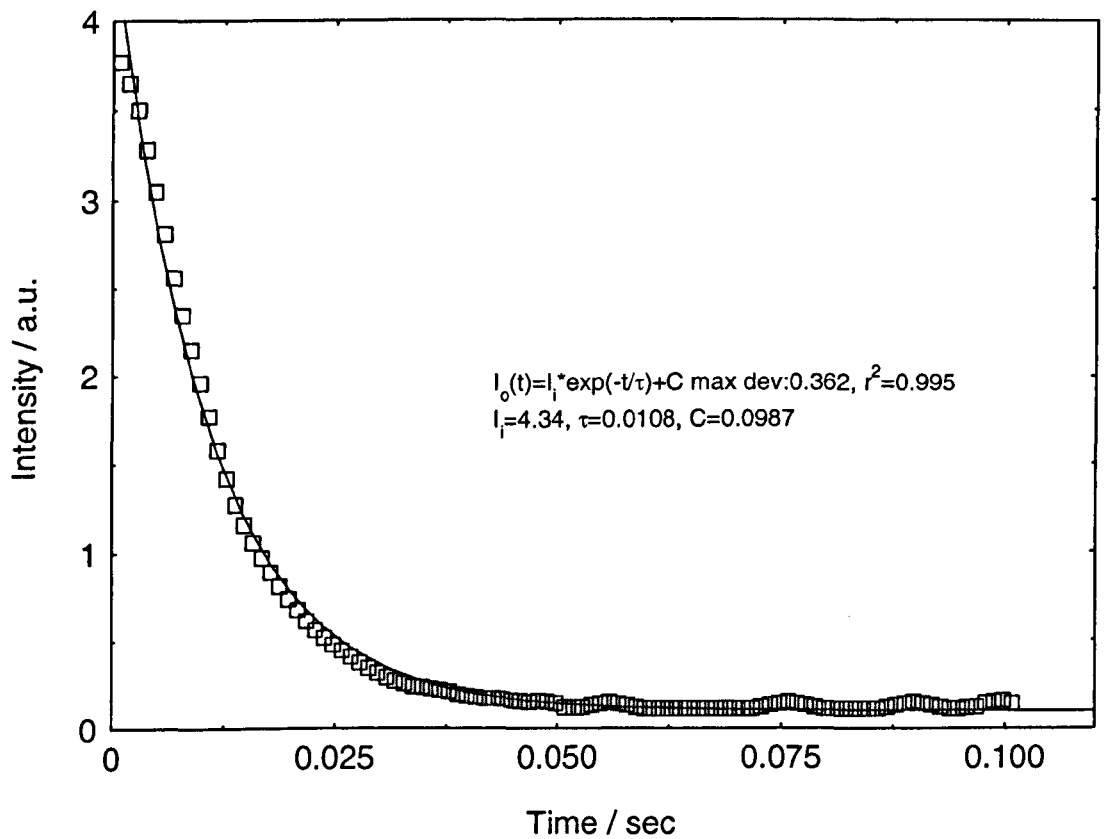

Figure 7.69: Spec 20 – $Y_2O_3:Er^{3+}$ (6mol%)
Fluorescence lifetime (τ) at $^4I_{13/2}$

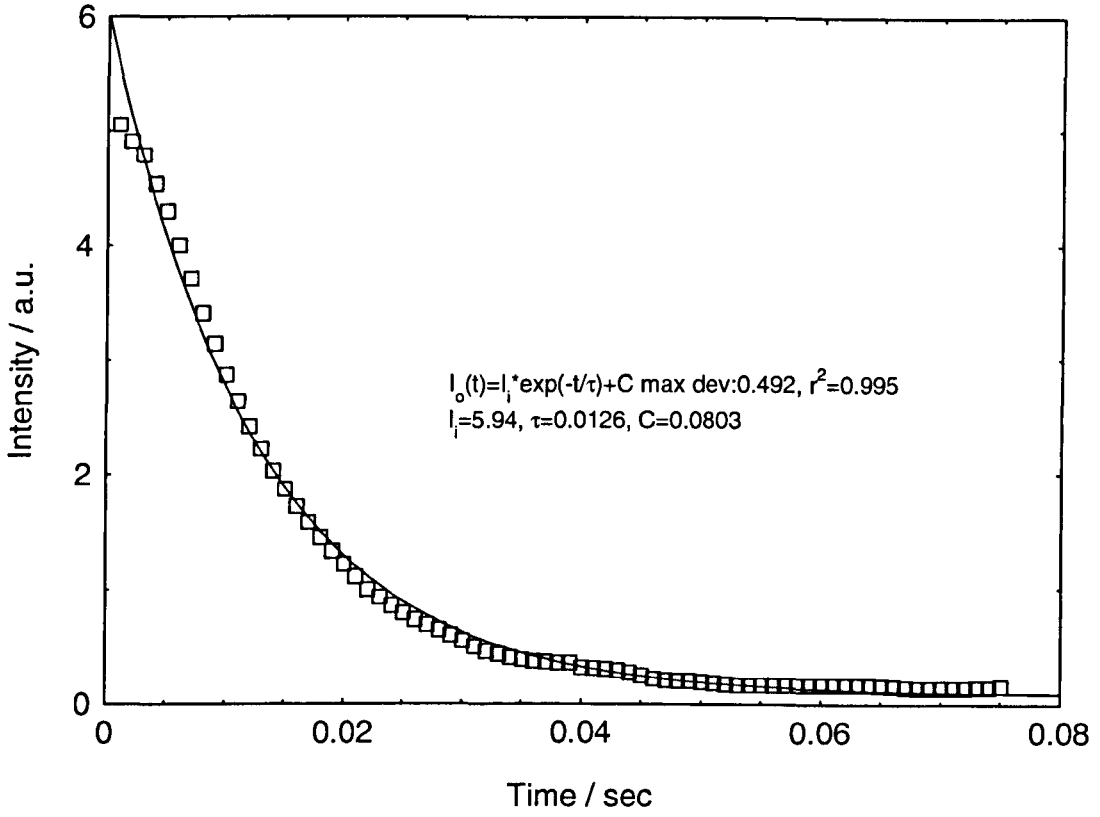

Figure 7.70: Spec 19 – $Y_2O_3:Er^{3+}$ (59mol%)
Fluorescence lifetime (τ) at $^4I_{13/2}$

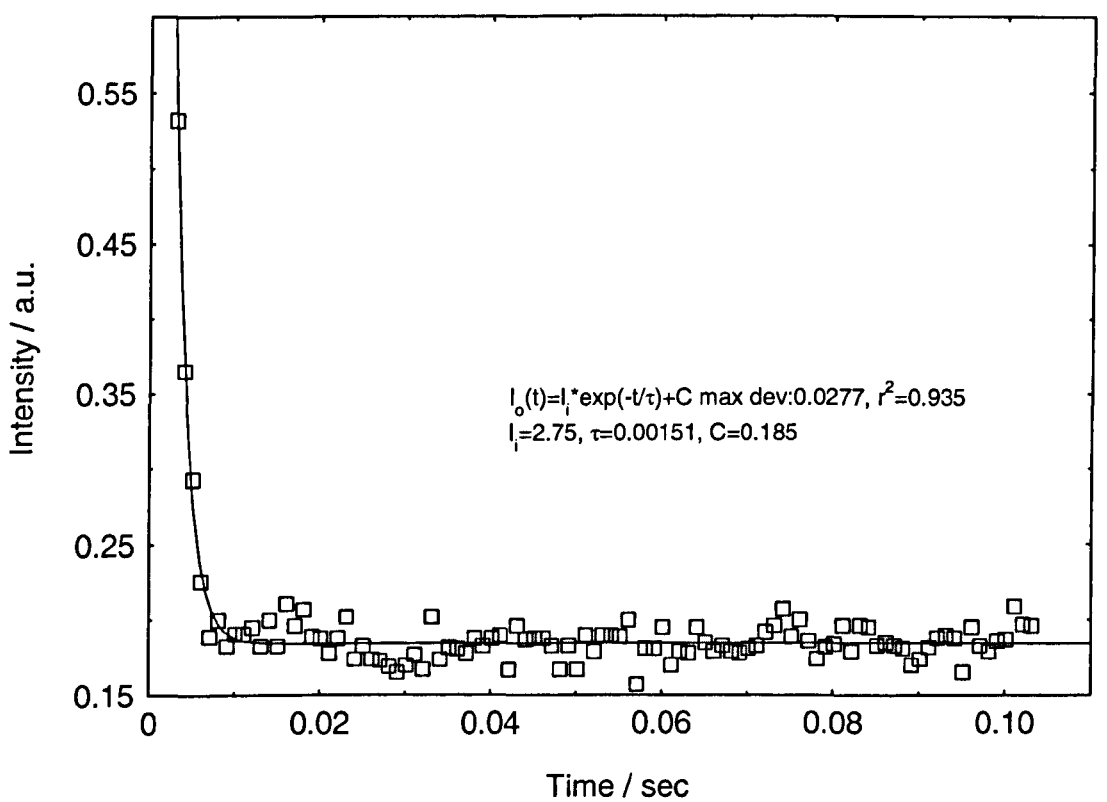

Figure 7.71: Y_2O_3:Er^{3+} Fluorescence lifetime (τ) at $^4I_{13/2}$

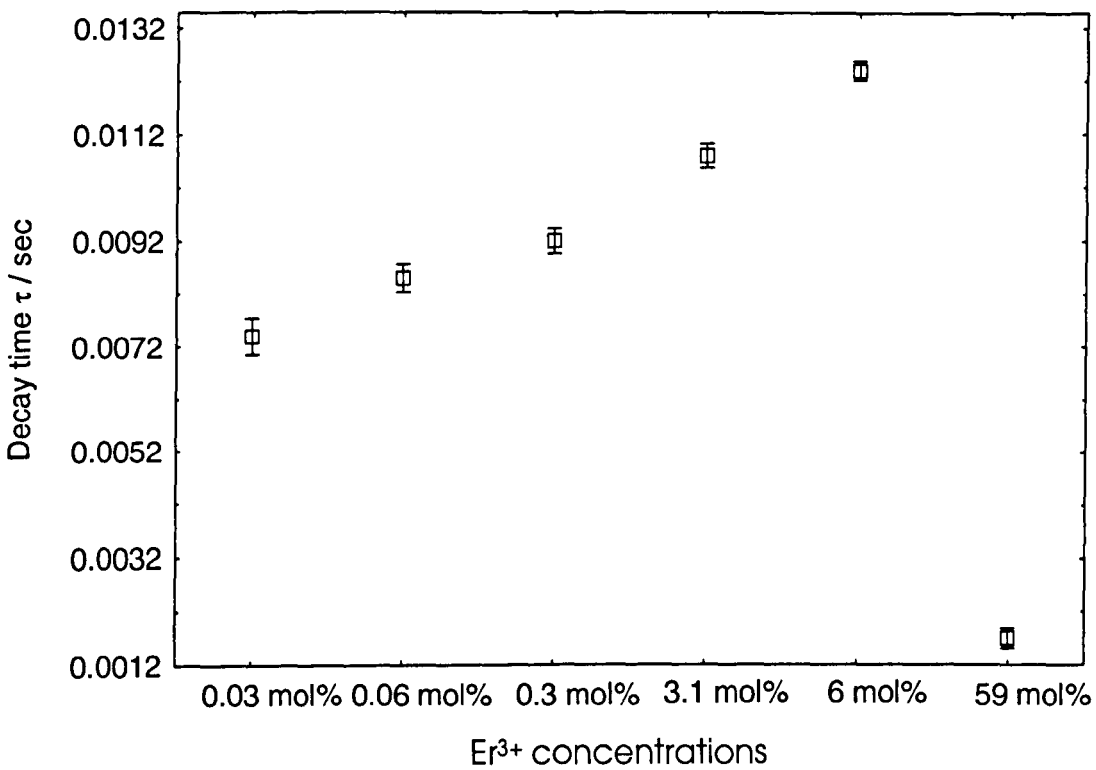

7.8 Reference

[7.1] A. Polman, *Erbium Implanted Thin Film Photonic Materials*, J. App. Phy., 82, 1, 1, 1997

[7.2] C. Goutaudier, F. S. Ermeneux, M. T. Cohen-Adad and R. Moncorge, *Growth of Pure and RE^{3+}-Doped Y_2O_3 Single Crystals by LHPG Technique*, J. Cryst. Growth, **210**, 4, 694, 2000

[7.3] A. O. G. Dikovska, P. A. Atanasov, M. Jiménez de Castro, A. Perea, J. Gonzalo, C. N. Afonso and J. G. López, *Optically Active Er^{3+}-Yb^{3+} Codoped Y_2O_3 Films Produced by Pulsed Laser Deposition*, Thin Sol. Film, **500**, 1-2, 336, 2006

[7.4] W. J. Miniscalco, *Optical and Electronic Properties of Rare Earth Ions in Glasses*, Rare Earth Doped Fiber Lasers and Amplifier, M. J. F. Digonnet (Ed), Marcel Dekker, Inc., 1993

[7.5] L. Laversenne, S. Kairouani, Y. Guyot, C. Goutaudier, G. Boulon and M. Th. Cohen-Adad, *Correlation Between Dopant Content and Excited-State Dynamics Properties in Er^{3+}-Yb^{3+}-Codoped Y_2O_3 by Using a New Combinatorial Method*, Opt. Mat., 19, 1, 59, 2002

[7.6] A. N. Georgobiani, A. N. Gruzintsev, T. V. Nikiforova, C. Barthou and P. Benalloul, *Luminescent Properties of Y_2O_3:Er^{3+}*, Inorg. Mat., 38, 10, 1199, 2002

[7.7] W. J. Miniscalco, *Optical and Electronic Properties of Rare Earth Ions in Glasses – Rare Earth Doped Fiber Lasers and Amplifiers*, M. J. F. Digonnet (ed), Marcel Dekker, Inc, New York, 1993

[7.8] M. B. Korzenski, Ph. Lecoeur, B. Mercey, P. Camy and J. L Doualan, *Low Propagation Losses of an Er:Y_2O_3 Planar Waveguide Grown by Alternate-Target Pulsed Laser Deposition*, App. Phy. Let., 78, 9, 1210, 2001

[7.9] F. Auzel, G. Baldacchini, L. Lasversenne and G. Boulon, *Radiation Trapping and Self-Quenching Analysis in Yb^{3+}, Er^{3+} and Ho^{3+} Doped Y_2O_3*, Opt. Mat., **24**, 1-2, 103, 2003

8 Al_2O_3 – Single Crystal Fibre

8.1 Introduction

Al_2O_3, or sapphire, has a broad transmission band (spanning from 0.24 to 4μm), high refractive index, high melting point (2040°C), good thermal conductivity, high tensile strength, and high hardness. Its mechanical properties are extremely attractive in structural reinforcement [8.1]. Work by *Haggerty* [2.7] showed that the mechanical strength of sapphire is excellent. Sapphire SCF's are also used for beam delivery in the medical field due to its excellent optical transmission in the mid infrared region. It is used as a waveguide delivering laser power at 2.9μm from a Er^{3+}:YAG laser [2.51]. Sapphire's low solubility in water, quality of being biologically inert, and its resistance to degradation under high powered beam delivery make it very attractive in this area. An appropriate length of fibre is essential in beam delivery. *Jundt* [8.2] was able to used LHPG to produce sapphire fibres of length 2m with a constant diameter of 110μm throughout this length. The tensile strength of sapphire fibre was discovered to be ten times that of fluoride and silver halide fibres. The sapphire fibre produced was also low in reflective losses. These observations showed that it was an excellent choice to be employed as a power delivery system for medical applications.

$Al_2O_3:Cr^{3+}$ (ruby) was the first material to be used as a solid state laser. $Al_2O_3:Cr^{3+}$ SCF's have been extensively investigated. Research carried out includes that of *Burrus* and *Stone* [2.12] on ruby clad fibres, and also work done on ruby tensile stress in relation to ruby's R lines [8.3]. Al_2O_3:Ti SCF lasers have also been greatly investigated [8.4]. Transitional metal ions like Cr^{3+} and Ti^{3+} are known to be easily incorporated into sapphire. However, the Al site is too small for substitutional replacement by rare earth ions. As such, there are difficulties in incorporating high contents of rare earth into sapphire [8.5]. Despite the difficulties, *Seat* [2.57] was able to dope at the tip of the sapphire fibre with Er^{3+} ion at a high concentration of ~12wt% where this fibre was used as a temperature sensor. In this work, pure Al_2O_3 fibres and doped fibres, both with rare earth and transition metal ions, were grown by LHPG and characterised. Diameter measurements, three-point bending tests, and absorption and fluorescence measurements were carried out. Discussions on each of

these works are made in the sections that follow. The results provided will give a review on the physical and optical status of the fibres produced.

8.2 Diameter Measurement

Al_2O_3 is relatively easy to grow. Therefore before growing other materials, Al_2O_3 was used as the initial 'test' material for the trial of the LPHG open loop growth system. Pure Al_2O_3 fibres and $Al_2O_3:Cr^{3+}$ (ruby) fibres diameters were measured. As the former's conditions of growth were kept similar, these pure Al_2O_3 fibres were used for mechanical testing measurements. In the case of the ruby fibres, two growth iterations were carried out from the bulk crystal which was the initial source material. Two ruby fibres of different diameters were produced and diameter measurements carried out. The larger diameter ruby fibre was grown from the bulk and was label in this work as 1st growth – Ruby 03 and the smaller diameter ruby fiber was grown from the Ruby 03 and was labelled as 2nd growth – Ruby 04. All fibres were in the c-axis orientation which had hexagonal cross-sections. Figure 4.4.3.4 shows the cross-section of a ruby fibre.

8.2.1 Results and Discussion

All the diameter data for the fibres were collected using the Filar Eyepiece Technique. The diameter of three pure Al_2O_3 fibres and one ruby fibre fell in the range of 400 and 450μm. The pure Al_2O_3 fibres were grown from source rods that were cold pressed. Wax binders were used to hold the Al_2O_3 powder together and this made handling easier for the roughing down process. Therefore, from Table 8.1, the diameter variation from fibre to fibre was more consistent, ~10μm, as compared to the first two materials mentioned in Chapters 6 and 7. Table 8.1 also shows the standard deviation of the fibres measured where the diameter variation error was not more than 3μm. The average diameters for the pure Al_2O_3 were in range of 393 to 402μm and fluctuations of the diameter were prominent. See Figure 8.1 to 4. For smaller diameter specimens like Ruby 04, a diameter fluctuation of 2.47% was seen which was the lowest when compared to the others. See Figure 8.4. Since Ruby 04 had a smaller diameter, the laser power required is also less. From Figure 4.3.1.3, it

can be seen that the power fluctuation was at low laser power. Again, the fluctuations along the length of the larger diameter fibres were caused by instabilities in the melt which was indirectly caused by the laser power fluctuation. Therefore, small diameter fibres such as Spec Ruby 04 generally have more consistent diameters throughout.

Table 8.1 – Al_2O_3 and $Al_2O_3:Cr^{3+}$ fibre diameter measurements

Specimen Name	Average Diameter (μm)	Standard Deviation (μm)	(%)
Spec Al30	401.60	16.27	4.05
Spec Al31	409.26	25.27	6.17
Spec Al32	393.12	17.74	4.51
Ruby 03 ($Al_2O_3:Cr^{3+}$)	444.79	40.52	9.11
Ruby 04 ($Al_2O_3:Cr^{3+}$)	226.16	5.33	2.47

Figure 8.1 : Spec Al30 – Al_2O_3 fibre diameter measurement

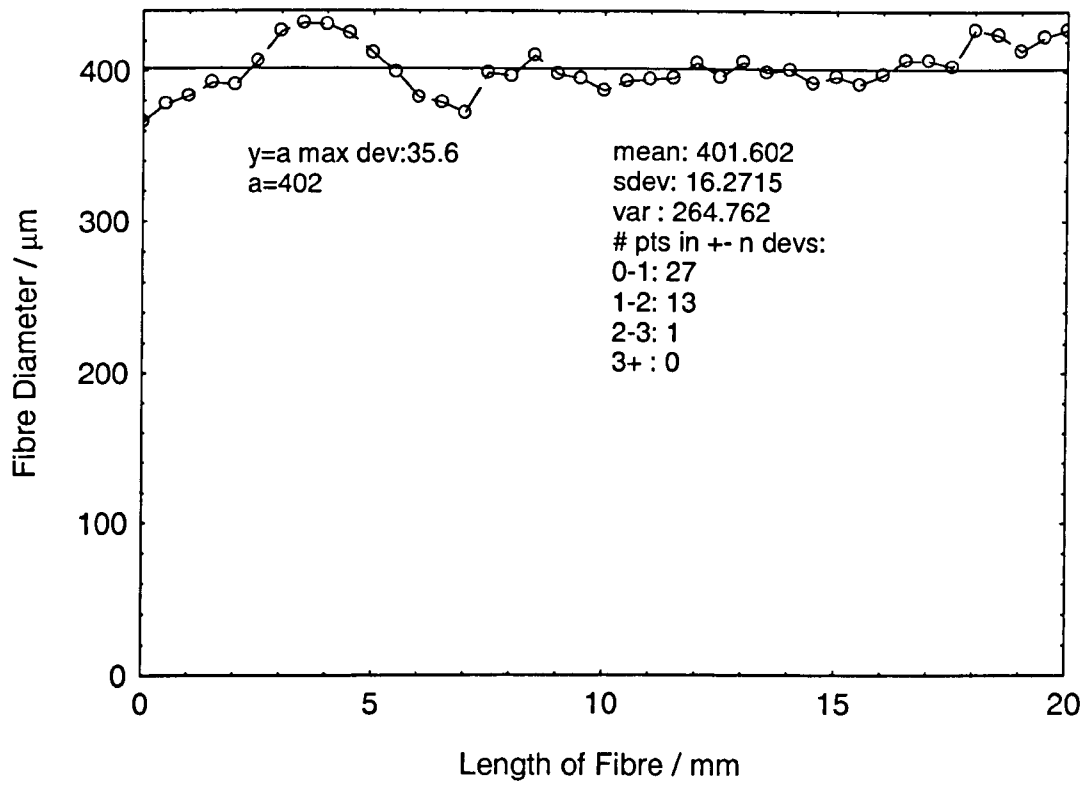

Figure 8.2 : Spec Al31 – Al_2O_3 fibre diameter measurement

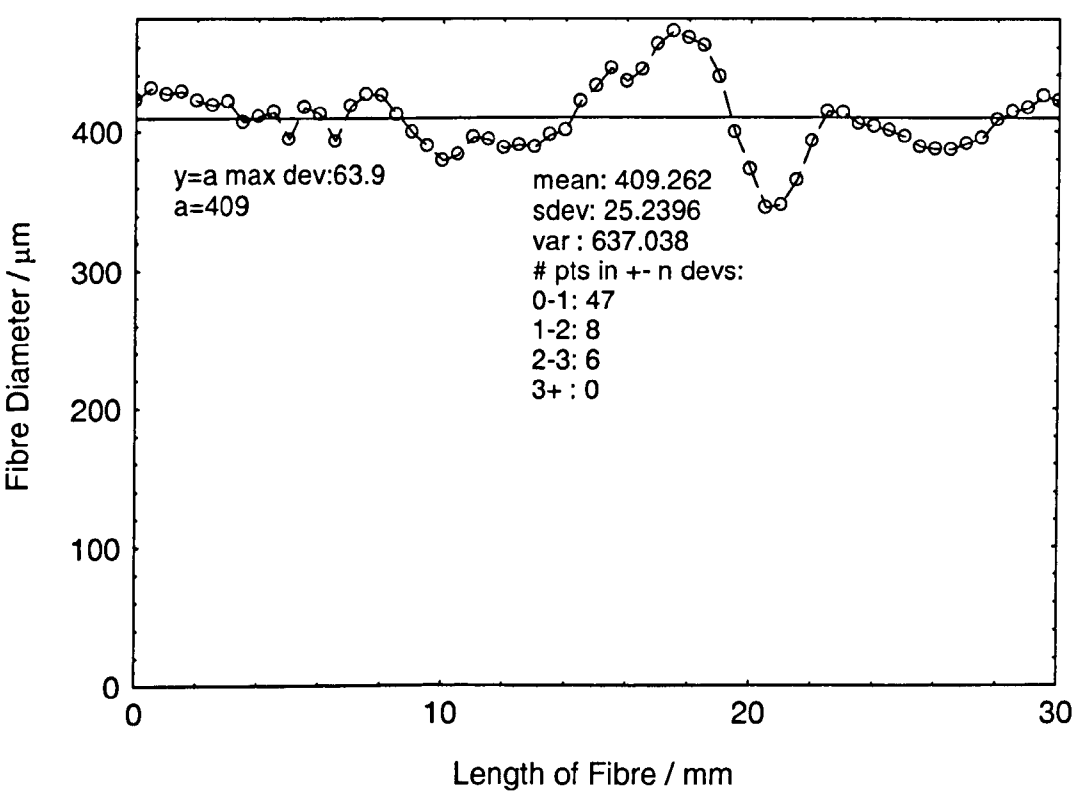

Figure 8.3 : Spec Al32 – Al_2O_3 fibre diameter measurement

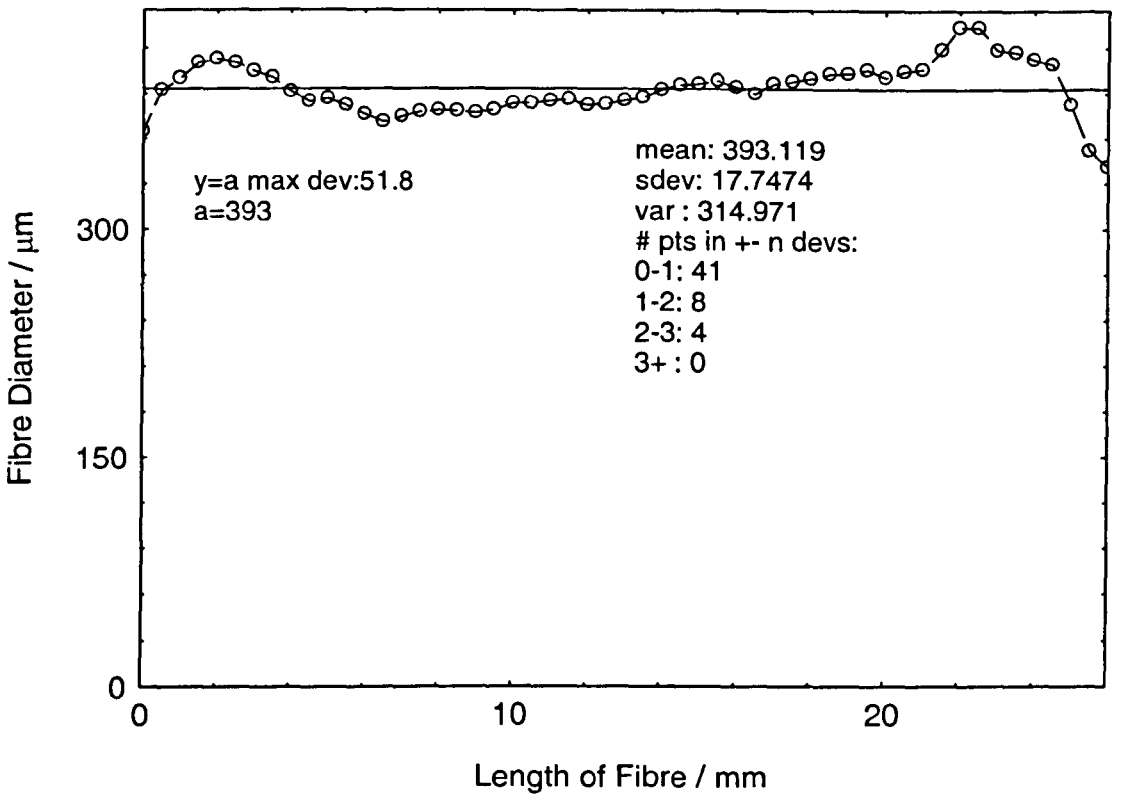

Figure 8.4 : $Al_2O_3:Cr^{3+}$ fibre diameter measurement

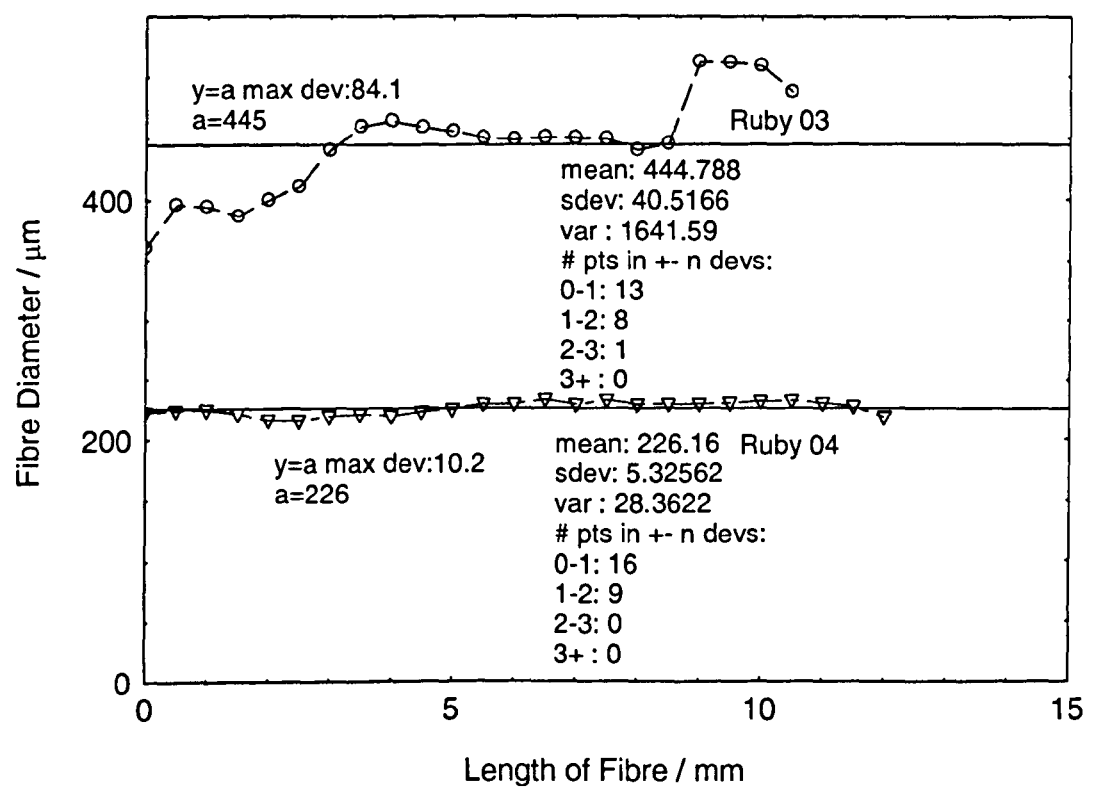

8.3 Mechanical Testing Measurement

During the growth process of Al_2O_3 fibres, no visual flaws were observed internally. The experimental layout and calculation method were discussed earlier in Chapter 5.2.2. All experiments were conducted at room temperature.

8.3.1 Results and Discussion

The three-point bending tests were conducted on three Al_2O_3 fibres and the forces, F, measured in the experiments are shown in Table 8.2. F and S values from the table are the highest among the three oxide materials. The larger the diameter, the larger the force required to strain the fibre to failure. The moment of resistance, M, was calculated taking into account the diameter. The F values were substituted in equation 5.2 to calculate the shear/bending strength, S. The increase of M decreases the shear/bending strength. Since the diameter is taken into account, it was observed that an increase in diameter might reduce the S value. The calculated mean shear/bending strength, S_m, was 5.07MPa and had a standard deviation of 0.34MPa. Figure 8.5 shows the force (N) versus deformation (mm) of *Spec Al32*. A deformation of 6.675mm was required to strain the fibre to failure. Figure 8.6 shows the bending of the fibre before breaking. The Al_2O_3 fibre has the highest deformation compared with the two other oxides discussed in Chapters 6 and 7. It had a very good physical strength and this was the primary reason for its investigation in structural reinforcement [2.8]. Figure 8.7 shows the forces required to strain a fibre to failure for the three oxide materials. Al_2O_3 fibres were approximately 65% stronger than YAG fibres and approximately 85% stronger than Y_2O_3. This simple experiment only gives a rudimental idea of the strength of fibres growth using LHPG. For a detailed study of the strength of fibres, one could model after reference [2.8].

Table 8.2 – Al_2O_3 fibre mechanical testing measurements

Specimen Name	Force, F (N)	$M = \pi d^3/32$ ($x10^{-12}$)	Shear/Bending Strength, S (MPa)
Spec Al30	7.00	6.39	5.20
Spec Al31	6.63	6.73	4.68
Spec Al32	6.68	5.32	5.32

Figure 8.5 : Three-point bending test on *Spec Al32*

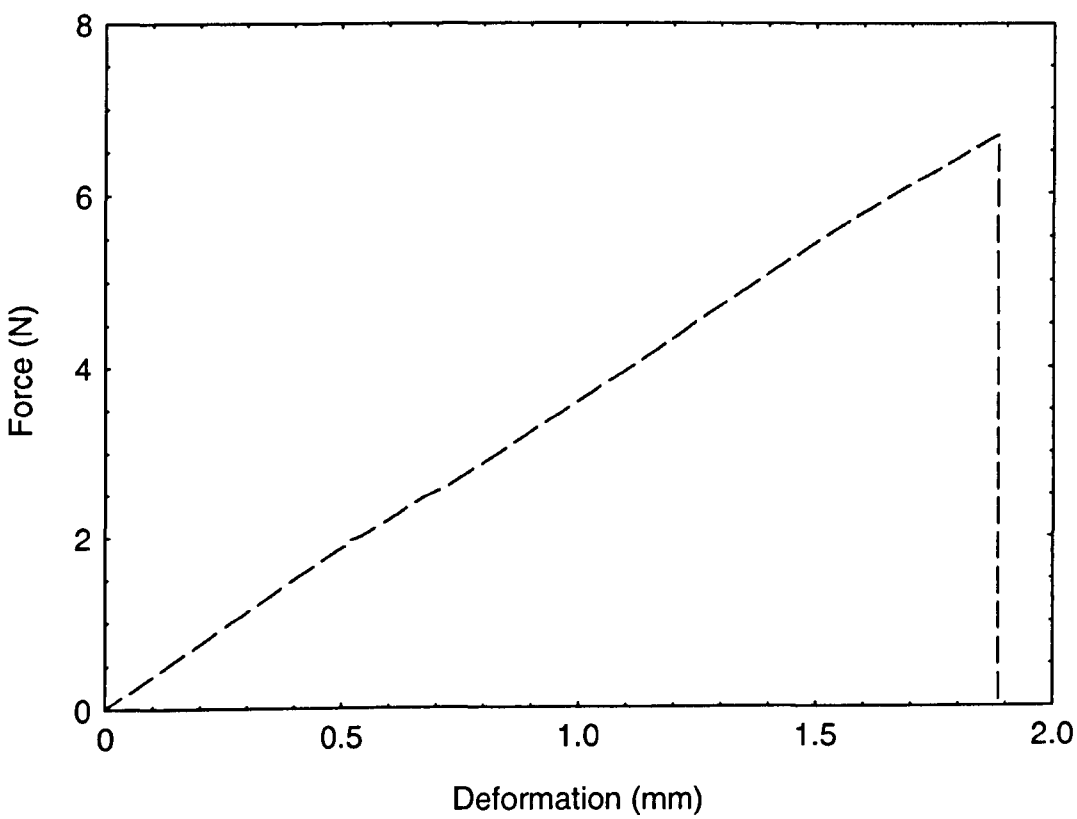

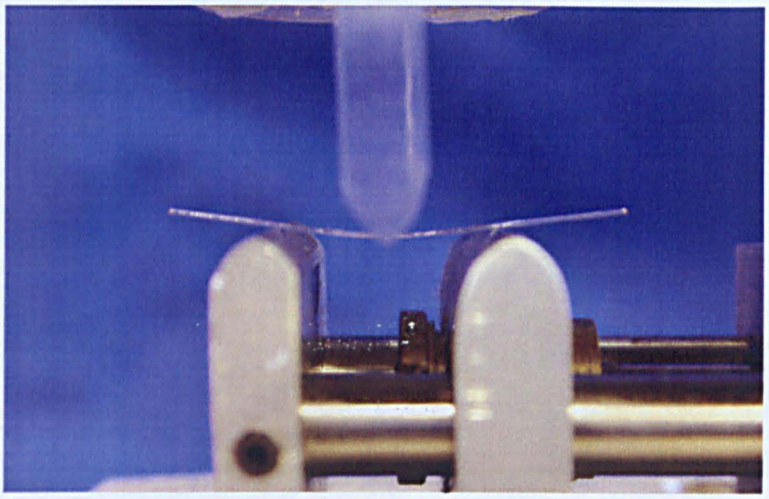

Figure 8.6 – Al_2O_3 fibre being bended before breaking

Figure 8.7 : Three-point bending test for oxide materials (Average Shear Strength)

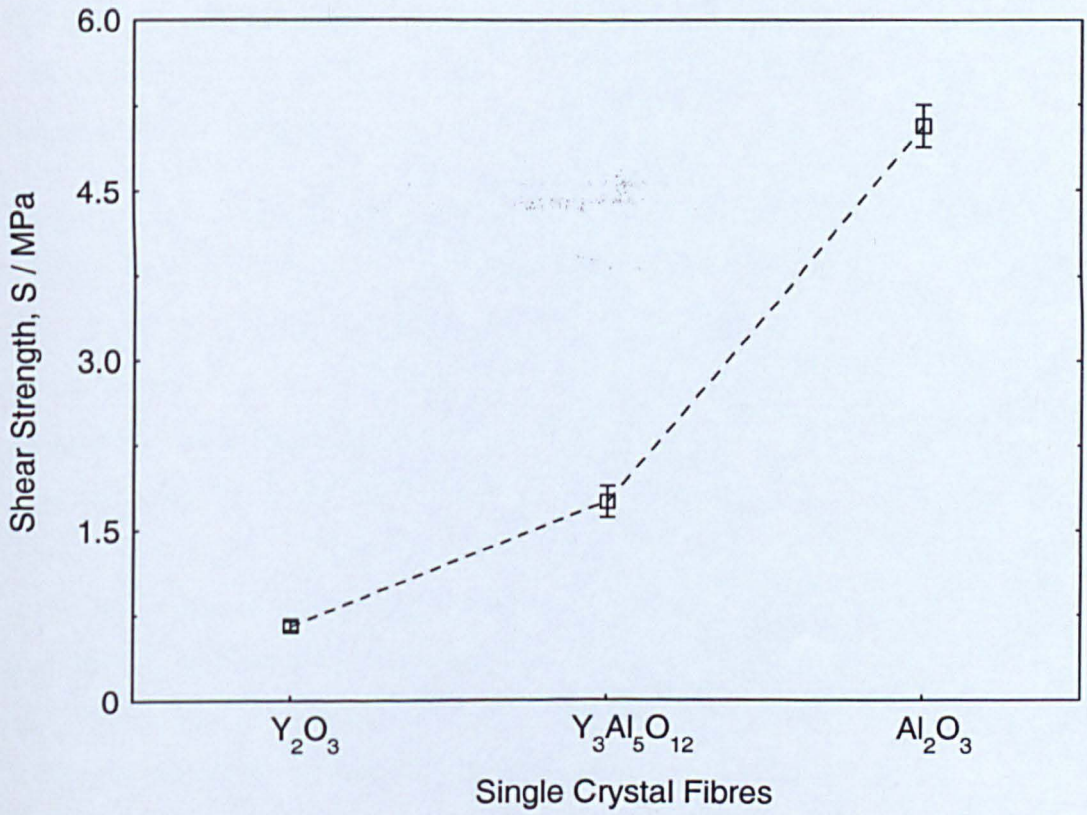

8.4 Absorption Spectrum Measurement

The absorption measurements were carried out on Er^{3+}:Al_2O_3 and Cr^{3+}:Al_2O_3 (ruby) fibres. The work on the former was abandoned because no absorption was observed when the fibres were nominally doped with 1mol% of Er^{3+}. The problem may be attributed to the bonding wax used to hold the powder of the Al_2O_3 when cold pressing. Further investigation is needed to confirm this assumption. However, in light of time constraints, no further investigation was made on Er^{3+}:Al_2O_3 fibres. Cr^{3+}:Al_2O_3 fibres were grown from bulk material and showed no major problems throughout the investigation.

8.4.1 Results and Discussion

The focal interest was ruby fibre emission at the 600nm to 700nm region. Therefore, absorption measurements were taken between 400nm and 800nm to locate the required excitation wavelength. The absorption experiments were carried out on the bulk material, first growth iteration ruby fibres and second growth iteration ruby fibres. Figure 8.8 shows the absorption spectra for all the three ruby materials. It was observed that there was only one broad absorption band in the 550nm region. The absorption peaks of the three materials coincided with each other and were at ~558nm. This shows that there was no obvious shift of the absorption spectrum from the original bulk material.

In the case of the bulk crystal, a broad absorption band was observed spanning from ~380 to ~700nm. Within this spectral region, there should be two broad bands [8.5, 8.6, 2.57] due to the transition from the ground state $^4A_2$ of the Cr^{3+} ion to the excited states $^4F_2$ and $^4F_1$ levels. Only one of the two broad peaks was observed in this work. The peak at the 400nm region could not be detected. This could be attributed to the (Quartz Halogen) light source used in the experiment. The intensity in the blue region of this light source was extremely low and this probably accounted for difficulty in observing the 400nm region of the absorption. Figure 5.6 shows that the intensity in the blue region was very close to zero and only started to pick up at the late 500nm region. In order to overcome this problem, a white lamp with a stronger UV region should be employed in future testing.

Figure 8.8 : $Al_2O_3:Cr^{3+}$ (ruby) absorption spectra

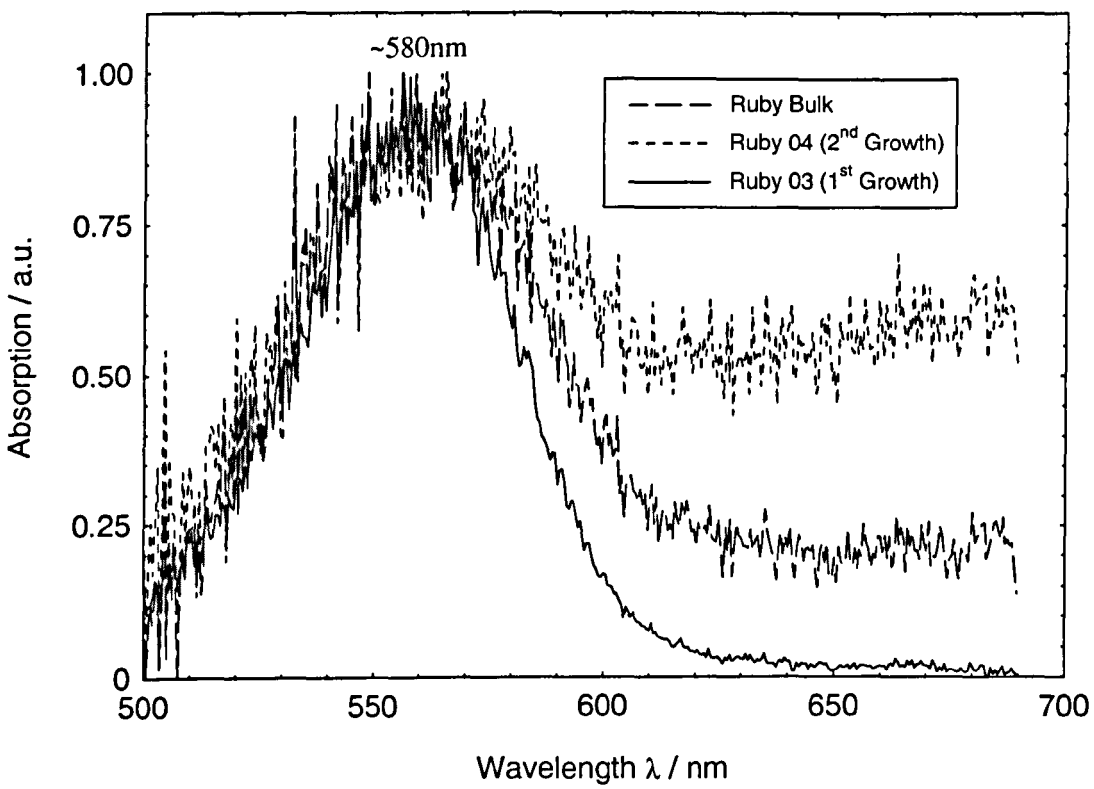

8.5 Fluorescence Measurement

From the absorption measurement, it can be concluded that the absorption in the 500nm to 600nm range was strong. A 532nm frequency doubled Nd:YAG laser was employed to excite the $Al_2O_3:Cr^{3+}$ fibre; the experimental layout was discussed earlier in Chapter 5.3.2.

8.5.1 Results and Discussion

Figure 8.9 shows the fluorescence spectra of the ruby fibres and the bulk ruby crystal. There are two pump bands (green ($18000cm^{-1}$) and violet ($25000cm^{-1}$)) for Cr^{3+} and are approximately a 100nm apart [8.7]. Two distinct emission peaks, R_1 and R_2, were observed when excited with a green laser. All three materials' R values coincided with each other. R_1 was at 691.6nm and R_2 was at 690.2nm. The 532nm laser raised the Cr^{3+} ions from the ground state, $^4A_2$, to the $^4T_2$ excited state. From this state, a non-radiative decay occurs to ^2E energy level which was divided into two metastable levels, $\bar{E}$ and 2A. The R_1 transition was from $\bar{E}$ metastable level to the ground state, $^4A_2$, and the R_2 transition was from the 2A level to the ground state. The separation between the R peaks was 1.4nm and energy gap between the two metastable levels was approximately $29cm^{-1}$. These were in agreement with the work done by *Seat* [2.57, 8.4.1]. The approximate spectral bandwidth for R_1 and R_2 were ~0.55nm and ~0.5nm respectively for the three investigated materials. There was no significant difference in the fluorescence spectrum between the three materials under the similar experimental conditions.

Figure 8.9 : $Al_2O_3:Cr^{3+}$ (ruby) fluorescence spectra

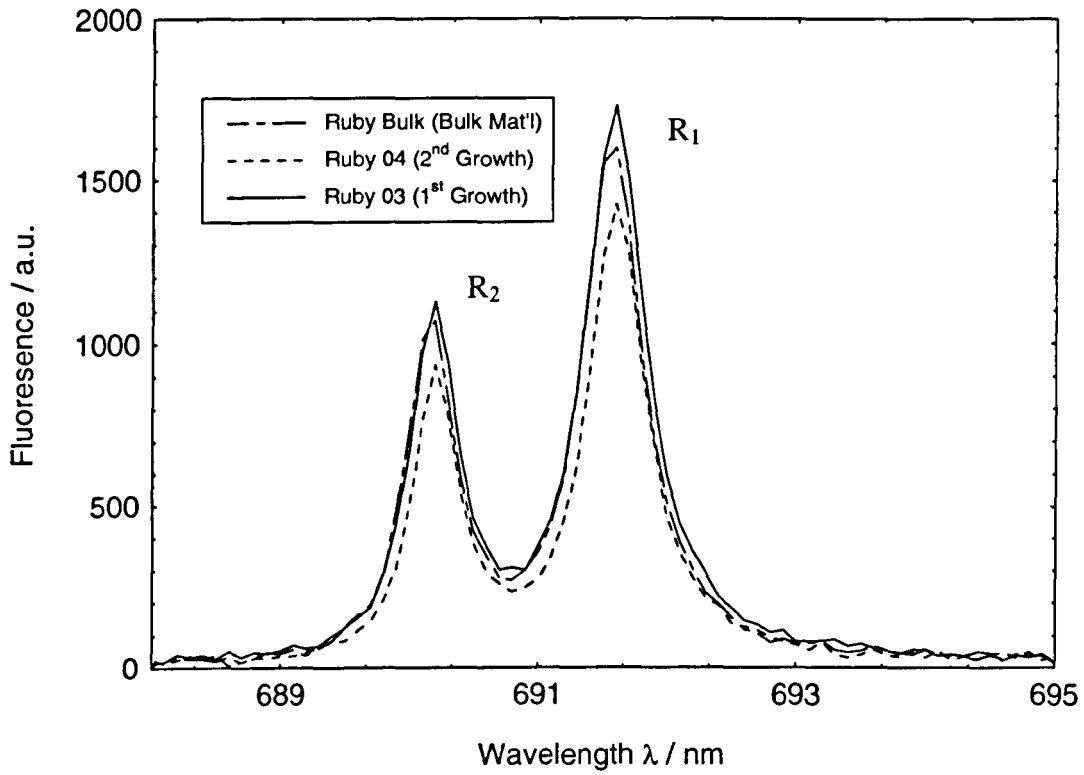

8.6 Reference

[8.1] G. N. Morscher, H. Sayir, *Bend Properties of Sapphire Fibres at Elevated Temperatures I: Bend Survivability*, Mat. Sci. Eng. A, **190**, 1-2, 267, 1995

[8.2] D. H. Jundt, M. M. Fejer and R. L. Byer, *Characterisation of Single-Crystal Sapphire Fibres for Optical Power Delivery Systems*, App. Phy. Let., **55**, 21, 2170, 1989

[8.3] H. Liu, K.S. Lim, W. Jia, E. Strauss and W. M. Yen, *Effects of Tensile Stress on the R Lines of Cr^{3+} in a Sapphire Fiber*, Opt. Let., **13**, 10, 931, 1988

[8.4] W. Jia, H. Liu, K. Lim and W. M. Yen, *Piezo-Spectroscopic Study of Ti^{3+}-Doped Sapphire Fibers*, J. Lum., **43**, 6, 323, 1989

[8.5] R. C. Powell, *Physics of Solid-State Laser Materials*, Spinger-Verlag New York, Inc., 1998

[8.6] C. Winnewusser, J. Schneider, M. Börsch, and H. W. Rotter, *In Situ Temperature Measurements via Ruby R lines of Sapphire Substrate Based InGaN Light Emitting Diodes During Operation*, J. App. Phy., **89**, 6, 3091, 2001

[8.7] W. Koechner, *Solid-State Laser Engineering*, Springer-Verlag Berlin Heidelberg New York, 1988

Section III

SCFs Applications

9 Applications of SCF – Temperature Sensors

9.1 Introduction

Knowing the temperature within a system is extremely vital. Almost all physical, chemical and biological processes react under the influence of temperature. Therefore, having a reliable and accurate method to measure temperature is desirable in many industries. Although there are a wide variety of temperature sensors available in the present market, traditional sensors have limitations which restrict their use for certain roles in these industries. An electronic thermometer, for example, would not be able to measure temperature in a transformer or a rotating turbine blade due to the high influence of the electromagnetic noise present in these systems. Also, traditional sensors do not function well or accurately in hostile environments where physical contact of the probe is impossible. Therefore, alternative sensing methods have been investigated to improve thermometry and one of the possible solutions is the use of fibre optics. The advantage of using fibre optics as temperature sensors is that they are impervious to radiofrequency, electromagnetic and magnetic interferences. They are extremely safe when operating in hazardous environments where electrical sparking is a concern. Fibre optic sensors are not powered electrically but by radiation from a light source that is some distance away from the measurement environment. The capabilities of remote measurement are ideal for complex equipment such as aircraft where accessibility is difficult and long term monitoring is desirable. Being small and light weight, its response to temperature is rapid. This is ideal in the thermometry industries [9.1].

Telecommunication has been the main focus in the use of fibre optics. However, the early 1970s saw the use of low-loss optical fibres as sensors [9.2]. This stirred up new interest in exploring fibre optics in sensing and measurement. Fibre optic sensing is considered by most a 'spin-off' from the optical communication industry, adopting the technology in this field modifying them and using them for the sensor industry. In the early years, traditional sensors maintained their popularity even though the performance of fibre optic sensors are comparable and in some instances, better. This was mainly due to the high production cost. In recent decades, however, progression in the telecommunication industry has benefited fibre optic sensing

research by reducing the cost of materials and components required in the sensing research arena [2.57]. This benefit gives researchers a new freedom, where the focus now is on developing fibre optic sensors to overcome difficulties where traditional sensors are presently limited and also to improve the present technology in this field.

Glass/silica-based fibres have been the dominating material used in fibre optics but there are limitations when these fibres are used as temperature sensors. The maximum operating temperature of glass based fibres is ~500°C while some silica based fibres have an operating temperature of ~1000°C [9.3]. When thulium was doped in a silica fibre, it was able to sustain a maximum effective operating temperature of ~1250°C [9.4]. Not only was it able to withstand high temperature, it also had a moderate sensitivity over this wide range of temperature of ~0.05μs/°C when the fluorescence lifetime was used to determine the temperature. When the temperature increases further, 'conventional' fibres degrade mechanically and optically. An alternative is required to measure temperature of 1250°C and above. SCFs were then chosen because of their high thermal resistance. *Dils* [2.53] was the pioneer for using SCF (sapphire) as a temperature sensor. The melting temperature of sapphire SCF is 2045°C and this temperature is much higher than for silica fibres. The limitations posted by silica fibres are now no longer a restriction when SCFs are used. Other single crystal materials like ruby [9.5], YAG [9.6, 7], ZrO_2 [2.55] and Y_2O_3-ZrO_3 [2.56] were investigated as high temperature sensors. Y_2O_3-ZrO_3 SCF, for instance, grown by LHPG were able to operate to temperatures as high as 2300°C [2.56]. The presence of ZrO_3 in Y_2O_3greatly increased the mechanical and optical quantities therefore making this SCF a potential candidate for ultra-high-temperature fibre sensors. The high melting temperatures of SCFs make them difficult to grow, hence most SCFs are shorter in length compared to conventional fibres. Integrating the two together into a single thermometry system, having the conventional fibres deliver the laser beam and the SCF being the sensing probe would be ideal for systems that require remote monitoring. An example would be *Dils's* [2.53] high temperature optical fibre thermometer which consisted of a sapphire fibre as the probe and a low temperature optical fibre to transmit the signal to the detector.

9.2 Fibre Optic Thermometry

The most common way of classifying fibre optical sensors are as intrinsic and extrinsic. Intrinsic sensors are sensors where the light remains at all times in the fibre. A modulating source is transmitted through the fibre to the section in the measurand field, a physical characteristic of the fibre is then changed by the measurand and the 'new' signal continues until it is collected by a detector. *Sun* [9.8] in her work described the use of intrinsic doped Nd fibre as a high temperature alarm sensor. The fluorescence behaviour of the Nd doped fibre corresponds to a change in temperature. The signal received by the detector at the other end was then treated mathematically to determine the temperature. Her work has shown that temperature can be measured to a precision of ±5°C which was acceptable for use as an alarm sensor. Extrinsic sensors depend on an external modulator attached to the fibre to modulate the signal. An extrinsic interferometric sensor system described by *Chen* [9.9] had a broadband optical source sent through a multimode optical fibre. The end is attached to a sensing interferometer which consisted of collimation lenses and mirrors. This sensing medium would respond to the measurand field and returned the modulated signal to the processing unit. Crystals such as yttrium orthovanadate (YVO_4), potassium gadolinium tungstate ($KGd(WO_4)^2$) and yttrium aluminium garnet (YAG) placed at the end of a silica fibre and secured mechanically by a quartz sheath and cement were another kind of extrinsic temperature sensor [9.10]. Figures 9.1 and 2 show the schematics of an intrinsic and extrinsic sensing device respectively.

There are a number of fibre optics sensing concepts that be can be applied to temperature measurement. Interferometric, in-fibre Bragg grating, distributed fibre optic and fluorescence sensing are a few common techniques employed to determine the temperature within a system. A brief account of these sensing methods will be discussed in this section.

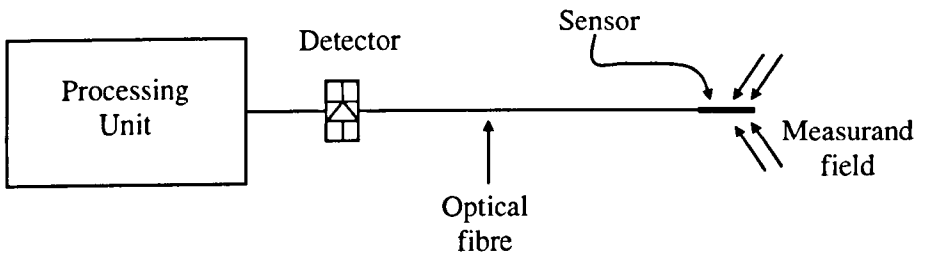

Figure 9.1 – Intrinsic sensing device

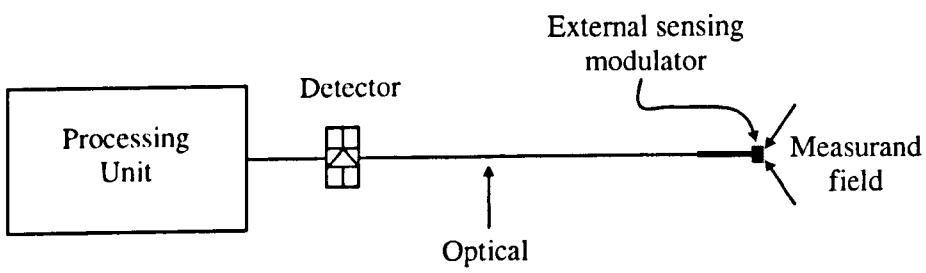

Figure 9.2 – Extrinsic sensing device

9.2.1 Interferometric Fibre Optic Sensors

Interferometric sensors are known to provide a high level of sensitivity and resolution to a number of measurands [9.11]. Therefore, this sensing method has been used in many different sensing fields. Work has been done on the use of interferometric sensors where the production of a phase shift proportional to the measurand is introduced to an optical fibre sensor. There are different approaches in the use of interferometric sensors, one of which is the Mach-Zehnder interferometer configuration [9.12]. The temperature can be measured using two single-mode fibre arms. The laser beam velocity is a function of refractive index where the refractive index is a function of the temperature. The variation of temperature changes either the dimension or refractive index of the fibre. This will also cause a change in the phase of the laser beam which can be observed through the displacement of the fringe pattern. These changes determine the temperature within the system. Knowing that the phase shift $\Delta\phi$ is a function of temperature change ΔT, the temperature sensitivity is given by the expression stated below [9.12, 13]:

$$\frac{\Delta\phi}{\Delta T} = \frac{2\pi L}{\lambda}\left(\frac{ndL}{LdT} + \frac{dn}{dT}\right) \tag{9.1}$$

where L is the length of the fibre length, λ is the wavelength and n is the refractive index. In the case of silica fibres, the refractive index changes dominate whereas for multi-components glasses the value of thermal expansion coefficients (dL/dT) and the temperature dependence of the refractive (dn/dT) vary significantly. For a typical glass fibre, calculated by the above equation, a temperature sensitivity of 4 to13x10^{-6} radians/°C is common [9.12]. Increasing the path length, L, will increase the sensitivity and if there are several more parallel interferometers, the dynamic range can be improved [9.14]. Cross-sensitivity might be taken as one of the problems within the system if the temperature variation is large [9.15]. Since there is a requirement to observe the fringes, aligning the system could be another disadvantage. Figure 9.3 shows the schematic of the Mach-Zehnder interferometric temperature sensor.

9.2.2 In-Fibre Bragg Gratings (FBG) Sensors

FBG sensors have shown great potential in both the telecommunication and the sensor industries. Being a more passive device in the optical telecommunication sector, FBGs have been employed as laser [9.16] and amplifier pump reflectors [9.17], dispersion compensation devices [9.18] and gain flattening devices [9.19]. FBG sensors are used in the measurement of strain [9.20], ultrasonics [9.21], chemicals [9.22], high magnetic-fields [9.23] and also temperature [9.24, 25]. The gratings that are found in the fibres can be created either by holographic side exposure [9.26] or phase mask imprinting [9.27]. The holographic side exposure process is where the fibres are exposed to two UV interference beams that production an interference grating. The grating period is determined by the incident wavelength and the angle between the two interference beams. For the latter method, a phase mask, from a precision photolithographic apparatus, is placed near or in contact normal to the axis of the optical fibre. An incident UV beam, directed through the diffractive phase mask, is then phase modulated spatially and diffracted forming an interference pattern which 'photoimprints' a refractive index modulation on the optical fibre creating the gratings. The basic Bragg wavelength at which light is reflected is given by:

$$\lambda_B = 2n\Lambda \tag{9.2}$$

where n is the refractive index of the fibre and Λ is the grating pitch or period [9.2]. The gratings imprinted on the fibre cause a periodic change in the refractive index where the phase front and the grating planes are spatially constant. When the Bragg grating condition is satisfied, the interferences created by the phase front and the grating plane add constructively otherwise interferences are destructive (out of phase). The reflected wavelength is a narrowband signal which is dependent on equation 9.2. Therefore, changes in the measurand which cause the Bragg grating to be altered physically changes the grating pitch. When measuring temperature, the change in temperature, ΔT, will influence the wavelength shift, $\Delta\lambda_{BT}$ and this is given by the expression:

$$\Delta\lambda_{BT} = \lambda_B(\alpha+\xi)\Delta T \tag{9.3}$$

where $\alpha = (1/\Lambda)(d\Lambda/dT)$ is thermal expansion coefficient and the thermo-optic coefficient is given by $\xi=(1/n)(dn/dT)$ [9.14]. Using the equation 9.3, the fractional wavelength shift for a typical silica fibre is ~6.8 pm $^{\circ}C^{-1}$ when an excitation at 0.83μm was used [9.28]. Figure 9.4 shows the common schematic of a fibre Bragg grating.

9.2.3 Distributed Fibre Optic Sensors

The initial development of distributed fibre optic sensors was based on the losses or scattering mechanisms present in the fibres. In the early 1990s, the use of the optical time domain reflectometry (OTDR) concept was employed in numerous distributed fibre optic sensor systems [9.29]. OTDR [9.30] was a common instrument used in optical telecommunication to locate faults or imperfections within a fibre. Due to the microscopic variation of the refractive index within the fibre core, Rayleigh scattering is present when a light is transmitted along the fibre. These losses (backscattering) are recaptured by the aperture of the fibre and transmitted back to the light source. With a pulsed light source, knowing the changes in the backscattering received by the detector could allow one to monitor/determine the intensity, spatial variations and attenuation. A similar technique is applied to sensing applications where influence by the measurand induces variations of the loss and scattering of the fibre, and this can be collected and analysed to determine the required sensing parameters [9.31]. There are several methods of distributed optic fibre temperature sensor, one of which is the Raman backscattering temperature sensor. This was to be the most successful distributed fibre optic sensor developed [9.2, 11] to date and this method has been commercialised [9.31]. Since Raman scattering is temperature sensitive, it is therefore ideal for use as distributed temperature sensors. To measure the temperature, an expression of the ratio of the anti-Stokes to Stokes intensity in the backscattering light is [9.11, 31]:

$$R_r = \left(\frac{\lambda_s}{\lambda_a}\right)^4 \exp\left(-\frac{hc\Delta\nu}{kT}\right) \tag{9.4}$$

where R_r is the ratio between anti-Stokes and Stokes, λ_s is the Stoke wavelength of the lower photon energy, λ_a is the anti-Stoke wavelength at the high photon energy, h

is Planck's constant, c is the velocity of light, $\Delta\nu$ is the optical frequency shift at which the measurement is made with reference to the pump frequency, k is Boltzmann's constant and lastly, T is the absolute temperature. Commercially, Raman scattering distributed fibre optic sensors are able to operate with fibre lengths as long as 10km and have resolution as high as ~1°C with 1m spatial resolution [9.11]. *Feced's* [9.32] work on distributed fibre optic sensors has improved the spatial resolution from 1m to 0.1m. Using Raman thermometry with the time-correlated single photon counting technique has greatly increased the spatial resolution. Figure 9.5 shows the schematic of the distributed sensing configuration.

9.2.4 Fluorescence Fibre Optic Sensors

Fluorescence emission can be used as a transduction mechanism when a measurand exerts influence on emission properties. This maybe to change the emission profile (spectral properties) or the spontaneous decay lifetime (temporal properties). The excitation source used is determined by the absorption spectrum of the material where the absorption energy of the material is then transferred into fluorescence. The fluorescence produced generally is of a lower photon energy and hence longer wavelength. Fluorescence fibre optic sensors generally involve the use of fluorescence optical materials for example, transitional metal and rare earth ions are commonly used. The transition metal ion, Cr^{3+}, has been greatly explored as a fluorescence-based temperature sensor in the past two decades [9.33, 34, 35]. Its strong interaction with the crystal field and lattice gives it a wide optical absorption spectrum from ultraviolet to the red region. These interactions also create an environment where the fluorescence characteristics are sensitive to temperature. Having a broad spectrum, it allows the use of many cheap and easily available excitation sources, such as high-power LEDs and visible laser diodes [9.33]. Alexandrite, $BeAl_2O_4:Cr^{3+}$, has an effective temperature measuring range up to 700°C [9.35]. Work done by *Ye* [9.36], shows that YAG doped with Cr^{3+}, using methods like fluorescence-based sensing, has an effective temperature range up to 500°C and when combined with radiation based measurements the effective temperature was as high as 1400°C. On the other hand, in rare earth ion doped fibre optical sensors fluorescence-based sensing can function beyond 700°C. When

incorporating rare earth into a suitable host, they can be ideal for high temperature sensing. One example is the use of Er^{3+} doped silica fibres as temperature sensors. The Er^{3+} doped sensor was excited with a 980nm laser diode and with a wavelength division multiplexer (WDM), the fluorescence emission at 1550nm was collected by a photodiode where the fluorescence decay-time at this wavelength was used to evaluate the temperature. It was able to assess temperatures up to ~900°C [9.37]. When the fibre was put through an annealing cycle, the effective working temperature increased to 1100°C [9.38]. *Kennedy* [9.39] showed that rare earths like Yb^{3+} and Tb^{3+} when doped in YAG, using fluorescence-based sensing, can have an effective temperature range up to ~1600°C. The advantage of fluorescence-based sensing is that it is able to solve cross sensitivity problems. The interest of this work is to look at fluorescence-based sensing in SCFs. Therefore a detailed discussion will be made in the following section. Figure 9.6 shows a fluorescence-based fibre optic sensor.

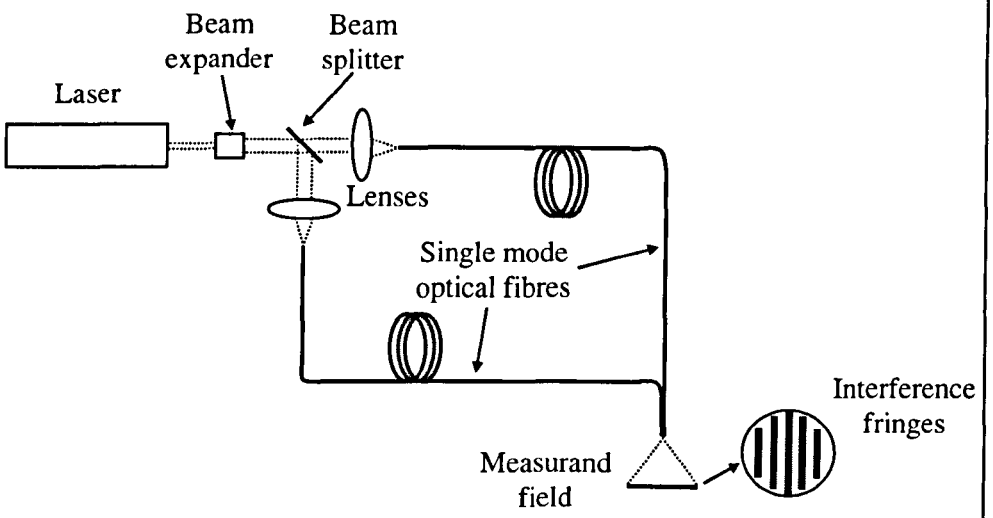

Figure 9.3 – Mach-Zehnder interferometer for temperature sensing

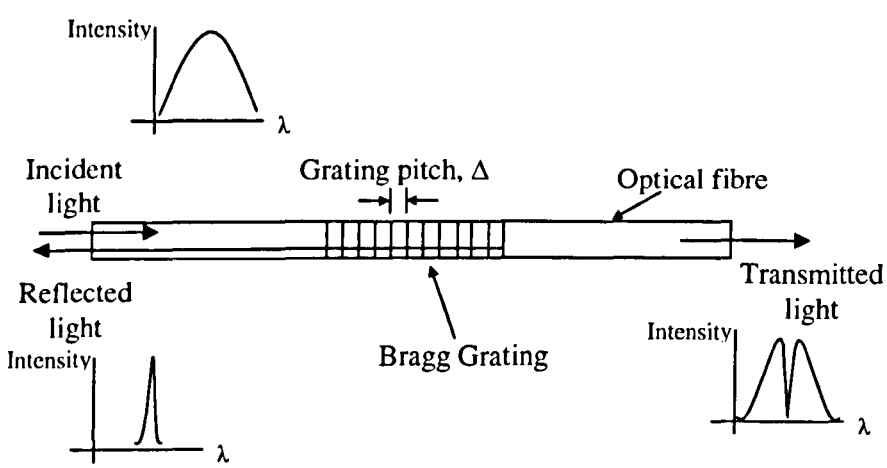

Figure 9.4 – Bragg grating imprinted on optical fibre

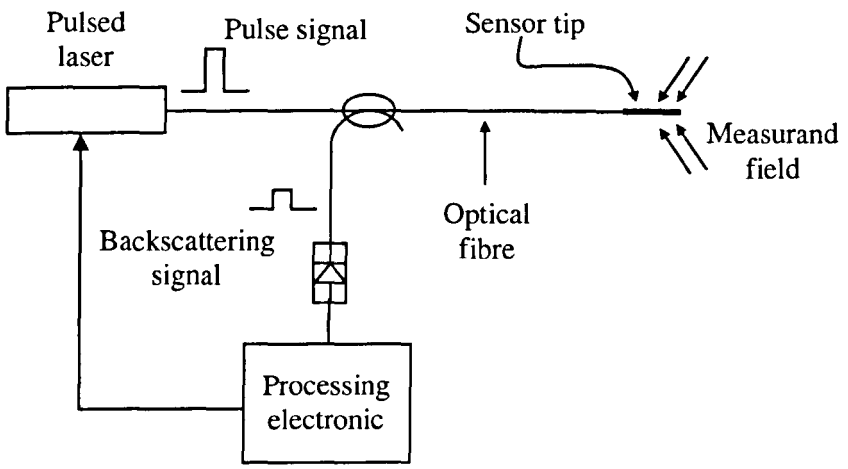

Figure 9.5 – Distributed fibre optic sensor configuration

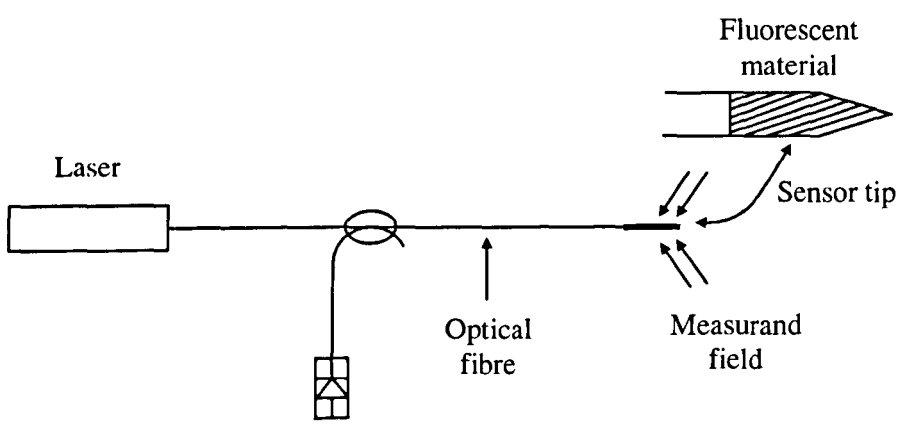

Figure 9.6 – Point fluorescence-based sensing

9.3 Rare Earth Fluorescence-Based Temperature Sensing

Fluorescence-based temperature sensing is the main sensing method employed in this work. The two techniques used were fluorescence intensity ratio (FIR) and fluorescence decay (FD) techniques. The former technique examining the ratio of two fluorescence lines within the spectrum. The latter technique explores temperature dependence of the fluorescence lifetime. A brief discussion will be made of these two techniques below.

9.3.1 Fluorescence Intensity Ratio (FIR) Technique

Under a suitable and constant pump rate, a rare earth doped system's fluorescence intensity variation can be influenced by several parameters, one of which is temperature. Due to the temperature dependence of the non-radiative rates between excited states, the fluorescence intensity changes with temperature. Measuring the temperature using this method involves the thermally linked populations of two energy levels within a rare earth ion. This thermally linked level is similar to a Boltzmann type population distribution. As temperature increases, the number of ions (N_1) in the lower energy excited state level decreases as more ions are raised to the higher energy excited state increasing number of ions (N_2). The ions (N_2) at a higher energy level will then depopulate increasing the N_1 population. A relationship is then developed since the fluorescence intensity is proportional to the populations of the two energy levels. The FIR is expressed by [9.40, 41]:

$$FIR = \frac{N_2}{N_1} = \frac{I_{2j}}{I_{1j}} = \frac{g_2\sigma_{2j}\omega_{2j}}{g_1\sigma_{1j}\omega_{1j}}\exp\left[\frac{-\Delta E}{kT}\right] = A\exp\left[\frac{-\Delta E}{kT}\right] \qquad (9.5)$$

with

$$A = \frac{g_{2j}\sigma_{2j}\omega_{2j}}{g_{2j}\sigma_{2j}\omega_{2j}}$$

where the term I_{ij} is the fluorescence intensity, g_i is the degeneracy, σ_{ij} is the emission cross section, ω_{ij} is the angular frequency of the fluorescence transition from the upper (i = 2) and lower (i = 1), thermalizing energy levels to the terminal

level j, ΔE is the energy difference between the two energy levels, k is the Boltzmann constant and T is the temperature in Kelvin. When using this technique, there are several advantages. Firstly, the energy levels used are closely spaced hence the fluorescence wavelengths are relatively close, in this way wavelength dependence effects which arises due to fibre bending would be greatly reduced. Secondly, the ratio of the population of the higher and lower energy excited states and the ratio of their fluorescence intensity is not dependence on the excitation power. The reason is that the individual thermally coupled levels' populations are directly proportional to the total population. Therefore changes in the excitation source will influence these levels to the same degree [9.40]. The sensitivity, S, of this temperature measuring technique can be determined by the equation [9.40, 41]:

$$S = \frac{1}{R}\frac{dR}{dT} = \frac{\Delta E}{kT^2} \tag{9.6}$$

where R is the fluorescence ratio between the two energy levels. From equation 9.6, the greater the energy difference the larger the sensitivity.

There are instances where offsets need to be added to equation 9.5 to measure the fluorescence intensity ratio. Effects such as stray light from other energy levels or coming from the pump source, and peaks from the fluorescence emission that are overlapping may be required to take into consideration. Therefore the modified equation that includes the above mentioned is given by [9.40]:

$$FIR = \left(\frac{n_2}{n_1}\right) A \exp\left[\frac{-\Delta E}{kT}\right] + \left(\frac{m_1}{n_1}\right) \tag{9.7}$$

where n_i (upper level i=2 and lower level i=1) is the ratio of the total fluorescence intensity of the transition from level i – actual intensity measured by detector from level i and m_i is the ratio of the total fluorescence intensity from level i – other thermalizing level measured by detector. When stray light is involved, a similar equation (9.7) can be used [9.40]. This modified equation was employed by *Beak* [9.42] to determine temperature with the FIR at emission at ~1 and ~1.5μm in silica doped with Er^{3+} and Yb^{3+}.

9.3.2 Fluorescence Decay (FD) Technique

When the rare earth within a medium is excited by an appropriate source, fluorescence emission occurs and the intensity falls rapidly when the source is terminated. Fluorescence Decay (FD) is the time taken for an ion to fall from the high excited state to the lower excited state radiatively. An exponential behaviour is observed during the termination of the source, and can be expressed as a function of time [9.43, 44, 45]:

$$I_o(t) = I_i e^{-t/\tau} + C \tag{9.8}$$

where $I_o(t)$ is the intensity of radiation emission at time t, I_i is the initial fluorescence amplitude, τ is the fluorescence lifetime and C is the signal baseline offset. A number of methods are available to determine the value, τ. It can be determined through either direct or indirect methods. For the latter, phased-locked analog-to-digital signal processing (A-DSP) can be used where τ is established. This is done by measuring the output modulation period T which is correlated to τ. In other words, the period T is adjusted in a way so that the measurement of this value is directly proportional to lifetime τ [9.45]. Therefore making this method an indirect way of measuring the fluorescence lifetime. As for the direct method, the value τ is determined directly from the output of a photodetector that is connected to a digital oscilloscope. By modulating the excitation source with a periodic rectangular signal, when excitation is turned off, an exponential decay curve is observed and is collected by the digital oscilloscope. At different temperatures, the lifetime τ is then evaluated from the exponential curves collected by the digital oscilloscope [9.45]. For this work, the direct method was employed.

9.4 Preparation, and Choices of Dopant Concentrations, of $Y_3Al_5O_{12}$ and Y_2O_3 Fibres for Temperature Sensors

For temperature sensing applications, two variants of $Y_3Al_5O_{12}$ (Er^{3+} singly doped and co-doped with Yb^{3+}) and one Y_2O_3 (Er^{3+} singly doped) SCFs were grown by LHPG techniques and employed as high temperature sensors. The approximate length of all fibres was 70mm. Table 9.1 shows the different rare earth content and diameters of the fibres used.

All temperature sensing fibres were prepared from powder oxide that was mixed with the required rare earth(s) and pressed into pellets by the cold pressing method. For sensing applications, just the tips of the fibres are required to be doped. Pellets were pressed with half just the basic oxide material and the other half containing rare earth dopant(s). See Chapter 4.4.1 for details on preparation processes. The initial source rods (15mm) were only able to produce fibres of reasonable quality of maximum length of 30mm which were too short to be used as temperature sensing fibres. Hence, one further reduction growth was made to all fibres to achieve a longer length that suitable for this application. Physical defects were observed and detailed discussion on these was done in Chapter 4.4.4. The conditions of the $Y_3Al_5O_{12}$ fibres were better as compared with the Y_2O_3 fibres. From Figure 9.7, it can be observed that the latter fibre did not have the clarity of the former. Visually the latter was seen to be cloudy along the whole length of the fibre. Figure 9.8 shows the tip of the temperature sensor and Figure 9.9 shows the upconversion emission in the green which signified that doping of the rare earth(s) took place only at the tip and not along the length of the fibre.

The decision on the concentration level of dopant used for the temperature sensors was based on work done in Chapters 6 and 7. For the YAG fibres, the work in Chapter 6 shows that 1 mol% Er^{3+} singly doped (Figure 6.21) had numerous distinct peaks throughout the $^4I_{13/2}$ manifold and that the 1500nm and 1600nm region intensities were equally strong; hence suggesting the use of these peaks as a possible candidate for the FIR technique to determine temperature. As the doped concentration increased to 5mol% (Figure 6.22) the peaks in the 1500nm region overlapped and the peaks were no longer able to be used in FIR technique. Based on these results, the concentration chosen must display strong/intense and distinct peaks

across the $^4I_{13/2}$ manifold. Since a further diameter reducing growth is required to increase the fibre length losses of dopant level through evaporation in the melt was would occur [3.7]. Bearing this in mind, 2mol% Er^{3+} was the chosen to be starting dopant concentration. The starting dopant concentration of the Yb^{3+} co-doping was 5mol% in orderto investigate if there were any significant changes in the $^4I_{13/2}$ manifold. The FIR for the singly doped and the co-doped YAG fibre temperature sensors of the 1528.5nm peak divided by 1612nm peak were 0.89 and 1.12, respectively. From the Figure 6.24, for 0.5 and 1mol% the FIR was 2.09 and 0.76 respectively. An assumption can be made that the singly doped fibre sensor had a concentration slightly higher than 1mol% (Er^{3+}) whereas the co-doped fibre was lower than 1mol% (Er^{3+}). For the Y_2O_3 fibre sensor (Figure 7.30) the majority of the peaks overlapped and created a broadening effect at a concentration of 3.1mol%. Therefore 2mol% singly doped Er^{3+} was the chosen concentration. FIR was calculated by dividing the intensity at peak wavelength 1010nm by the peak at 1530nm and the result was 2.44. At 3.1mol% the FIR was 3.77, see Figure 7.36. Again from this figure, assumption can be made that the dopant concentration for this Y_2O_3 temperature sensing fibre was ~2mol%. All the fibres grown for temperature sensing applications demonstrated the presence of upconversion. Bright visible green emission was observed at the tip and from this we could determine the length of the doped section in the fibres. The doped length of all the fibres was ~20mm from the tip.

Table 9.1 – SCF temperature sensors

Specimen No.	Oxide Materials & Rare earth(s)	Starting Dopant concentration (mol%)	Diameter (μm)	Length (mm)
Spec YAl 26	$Y_3Al_5O_{12}:Er^{3+}$	2	285.9	~70
Spec YAl 32	$Y_3Al_5O_{12}:Er^{3+}+Yb^{3+}$	2+5	330.0	~68
Spec 64	$Y_2O_3:Er^{3+}$	2	292.8	~66

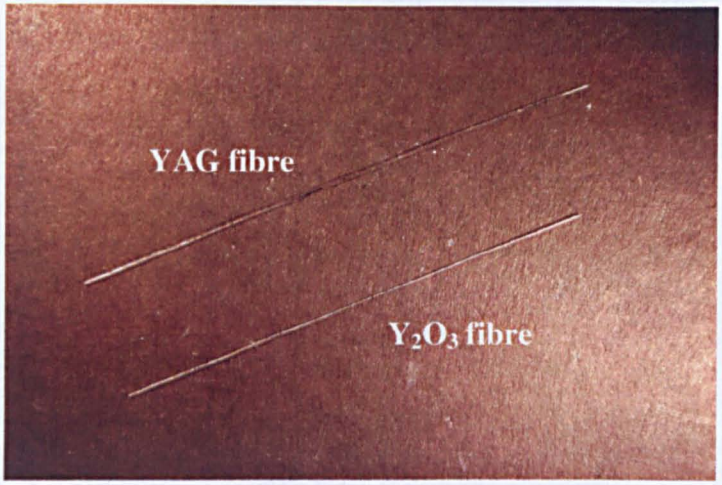

Figure 9.7 – SCFs temperature sensors

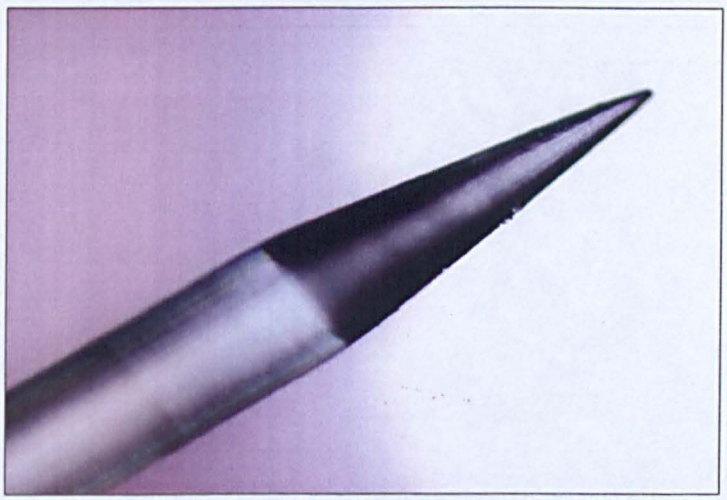

Figure 9.8 – SCF temperature sensor tip

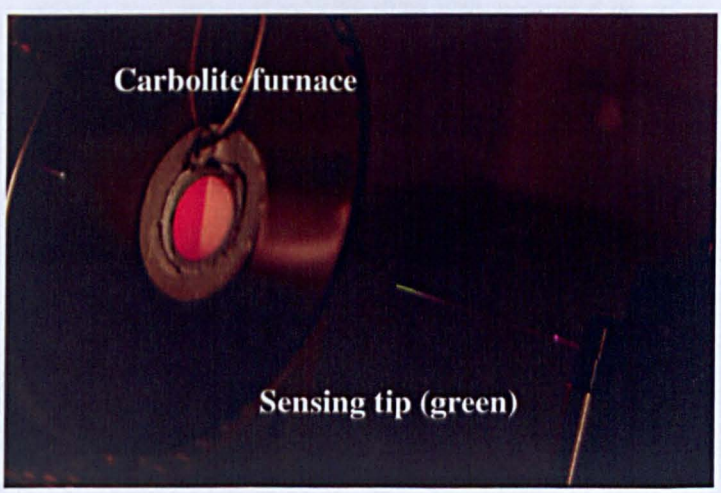

Figure 9.9 – Upconversion (visible green) seen at the tip of the fibre sensor

9.5 Experimental Set-Up for Temperature Sensors

All fibres underwent a similar experimental set-up for the temperature dependent measurements. Temperature measurements were done in the infrared and the visible region. The only difference between the two was the use of a different photodetector. A brief account of the layout will be explained in this section. FIR and FD employ a similar experimental set-up. For these experiments, a 965nm laser diode was used to excite the fibres. Figure 9.10 shows the schematic of the experimental layout. This pump source (*LACRYS – model 402*) was directed into a pair of collimating lenses and then into a 20x microscope objective. An opto-mechanical chopper was placed at the focused spot that was in between the two collimating lenses. It was used to modulate the excitation source. The output beam from the microscope objective was then focussed into the polished end of the fibre. Figure 9.9 clearly shows the green upconversion at the tip of the sensing fibre. The sensing tip was inserted into the *Carbolite Eurotherm* (model *MTF 12/25/250*) tube furnace. The maximum heating temperature of the furnace was 1473K hence all temperature sensing experiments were carried out from room temperature (~293K) to 1473K. Having a taper tip at the sensing end, the beam that travelled to the tip was then reflected back toward the excitation source. A beam splitter, placed in the path of the incoming and reflected beams, was used to redirect the reflected laser beam from the sensing tip to a focusing lens. The reflected laser beam was then focussed into the monochromator by a lens. Two different kinds of photodetectors were used in these experiments. A photomultiplier tube (*PMT – Hamamsutsu model R928*) was used for the visible region and an InGaAs/PIN photodetector (*IR Femto Watt Photoreceiver*) was used for the infrared region. The signal from the photodetectors was then sent to a lock-amplifier to enhance the signal. The processed signal will be then sent to the computer for storage and further processing. The scanning range by the monochromator for the visible region was from 500nm to 700nm and for the infrared region from 1000nm to 1700nm. When acquiring the fluorescence decay, the gratings of the monochromator were position at the required wavelength, and a digital oscilloscope were used to collect the data from the photodetector and storing them for further processing. Due to the weak visible signal, upconversion decay was not investigated in this work.

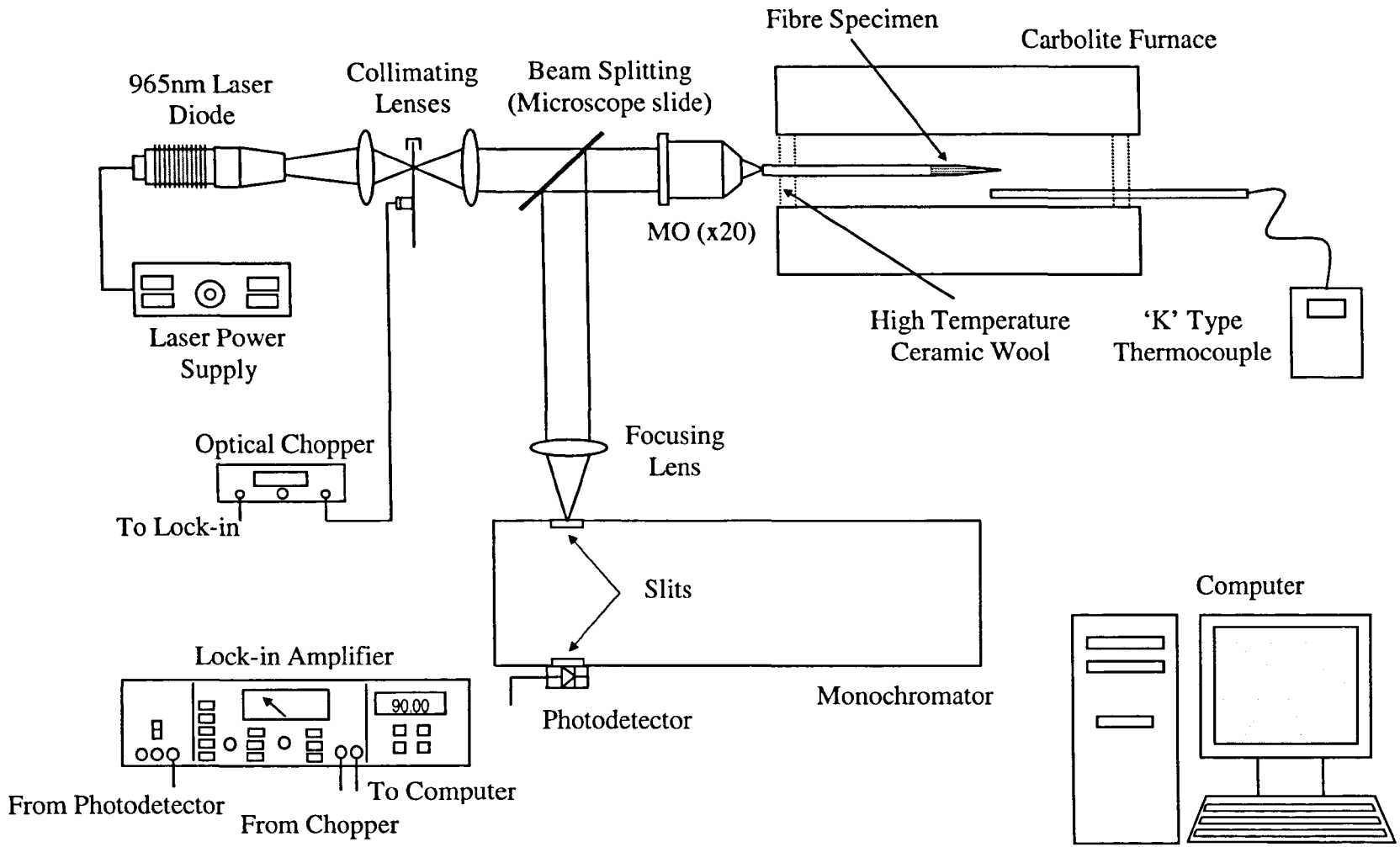

Figure 9.10 – Experimental set-up for temperature sensing using FIR, UIR and FD method

9.6 $Y_3Al_5O_{12}:Er^{3+}$ - Temperature Sensor

In this section, investigation was made using YAG:Er^{3+} as a temperature sensor, employing FIR (infrared), upconversion intensity ratio (UIR – visible region) and FD to measure temperature as high as 1473K. Results of these investigations are presented and discussed.

9.6.1 Fluorescence Intensity Based Sensing – $Y_3Al_5O_{12}:Er^{3+}$

Several peaks in the transition $^4I_{13/2}$ were observed in the YAG fibre doped with Er^{3+} when excited at 965nm. These peaks (IR lines), at room temperature, are shown in Figure 9.11. Monitoring of the intensity of these IR lines, from room temperature (293K) to 1473K, was carried out to establish a relationship between ratios of IR line intensities as a function of temperature. Exploiting the 1500nm region as a means of temperature sensing was reported by *Imai* [9.46], who used the intensity ratio of the fluorescence emission at 1530nm and 1552nm for temperature sensing. Investigations were then made in this work to determine which of these fluorescence intensity ratios (FIRs) would be appropriated to use as potential thermometric applications. The FIR can be calculated by having the upper thermalizing energy level divided by the lower thermalizing energy level and the results can be fitted to the FIR equations mentioned in section 9.3.1.

9.6.1.1 Results and Discussion

Figure 9.12 and 13 show the fluorescence spectra of Er^{3+} from the $^4I_{13/2}$ state at various temperatures. Strong signals were observed throughout the entire experiment. The fluorescence emission seen at a temperature of 1473K signified that the signal to noise ratio was low. The fluorescence profile is divided into three regions, labelled as A, B and C, for easy explanation. For the 1400nm to 1500nm region (Region A), the fluorescence intensity profile increases with the increase in temperature. At room temperature, there were several distinct peaks but as the temperature was raised to 637K these were no longer obvious and at 973K they completely merged and formed a broaden lineshape. Although the fluorescence intensity at 1473K is slightly lower than at 1373K the fluorescence intensity profile at this temperature had a ~80%

increased from 293K. For the 1500nm to 1600nm region (Region B), a similar broadening effect was observed with increasing temperature. The peaks at 1528.5nm remained the most intense IR line throughout the temperature sensing experiment. An increase of 61% in its fluorescence intensity was also observed. The 1600nm to 1700nm region (Region C) was the only region that saw a decrease in fluorescence intensity with the increase in temperature. The 'five fingers' profile of this region also gradually disappears with the increasing temperature. The increase of Regions A and B with temperature and the decreases in where Region C could be due to the increasing overlapping of the fluorescence peaks. The fluorescence from the lower energy level overlaps the upper thermally coupled energy levels resulting in the decreasing (Region C) and increasing (Region A and B) of the fluorescence intensity [9.40]. A similar phenomenon has also been observed in Nd^{3+} when it was used in temperature sensing [9.40]. Figure 9.14 shows the plots of the integrated intensities over the three mentioned regions as a function of temperature. Both Regions A and B show an increase as the temperature increases whereas changes of Region C remained relatively minimal throughout the experiment. The curves of the integrated intensities of Region A and B could be selected for possible thermometric application, with an effective temperature range from 293K to ~1373K. The integral under the fluorescence profiles were calculated using the EASYPLOT software package.

Table 9.2 shows the denotation of the IR lines used for the temperature dependent intensity ratios. FIR can be calculated by dividing the upper by the lower thermalizing level. FIR_{ij}^{a} is an example of a denotation where the superscript a represents the specimen number and the subscripts i and j represent the ratio between the two IR lines. For FIR_{12}^{26}, superscript *26* is the specimen number and subscript *12* is the fluorescence intensity ratio between 1453nm and 1470nm IR lines. The first set of FIR plots with 1453nm as the higher energy IR line is shown in Figures 9.15a to c. Generally, all the curves exhibited increases as the temperature increased. Figure 9.15c showed the widest intensity change with the steepest slopes when the higher energy IR line was divided by the IR lines in the 1600nm region. Figures 9.15d to g show the FIR curves being fitted by equation 9.7. Due to the overlapping of the fluorescence from the thermally coupled levels, equation 9.7 is a better fit as compared to equation 9.5 [9.40]. Figure 9.15d shows (fitted curve) an exponential

increase and has an effective temperature range starting from 273K. The curve starts off steep therefore higher sensitive would be expected at the lower temperature region as compared to the high temperature region. Figures 9.15e to g show that the effective sensing range only starts at approximately 673k to 873K followed by a gradual increase. FIR_{18}^{26} - fitted in Figure 9.15f demonstrated the steepest increase in the ~873K to 1473K region making it extremely useful for sensing in the high temperature region. Figures 9.16a and b show the FIR of upper energy IR line 1470nm. The curves in both the figures are non-monotonic and have similar features where a gradual increase with increasing temperature was observed. The curves in Figure 9.16b a wider fluorescence intensity ratio and hence were selected to fit to equation 9.7. Figures 9.16c and d shows the fitted curves. Among the fitted curves, FIR_{26}^{26} (Figure 9.16d) has the lowest effective working temperature at ~473K. While the other fitted curves basically have a 'flat' line at the lower temperature region before increasing at a temperature of approximately 673k to 873K. The majority of FIR curves with 1453nm and 1470nm as upper energy lines shown in the figures have similar curve profiles. These signified that the changes of intensities with temperature within this region were consistent for these two lines. Figures 9.17a and b show 1528.5nm as higher energy IR lines. The only usable FIRs for temperature sensing are shown in Figure 9.17b. To further determine the usability of these curves for thermometric application, these FIRs are fitted with equation 9.7. The good fit and linearity of FIR_{35}^{26}, FIR_{37}^{26} and FIR_{38}^{26} are possible candidates for thermometric applications. When using 1568nm as the base IR line, similar FIR curves profiles were observed, see Figure 9.18a. When fitted with FIR equation 9.7, only FIR_{46}^{26} does not linearly increases, see Figures 9.18b and c. The other curves showed great potential for temperature sensing due to the consistent linear increment with temperature and a good fitted model was achieved with these ratios. When using 1612nm as the higher energy IR line. The results were not promising. None of the FIRs seem to be appropriate for temperature sensing, see Figure 9.19. There was no consistency in either the trend of the curves plotted with this IR line. Figure 9.20a shows two curves plotted with 1628.5nm. Changes in FIR at the lower temperature were minimal and only picked up after ~773K. Since FIR_{68}^{26} has a much steeper increment at the high temperature region, it was selected and was re-plotted in Figure 9.20b. The fitted curve matches the original curve well and has a r^2 value of 0.999.

However the only setback with this is that it is not possible to register lower temperatures. The last IR line used for FIR was at 1640.5nm. Figure 9.21 shows both the experimental and fitted curves. The width of the FIR for experimental curve is relatively small but it has a consistent increment with increasing temperature, hence the attempt to fit the model curve to it. The effective working temperature for this IR line starts at ~573K and again the ability to measure the lower temperature region would not be possible. From the above discussion, the most ideal IR line plots that demonstrated potential to measure temperature from ~273K to 1473K are 1528nm and 1568nm. Using these two lines, curves encompassed a wide range of FIR with linear increase with to increasing temperatures and the standard deviation for the FIR points recorded were between ~0.8 to ~1.5%.

FIR was also carried out across each of three regions. A similar method is reported in references [9.41, 47]. From the fluorescence spectra collected for each temperature, the integrated fluorescence intensities across each of the region A, B and C were calculated. The ratios of the upper and lower thermalizing regions were taken, and plotted in Figure 9.22a. From this figure, it was observed that FIR_{AB}^{26} and FIR_{AC}^{26} increased with temperature and seem suitable for temperature sensing. A re-plot of these two curves was shown in Figure 9.22b. A gradual increase with temperature can be seen from the figure and the curves have an effective working temperature from ~573K.

Figure 9.11: Spec YAl 26 $Y_3Al_5O_{12}:Er^{3+}$ fluorescence in room temperature, 293K

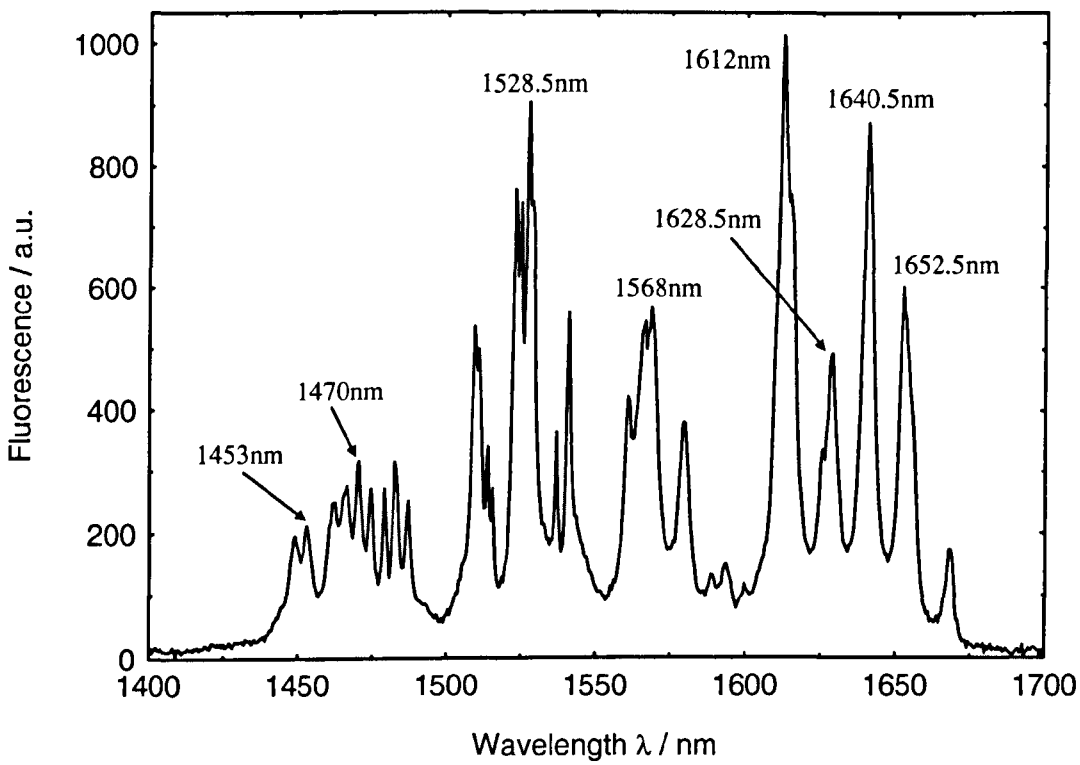

Figure 9.12: Spec YAl 26 $Y_3Al_5O_{12}:Er^{3+}$ fluorescence spectra ($^4I_{13/2}$) – room temperature to 837K

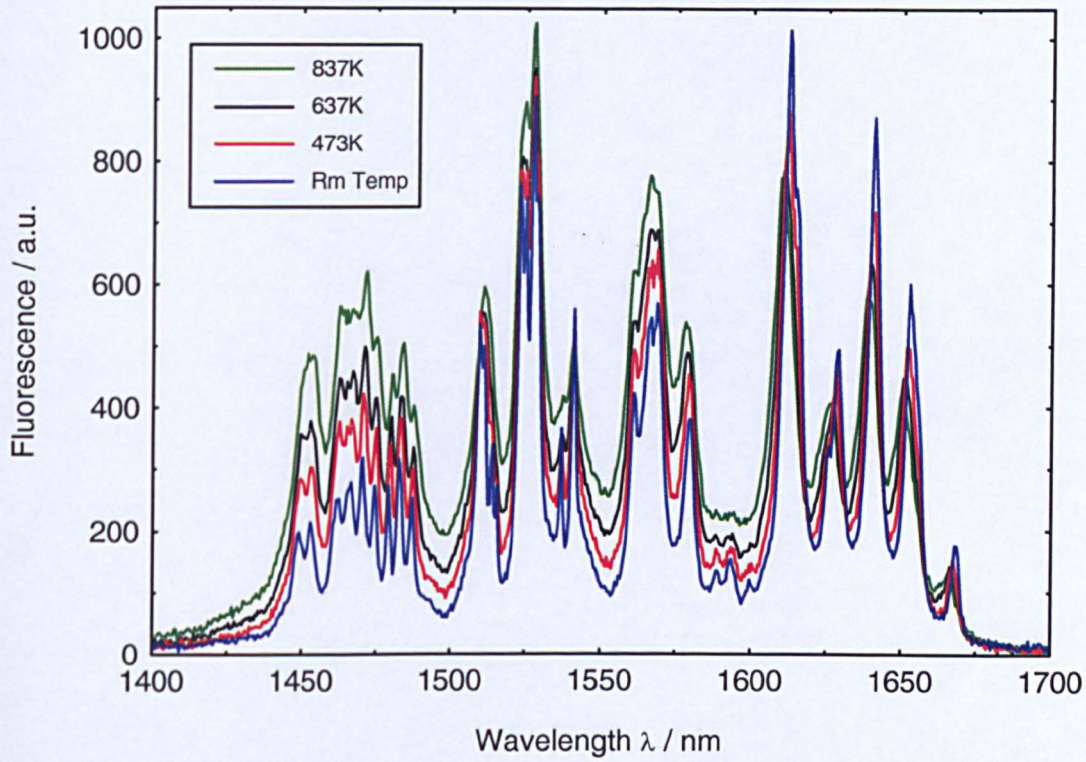

Figure 9.13: Spec YAl 26 $Y_3Al_5O_{12}:Er^{3+}$ fluorescence spectra ($^4I_{13/2}$) – 937K to 1473K

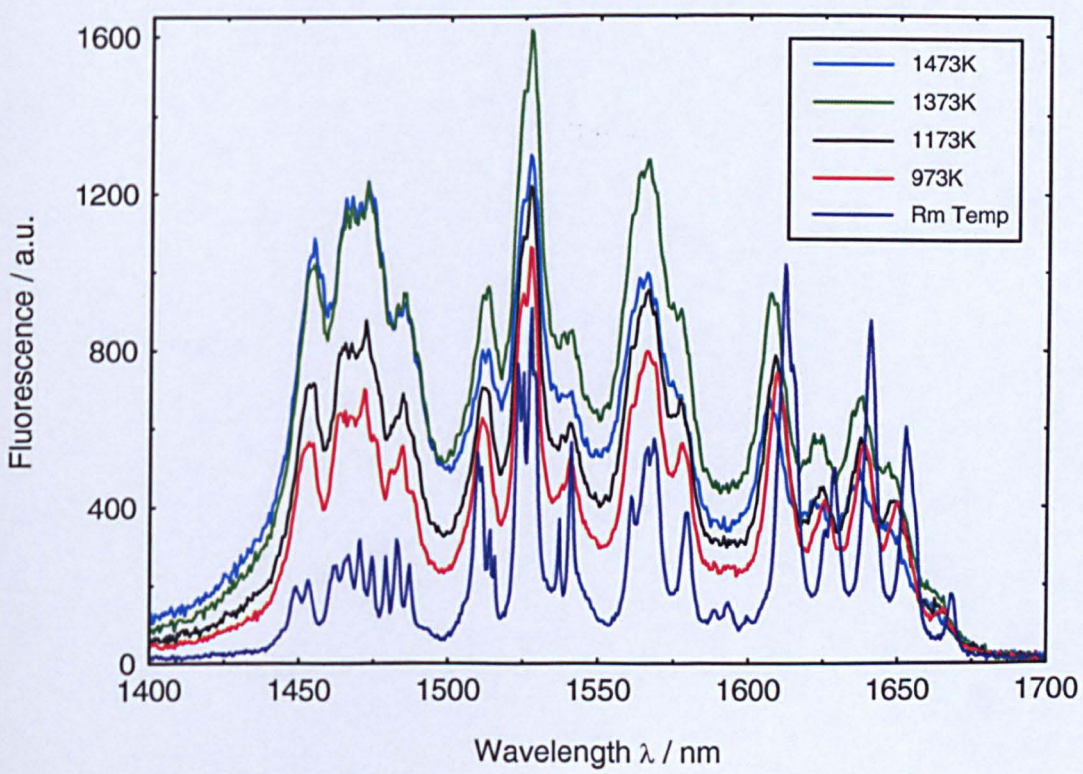

Figure 9.14: Spec YAl 26 $Y_3Al_5O_{12}:Er^{3+}$ - Integrated intensity

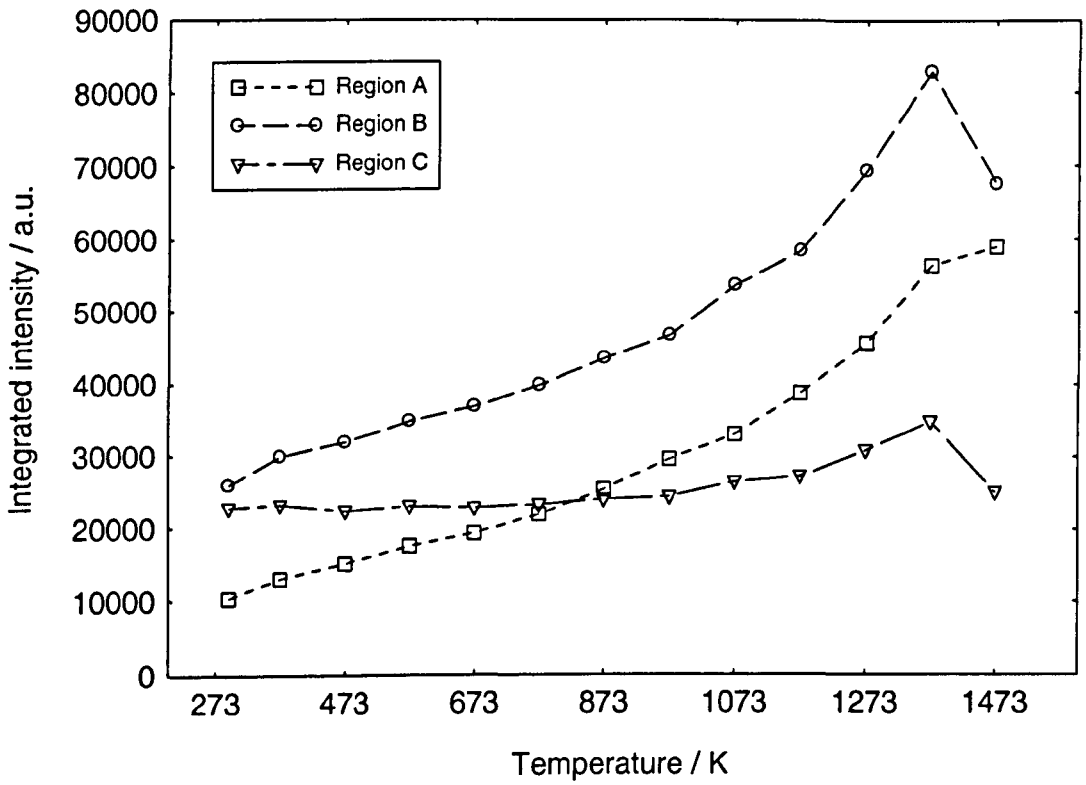

Table 9.2 – Spec YAl 26:$Y_3Al_5O_{12}$:Er^{3+} temperature sensor FIR denotations

Denotations	IR lines	Denotations	IR lines
FIR_{12}^{26}	I_{1453}/I_{1470}	FIR_{35}^{26}	$I_{1528.5}/I_{1612}$
FIR_{13}^{26}	$I_{1453}/I_{1528.5}$	FIR_{36}^{26}	$I_{1528.5}/I_{1628.5}$
FIR_{14}^{26}	I_{1453}/I_{1568}	FIR_{37}^{26}	$I_{1528.5}/I_{1640.5}$
FIR_{15}^{26}	I_{1453}/I_{1612}	FIR_{38}^{26}	$I_{1528.5}/I_{1652.5}$
FIR_{16}^{26}	$I_{1453}/I_{1628.5}$	FIR_{45}^{26}	$I_{1528.5}/I_{1612}$
FIR_{17}^{26}	$I_{1453}/I_{1640.5}$	FIR_{46}^{26}	$I_{1528.5}/I_{1628.5}$
FIR_{18}^{26}	$I_{1453}/I_{1652.5}$	FIR_{47}^{26}	$I_{1528.5}/I_{1640.5}$
FIR_{23}^{26}	$I_{1470}/I_{1528.5}$	FIR_{48}^{26}	$I_{1528.5}/I_{1652.5}$
FIR_{24}^{26}	I_{1470}/I_{1568}	FIR_{56}^{26}	$I_{1612}/I_{1628.5}$
FIR_{25}^{26}	I_{1470}/I_{1612}	FIR_{57}^{26}	$I_{1612}/I_{1640.5}$
FIR_{26}^{26}	$I_{1470}/I_{1628.5}$	FIR_{58}^{26}	$I_{1612}/I_{1652.5}$
FIR_{27}^{26}	$I_{1470}/I_{1640.5}$	FIR_{67}^{26}	$I_{1628.5}/I_{1640.5}$
FIR_{28}^{26}	$I_{1470}/I_{1652.5}$	FIR_{68}^{26}	$I_{1628.5}/I_{1652.5}$
FIR_{34}^{26}	$I_{1528.5}/I_{1568}$	FIR_{78}^{26}	$I_{1640.5}/I_{1652.5}$

Figure 9.15a: Spec YAl 26 – $Y_3Al_5O_{12}:Er^{3+}$ FIR_{12}^{26} vs temperature

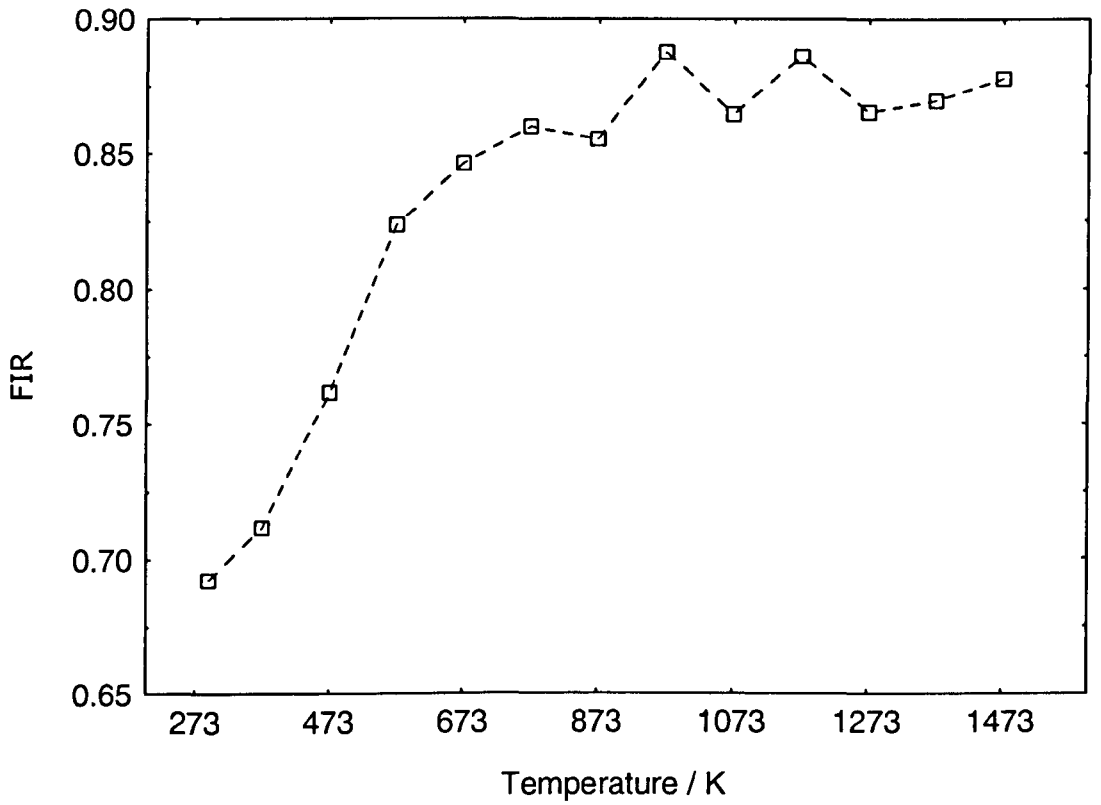

Figure 9.15b: Spec YAl 26 – $Y_3Al_5O_{12}:Er^{3+}$ FIR_{13}^{26} & FIR_{14}^{26} vs temperature

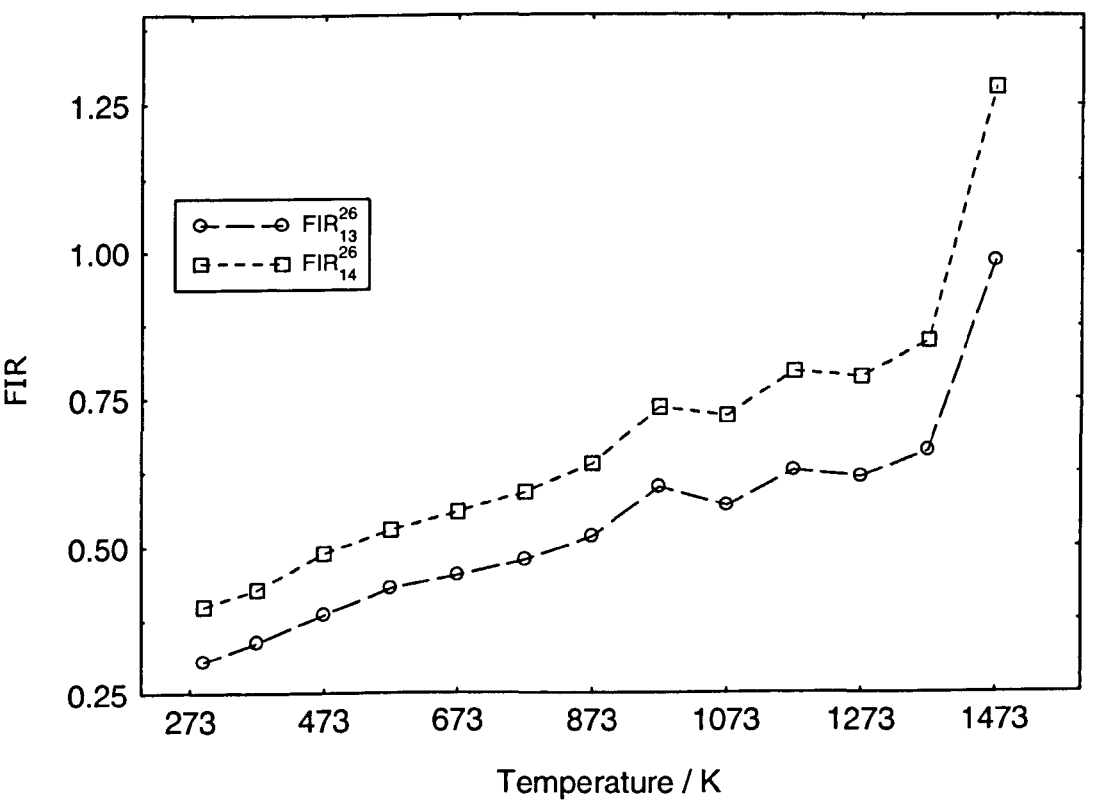

Figure 9.15c: Spec YAl 26 – $Y_3Al_5O_{12}:Er^{3+}$ FIR_{15}^{26} to FIR_{18}^{26} vs temperature

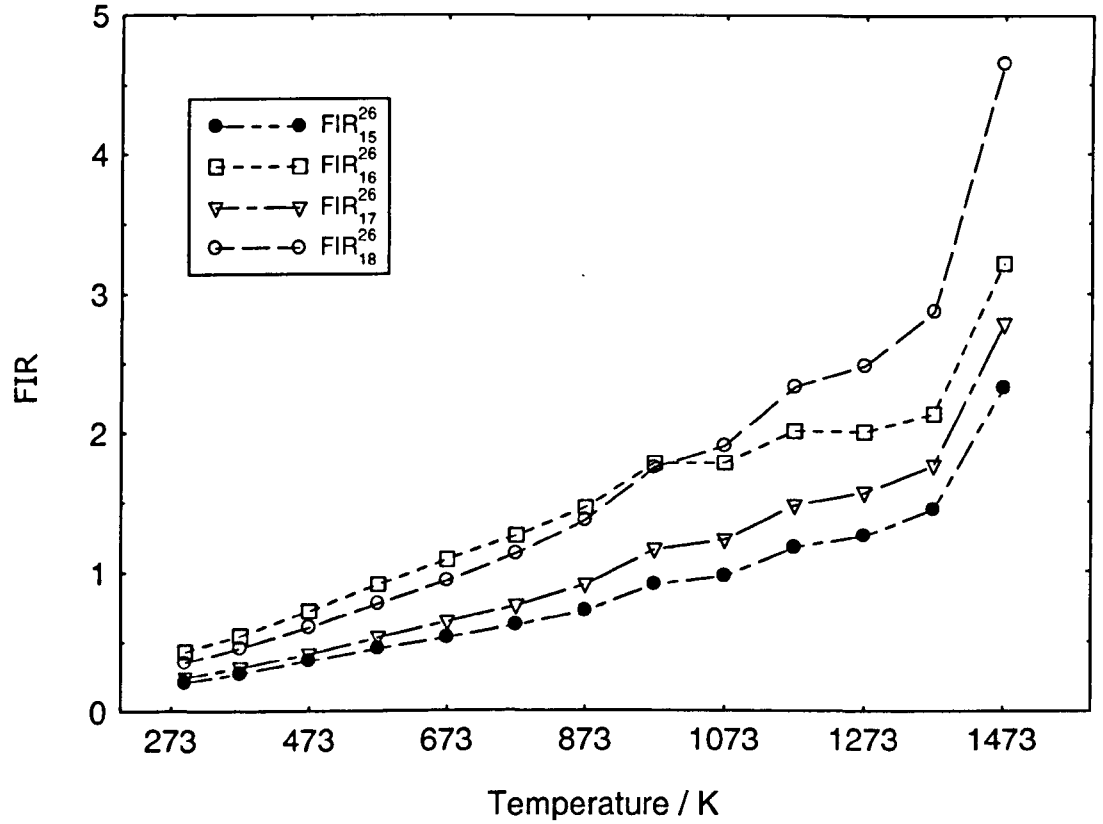

Figure 9.15d: Spec YAl 26 – $Y_3Al_5O_{12}:Er^{3+}$ FIR_{12}^{26} (fitted with Eq. 9.7) vs temperature

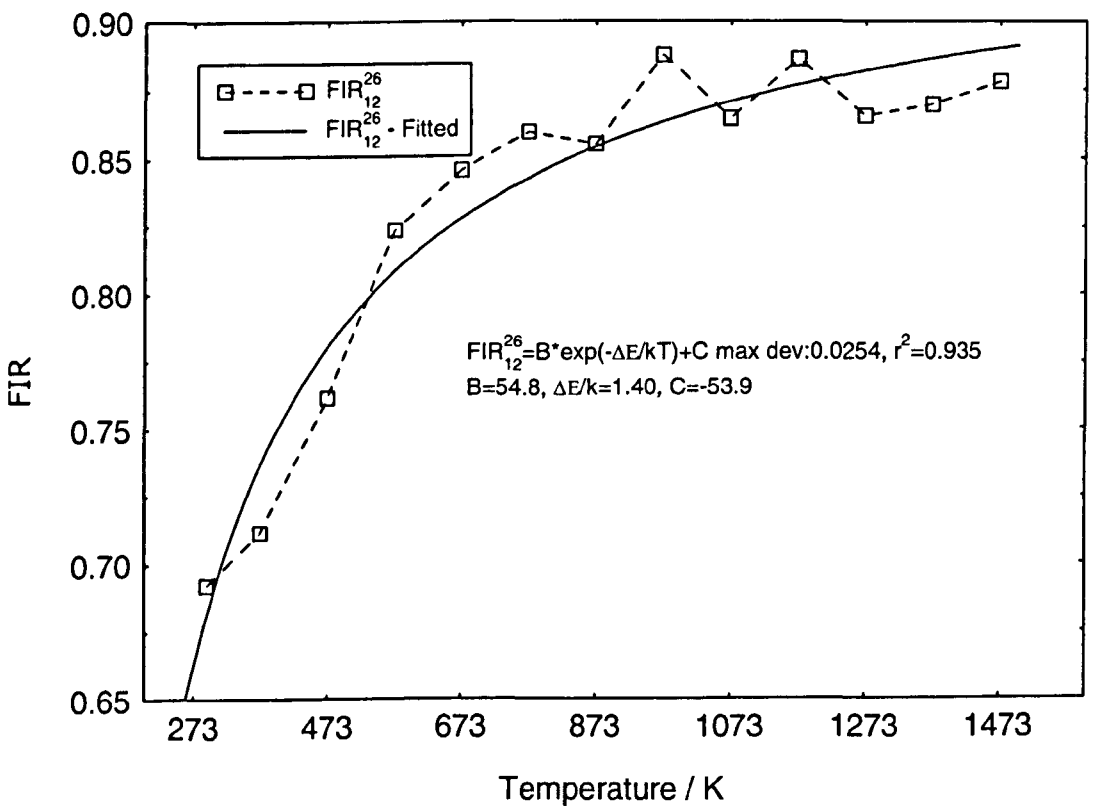

Figure 9.15e: Spec YAl 26 – $Y_3Al_5O_{12}:Er^{3+}$ FIR_{13}^{26} & FIR_{14}^{26} (fitted with Eq. 9.7) vs temperature

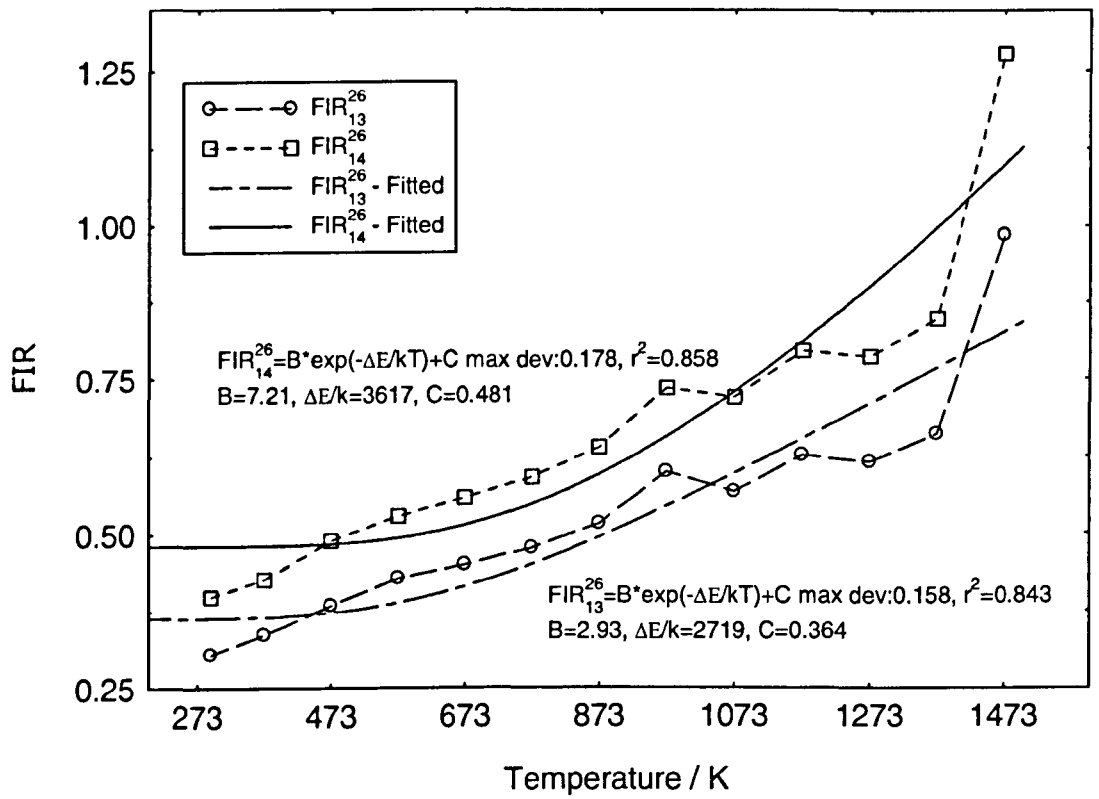

Figure 9.15f: Spec YAl 26 – $Y_3Al_5O_{12}:Er^{3+}$ FIR_{15}^{26} & FIR_{18}^{26} (fitted with Eq. 9.7) vs temperature

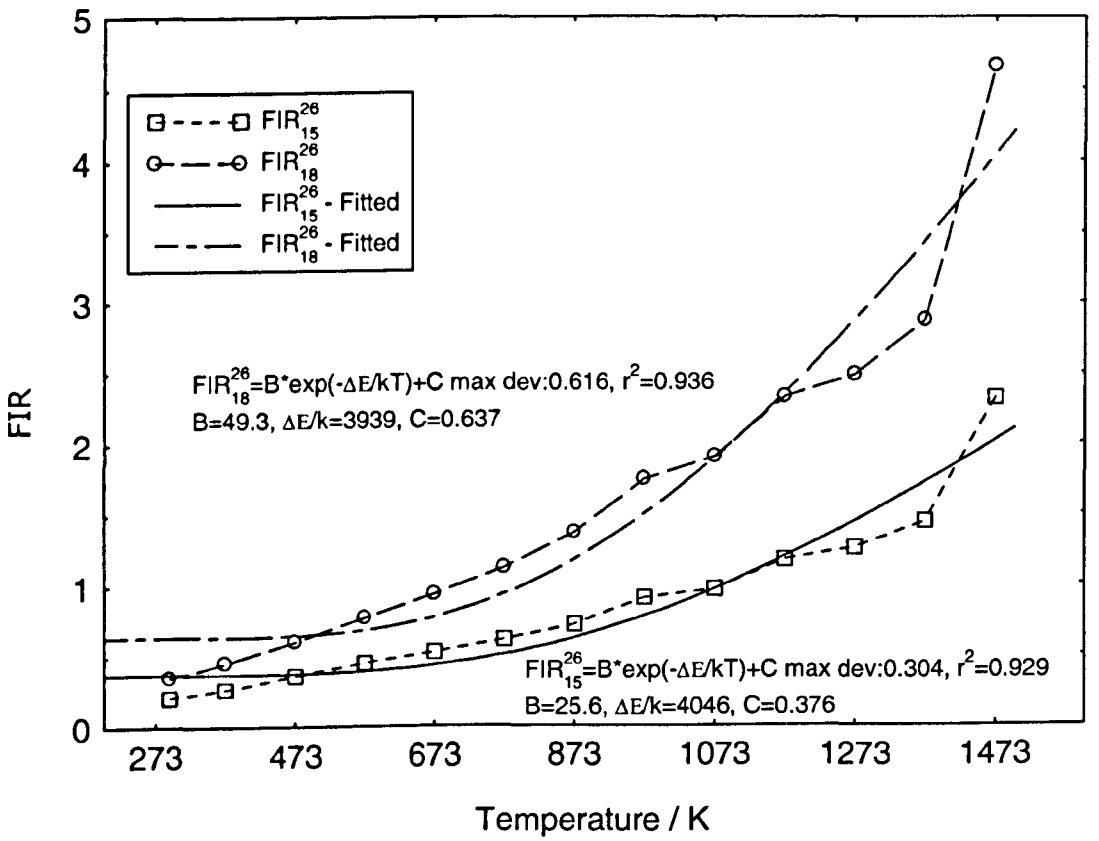

Figure 9.15g: Spec YAl 26 – $Y_3Al_5O_{12}:Er^{3+}$ FIR_{16}^{26} & FIR_{17}^{26} (fitted with Eq. 9.7) vs temperature

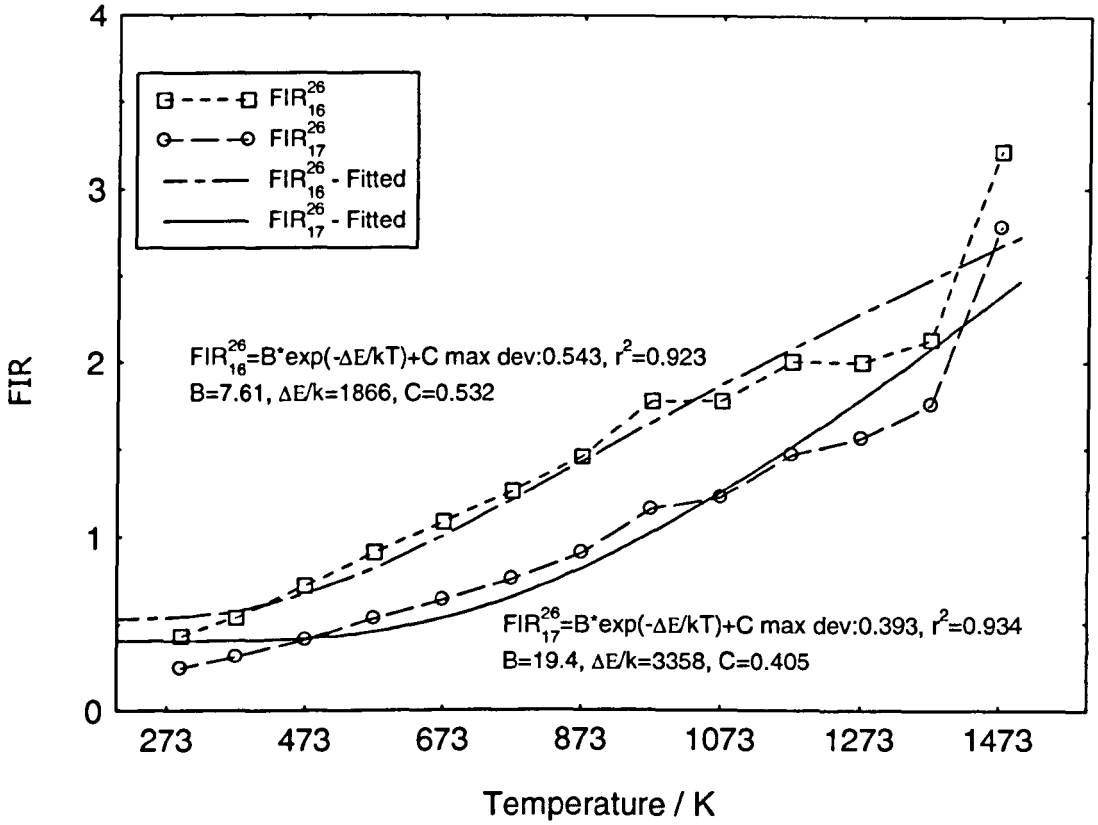

Figure 9.16a: Spec YAl 26 – $Y_3Al_5O_{12}:Er^{3+}$ FIR_{23}^{26} & FIR_{24}^{26} vs temperature

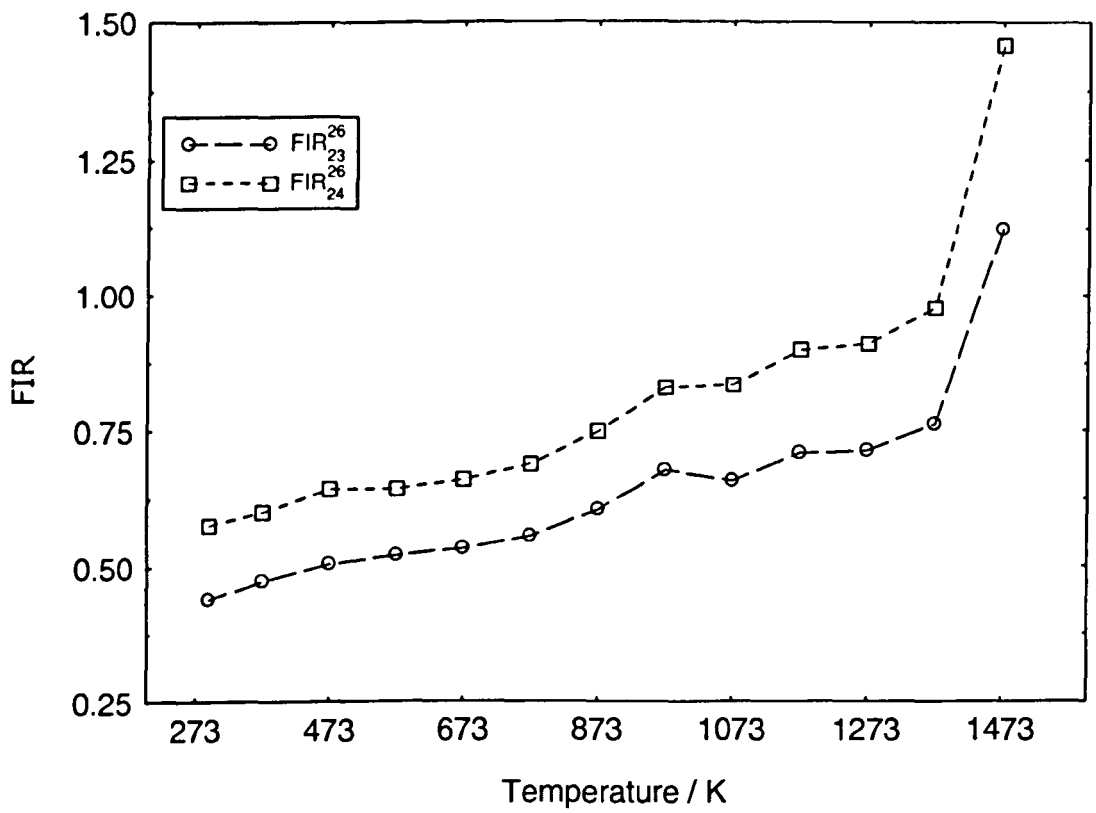

Figure 9.16b: Spec YAl 26 – $Y_3Al_5O_{12}:Er^{3+}$ FIR_{25}^{26} to FIR_{28}^{26} vs temperature

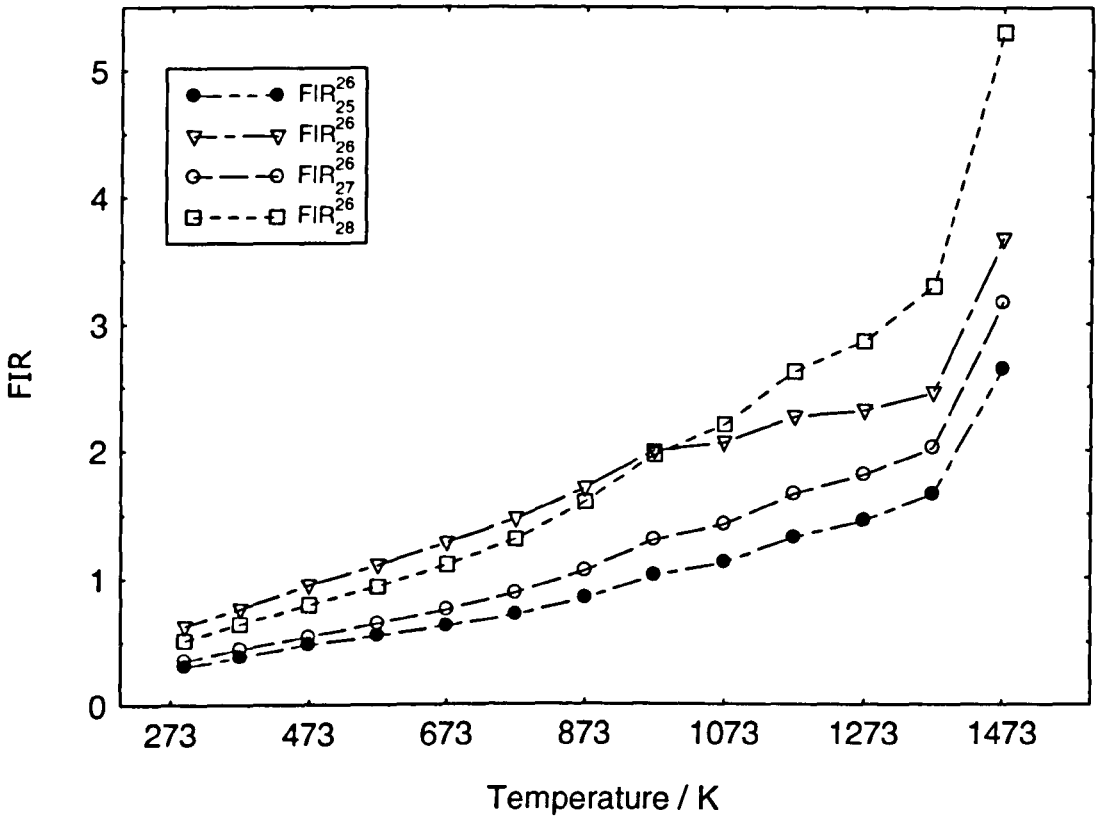

Figure 9.16c: Spec YAl 26 – $Y_3Al_5O_{12}:Er^{3+}$ FIR_{25}^{26} & FIR_{28}^{26} (fitted with Eq. 9.7) vs temperature

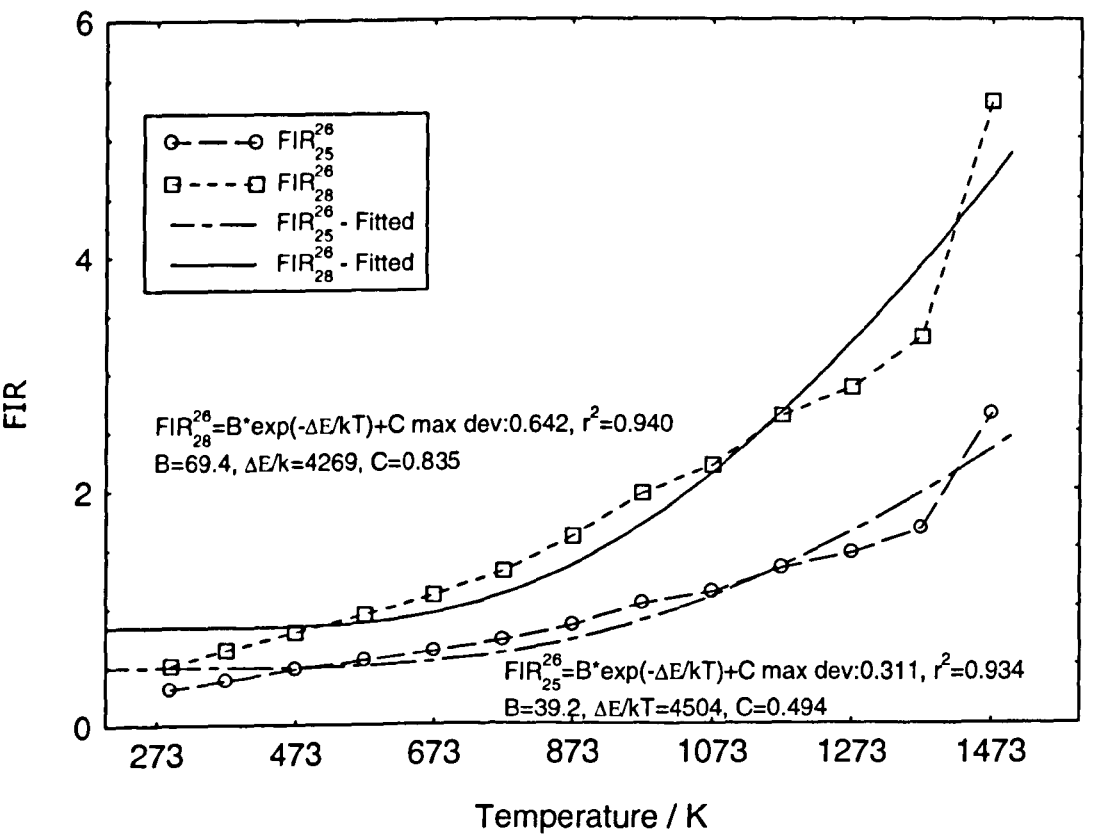

Figure 9.16d: Spec YAl 26 – $Y_3Al_5O_{12}:Er^{3+}$ FIR_{26}^{26} & FIR_{27}^{26} (fitted with Eq. 9.7) vs temperature

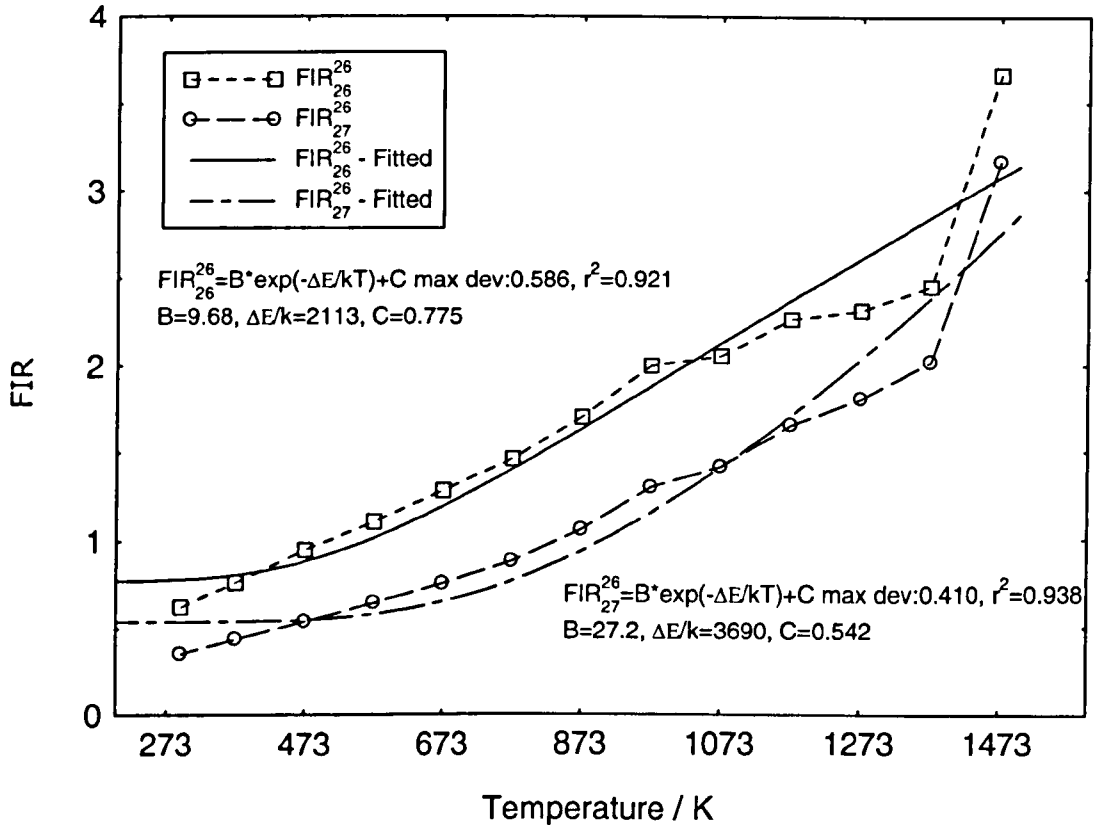

Figure 9.17a: Spec YAl 26 – $Y_3Al_5O_{12}:Er^{3+}$ FIR_{34}^{26} vs temperature

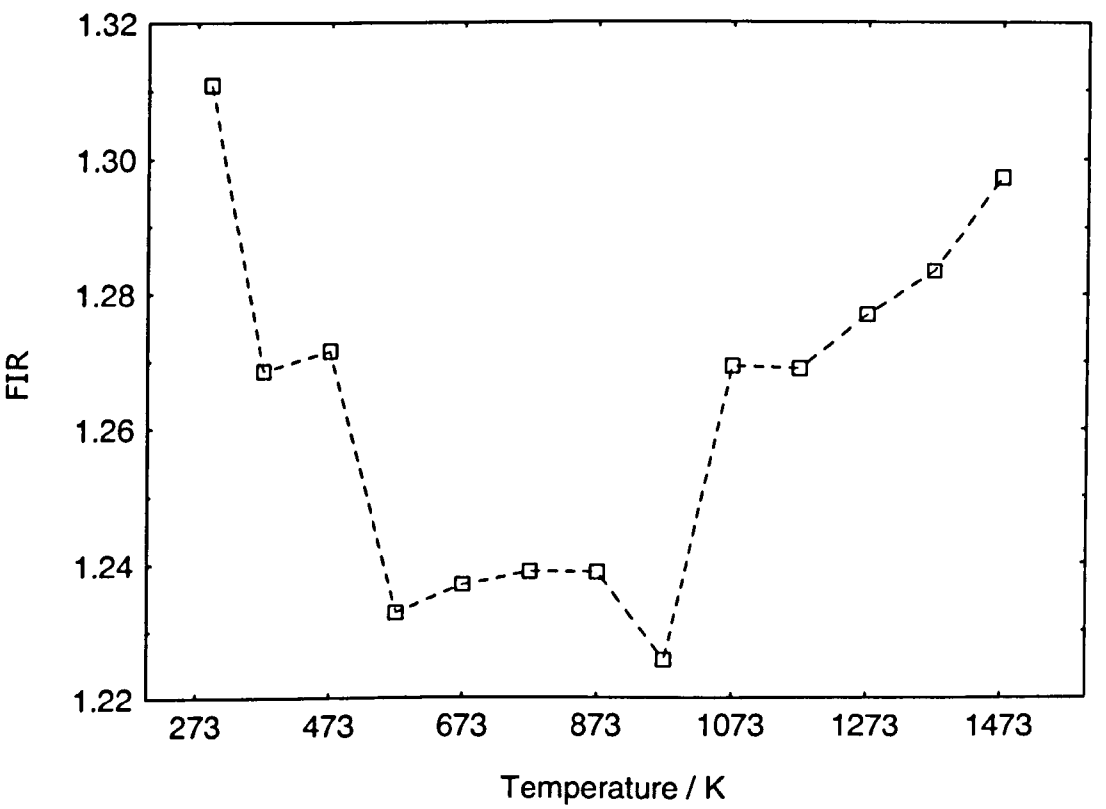

Figure 9.17b: Spec YAl 26 – $Y_3Al_5O_{12}:Er^{3+}$ FIR_{35}^{26} to FIR_{38}^{26} vs temperature

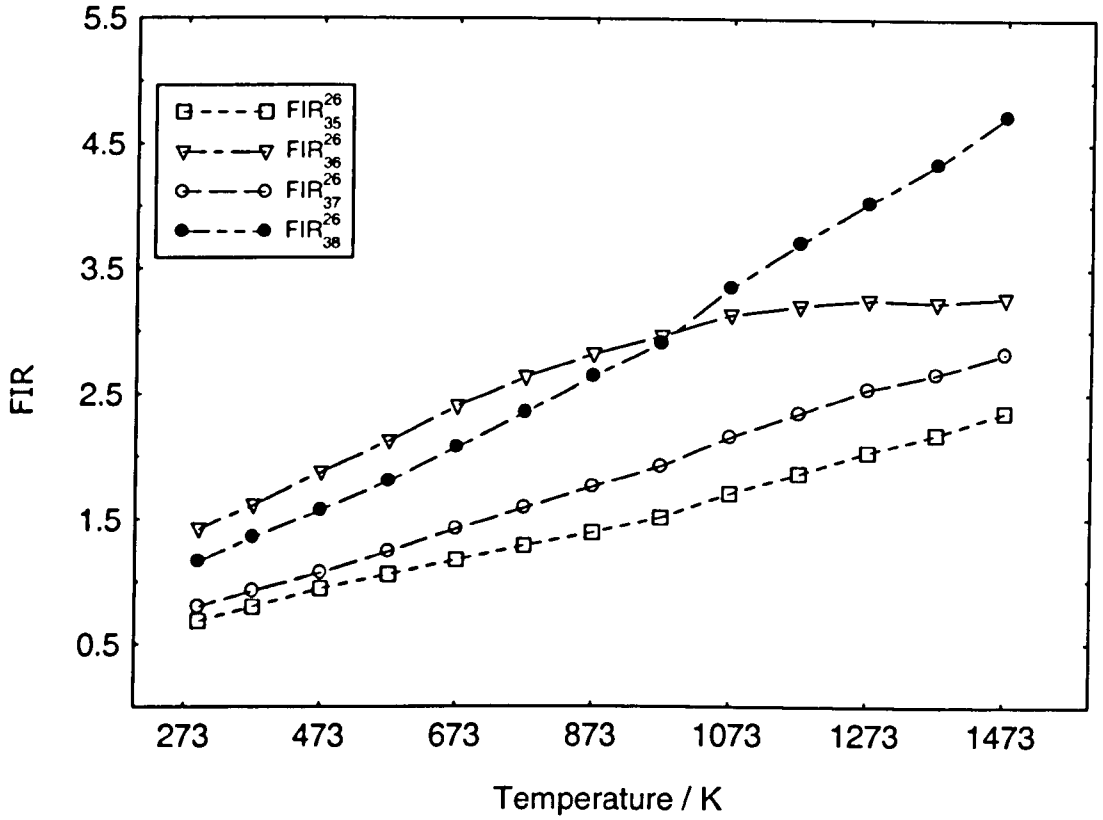

Figure 9.17c: Spec YAl 26 – $Y_3Al_5O_{12}:Er^{3+}$ FIR_{35}^{26} & FIR_{37}^{26} (fitted with Eq. 9.7) vs temperature

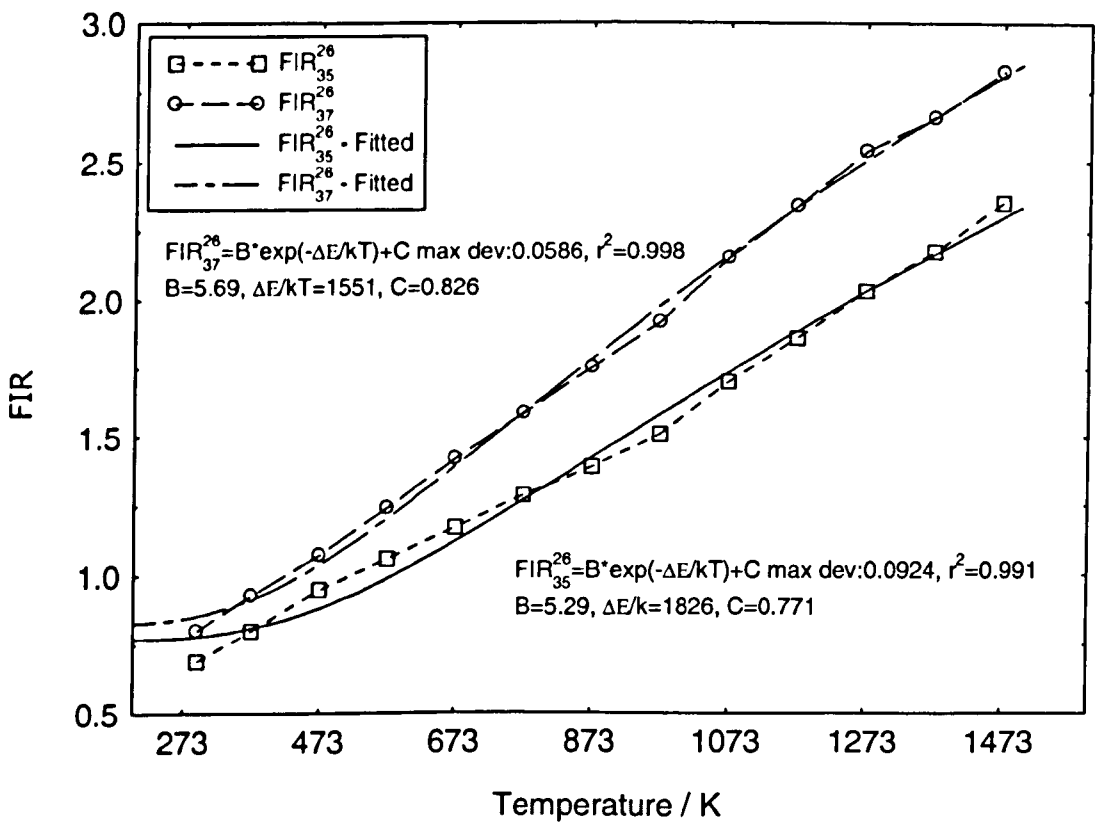

Figure 9.17d: Spec YAl 26 – $Y_3Al_5O_{12}:Er^{3+}$ FIR_{36}^{26} to FIR_{38}^{26} (fitted with Eq. 9.7) vs temperature

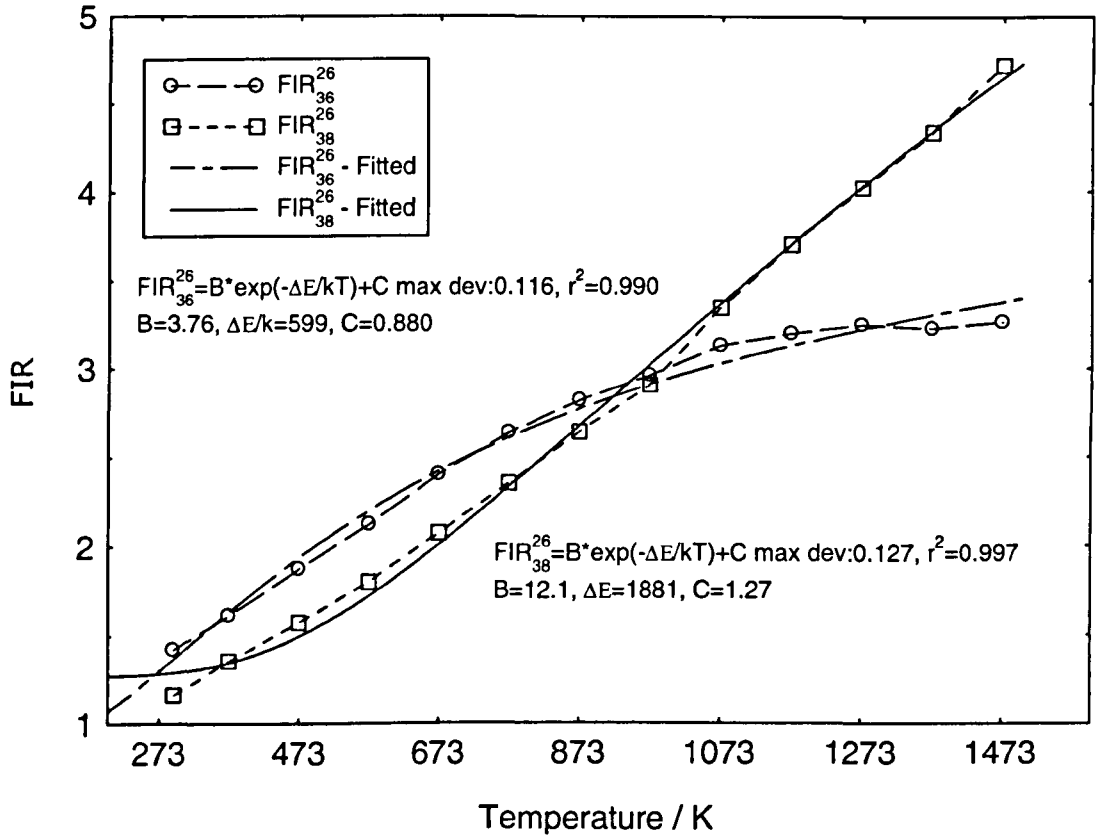

Figure 9.18a: Spec YAl 26 – $Y_3Al_5O_{12}:Er^{3+}$ FIR_{45}^{26} to FIR_{48}^{26} vs temperature

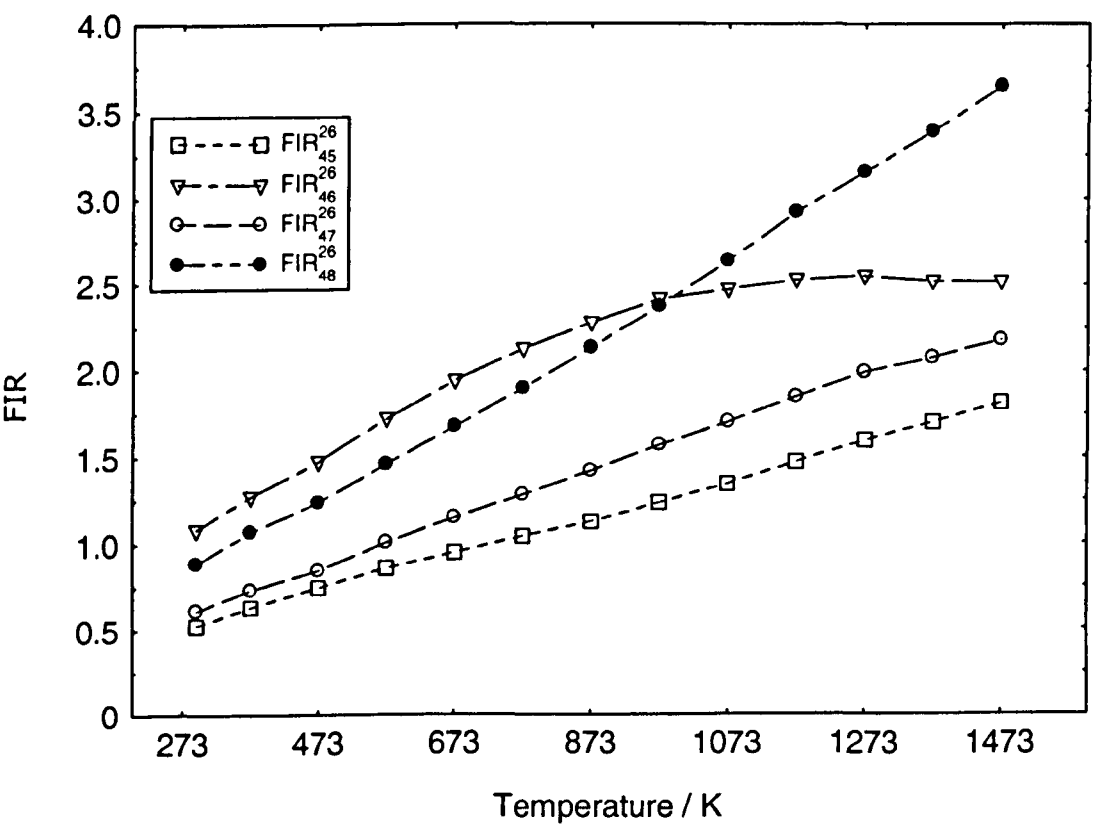

Figure 9.18b: Spec YAl 26 – $Y_3Al_5O_{12}:Er^{3+}$ FIR_{45}^{26} & FIR_{47}^{26} (fitted with Eq. 9.7) vs temperature

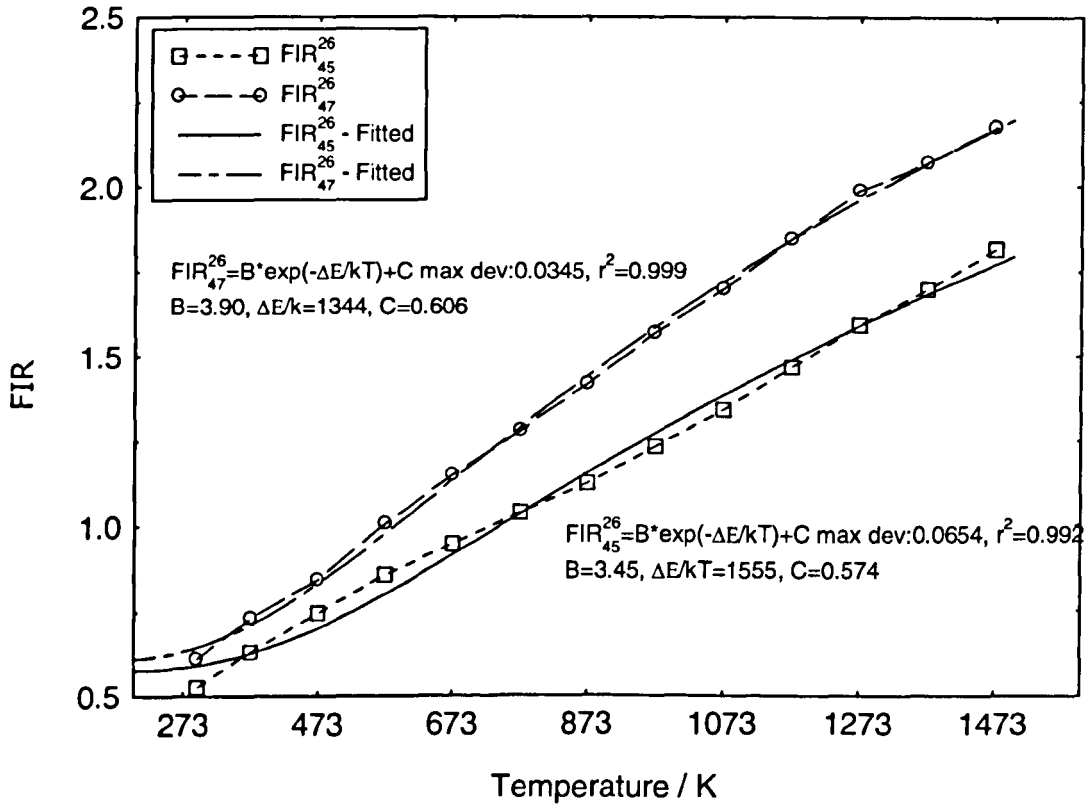

Figure 9.18c: Spec YAl 26 – $Y_3Al_5O_{12}:Er^{3+}$ FIR_{46}^{26} & FIR_{48}^{26} (fitted with Eq. 9.7) vs temperature

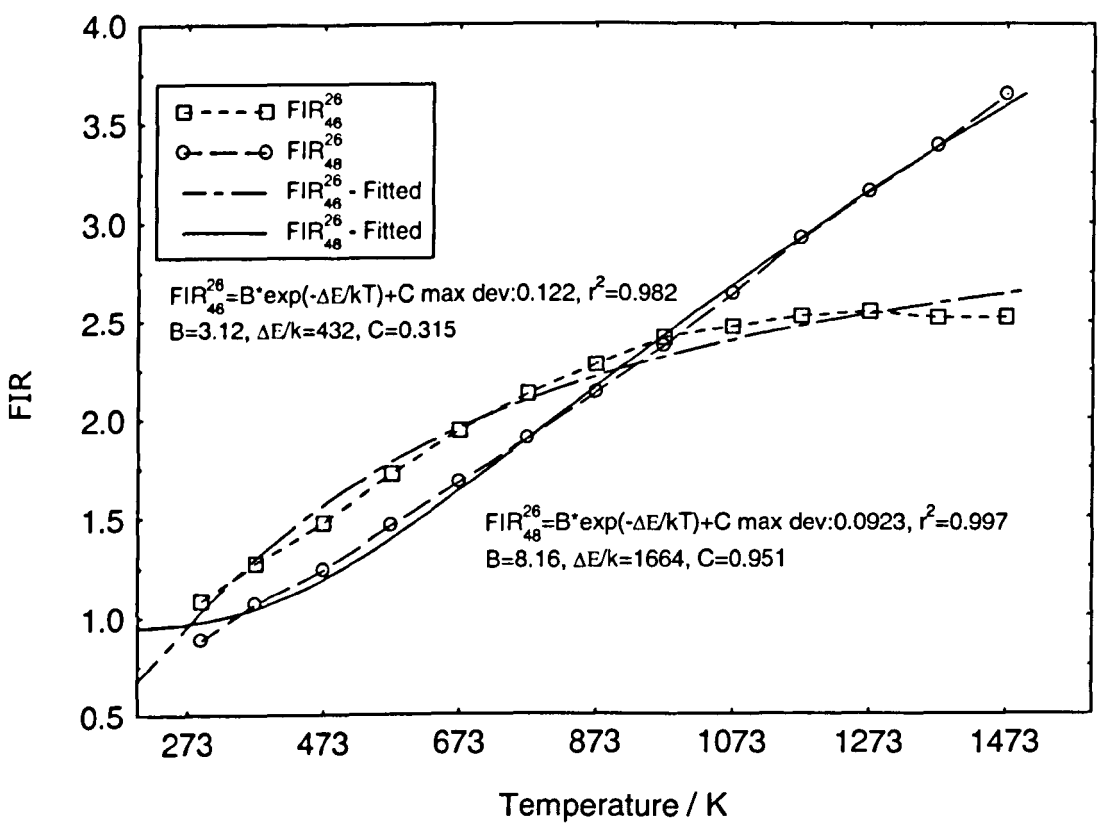

Figure 9.19: Spec YAl 26 – $Y_3Al_5O_{12}:Er^{3+}$ FIR_{56}^{26} to FIR_{58}^{26} vs temperature

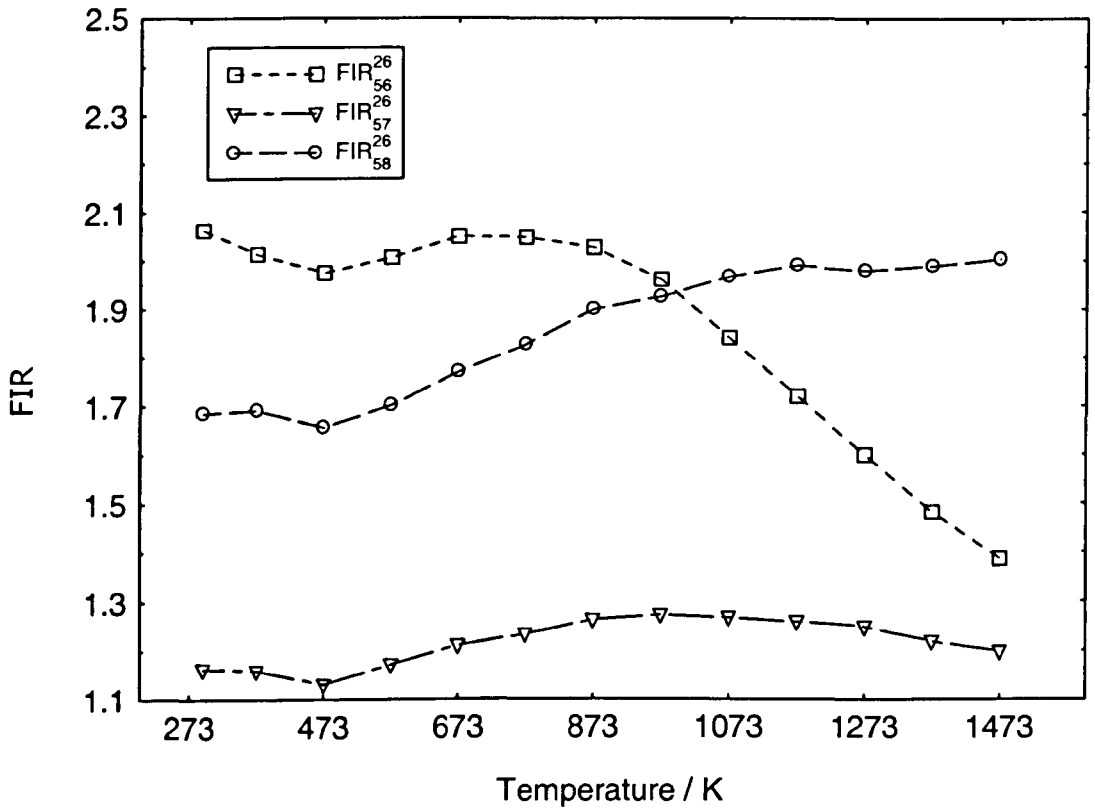

Figure 9.20a: Spec YAl 26 – $Y_3Al_5O_{12}:Er^{3+}$ FIR_{67}^{26} & FIR_{68}^{26} vs temperature

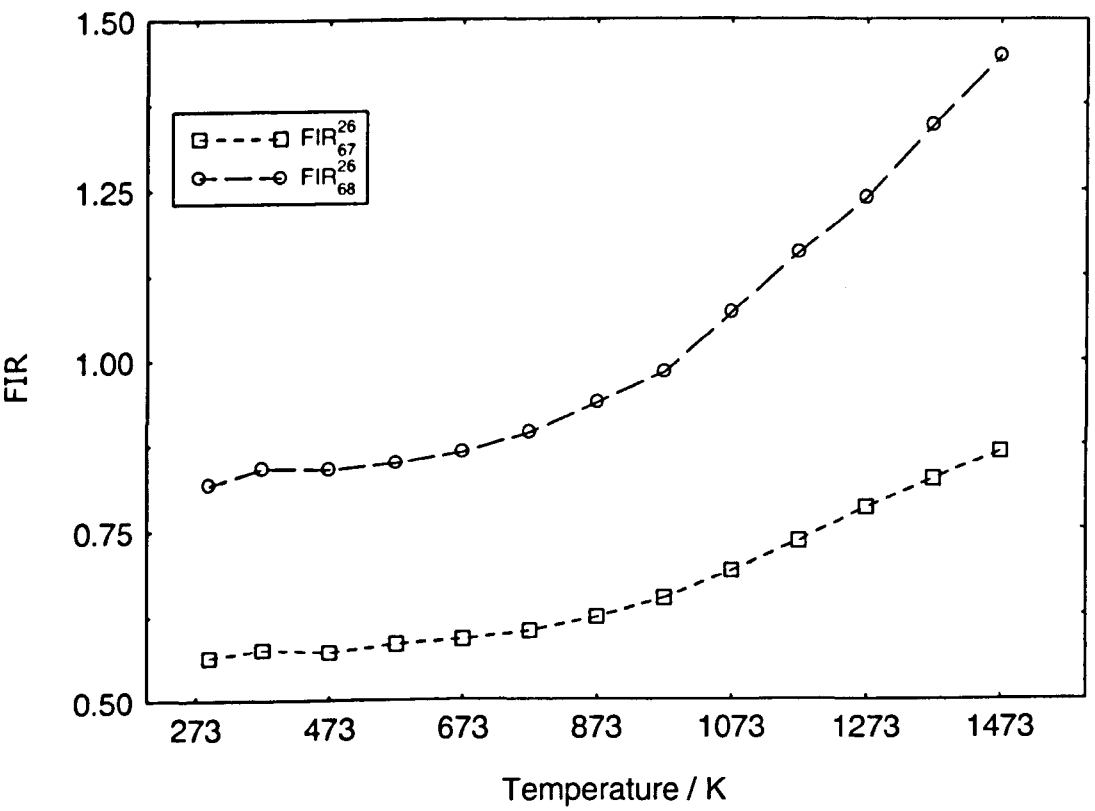

Figure 9.20b: Spec YAl 26 – $Y_3Al_5O_{12}:Er^{3+}$ FIR_{68}^{26} (fitted with Eq. 9.7) vs temperature

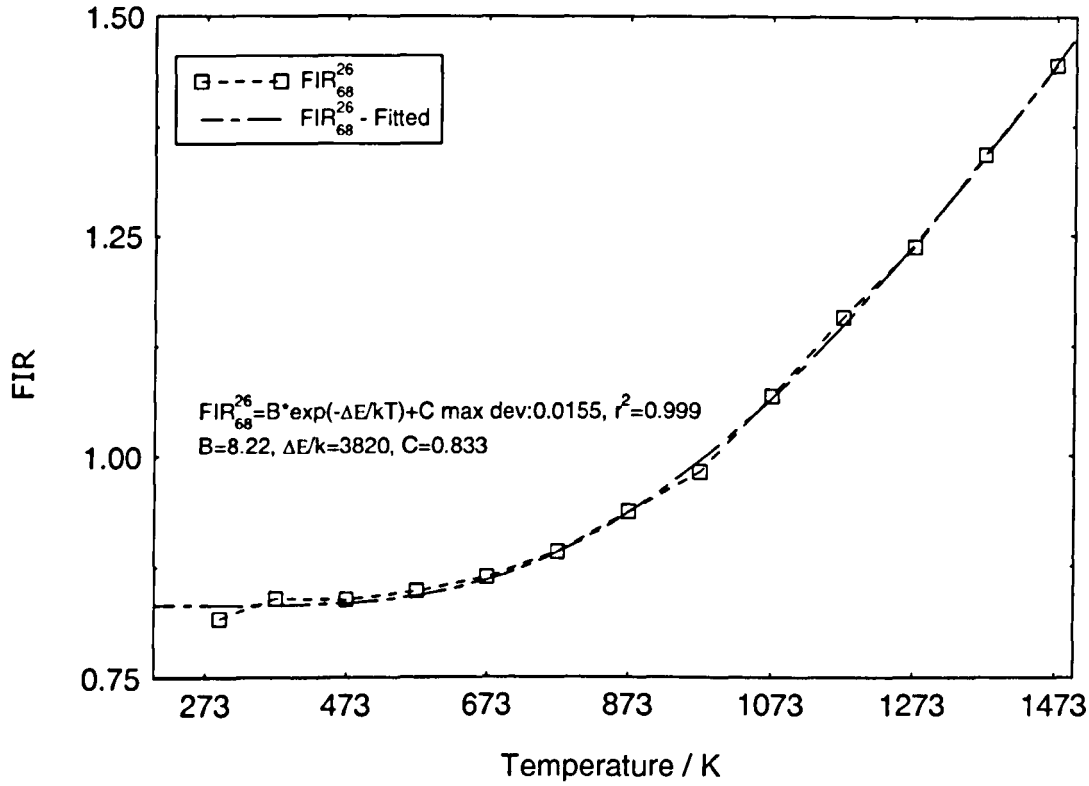

Figure 9.21: Spec YAl 26 – $Y_3Al_5O_{12}:Er^{3+}$ FIR_{78}^{26} (actual and fitted with Eq. 9.7) vs temperature

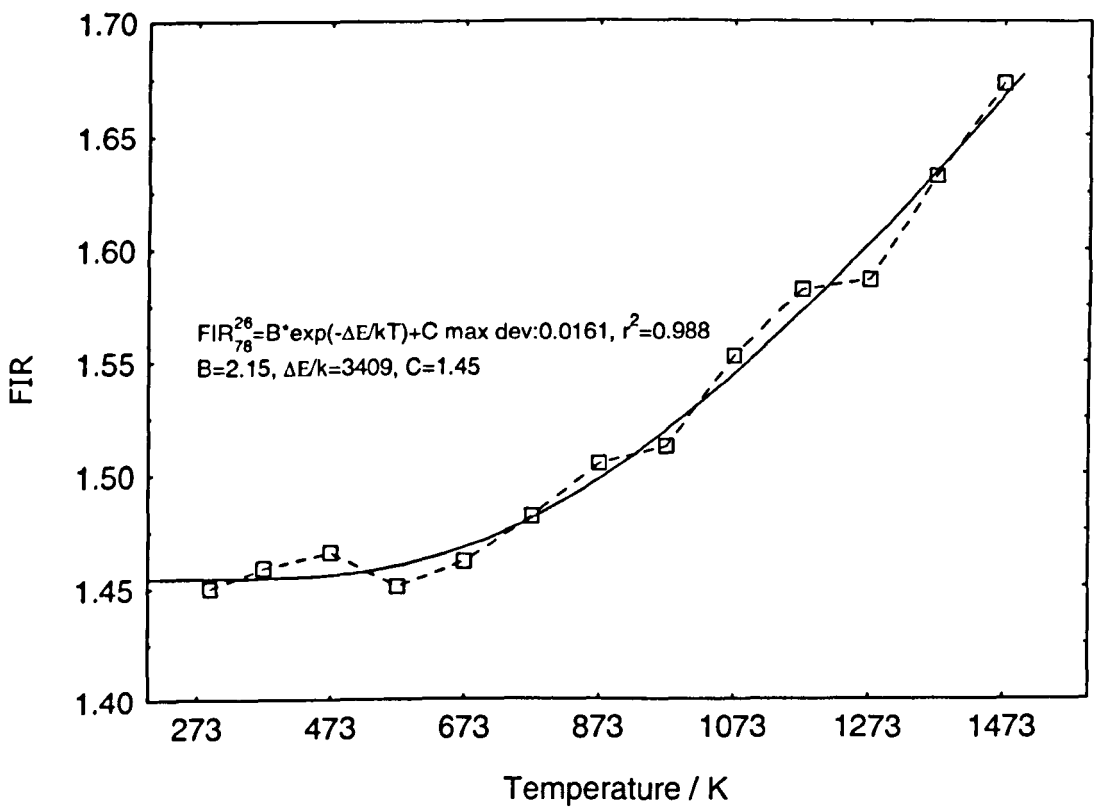

Figure 9.22a: Spec YAl 26 – $Y_3Al_5O_{12}:Er^{3+}$ FIR_{AB}^{26}, FIR_{AC}^{26} & FIR_{BC}^{26} - integrated intensity vs temperature

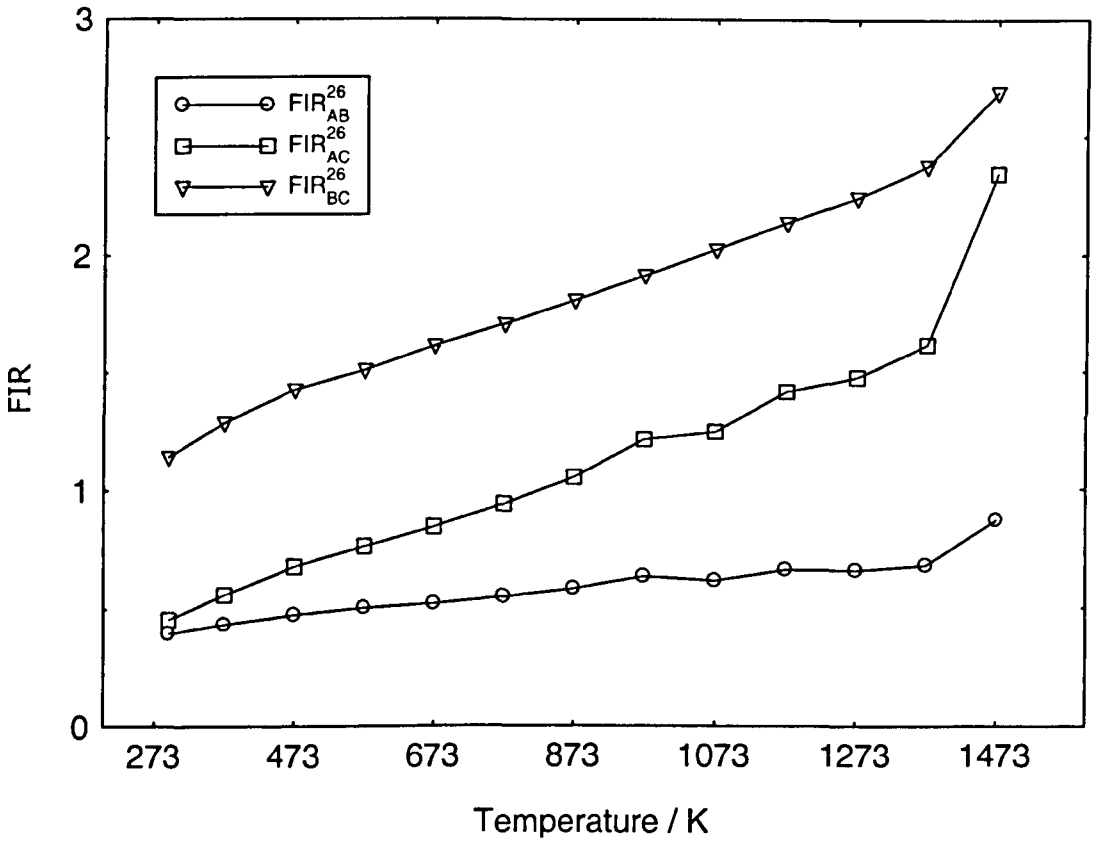

Figure 9.22b: Spec YAl 26 – $Y_3Al_5O_{12}:Er^{3+}$ FIR_{AC}^{26} & FIR_{BC}^{26} - integrated intensity (fitted with Eq. 9.7) vs temperature

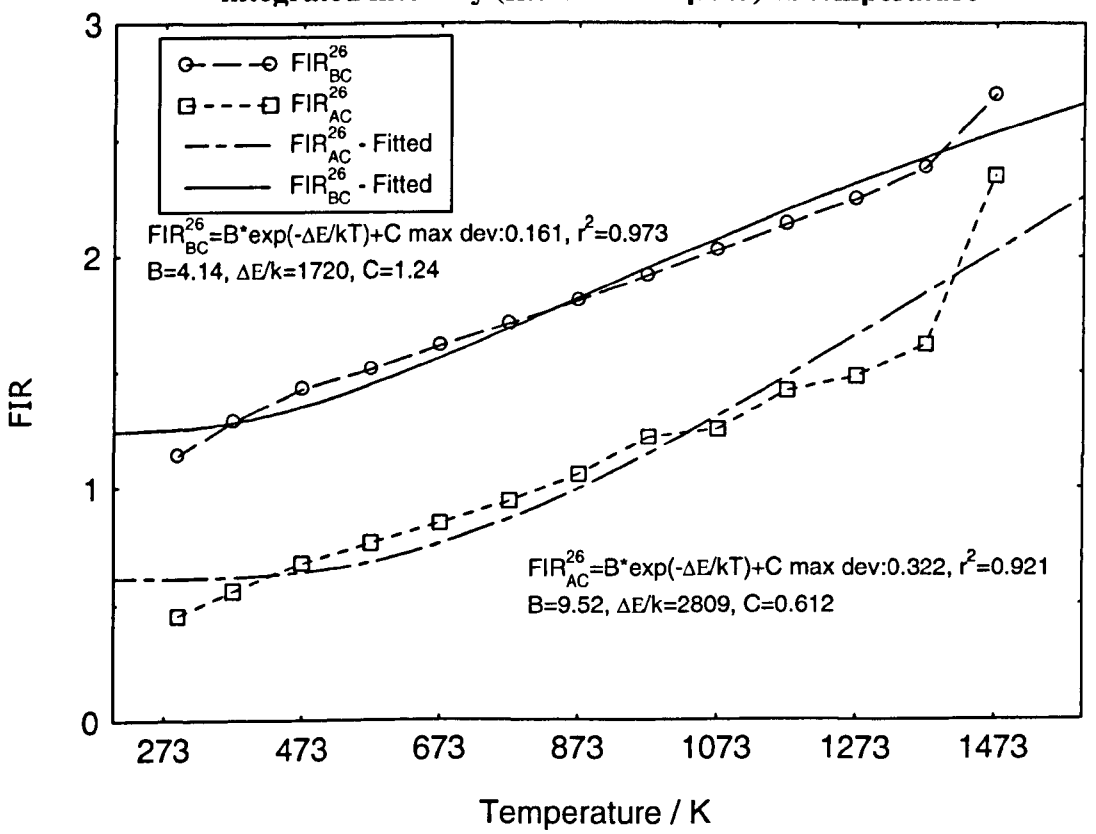

9.6.2 Upconversion Intensity Based Sensing – $Y_3Al_5O_{12}:Er^{3+}$

The temperature dependence of the upconversion emission in the visible region was investigated. Under the excitation of a 965nm laser diode, visible green and red light was observed. The behaviour of the emission will give us a clearer understanding of the practicality of temperature sensing using the visible region. Figure 9.23 shows the upconversion emission at room temperature. The total green emission is approximately 80% more intense as compared with the red intensity. The green lines (541nm, 553.5nm and 560nm) and one red line (676nm) intensities were monitored and recorded for the calculation of the upconversion intensity ratio (UIR). Integrating the upconversion wavelength ranges corresponding to the transitions from $^2H_{11/2}$ and $^4S_{3/2}$ were also investigated to determine the UIR. The highest reported temperature measured using upconversion for Er^{3+} doped silica fibres is ~1000K by *Maurice* [9.49]. This work presents the possibility of detecting temperatures as high as 1473K using upconversion.

9.6.2.1 Results and Discussion

Figure 9.24 shows the upconversion spectra of both the green and red as a function of temperature over the whole temperature range (273K to 1473K) investigated in this work. At $^4S_{3/2}$ and $^2H_{11/2}$ transition (Figures 9.25 and 26) intensities decreased as the temperature increased. Broadening effects on linewidths were observed at 1173K and above. From Figure 9.26, it can be seen that the intensity of transition $^4S_{3/2}$ decreases with temperature but $^2H_{11/2}$ decreases initially but increases progressively from approximately 773K. This can be clearly seen in Figure 9.29 (insert). By integrating the wavelength range of each transition one can clearly see the variation of the intensities. A similar phenomenon was observed in Er^{3+} doped silica fibres where the transition $^2H_{11/2}$ was not visible at 77K but as temperature increased the upconversion intensity increased as well [9.48]. The possible reason for this increase when the doped fibre is heated could due to the effect of the thermal population of the energy levels of Er^{3+} [9.48]. In the thermal equilibrium a Boltzmann distribution would suggest upper energy levels should increase in population with increasing temperature and this was observed (Figure 9.26). Transitions from level $^4S_{3/2}$ (lower energy level) decreased as temperature increased but the transition from level $^2H_{11/2}$

(upper energy level) increased. Its linewidth started at ~500nm where the initial linewidth started at ~530nm at room temperature. Figures 9.27 and 28 show the upconversion spectra from the $^4F_{9/2}$ manifold. The red upconversion intensity was observed to initially decrease with temperature, however the intensity began to increase after ~873K. Figure 9.29 shows the integrated intensity of the wavelengths from the $^4F_{9/2}$ manifold where a steep increase is observed. This could be very useful for measuring temperature due to the wide dynamic intensity range.

From the above work, it was observed that it was possible to monitor the temperature just based on the intensity of the upconversion emission. Figures 9.30a and b show the intensities of emission lines at 541mn ($^2H_{11/2}\rightarrow{}^4I_{15/2}$), 553.5nm and 560nm ($^4S_{3/2}\rightarrow{}^4I_{15/2}$) as a function of temperature. The intensities of these emission lines decrease as the temperature rises and, when plotted, distinguishable exponential decay profiles can be observed. These curves (I_{541}, $I_{553.5}$ and I_{560}) have a maximum effective measuring temperature of ~1173K and the maximum error obtained for these curves during the intensity measurement was ~4%. The red emission line at 679nm ($^4S_{3/2}\rightarrow{}^4I_{15/2}$) was appropriate for use due to large changes from decreasing to increasing intensity, see Figure 9.31. Table 9.3 shows the denotations of the upconversion intensity ratios (UIR) of the Er^{3+} doped YAG SCF and the ΔE for both theoretical and fitted which was obtained using equation 9.7. From Figures 9.32 and 33 the progressive increase in the UIRs as temperature increases can be seen. From the UIRs, measurement to a high temperature of 1473K (maximum temperature for this work) was possible but with a relatively large error of ~8%. This error can be greatly reduced if the fibre sensor can be properly coupled to the excitation source and other optics, and by replacing the mechanical chopper with an electronic modulator. By doing so the signal-to-noise ratio could be increased and the temperature measuring system improved. There were differences between the theoretical and fitted values of ΔE. When adopting equation 9.7, one would expect some variation as this equation is commonly used for silica based fibres. Discrepancies were also observed in work reported by *Seat* [2.57] when Al_2O_3 SCF fibres were employed for temperature sensing. Modification could be made to the present equation 9.7 to improve the condition of the fitting to oxide based materials. For now, a close approximation is sufficient for the current investigation. Due to the

non-monotonic changes of the intensity with temperature in the $^4F_{9/2}$ manifold, emission lines at 679nm was not made use of for UIR calculation.

Integral intensities of the wavelengths from $^2H_{11/2}$ transition (530nm to 550nm – subscript *A*) and $^4S_{3/2}$ (550nm to 570nm – subscript *B*) were monitored. Figure 9.34 shows the intensity ratio between the two transitions. The UIR plot is linear making it desirable for temperature sensing application. The UIR_{AB}^{26} is both fitted with a straight line and equation 9.7, the points were thoroughly fitted. The ratio of the integrated intensity between transitions $^2H_{11/2}$ + $^4S_{3/2}$ with $^4F_{9/2}$ $\left(UIR_{ABC}^{26}\right)$ is presented in Figure 9.35 (subscript *C* refers to region 630nm to 700nm). The very steep slope observed in the higher temperature region signified that there are large changes in the temperature dependent ratio making it extremely useful for measuring extreme temperature environments.

Figure 9.23: Spec YAl 26 $Y_3Al_5O_{12}:Er^{3+}$ upconversion in room temperature, 293K

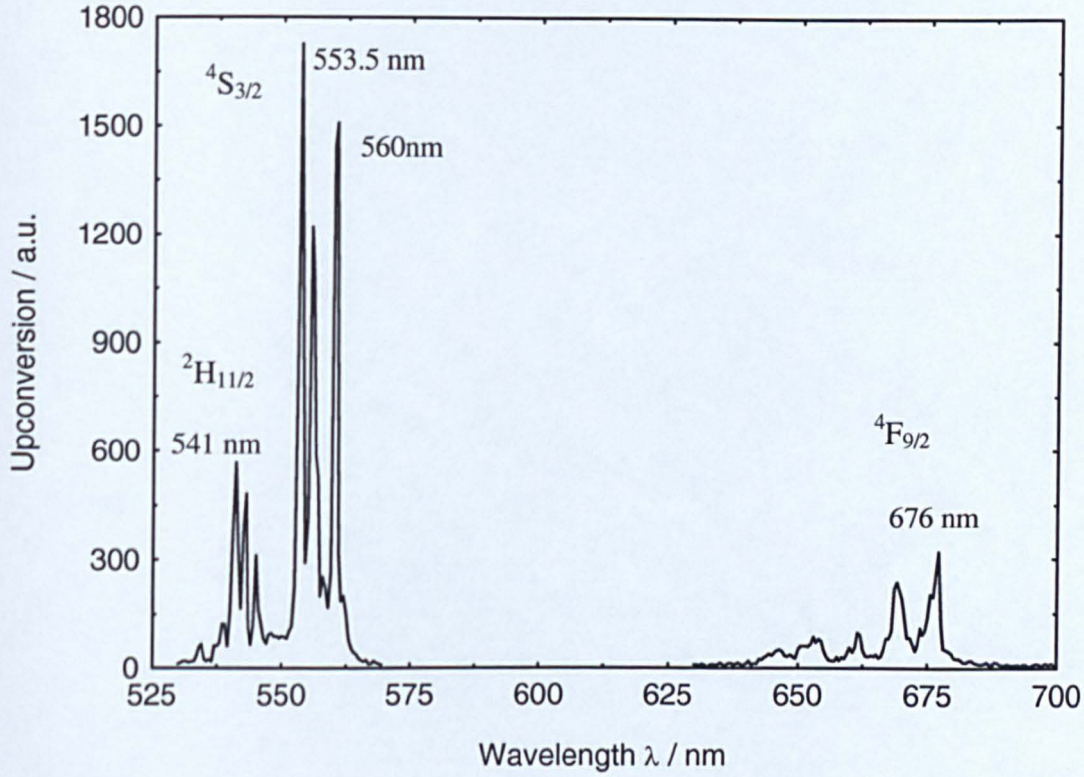

Figure 9.24: Spec YAl 26 $Y_3Al_5O_{12}:Er^{3+}$ upconversion spectra from room temperature to 1473K

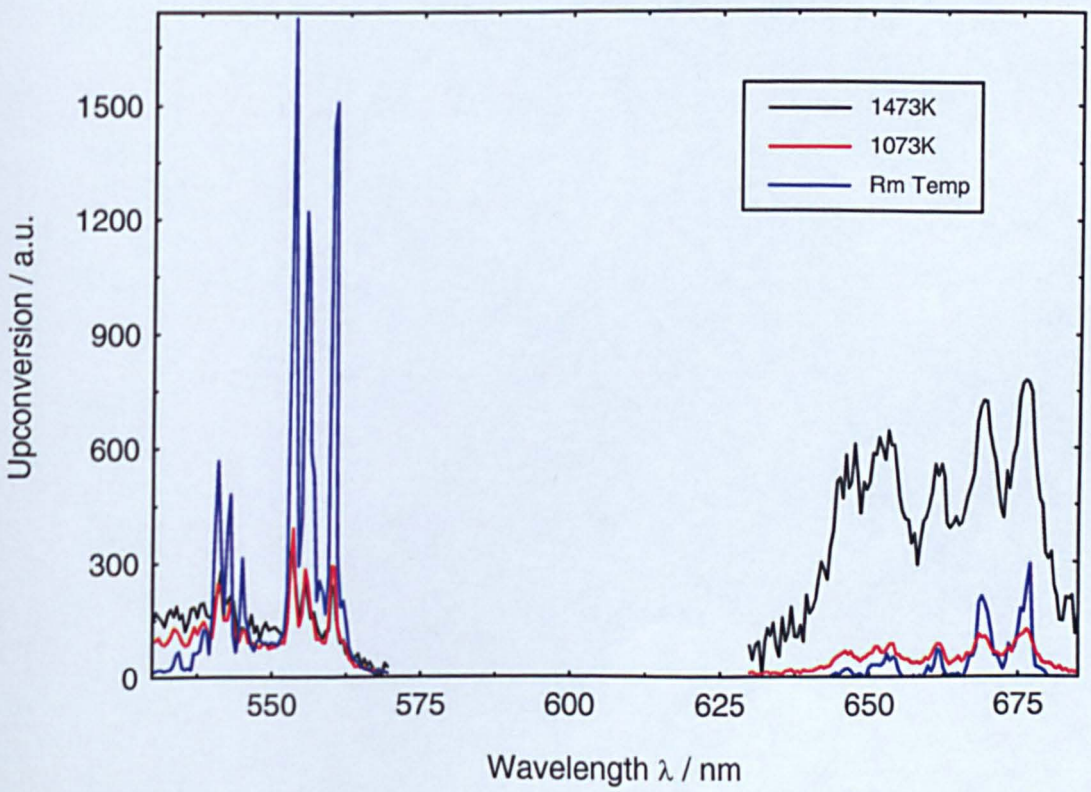

Figure 9.25: Spec YAl 26 $Y_3Al_5O_{12}:Er^{3+}$ upconversion spectra from room temperature to 873K, $^2H_{11/2} + {}^4S_{3/2}$

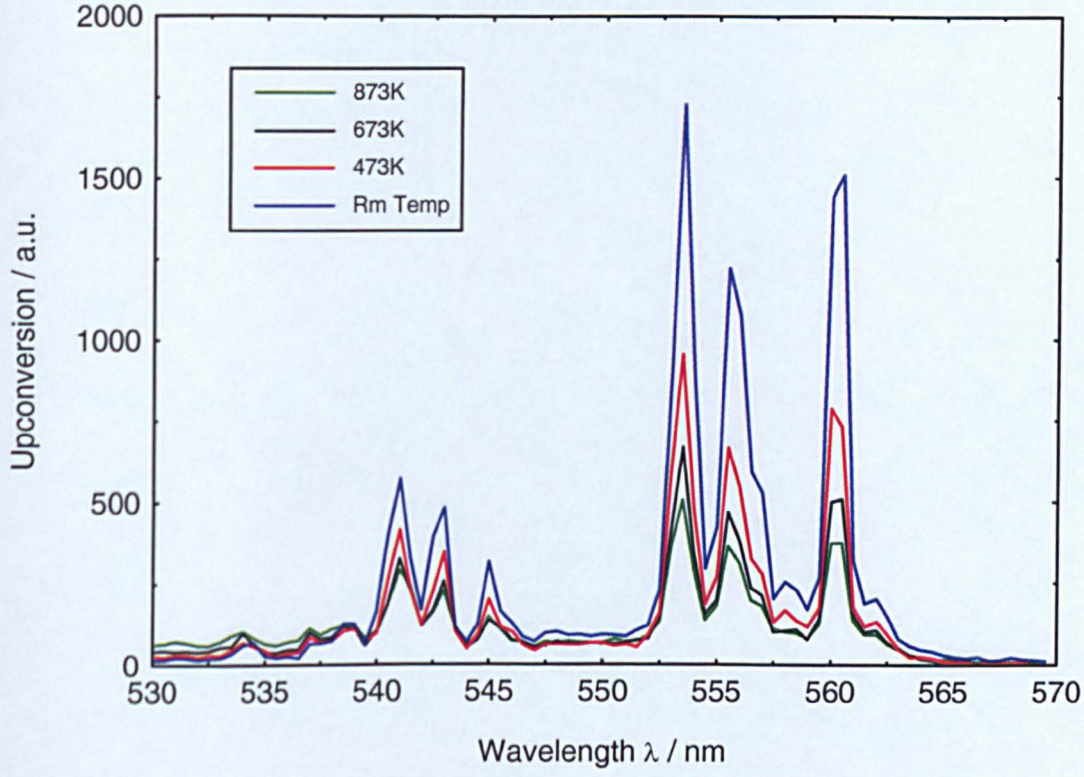

Figure 9.26: Spec YAl 26 $Y_3Al_5O_{12}:Er^{3+}$ upconversion spectra from 1173K to 1473K, $^2H_{11/2} + {}^4S_{3/2}$

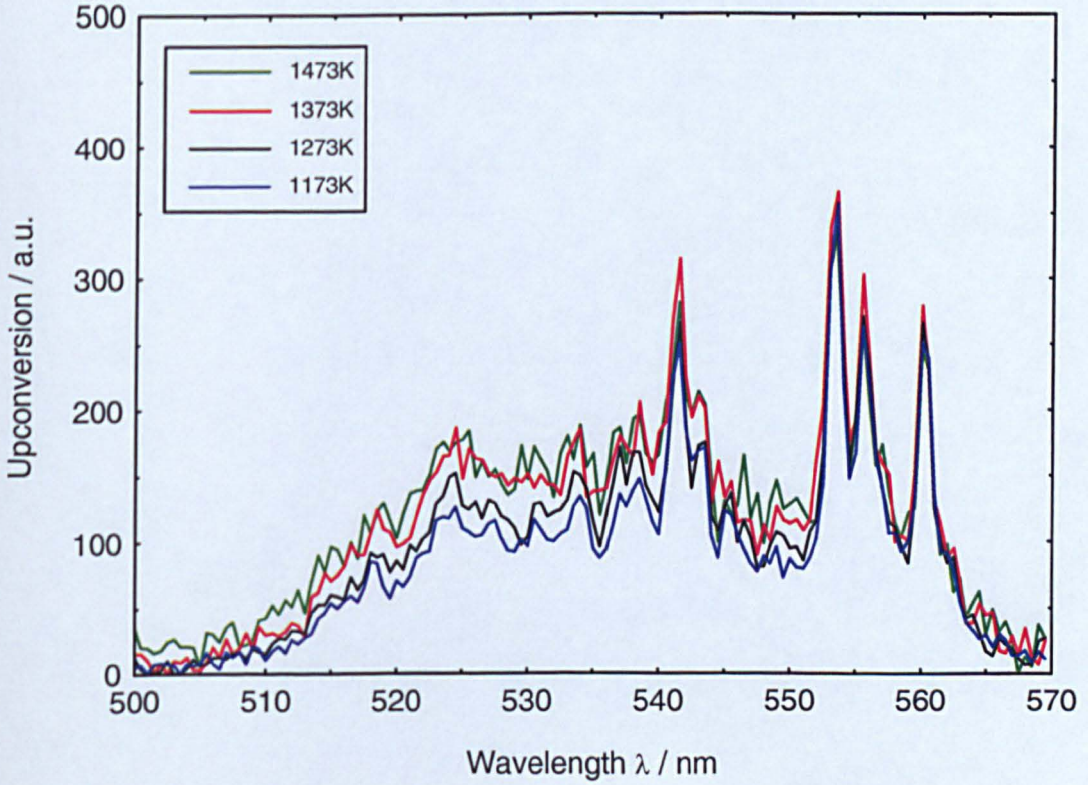

Figure 9.27: Spec YAl 26 $Y_3Al_5O_{12}:Er^{3+}$ upconversion spectra from room temperature to 873K, $^2F_{9/2}$

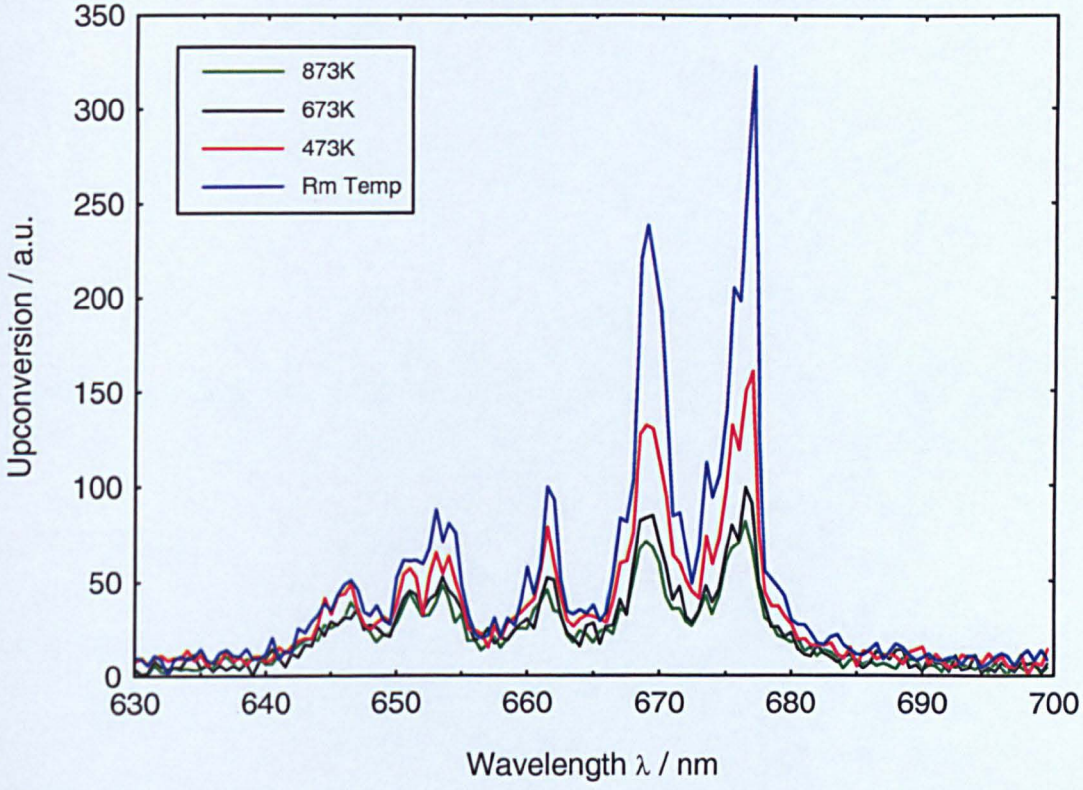

Figure 9.28: Spec YAl 26 $Y_3Al_5O_{12}:Er^{3+}$ upconversion spectra from 973K to 1473K & 273K, $^2F_{9/2}$

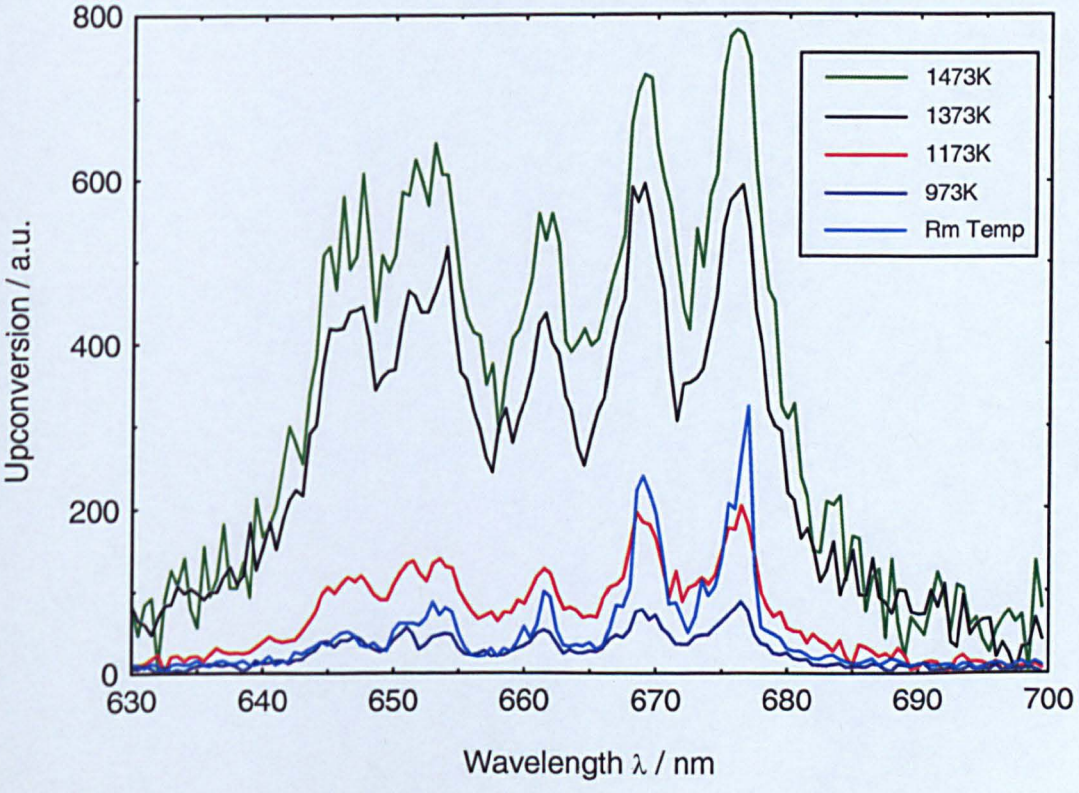

Table 9.3 – Spec YAl 26:$Y_3Al_5O_{12}:Er^{3+}$ temperature sensor UIR denotations

Denotations	Visible line	ΔE (cm^{-1})	
		Theoretical	Fitted
UIR_{12}^{26}	$I_{541}/I_{553.5}$	417.44	517.73
UIR_{13}^{26}	I_{541}/I_{560}	627.14	678.96
UIR_{23}^{26}	$I_{553.5}/I_{560}$	209.7	598.34

Figure 9.29: Spec YAl 26 $Y_3Al_5O_{12}:Er^{3+}$ - Integrated intensity at $^2H_{11/2}$, $^4S_{3/2}$ and $^4F_{9/2}$

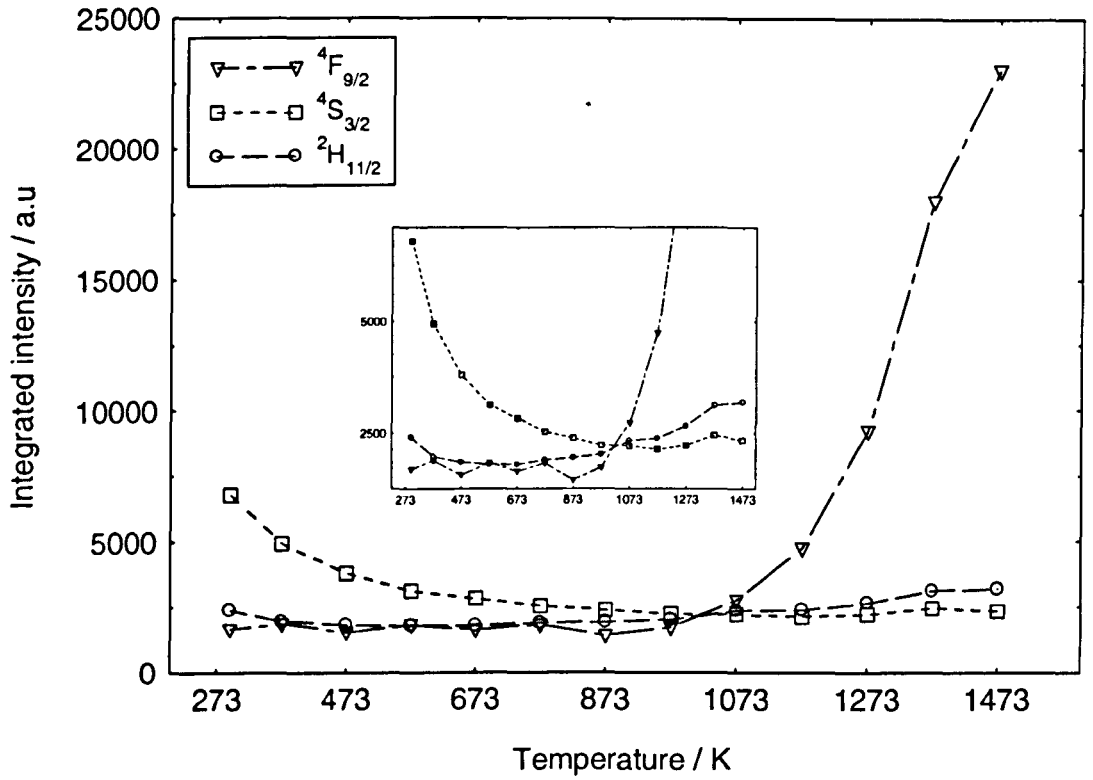

Figure 9.30a: Spec YAl 26 $Y_3Al_5O_{12}:Er^{3+}$ intensity based sensing at 541nm (I_{541})

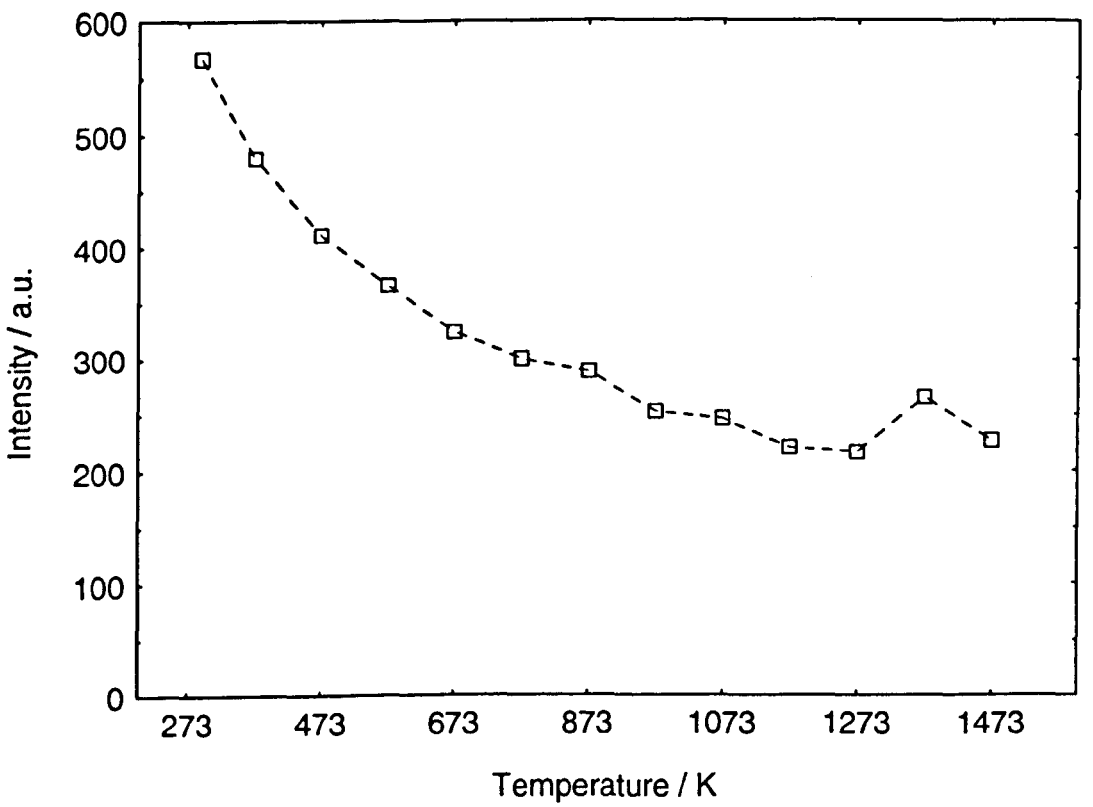

Figure 9.30b: Spec YAl 26 $Y_3Al_5O_{12}:Er^{3+}$ intensity based sensing at 553.5nm & 560nm ($I_{553.5}$ & I_{560})

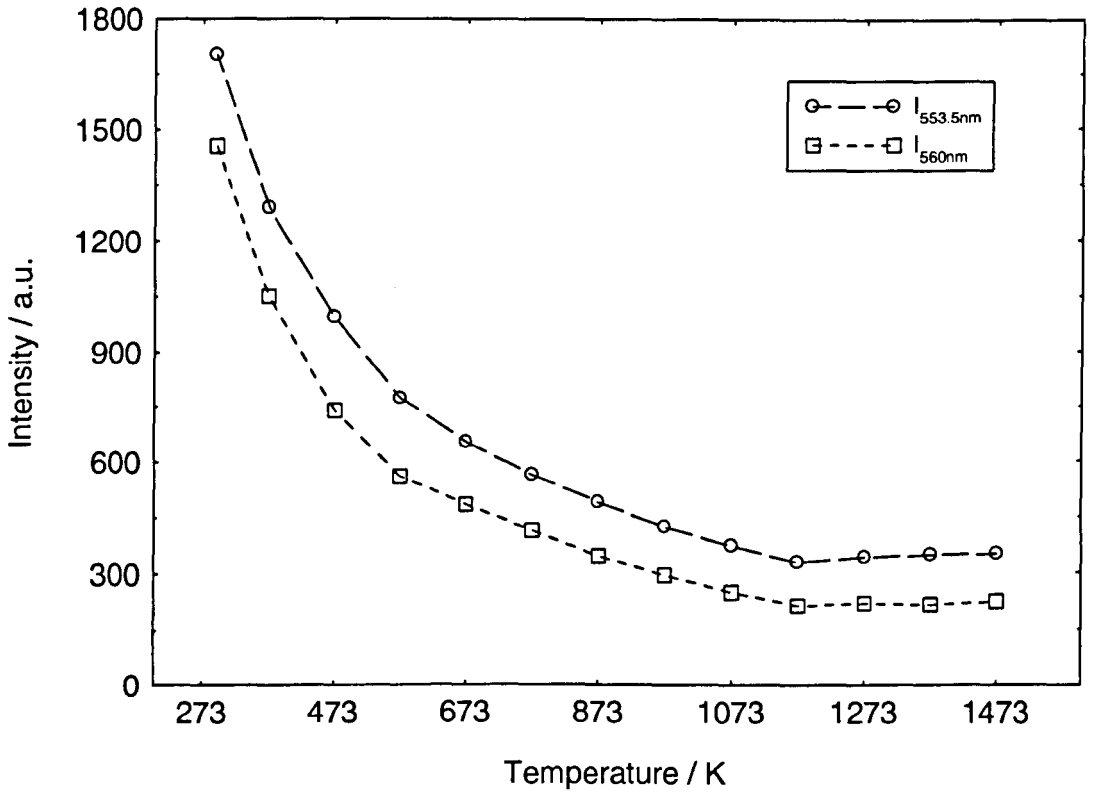

Figure 9.31: Spec YAl 26 $Y_3Al_5O_{12}:Er^{3+}$ intensity based sensing at 676nm (I_{676})

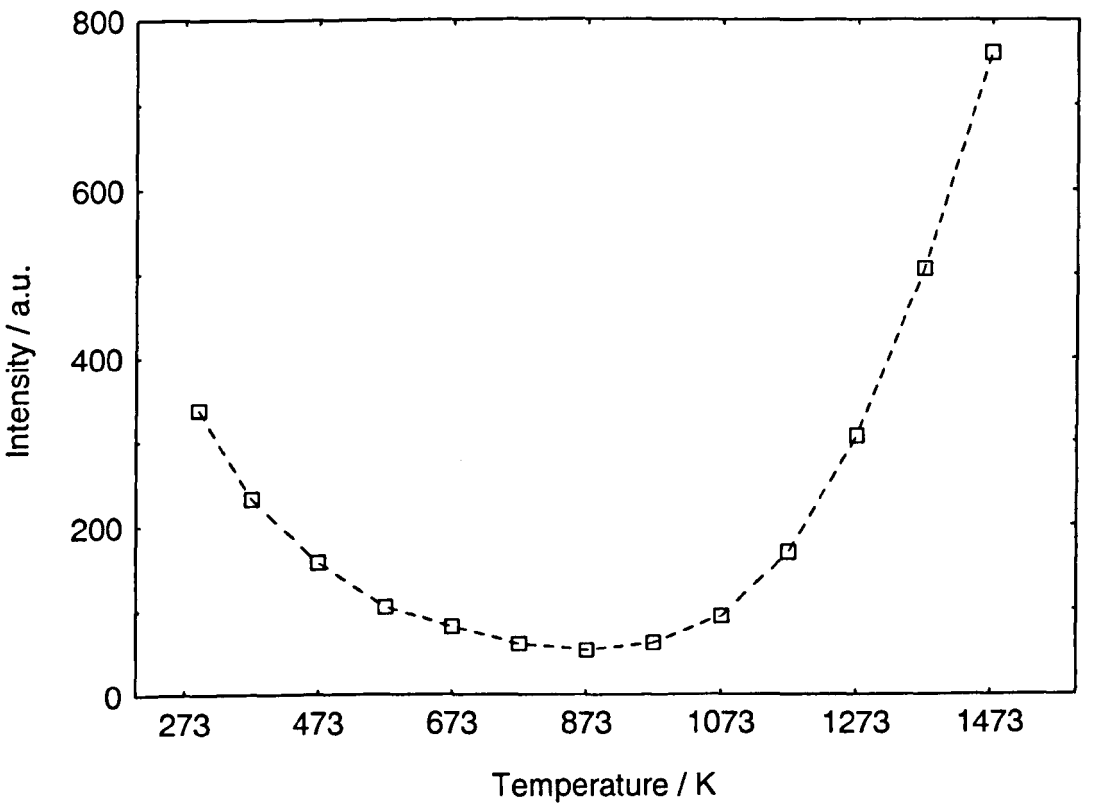

Figure 9.32: Spec YAl 26 $Y_3Al_5O_{12}:Er^{3+}$ UIR_{12}^{26} & UIR_{13}^{26} (actual and fitted with Eq 9.7) vs temperature

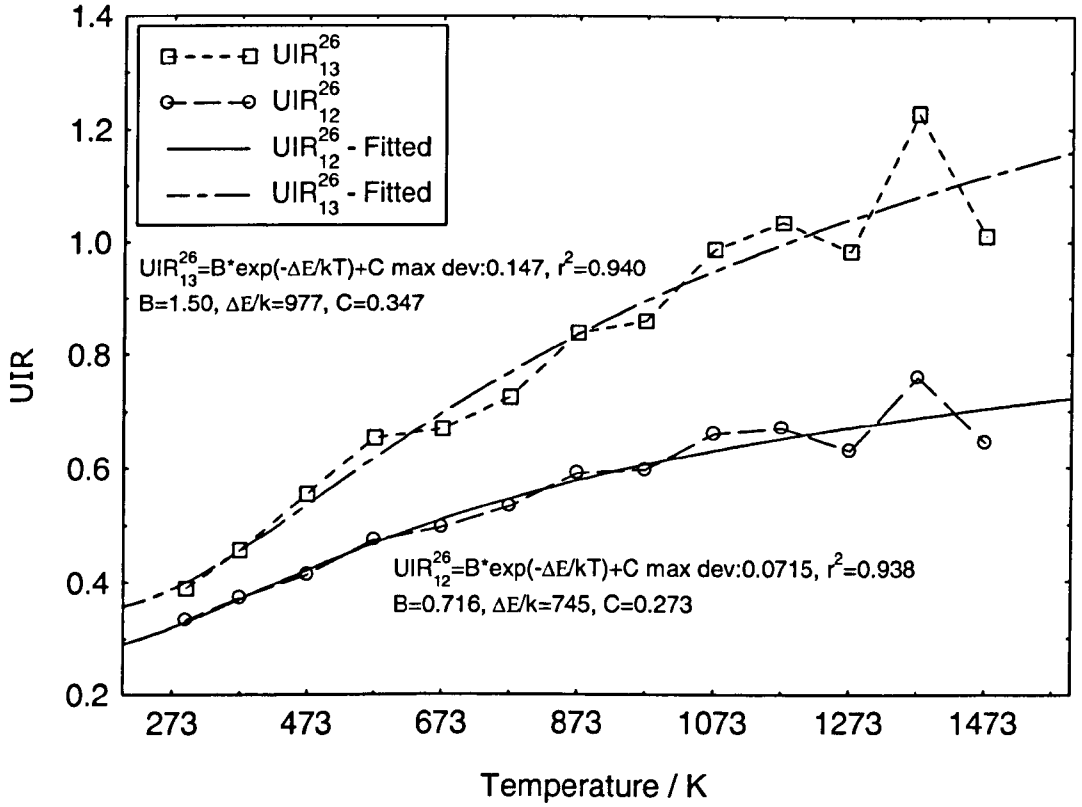

Figure 9.33: Spec YAl 26 $Y_3Al_5O_{12}:Er^{3+}$ UIR_{23}^{26} (actual and fitted with Eq 9.7) vs temperature

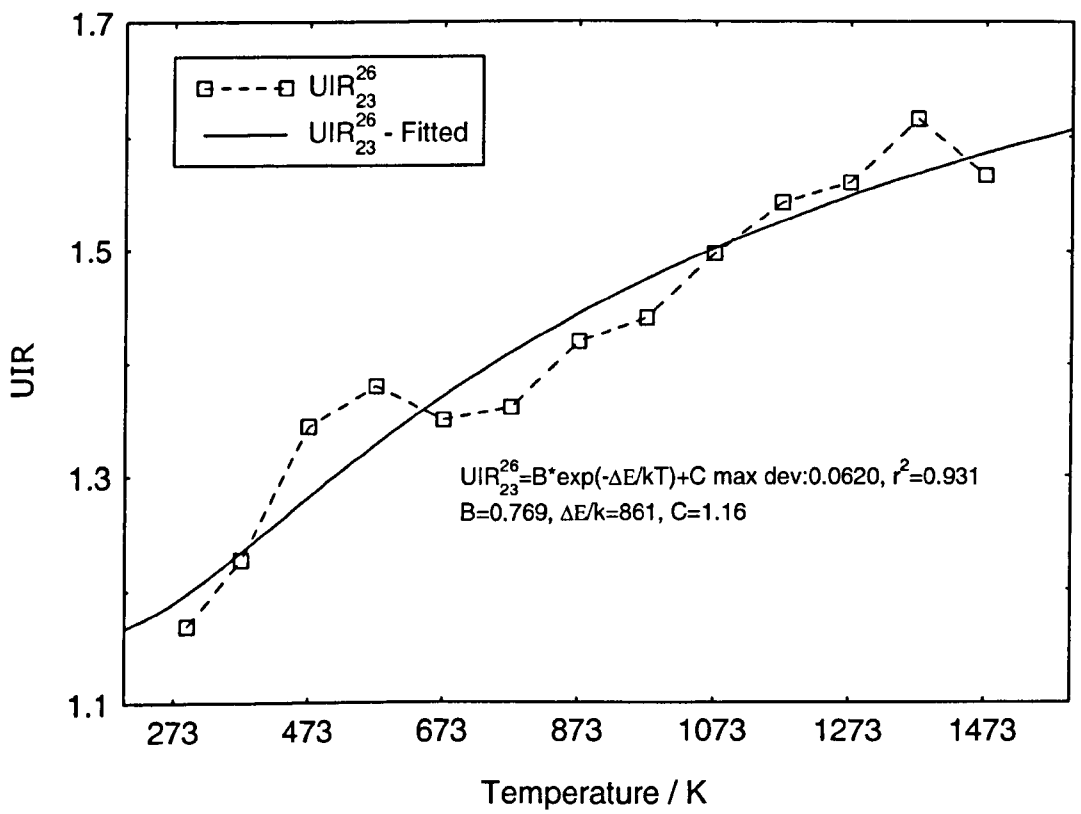

Figure 9.34: Spec YAl 26 $Y_3Al_5O_{12}:Er^{3+}$ UIR_{AB}^{26} (actual and fitted) vs temperature

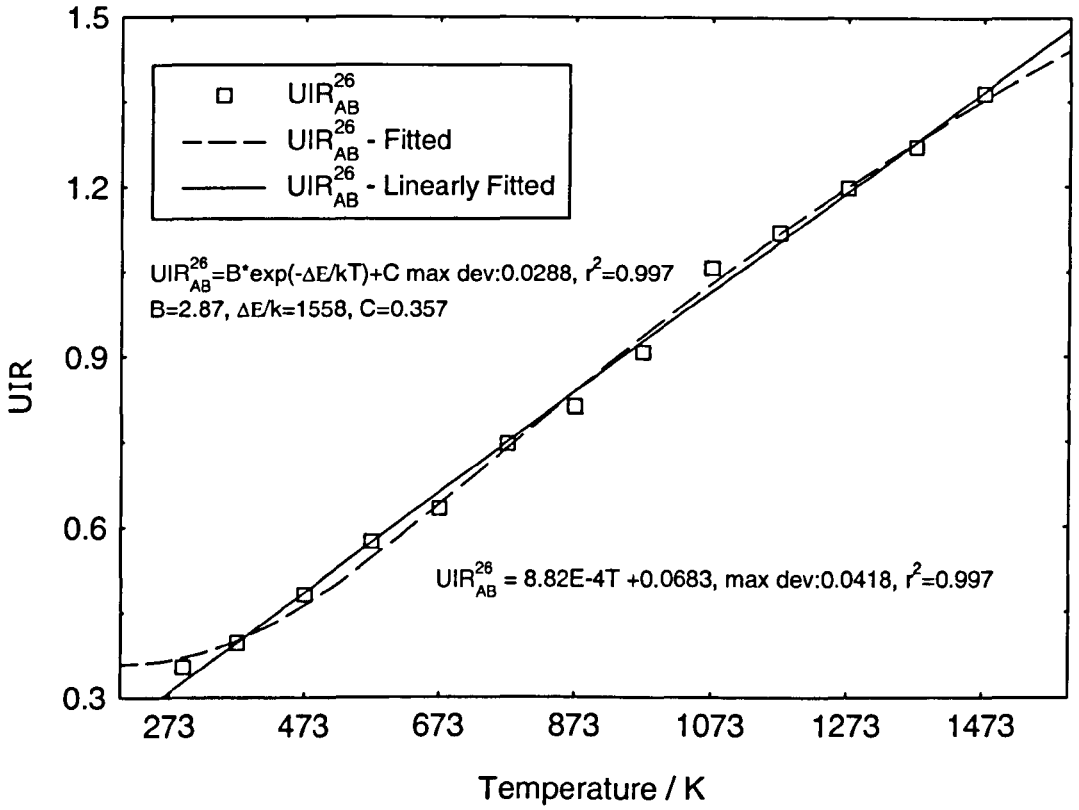

Figure 9.35: Spec YAl 26 $Y_3Al_5O_{12}:Er^{3+}$ UIR_{ABC}^{26} (actual and fitted with Eq. 9.7) vs temperature

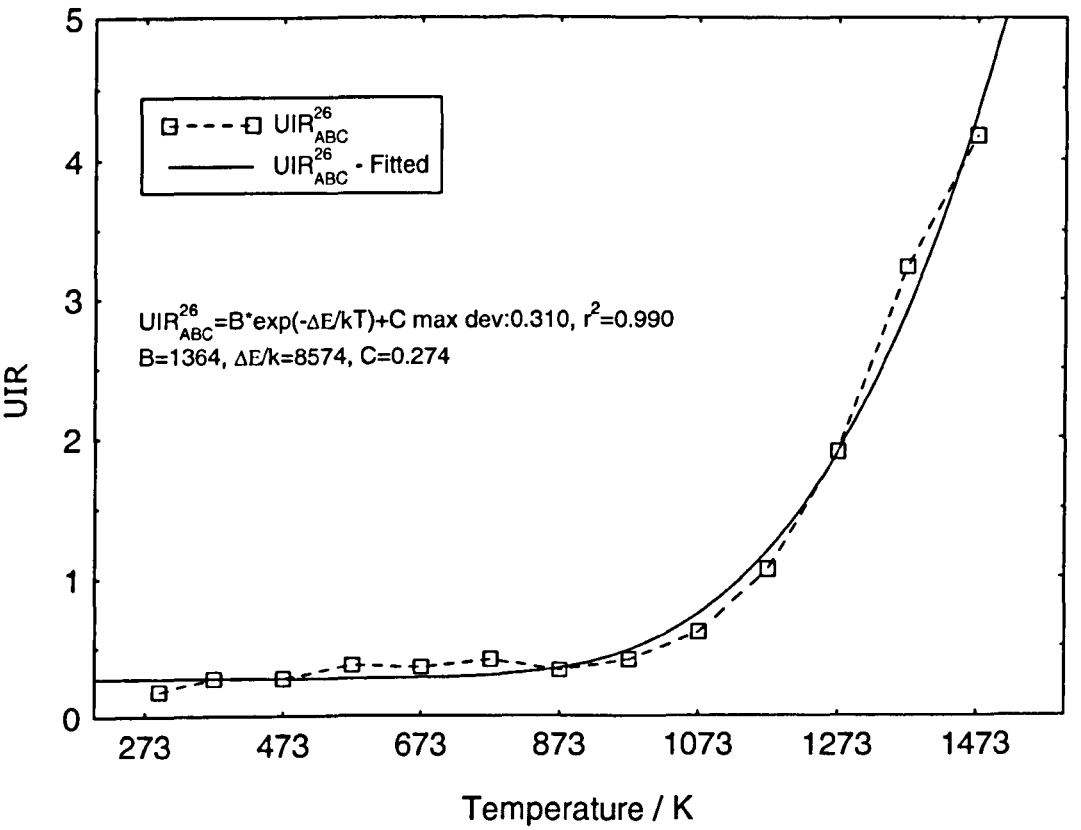

9.6.3 Fluorescence Decay Sensing – $Y_3Al_5O_{12}:Er^{3+}$

Measuring the fluorescence decay time of a rare earth ion can be another method to determine the temperature of an environment. From section 9.6.1, we have observed the presence of strong Er^{3+} emission from the $^4I_{12/3}$ transition. The study of the FIR has shown that the fluorescence emissions are dependent on changes in temperature. With this knowledge, the rare earth fluorescence lifetime temperature dependence at transition $^4I_{12/3}$ was investigated in this work. Attempt was made to measure the integrated lifetime of this transition but was not successful. The intensity blackbody radiation from the furnace and the lack of appropriate IR filters led to saturation of the photodetector. Therefore study was made on the individual IR lines that were used in the FIR measurements. The IR lines are seen in Figure 9.11. To prevent the influence of unwanted IR radiation, the monochromator was used as a filter to shield the photodetector. When employing fluorescence decay (FD), the effect of having to measure light intensity accurately was not a concern and FD is commonly of the order of hundreds of microseconds which can easily be detected and measured accurately [9.43]. In this experiment, the signal from the photodetector was processed by a digital oscilloscope and the results then stored on a computer and the curves fitted using the EASYPLOT software package.

9.6.3.1 Results and Discussion

Within the $^4I_{13/2}$ transition, the nine IR lines employed for FD experiment all exhibited a single exponential decay curve. Refer to Appendix B to see these curves at 1612mn. The maximum temperature investigated in this work was 1473K. Figures 9.36 to 43 show the lifetime of individual wavelengths as a function of temperature. *Zhang* [3.28] reported that when Er^{3+} ion doped in silica fibres a decrease in lifetime was evident and the explanation to this was the thermal quenching of the Er^{3+} fluorescence. The same effect was present in the current work. The rare earth ions experience a single step decay from the $^4I_{13/2}$ level to the ground level $^4I_{15/2}$ and under the influence of temperature this radiative decay rate increases. Generally all plots from the figures reflect a decreasing trend but not all are suitable for temperature measurements. Figure 9.36 show the decay of the IR line 1453nm. The error bars at the lower temperature region were large and the difference in lifetime, τ, between the

lower and upper temperature regions were very small. Using the FD at this wavelength does not seem practical. The large variation in the readings at the lower temperature region was due to the weak emission signal. From the fluorescence emission spectrum in Figure 9.13 it can be seen that at room temperature it has one of the lowest intensities but increases as temperature rises. Figure 9.41 illustrates the response of the IR line 1628.5nmn and again the unstable variation of τ makes it unsuitable for use as a temperature sensing fluorescence decay line. One possible solution to reduce this large variation error would be to reduce the coupling losses between the excitation source, photodetector and fibre.

From among the nine data sets two were selected to be fitted by a least-squares fit routine [9.49]. The selection was based on the consistency of the response. These curves are fitted using the software package EASYPLOT. There is no physical significance for this fit, but it purely provides the best possible fit to the experimental data acquired, see Figures 9.39 and 40. Observation from these two fitted curves showed clearly the decrease in lifetime. The slower decrease seen at the higher temperature region (approximate above 973K) could possibly be due to phonon-induced transitions or more radiative transitions initiated from the higher energy levels since these levels have a higher transfer rate [3.28]. Figure 9.44 shows the value of τ at different wavelengths at different temperatures. From this plot, the maximum average decay at room temperature was ~7.5ms and the difference in τ between 273K and 1273K was ~0.98ms. On the other hand, Er^{3+} doped silica fibres have a difference of ~6ms [3.28] therefore making it more sensitive. The setback of silica fibre is that it has a maximum operating temperature of ~1273K.

Figure 9.36: Spec YAl 26 $Y_3Al_5O_{12}:Er^{3+}$ fluorescence decay at 1453nm

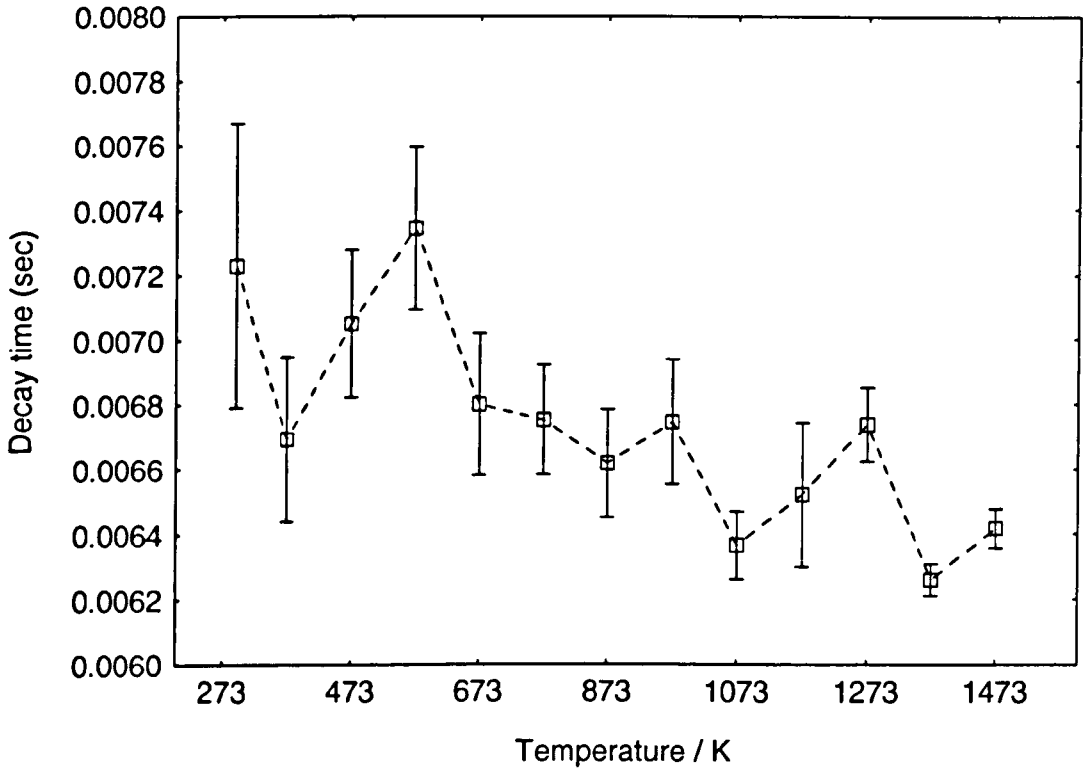

Figure 9.37: Spec YAl 26 $Y_3Al_5O_{12}:Er^{3+}$ fluorescence decay at 1470nm

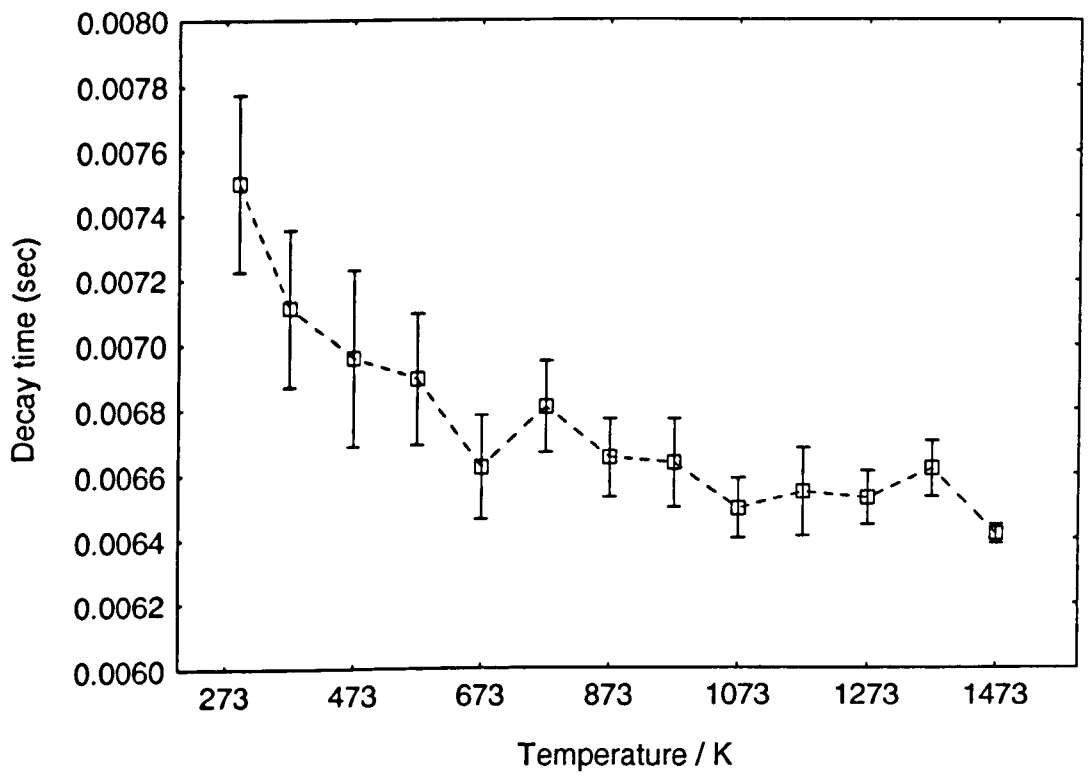

Figure 9.38: Spec YAl 26 $Y_3Al_5O_{12}:Er^{3+}$ fluorescence decay at 1528.5nm

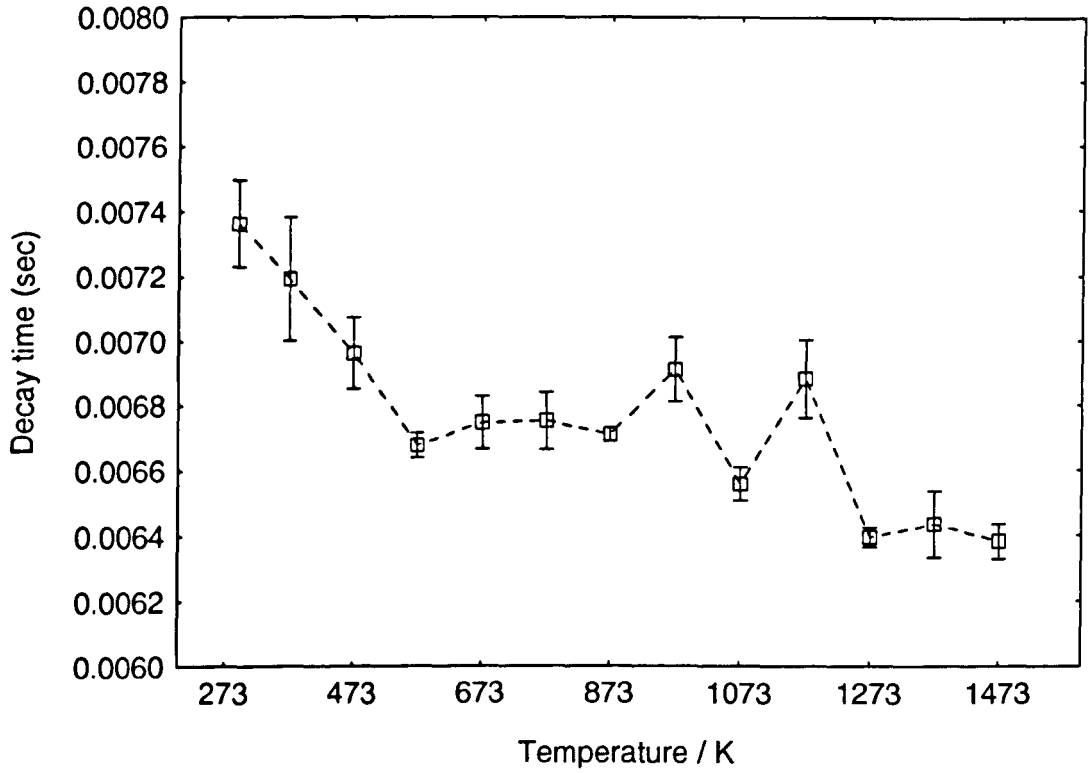

Figure 9.39: Spec YAl 26 $Y_3Al_5O_{12}:Er^{3+}$ fluorescence decay at 1568nm

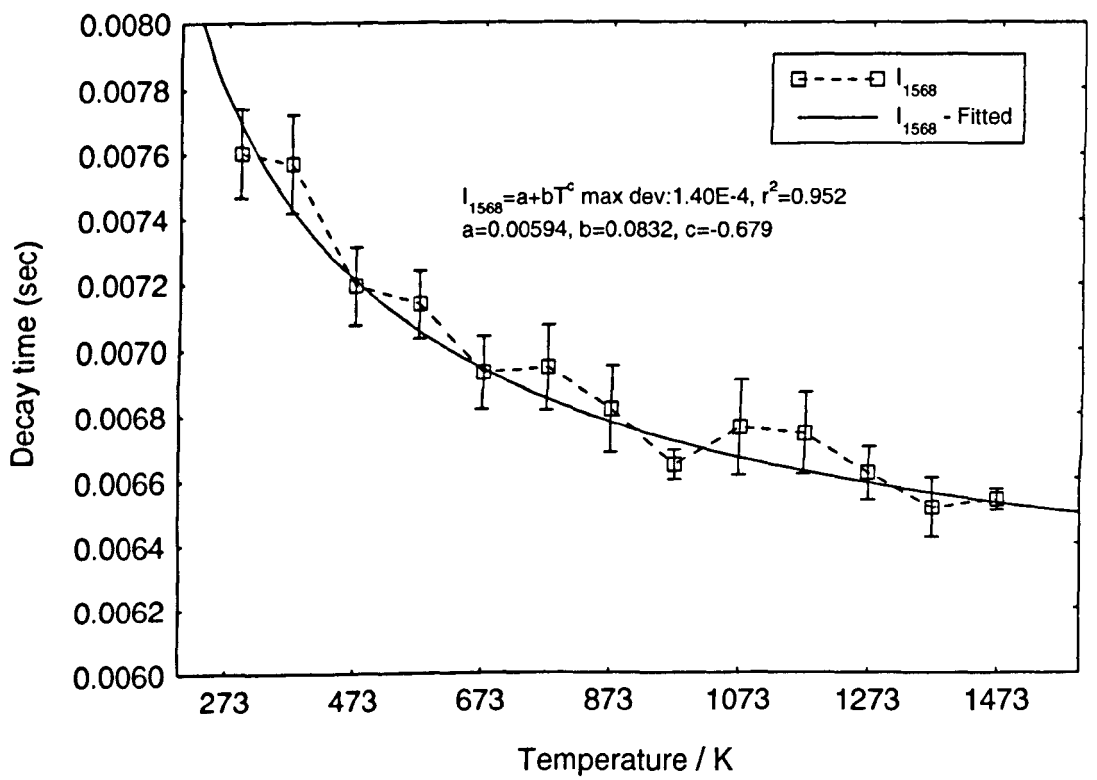

Figure 9.40: Spec YAl 26 $Y_3Al_5O_{12}:Er^{3+}$ fluorescence decay at 1612nm

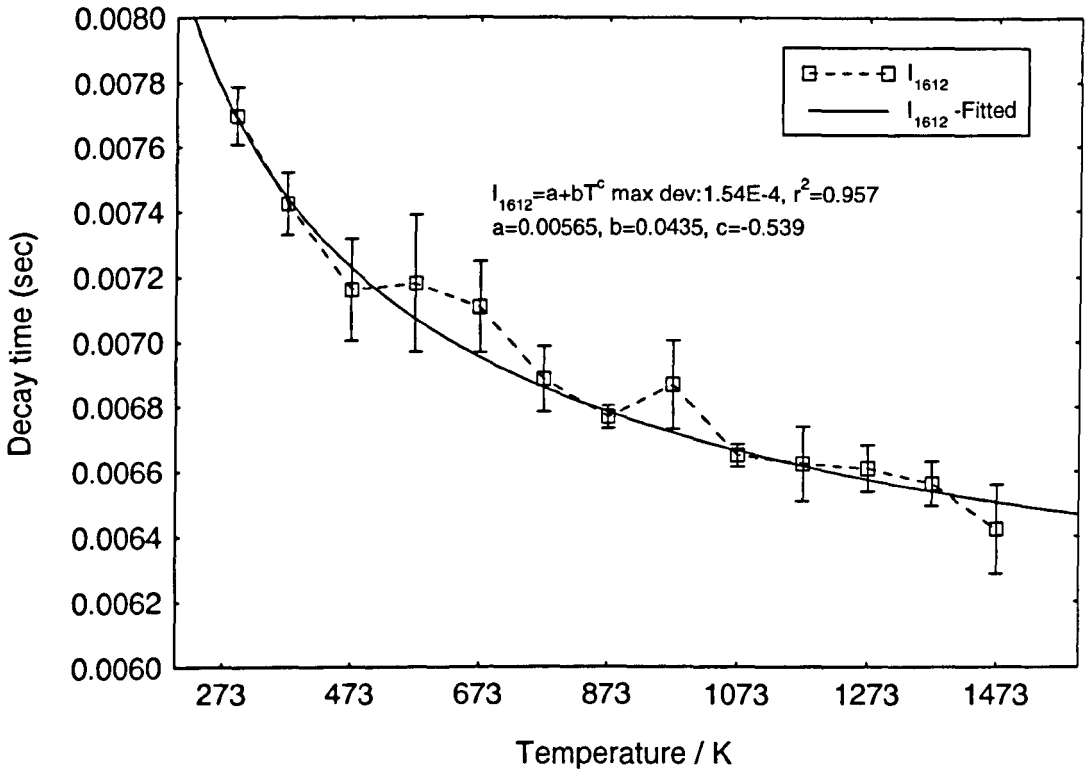

Figure 9.41: Spec YAl 26 $Y_3Al_5O_{12}:Er^{3+}$ fluorescence decay at 1628.5nm

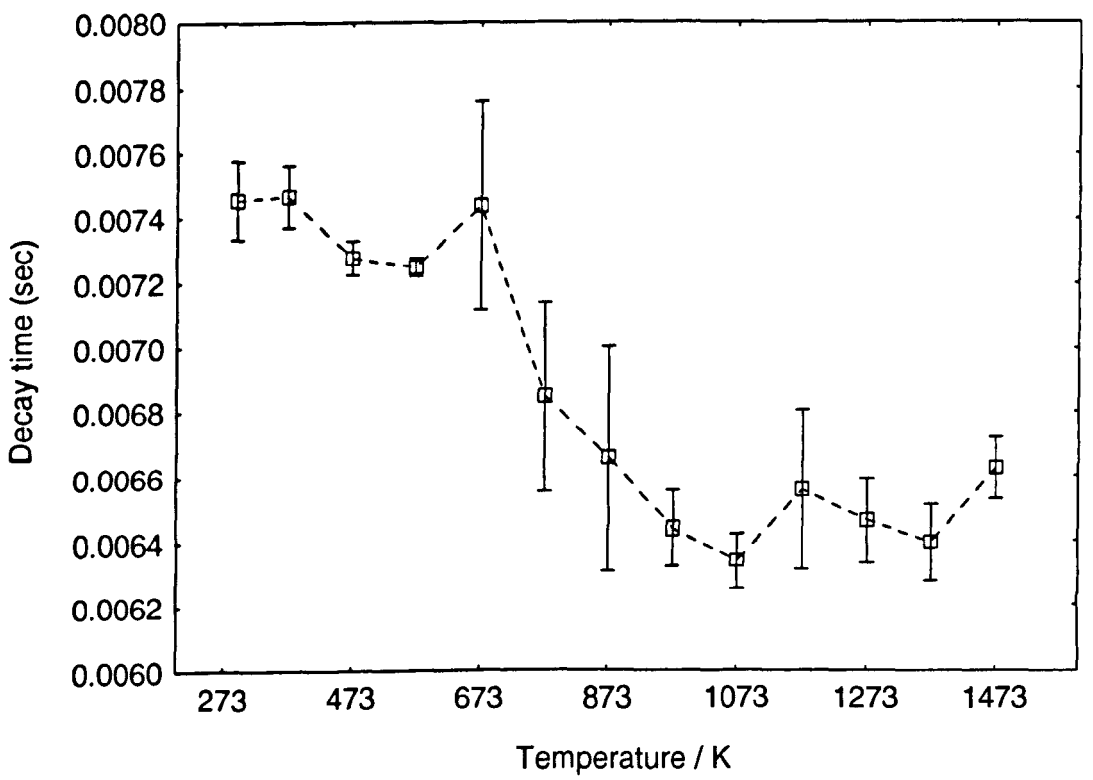

Figure 9.42: Spec YAl 26 $Y_3Al_5O_{12}:Er^{3+}$ fluorescence decay at 1640.5nm

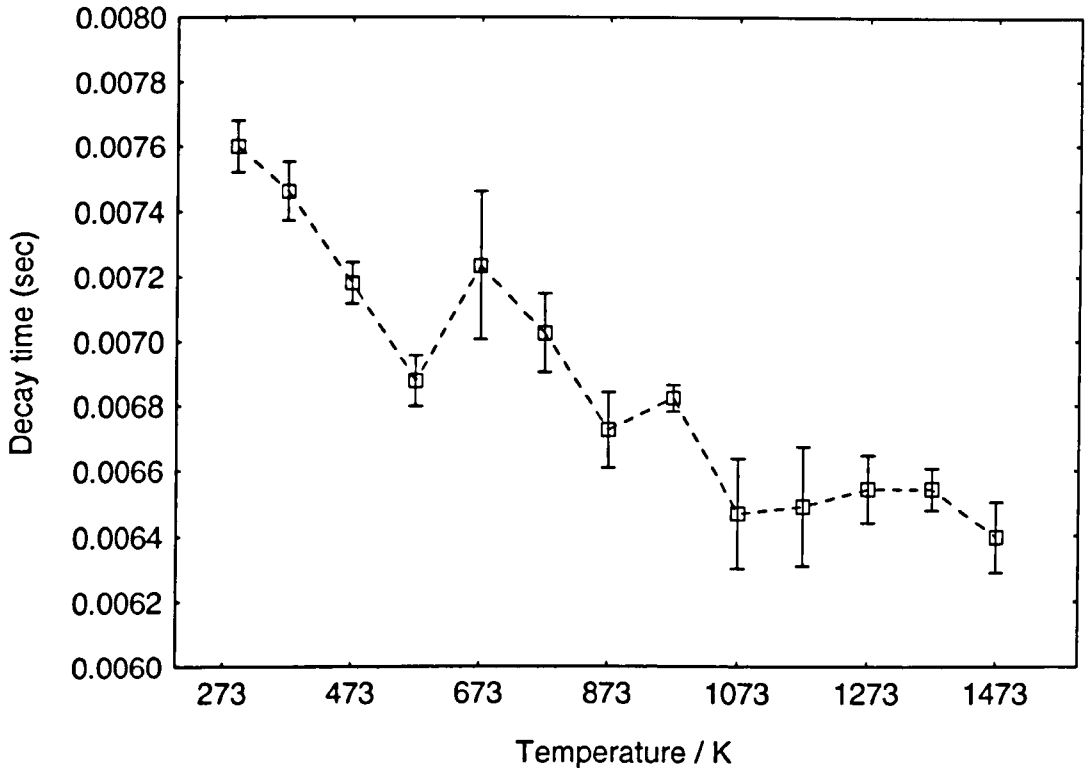

Figure 9.43: Spec YAl 26 $Y_3Al_5O_{12}:Er^{3+}$ fluorescence decay at 1652.5nm

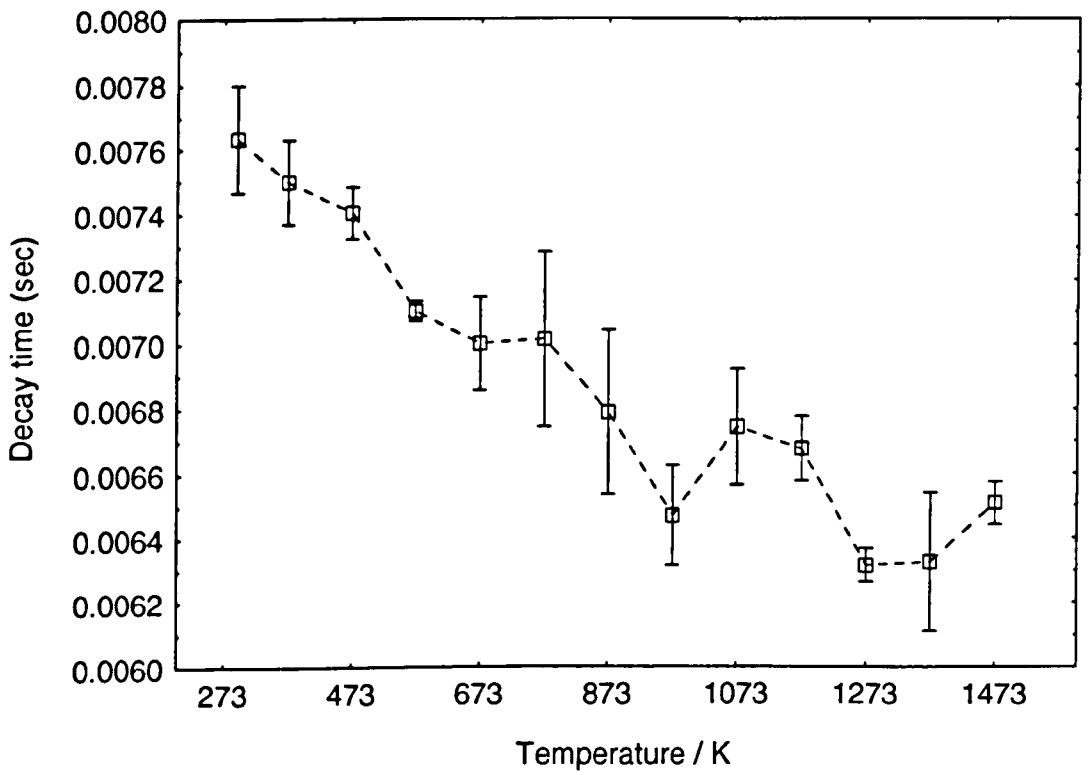

Figure 9.44: Spec YAl 26 $Y_3Al_5O_{12}:Er^{3+}$ fluorescence decay of different temperatures at varies wavelengths

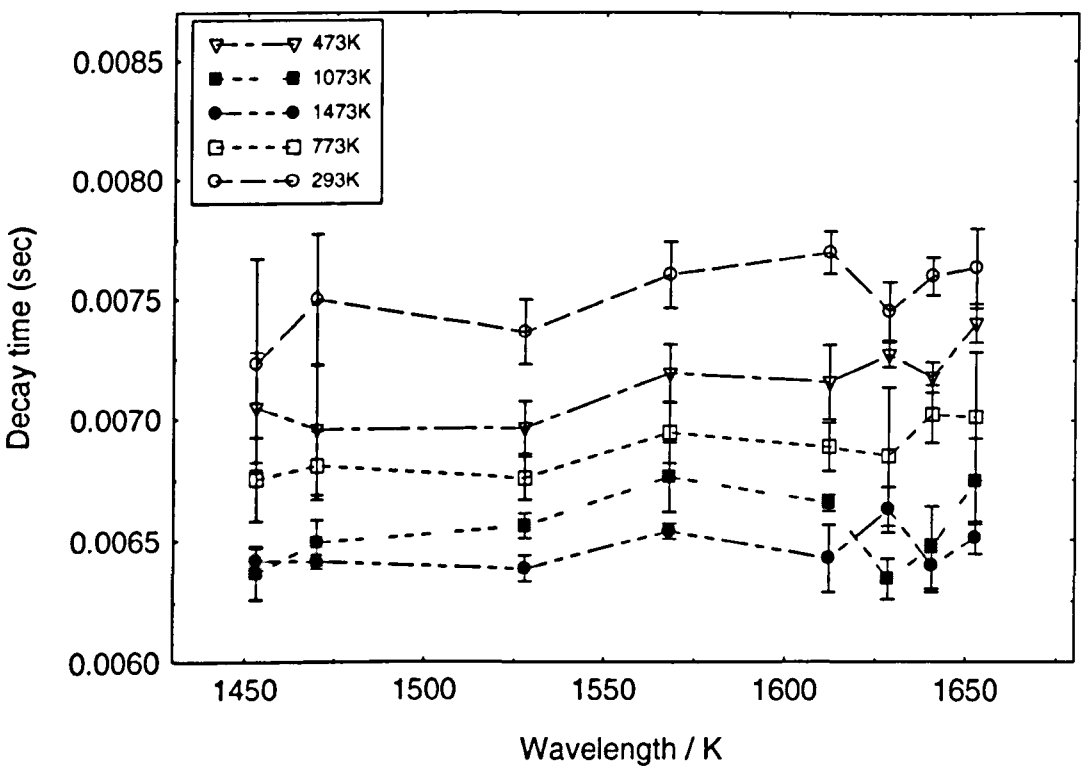

9.7 $Y_3Al_5O_{12}:Er^{3+} + Yb^{3+}$ - Temperature Sensor

9.7.1 Fluorescence Intensity Based Sensing - $Y_3Al_5O_{12}:Er^{3+}+Yb^{3+}$

From previous work in Chapter 6, it was observed that when Yb^{3+} was co-doped it facilitated a better absorption (at 950nm<λ<1100nm region) which improved the energy transfer processes within the fibres where the pumping efficiency in the IR region can increase by two orders of magnitude [3.38]. *Baek* [9.43] stated that the energy transfer rate between the two ions is thermally coupled due to the population densities which are temperature dependent. When excited with a 965nm laser diode, it was observed that fluorescence emission took place from the $^4F_{5/2}$ (Yb^{3+}) and $^4I_{13/2}$ (Er^{3+}) transition levels. Figure 9.45 shows the fluorescence emission at room temperature. An additional IR line at 1027nm was included in this experiment when the FIR is calculated. Another eight lines are used similar those used in the singly doped YAG fibres (see Figure 9.11 for the other IR lines used). These lines were employed to monitor temperature from 293k to 1473K and the results were then fitted with equation 9.7.

9.7.1.1 Results and Discussion

The fluorescence emission intensity at transition $^4I_{11/2}$ (at 1010nm) was ~40% more intense than the next highest peak at 1528.5nm (see Figure 9.46. Figures 9.46 to 50 show the fluorescence emission profile over various temperate ranges. For easy discussion, the fluorescence emissions are divided into 4 different regions, Region Y – 1000nm to 1100nm and Regions A, B and C similar to that of *Spec YAl 26* in section 9.6.1.1. Figures 9.47 and 48 showed that the intensity from $^4I_{11/2}$ decreases as temperature is applied to the sensor. A possible cause could be that the upper thermal energy level ($^4F_{9/2}\rightarrow{}^4I_{15/2}$ transition) experiences a certain amount of overlapping by the fluorescence at the lower thermally coupled energy level ($^4F_{5/2}\rightarrow{}^4F_{7/2}$ transition) [9.40] and possible energy back transfer. From Figure 9.48, it was observed that the peak at 1027nm at a temperature of 1473K had completely disappeared. Figures 9.49 and 50 show the fluorescence spectra at transition $^4I_{13/2}$ under the influence of temperature. The co-doped fibre reacted similarly to the singly doped fibres discussed in section 9.6.1. Intensity in Regions A and B increases when temperature

rises whereas Region C decreases. By integrating the fluorescence intensity over each region, a clearer comparison could be made between them. These results are shown in Figure 9.51. Regions A and B exhibited an increasing intensity as the temperature rises. These increments could be again attributed to the overlapping of the fluorescence from the lower to the upper energy level and these regions could be selected for potential sensing application. Region C showed minimal changes throughout the temperature scale.

Table 9.4 shows the denotations of the FIR for *Spec YAl 32*. The presence of Yb^{3+} ions has given this fibre an additional IR line at 1027nm. Figures 9.52a and b, illustrate the intensity ratios of the IR lines with the 1027nm line as a function of temperature. As temperature increases a decrease in FIR is seen for all the curves with only four of the eight demonstrating a wide FIR range with a steady exponential decrease in FIR. Hence these four curves, FIR_{Y1}^{32} to FIR_{Y4}^{32}, were chosen to be fitted with equation 9.7. The theoretical model fitted the experimental data perfectly with the r^2 values all near unity, see Figures 9.52c and d. The IR line observed has no significant change in FIR after ~673K making it insensitive at high temperatures. Furthermore, when the FIR data were fitted to equation 9.7 a negative sign to ΔE was obtained. This was similar to the work of *Baek* [9.43] and could be due to the higher energy level $^5F_{5/2}$ of the Yb^{3+} ion compared to that of the energy level $^4I_{13/2}$ of the Er^{3+} ion. However, it is possible to use these ratios for temperature measurements although perhaps not recommended; further work would be needed to be done to identify why the negative value of ΔE occurs.

Several FIR curves are plotted in Figures 9.53a and b where 1443nm was used as the reference IR line. Although the characteristics of these curves were non-monotonic, after close examination only three showed potential and were selected for temperature sensing applications. The re-plotted curves are shown in Figures 9.53c and d. FIR_{15}^{32}, FIR_{17}^{32} and FIR_{18}^{32} showed a steady increase with temperature rises. Figure 9.54a and b, show the FIR for 1470nm as reference line. Observations made from the plots showed that the FIRs calculated with the IR lines in the 1600nm region to be more temperature dependent as compared to that of the 1500nm region. The larger change in intensity ratio would be extremely useful for temperature sensing applications. Three curves were re-plotted and are shown in Figures 9.54c

and d. The theoretical curves fit adequately with the experimental results. FIRs for 1528.5nm as the reference IR line are shown in Figures 9.54a and b. The ratio between 1528.5nm and 1568nm produces a decreasing curve as temperature increases. On the other hand, others showed an increase and also have a wider intensity ratio. Selected curves fitted with the theoretical equation 9.7 are show in Figures 9.55c to e. Again, the ratio of 1528.5nm with IR lines in the 1600nmn showed good results when fitted theoretically. Results of the FIRs for the 1568nm line were just as promising, see Figure 9.56a. Three of the four FIRs showed a consistently and linear increase. When fitted (see Figures 9.56b and c) the results again showed the FIRs could be employed for temperature sensing applications. At 1612nm, FIRs plotted were not as ideal because the curves are mainly 'flat', see Figure 9.57. The two plots of 1628.5 as reference IR line seen in Figure 9.58a have minimal changes at lower temperature and were only effective above ~773K. The theoretical fits were again close to unity but the FIRs could only be used in the higher temperature region, see Figure 9.58b. The last IR line investigated was 1640.5nm and Figure 9.59 illustrates the results. A gradual increase was observed with temperature and an appropriate line could to be fitted to it.

FIR method using the integrated intensity across the four regions (Y, A, B and C) was also investigated as a possible method to determine changes in temperature. See Figures 9.60a and b. When Region Y was employed as the reference, the FIR curves plotted exhibited an exponential decay profile. FIR_{YA}^{32} was chosen as it has a wider intensity ratio and the changes in intensity ratio with temperature were consistent. Figures 9.60c shows an adequate fit to this curve. It is observed that it has better sensitivity in the lower temperature range rather than the higher region. Figure 9.60b shows that only two plots were usable as one was flat throughout. Figure 9.60d illustrate the fitted theoretical curves with an effective measuring temperature range from ~273K to ~1473K. It is worth mentioning that experimental investigation in this work showed to be in good agreement with the theoretical model and many IR lines and regions have great potential for use as fluorescence-based temperature sensors. Lastly, adding Yb^{3+} did not see any marked influence in fluorescence emission at transition $^4I_{13/2}$, the behaviour was greatly dominated by the Er^{3+} ions present in the fibre.

Figure 9.45: Spec YAl 32 $Y_3Al_5O_{12}$:Er^{3+}+Yb^{3+} fluorescence in room temperature, 293K

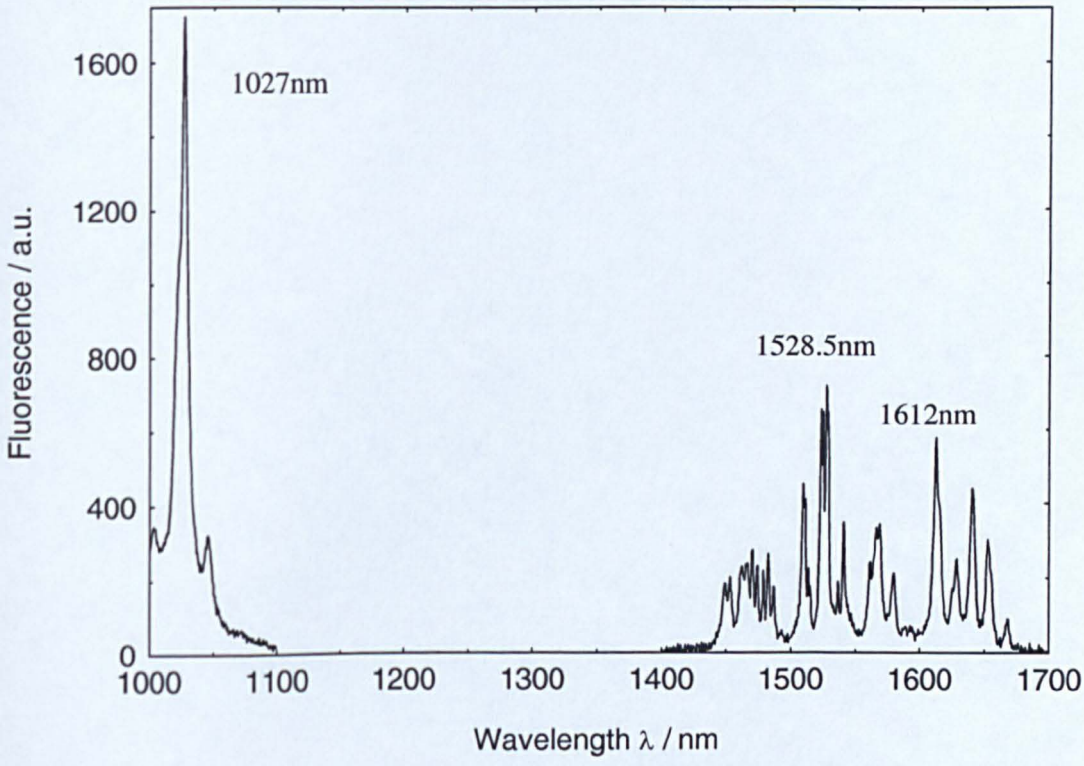

Figure 9.46: Spec YAl 32 $Y_3Al_5O_{12}$:Er^{3+}+Yb^{3+} fluorescence spectra from room temperature to 1473K

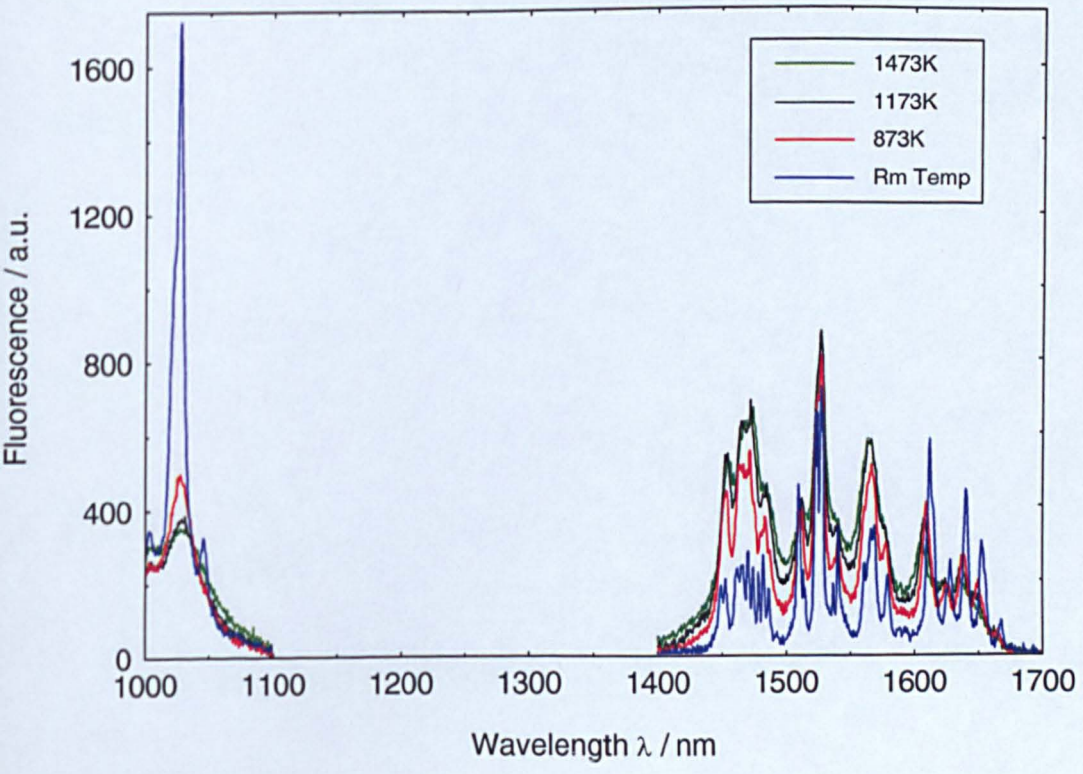

Figure 9.47: Spec YAl 32 $Y_3Al_5O_{12}:Er^{3+}+Yb^{3+}$ fluorescence spectra ($^4I_{11/2}$) – room temperature to 873K

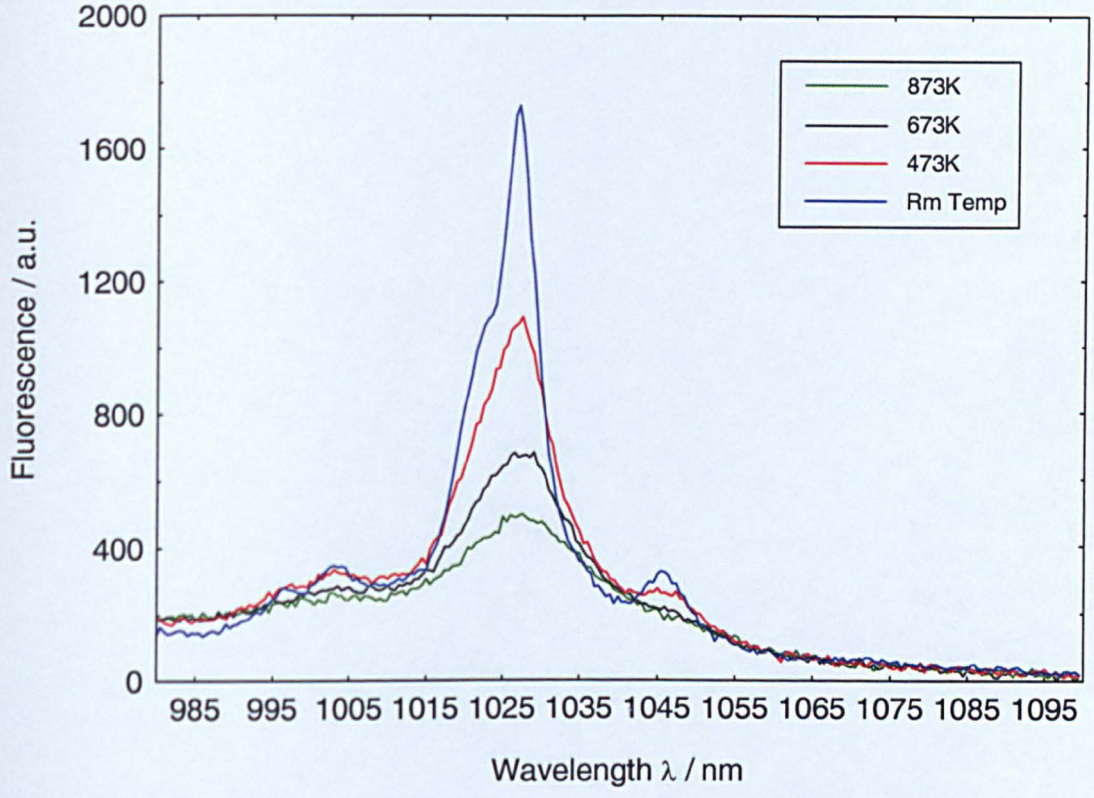

Figure 9.48: Spec YAl 32 $Y_3Al_5O_{12}:Er^{3+}+Yb^{3+}$ fluorescence spectra ($^4I_{11/2}$) – room temperature to 1473K

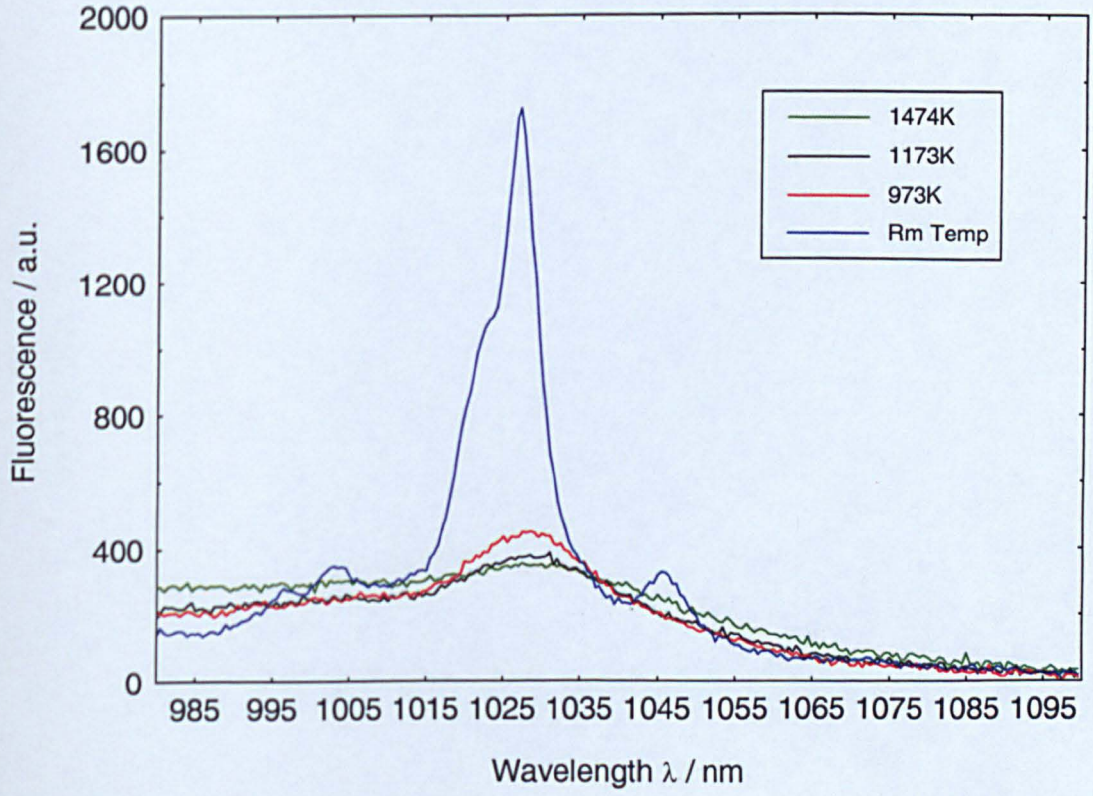

Figure 9.49: Spec YAl 32 $Y_3Al_5O_{12}:Er^{3+}+Yb^{3+}$ fluorescence spectra ($^4I_{13/2}$) – room temperature to 873K

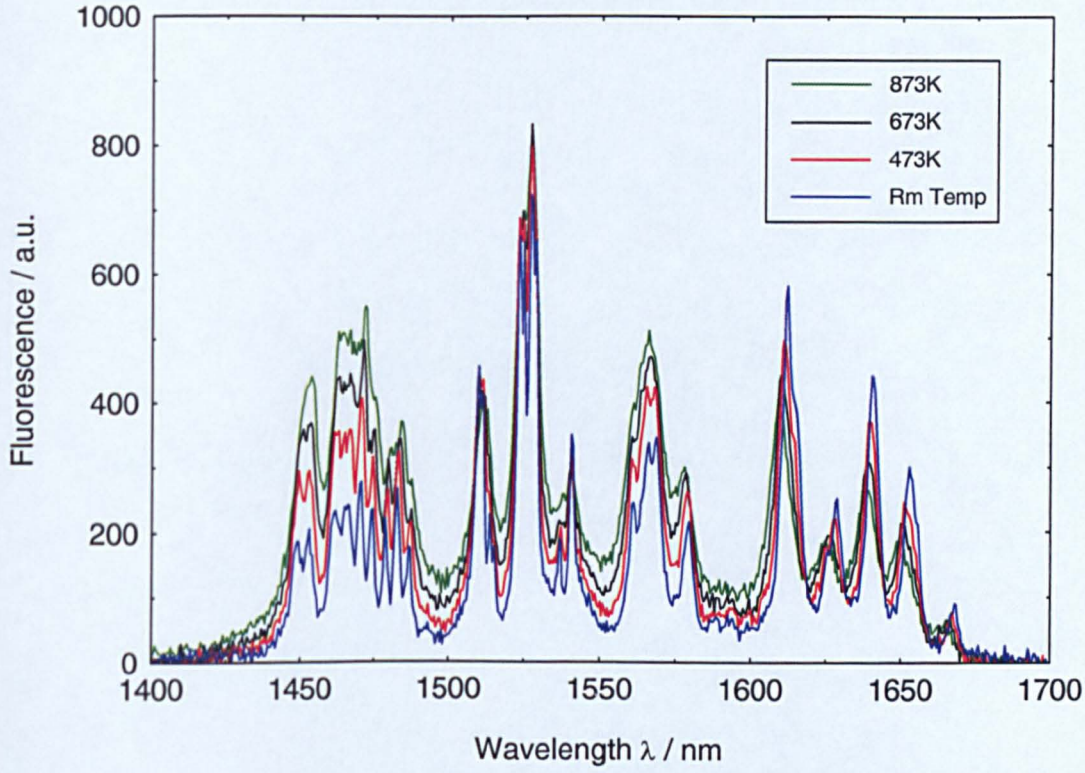

Figure 9.50: Spec YAl 32 $Y_3Al_5O_{12}:Er^{3+}+Yb^{3+}$ fluorescence spectra ($^4I_{13/2}$) – room temperature to 1473K

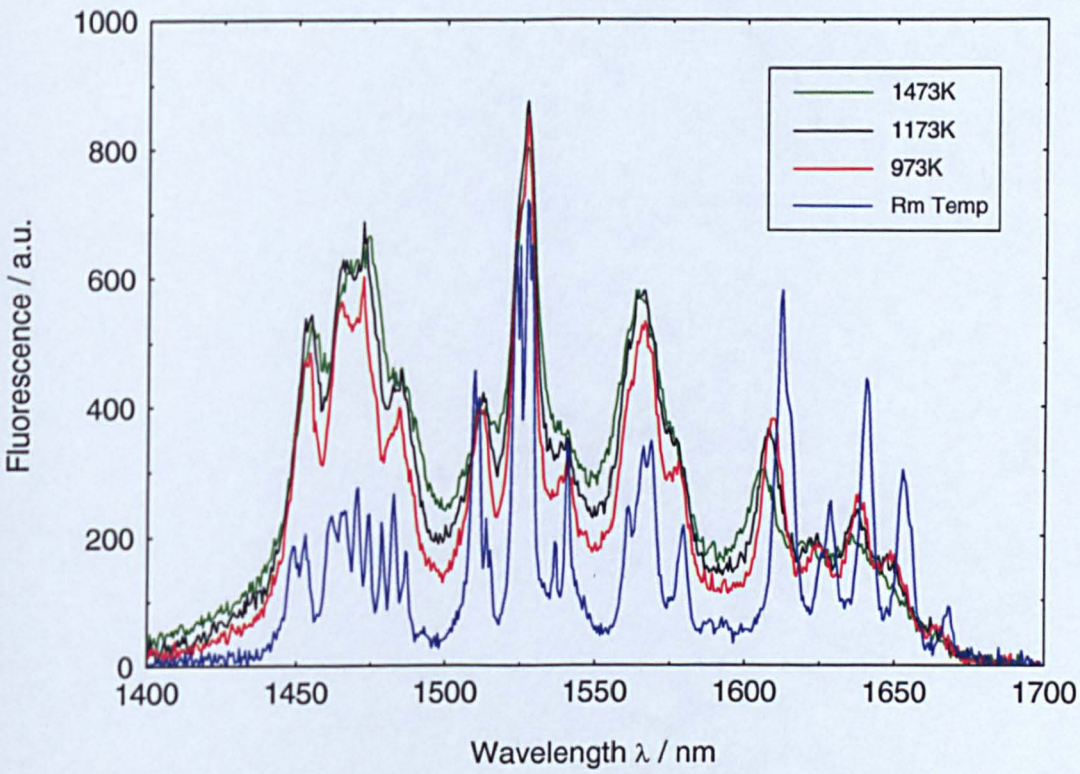

Figure 9.51: Spec YAl 32 $Y_3Al_5O_{12}:Er^{3+}+Yb^{3+}$ - Integrated intensity

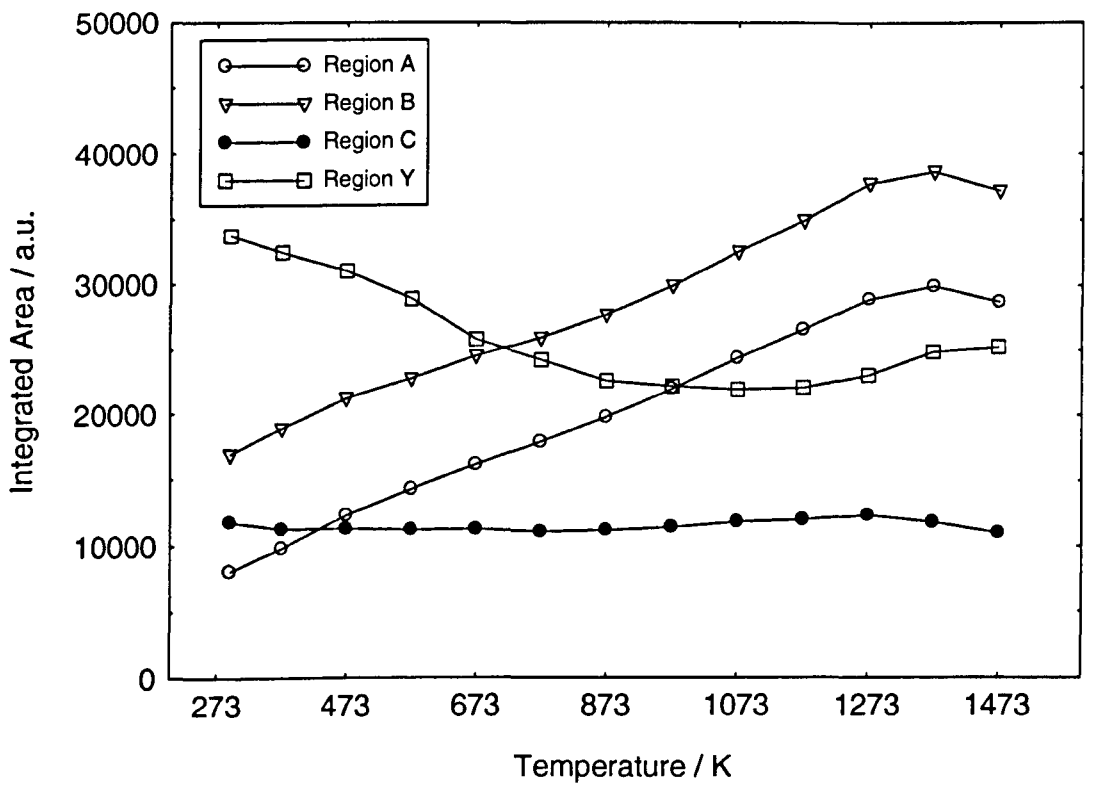

Table 9.4 – Spec YAl 26:$Y_3Al_5O_{12}$:Er^{3+}+Yb^{3+} temperature sensor FIR denotations

Denotations	IR lines	Denotations	IR lines	Denotations	IR lines
FIR_{Y1}^{32}	I_{1027}/I_{1453}	FIR_{16}^{32}	$I_{1453}/I_{1628.5}$	FIR_{37}^{32}	$I_{1528.5}/I_{1640.5}$
FIR_{Y2}^{32}	I_{1027}/I_{1470}	FIR_{17}^{32}	$I_{1453}/I_{1640.5}$	FIR_{38}^{32}	$I_{1528.5}/I_{1652.5}$
FIR_{Y3}^{32}	$I_{1027}/I_{1528.5}$	FIR_{18}^{32}	$I_{1453}/I_{1652.5}$	FIR_{45}^{32}	$I_{1528.5}/I_{1612}$
FIR_{Y4}^{26}	I_{1027}/I_{1568}	FIR_{23}^{32}	$I_{1470}/I_{1528.5}$	FIR_{46}^{32}	$I_{1528.5}/I_{1628.5}$
FIR_{Y5}^{26}	I_{1027}/I_{1612}	FIR_{24}^{26}	I_{1470}/I_{1568}	FIR_{47}^{26}	$I_{1528.5}/I_{1640.5}$
FIR_{Y6}^{32}	$I_{1027}/I_{1628.5}$	FIR_{25}^{32}	I_{1470}/I_{1612}	FIR_{48}^{32}	$I_{1528.5}/I_{1652.5}$
FIR_{Y7}^{32}	$I_{1027}/I_{1640.5}$	FIR_{26}^{32}	$I_{1470}/I_{1628.5}$	FIR_{56}^{32}	$I_{1612}/I_{1628.5}$
FIR_{Y8}^{32}	$I_{1027}/I_{1652.5}$	FIR_{27}^{32}	$I_{1470}/I_{1640.5}$	FIR_{57}^{32}	$I_{1612}/I_{1640.5}$
FIR_{12}^{32}	I_{1453}/I_{1470}	FIR_{28}^{32}	$I_{1470}/I_{1652.5}$	FIR_{58}^{32}	$I_{1612}/I_{1652.5}$
FIR_{13}^{32}	$I_{1453}/I_{1528.5}$	FIR_{34}^{32}	$I_{1528.5}/I_{1568}$	FIR_{67}^{32}	$I_{1628.5}/I_{1640.5}$
FIR_{14}^{32}	I_{1453}/I_{1568}	FIR_{35}^{32}	$I_{1528.5}/I_{1612}$	FIR_{68}^{32}	$I_{1628.5}/I_{1652.5}$
FIR_{15}^{32}	I_{14nm}/I_{1612}	FIR_{36}^{32}	$I_{1528.5}/I_{1628.5}$	FIR_{78}^{32}	$I_{1640.5}/I_{1652.5}$

Figure 9.52a: Spec YAl 32 $Y_3Al_5O_{12}:Er^{3+}+Yb^{3+}$ FIR_{Y1}^{32} to FIR_{Y4}^{32} vs temperature

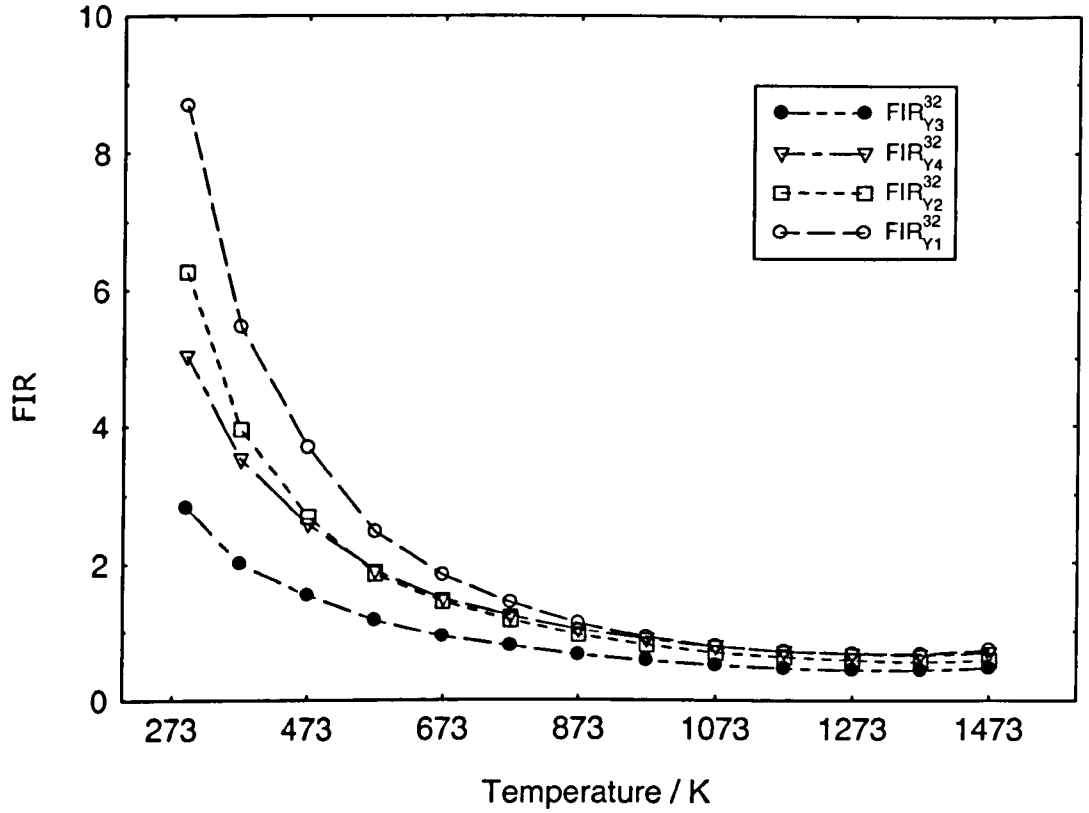

Figure 9.52b: Spec YAl 32 $Y_3Al_5O_{12}:Er^{3+}+Yb^{3+}$ FIR_{Y5}^{32} to FIR_{Y8}^{32} vs temperature

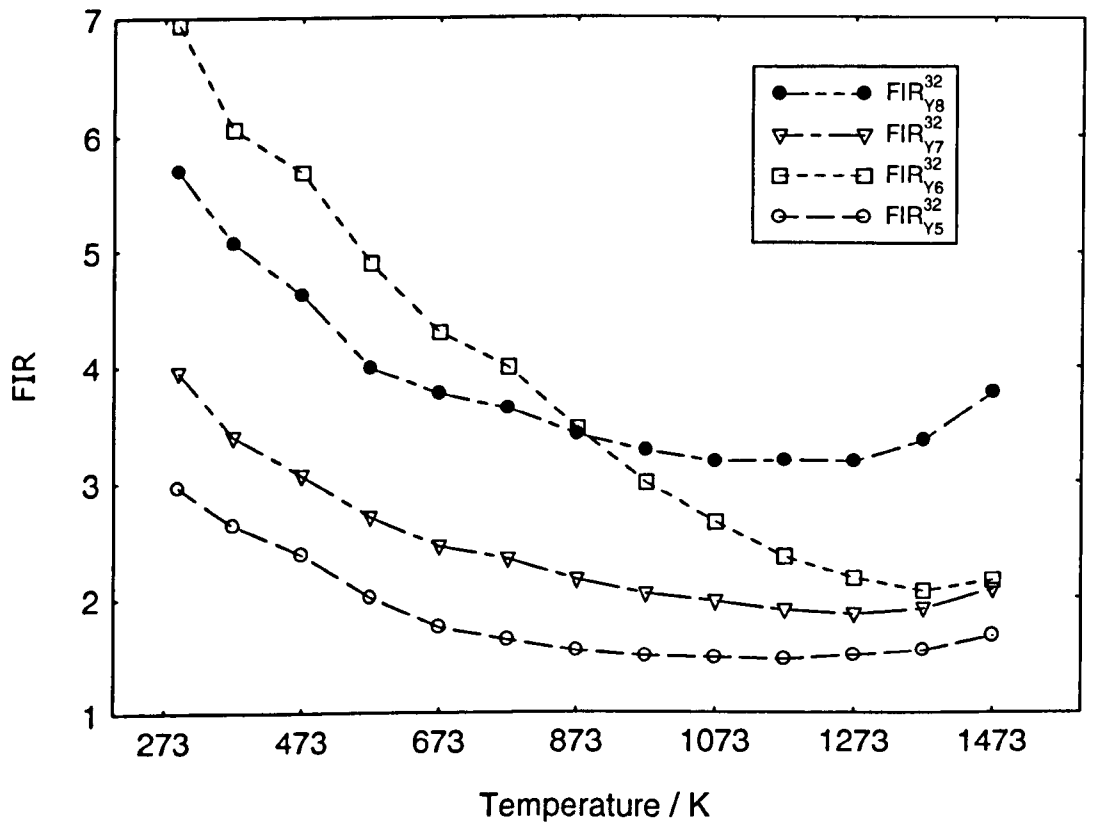

Figure 9.52c: Spec YAl 32 $Y_3Al_5O_{12}$:Er^{3+}+Yb^{3+} FIR_{Y1}^{32} & FIR_{Y2}^{32} (fitted with Eq. 9.7) vs temperature

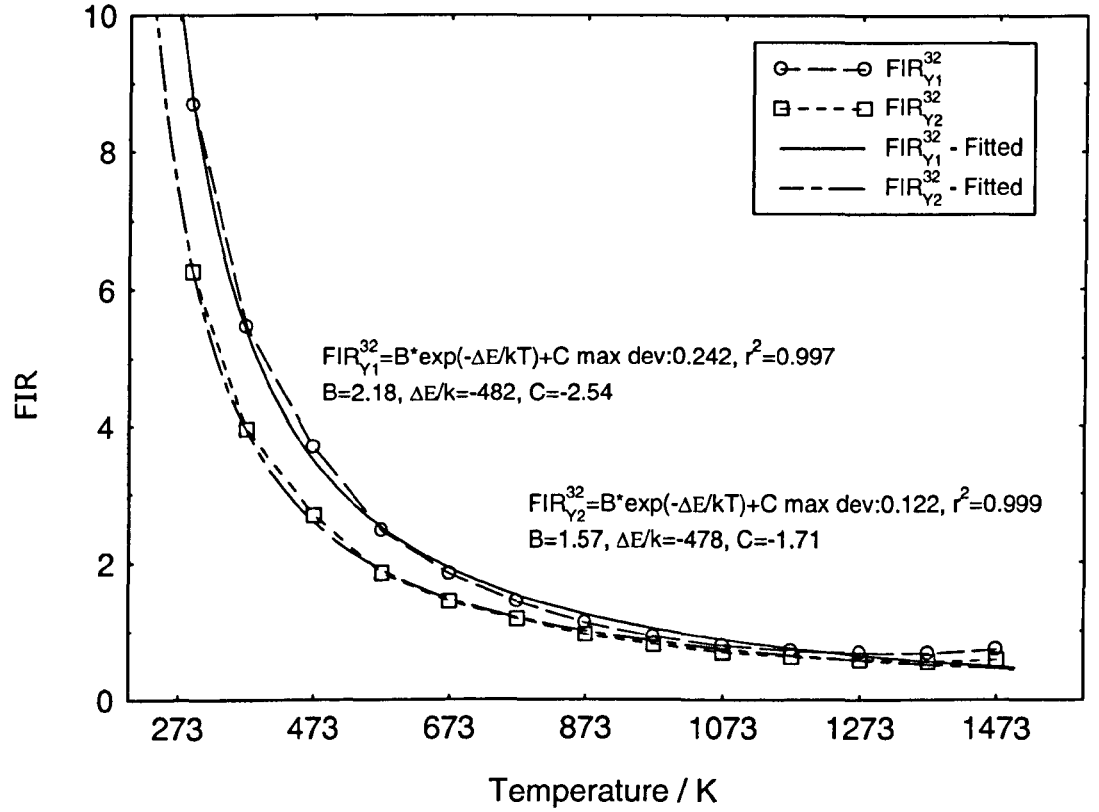

Figure 9.52d: Spec YAl 32 $Y_3Al_5O_{12}$:Er^{3+}+Yb^{3+} FIR_{Y3}^{32} to FIR_{Y4}^{32} (fitted with Eq. 9.7) vs temperature

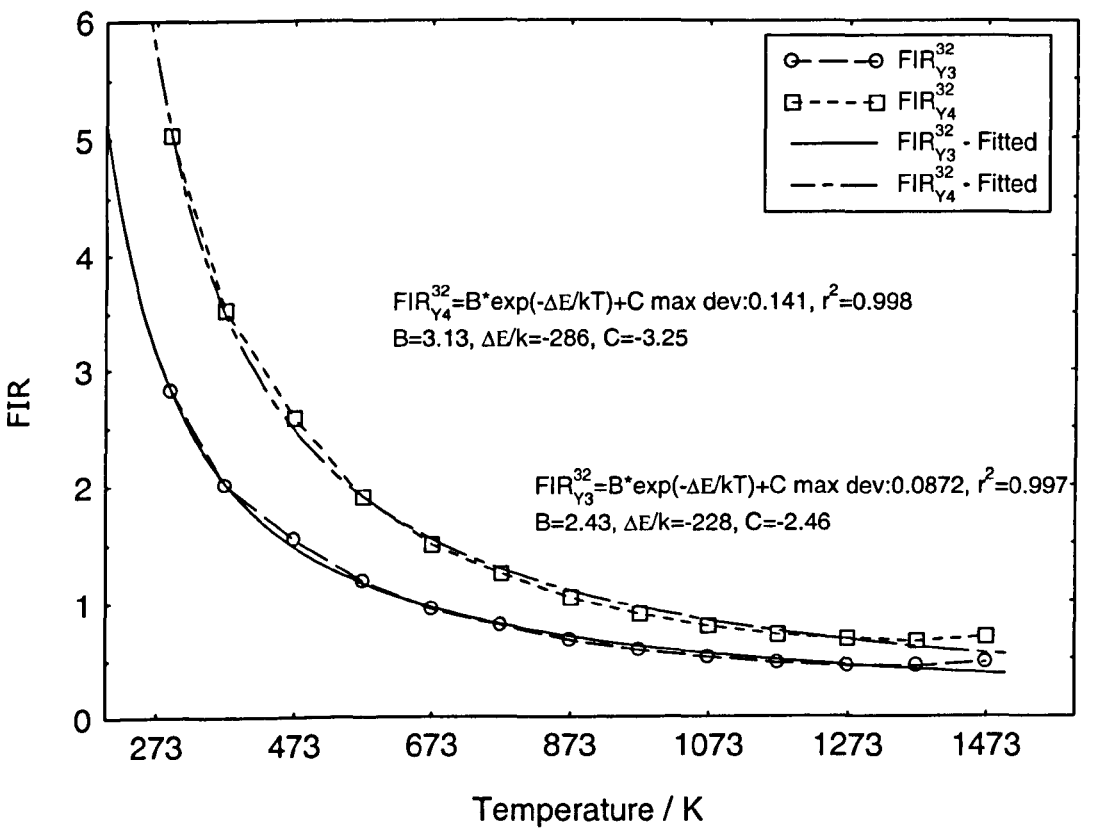

Figure 9.53a: Spec YAl 32 $Y_3Al_5O_{12}$:Er^{3+}+Yb^{3+} FIR_{12}^{32} to FIR_{14}^{32} vs temperature

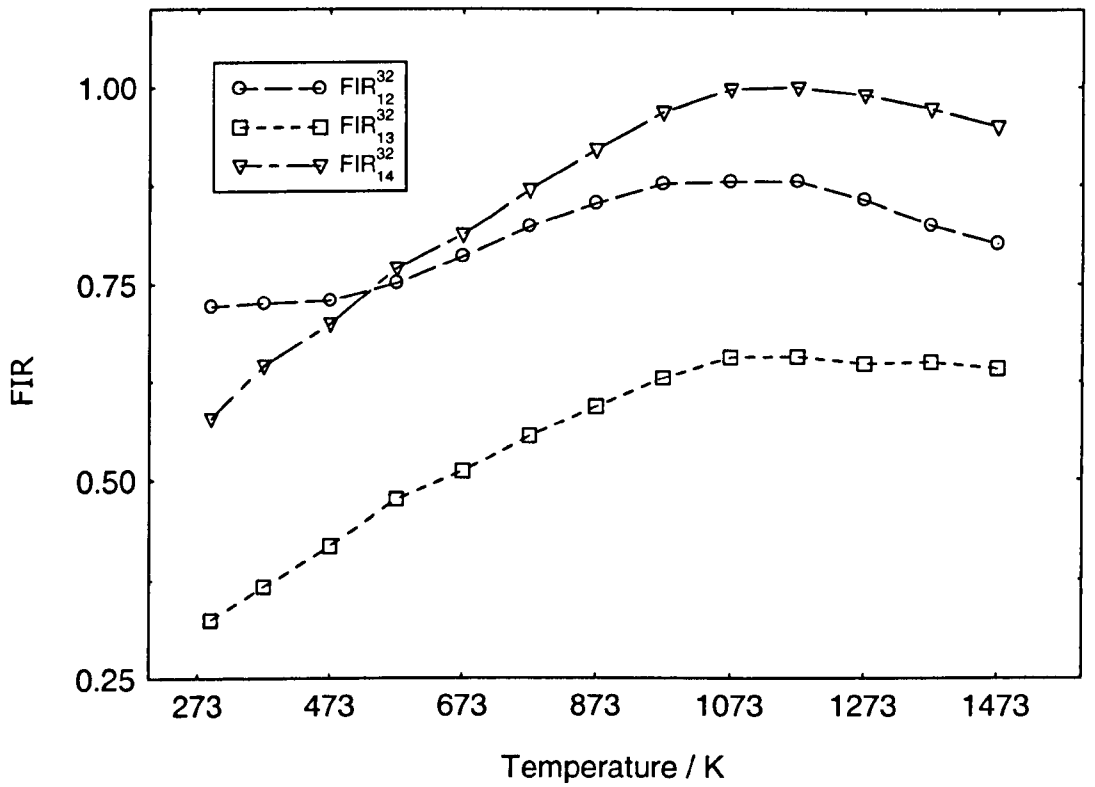

Figure 9.53b: Spec YAl 32 $Y_3Al_5O_{12}$:Er^{3+}+Yb^{3+} FIR_{15}^{32} to FIR_{18}^{32} vs temperature

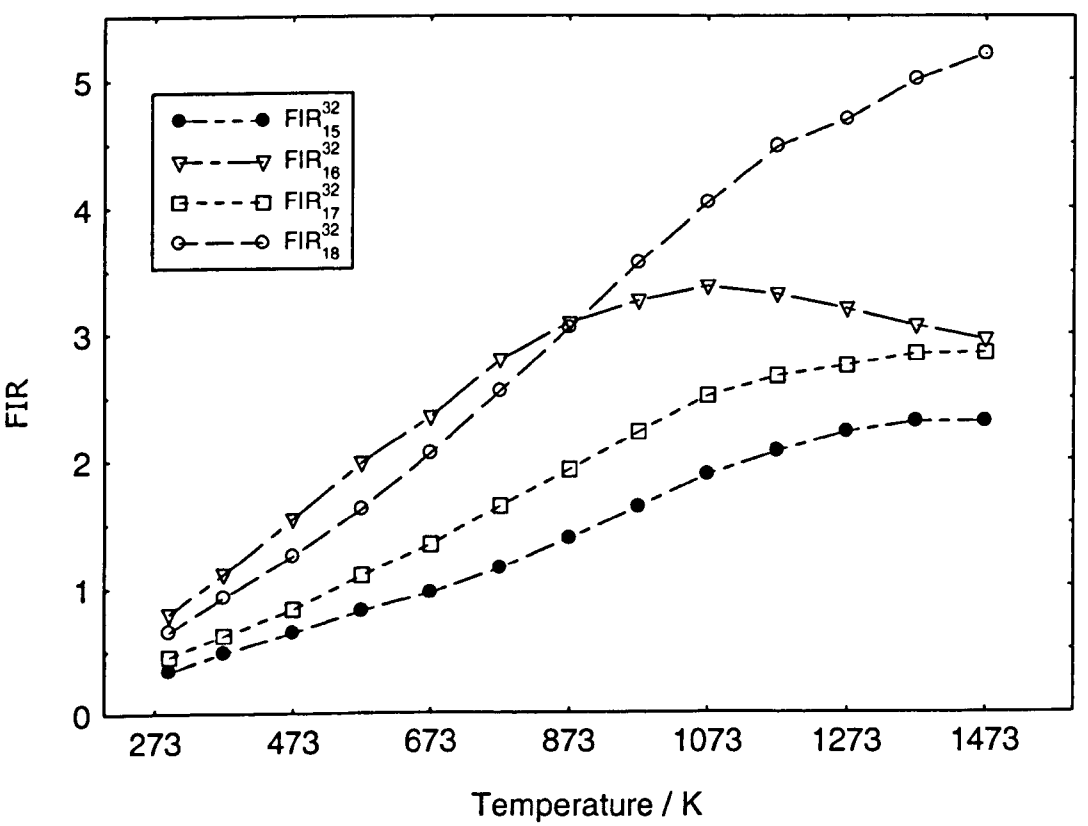

Figure 9.53c: Spec YAl 32 $Y_3Al_5O_{12}:Er^{3+}+Yb^{3+}$ FIR_{15}^{32} & FIR_{17}^{32} (fitted with Eq. 9.7) vs temperature

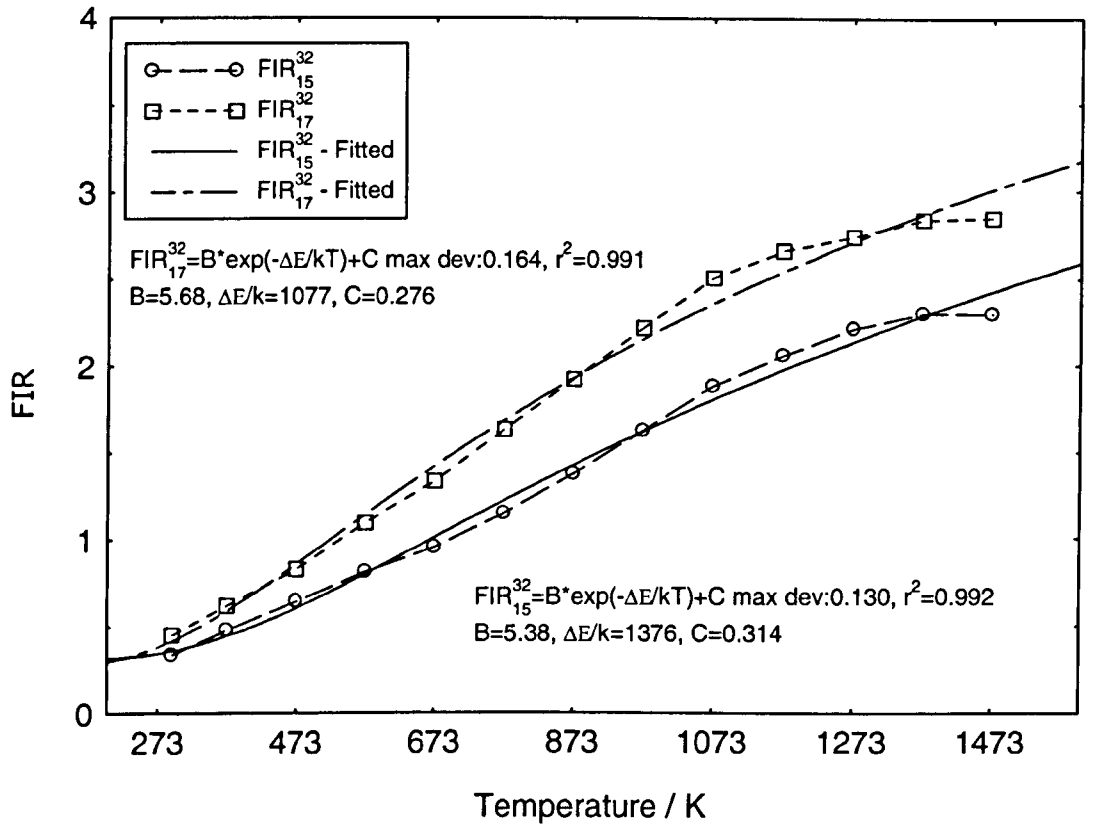

Figure 9.53d: Spec YAl 32 $Y_3Al_5O_{12}:Er^{3+}+Yb^{3+}$ FIR_{18}^{32} (fitted with Eq. 9.7) vs temperature

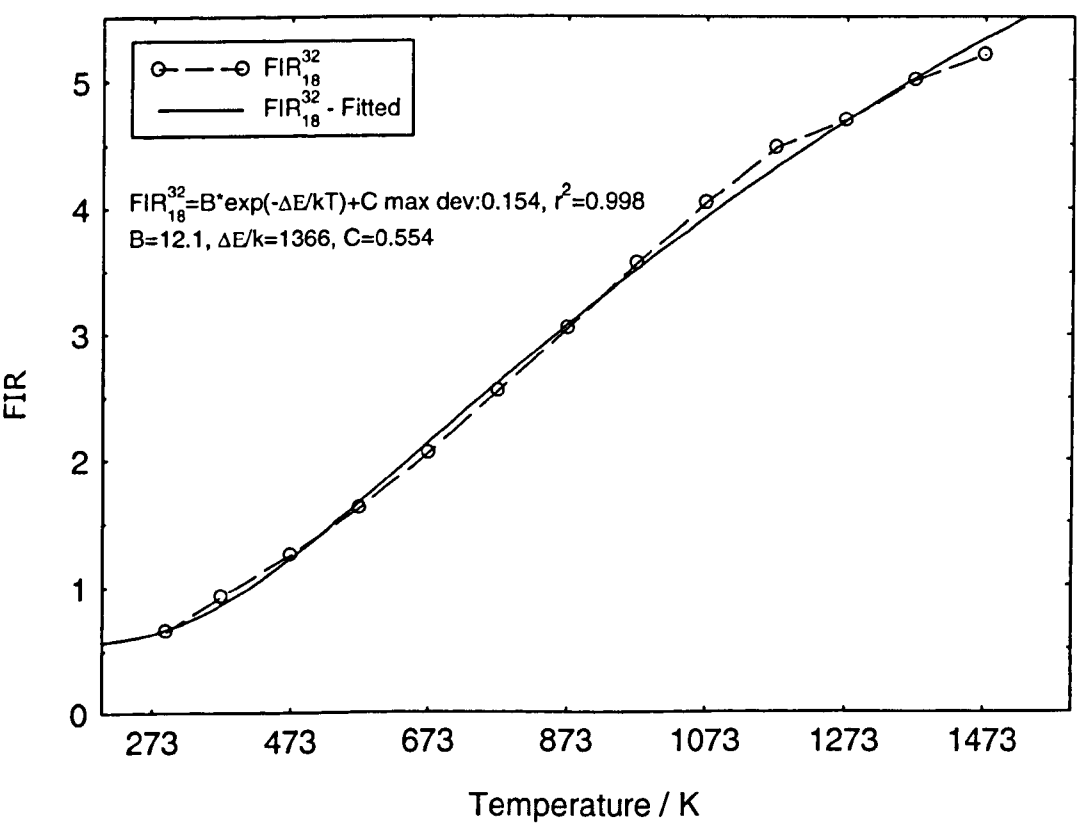

Figure 9.54a: Spec YAl 32 $Y_3Al_5O_{12}$:Er^{3+}+Yb^{3+} FIR_{23}^{32} & FIR_{24}^{32} vs temperature

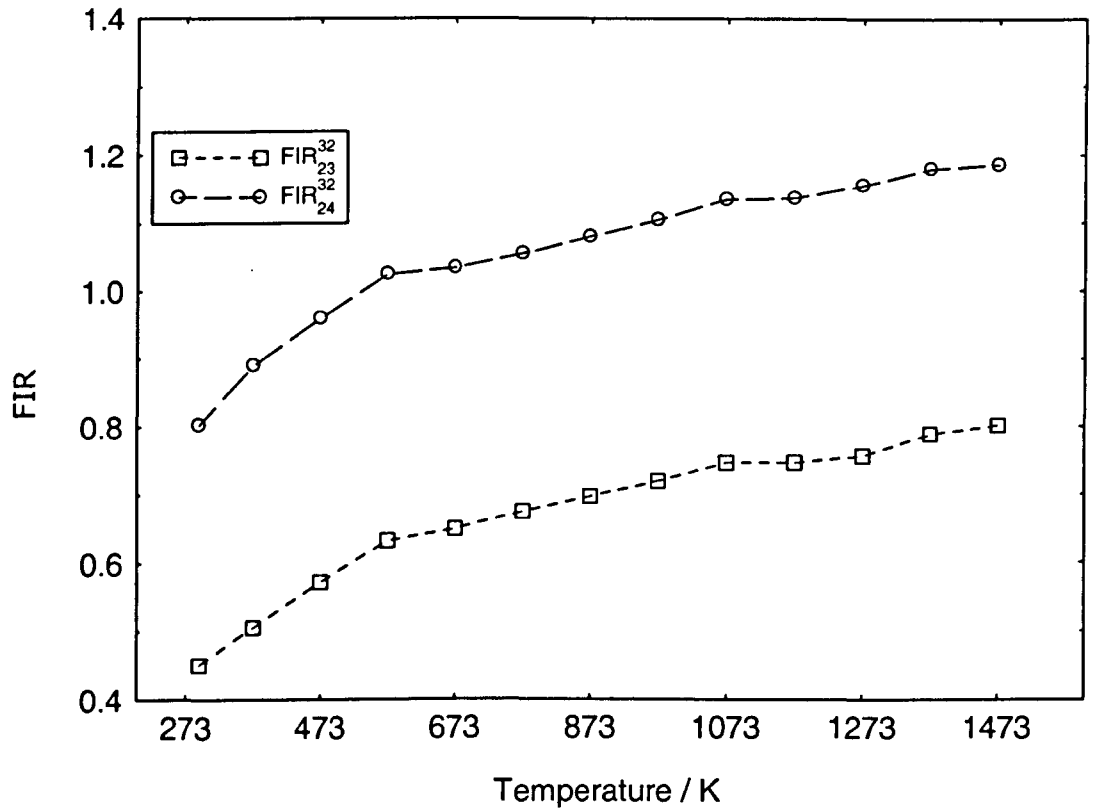

Figure 9.54b: Spec YAl 32 $Y_3Al_5O_{12}$:Er^{3+}+Yb^{3+} FIR_{25}^{32} to FIR_{28}^{32} vs temperature

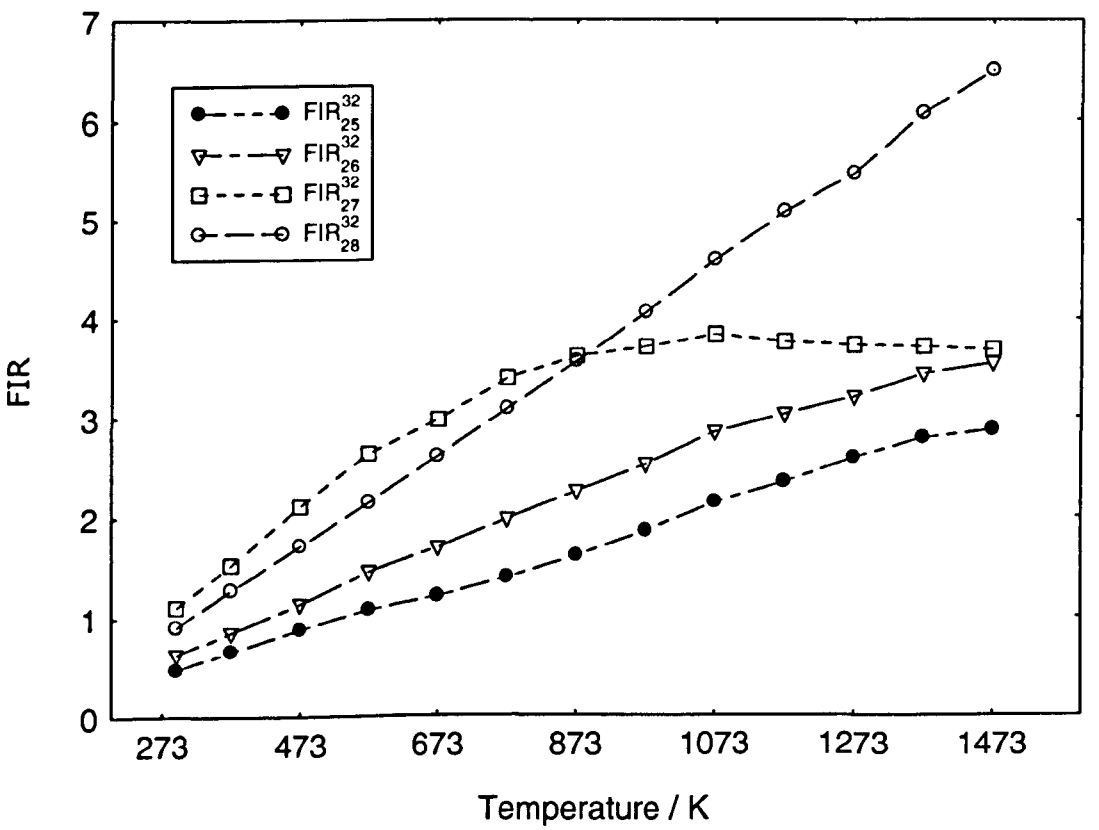

Figure 9.54c: Spec YAl 32 $Y_3Al_5O_{12}:Er^{3+}+Yb^{3+}$ FIR_{25}^{32} & FIR_{26}^{32} (fitted with Eq. 9.7) vs temperature

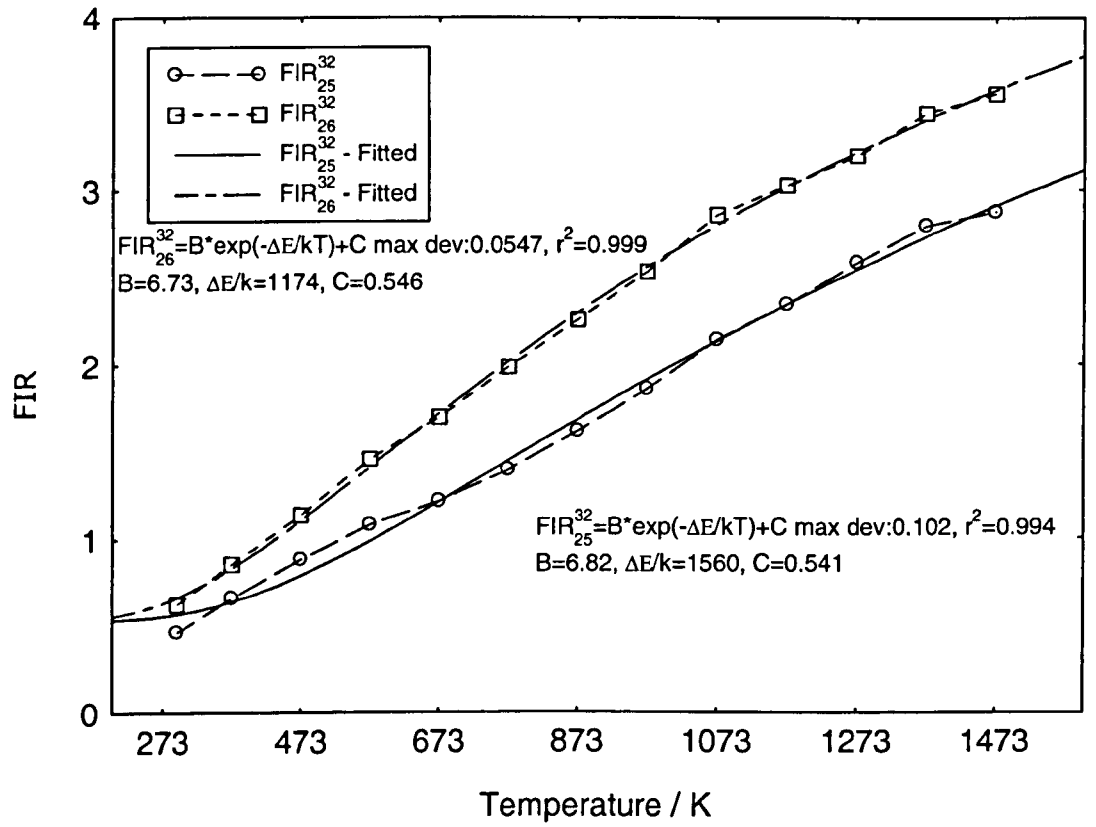

Figure 9.54d: Spec YAl 32 $Y_3Al_5O_{12}:Er^{3+}+Yb^{3+}$ FIR_{28}^{32} (fitted with Eq. 9.7) vs temperature

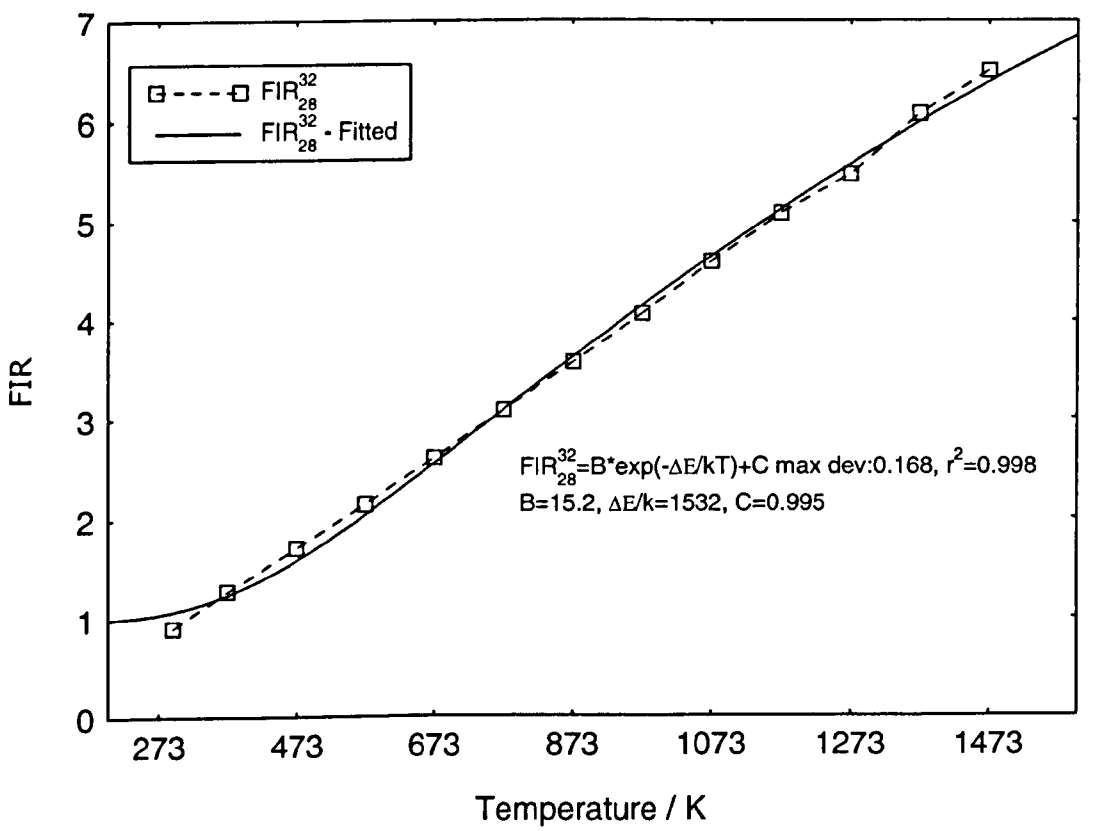

Figure 9.55a: Spec YAl 32 $Y_3Al_5O_{12}:Er^{3+}+Yb^{3+}$ FIR_{34}^{32} vs temperature

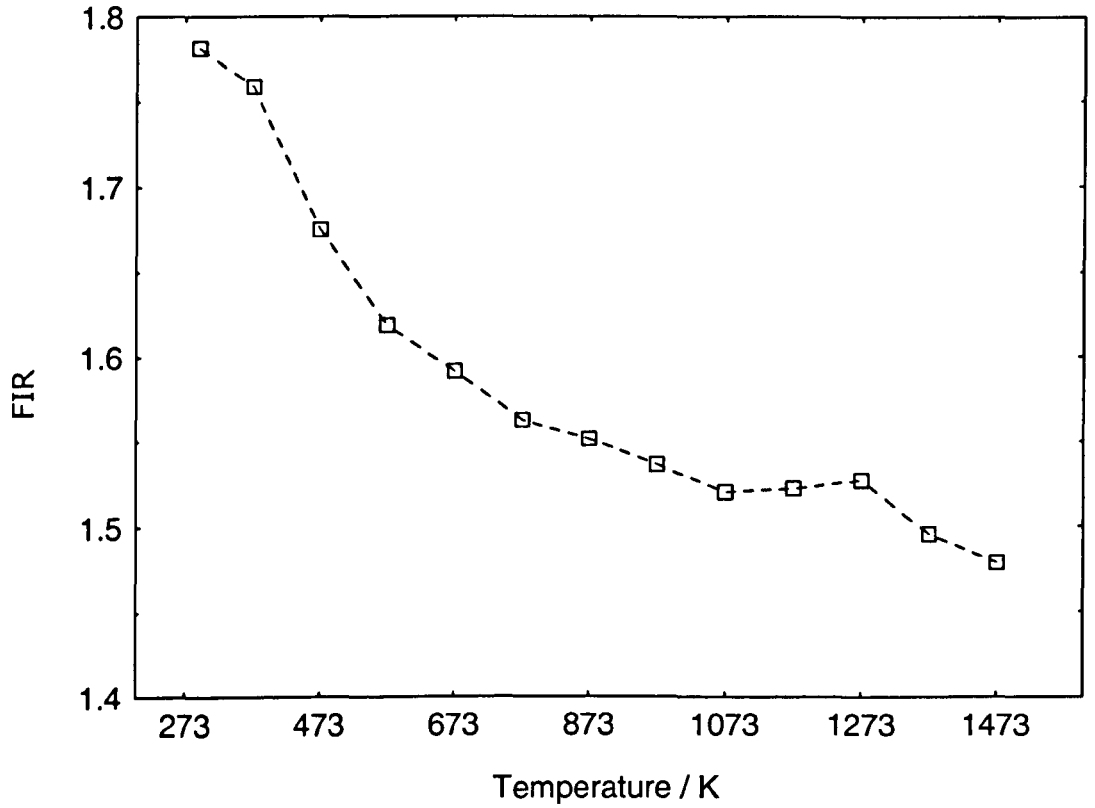

Figure 9.55b: Spec YAl 32 $Y_3Al_5O_{12}:Er^{3+}+Yb^{3+}$ FIR_{35}^{32} to FIR_{38}^{32} vs temperature

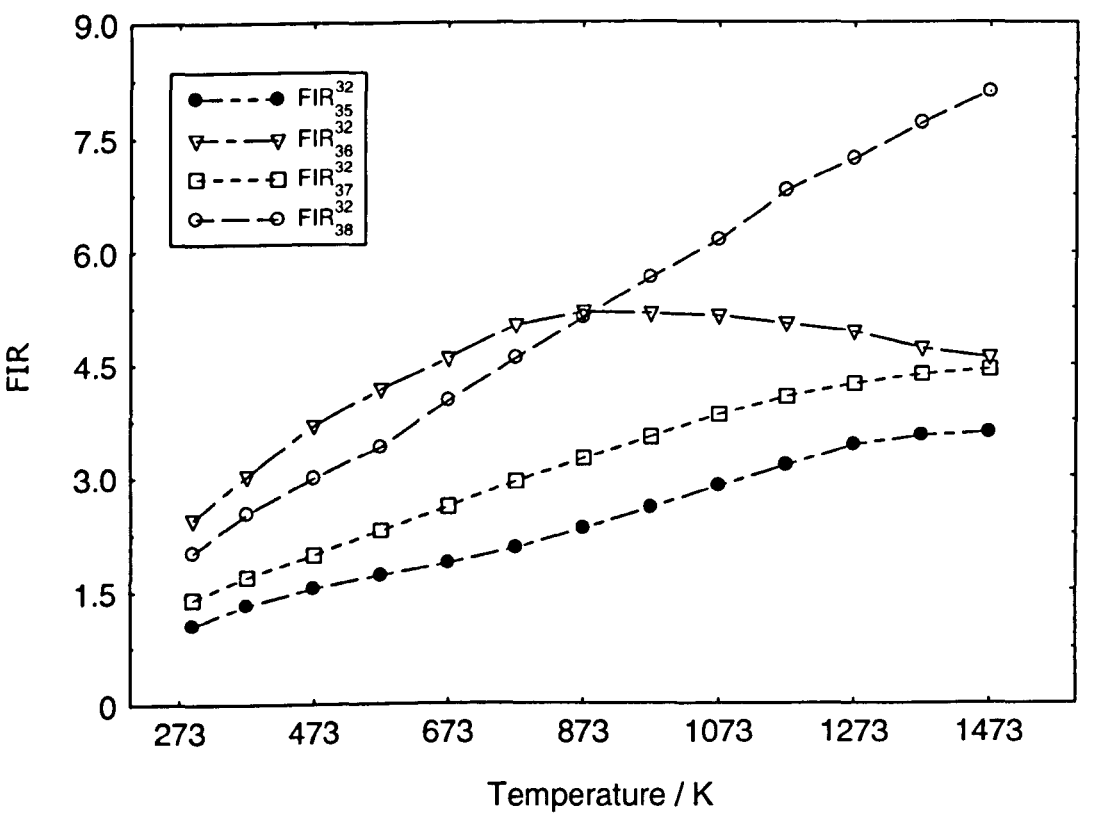

Figure 9.55c: Spec YAl 32 $Y_3Al_5O_{12}:Er^{3+}+Yb^{3+}$ FIR_{34}^{32} (fitted with Eq. 9.7) vs temperature

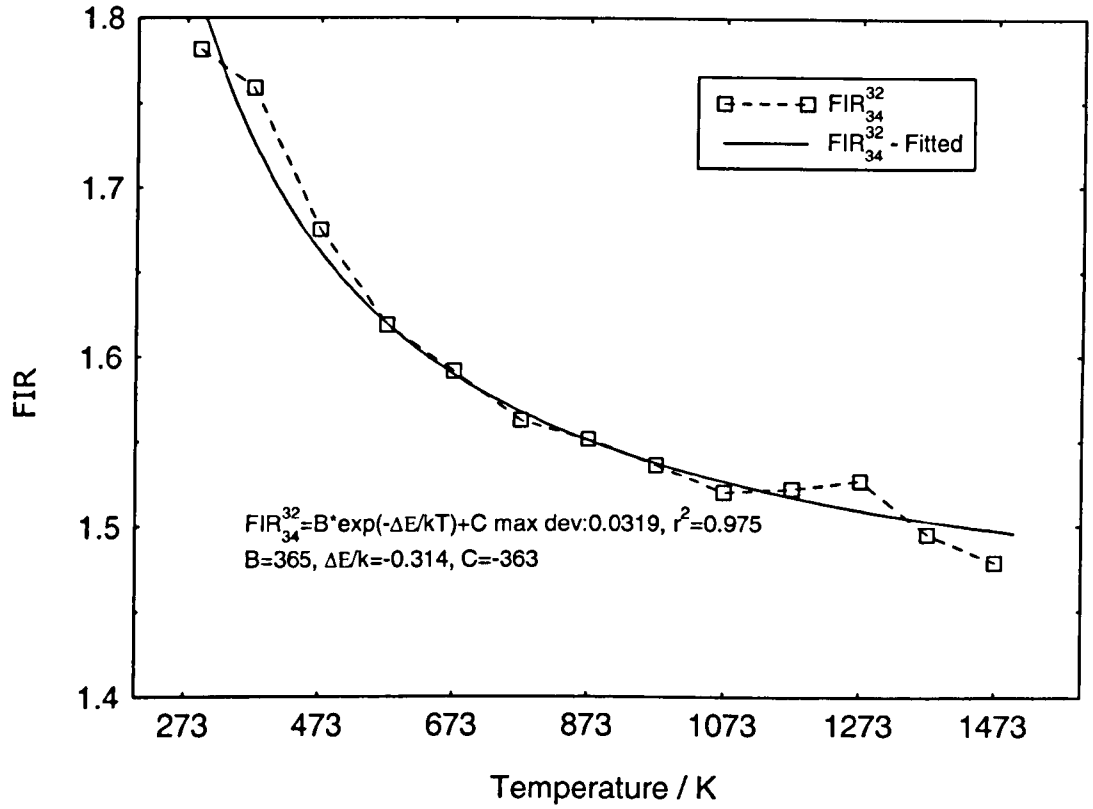

Figure 9.55d: Spec YAl 32 $Y_3Al_5O_{12}:Er^{3+}+Yb^{3+}$ FIR_{35}^{32} & FIR_{37}^{32} (fitted with Eq. 9.7) vs temperature

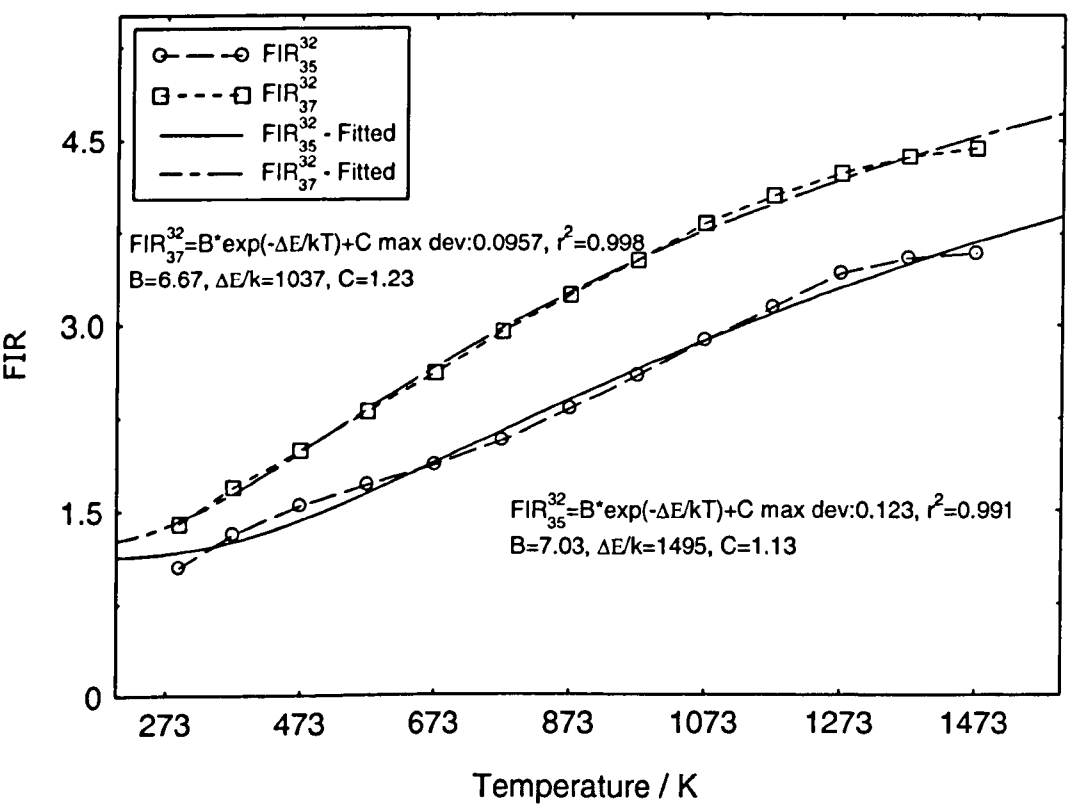

Figure 9.55e: Spec YAl 32 $Y_3Al_5O_{12}:Er^{3+}+Yb^{3+}$ FIR_{38}^{32} (fitted with Eq. 9.7) vs temperature

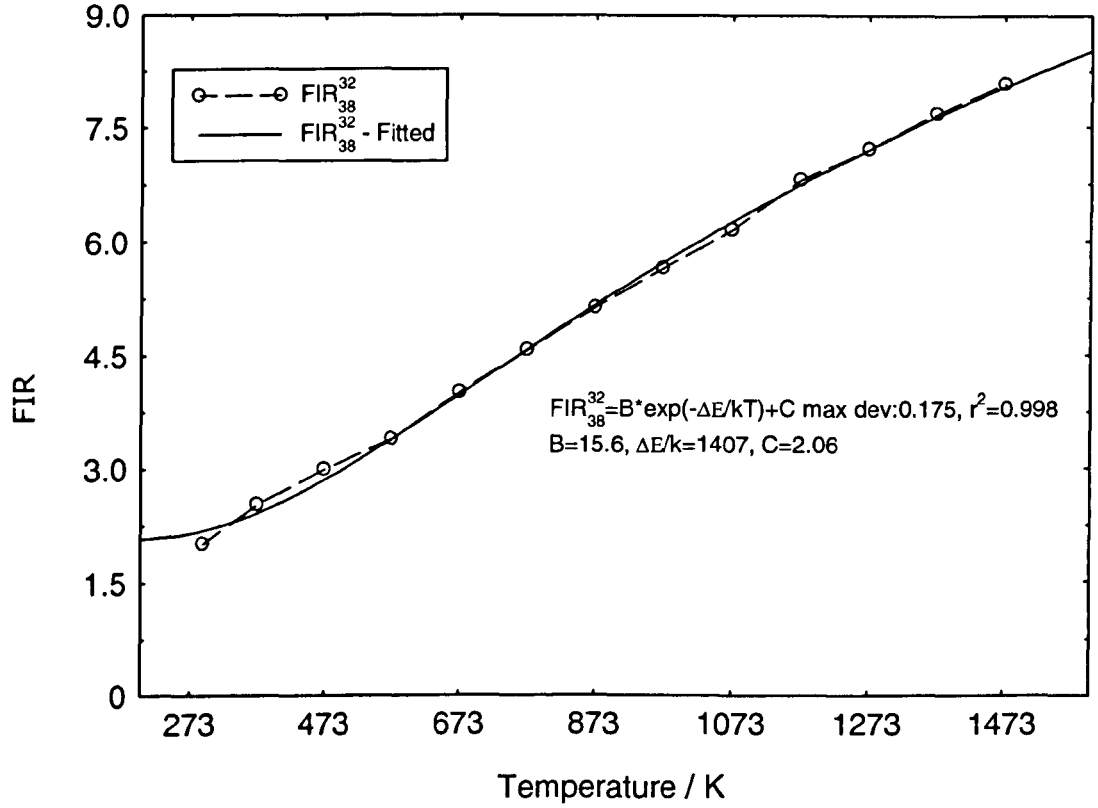

Figure 9.56a: Spec YAl 32 $Y_3Al_5O_{12}:Er^{3+}+Yb^{3+}$ FIR_{45}^{32} to FIR_{48}^{32} vs temperature

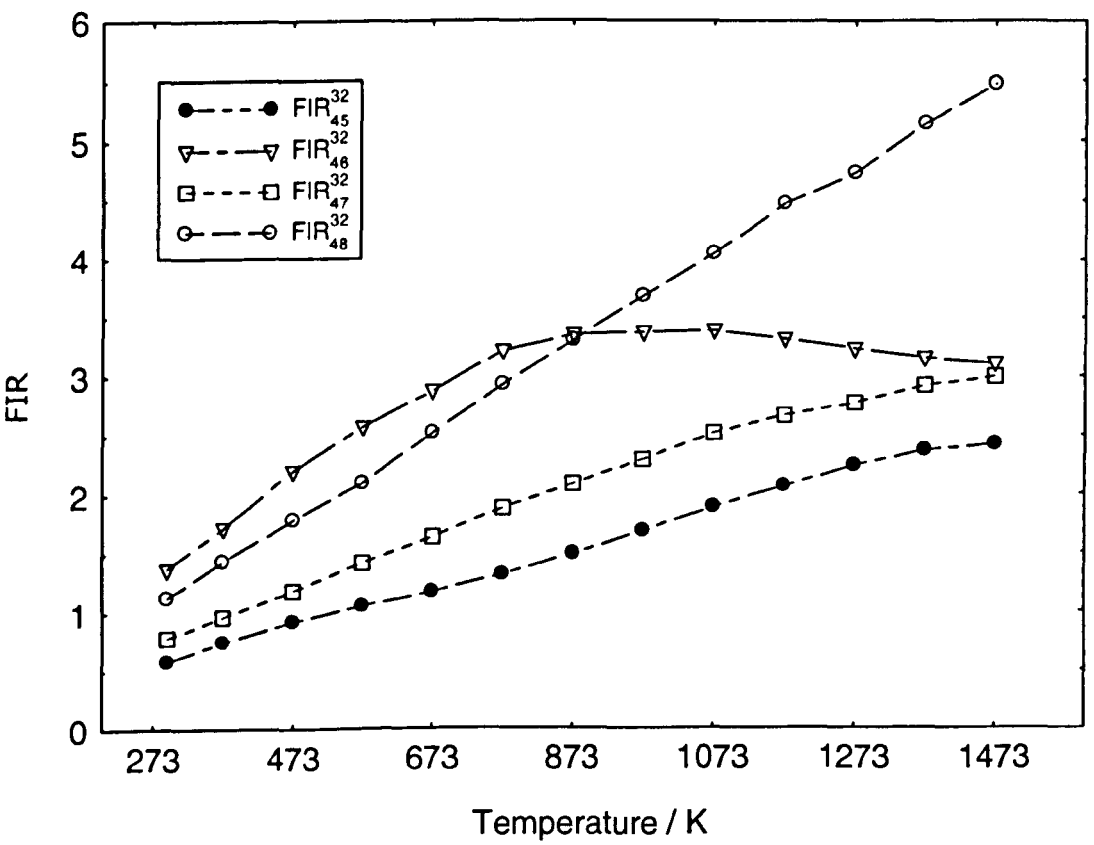

Figure 9.56b: Spec YAl 32 $Y_3Al_5O_{12}$:Er^{3+}+Yb^{3+} FIR_{45}^{32} & FIR_{47}^{32} (fitted with Eq. 9.7) vs temperature

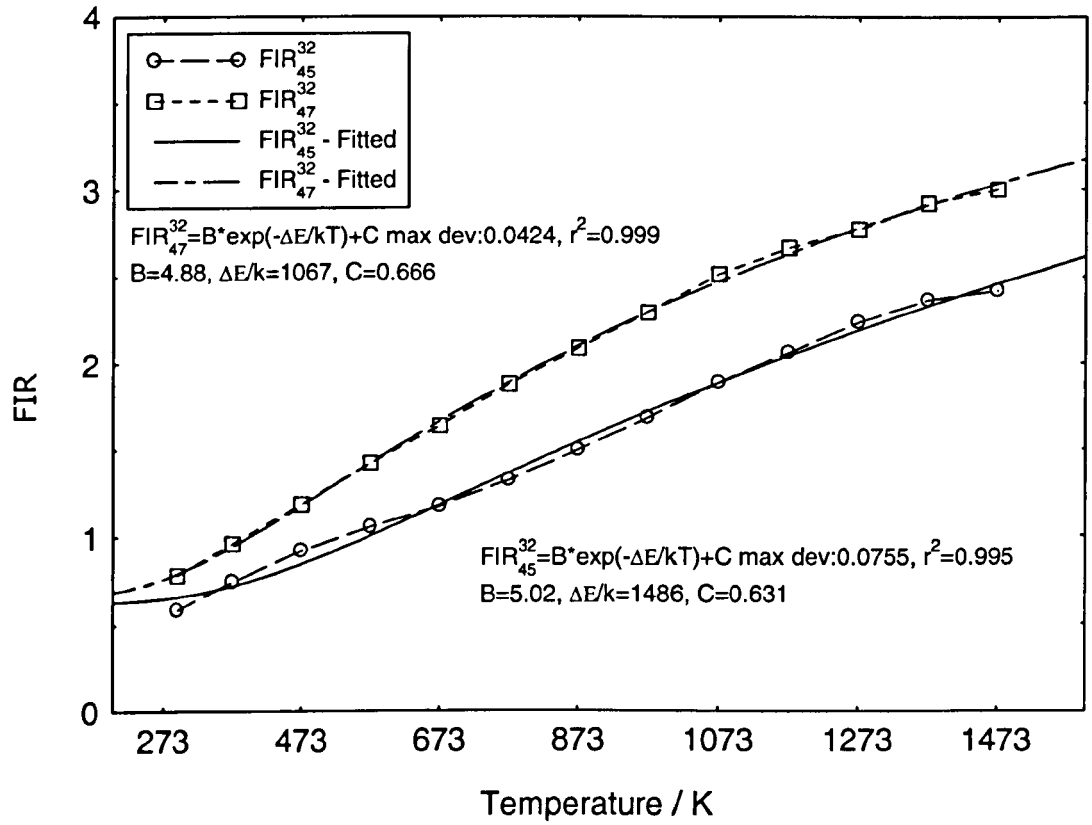

Figure 9.56c: Spec YAl 32 $Y_3Al_5O_{12}$:Er^{3+}+Yb^{3+} FIR_{48}^{32} (fitted with Eq. 9.7) vs temperature

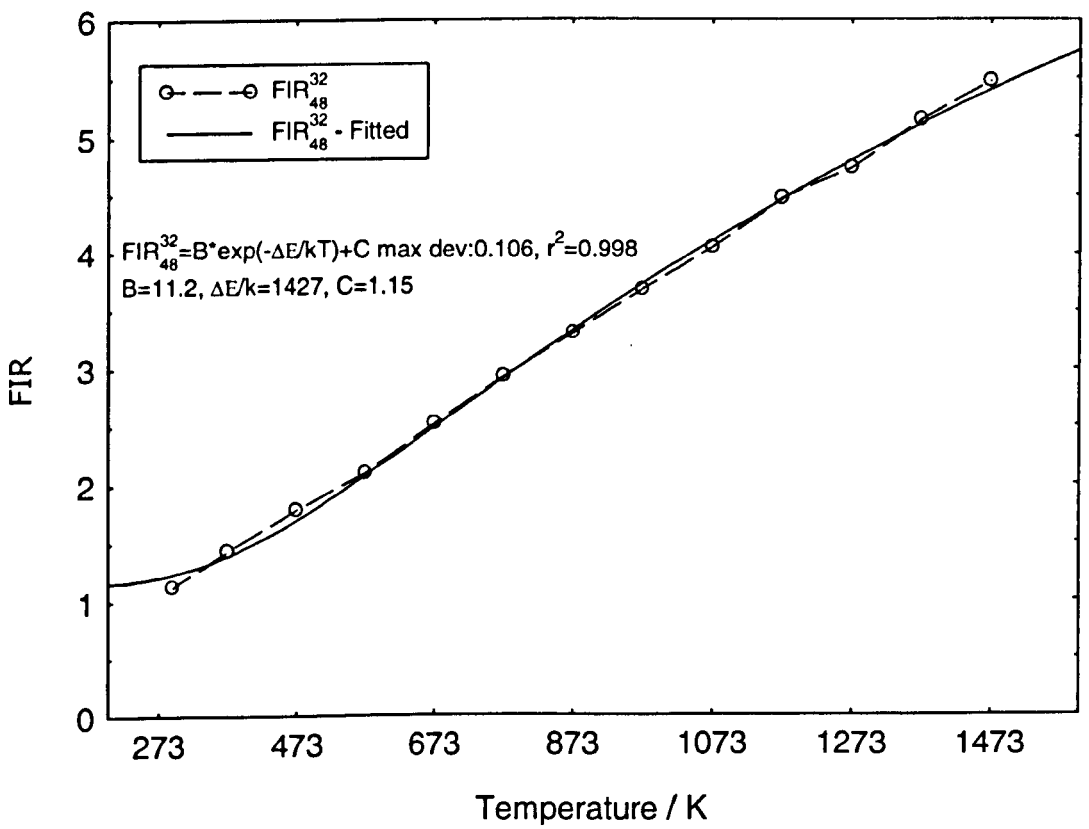

Figure 9.57: Spec YAl 32 $Y_3Al_5O_{12}:Er^{3+}+Yb^{3+}$ FIR_{56}^{32} to FIR_{58}^{32} vs temperature

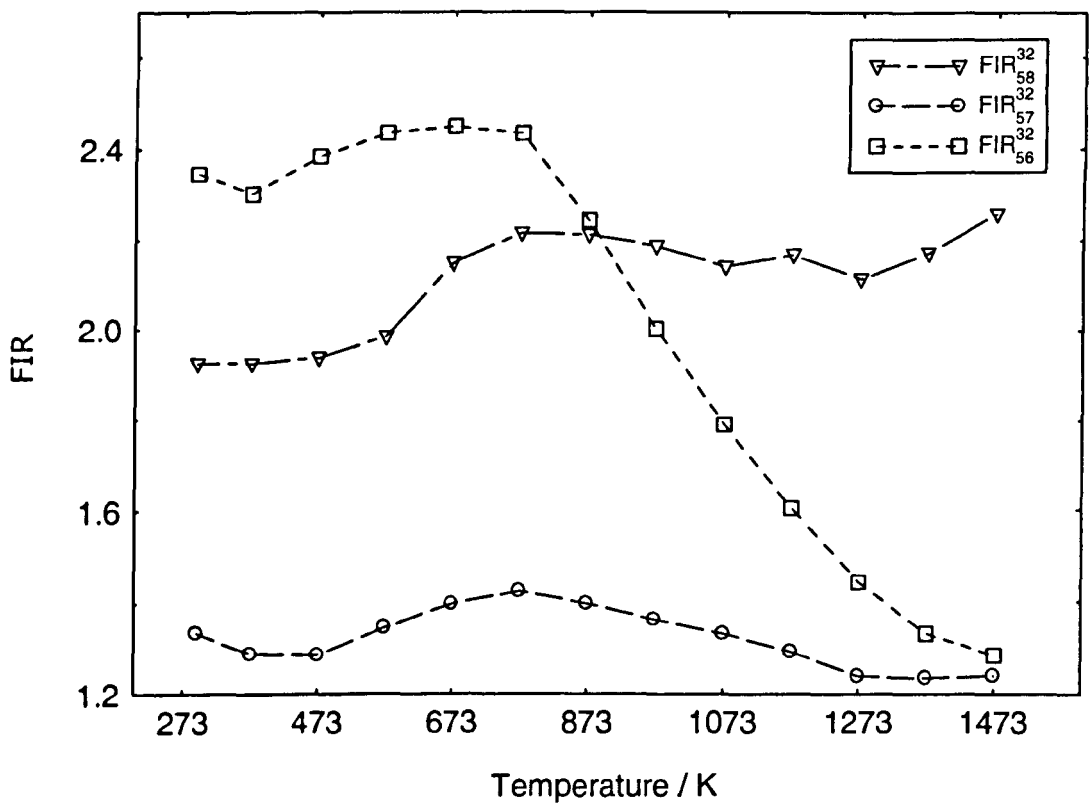

Figure 9.58a: Spec YAl 32 $Y_3Al_5O_{12}:Er^{3+}+Yb^{3+}$ FIR_{67}^{32} & FIR_{68}^{32} vs temperature

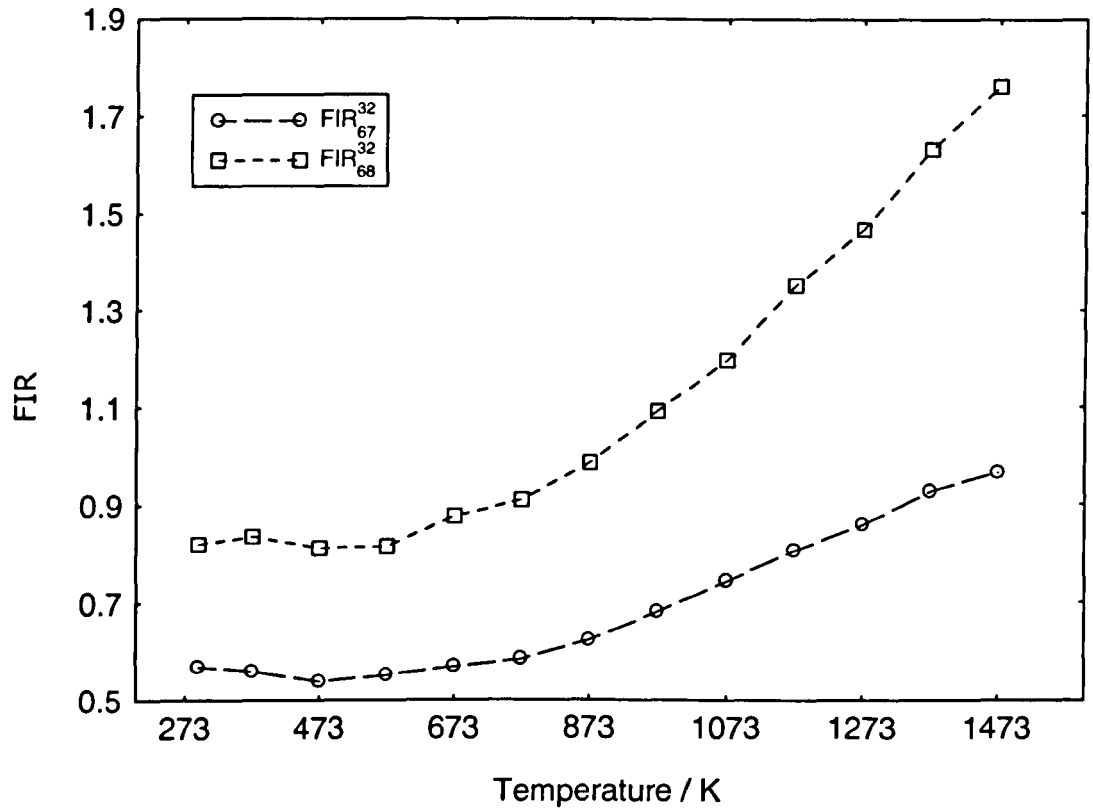

Figure 9.58b: Spec YAl 32 $Y_3Al_5O_{12}:Er^{3+}+Yb^{3+}$ FIR_{67}^{32} & FIR_{68}^{32} (fitted with Eq. 9.7) vs temperature

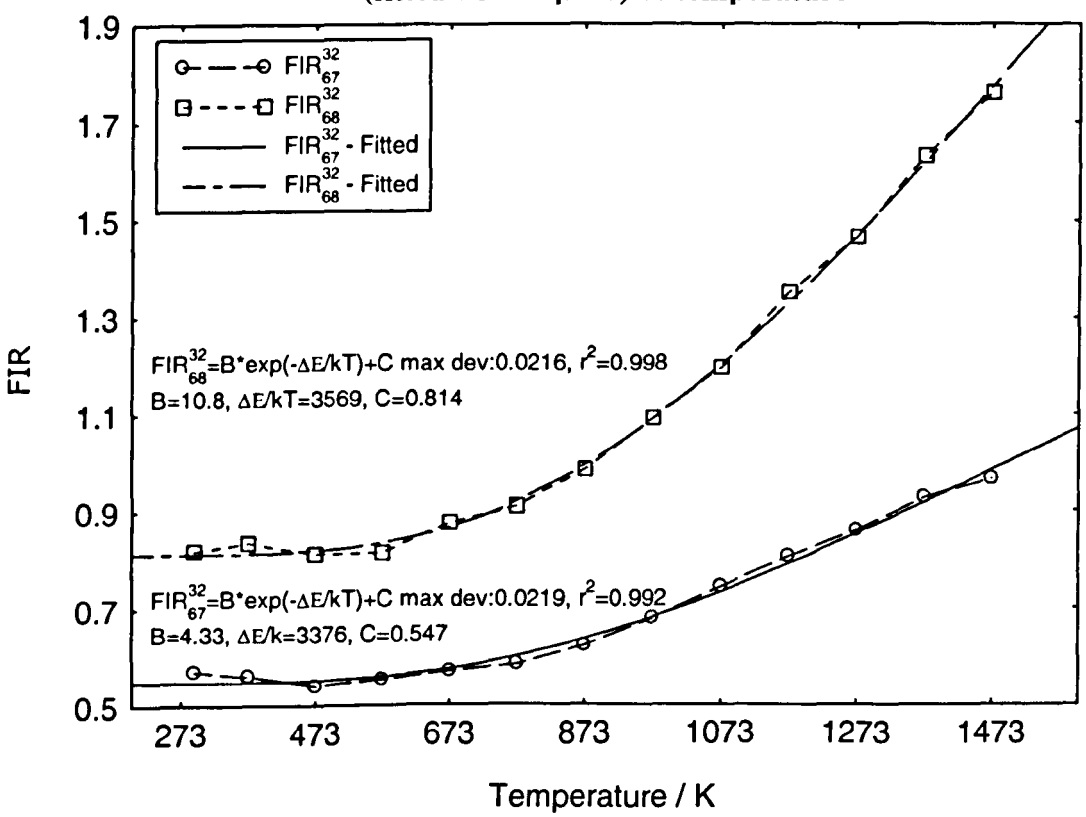

Figure 9.59: Spec YAl 32 $Y_3Al_5O_{12}:Er^{3+}+Yb^{3+}$ FIR_{78}^{32} (actual and fitted with Eq. 9.7) vs temperature

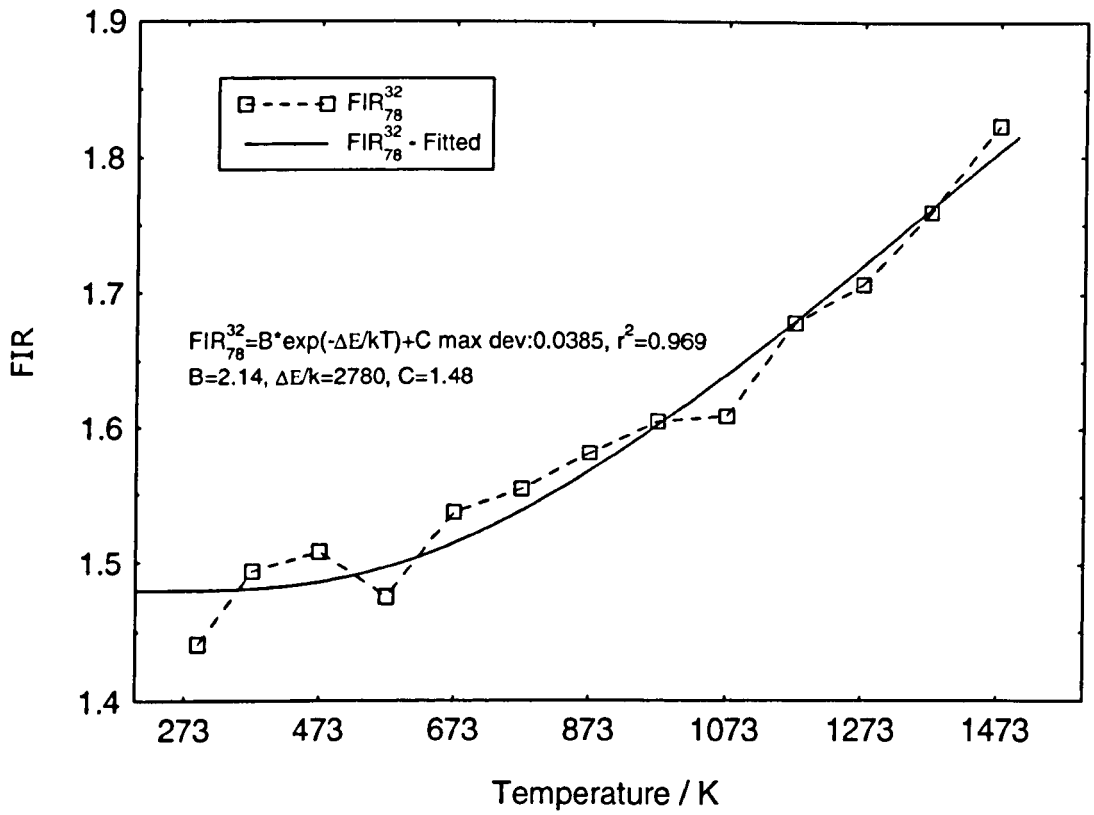

Figure 9.60a: Spec YAl 32 – $Y_3Al_5O_{12}:Er^{3+}+Yb^{3+}$ FIR_{YA}^{32} to FIR_{YC}^{32} - integrated intensity vs temperature

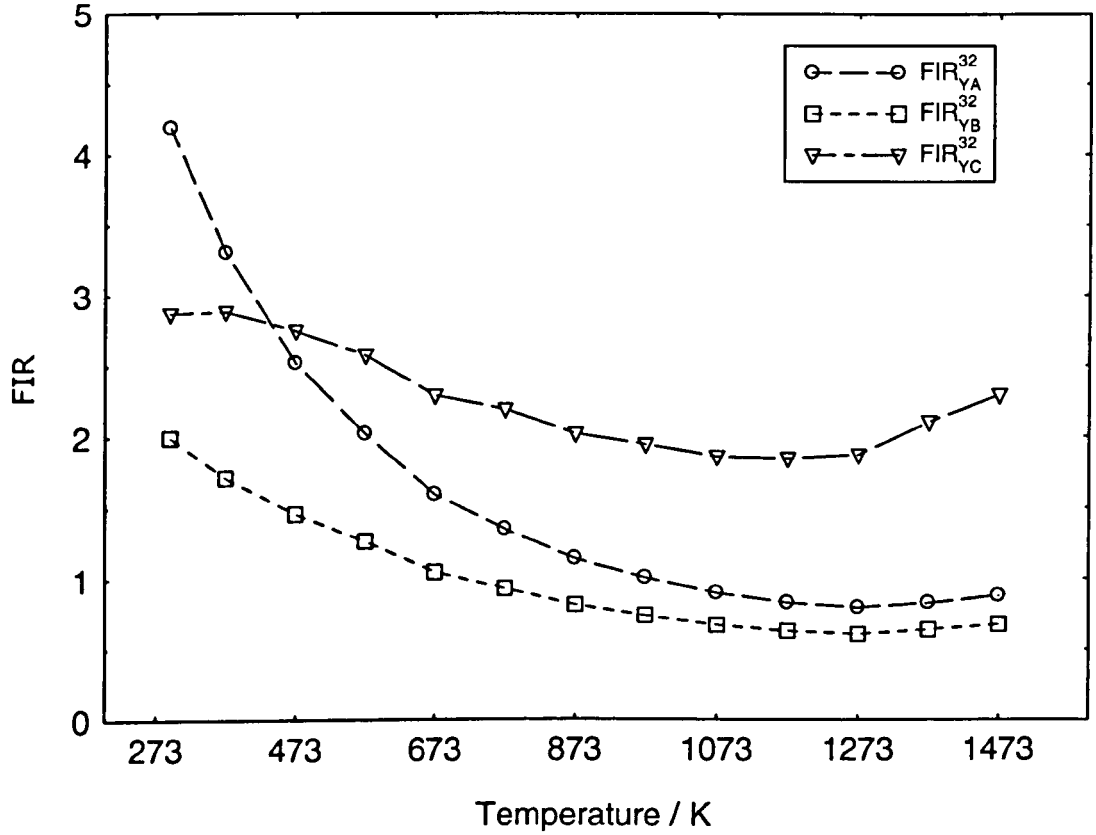

Figure 9.60b: Spec YAl 32 – $Y_3Al_5O_{12}:Er^{3+}+Yb^{3+}$ FIR_{AB}^{32}, FIR_{AC}^{32} & FIR_{BC}^{32} - integrated intensity vs temperature

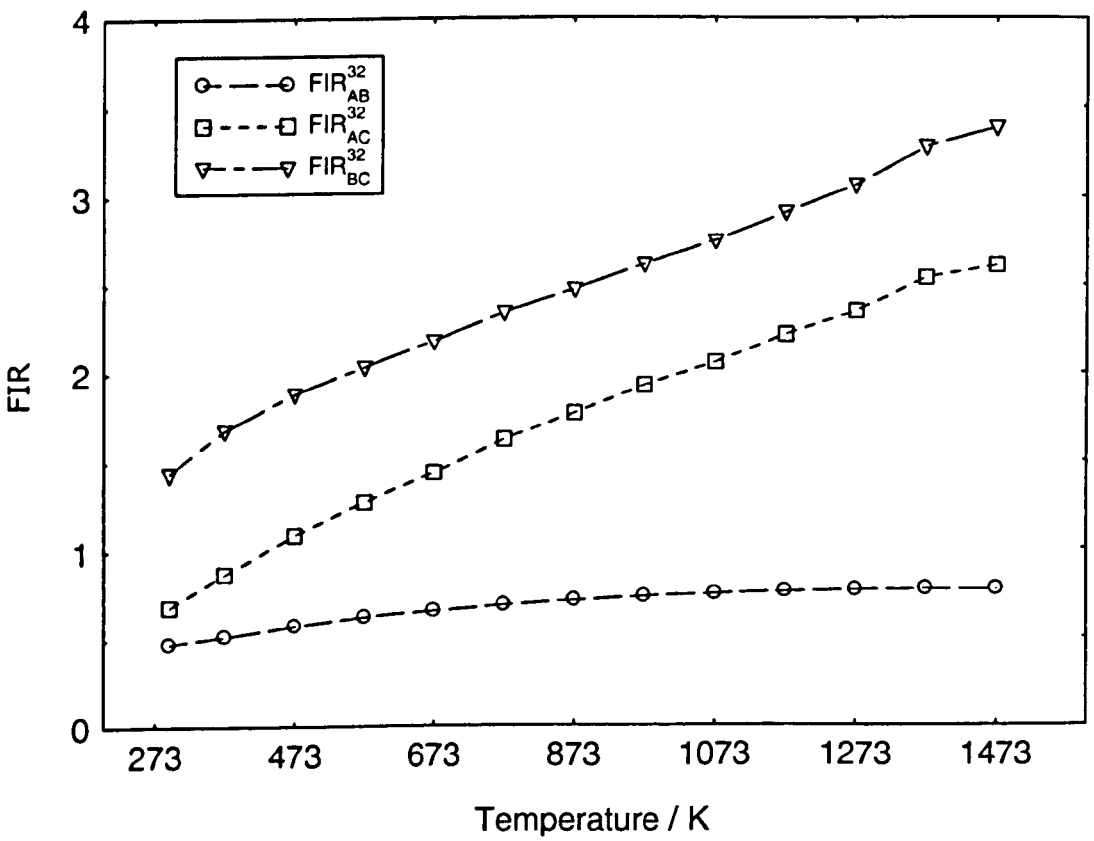

Figure 9.60c: Spec YAl 32 – $Y_3Al_5O_{12}:Er^{3+}+Yb^{3+}$ FIR_{YA}^{32} - integrated intensity (fitted with Eq. 9.7) vs temperature

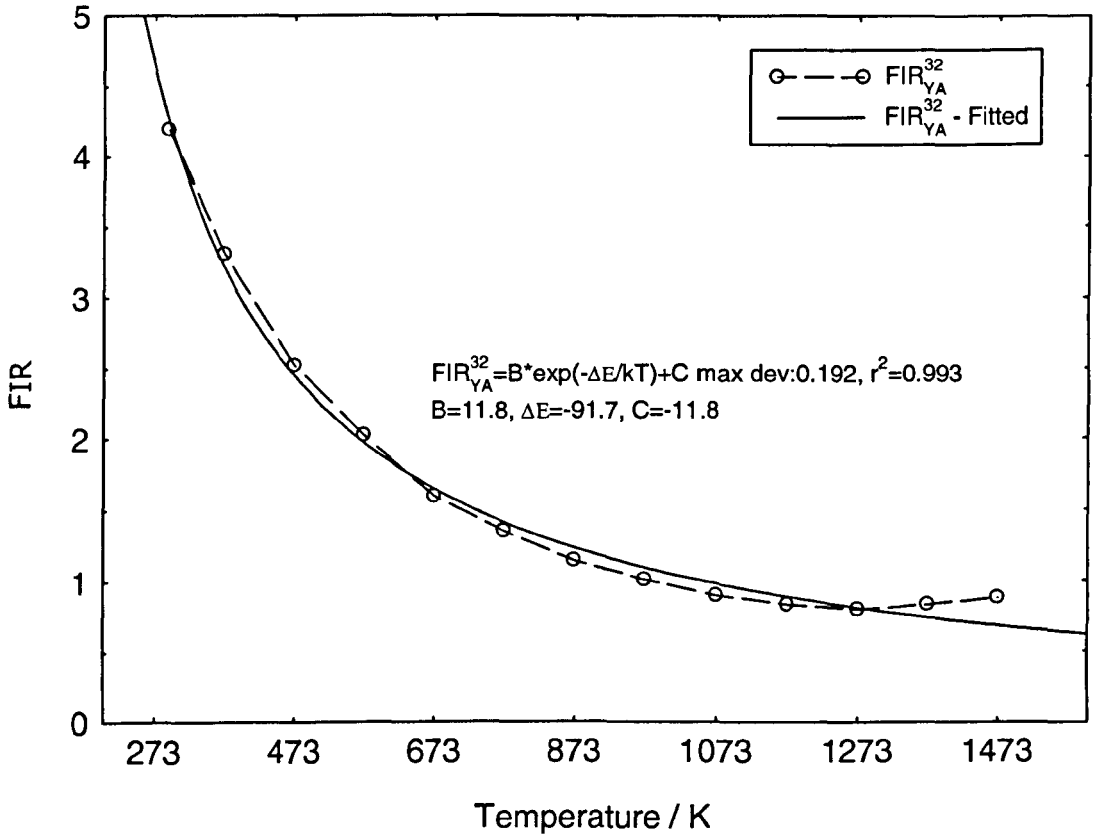

Figure 9.60d: Spec YAl 32 – $Y_3Al_5O_{12}:Er^{3+}+Yb^{3+}$ FIR_{AC}^{32} & FIR_{BC}^{32} - integrated intensity (fitted with Eq. 9.7) vs temperature

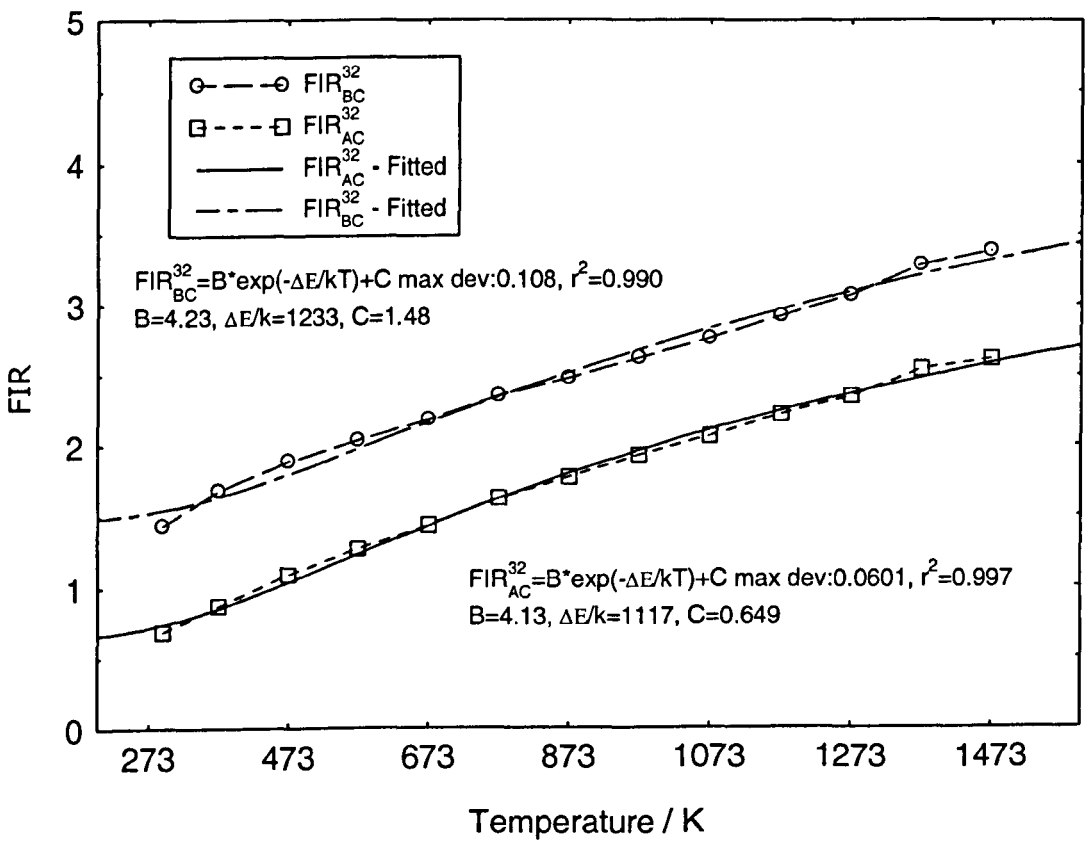

9.7.2 Upconversion Intensity Based Sensing - $Y_3Al_5O_{12}:Er^{3+}+Yb^{3+}$

There are a number of advantages in having Yb^{3+} as a co-doped ion. One of which is the optimization of the energy transfer by broadening of the absorption band at 900nm to 1000nm region. Several works have reported incorporating $Er^{3+}+Yb^{3+}$ ions and using upconversion intensities for temperature sensing in fibres at the lower temperature region (~293K to 493K) [9.50, 51]. The use of co-doped Al_2O_3 SCF as host for temperatures up to ~1470K has also been discussed [2.23]. Investigations carried out in this section are on the temperature dependent green and red spectral regions of the YAG co-doped SCF. Under the excitation by a 965nm laser diode, a strong green and red emission was observed at room temperature (Figure 9.61). The red emission is about ~41% of the green. A relationship between temperature changes and intensity changes was examined by monitoring the visible lines at 541nm, 553.5nm, 560nm and 676nm. Work presented in this section demonstrates that possibility of achieving and measurement temperature range as high as ~1473K. Intensity based sensing, using UIR and integrated intensities in the different transition levels are methods employed to determine the temperature change.

9.7.2.1 Results and Discussion

A general overview of the upconversion spectra under the influence of temperature is presented in Figure 9.62. It clearly shows that as temperature increases the intensity of several strong peaks in the green region decreases and the red emission intensity was at its strongest at 1473K. Transitions from the $^4S_{3/2}$ level decrease as the temperature rises. With increasing temperature, broadening of the linewidth at the base of the upconversion profile is evident. Figure 9.67 (insert) illustrates the integrated intensity changes of the three transitions. Transitions $^2H_{11/2}$ and $^4F_{9/2}$ decrease with temperature, however, at ~773K the two experience an increase in the integrated intensities. Figures 9.63 and 64 show the upconversion emission spectra at different temperatures for the transitions from $^2H_{11/2}$ and $^4S_{3/2}$. The increase in the former transition, as mentioned in singly doped YAG, was possibly due to the thermal equilibrium within energy levels of the rare earths [9.48]. The reduction of the $^4S_{3/2}$ level could be due to the homogeneous line broadening and population redistribution between the Stark lines at the ground level $^4I_{15/2}$. This possible

redistribution has then increased the integrated intensity from the $^2H_{11/2}$ transition. Figure 9.64 illustrates the linewidth started at wavelength 530nm initially then increase to start at wavelength ~500nm. At 1473K, transitions from $^2H_{11/2}$ increased by ~55%. The plots in Figures 9.65 and 66 show the temperature dependent upconversion emission spectra from $^4F_{9/2}$. Broadening of linewidths were again seen in this transition. The red emission exhibited an initial decrease before increasing with temperature. This rapid increase of the integrated intensity makes it very sensitive to temperature changes at the high temperature region, Figure 9.67.

Using the upconversion emission intensity as a function of temperature could be another way to monitor the temperature change within a system. Figures 6.68a and b shows the visible lines in the $^2H_{11/2}$ and $^4S_{3/2}$ transitions and Figure 6.69 illustrates the line in the $^4F_{9/2}$ transition. In the green region, exponential decrease was observed in plots as the temperature increases. These rapidly decreasing curves have a maximum effective temperature of only ~1173K. The I_{676} intensity line in the red was not ideal for temperature sensing due to non-monotonic changes in the intensity.

Table 9.5 shows the denotation used for the UIRs. When 541nm was chosen as the upper energy level in the UIR calculation, the results could not be fitted well with equation 9.7. The results did not follow the ideal behaviour this could be due to the broadening of the line shapes at high temperatures. As reported by *Maurice* upconversion intensity ratios do not fellow theoretical predictions closely [3.36]. Figure 9.70 shows the plots UIR_{12}^{32} & UIR_{13}^{32} and a 4th order polynomial fitted carried out on the curves. Mentioned in the work by *Sidiroglou* [9.41], this polynomial fitting method is commonly used in thermometry sensing thereby creating another avenue by which data can be analysed. Figure 9.71 illustrates the UIR between the ratio of 553.5nm and 560nm and its fitted curve. An increase in UIR was observed as the temperature rises. The calculated energy difference from the fitted curve is 1662cm^{-1} whereas the theoretical value of ΔE is 209.7cm^{-1}. The large discrepancy could be attributed to the material used, as equation 9.7 was intended for silica based sensors. Once again study of the visible line at 679nmn was abandoned due to non-monotonic changes in the intensity.

Figure 9.72 shows the intensity ratio and fitted plots (both linear and with equation 9.7) of the integrated wavelengths between transitions $^2H_{11/2}$ and $^4S_{3/2}$. The linear

behaviour make it ideal for use in thermometry. Lastly, the integrated intensity ratio between the green ($^2H_{11/2}$ + $^4S_{3/2}$) and the red ($^4F_{9/2}$) is presented in Figure 9.73. A rapid increase is observed after 1073K. The exponential increase makes it ideal for temperature sensing since small changes in temperature will result large changes in UIR. Even though there are variations in the intensity for the transitions seen in Figure 9.67, the UIR results show a consistent increase; similarity kinds of fluctuation of intensity have also been reported in reference [9.50]. This consistency in the UIR confirms the self-referencing property and concludes that it is independent of pump power fluctuation [3.36, 9.50]. From the above work, several ways can be adopted for temperature sensing as the rare earth ions in YAG have shown to be dependent to temperature.

Figure 9.61: Spec YAl 32 $Y_3Al_5O_{12}:Er^{3+} + Yb^{3+}$ upconversion in room temperature, 293K

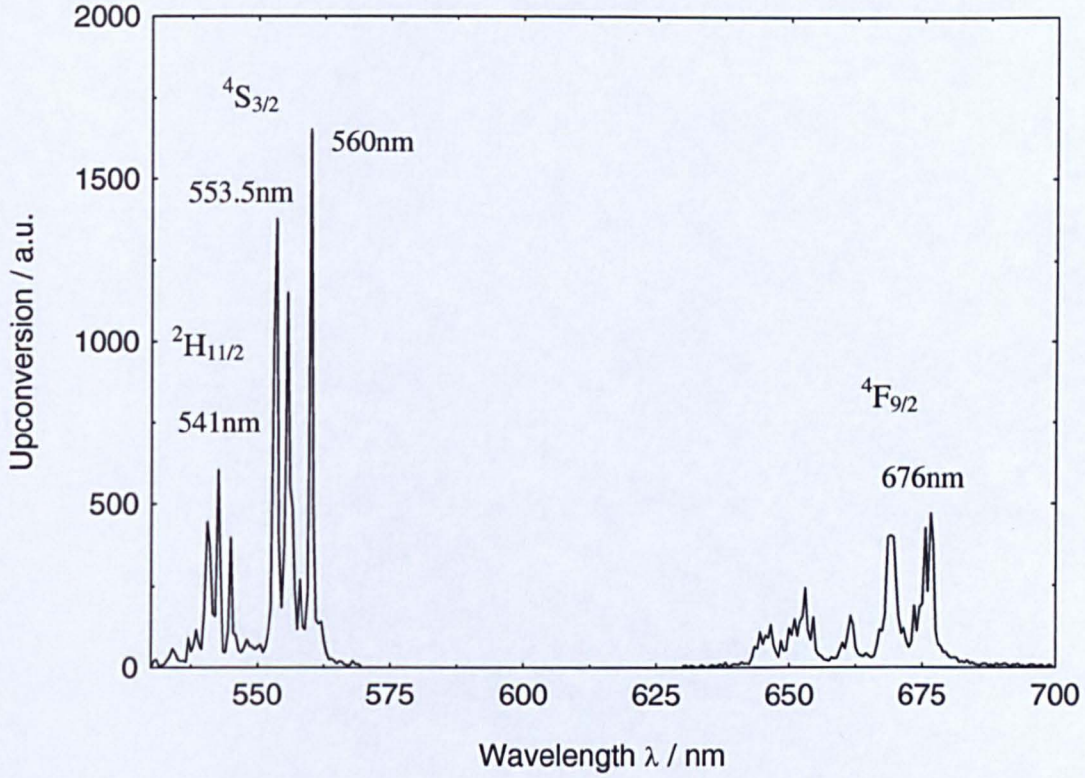

Figure 9.62: Spec YAl 32 $Y_3Al_5O_{12}:Er^{3+} + Yb^{3+}$ upconversion spectra from room temperature to 1473K

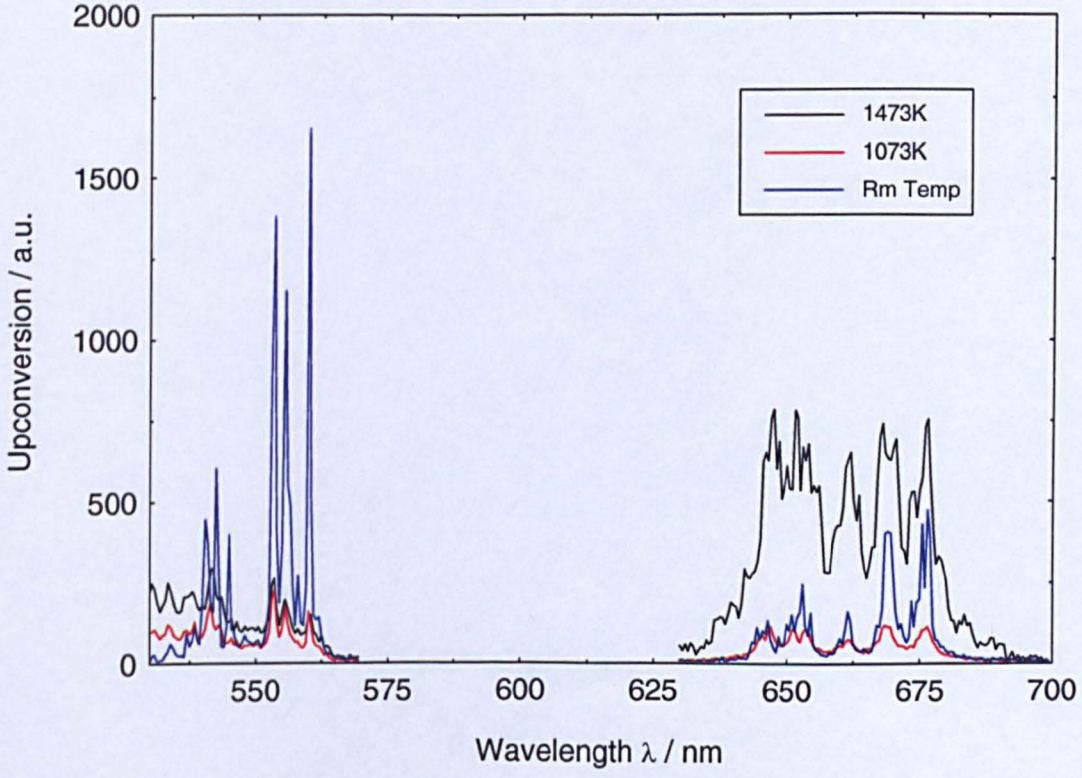

Figure 9.63: Spec YAl 32 $Y_3Al_5O_{12}:Er^{3+} + Yb^{3+}$ upconversion spectra from room temperature to 873K, $^2H_{11/2} + {}^4S_{3/2}$

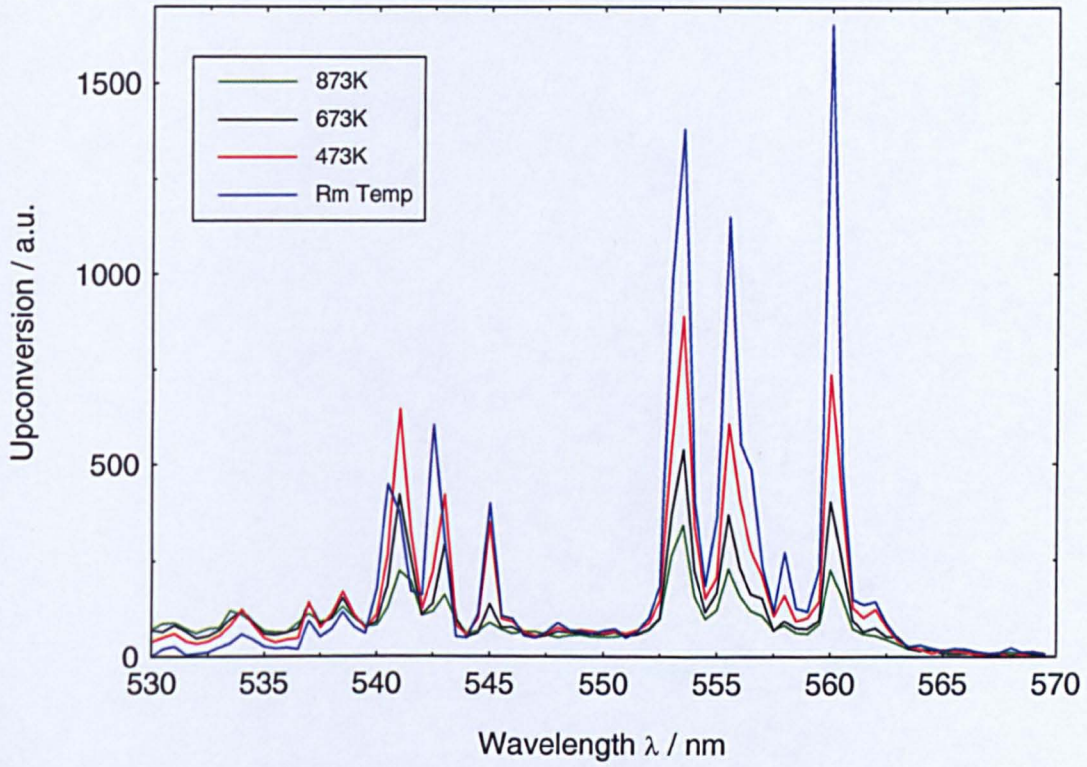

Figure 9.64: Spec YAl 32 $Y_3Al_5O_{12}:Er^{3+} + Yb^{3+}$ upconversion spectra from 873K to 1473K, $^2H_{11/2} + {}^4S_{3/2}$

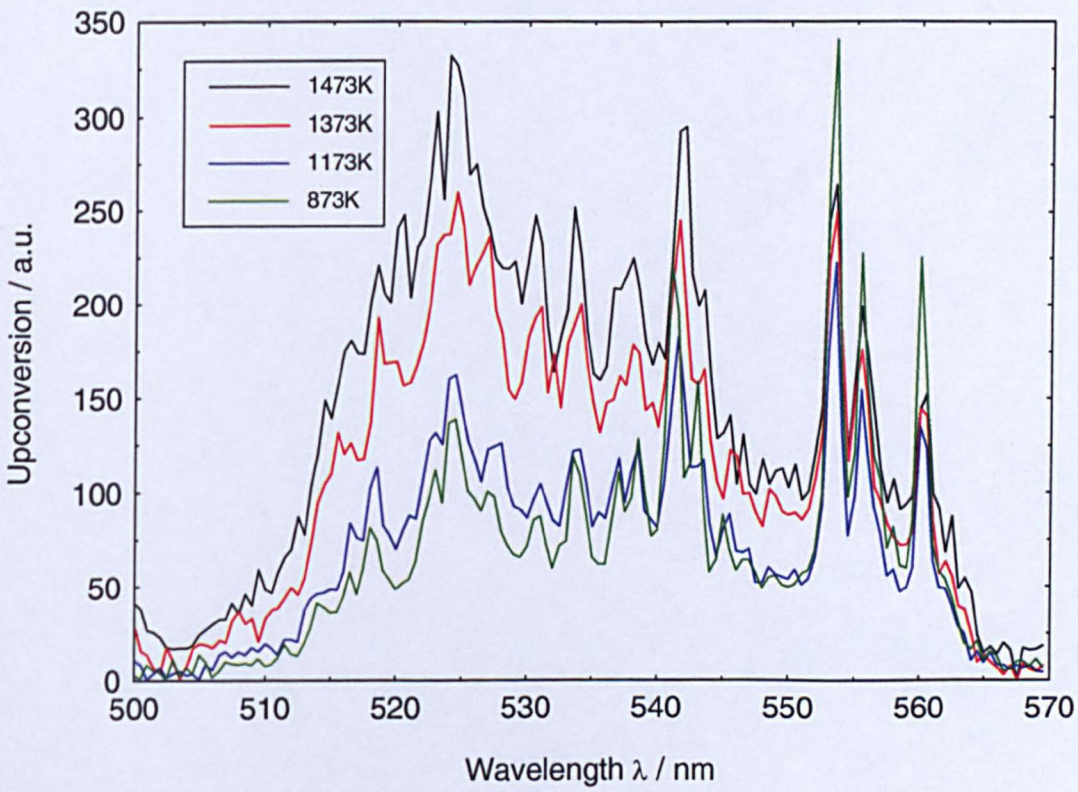

Figure 9.65: Spec YAl 32 $Y_3Al_5O_{12}:Er^{3+} + Yb^{3+}$ upconversion spectra from room temperature to 873K, $^4F_{9/2}$

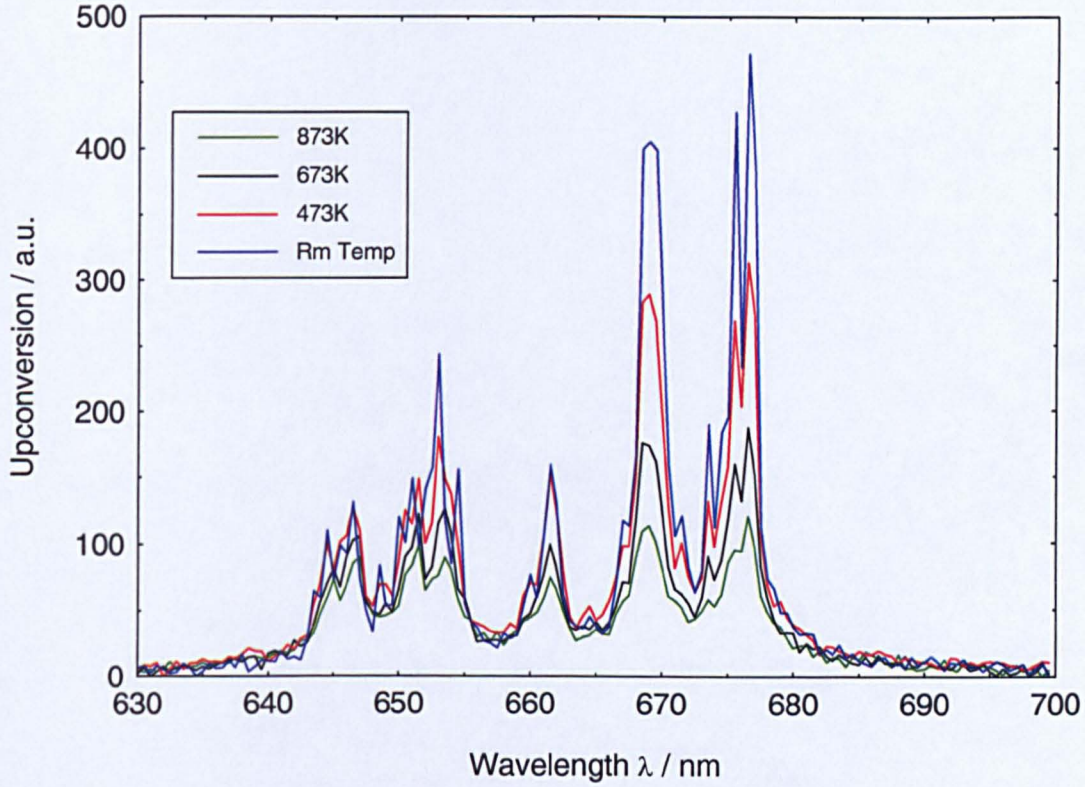

Figure 9.66: Spec YAl 32 $Y_3Al_5O_{12}:Er^{3+} + Yb^{3+}$ upconversion spectra from 873K to 1473K, $^4F_{9/2}$

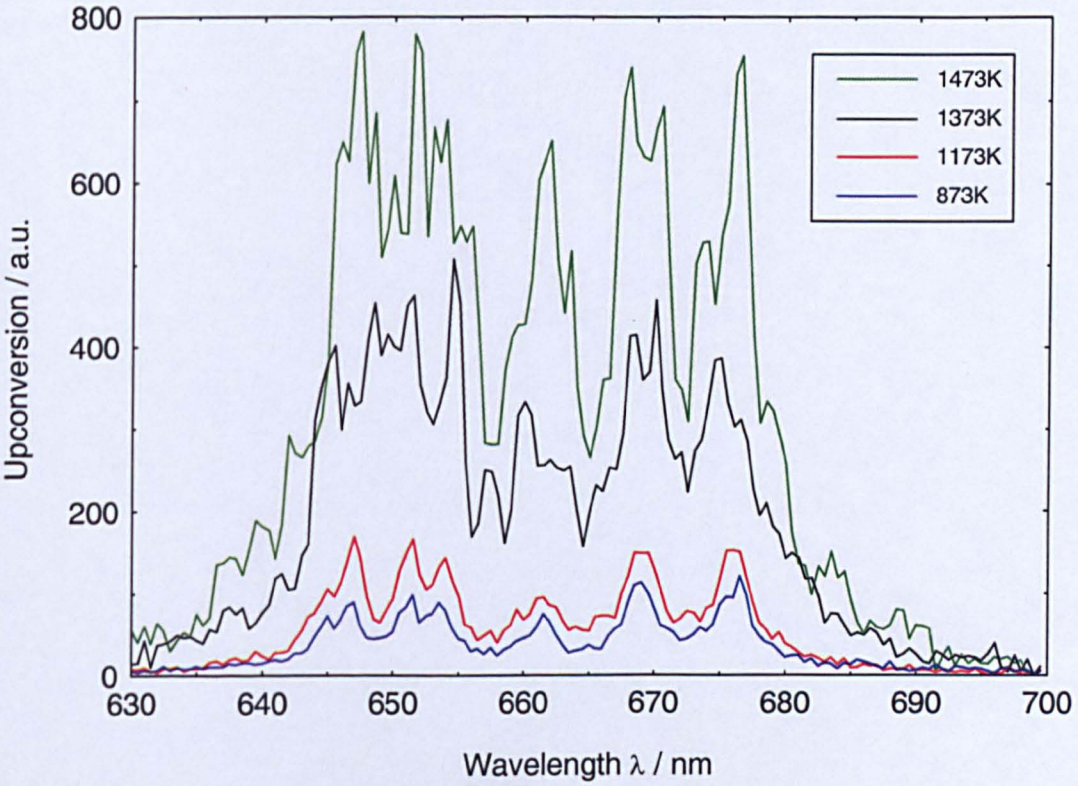

Table 9.5 – Spec YAl 26:$Y_3Al_5O_{12}$:Er^{3+} + Yb^{3+} temperature sensor UIR denotations

Denotations	Visible lines
UIR_{12}^{32}	$I_{541}/I_{553.5}$
UIR_{13}^{32}	I_{541}/I_{560}
UIR_{23}^{32}	$I_{553.5}/I_{560}$

Figure 9.67: Spec YAl 32 $Y_3Al_5O_{12}:Er^{3+} + Yb^{3+}$ - Integrated intensity at $^2H_{11/2}$, $^4S_{3/2}$ and $^4F_{9/2}$

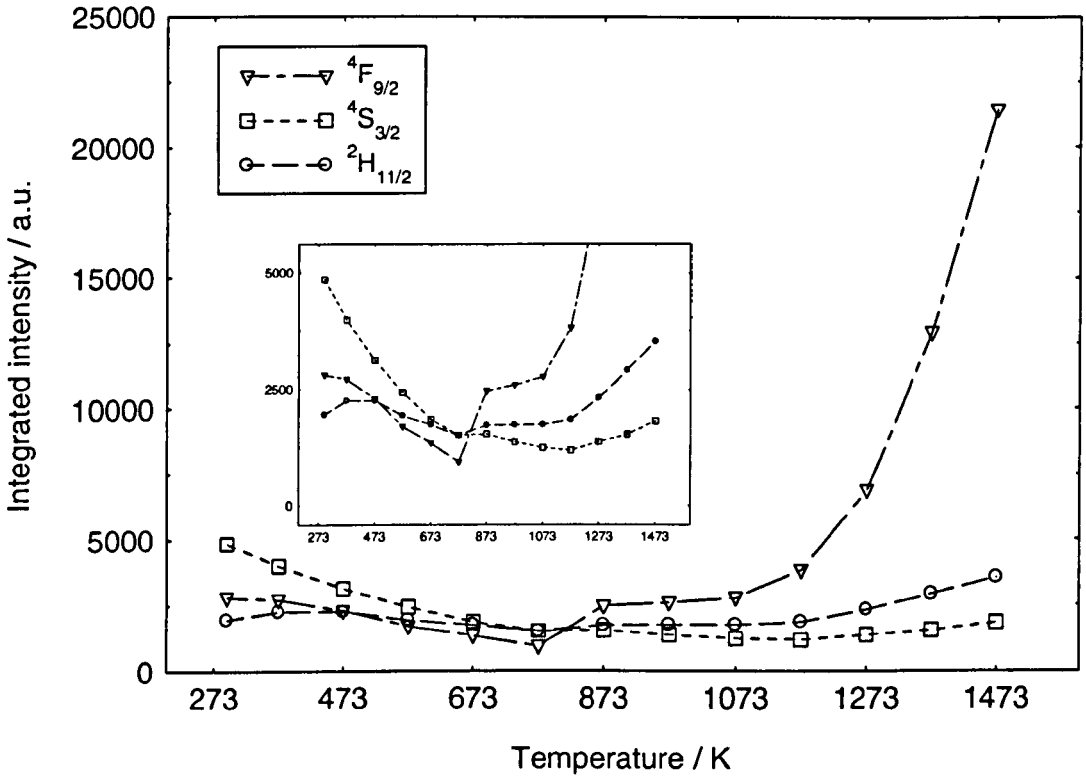

Figure 9.68a: Spec YAl 32 $Y_3Al_5O_{12}:Er^{3+} + Yb^{3+}$ intensity based sensing at 541nm (I_{541})

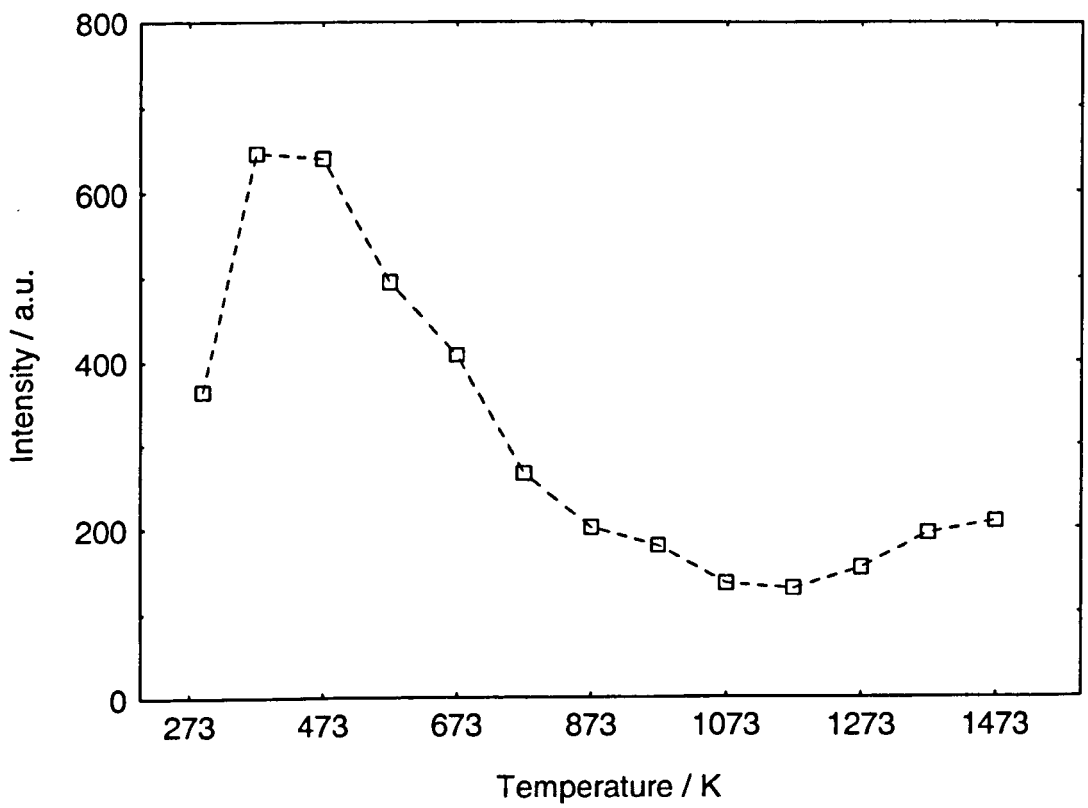

Figure 9.68b: Spec YAl 32 $Y_3Al_5O_{12}:Er^{3+} + Yb^{3+}$ intensity based sensing at 553.5nm & 560nm ($I_{553.5}$ & I_{560})

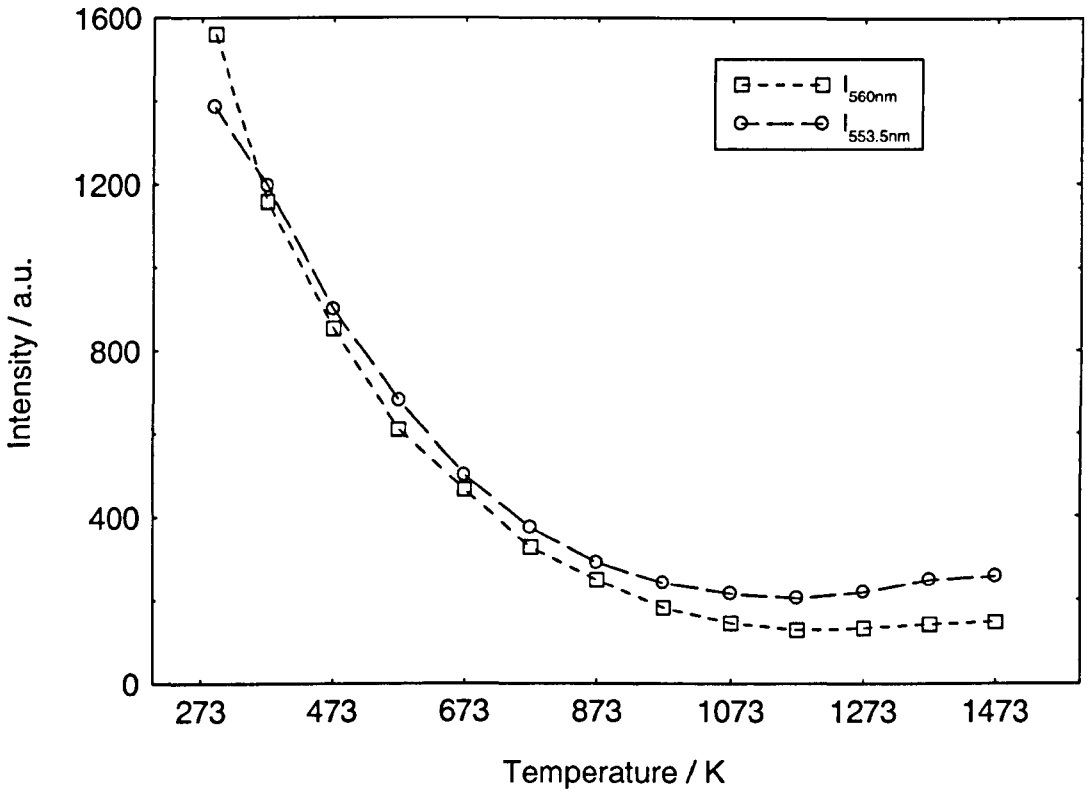

Figure 9.69: Spec YAl 32 $Y_3Al_5O_{12}:Er^{3+} + Yb^{3+}$ intensity based sensing at 676nm (I_{676})

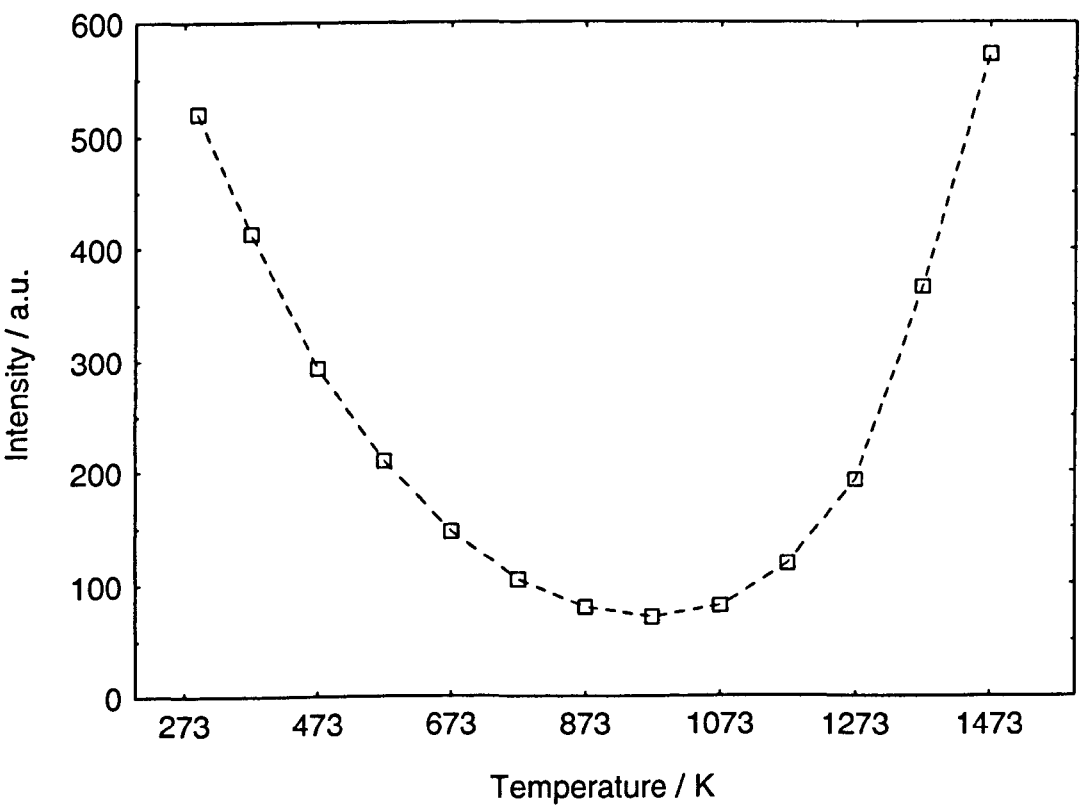

Figure 9.70: Spec YAl 32 $Y_3Al_5O_{12}:Er^{3+} + Yb^{3+}$ UIR_{12}^{32} & UIR_{13}^{32} (actual and polynomial fit) vs temperature

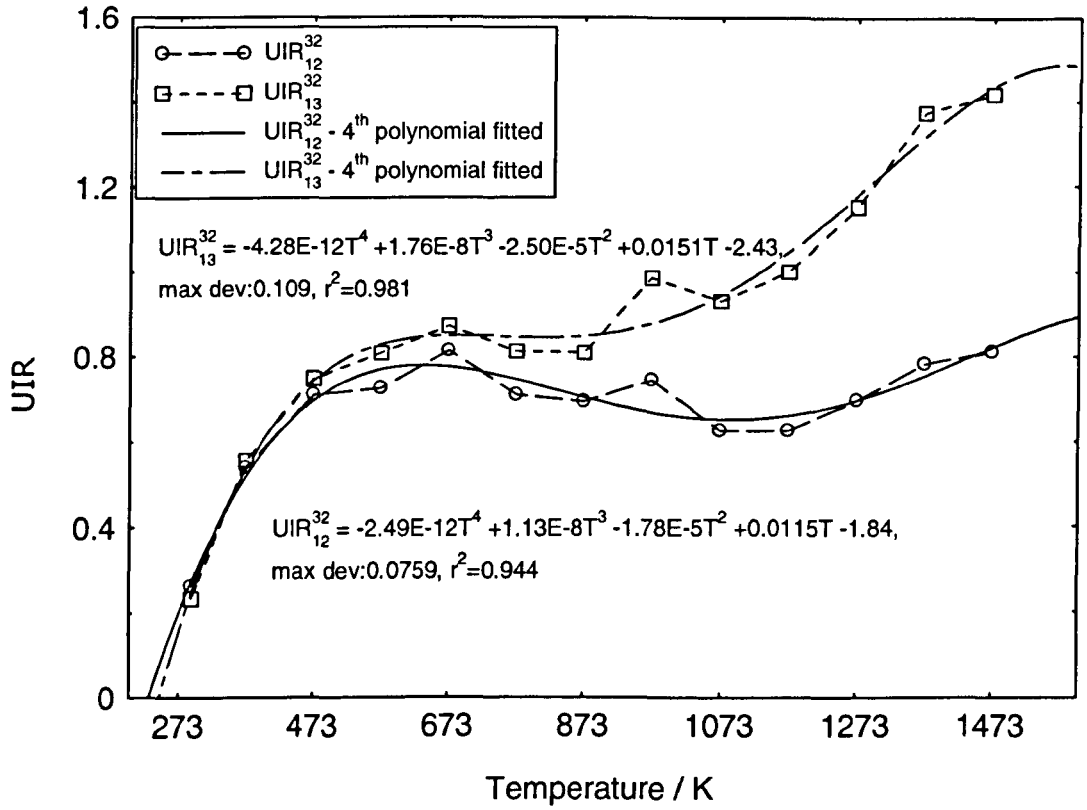

Figure 9.71: Spec YAl 32 $Y_3Al_5O_{12}:Er^{3+} + Yb^{3+}$ UIR_{23}^{32} (actual and fitted with Eq 9.7) vs temperature

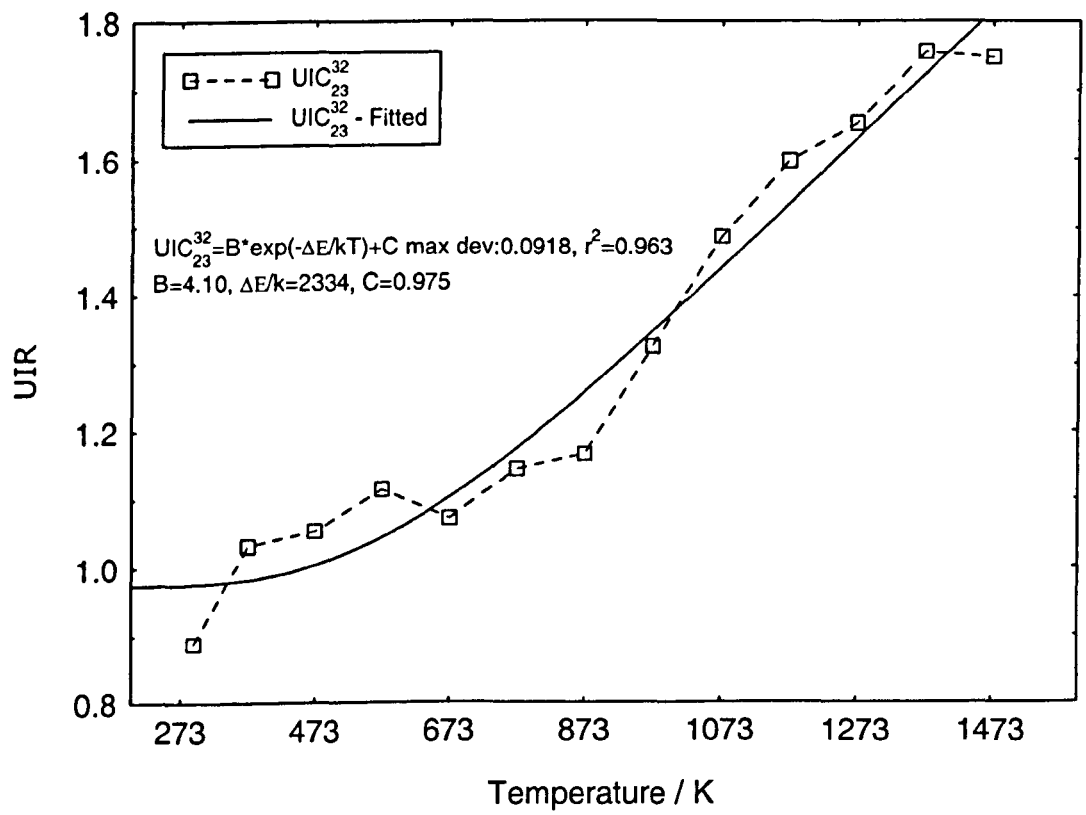

Figure 9.72: Spec YAl 32 $Y_3Al_5O_{12}:Er^{3+} + Yb^{3+}$ UIR^{32}_{AB} (actual and fitted with Eq 9.7) vs temperature

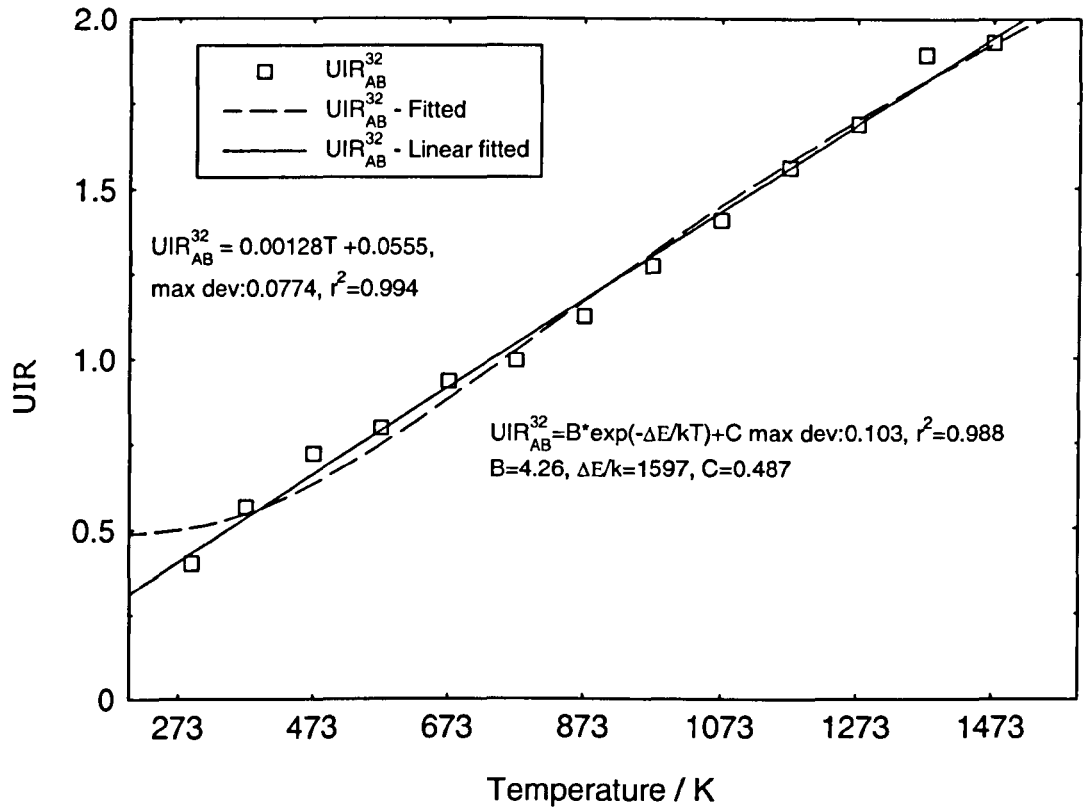

Figure 9.73: Spec YAl 32 $Y_3Al_5O_{12}:Er^{3+} + Yb^{3+}$ UIR^{32}_{ABC} (actual and fitted with Eq 9.7) vs temperature

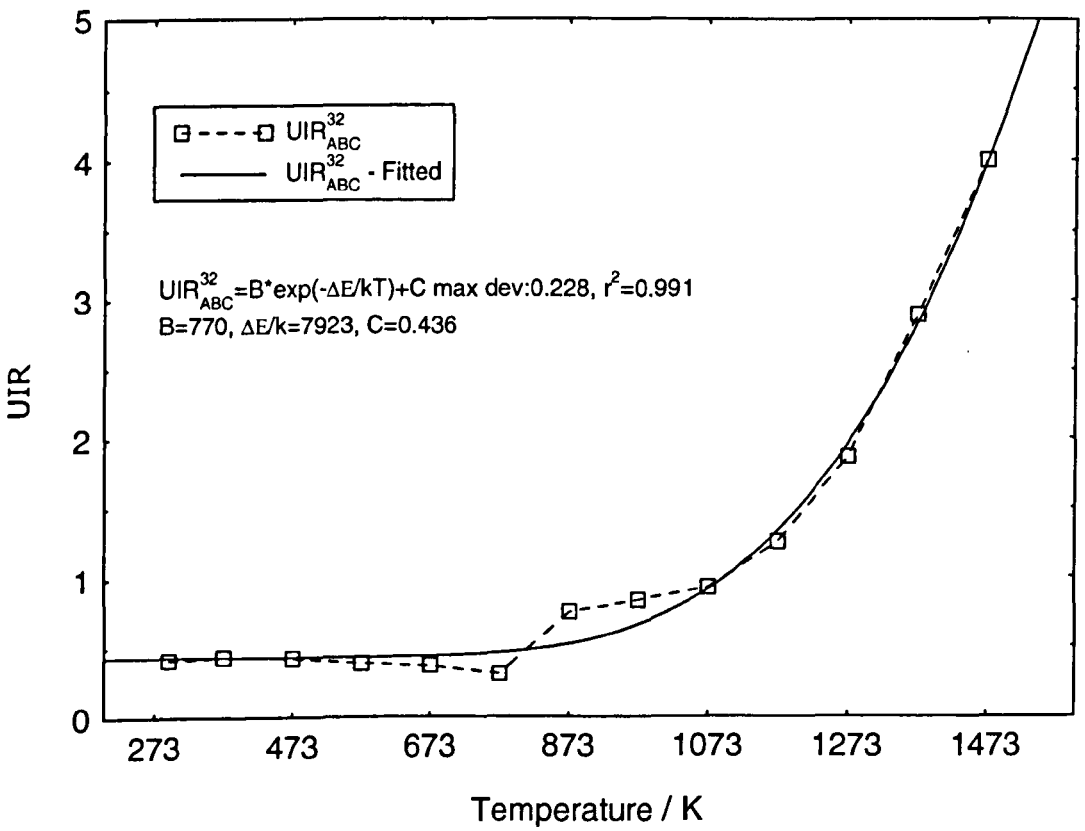

9.7.3 Fluorescence Decay Sensing – $Y_3Al_5O_{12}:Er^{3+}+Yb^{3+}$

The previous section 9.7.2 has demonstrated the increased efficiency in the red emission region when Yb^{3+} was added as a sensitizer. Work reported by *Sun* [3.38] shows that Yb^{3+} not only enhances the optical excitation of the 960nm region but also changes the thermal characterises at high temperatures and reduces the drift in lifetime due to annealing. In this work, investigation was made on YAG:Er^{3+} + Yb^{3+} fibre's FD as a function of temperature. The thermal range for this work was from 273K to 1473K. FD at individual IR lines at the transitions $^4I_{13/2}\rightarrow{}^4I_{15/2}$ and $^4F_{5/2}\rightarrow{}^4F_{7/2}$ were recorded at different temperatures.

9.7.3.1 Results and Discussion

All lifetimes recorded in this experiment displayed a single exponential decay curve. Examples of some of the curves are shown in Appendix B. When Yb^{3+} was added as a co-doped ion in YAG, an additional IR line was observed at 1027nm. The recorded FD as a function of temperature is shown in Figure 9.74. At room temperature it has a decay of ~0.95ms. This was the only line investigated that exhibited an increase in τ with increasing temperature. This work presented, was in agreement with the report by *Kennedy* [6.4], which showed that in Yb^{3+} doped YAG the τ values increases with rising temperature. From the Figure 9.74, it is observed that errors could be as high as ~21%. Although there is an increase in τ, this increase was not progressive but staggered. The lifetime difference between 293K and 1473K was ~220μs which was very small making it very difficult to be employed as a temperature sensor. Figures 9.45 to 82 show the FD of the emissions lines at transitions $^4I_{13/2}\rightarrow{}^4I_{15/2}$. It is seen in these figures that increment of temperature brings about a decrease of lifetime. Under the influence of temperature, the Er^{3+} ion experienced thermal quenching that resulted in the decrease in fluorescence lifetime which was evident throughout all the IR emission lines [3.28]. All profiles showed a common linear trend and the maximum error for these plots was ~4%. Linear fits were made to each plot at this transition. Again there is no physical significance for these fitted lines but they merely demonstrate the best fit for the results acquired. FD at 1612nm showed a sensitivity of 1.17μs/K which is calculated from the slope of the fitted line, see Figure 9.79. Analysis of these plots also revealed that at approximately 1173K the

decrease in τ was a little more rapid as compared to the lower temperature region. The slower decrease in the τ, at the lower temperature region, as mentioned in reference [3.28] could be possibly due to phonon-induced transitions from higher energy levels.

The average lifetime at room temperature for the transition $^4I_{13/2}$ was ~6.9ms. When referred to the work in Chapter 6, this τ value, indicates that the dopant concentration in this fibre is approximately 1mol% Er^{3+}. This approximation is close to that when using the FIR method mentioned in section 9.4. Figure 9.83 shows that there is consistency in the decay at different wavelengths and clearly illustrates the decrease of lifetime with increasing temperature. However, the maximum difference in τ from 273K to 1273K is ~1.2ms; larger than the singly doped fibre but smaller than Er^{3+} doped in silica [3.28]. Similar to the work reported by *Sun* [3.38], Yb^{3+} does change the thermal characteristics especially in the higher temperature region which can be seen from the plots studied in this work.

Figure 9.74: Spec YAl 32 $Y_3Al_5O_{12}:Er^{3+} + Yb^{3+}$ fluorescence decay at 1027nm

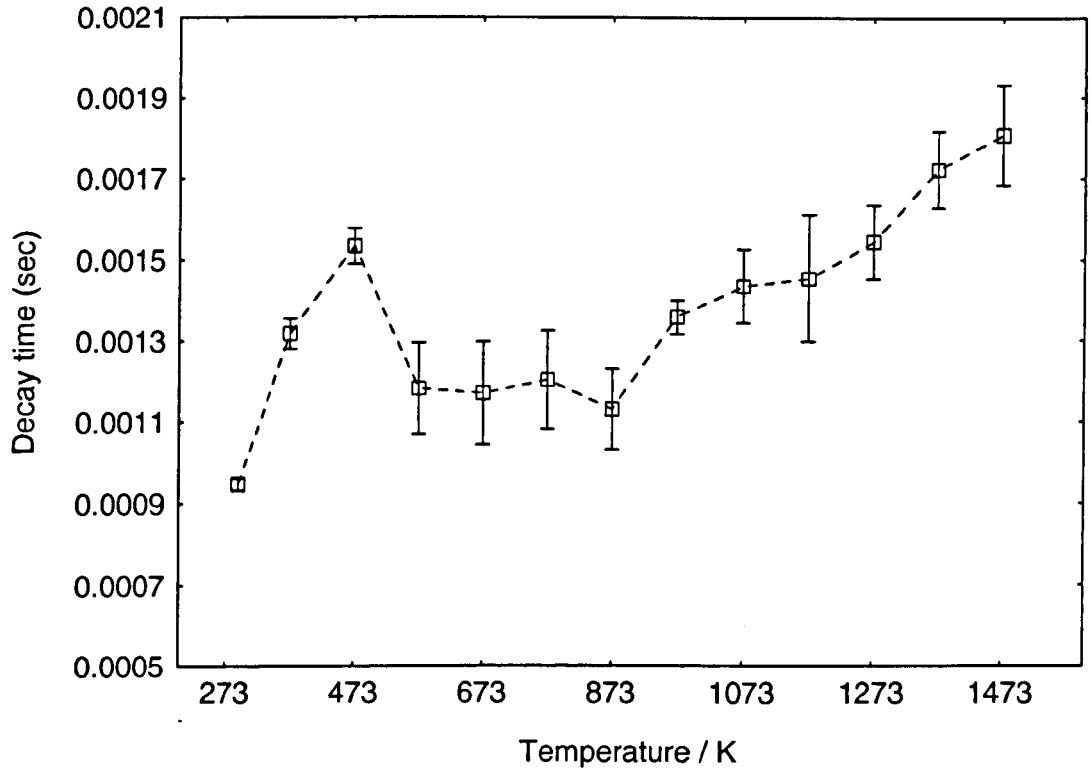

Figure 9.75: Spec YAl 32 $Y_3Al_5O_{12}:Er^{3+} + Yb^{3+}$ fluorescence decay at 1453nm

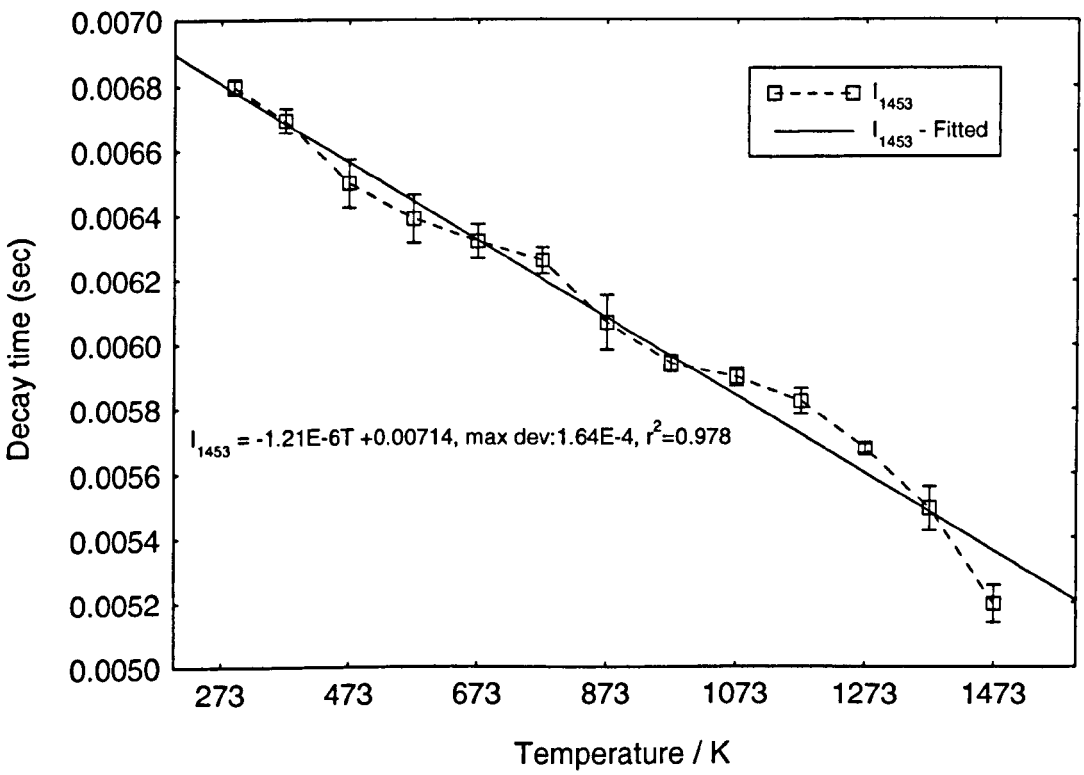

Figure 9.76: Spec YAl 32 $Y_3Al_5O_{12}:Er^{3+} + Yb^{3+}$ fluorescence decay at 1470nm

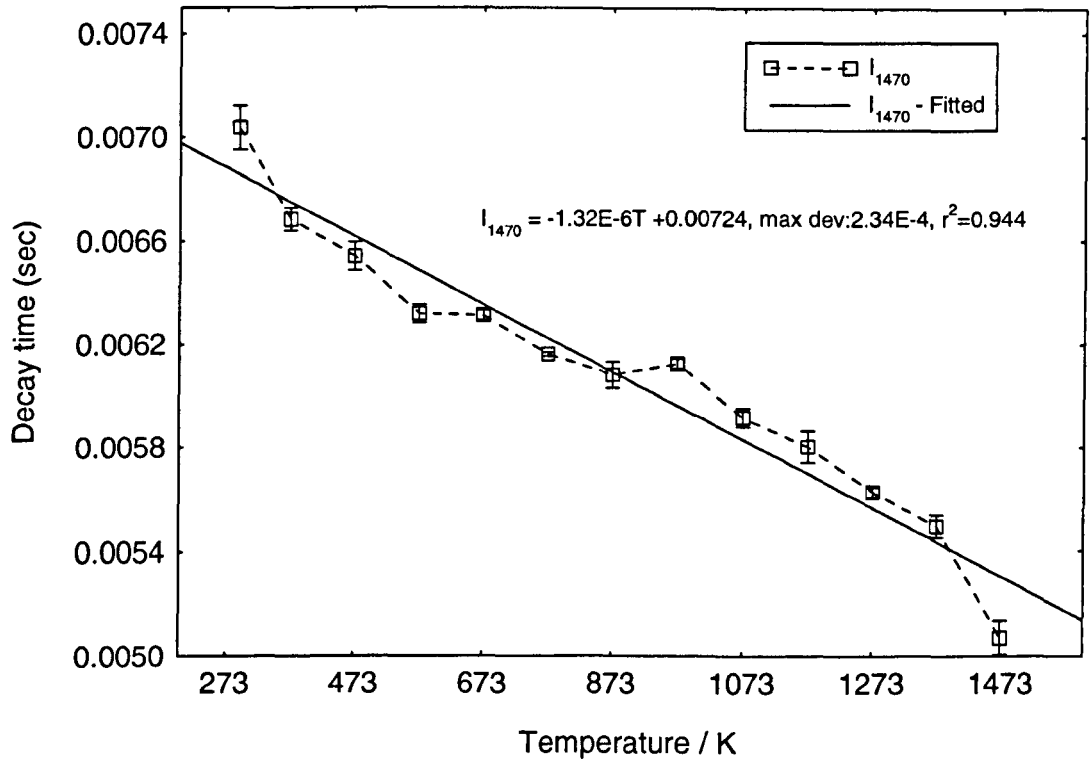

Figure 9.77: Spec YAl 32 $Y_3Al_5O_{12}:Er^{3+} + Yb^{3+}$ fluorescence decay at 1528.5nm

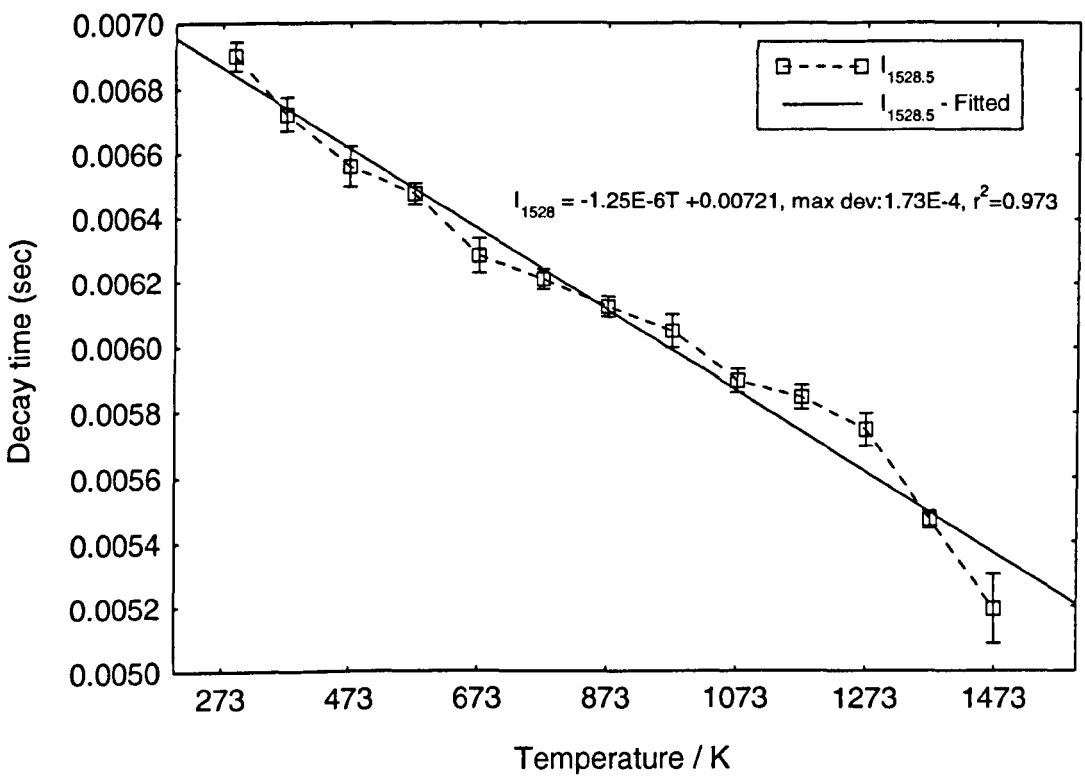

Figure 9.78: Spec YAl 32 $Y_3Al_5O_{12}:Er^{3+} + Yb^{3+}$ fluorescence decay at 1568nm

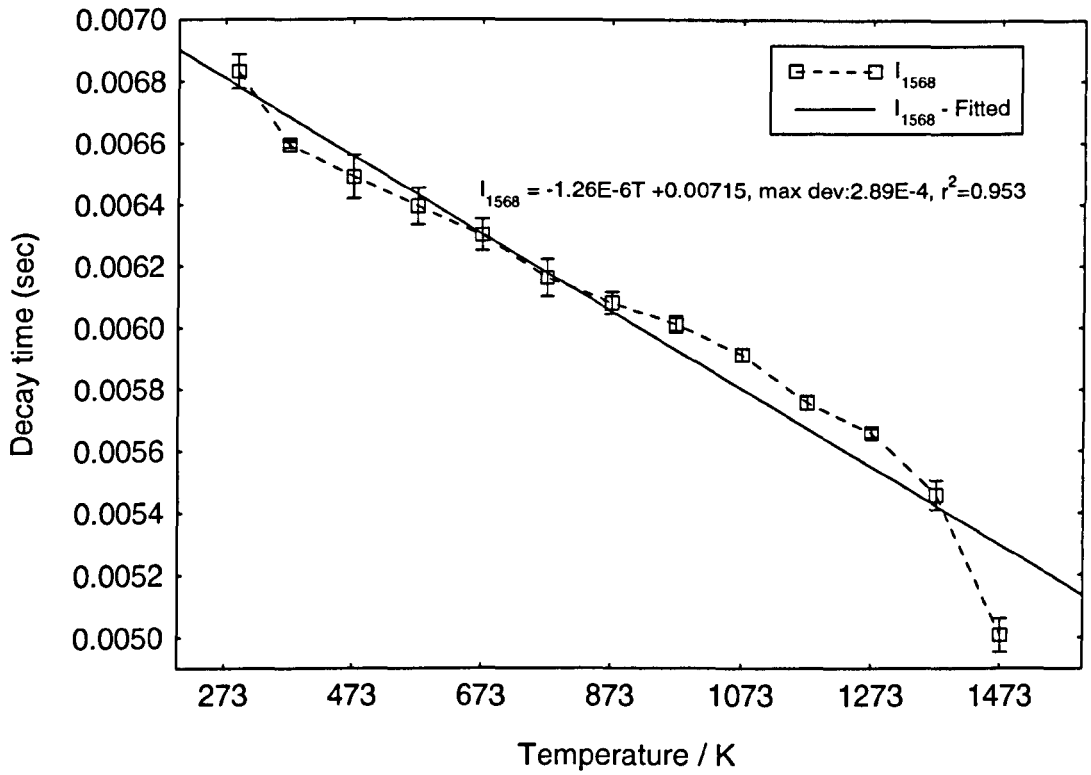

Figure 9.79: Spec YAl 32 $Y_3Al_5O_{12}:Er^{3+} + Yb^{3+}$ fluorescence decay at 1612nm

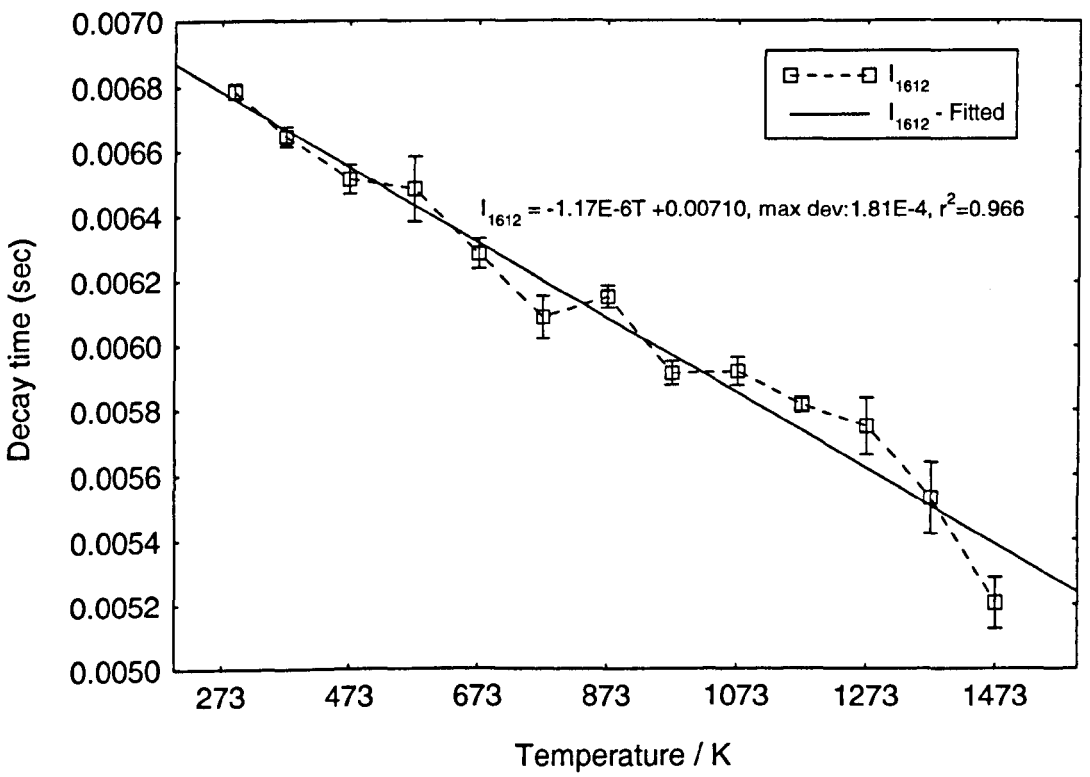

Figure 9.80: Spec YAl 32 $Y_3Al_5O_{12}:Er^{3+} + Yb^{3+}$ fluorescence decay at 1628.5nm

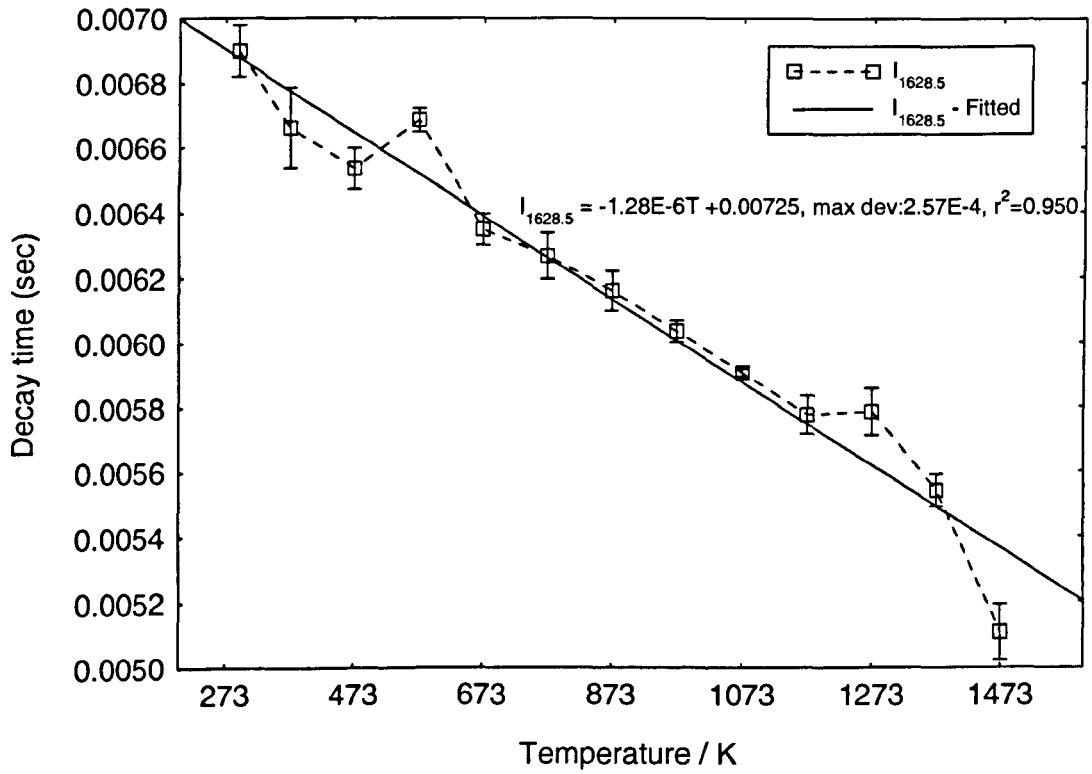

Figure 9.81: Spec YAl 32 $Y_3Al_5O_{12}:Er^{3+} + Yb^{3+}$ fluorescence decay at 1640.5nm

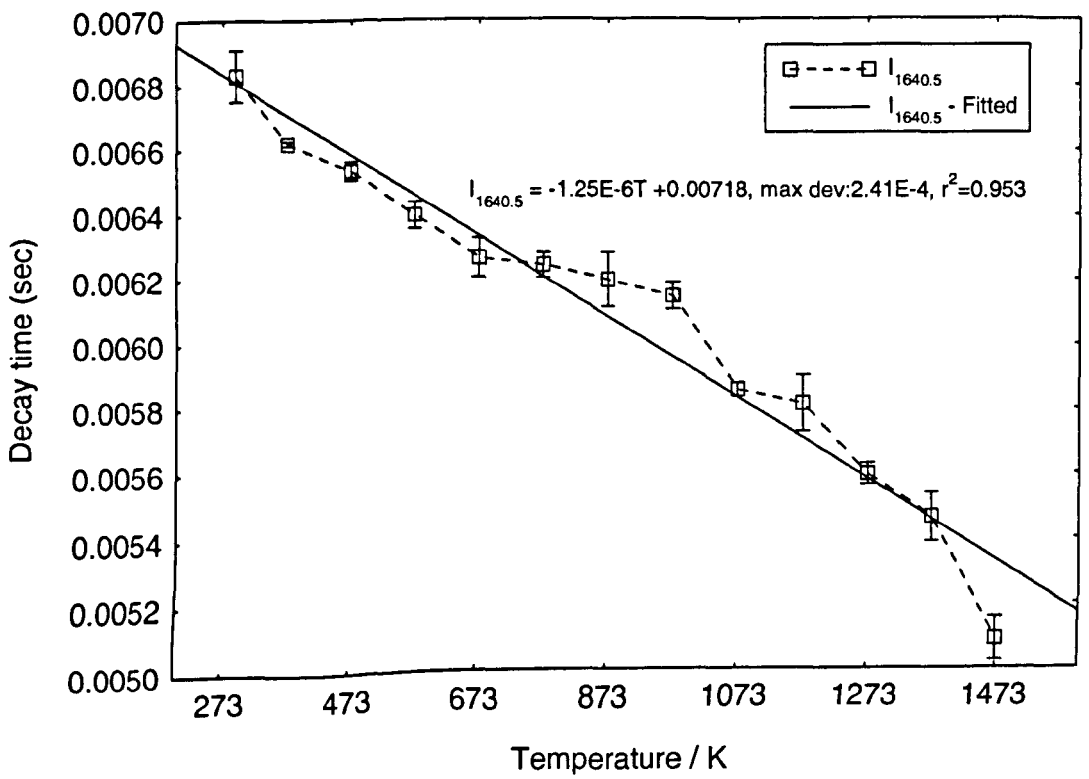

Figure 9.82: Spec YAl 32 $Y_3Al_5O_{12}:Er^{3+} + Yb^{3+}$ fluorescence decay at 1652.5nm

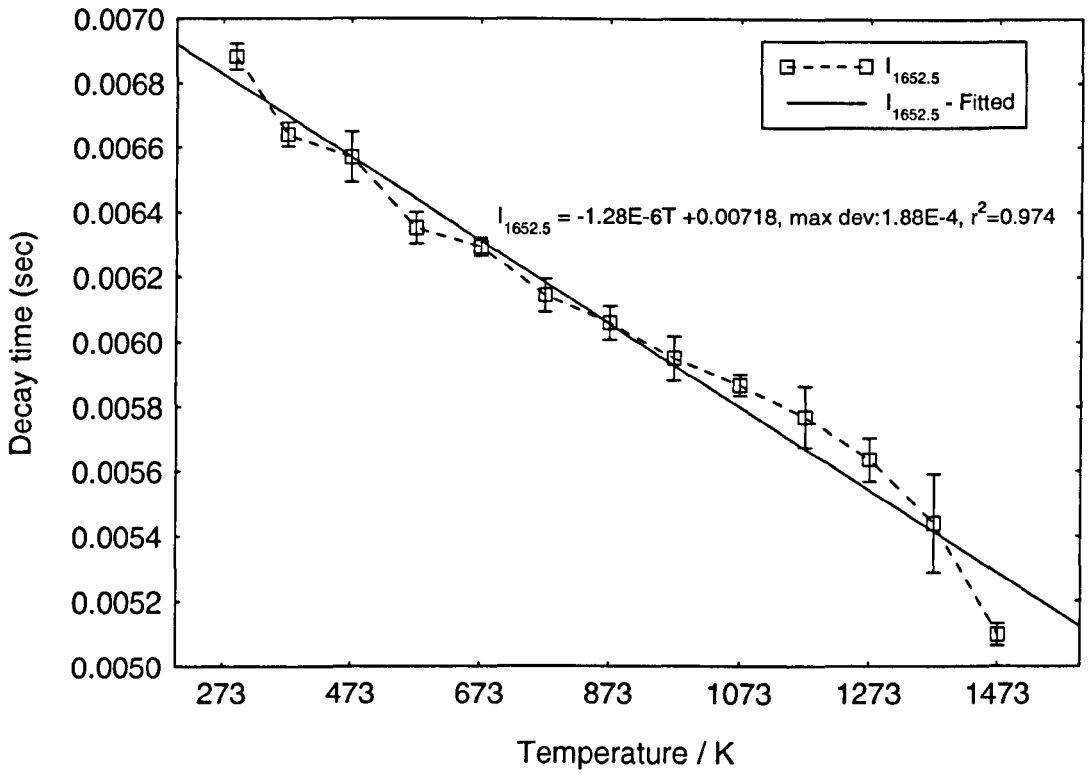

Figure 9.83: Spec YAl 32 $Y_3Al_5O_{12}:Er^{3+} + Yb^{3+}$ fluorescence decay of different temperatures at varies wavelengths

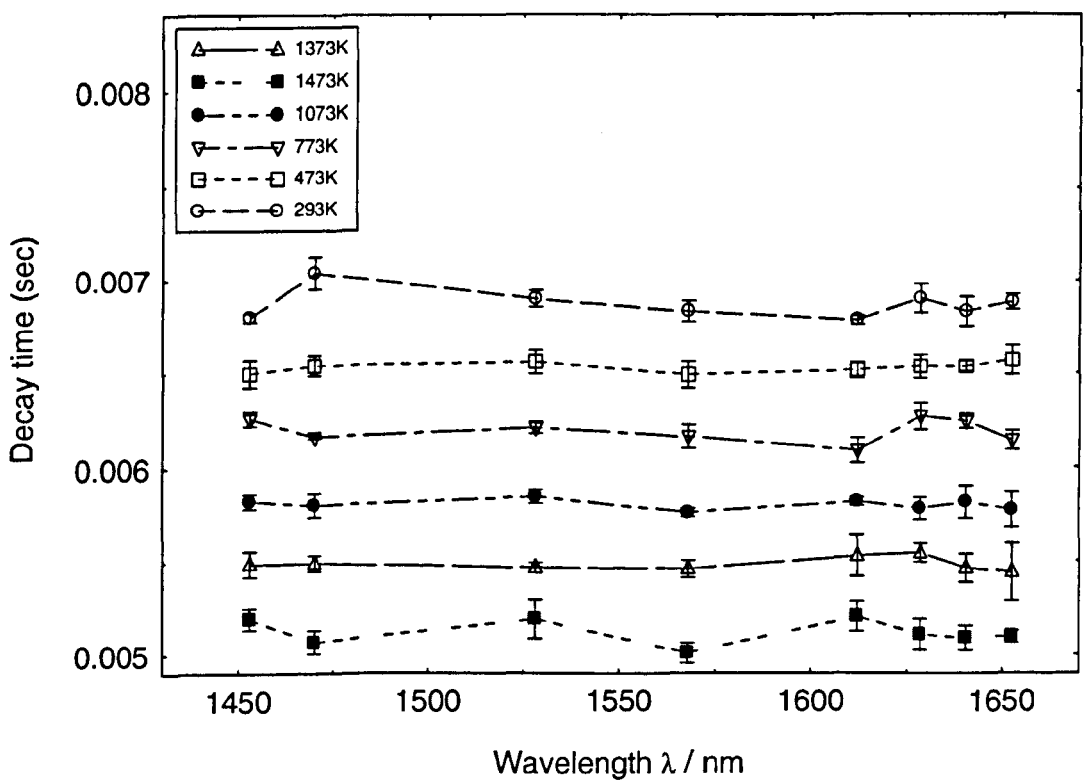

9.8 $Y_2O_3:Er^{3+}$ - Temperature Sensor

Investigations were carried on using $Y_2O_3:Er^{3+}$ SCF for application as temperature sensors. Methods like FIR, UIR and FD were used to determine the temperature changes. All results are presented in this section. The interest of this work was to investigate the response of rare earth in Y_2O_3 SCF under the influence of temperature and the condition of the host during and after the temperature cycle.

9.8.1 Fluorescence Intensity Based Sensing - $Y_2O_3:Er^{3+}$

Y_2O_3 – stabilized ZrO_2 was reported by *Tong* [2.56] as a promising sensing material due to the high melting point at ~3000K. Work by *Allision* [9.53] examined the used of ceramic phosphors doped with rare earth, for example $Y_2O_3:Eu^{3+}$, as remote thermometers. Ceramic based Y_2O_3 is a common host used in thermometry applications. The advantage is its effective working temperature ranges from cryogenic temperatures to ~2200K. In this work, $Y_2O_3:Er^{3+}$ SCF fibres are used as fluorescence based temperature sensors. Fluorescence emissions were observed at transitions $^4I_{11/2}$ and $^4I_{13/2}$. Two IR lines from the former and seven IR lines from the latter transitions were monitored during the temperature sensing experiment in order to determine the fluorescence intensity ratio as a function of temperature. Figures 9.84 and 85 show the fluorescence at room temperature and the IR lines used for the FIR experiments.

9.8.1.1 Results and Discussion

A general overview of the fluorescence spectra with respect to temperature is shown in Figure 9.86. It is observed that the fluorescence intensity at emission $^4I_{11/2}$ (Region A – 1000 to 1100nm) decreases as the temperature increases. Although the signal-to-noise ratio decreases with increasing temperature the two peaks observed remained noticeable at 1473K, see Figures 9.87 and 88. This phenomenon is similar to that seen in $Y_3Al_5O_{12}:Er^{3+}+Yb^{3+}$, discussed in section 9.7. Figures 9.89 and 90 show the fluorescence spectra from transition $^4I_{13/2}$ at different temperature. The fluorescence spectrum at this transition is divided into three regions, B (1400 to 1500nm), C (1500 to 1600nm) and D (1600 to 1700nm). One common observation throughout these

regions is that the fluorescence spectra intensities increase with rising temperature. This continued on until the temperature reached ~1273K, where the intensity begins to decrease. This decrease could be possibly associated with fluorescence quenching and chemical/material changes under the influence of high temperature [9.38]. The peak at wavelength ~1528nm remained the strongest even at this temperature. The changes in the intensities within different regions are clearly illustrated in Figure 9.91. The transition $^4I_{13/2} \rightarrow {}^4I_{15/2}$ generally experiences an increase as temperature increases and Region C has the steepest slope indicating that this region experienced the largest increase. In the transition $^4I_{11/2} \rightarrow {}^4I_{15/2}$, Region A, decreases as temperature rises and levels out at ~873K. The integrated intensity for each region presented in this figure are derived from using EASYPLOT software package. By monitoring these regions, the temperature within an environment could be determined.

When the Y_2O_3:Er^{3+} SCFs were excited with the 965nm laser diode, several IR lines within the fluorescence emission at the transitions $^4I_{11/2}$ and $^4I_{13/2}$ were selected to be used in the FIR method. To determine the FIRs, the intensities of each of the IR lines were recorded using LABVIEW software package and were then transported to EASYPLOT. Tables 9.6 and 7 show the denotation of the IR lines employed in the Y_2O_3:Er^{3+} SCF temperature sensor when using the FIR method. For transitions in the $^4I_{11/2}$ manifold peak intensities at 1010nm and 1028.5nm were used as the numerator ratio calculation, see Figures 9.92a to c and 9.93a to b. Negative ΔE was observed, (see Figures 9.92e, 92f, 93c and 93d), although it is possible to use these ratios for temperature sensing but perhaps not recommended. Further work would be required to investigate the occurrence of the negative value for ΔE. From the graphs only FIR_{12}^{64} increase as the temperature increases. Fitted with equation 9.7, the curve increases progressively with an effective maximum temperature of 1473K. The theoretical and calculated values of ΔE were 178.9cm^{-1} and 346.08cm^{-1} respectively, see Figure 9.92d. The remaining plots were in the form of exponential decay curves which were only sensitive up to ~1073K.

In the emission $^4I_{13/2}$ numerous FIR curves are possible candidates for use in thermometry applications. A large majority of these curves increase with rising temperature. Figures 9.94a to 99 clearly illustrated the intensity ratio as a function of temperature. The 1500nmn region exhibited the highest intensity ratio change

whereas the 1600nm region showed the lowest. In the 1400 region, FIR_{39}^{64} exhibited a relatively large intensity ratio change moreover when fitted with the model equation, it has an effective working temperature range starting at ~573K. This curve has a ΔE of 1649cm^{-1} (fitted) and 755cm^{-1} (theoretical). The large difference between the two could be due to the equation that was adopted for this work which is commonly used for silica based fibres. Figures 9.95a to 96d illustrate the case where peak intensities at 1530.5nm and 1550nm used as the numerators for FIR. These curves exhibited a large change in intensity ratio, however, the effective working temperature only starts at ~1073K. For the peak at 1572nm, FIR_{67}^{64} to FIR_{69}^{64} , a larger effective temperature range is seen which starts at 573K but with a small change in of FIR. The small and erratic changes in FIR_{78}^{64}, FIR_{79}^{64} and FIR_{89}^{64} make them unsuitable for use in thermometry.

The FIR as a function of temperature can also be calculated using the ratio of the peak at higher energy to peak at lower energies. Figure 9.100a shows curves when Region A was chosen as N_2 and Region B N_1 in equation 9.7. FIR_{AB}^{64} and FIR_{AD}^{64} from this figure shows a larger intensity ratio change at the lower temperature region but at higher temperatures. Only FIR_{CD}^{64} in Figure 9.100b responded well to temperature while FIR_{BC}^{64} and FIR_{BD}^{64} were less sensitive to temperature. Fitted curves using equation 9.7 are seen in Figures 9.100c and d. Most of the FIRs discussed in this section can either be used at higher temperatures only or lower temperature regions.

Figure 9.84: Spec 64 Y_2O_3:Er^{3+} fluorescence in room temperature, 293K, $^2I_{11/2}$

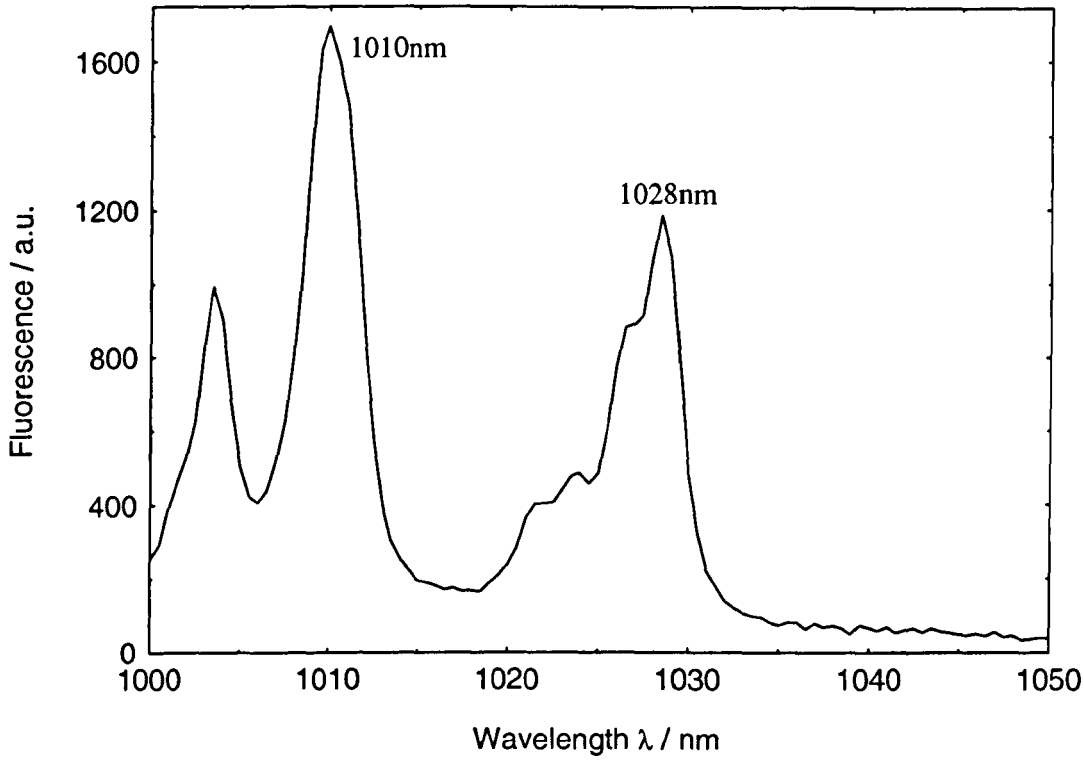

Figure 9.85: Spec 64 Y_2O_3:Er^{3+} fluorescence in room temperature, 293K, $^4I_{13/2}$

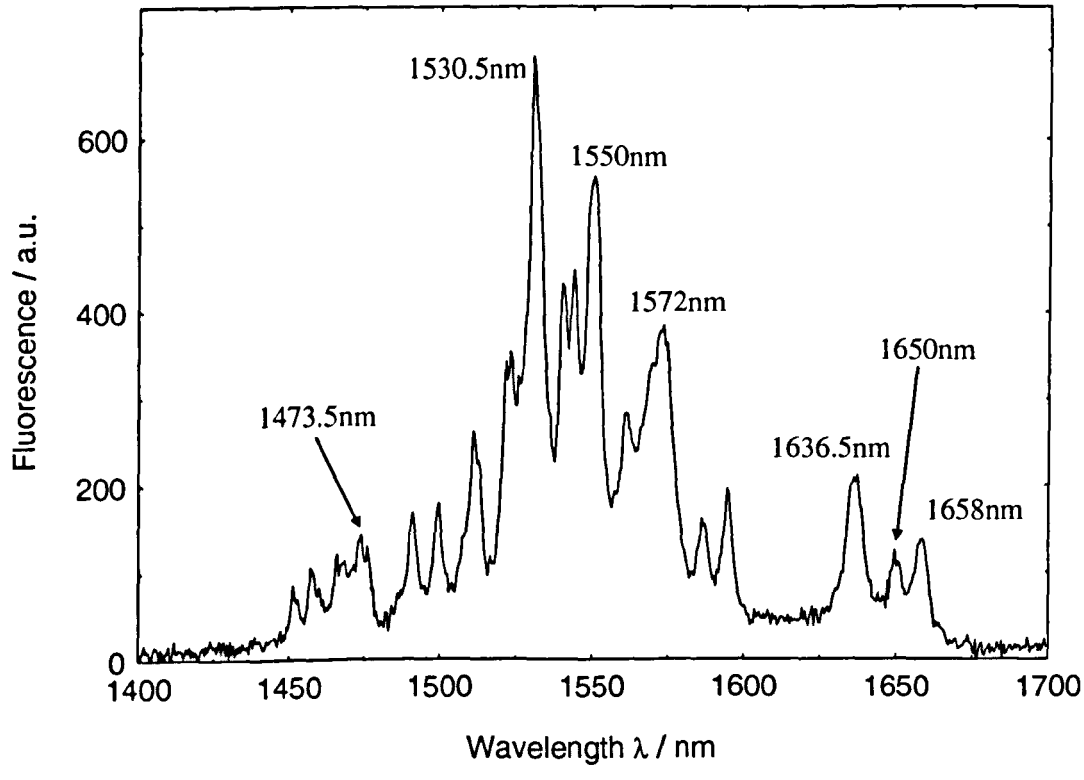

Figure 9.86: Spec 64 $Y_2O_3:Er^{3+}$ fluorescence spectra from room temperature to 1473K

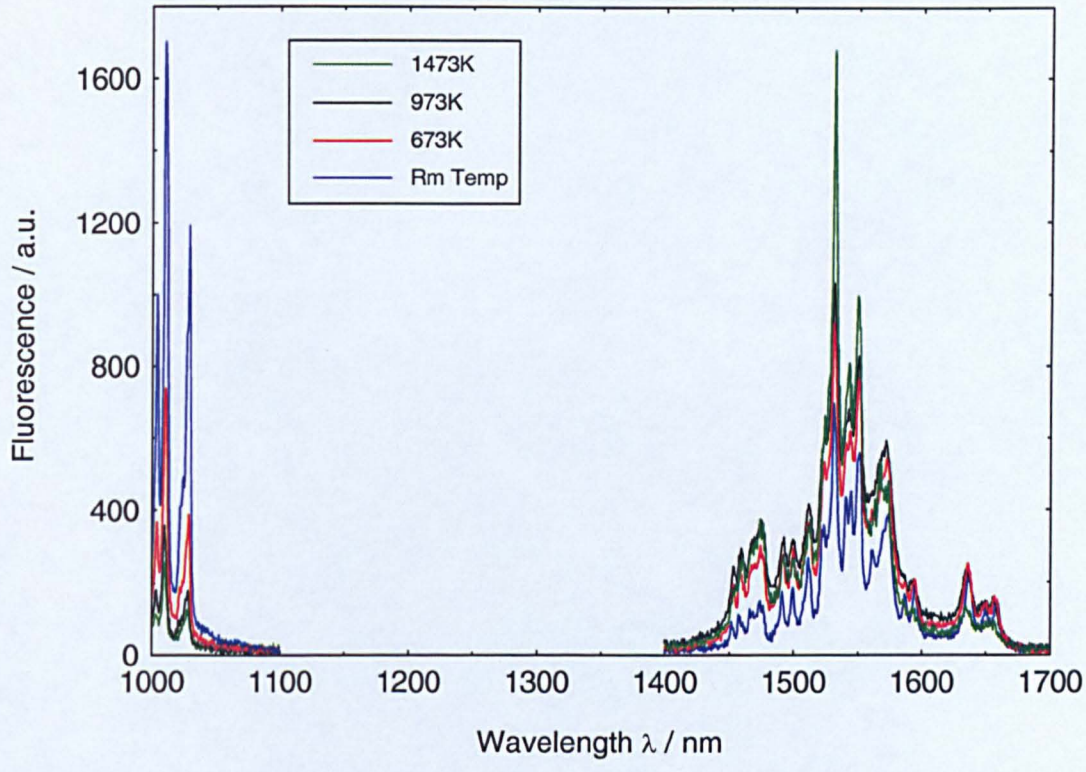

Figure 9.87: Spec 64 $Y_2O_3:Er^{3+}$ fluorescence spectra ($^4I_{11/2}$) – room temperature to 873K

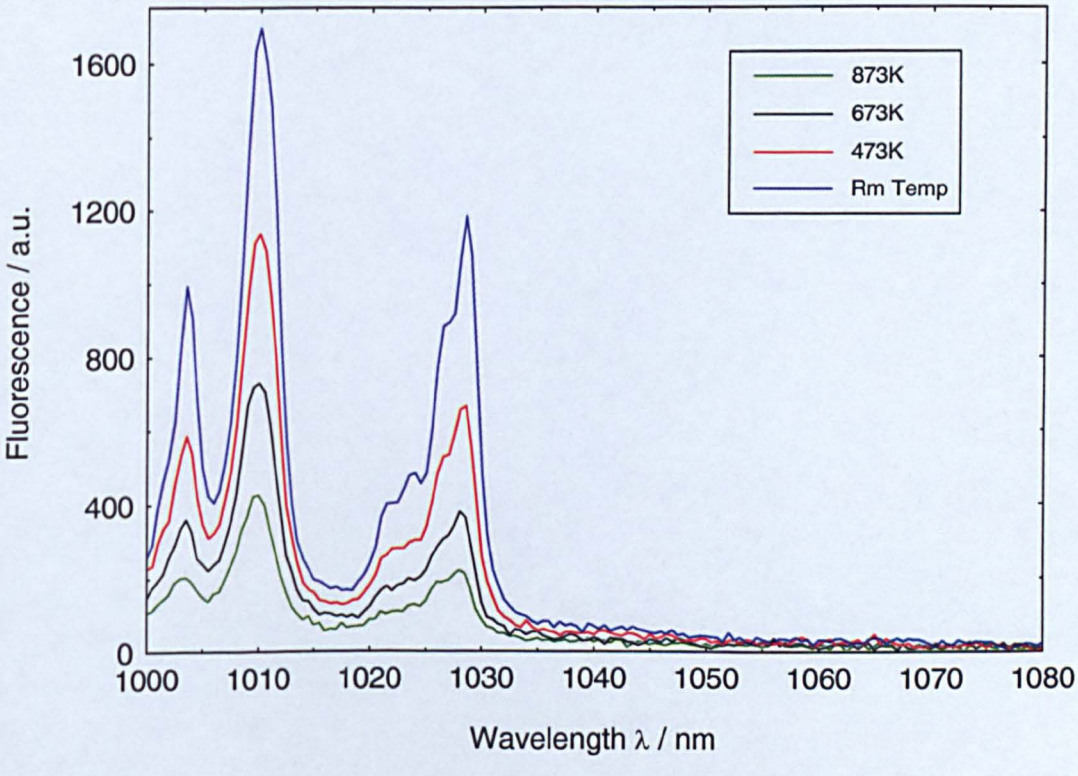

Figure 9.88: Spec 64 $Y_2O_3:Er^{3+}$ fluorescence spectra ($^4I_{11/2}$) – 873K to 1473K

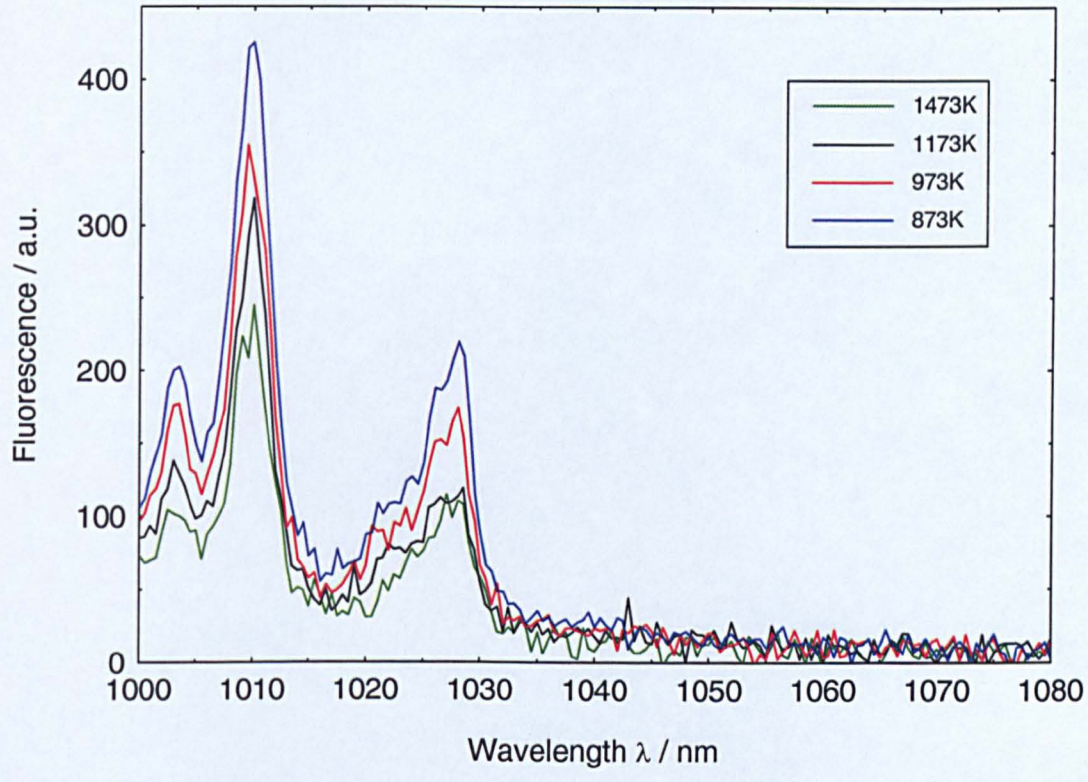

Figure 9.89: Spec 64 $Y_2O_3:Er^{3+}$ fluorescence spectra ($^4I_{13/2}$) – room temperature to 873K

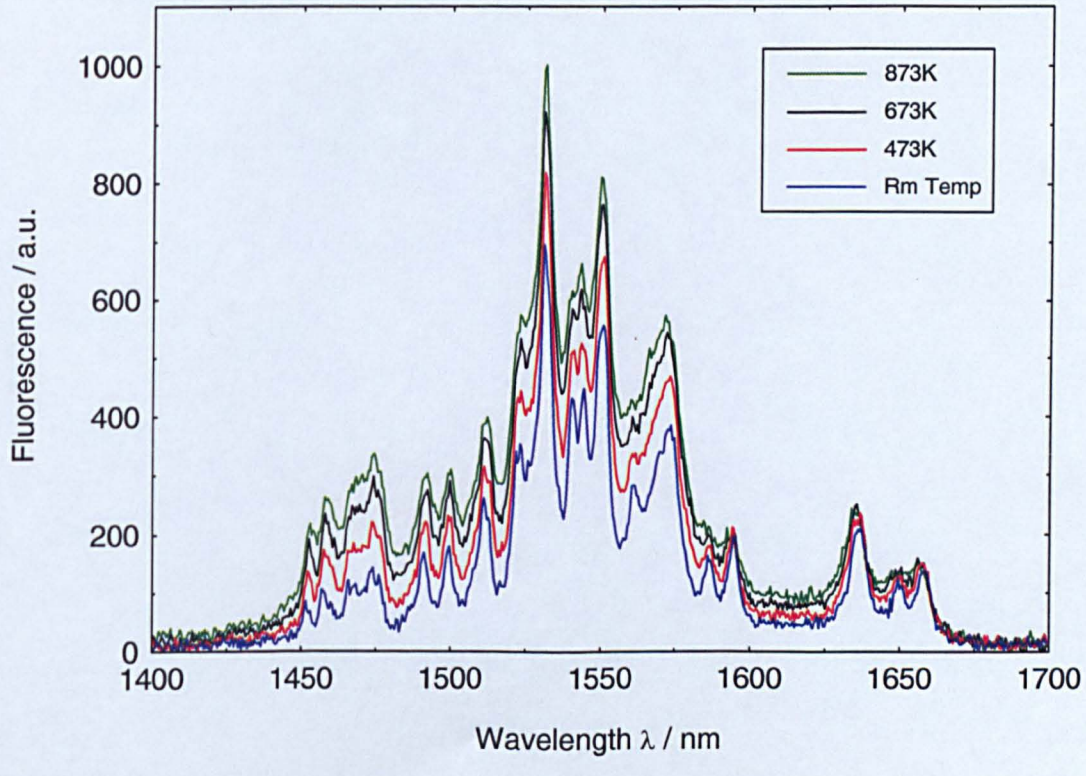

Figure 9.90: Spec 64 Y_2O_3:Er^{3+} fluorescence spectra ($^4I_{13/2}$) – 873K to 1473K

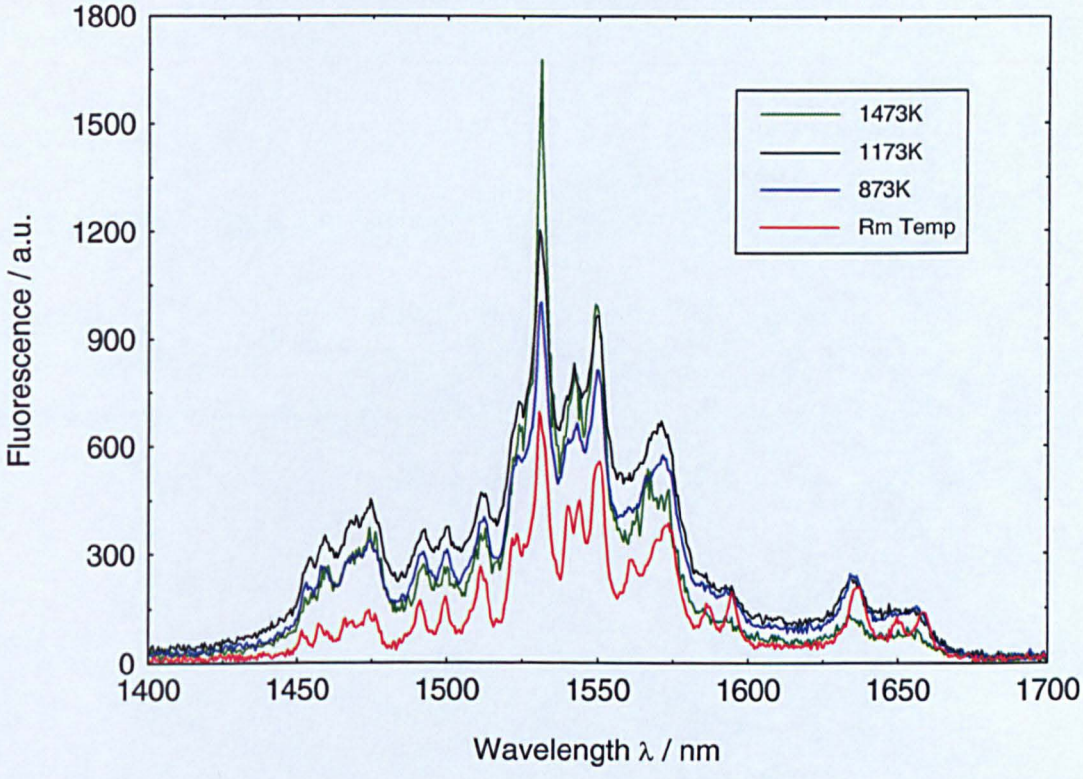

Figure 9.91: Spec 64 Y_2O_3:Er^{3+} fluorescence spectra – Integrated intensity

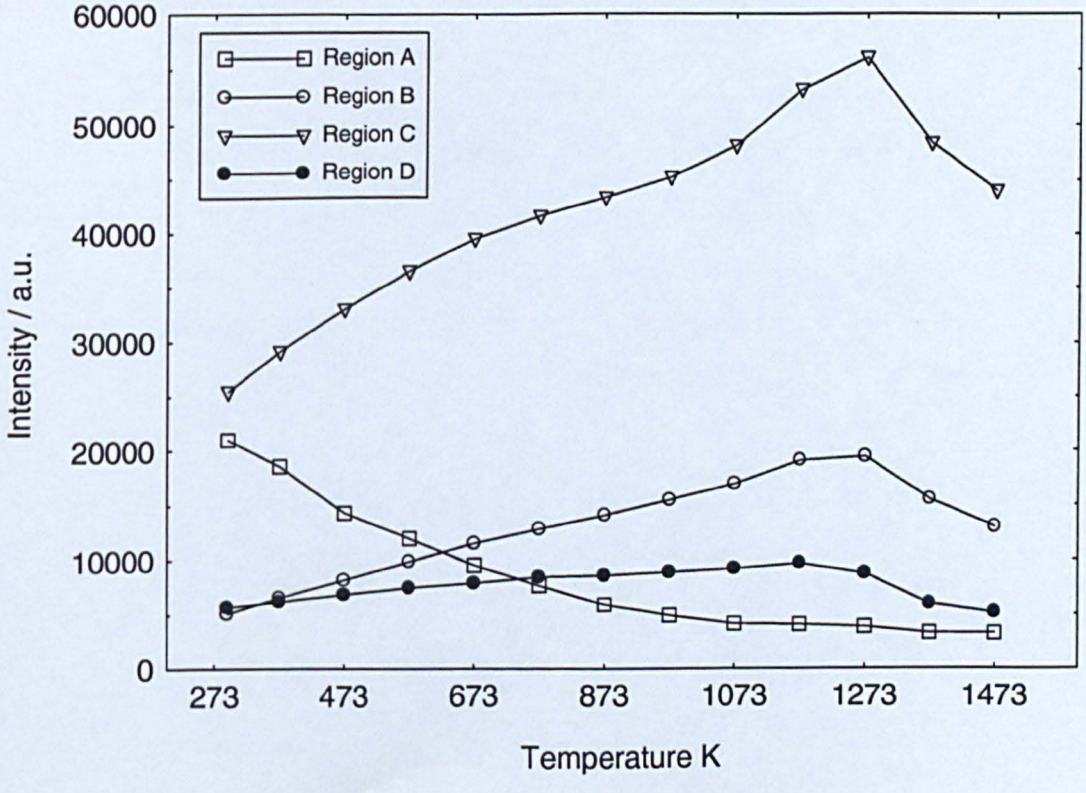

Table 9.6 – Spec 64 $Y_2O_3:Er^{3+}$ temperature sensor FIR denotations $^4I_{11/2}$

Denotation	IR lines	Denotation	IR lines
FIR_{12}^{64}	$I_{1010}/I_{1028.5}$	FIR_{23}^{64}	$I_{1028.5}/I_{1473.5}$
FIR_{13}^{64}	$I_{1010}/I_{1473.5}$	FIR_{24}^{64}	$I_{1028.5}/I_{1530.5}$
FIR_{14}^{64}	$I_{1010}/I_{1530.5}$	FIR_{25}^{64}	$I_{1028.5}/I_{1550}$
FIR_{15}^{64}	I_{1010}/I_{1550}	FIR_{26}^{64}	$I_{1028.5}/I_{1572}$
FIR_{16}^{64}	I_{1010}/I_{1572}	FIR_{27}^{64}	$I_{1028.5}/I_{1636.5}$
FIR_{17}^{64}	$I_{1010}/I_{1636.5}$	FIR_{28}^{64}	$I_{1028.5}/I_{1650}$
FIR_{18}^{64}	I_{1010}/I_{1650}	FIR_{29}^{64}	$I_{1028.5}/I_{1658}$
FIR_{19}^{64}	I_{1010}/I_{1658}		

Table 9.7 – Spec 64 Y_2O_3:Er^{3+} temperature sensor FIR denotations $^4I_{13/2}$

Denotation	IR lines	Denotation	IR lines
FIR_{34}^{64}	$I_{1473.5}/I_{1530.5}$	FIR_{56}^{64}	I_{1550}/I_{1572}
FIR_{35}^{64}	$I_{1473.5}/I_{1550}$	FIR_{57}^{64}	$I_{1550}/I_{1636.5}$
FIR_{36}^{64}	$I_{1473.5}/I_{1572}$	FIR_{58}^{64}	I_{1550}/I_{1650}
FIR_{37}^{64}	$I_{1473.5}/I_{1636.5}$	FIR_{59}^{64}	I_{1550}/I_{1658}
FIR_{38}^{64}	$I_{1473.5}/I_{1650}$	FIR_{67}^{64}	$I_{1572}/I_{1636.5}$
FIR_{39}^{64}	$I_{1473.5}/I_{1658}$	FIR_{68}^{64}	I_{1572}/I_{1650}
FIR_{45}^{64}	$I_{1530.5}/I_{1550}$	FIR_{69}^{64}	I_{1572}/I_{1658}
FIR_{46}^{64}	$I_{1530.5}/I_{1572}$	FIR_{78}^{64}	$I_{1636.5}/I_{1650}$
FIR_{47}^{64}	$I_{1530.5}/I_{1636.5}$	FIR_{79}^{64}	$I_{1636.5}/I_{1658}$
FIR_{48}^{64}	$I_{1530.5}/I_{1650}$	FIR_{89}^{64}	I_{1658}/I_{1658}
FIR_{49}^{64}	$I_{1530.5}/I_{1658}$		

Figure 9.92a: Spec 64 Y_2O_3:Er^{3+} FIR_{12}^{64} vs temperature

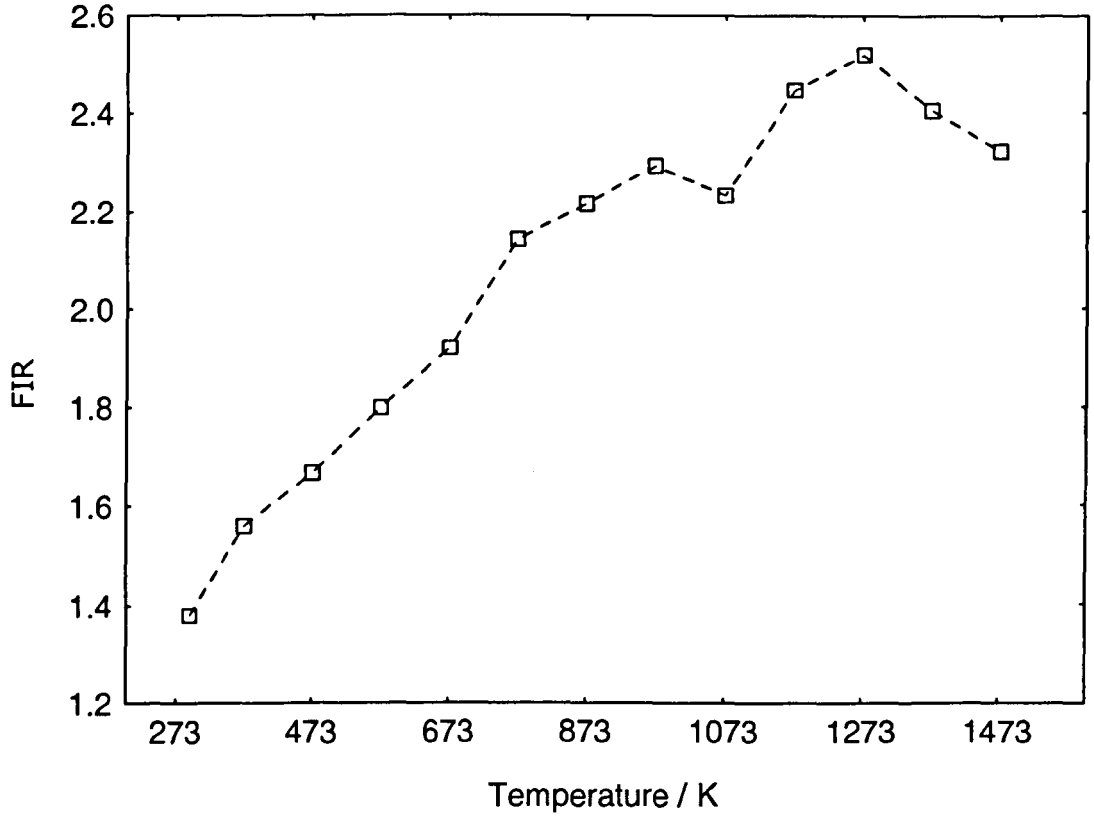

Figure 9.92b: Spec 64 Y_2O_3:Er^{3+} FIR_{14}^{64} to FIR_{16}^{64} vs temperature

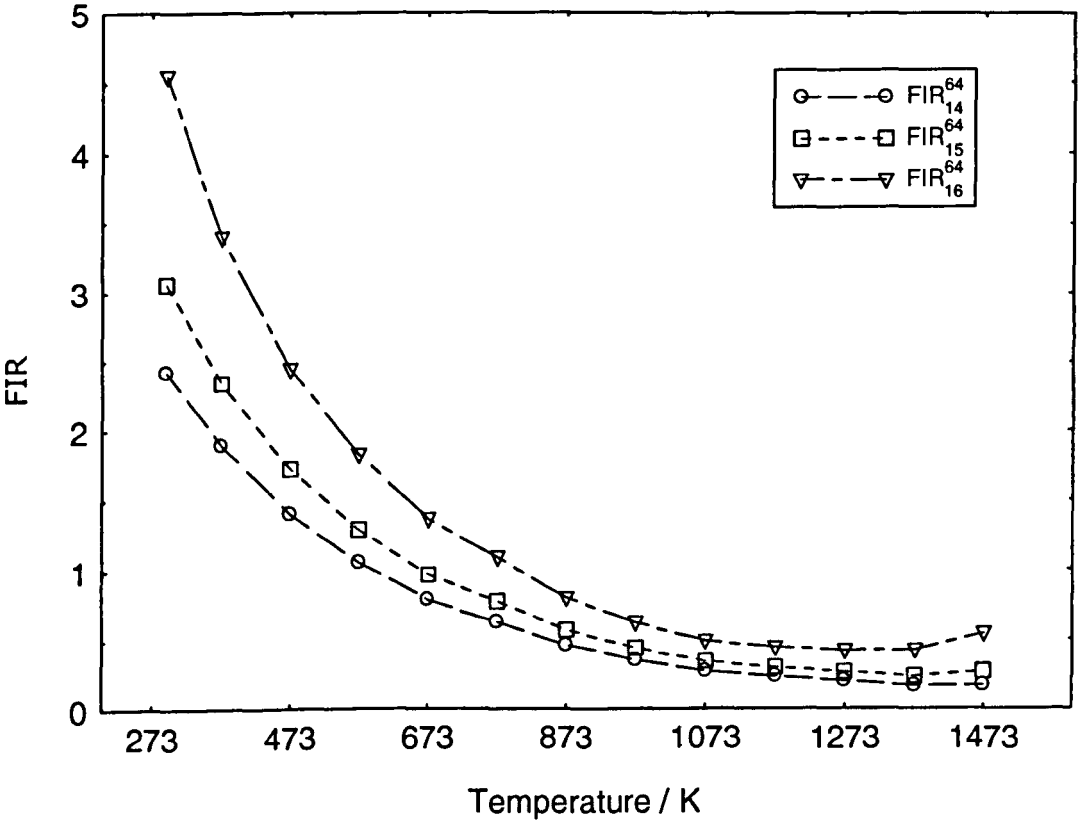

Figure 9.92c: Spec 64 Y_2O_3:Er^{3+} FIR_{13}^{64}, FIR_{17}^{64} to FIR_{19}^{64} vs temperature

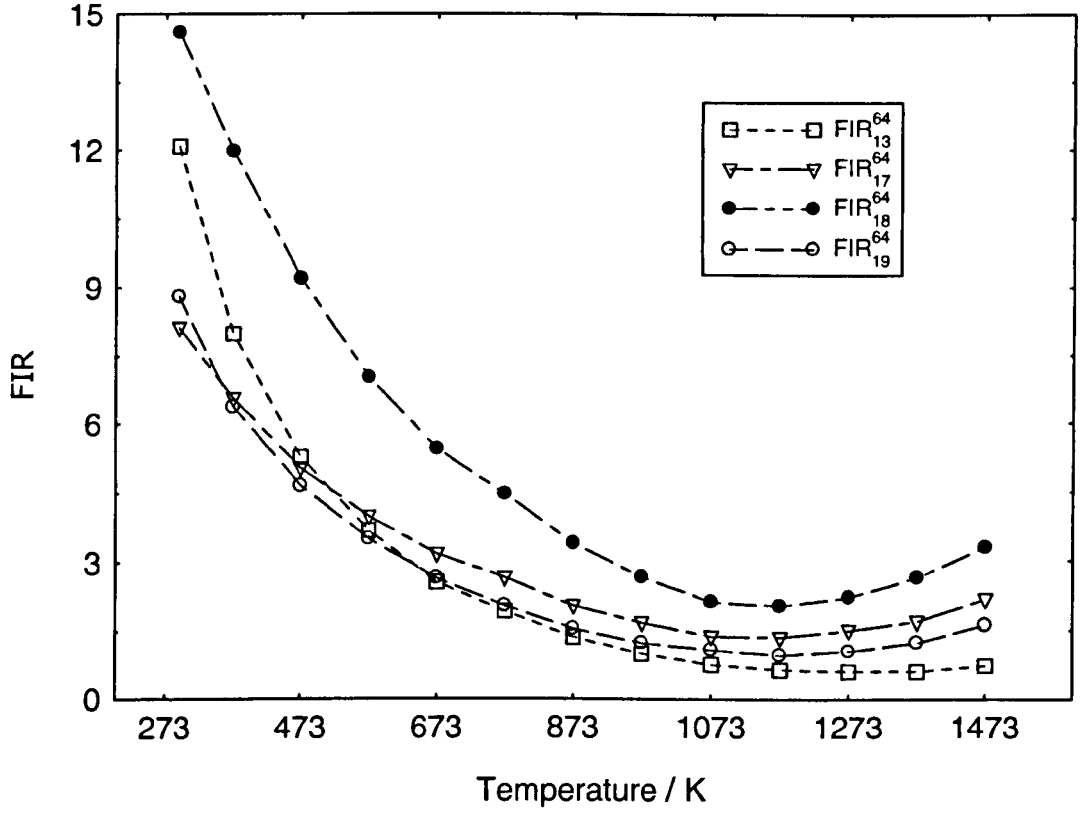

Figure 9.92d: Spec 64 Y_2O_3:Er^{3+} FIR_{12}^{64} (fitted with Eq. 9.7) vs temperature

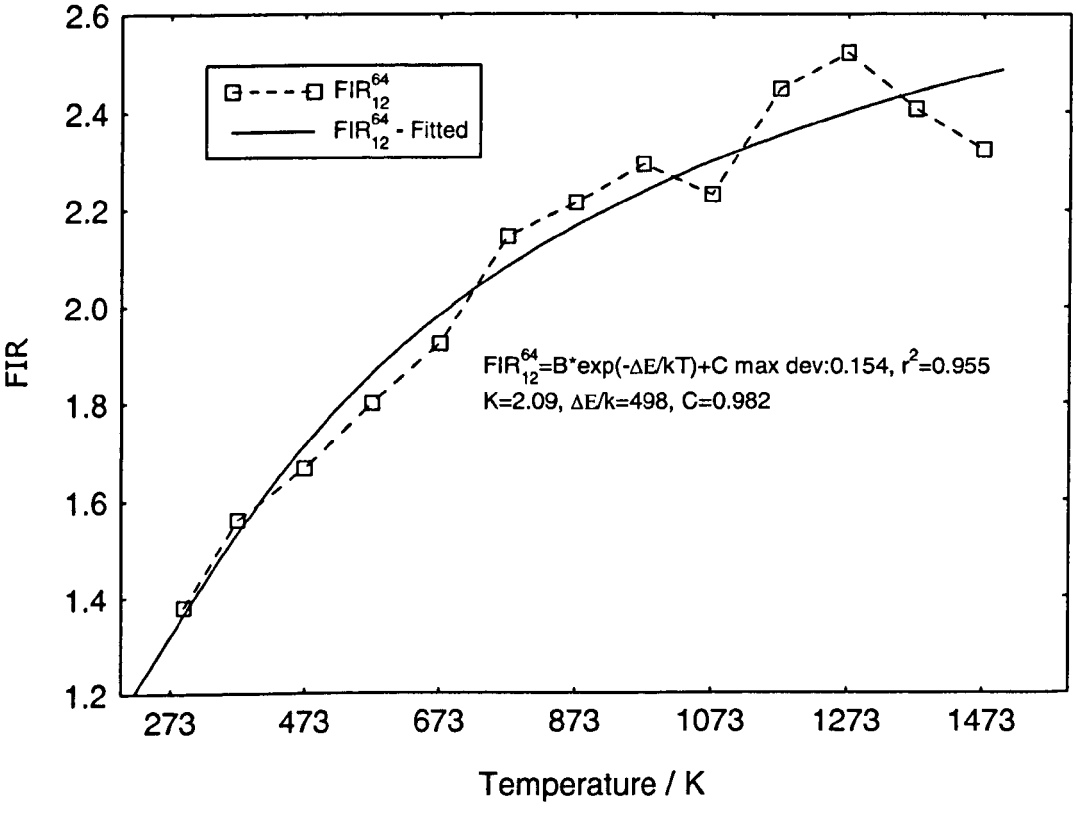

Figure 9.92e: Spec 64 Y_2O_3:Er^{3+} FIR_{13}^{64} (fitted with Eq. 9.7) vs temperature

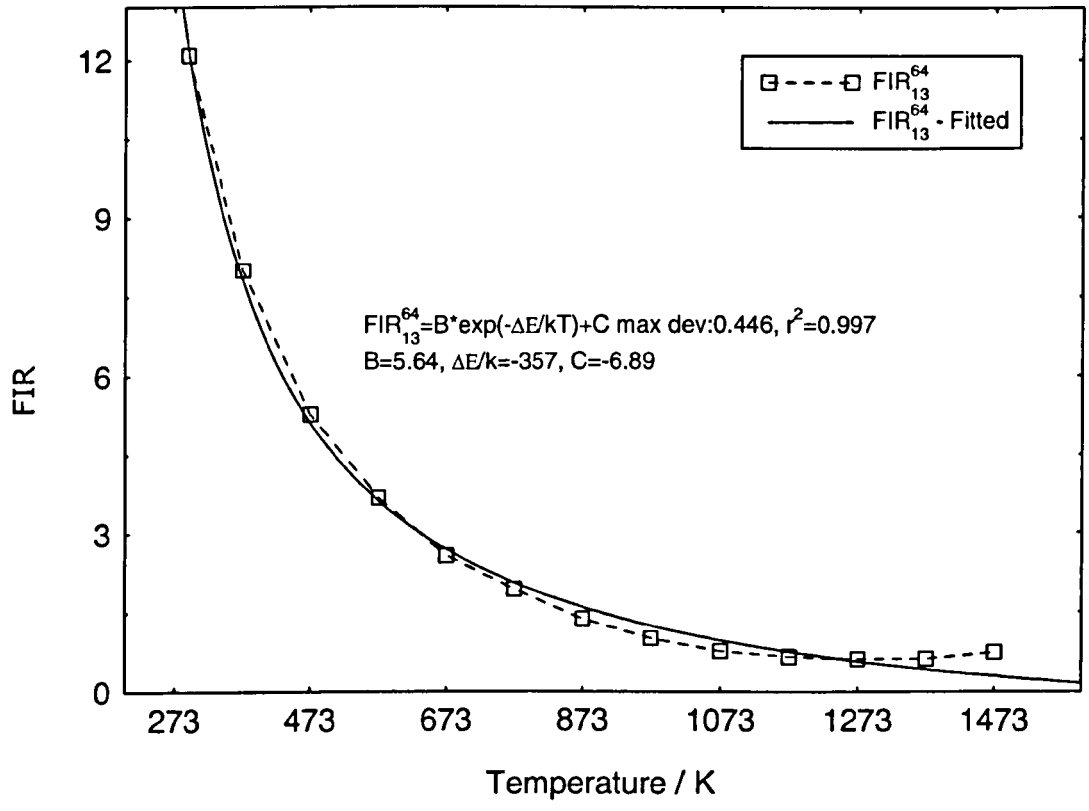

Figure 9.92f: Spec 64 Y_2O_3:Er^{3+} FIR_{14}^{64} & FIR_{15}^{64} (fitted with Eq. 9.7) vs temperature

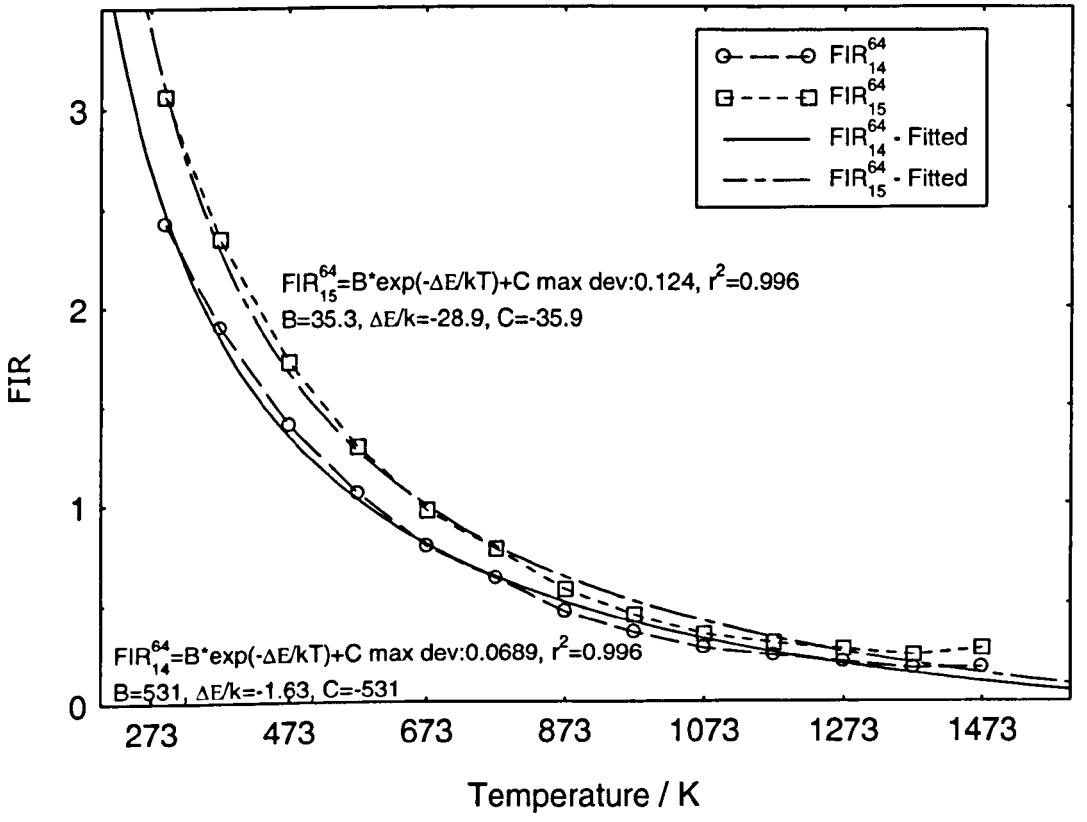

Figure 9.93a: Spec 64 Y_2O_3:Er^{3+} FIR_{24}^{64} to FIR_{26}^{64} vs temperature

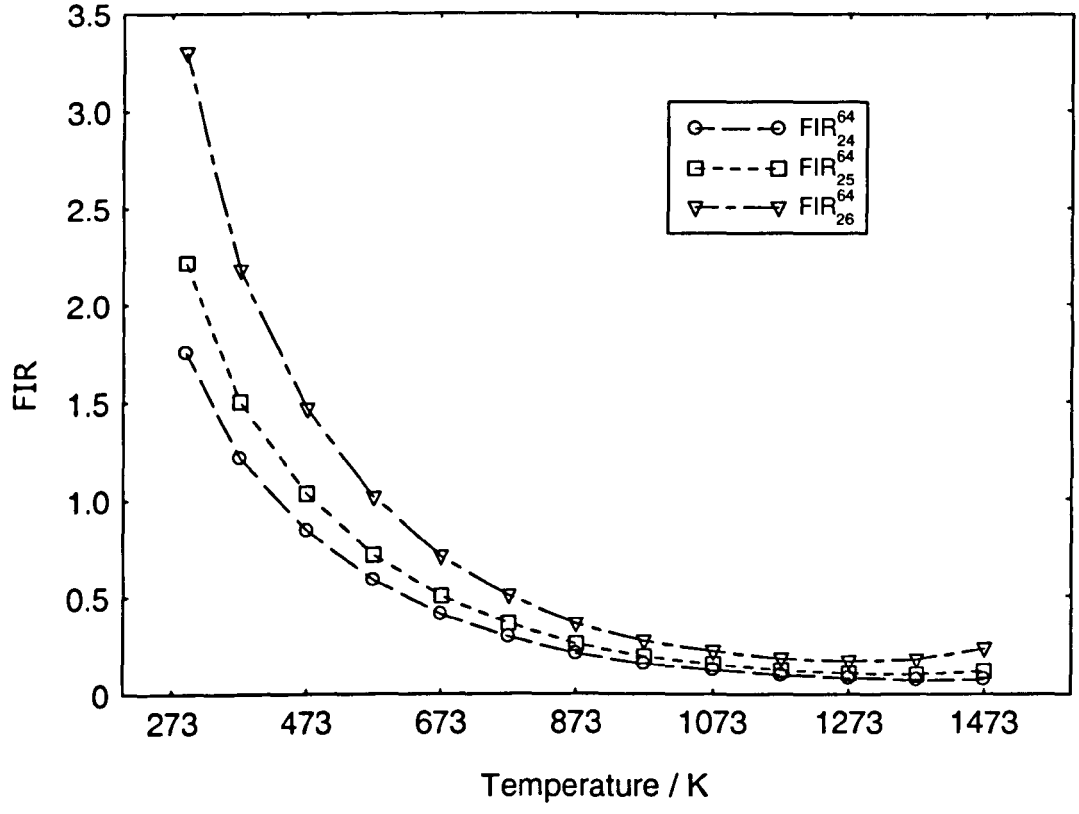

Figure 9.93b: Spec 64 Y_2O_3:Er^{3+} FIR_{23}^{64}, FIR_{27}^{64} to FIR_{29}^{64} vs temperature

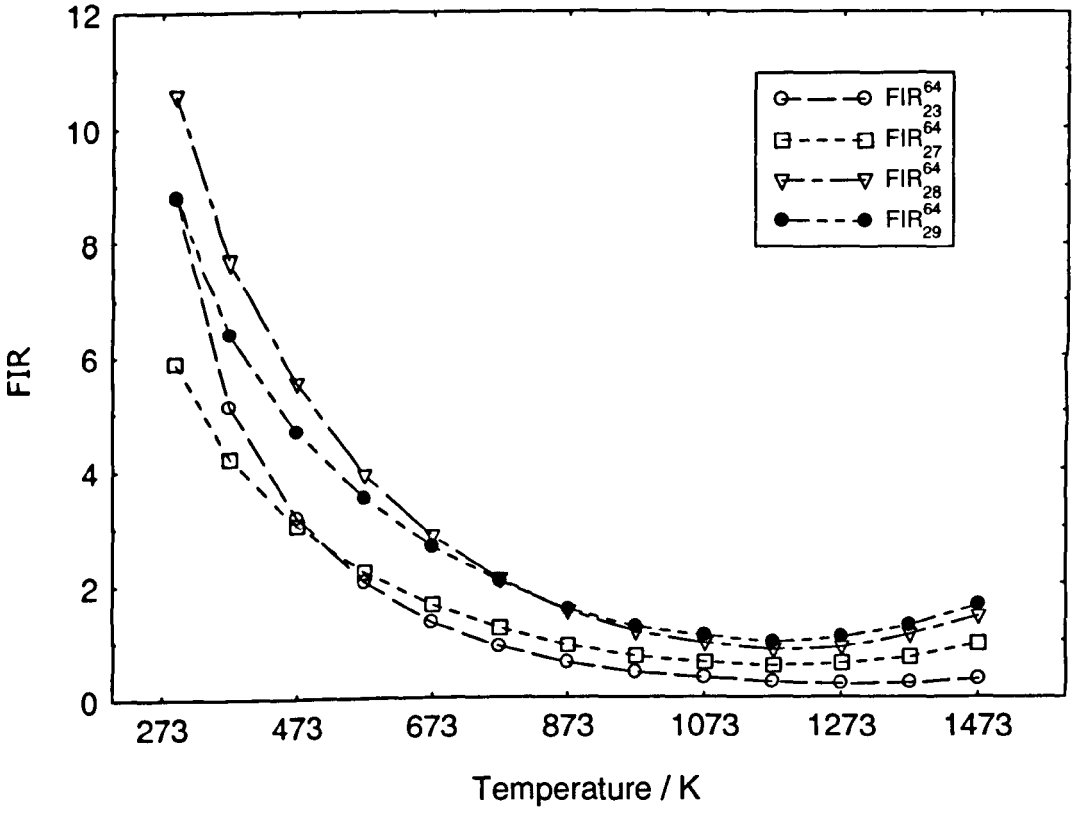

Figure 9.93c: Spec 64 $Y_2O_3:Er^{3+}$ FIR_{23}^{64} (fitted with Eq. 9.7) vs temperature

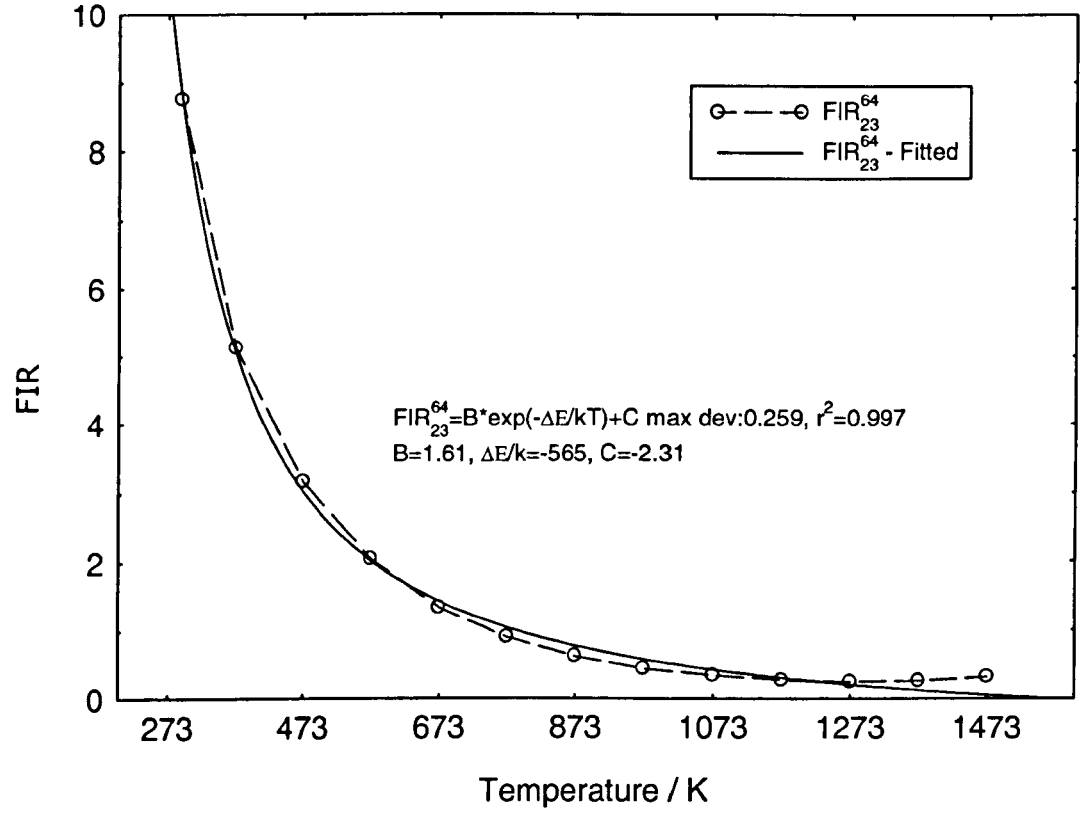

Figure 9.93d: Spec 64 $Y_2O_3:Er^{3+}$ FIR_{24}^{64} (fitted with Eq. 9.7) vs temperature

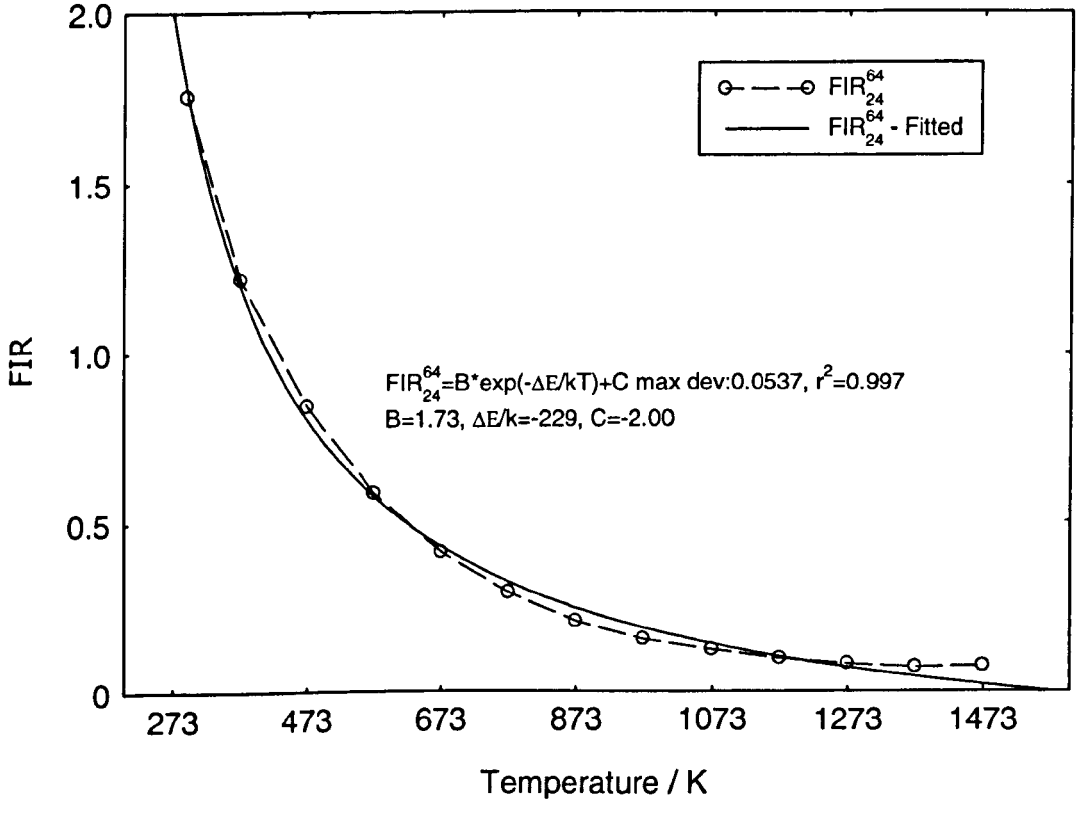

Figure 9.94a: Spec 64 Y_2O_3:Er^{3+} FIR_{34}^{64} to FIR_{36}^{64} vs temperature

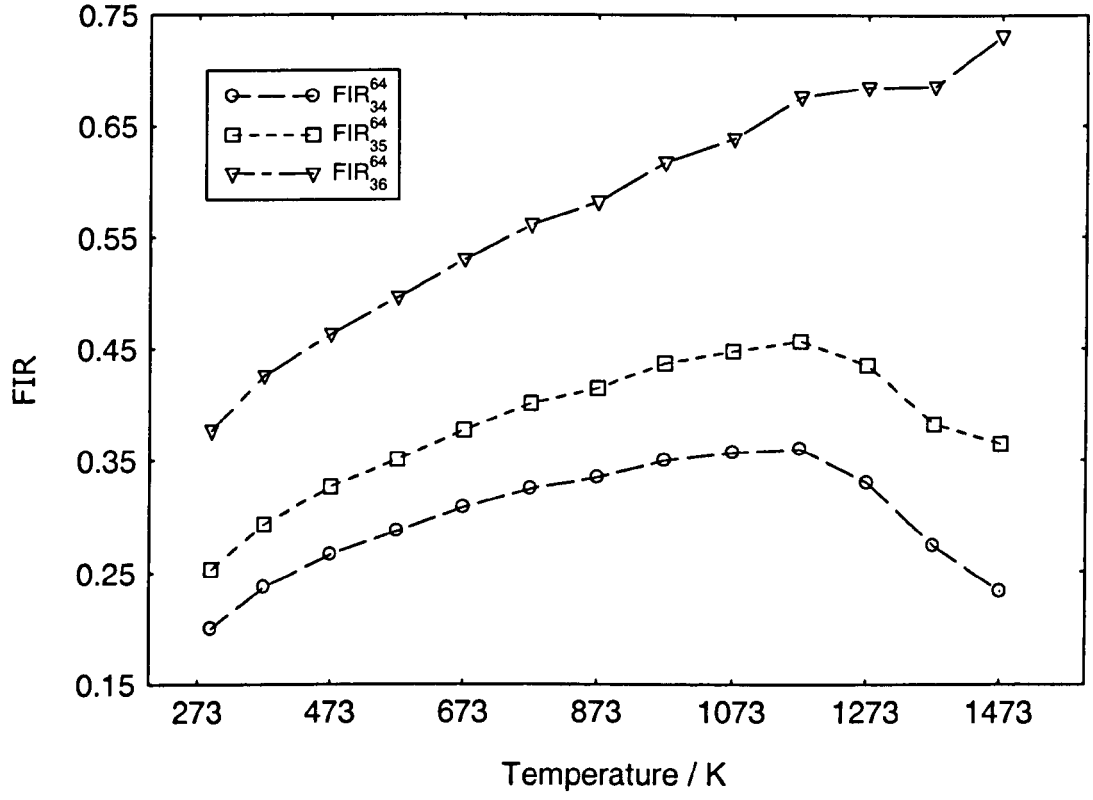

Figure 9.94b: Spec 64 Y_2O_3:Er^{3+} FIR_{37}^{64} to FIR_{39}^{64} vs temperature

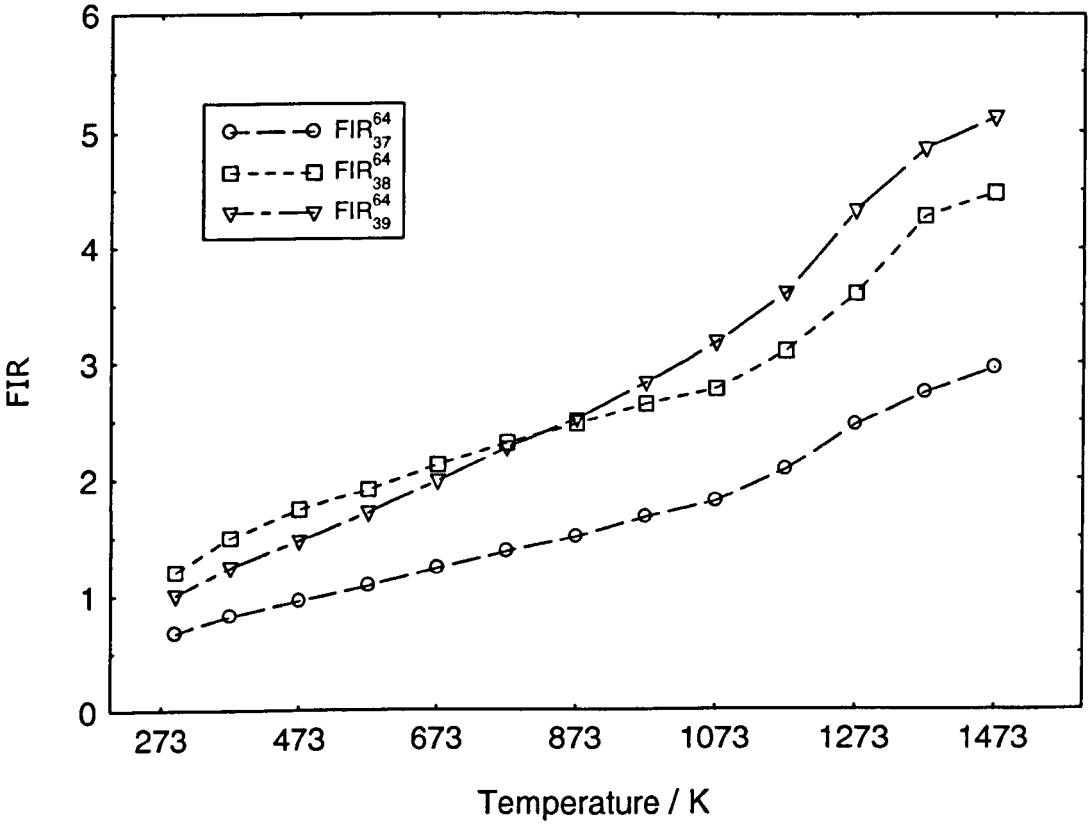

Figure 9.94c: Spec 64 Y_2O_3:Er^{3+} FIR_{36}^{64} (fitted with Eq. 9.7) vs temperature

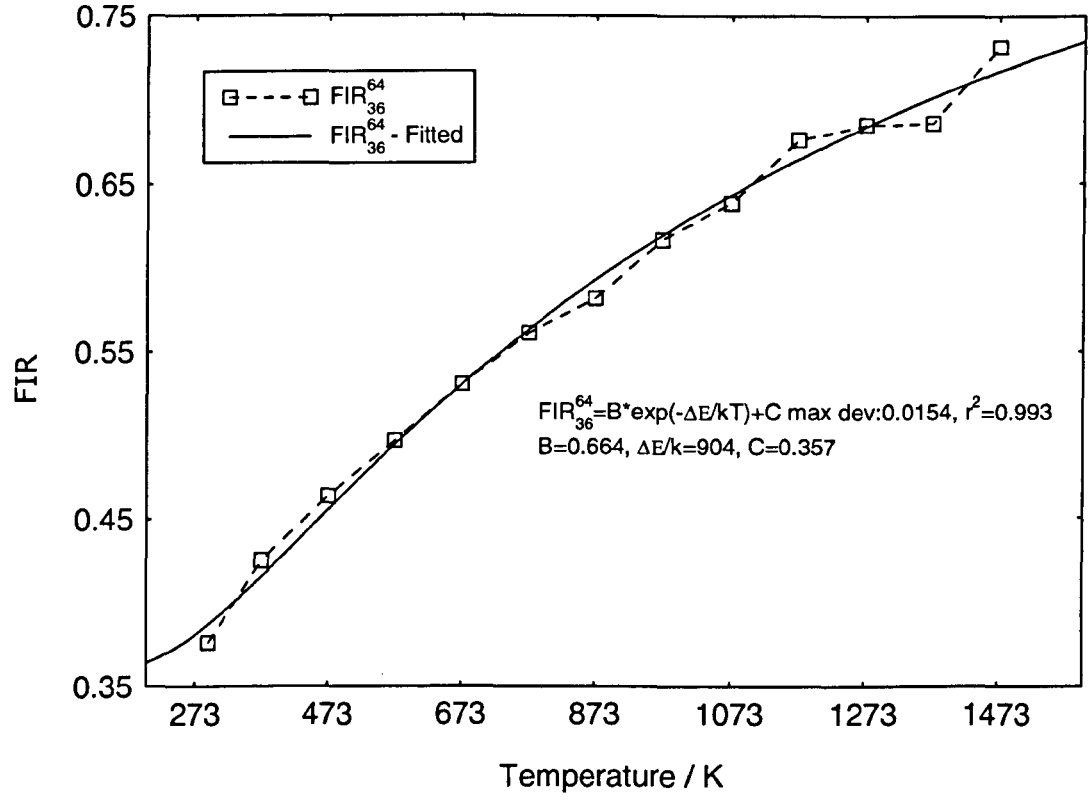

Figure 9.94d: Spec 64 Y_2O_3:Er^{3+} FIR_{37}^{64} & FIR_{38}^{64} (fitted with Eq. 9.7) vs temperature

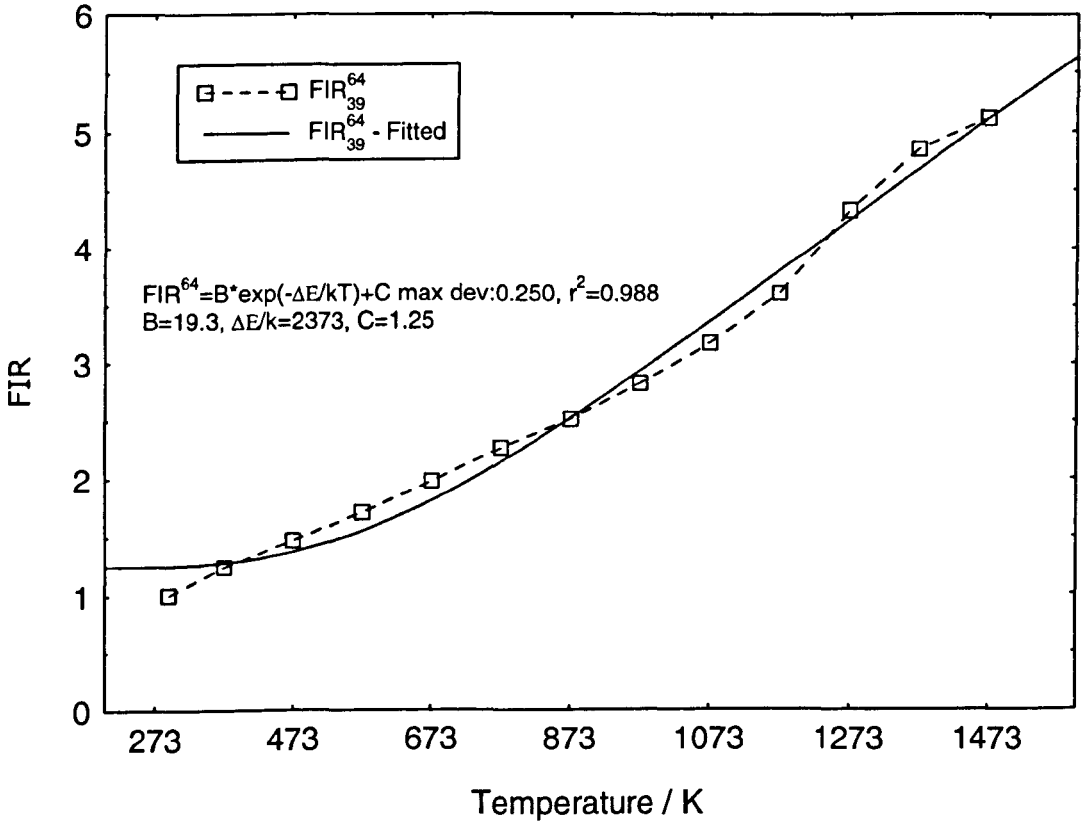

Figure 9.95a: Spec 64 Y_2O_3:Er^{3+} FIR_{45}^{64} & FIR_{46}^{64} vs temperature

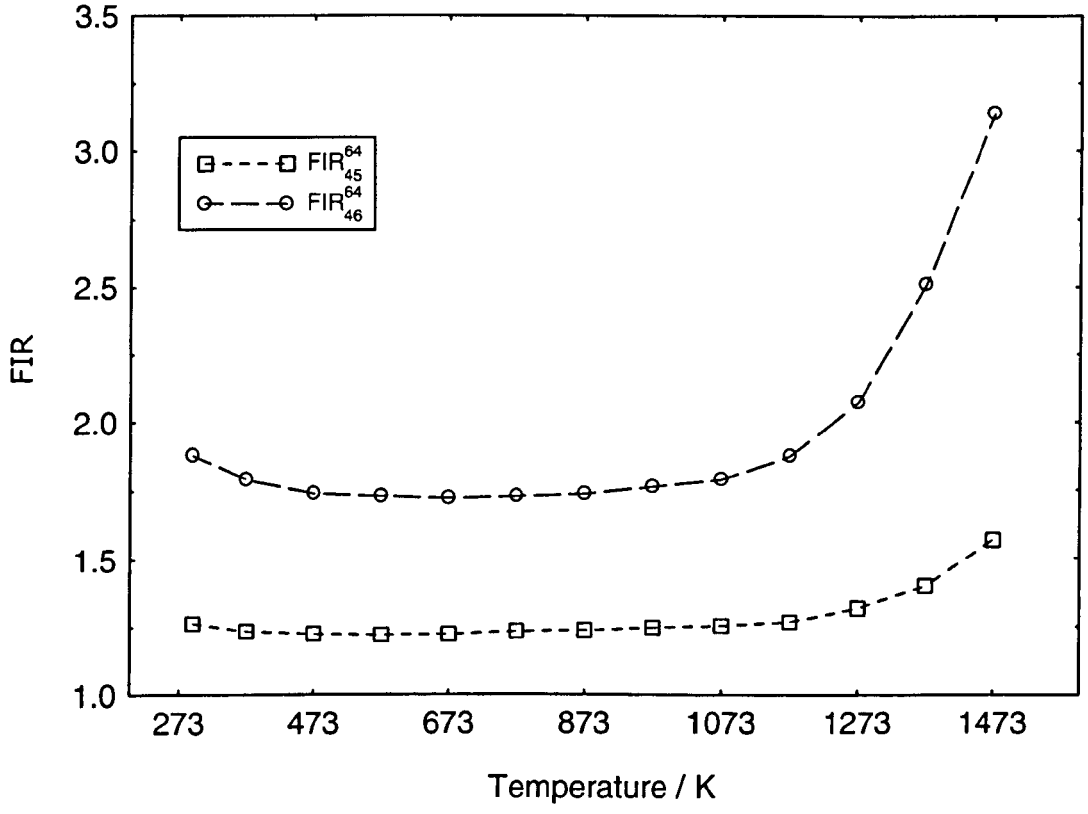

Figure 9.95b: Spec 64 Y_2O_3:Er^{3+} FIR_{47}^{64} to FIR_{49}^{64} vs temperature

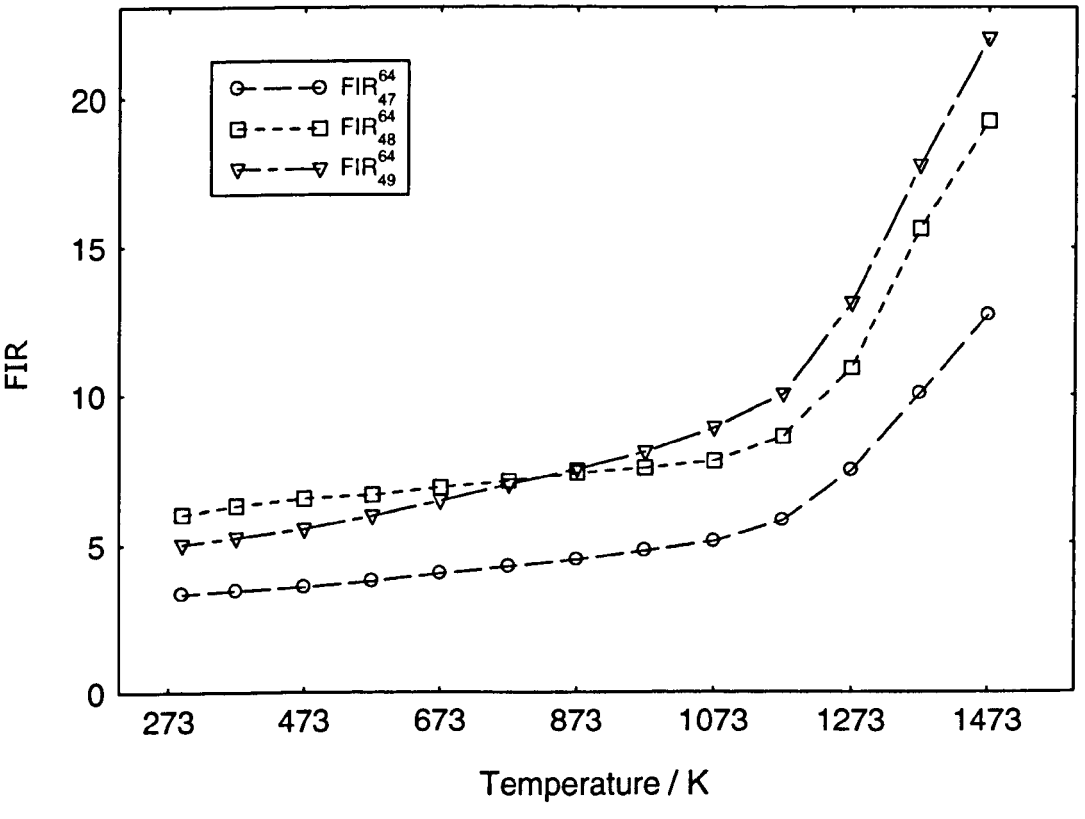

Figure 9.95c: Spec 64 Y_2O_3:Er^{3+} FIR_{47}^{64} & FIR_{48}^{64} (fitted with Eq. 9.7) vs temperature

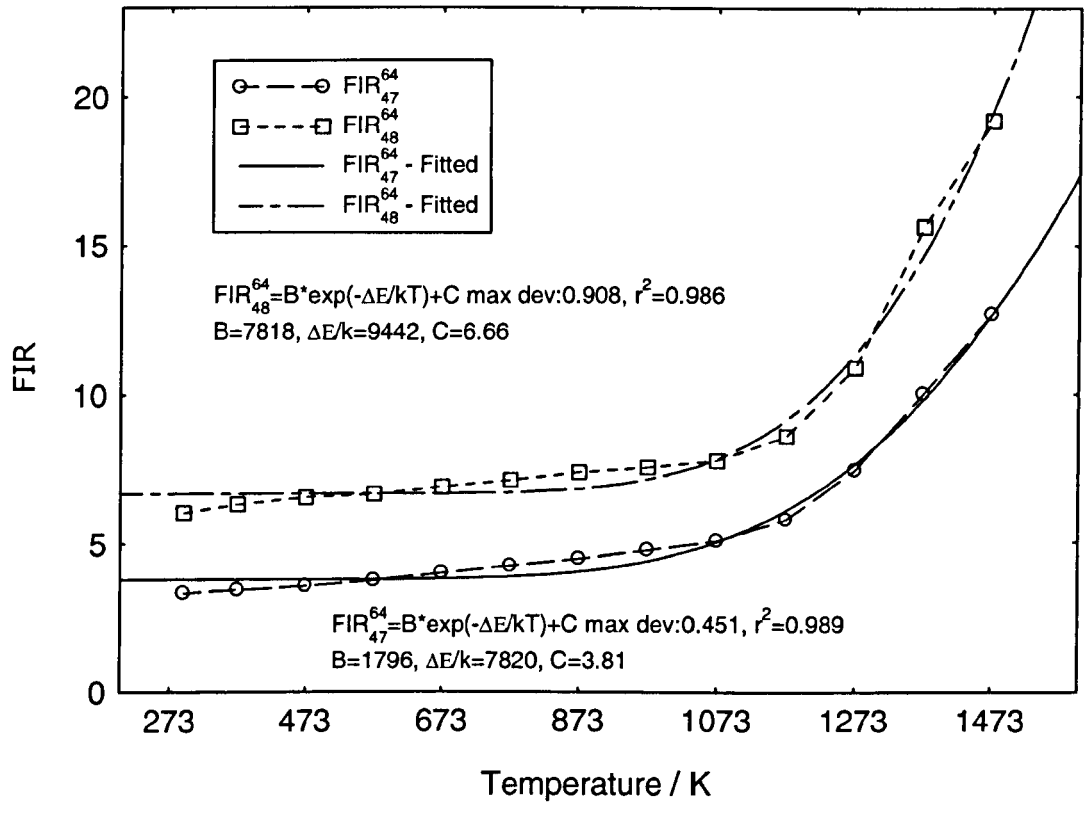

Figure 9.95d: Spec 64 Y_2O_3:Er^{3+} FIR_{49}^{64} (fitted with Eq. 9.7) vs temperature

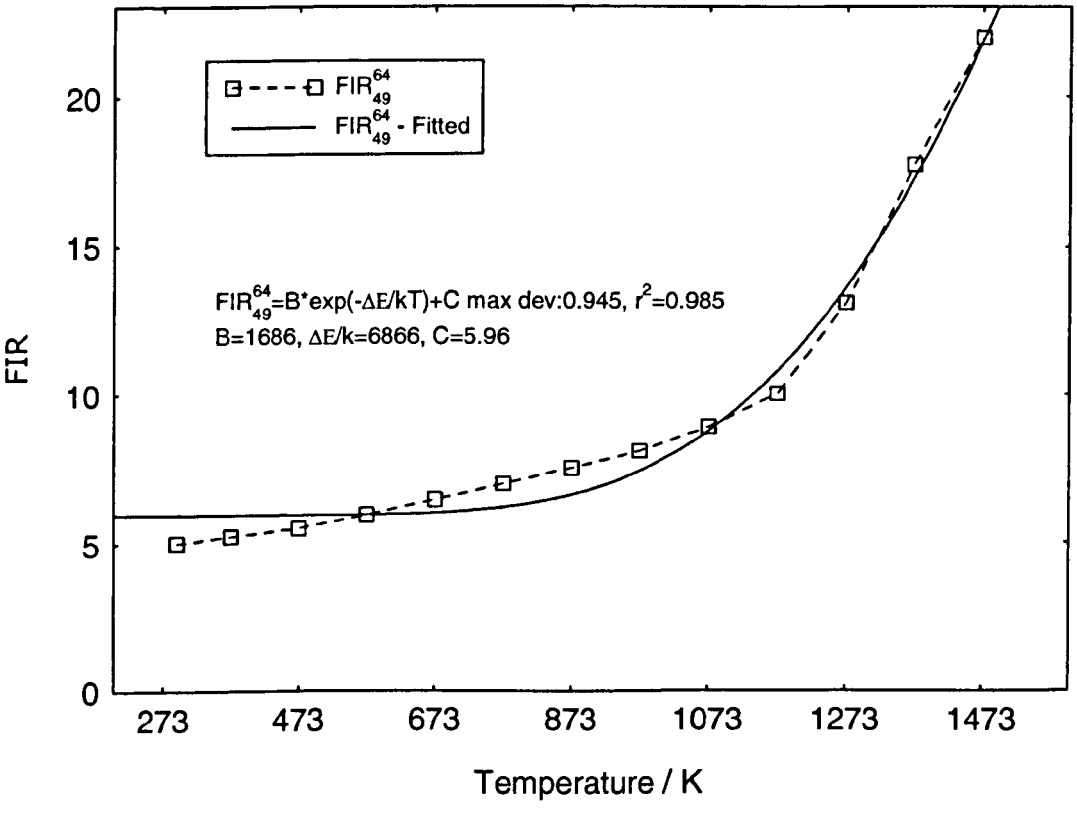

Figure 9.96a: Spec 64 Y_2O_3:Er^{3+} FIR_{56}^{64} vs temperature

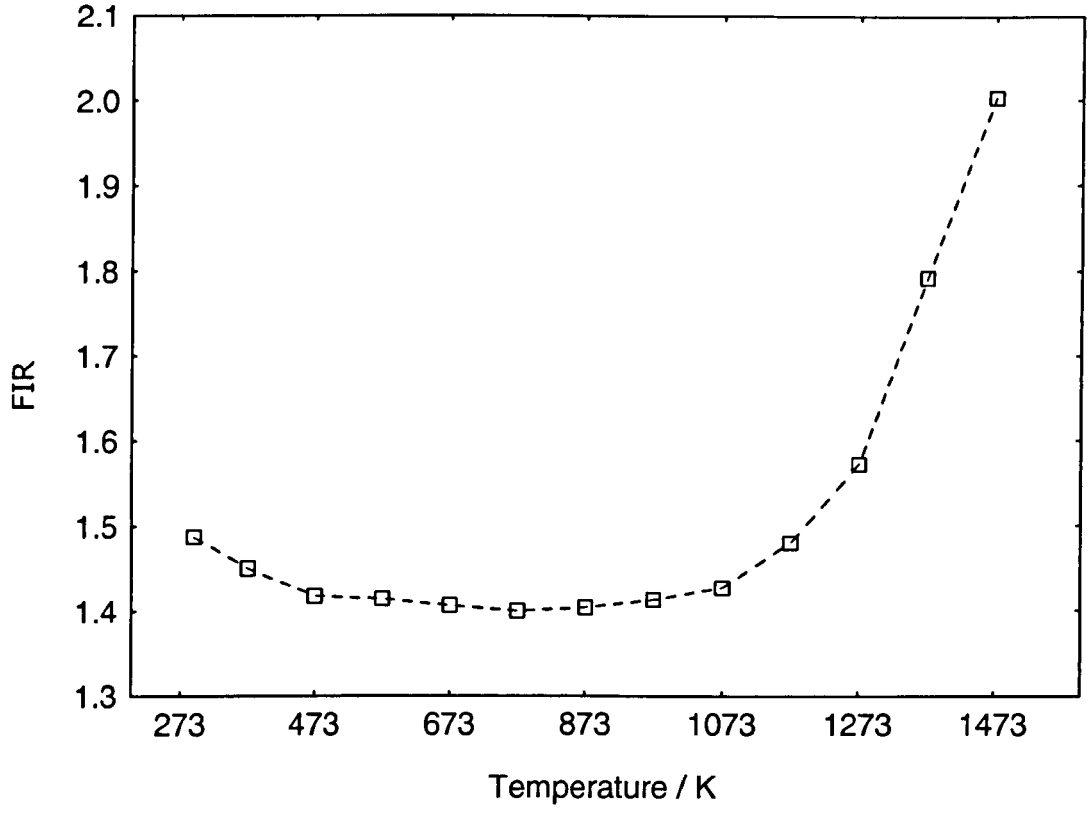

Figure 9.96b: Spec 64 Y_2O_3:Er^{3+} FIR_{57}^{64} to FIR_{59}^{64} vs temperature

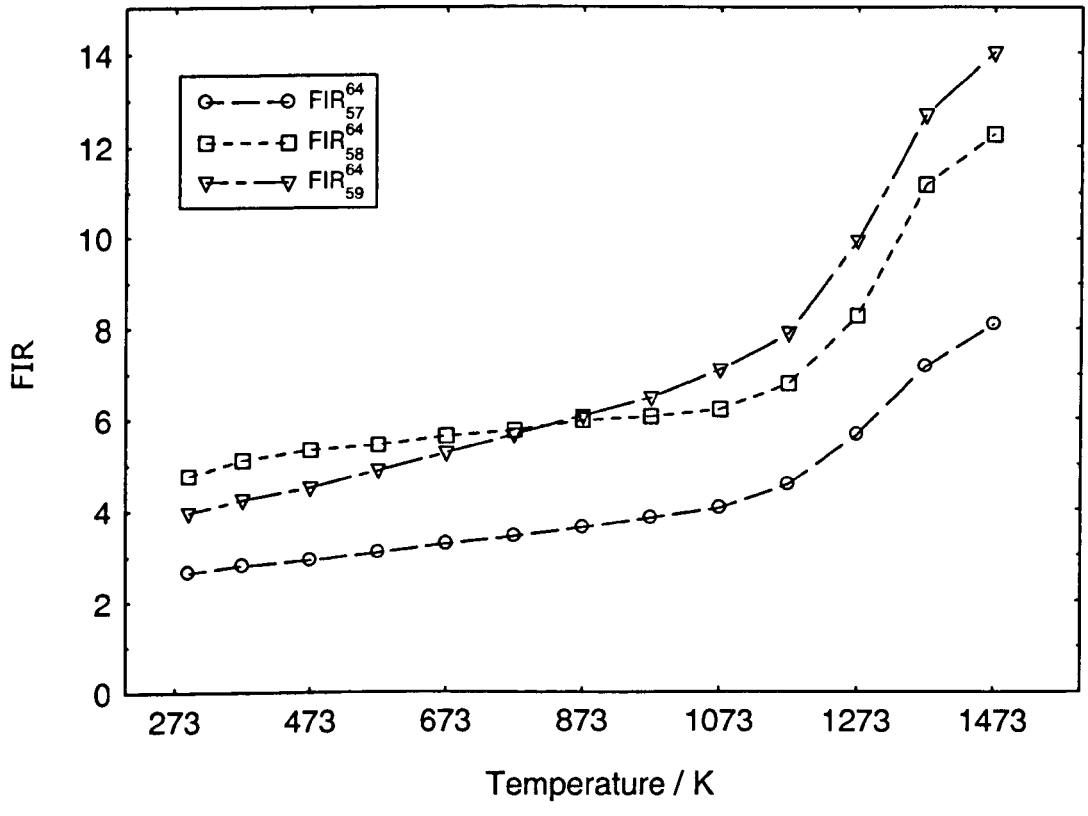

Figure 9.96c: Spec 64 Y_2O_3:Er^{3+} FIR_{57}^{64} & FIR_{58}^{64} (fitted with Eq. 9.7) vs temperature

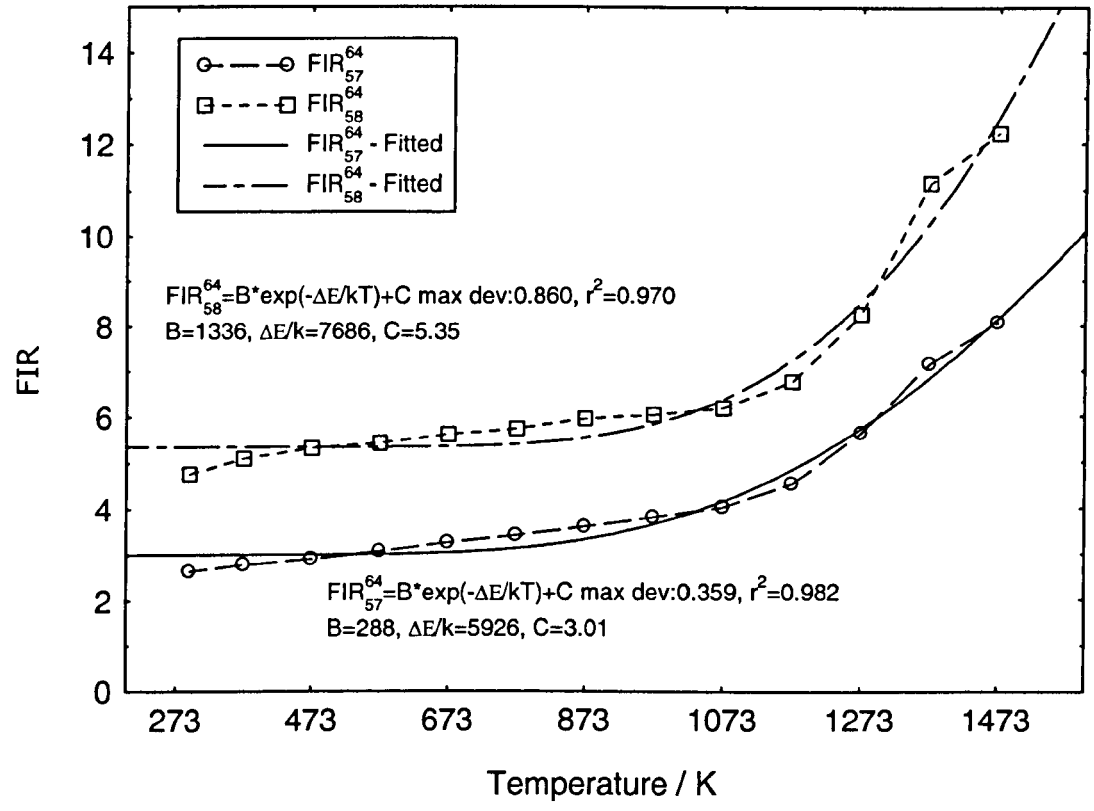

Figure 9.96d: Spec 64 Y_2O_3:Er^{3+} FIR_{59}^{64} (fitted with Eq. 9.7) vs temperature

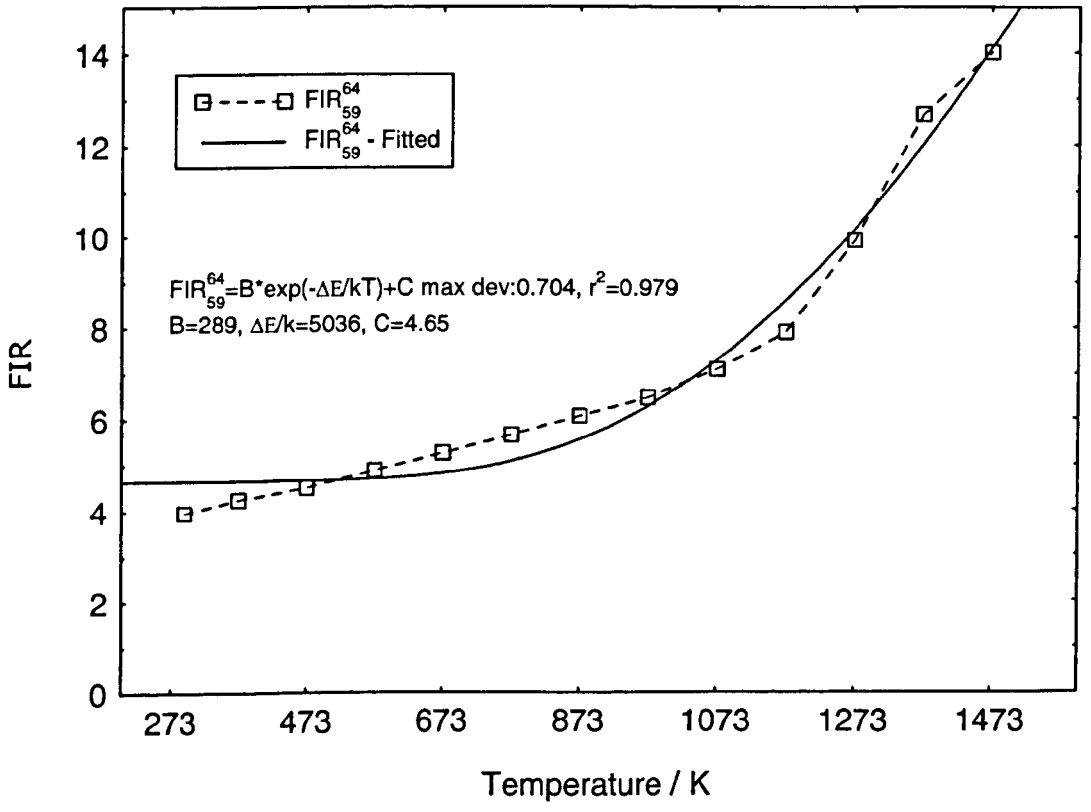

Figure 9.97a: Spec 64 Y_2O_3:Er^{3+} FIR_{67}^{64} to FIR_{69}^{64} vs temperature

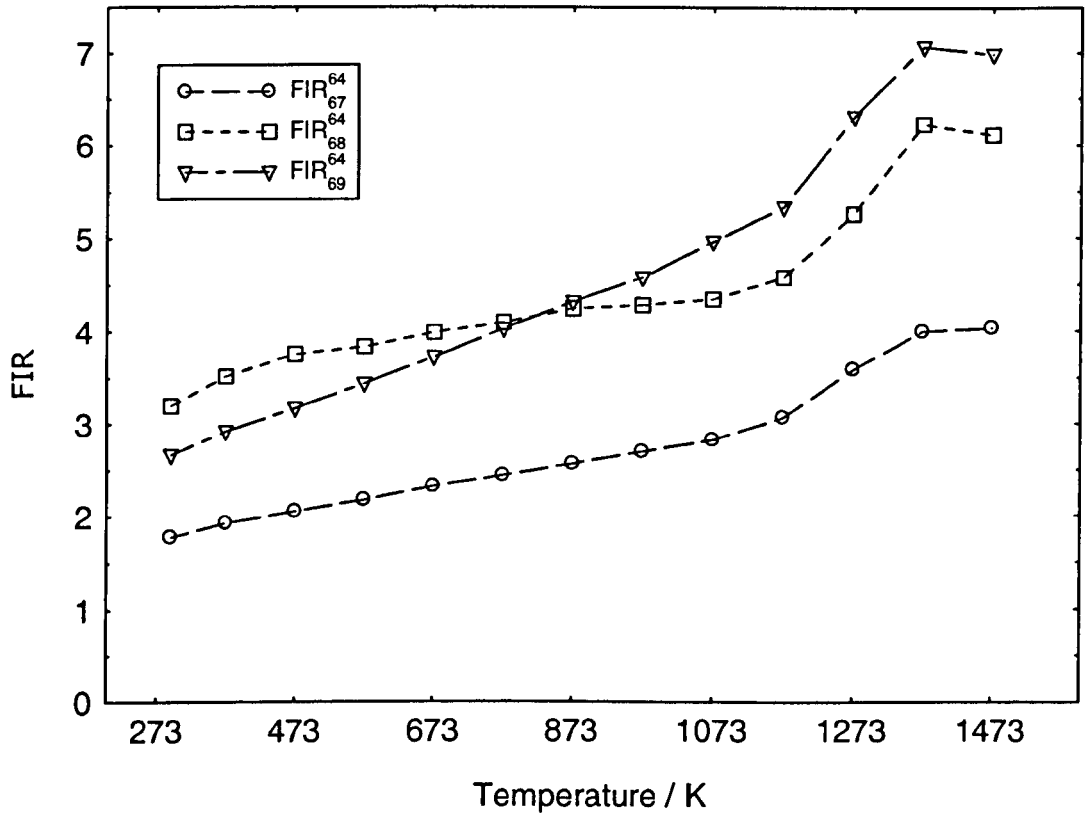

Figure 9.97b: Spec 64 Y_2O_3:Er^{3+} FIR_{67}^{64} to FIR_{68}^{64} (fitted with Eq. 9.7) vs temperature

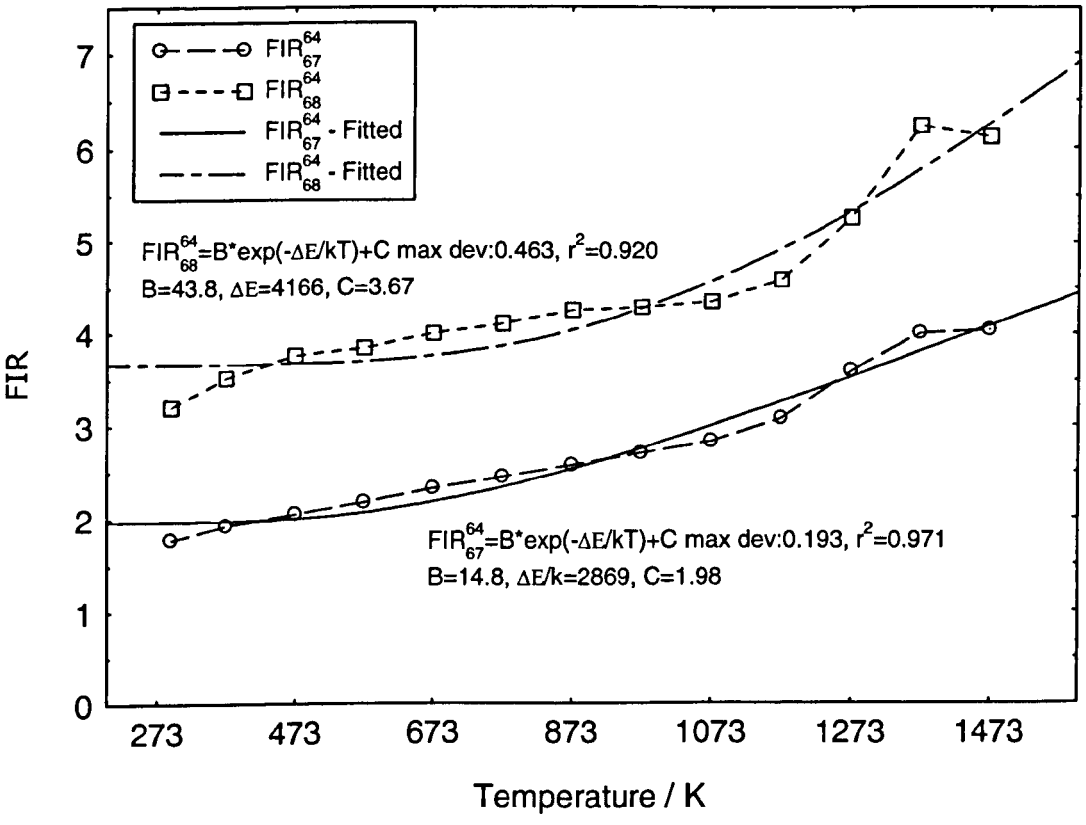

Figure 9.97c: Spec 64 $Y_2O_3:Er^{3+}$ FIR_{69}^{64} (fitted with Eq. 9.7) vs temperature

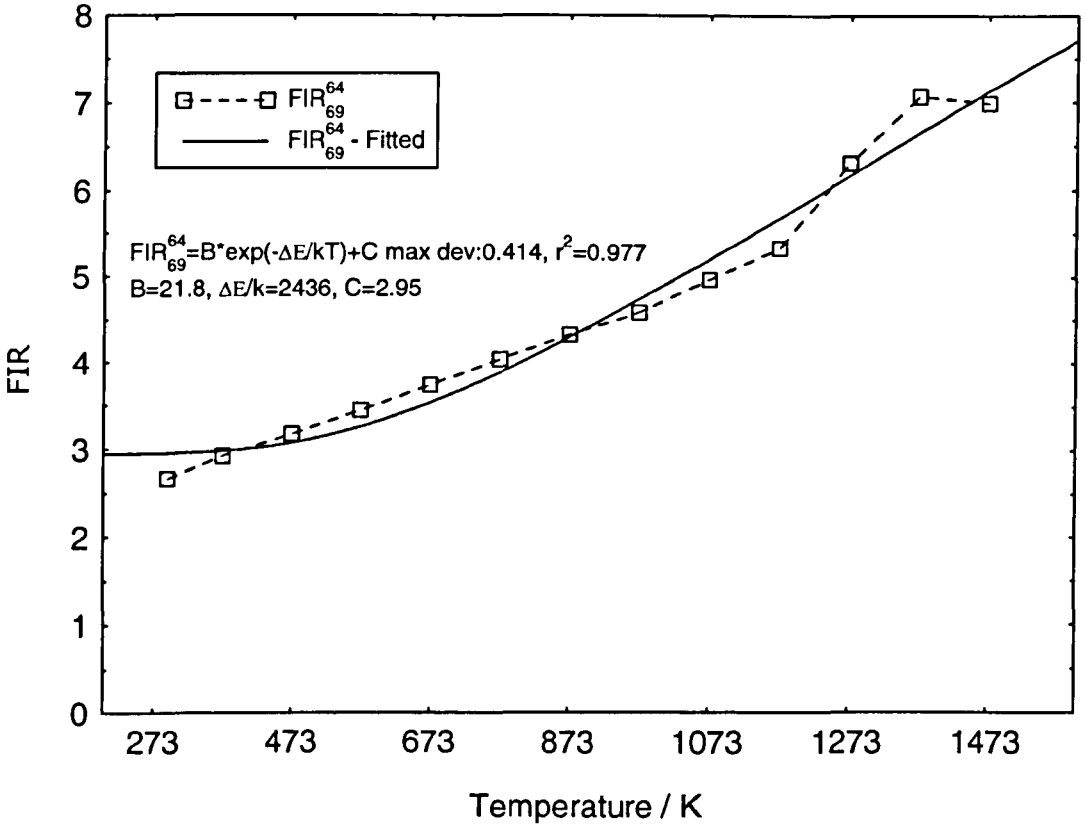

Figure 9.98: Spec 64 Y_2O_3:Er^{3+} FIR_{78}^{64} & FIR_{79}^{64} vs temperature

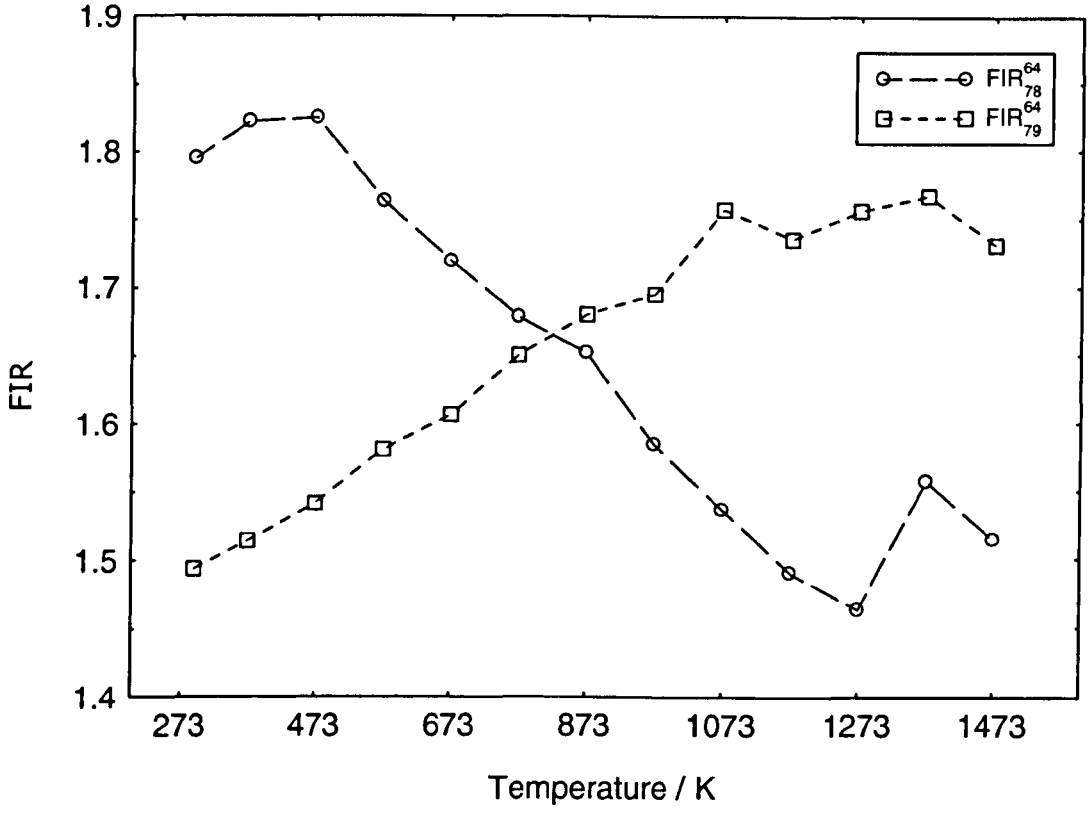

Figure 9.99: Spec 64 Y_2O_3:Er^{3+} FIR_{89}^{64} vs temperature

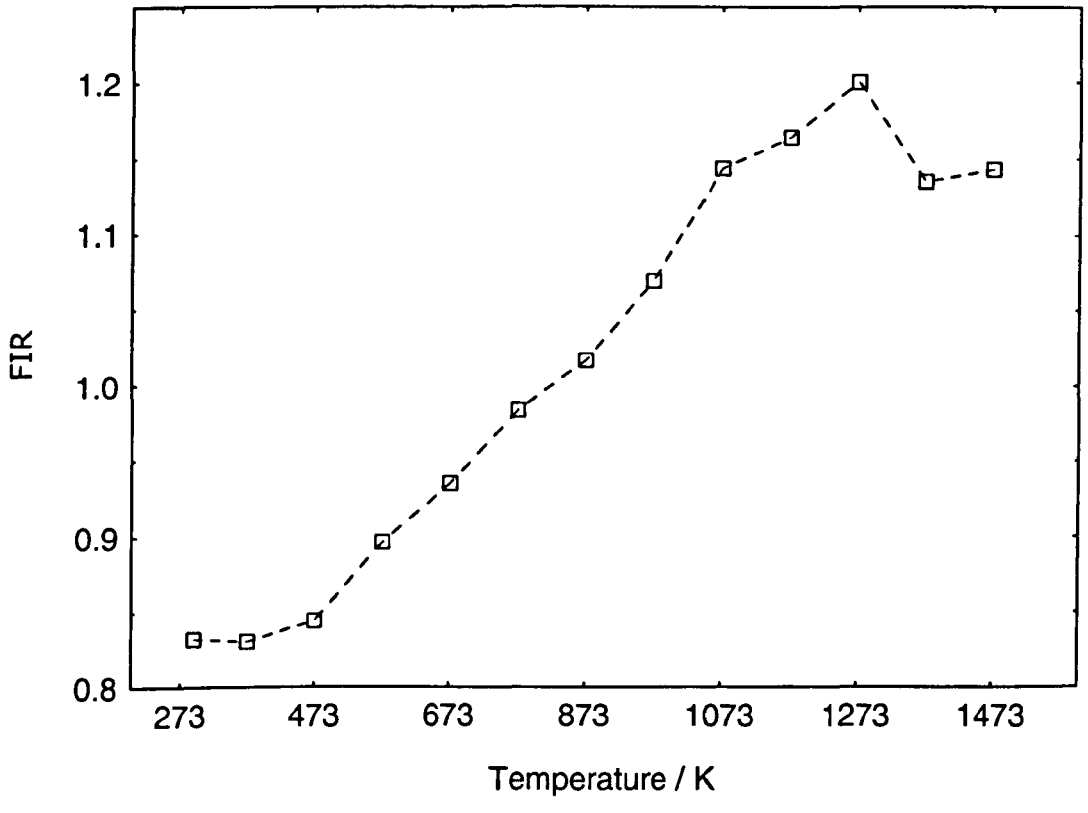

Figure 9.100a: Spec 64 Y_2O_3:Er^{3+} FIR^{64}_{AB}, FIR^{64}_{AC} & FIR^{64}_{AD} vs temperature

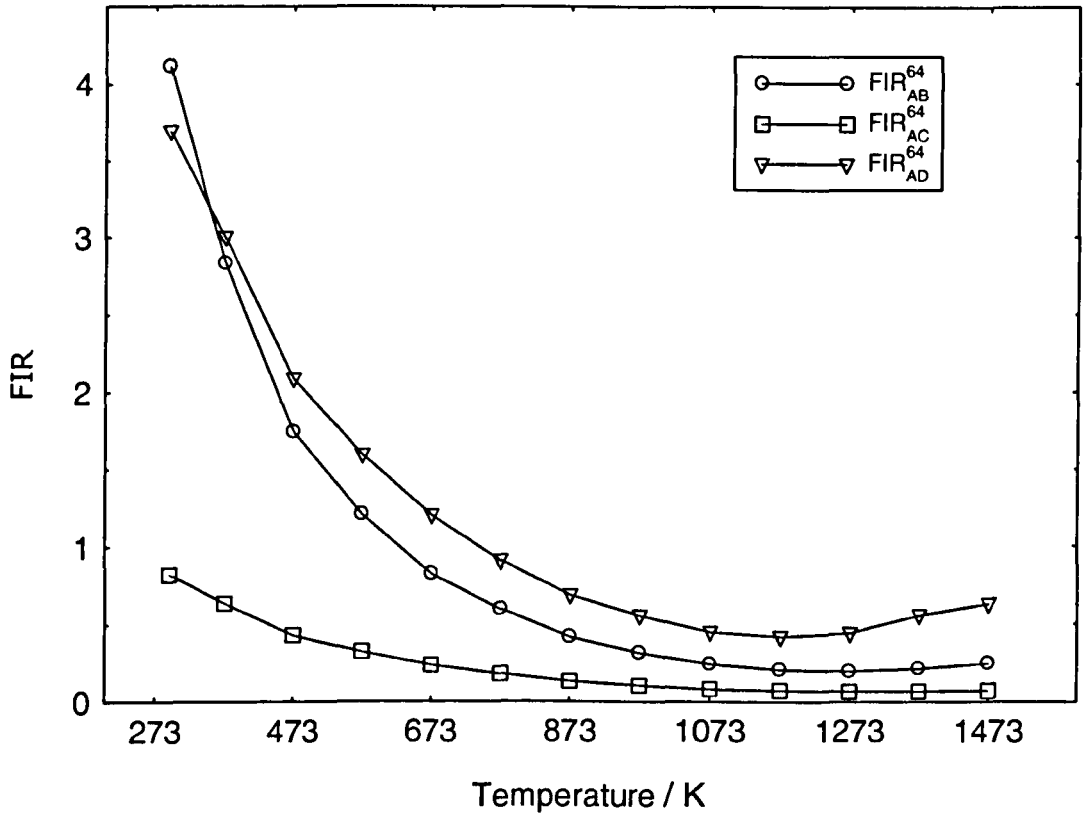

Figure 9.100b: Spec 64 Y_2O_3:Er^{3+} FIR^{64}_{BC}, FIR^{64}_{BD} & FIR^{64}_{CD} vs temperature

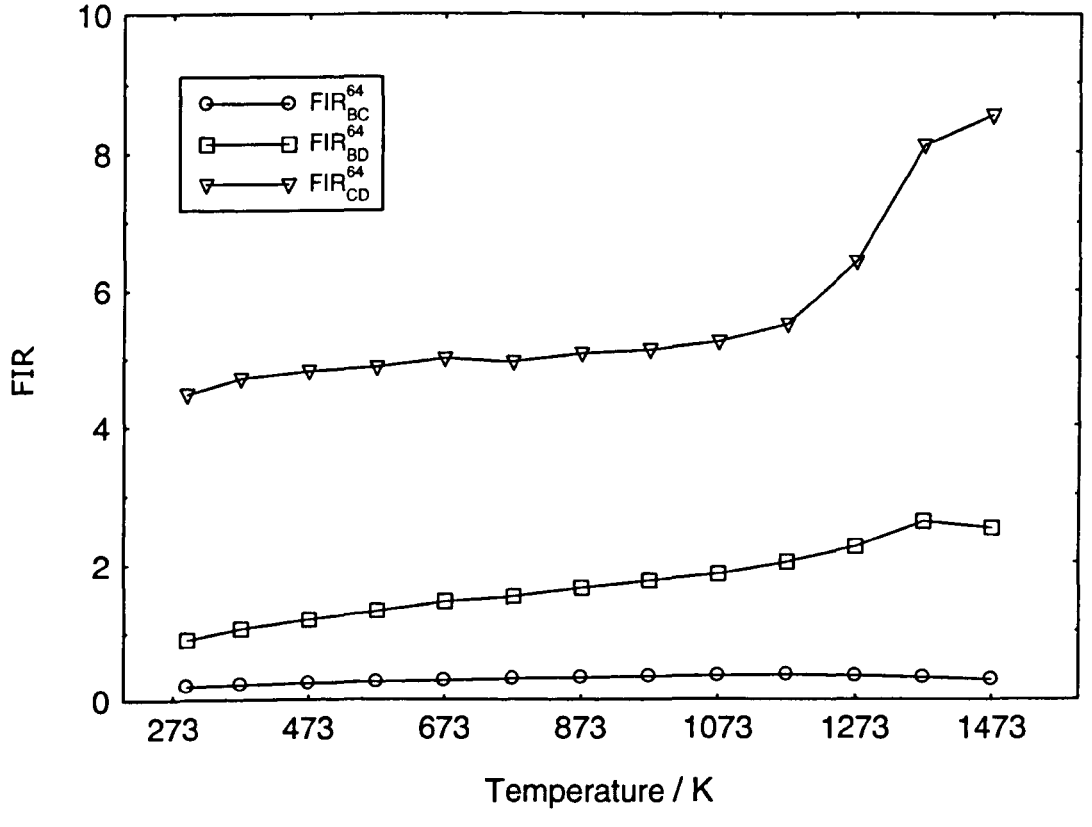

Figure 9.100c: Spec 64 $Y_2O_3:Er^{3+}$ FIR_{AC}^{64} (fitted with Eq. 9.7) vs temperature

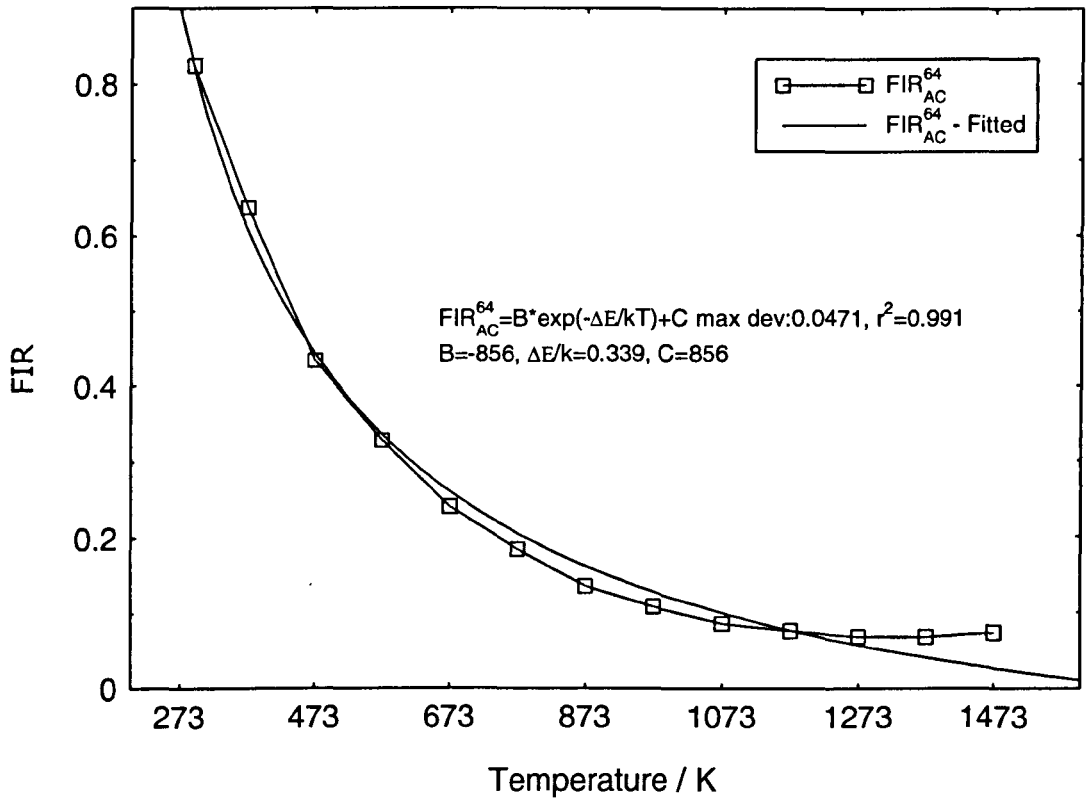

Figure 9.100d: Spec 64 $Y_2O_3:Er^{3+}$ FIR_{CD}^{64} (fitted with Eq. 9.7) vs temperature

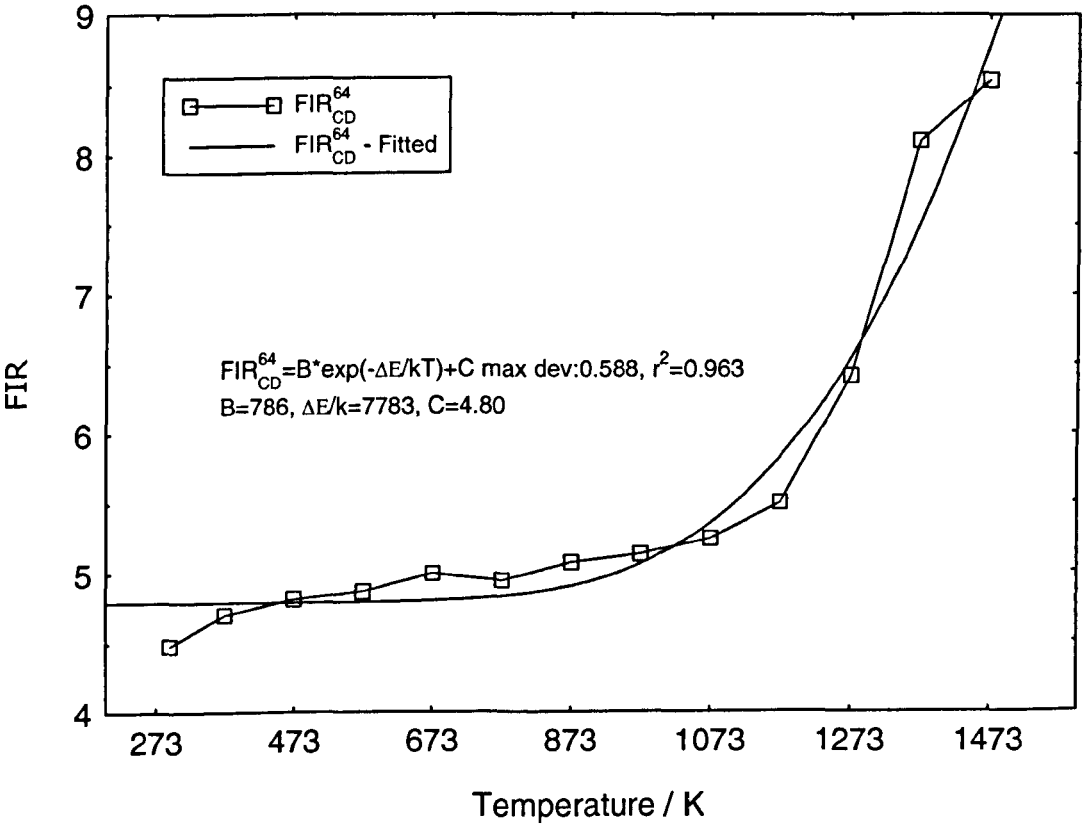

9.8.2 Upconversion Intensity Based Sensing - $Y_2O_3:Er^{3+}$

A visible green light was observed coming from the tip of $Y_2O_3:Er^{3+}$ sensing fibre when excited with a 965nm laser diode. Investigation was carried out to apply the upconversion emission as a function of temperature and further investigate its functionality for use as a SCF sensor. A spectral scan was carried out at room temperature and it is illustrated in Figure 9.101. Comparing this upconversion spectrum with that of YAG singly and co-doped, the red emission was very weak. Although both hosts were doped with Er^{3+} ions, the upconversion spectra were slightly different. The intensities of the visible lines at 538.5nm, 553nm, 563nm and 681nm were needed for UIR calculations. Study was made of the transitions $^2H_{11/2}$ + $^4S_{3/2}$ (green) and $^4F_{9/2}$ (red) was monitored as a function of temperature up to 1473K and ~673K, respectively.

9.8.2.1 Results and Discussion

Figures 9.103 to 105 show the upconversion spectra from the experiment. At the emission $^2H_{11/2}$ when temperature increases, only a slight increase in intensity was observed. In Figure 9.104, comparison is made between the spectrum at room temperature and at 1473K. It can be seen that the only increase in intensity occurs between wavelengths ~518nm to ~527nm. When the integrated intensity of the transition was calculated the increase was not significant enough to be apparent in the plot shown in Figure 9.106. This only reflected a gradual decrease in integrated intensity. At transition $^4S_{3/2}$, it was observed that the intensity decreases with rising temperature. Figures 9.103 and 104 show the change in of the upconversion across the temperature range. From Figure 9.106, an exponential decay for transition $^4S_{3/2}$ was seen. This is useful to measure lower temperatures due to the rapid changes with intensity to small temperature increments. The reduction of intensity could possibly be due to homogeneous line broadening and redistribution of the ions' population within the Stark lines. Unlike in the results for YAG, the redistribution to transition $^2H_{11/2}$ was not obvious and can't be observed in the upconversion spectra. Another noticeable difference is that Y_2O_3 upconversion spectrum profile at 1473K maintained good resolution when compared to YAG. No obvious broadening was experienced during the temperature changes. The upconversion emission spectrum

from $^4F_{9/2}$, seen in Figure 9.105, was only effective until ~673K. The profile of the emission after this temperature was dominated by the background noise and no meaningful results could be obtained from the data collected.

Figures 9.107 to 109 show the upconversion emission lines as a function of temperature. The plots show a decrease in intensity as the temperature increases. In Figure 9.107, $I_{538.5}$ exhibits steady decrease as temperature increases hence a linear line was fitted to the plot. Emission lines at 553nm and 563nm experience a progressive decrease. The gradual decrease was also observed in the red emission having a maximum effective temperature of ~673K, see Figure 9.109. It is worth mentioning that in the green transition, due to the Stark level splitting several other peaks (521nm, 547.5nm, 555nm and 560nm) were observed and remained relatively strong throughout the thermal cycle. It was clear that these sublevels are temperature dependent and could be considered for use in future thermometry experiments.

Table 9.8 shows the denotations of the UIRs assigned to each intensity ratio and both the theoretical and calculated energy differences. The presentations of all the UIRs are shown in Figures 9.110 to 112. UIR_{23}^{64} was not ideal for temperature sensing as the curve only showed a small variation in the UIR. UIR_{12}^{64} & UIR_{13}^{64} showed a gradual increase but with a small increment in UIR with respect to temperature. For UIR_{24}^{64} & UIR_{34}^{64} shown a large change in intensity ratios is seen suitable for the lower temperature region. Once again the ΔE of the fitted and theoretical are not in agreement. Modification of the present equation 9.7 might be a way to improve the fit to cater for crystalline oxide based materials.

From the upconversion emission spectra, the integrated intensity from the transitions $^2H_{11/2}$ (520nm to 550nm) and $^4S_{3/2}$ (550nm to 570nm) could be used to calculate the UIR. Figure 9.113 shows that UIR_{AB}^{64} has a progressive increase with temperature. It was also observed that the maximum effective temperature was as high as 1473K. When UIR_{ABC}^{64} was plotted, it showed a monotonic line with no significant changes in the UIR therefore it was appropriate for thermometry applications.

Figure 9.101: Spec 64 $Y_2O3:Er^{3+}$ upconversion in room temperature, 293K

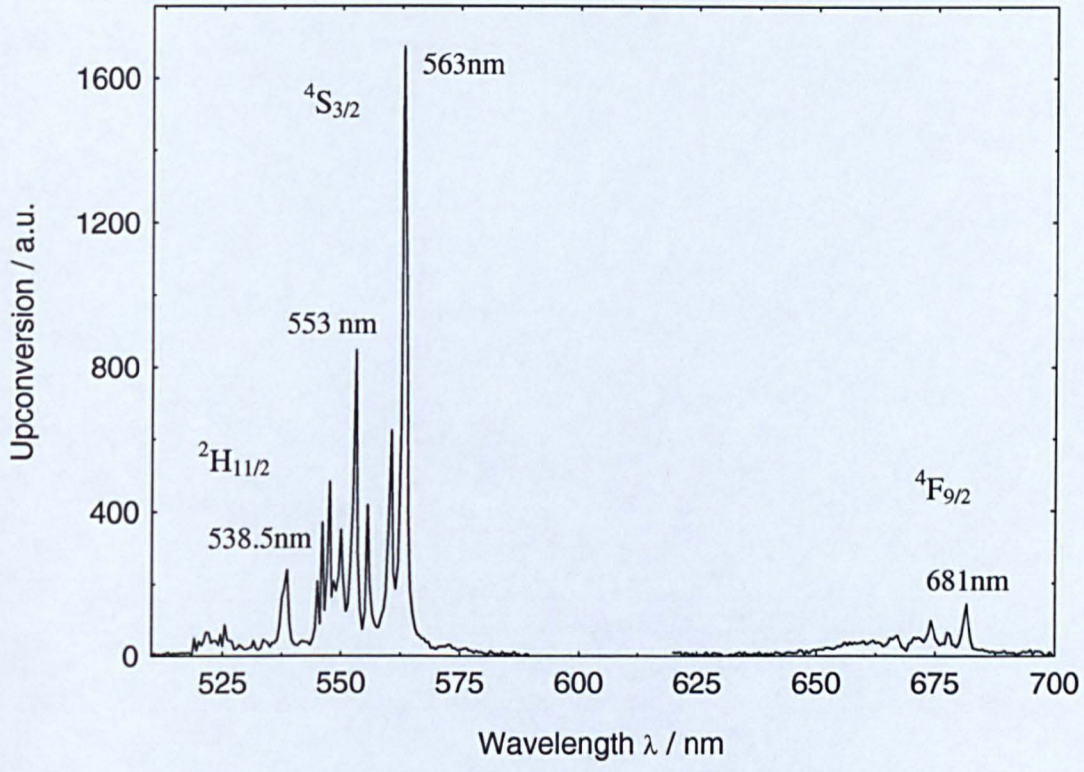

Figure 9.102: Spec 64 $Y_2O3:Er^{3+}$ upconversion spectra from room temperature to 1473K

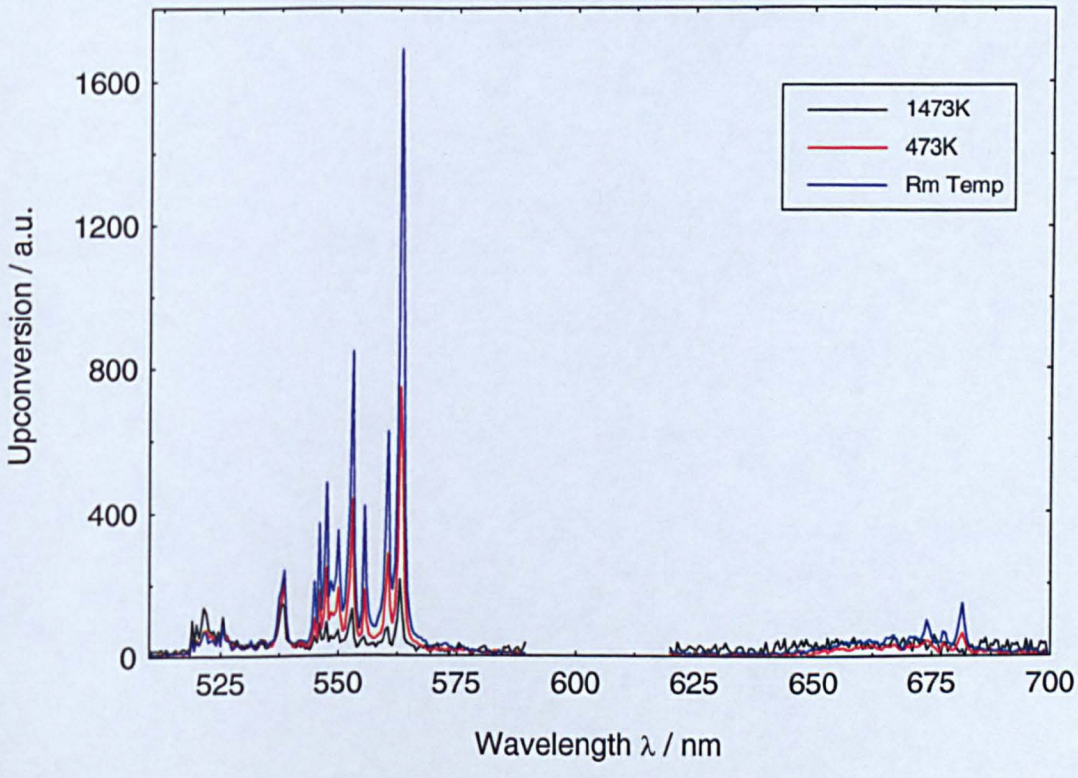

Figure 9.103: Spec 64 $Y_2O3:Er^{3+}$ upconversion spectra from room temperature to 873K, $^2H_{11/2} + {}^4S_{3/2}$

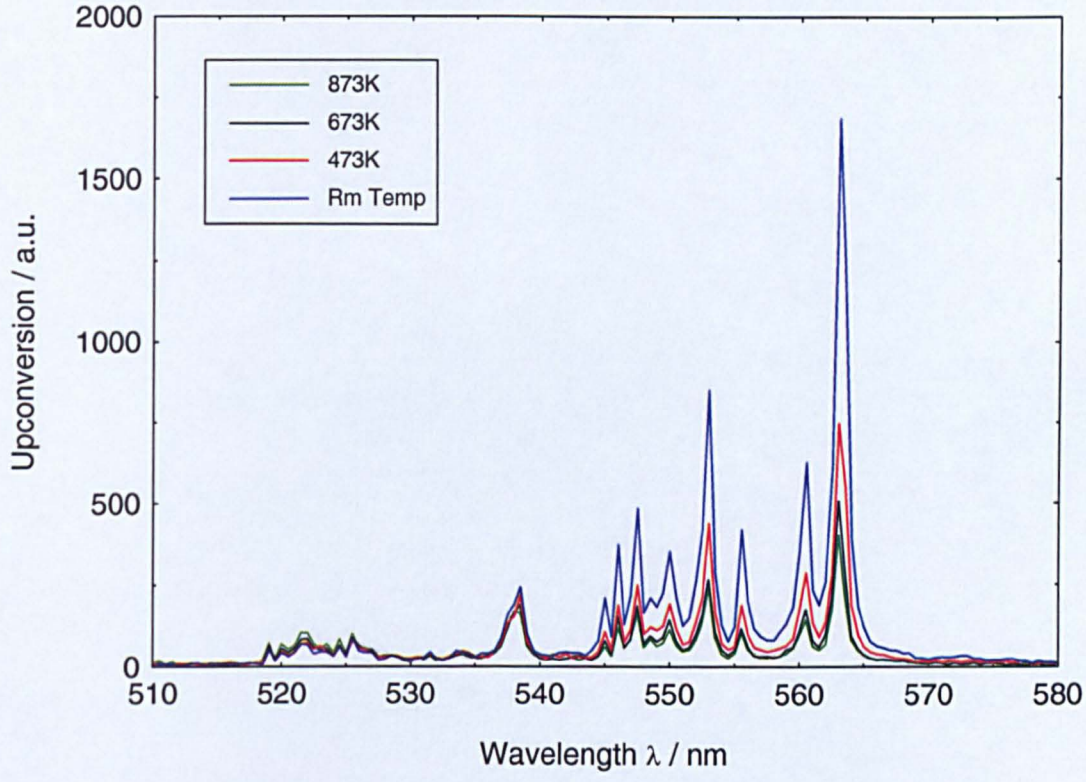

Figure 9.104: Spec 64 $Y_2O3:Er^{3+}$ upconversion spectra from room temperature to 1473K, $^2H_{11/2} + {}^4S_{3/2}$

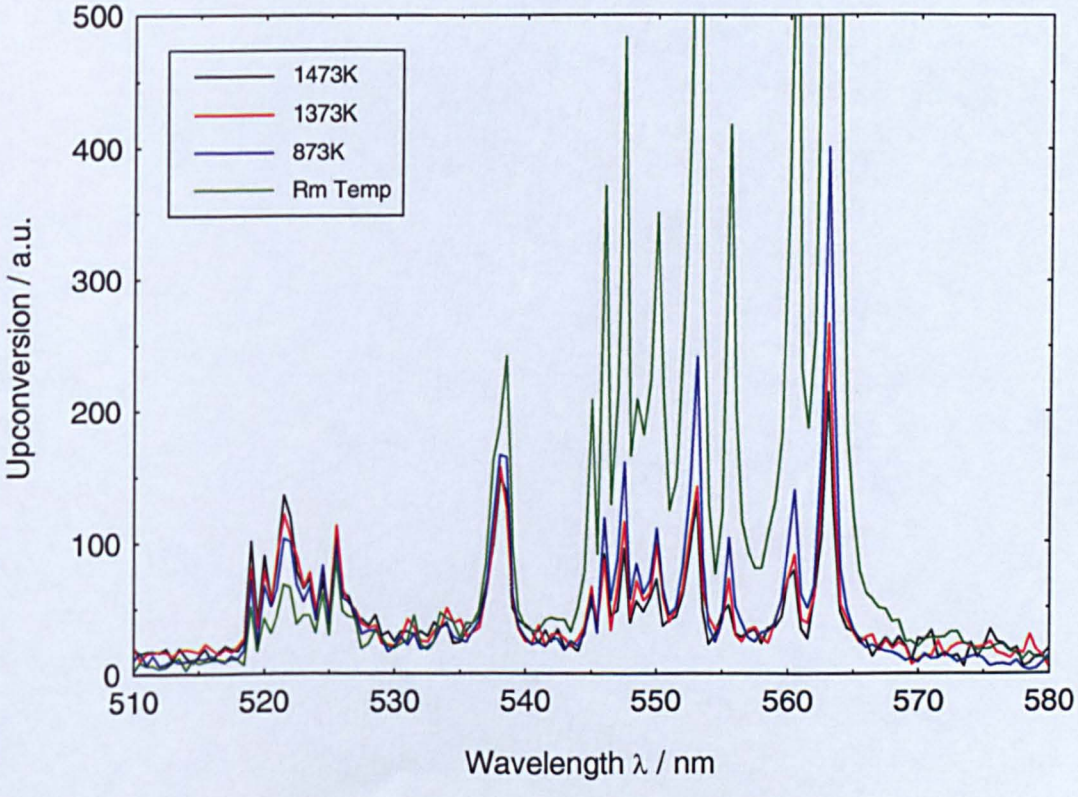

Figure 9.105: Spec 64 $Y_2O3:Er^{3+}$ upconversion spectra from room temperature to 773K, $^4F_{9/2}$

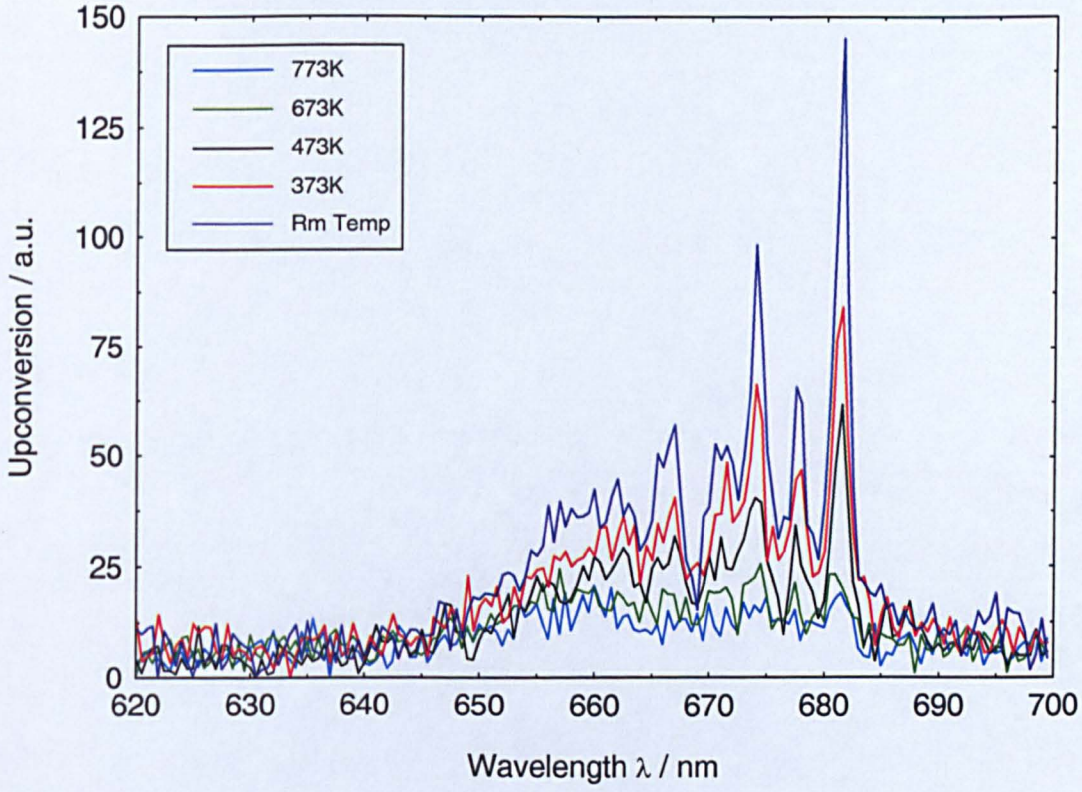

Table 9.8 – Spec 64:Y_2O_3:Er^{3+} temperature sensor UIR denotations

Denotations	Visible line	ΔE (cm^{-1})	
		Theoretical	Fitted
UIR_{12}^{64}	$I_{538.5}/I_{553}$	486.92	606.69
UIR_{13}^{64}	$I_{538.5}/I_{563}$	808.0	307.17
UIR_{23}^{64}	I_{553}/I_{563}	-	-
UIR_{24}^{64}	I_{553}/I_{681}	3398.87	1589.34
UIR_{34}^{26}	I_{563}/I_{681}	3077.68	1881.9

Figure 9.106: Spec 64 $Y_2O3:Er^{3+}$ - Integrated intensity at $^2H_{11/2}$, $^4S_{3/2}$ and $^4F_{9/2}$

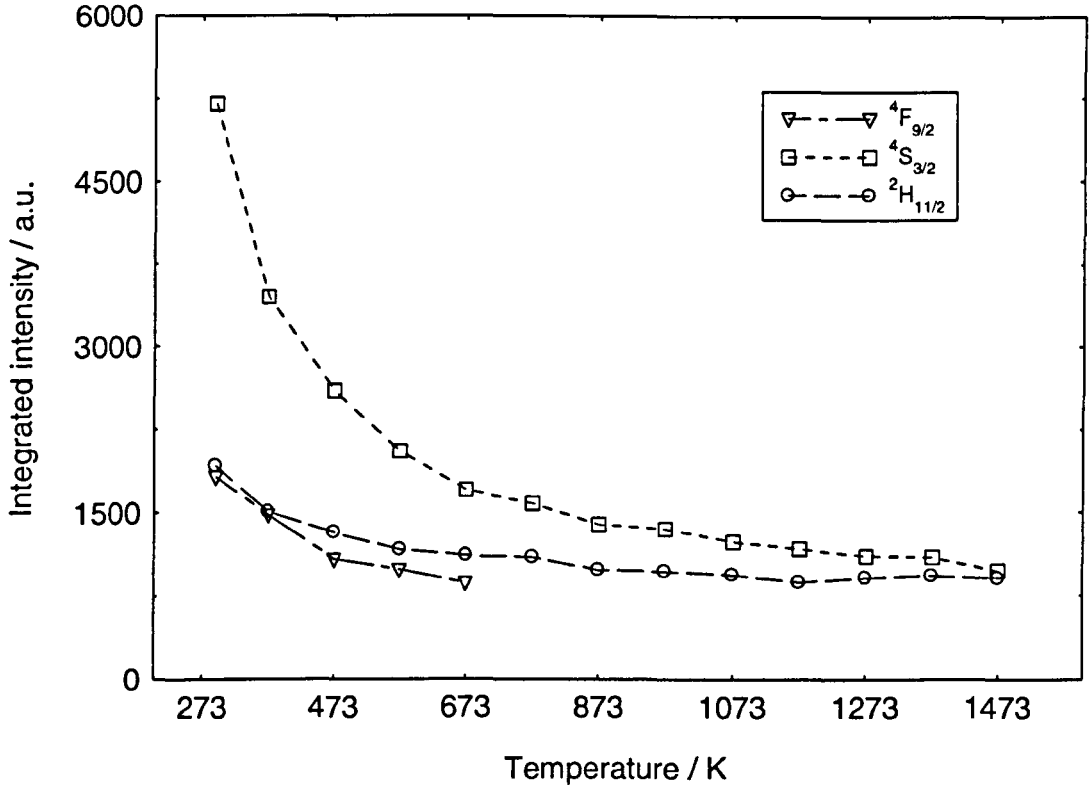

Figure 9.107: Spec 64 $Y_2O3:Er^{3+}$ intensity based sensing at 538.5nm ($I_{538.5}$)

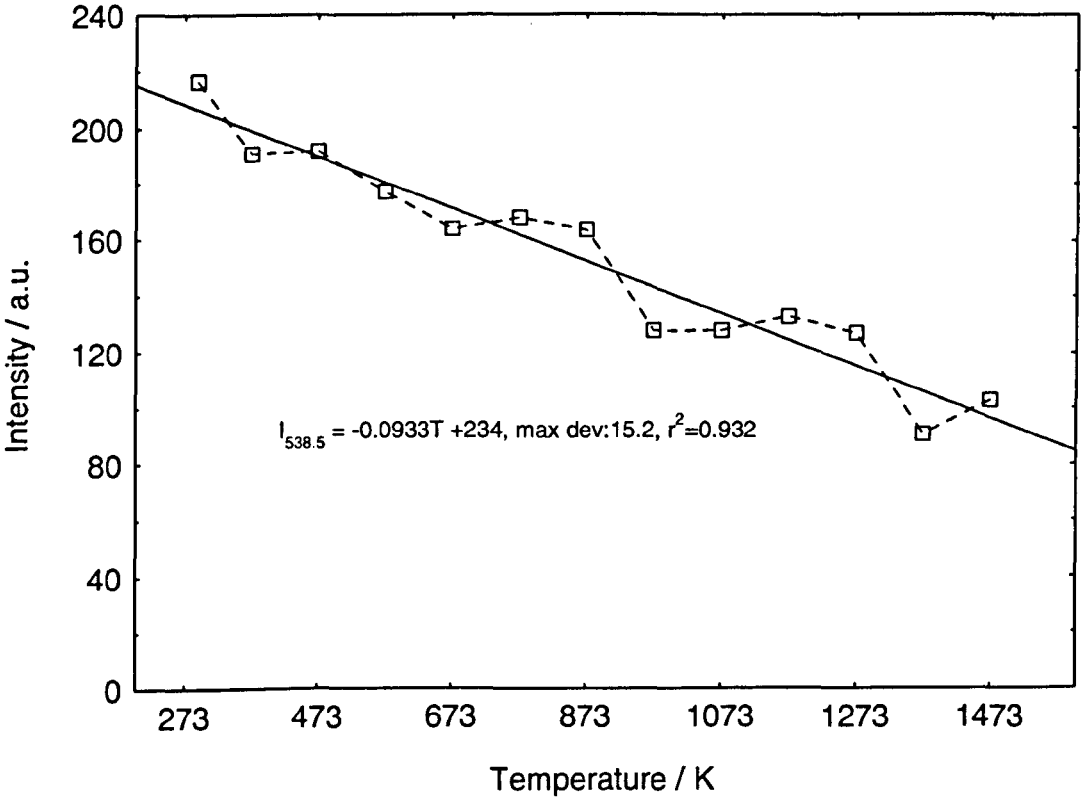

Figure 9.108: Spec 64 $Y_2O3:Er^{3+}$ intensity based sensing at 553nm and 563nm ($I_{538.5}$ & I_{563})

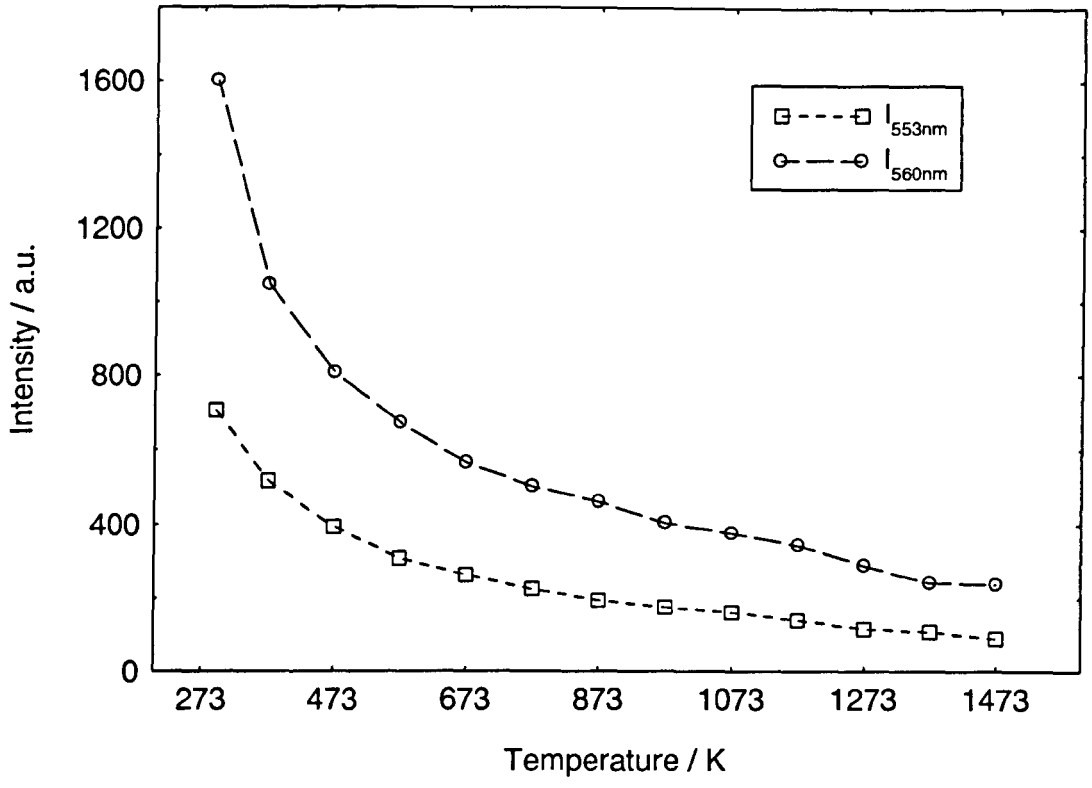

Figure 9.109: Spec 64 $Y_2O3:Er^{3+}$ intensity based sensing at 681nm (I_{681})

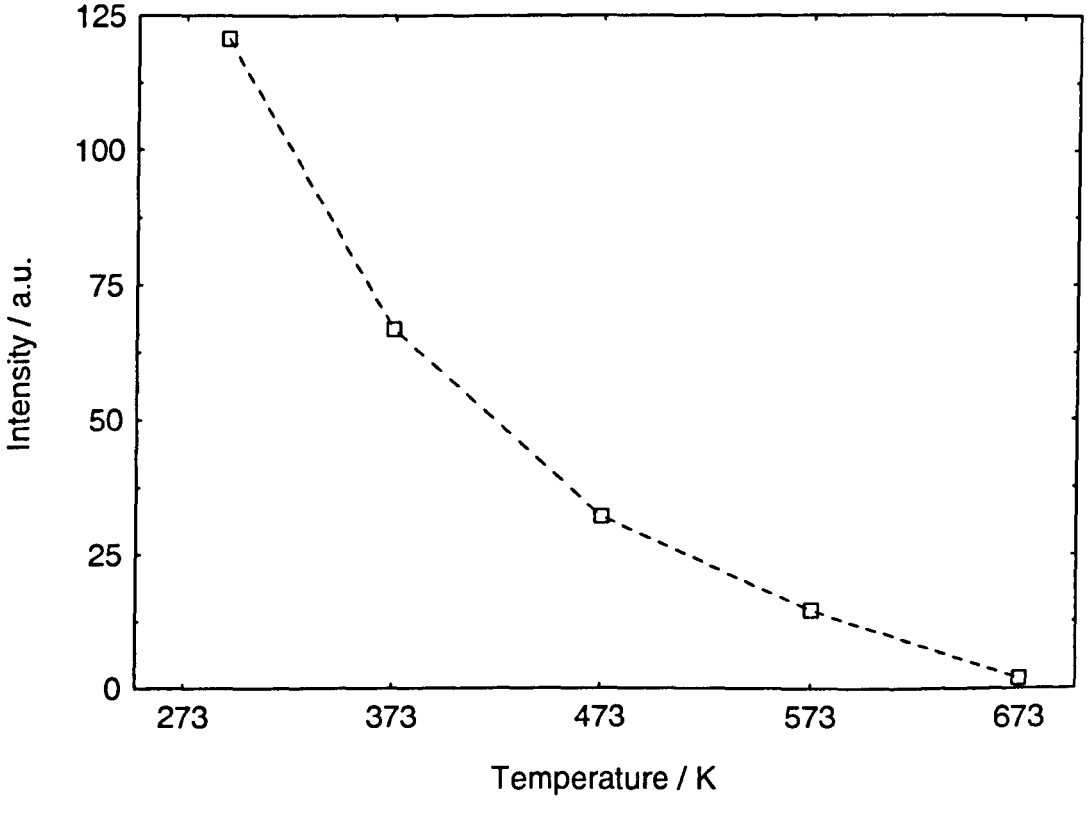

Figure 9.110: Spec 64 $Y_2O3:Er^{3+}$ UIR_{12}^{64} & UIR_{13}^{64} (actual and fitted with Eq 9.7) vs temperature

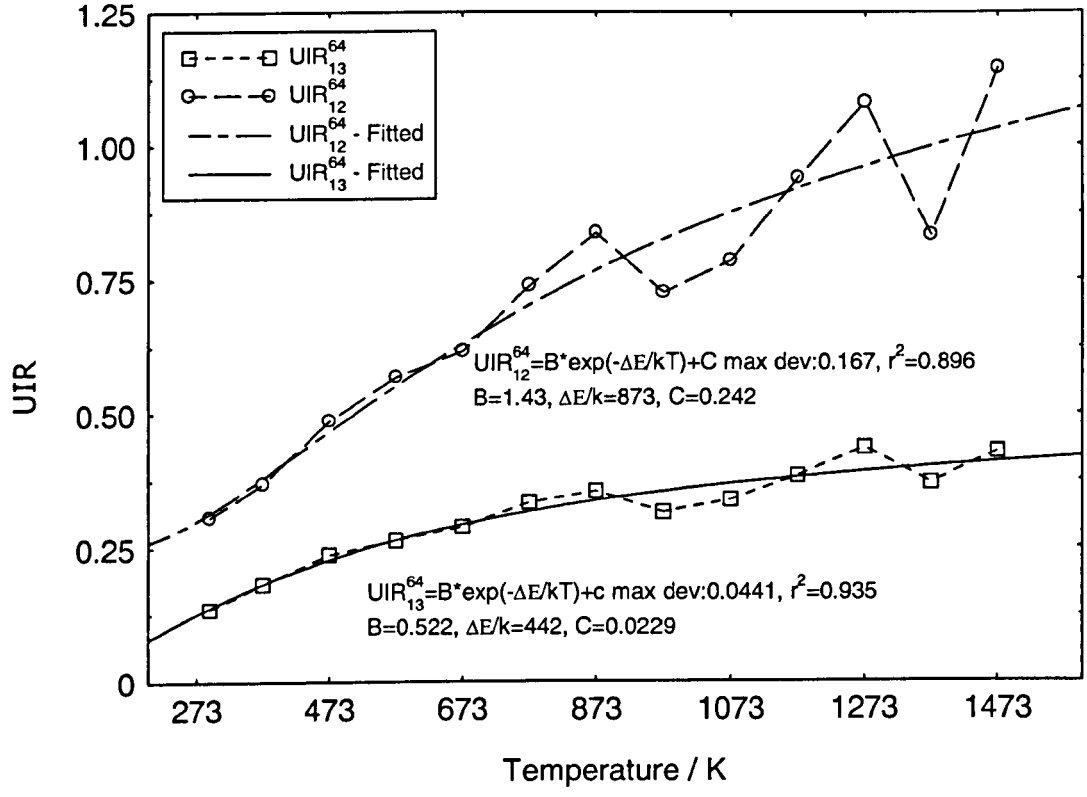

Figure 9.111: Spec 64 $Y_2O3:Er^{3+}$ UIR_{23}^{64} vs temperature

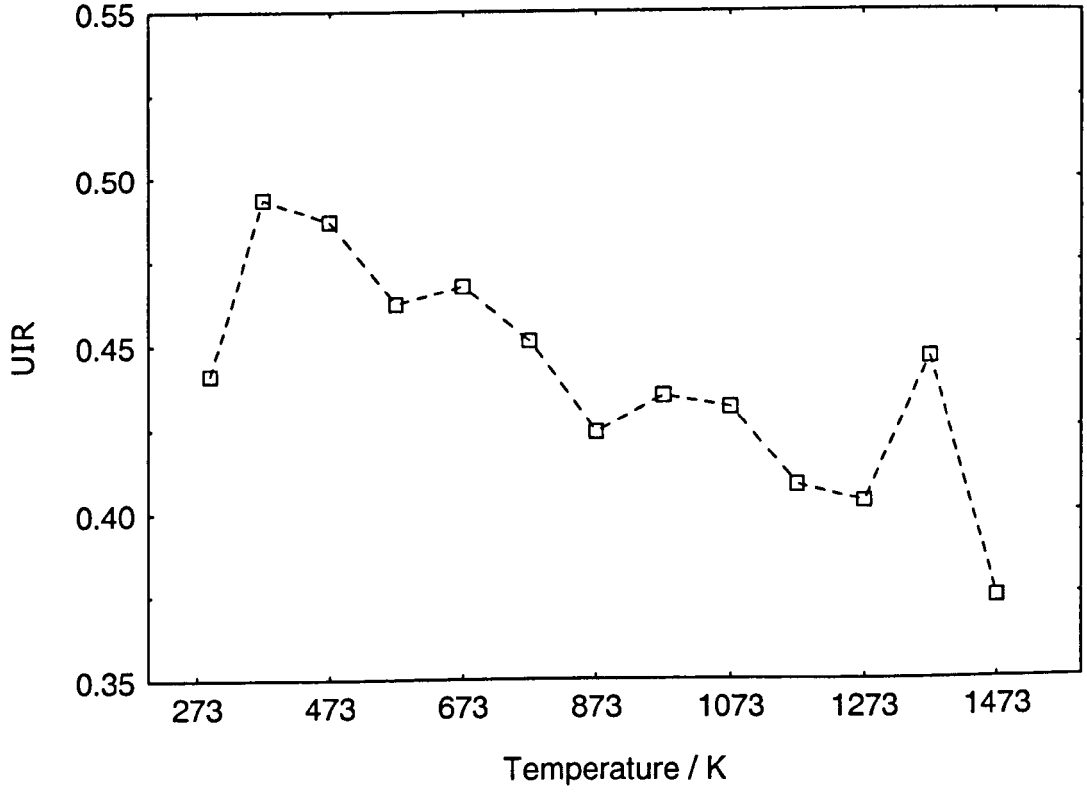

Figure 9.112: Spec 64 $Y_2O3:Er^{3+}$ UIR_{24}^{64} & UIR_{34}^{64} (actual and fitted with Eq 9.7) vs temperature

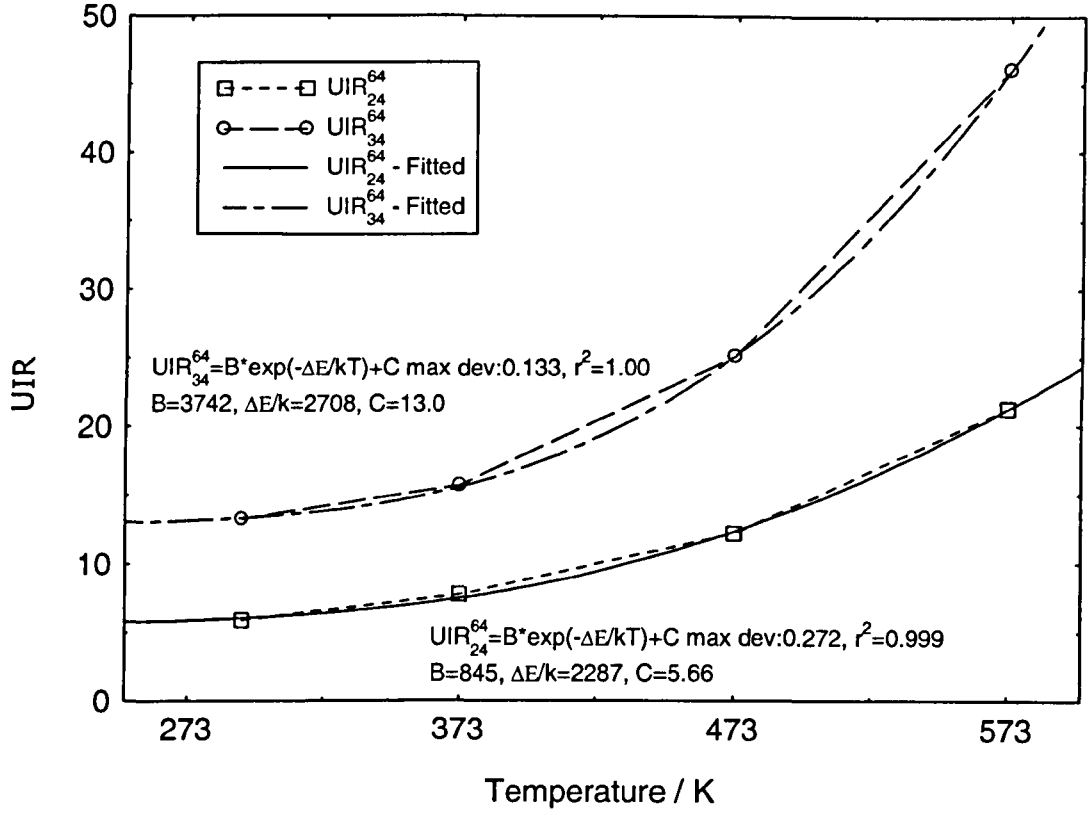

Figure 9.113: Spec 64 $Y_2O3:Er^{3+}$ UIR_{AB}^{64} (actual and fitted with Eq 9.7) vs temperature

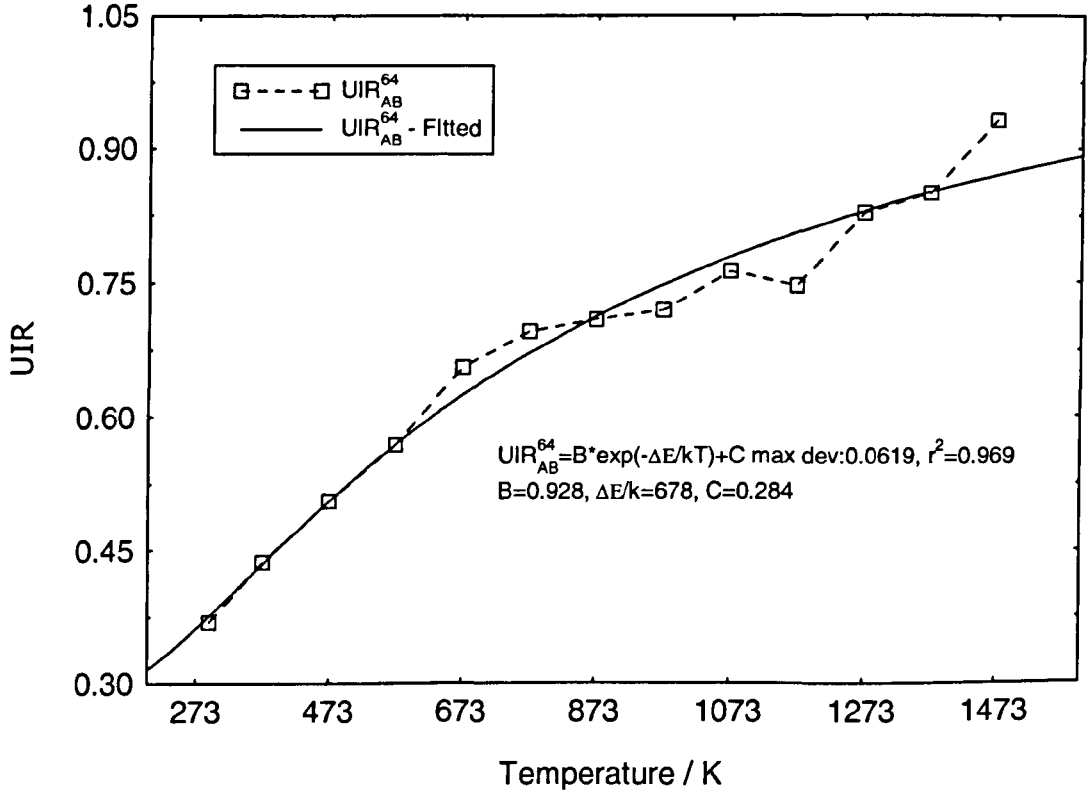

Figure 9.114: Spec 64 $Y_2O3:Er^{3+}$ UIR_{ABC}^{64} vs temperature

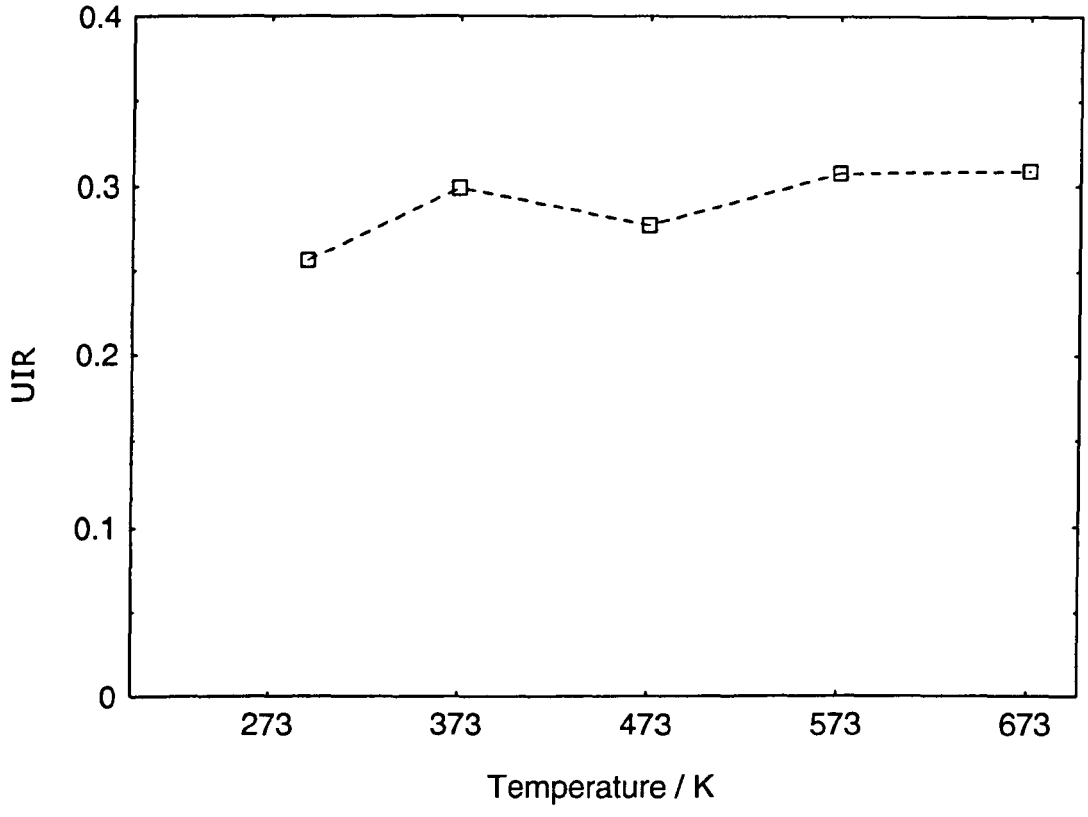

9.8.3 Fluorescence Decay Sensing – $Y_3O_3:Er^{3+}$

The fluorescence lifetime of the Er^{3+} ion is determined by the host material in which it is doped. There are differences when Er^{3+} is doped in silica fibre and silicon reported by *Zhang* [9.53]. The work presented in this thesis shows that under the influence of different host materials the fluorescence lifetime varies as shown in Chapter 6 and 7. Er^{3+} was doped in Y_2O_3, with a starting concentration of 2mol% and was investigated using the dependence of rare earth's lifetime on temperature to perform sensing applications under temperatures as high as 1473K. Similar to the results seen for YAG singly doped SCF several IR lines in $Y_2O_3:Er^{3+}$ were selected and closely monitored throughout the temperature range. Among the nine IR lines examined (Figure 9.85) four at 1010nm, 1028.5nm, 1530.5nm and 1550nm were selected for closer study. The remaining lines were not suitable due to the signal from the fibre being too weak. Among these four only those in the 1500 region were able to be effective up to 1473K whereas the others only have an effective maximum working temperature only up to ~973K.

9.8.3.1 Results and Discussion

The FD recorded was from the transitions $^4I_{11/2} \rightarrow {}^4I_{15/2}$ and $^4I_{13/2} \rightarrow {}^4I_{15/2}$, and all demonstrated single exponential decay curves, see Appendix B. Emission from the $^4I_{11/2}$ manifold consists of IR lines at 1010nm and 1028nm. Figures 9.115 and 116, show the lifetime at these points. It was observed that generally τ decreases as the increases temperature. The maximum temperature for observation of these two lines was ~973K, higher than this and the signal is obscured by noise and no lifetime can be recorded. The decrease in lifetime was approximately linear therefore attempt was made to fit a straight line to the plots. These fitted lines provide the best fit for these two fluorescence decay values. The sensitivity at 1010nm and 1028nm were 3.05μs/K and 3.52μs/K respectively. This is calculated by the slope of the fitted line. The maximum average τ value for this transition is ~3.4ms. The strongest fluorescence emission observed from the spectrum was in the 1500nm region. Figures 9.117 and 118, show the FD for the IR lines at 1530.54nm and 1550nm. The maximum effective range for these two emission lines were 1473K. The decrease in τ with temperature was similar to that seen in the singly doped YAG SCFs. A

possible reason for this was due to thermal quenching of the Er^{3+} ion in the fibre. The maximum error encountered for these IR lines was ~7%. Data was fitted using a least-square fit routine [9.49]. From the fitted curves, it was observed that the decrease in lifetime with increasing temperature has a more rapid decline at lower temperatures. The maximum difference in τ from 293K to 1273K was ~2.3ms which was the highest in the course of this work. Again silica doped Er^{3+} fibres still have a wider range of τ values ~6ms.

An estimation of the Er^{3+} dopant concentration in this SCF could be obtained from referring to data presented in Chapter 7. The τ value at room temperature was ~9.5ms which falls between 9.1ms for 0.3mol% and 10.4ms for 6mol%. A rough estimation of the dopant concentration within the fibre from it's lifetime can be determined. Using the FIR presented in section 9.4, another way of approximating the dopant level, estimates the concentration to be ~2mol% Er^{3+} in the SCF. From this work, YAG and Y_2O_3 fibres have approximately the same dopant concentration but there is a large difference in lifetime decay, which is in agreement with reference [9.53]. The general problem when using Y_2O_3 SCF as a temperature sensor was the presence of internal cracks within the fibre. This problem increases the losses and will therefore reduce its accuracy.

Figure 9.115: Spec 64 Y_2O_3:Er^{3+} fluorescence decay at 1010nm

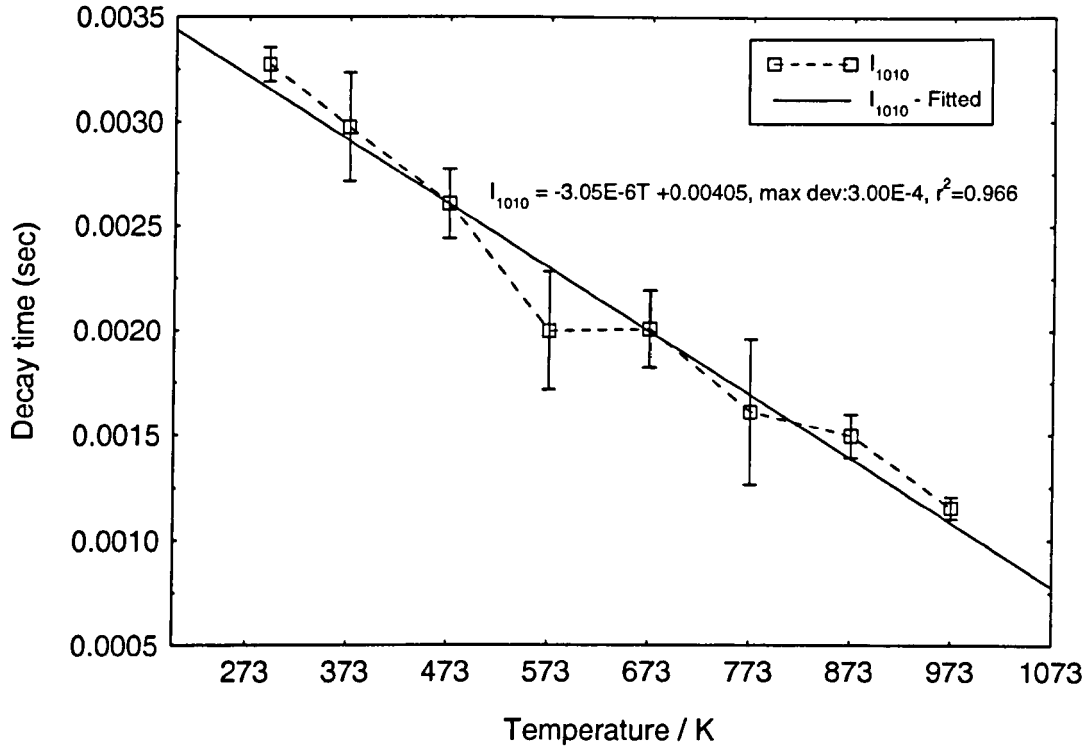

Figure 9.116: Spec 64 Y_2O_3:Er^{3+} fluorescence decay at 1028.5nm

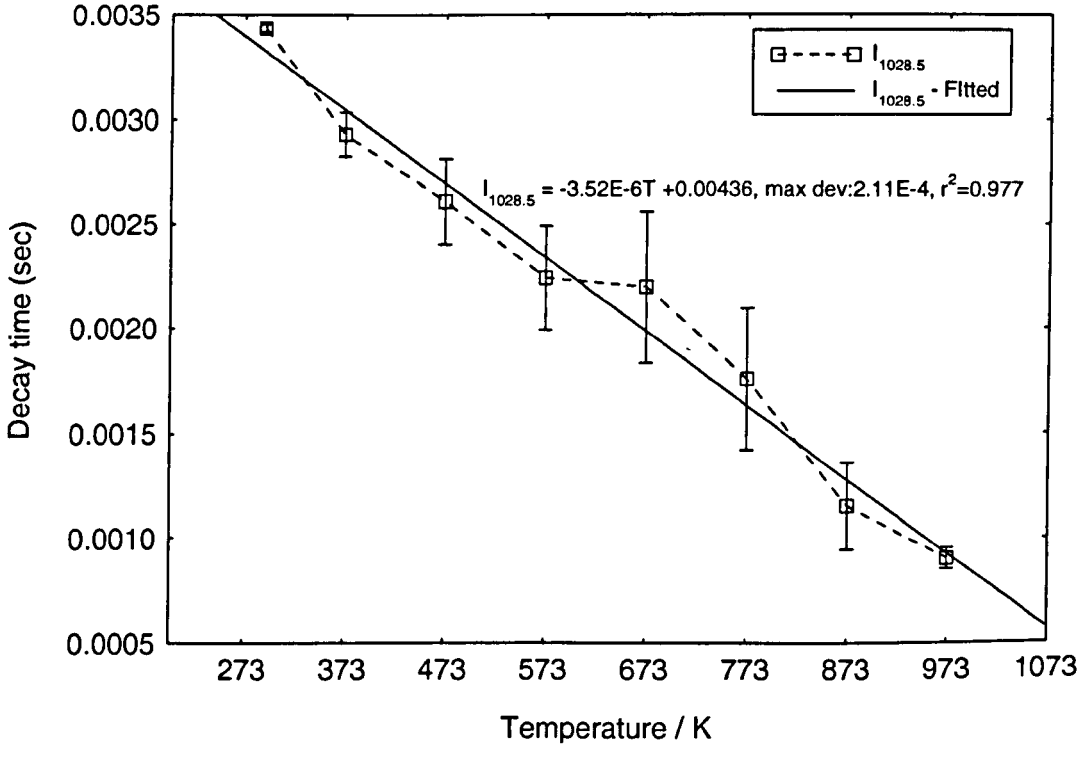

Figure 9.117: Spec 64 Y_2O_3:Er^{3+} fluorescence decay at 1530.5nm

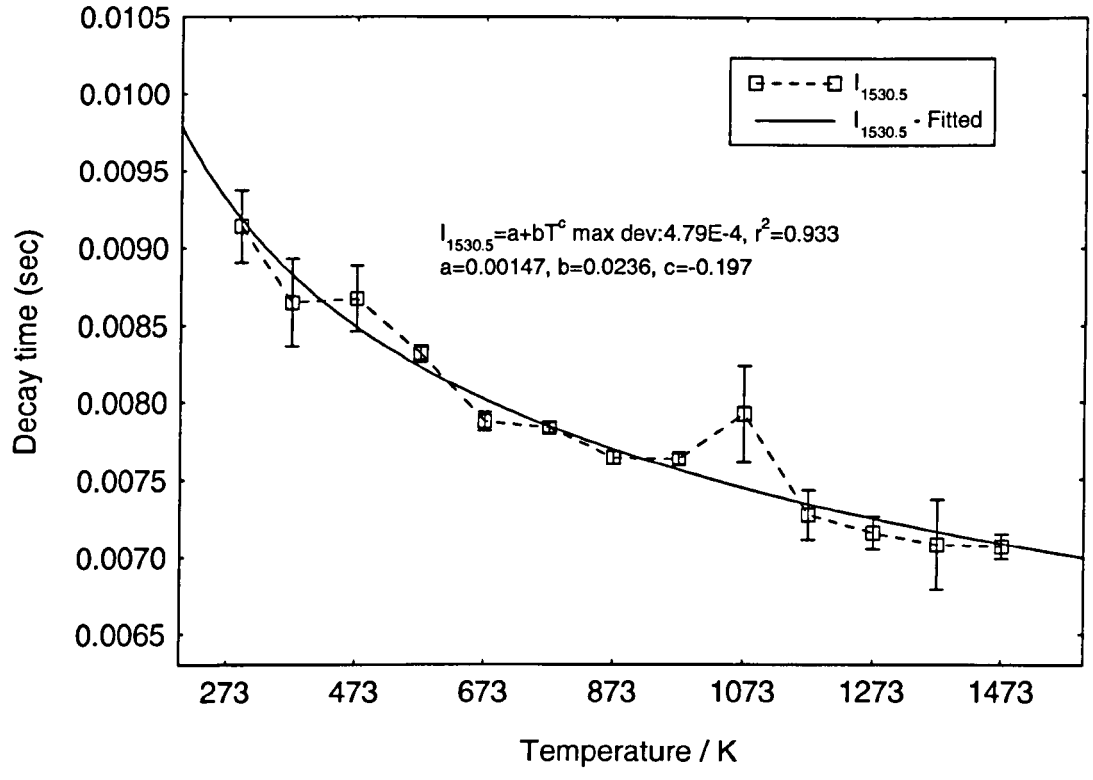

Figure 9.118: Spec 64 Y_2O_3:Er^{3+} fluorescence decay at 1550nm

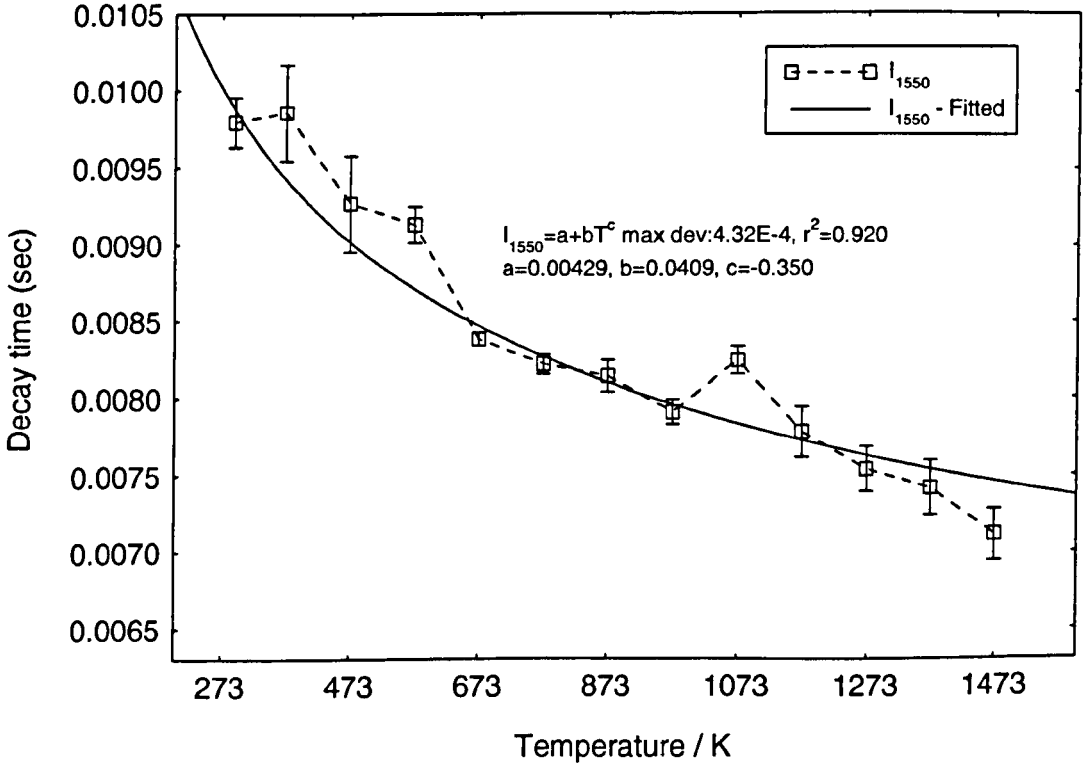

9.9 Reference

[9.1] K. T. V. Grattan and Z. Y. Zhang, *Fibre Optic Fluorescence Thermometry*, Chapman and Hall, 1995

[9.2] K .T. V. Grattan and T. Sun, *Fibre Optic Sensor Technology: An Overview*, Sensors and Actuators A, **82**, 1-3, 40, 2000

[9.3] M. Gottlied and G. B. Brandt, *Fiber-Optic Temperature Sensor Based on Internally Generated Thermal Radiation*, Appl. Opt., **20**, 19, 3408, 1981

[9.4] Z. Y. Znag, K. T. V. Grattan, A. W. Palemer and B. T. Meggitt, *Thulium-Doped Intrinsci Fibe Optic Sensor for High Temperature Measurements*, Rev. Sci. Inst., **69**, 9, 3210, 1998

[9.5] K. T. V. Grattan, Z. Y. Zhang, T. Sun, Y. Shen, L. Tong and Z. Ding, *Sapphire-Ruby Single-Crystal Fibre for Application in High Temperature Optical Fibre Thermometers: Studies at Temperature 1500°C*, Meas. Sci. Tech., **12**, 7, 981, 2001

[9.6] Y. Shen, W. Zhao, T. Sun and K. T. V. Grattan, *Characterisation of an Optical Fiber Thermometer Using Tm^{3+}:YAG Crystal, Based on the Fluorescence Lifetime Approach*, Sensors and Actuators A, **109**, 1-2, 53, 2003

[9.7] Y. Shen, W. Zhao, J. He, T. Sun and K. T. V. Grattan, *Fluorescence Decay Characteristic of Tm-Doped YAG Crystal Fibre for Sensor Applications, Investigated From Room Temperature to 1400°C*, J. Sensor IEEE, **3**, 4, 507, 2003

[9.8] T. Sun, Z. Y. Zhang, K. T. V. Grattan and A. W. Palmer, *Intrinsic Doped Fluorescence-Lifetime Based High Temperature Alarm*, Sensor and Actuators A, **76**, 1-3, 67, 1999

[9.9] S. Chen, A. W. Palmer, K. T. V. Grattan and B. T. Meggitt, *Extrinsic Optical Fiber Interferometric Sensor That Uses Multimode Optical Fibers: System and Sensing-Head Design for Low-Noise Operation*, Opt. Let, **17**, 10, 701, 1992

[9.10] Z. Y. Zhang, K. T. V. Grattan, A. W. Palmer and B. T. Meggitt, *Potential for Temperature Sensor Applications of Highly Neodymium-Doped Crystals and Fiber at Up to Approximately 1000°C*, Rev. Sci. Inst., **68**, 7, 2759, 1997

[9.11] A. D. Kersey, *A Review of Recent Developments in Fiber Optic Sensor Technology*, Opt. Fiber Tech., **2**, 3, 291, 1996

[9.12] G. B. Hocker, *Fiber-Optic Sensing of Pressure and Temperature*, App. Opt., **18**, 9, 1445, 1979

[9.13] T. G. Giallorenzi, J. A. Bucaro, A. Dandridge, G. H. Sigel, J. H. Cole, S. C. Rashleigh and R. G. Priest, *Optic Fiber Sensor Technology*, IEEE J. Quant. Elect., **18**, 4, 626, 1982

[9.14] D. A. Krohn, *Fibre Optic Sensors- Fundamental and Applications*, 3rd ed, Instrument Society of America, 2000

[9.15] F. Farahi, D. J. Webb, J. D. C. Jones and D. A. Jackson, *Simultaneous Measurement of Temperature and Strain: Cross-Sensitivity Considerations*, J. Light. Tech., **8**, 2, 138, 1990

[9.16] G. A. Ball, W. W. Morey and P. K. Cheo, *Fiber Laser Source/Analyzer for Bragg Grating Sensor Array Interrogation*, J. Light. Tech., **12**, 4, 700, 1994

[9.17] M. C. Farries, C. M. Ragdale and D. C. J. Reid, *Broadband Chirped Fibre Bragg Filters for Pump Rejection and Recycling in Erbium Doped Fibre Amplifiers*, Elect. Let., **28**, 5, 487, 1992

[9.18] F. Ouellette, *All-Fiber Filter for Efficient Dispersion Compensation*, Opt. Let., **16**, 5, 303, 1991

[9.19] R. Kashyap, R. Wyatt and R. J. Campbell, *Wideband Gain Flattened Erbium Fibre Amplifier Using a Photosensitive Fibre Blazed Grating*, Elect. Let., **29**, 2, 154, 1993

[9.20] I. J. Read and P. D. Foote, *Sea and Flight Trials of Optical Fibre Bragg Grating Strain Sensing Systems*, Smart. Mat. Structures, **10**, 5, 1085, 2001

[9.21] D. J. Webb, J. Surowiec, M. Sweeney and D. A. Jackson, *Miniature Fiber Optic Ultrasonic Probe*, Conf Fibre Optic and Laser Sensors XVI, Proc. SPIE, **2839**, 79, 1996

[9.22] G. Meltz, W. W. Morey and J. R. Dunphy, *Fiber Bragg Grating Chemical Sensor*, Chemical, Biochemical and Environmental Fiber Sensors III, Proc. SPIE, **1587**, 350, 1992

[9.23] A. D. Kersey and M. J. Marrone, *Fiber Bragg Grating High-Magnetic-Field Probe*, 10th Inter. Conf. Optical Fibre Sensors, Proc. SPIE, **2360**, 53, 1994

[9.24] M. G. Xu, J.-L. Archambault, L. Reekie and J. P. Dakin, *Discrimination Between Strain and Temperature Effects Using Dual-Wavelength Fibre Grating Sensors*, Elect. Let., **30**, 13, 1085, 1994

[9.25] W. W. Morey and G. Meltz, *High-Temperature Capabilities and Limitations of Fiber Grating Sensors*, 10th Inter. Conf. Optical Fibre Sensors, Proc. SPIE, **2360**, 234, 1994

[9.26] G. Meltz, W. W. Morey and W. H. Glenn, *Formation of Bragg Gratings in Optical Fibers by a Transverse Holographic Method*, Opt. Let., **14**, 15, 823, 1989

[9.27] K. O. Hill, B. Malo, F. Bilodeau, D. C. Johnson and J. Albert, *Bragg Gratings Fabrication in Monomode Photosensitive Optical Fiber by UV Exposure Through a Phase Mask*, App. Phy. Let., **62**, 10, 1035, 1993

[9.28] W. W. Morey, G. Meltz and W. H. Glenn, *Fibre Optic Bragg Grating Sensors*, Conf. Fibre Optics and Laser Sensors 7, Proc. SPIE, **1169**, 98, 1990

[9.29] J. P. Dakin, *Distributed Optical Fiber Sensors*, Distributed and Multiplex Fiber Optic Sensor II, Proc. SPIE, **1797**, 76, 1993

[9.30] M. K. Barnoski and S. M. Jensen, *Fiber Waveguides: A Novel Technique for Investigating Attenuation Characteristics*, App. Opt., **15**, 9, 2112, 1976

[9.31] A. D. Kersey, *Distributed and Multiplexed Fiber Optic Sensors*, Fiber Optic Sensors – Introduction for Engineers and Scientists, Ed (E. Udd), John Wiley & sons, Inc, 327, 1991

[9.32] R. Feced, M. Farhadiroushan, V. A. Handerek and A. J. Rogers, *A High Spatial Resolution Distributed Optical Fiber Sensor for High-Temperature Measurements*, Rev. Sci. Inst., **68**, 10, 3372, 1997

[9.33] Z. Zhang, K. T. V. Grattan and A. W. Palmer, *Temperature Dependences of Fluorescence Lifetimes in Cr^{3+}-Doped Insulating Crystals*, Phy. Rev. B, **48**, 11, 7772, 1993

[9.34] R. R. Sholes, J. G. Small, *Fluorescent Decay Thermometer with Biological Applications*, Rev. Sci. Inst., **51**, 7, 882, 1980

[9.35] Z. Zhang, K. T. V. Grattan and A. W. Palmer, *Fiber-Optic High – Temperature Sensor Based on the Fluorescence Lifetime of Alexandrite*, Rev. Sci. Inst., **63**, 8, 3869, 1992

[9.36] L. Ye, Y. Qiu, Y. Shen and S. He, *Fiber Thermometer Based on the Cross Detection of the Fluorescence Lifetime of Cr^{3+}:YAG Crystal Fiber and Plank's Blackbody Radiation from Cryogenic Up to 1400°C*, Adv. Sen. Sys. Appl., Proc. SPIE **5634**, 389, 2005

[9.37] Z. Y. Zhang, K. T. K. Grattan, A. W. Palmer, B. T. Meggitt and T. Sun, *Fluorescence Decay-Time Characteristics of Erbium-Doped Optical Fiber at Elevated Temperatures*, Rev. Sci. Inst., **68**, 7, 2764, 1997

[9.38] Z. Y. Zhang, K. T. K. Grattan, A. W. Palmer, B. T. Meggitt and T. Sun, *Characterization of Erbium-Doped Intrinsic Optical Fiber Sensor Probes at High Temperatures*, Rev. Sci. Inst., **69**, 8, 2924, 1998

[9.39] J. L. Kennedy and N. Djeu, *Energy Transfer in Rare Earth Doped $Y_3Al_5O_{12}$ at Very High Temperatures*, J. Lum., **101**, 1-2, 147, 2003

[9.40] S. A. Wade, S. F. Collins and G. W. Baxter, *Fluorescence Intensity Ratio Technique for Optical Fiber Point Temperature Sensing*, J. App. Phy., **94**, 8, 4743, 2003

[9.41] F. Sirdiroglou, S. A. Wade, N. M. Dragomir, G. W. Baxter and S. F. Collins, *Effects of High-Temperature Heat Treatment on Nd^{3+}-Doped Optical Fibers for Use in Fluorescence Intensity Ratio Based Temperature Sensing*, Rev. Sci. Inst. **74**, 7, 3524, 2003

[9.42] S. Baek, Y. Jeong, J. Nilsson, J. K. Sahu and B. Lee, *Temperature-Dependent Fluorescence Characteristics of an Ytterbium-Sensitized Erbium-Doped Silica Fiber for Sensor Applications*, Opt. Fiber Tech., **12**, 1, 10, 2006

[9.43] K. T. V. Grattan and A. W. Palmer, *Infrared Fluorescence "Decay-Time" Temperature Sensor*, Rev. Sci. Inst., **56**, 9, 1784, 1985

[9.44] T. Sun, Z. Y. Zhang, K. T. V. Grattan, A. W. Palmer and S. F. Collins, *Temperature Dependence of the Fluorescence Lifetime in Pr^{3+}:ZBLAN Glass for Fiber Optic Thermometry*, Rev. Sci. Inst., **68**, 9, 3447, 1997

[9.45] V. C. Fernicola, L. Rosss, R. Galleano, T. Sun, Z. Y. Zhang and K. T. V. Grattan, *Investigations on Exponential Lifetime Measurements for Fluorescence Thermometry*, Rev. Sci. Inst., **71**, 7, 2938, 2000

[9.46] Y. Imai and T. Hokazono, *Fluorescence-Based Temperature Sensing Using Erbium-Doped Optical Fibers with 1.48μm Pumping*, Opt. Rev., **4**, 1A, 117, 1997

[9.47] S.A. Wade, J. C. Muscat, S. F. Collins and G. W. Baxter, *Nd^{3+}-Doped Optical Fiber Temperature Sensor Using the Fluorescence Intensity Ratio Technique*, Rev. Sci. Inst., **70**, 11, 4279, 1999

[9.48] E. Maurice, G. Monnom, B. Dussardier, A. Saïssy and D. B. Ostrowsdy, *Thermalization Effects Between Upper Levels of Green Fluorescence in Er-Doped Silica Fibres*, Opt. Let., **19**, 13, 990, 1994

[9.49] A. K. Kewell, G. T. Reed and F. Namavar, *Integrated Temperature Sensor in Er-Doped Silicon*, Sensor and Actuator A, **65**, 2-3, 160, 1998

[9.50] H. Berthou and C. K. Jörgensen, *Optical-Fibre Temperature Sensor Based on Upconversion-Excited Fluorescence*, Opt. Let., **15**, 19, 1100, 1990

[9.51] P. V. dos Santos, M. T. de Araujo, A. S. Gouveia-Neto, J. A. Medeiros Neto and A. S. B Sombra, *Optical Thermometry Through Infrared Excited Upconversion Fluorescence Emission in Er^{3+}- and Er^{3+}-Yb^{3+}-Doped Chalcogenide Glasses*, J. Quant. Elect., **35**, 2, 395, and 1999

[9.52] S. W. Allison, G. T. Gillies, *Remote Thermometry with Thermographic Phosphors: Instrumentation and Applications*, Rev. Sci. Inst., **68**, 7, 2615, 1997

[9.53] Z. Y. Zhang, T. Sun, K. T. V. Grattan and A. W. Palmer, *Erbium-Doped Intrinsic Fibre Sensor for Cryogenic Temperature Measurement*, Sensors and Actuators A, **71**, 3, 183, 1998

10 Conclusion and Future Work

10.1 Conclusion

The growing interest in the area of Single Crystal Fibres (SCF) and their applications has being the main driving force of this project. Incorporating different dopant concentrations of rare earths into SCFs in order to have a clear understanding of the effects of different oxides was another area of motivation. Basically, this work can be divided into three major sections. The first of which was the employment of the laser hearted pedestal growth (LHPG) system to grow SCFs. Studies were carried to demonstrate the possibility of using the present technique to grow different oxide based SCF materials that are doped with different rare earths of various concentration levels. Secondly, to characterise the grown fibres. The third and last section was to apply these SCFs in practical aspects.

One of the many reasons for choosing LHPG was that it is a versatile crystal growth technique. With the ease of preparation, this technique is able to be employed to grow a large variety of materials ranging from oxide, fluoride, eutectics, etc. The present system follows the model designed by Stanford University. It consists of a 30W CO_2 laser and various optics that deliver the laser to the source material. The pull and feed mechanisms are driven by precision DC motors. The holding devices for the seed fibre had been modified and have greatly improved the alignment during the growth process. Three materials (Y_2O_3, Al_2O_3 and $Y_3Al_5O_{12}$) were investigated and the source materials used for growth were either from bulk material or cold pressed powders. The half pellet method was used to produce a fibre that is monolithic where only the tip of the fibre was doped with rare earth. The size of the square rods cut from the pressed pellets were required to be relatively small (~0.8 x ~0.8 x ~13mm) so that they could be fitted in a miniature chuck. It was observed during the growth process of Al_2O_3 and $Y_3Al_5O_{12}$ that bubbles were evident in the melt. The melt became unstable when the dopant concentration level increased. For Al_2O_3 fibres, this instability happens when Er^{3+} dopant concentrations were at 1mol%. The fibres produced at concentrations higher than 2mol% would opaque and be pinkish in colour. $Y_3Al_5O_{12}$ fibres had a higher acceptance of rare earth content. Only when dopant levels reached 15mol% would the melt become unstable and

clouding would then be evident in the fibres. This cloudiness is formed by microviods that appear in the fibres. Y_2O_3 fibres were highly receptive to rare earth doping. The highest doping concentration used in this work was 59mol% for Y_2O_3. Although the physical appearance of the fibre at this concentration was pink, no instability in the melt was observed throughout the growth process. Among the three oxide materials investigated, Y_2O_3 was the most brittle and internal cracks were common for all concentration levels. Defects like inclusions and ridges were seen on the surface of the fibres due to CO_2 laser power instability. Irregularities in diameter along the fibres were observed for fibres with a diameter ~300μm and above. Fluctuation of the laser tends to take place at higher powers. Since larger diameters require higher powers to grow this explained the inconsistency of the diameters encountered.

$Y_3Al_5O_{12}$ SCFs grown had diameters ranging from ~390μm to ~420μm. Physical and optical characterisation was carried out on these fibres. During the physical characterisation, results revealed that these fibres had a shear strength of ~2.3MPa when a three-point bending test was carried out. The knowledge of the absorption wavelengths was used in identifying the type of excitation source needed to induce fluorescence. Observation was made that the absorption spectra changed under the influence of different rare earths and their concentrations. Er^{3+} singly doped fibres experience broadening of their linewidths, especially in the $^4I_{13/2}$ level, when the dopant concentration increases from 0.5 to 10mol%. When Yb^{3+} was co-doped in YAG, linewidth broadening from ~900nm to ~1050nm was observed. This suggested that the energy transfer efficiency when pumped at this wavelength would increase. Fluorescence emission was observed when the fibres were excited by a 975nm pump source and the 'five finger' spectrum profile which is characteristic of Er^{3+} in YAG was seen in the 1600nm region. Increasing the dopant concentration causes distortion within the lattice of the crystal that resulted in the broadening effects seen. When co-doped with Yb^{3+}, emission at the $^4I_{11/2}$ level was observed and increasing the concentration of Yb^{3+} increased the fluorescence intensity from this level. Green emission from the fibres was the telltale sign of the presence of upconversion. Experiments were carried out to characterise the emission in the visible region. Under the influence of higher Er^{3+} and Yb^{3+} concentrations the red emission intensity was seen to increase. The emission from $^2H_{11/2}$ + $^4S_{3/2}$ (green region) were the

strongest for all concentration levels. The fluorescence decay lifetime for these fibres was investigated and single exponential curves were seen for all fibres. Increasing dopant concentration levels in this work did not result in concentration quenching but an increase in lifetime from 6.5ms at 0.5mol% to 8ms at 10mol% was observed.

Special care was required when handling the Y_2O_3 SCFs due to their brittleness. With a shear strength of only ~0.71MPa, it was physically the weakest of the three oxide materials investigated in this work. Diameters of the fibres grown ranged from ~390μm to ~430μm. Being a tough material with a high melting temperature of 2450°C, high quality fibres were difficult to grow due to the limitation of the laser's power. The advantage of this oxide was its acceptance of rare earth dopants. Fibres were doped with Er^{3+} ions from 0.03 to 59mol%. Linewidth broadening was seen as the concentration levels increased and especially at 59mol% in the transition $^4I_{13/2}$ which had a linewidth of 174nm. Similar broadening effects were also observed throughout the wavelengths investigated as dopant levels increased. The merging of narrow peaks resulted in the formation of wider linewidths, possibly caused by the inhomogeneous broadening under the strong influence of the presence of Er^{3+} ions. Under excitation by a 965nm laser a strong fluorescence emission from the $^4I_{13/2}$ transition was seen and at a concentration of 3.1mol% and above an increase in the intensity from the $^4I_{11/2}$ transition was also witnessed. At 59mol%, the telecommunication emission line at 1550nm was no longer seen but the 1600nm region experienced an overlapping of emission lines which resulted in broadening of the linewidth. At low dopant concentrations, emission in the red region was extremely weak. Increasing the Er^{3+} level also increased the red emission in the visible region. Visible green light was seen emitting from the fibre but orange/reddish colour was seen with the 59mol% fibres. Y_2O_3 doped Er^{3+} fibres have a slower lifetime when compared to YAG fibres. At 0.03mol%, the decay was found to be 7.4ms and at 6mol% was 12.4ms. Fluorescence quenching was observed at 59mol% where the decay decreases to 1.7ms.

Growth of Al_2O_3 fibres was carried out as an initial 'test' material to examine LHPG using open loop control. Among the three materials studied Al_2O_3 was the easiest to grow therefore making it the ideal testing material. $Al_2O_3:Cr^{3+}$ (ruby) fibres grown had diameters of ~200μm and did not have any surface irregularity. The laser power

required to grow these fibres was ~11W and at this setting the fluctuation in laser power was minimal therefore resulting in good quality fibres. These fibres have the highest shear strength (~5MPa) when compared with YAG and Y_2O_3 fibres. Absorption and fluorescence characterisation was done for the ruby fibres and bulk material. The absorption and emission profiles were similar for the two ruby fibres and bulk materials.

Investigations were carried out on the use of YAG singly and co-doped fibres, and Y_2O_3 singly doped fibres as temperature sensors. Methods such as fluorescence intensity ratio (FIR), upconversion intensity ratio (UIR), fluorescence decay (FD) and emission intensity were examined as a function of temperature. All three types of fibre exhibited qualities which could be employed as fibre sensors for high temperature measurement. $Y_3Al_5O_{12}:Er^{3+}$ fibre sensing using the FIR method was seen to have several IR lines that could be used in thermometry sensing. Generally, the majority of the FIR curves experience an intensity ratio increment under the influence of increasing temperature where the theoretical curve can be easily fitted to the experimental results. IR line at 1528nm and 1568nm were the most ideal for they were able to detect temperatures ranging from ~273K to ~1473K whereas some were either effective at lower temperatures or only at higher temperature ranges. The introduction of Yb^{3+} did not see much improvement in thermal behaviour compared to that of the singly doped YAG fibres. With the addition of Yb^{3+} ions, fluorescence emission in the $^4F_{5/2}$ transition was observed. When the peak at 1027nm was used for the intensity ratio measurement, an exponential decay curve was seen. These curves were only effective at the lower temperatures. As for Y_2O_3 SCFs temperature sensing, experiments showed that the IR lines at 1530.5nm and 1550nm had potential for temperature sensing. The majority of the FIRs investigated for this material were either effective in the lower or higher temperature regions only.

Upconversion emission, for three types of fibres, in the green and the red regions were temperature dependent. For the YAG based fibres, as temperature rises, it was observed that there was a slight increase in $^2H_{11/2}$ emission. $^4S_{3/2}$ emission experiences an 'exponential decay' type of decrease in intensity as the temperature increases. This response in the green emission can be employed for temperature sensing. The thermal behaviour of emission in the visible region was similar for the

singly and co-doped YAG fibres. For Y_2O_3 SCF, when using the temperature dependence of the green and red emission, the maximum effective working temperatures were ~1473K and ~673K, respectively. The red emission intensity was dominated by noise at high temperatures and it was not possible to detect any reasonable signal.

FD dependence on temperature was investigated. The difference between the lifetime at low and high temperatures for the YAG singly doped and co-doped, and Y_2O_3 SCFs were ~0.98ms, ~1.2ms and ~2.3ms, respectively. Particularly for YAG singly doped SCFs, the noise level in the FD experiment was relatively low. Decay at 1612nm had a sensitivity of ~1.17 μs/K. As for Y_2O_3 SCFs, only four IR lines were employed due to the poor signal-to-noise ratio. IR lines at 1010nm and 1028nm have an effective measuring temperature up to 1073K whereas 1530.5nm and 1550nmn were able to measure up to 1473K.

10.2 Future Work

Insufficient CO_2 laser power was the major problem encountered during growth of Y_2O_3. It is extremely difficult to grind the cold pressed source rod down and most of the commercial fibre source materials are of diameters around 1mm. The present CO_2 laser cannot handle high refractory materials that are larger than 1mm. It would be ideal to have a higher power CO_2 laser of approximate 100W so that a wider variety of materials can be studied. Replacement by a higher power laser would also eliminate fluctuation problems caused by the present laser. All fibres in this work were grown without a closed loop diameter monitoring system. At present final quality is greatly dependent on the experience of the person growing the fibres but there are obvious limitations. Having a closed loop control system that is able to communicate with the laser power, pull and feed mechanism, and the x-y control would improve the quality of the fibres grown. With this system in place, by monitoring the changes of diameter during the growth, adjustment of the other parameters could be made accordingly so that high quality fibre diameters can be achieved. Another area for improvement would be the limitation of the present pull mechanism where only a short length of fibre can be grown. Modifying the pull/feed mechanism into a continuous belt configuration would help to increase the length of

the grown fibres. Monitoring CCTV can be used to replace the viewfinders that are used presently. It is extremely tiring for one to view through the viewfinders for a long period of time and also one can only monitor one direction at a time. These problems could be solved using cameras to monitor the two axes simultaneously and also the capability of recording the growth process for future studies would be of advantage.

Sol-gel was another area that was of interest in the cladding of the present SCFs grown by LHPG. Relatively high transmission losses were evident in the present fibres. The growth system is not able to grow or coat a cladding on the crystal fibres therefore one method of doing so would be to use the sol-gel method. Work is currently in progress investigating the use of alumina thin-film coatings through sol-gel techniques. This 'cladding' by dip-coating is put onto the fibres to reduce losses and also act a form of protection to the core fibres. Alumina was chosen due its high temperature resistance where it can be employed in the thermometry. The difficulty of this work is the inability to increase the thickness of the alumina film on the fibres but surely this is an area worth investigating.

Further improvement can be done on the coupling system between the fibres and the present equipment required for the temperature or other experiments. Improvement of the growth system would give quality fibres which could then be properly connected to commercial couplers. This would greatly improve the signal-to-noise ratio and also make the fibres more commercially viable. For the dopant concentration studies in this work, a deeper study could be carried out to further understand the actual amount of concentration entering the fibres and the losses of the dopant. Ways of approaching this can be carried out through physical studies using SEM. Finally it would be interesting to look at monolithic upconversion lasers. Success has been seen in doping fibres through cold pressing by the half pellet method discussed in this work. Using the same method one could produce Al_2O_3 fibres that are on one end Ti^{3+} and the other Er^{3+}. The green visible emission from the Er^{3+} can then be used to excite the Ti^{3+} ion on the other end of the fibre.

Appendix A

Table A1 – Materials growth by LHPG

Materials	Common Name	Melting Point (°C)	Orientation	Diameter (μm)	Application
Oxide					
Al_2O_3	Sapphire	2045	a, c	55 – 800	Beam Delivery[1]
$Al_2O_3:Cr^{3+}$	Ruby	2045	C	3 – 170	Laser[1]
$Al_2O_3:Ti^{3+}$	Ti:sapphire	2045	C	200 – 800	Laser[1]
BaB_2O_4	BBO	1095		500	NLO[1]
$BaTiO_3$	Barium Titantate	1618	c (Hex phase)	300 – 800	Ferroelectric[1]
$BaTiO_3$	Barium Titantate	1618	c (Cubic phase)	300 – 800	Ferroelectric[1]
$B_{12}SiO_{20}$	BSO		[011], [001]	650 – 1200	Photorefractive[4]
$B_{12}TiO_{20}$	BTO		[011], [001]	650 – 1200	Photorefractive[4]
$CaSc_2O_{20}$		2200	a, b, c	100 – 600	Model[1]
$CaSc_2O_{20}$:Nd		2200	c	600	Model[1]
$Gd_2(MoO_4)_3$		1157	[110]	200 – 600	Ferroelastic[1]
$Gd_3Sc_2Al_3O_{12}$	GSAG	1900		800	Laser[1]
$K_3Li_{2-x}Nb_{5+x}O_{15+2x}$	KLN		a	500	NLO[9]
$K_3Li_{2-x}Nb_{5+x}O_{15+2x}$	Nd:KLN		a	500	NLO,Laser[9]
$KTa_{1-x}Nb_xO_3$	KTN	<1370	[100]	600	Photorefractive[3]
$LaMgAl_{11}O_{19}$		1700 – 2000	c	100 – 600	Laser[1]
Li_2GeO_3		1170	a, c	100 – 600	Raman[1]
L_2O-$3B_2O_3$	LBO	834		200	NLO[6]
$LiNbO_3$	Lithium Niobate	1260	a, c	20 – 800	NLO, SAW[1]
$LiNbO_3:Nd^{3+}$		1260	c	600	Laser[1]
$LiNbO_3$:MgO		1260	a, c	50 - 200	NLO, Laser Host[8]
$LiTaO_3$	Lithium Tantalate	1650	[110]	600	SAW[1]
$LiYF_4$:Nd	Nd:YLF	825		1000 – 3000	Laser[5]
$LiYF_4$:Tm	Tm:YLF	825		1000 – 3000	Laser[5]
Lu_2O_3:Cr		2400	c, [110]	600	Laser[1]
$MgAl_2O_4$:Ti		2150		1000	Laser[1]
Mg_2SiO_4:Cr	Cr: forsterite	1890		700	Laser[7]
Nb_2O_5		1495		700 – 1700	Optical Prop.[1]
Nd_2SiO_5		1980		750	Laser[1]
Sc_2O_3:Cr		2400	c, [110]	600	Laser[1]
$SctaO_4$		2300	a	200 – 600	Ferrolelactric[1]
$ScNbO_4$		2100		200 – 600	Ferrolelactric[1]
$SrBaNb_2O_6$		1700	a, c	200 – 600	Ferrolelactric[1]
$SrBaTi_2O_6$		1500	a, c	600 – 1700	Photorefractive[1]
Sr_2RuO_4			[001]	800	Superconductor[2]

$SrSc_2O_4$		2200		600	Model[1]
$SrTiO_3$	Strontium Titanate	1860		600	Optical Prop[1]
TiO_2		1850		500 – 1000	Material Study[1]
$YAlO_3$:Ti	Ti:YAP	1875		500 – 1000	Laser[1]
$Y_3Al_5O_{12}$	YAG	1940	[111], [100]	100 – 1000	Model[1]
$Y_3Al_5O_{12}$:Nd	Nd:YAG	1940	[111], [100]	6 – 1000	Laser[1]
YFe_5O_{12}	YIG	1555	[110]	110 – 600	Isolator[1]
Y_2O_3:Cr		2400	c, [110]	600	Laser[1]
Y_2O_3:Eu		2410	c	500 – 800	Laser[1]
$Y_3Sc_2Al_3O_{12}$:Cr	Cr:YSAG	1900	[111]	800	Laser[1]
Fluorides					
BaF_2	Barium Fluoride	1280	[100]	200 – 800	IR Guide[1]
CaF_2	Calcium Fluoride	1360	[111]	600	IR Guide[1]
Eutectics					
LiF-NaF		676			Eutectics[1]
Li_2O-GeO_2		1106			Eutectics[1]
NaF-NaCl		640			Eutectics[1]
PbF_2-Al_2F_3		565		1000	Material Study[1]
Semiconductors & Metallics					
B_9C		2400		200	Thermoelectric[1]
$Bi_2Sr_2CaCu_2O_8$		900		250 – 1000	Superconductor[1]
Co		1495		100 – 600	Magnetics[1]
Fe		1539		100 – 600	Magnetics[1]
Fe-Co		1500		100 – 600	Magnetics[1]
Ge		960		200	IR Guide[1]
LaB_6		2716		200	Cathode Filament[1]
Nb		2468		200	Superconductor[1]
Si		1420	[111]	200	Model

[A.1] R. S. Feigelson, *Opportunities for Research on Single-Crystal Fibers*, Mat. Sci. Eng. B1, **1**, 1, 67, 1988

[A.2] D. R. Ardila, M. R. B. Andreeta, S. L. Cuffini, A. C. Hernandes, J. P. Andreeta and Y. P. Mascarenhas, *Laser Heated Pedestal Growth of Sr_2RuO_4 Single-Crystal Fibers from $SrRuO_3$*, J. Cryst. Growth, **177**, 1-2, 52, 1997

[A.3] T. Imai, S. Yagi, Y. Sugiyama and I. Hatakeyama, *Growth of Potassium Tantalate Niobate Single Crystal Fibers by Laser-Heated Pedestal Growth Method Assisted by a Crystal Cooling Technique*, J. Cryst. Growth, **147**, 3-4, 350, 1995

[A.4] V. V Prokofiev, J. P. Andreeta, C. J. de Lima, M. R. B. Andreeta, A. C. Hernandes, J. F. Carvalho, A. A. Kamshilin and T. Jääskeläinen, *Growth of Single-Crystal Photorefractive Fibers of $Bi_{12}SiO_{20}$ and $Bi_{12}TiO_{20}$ by the Laser-Heated Pedestal Growth Method*, J. Cryst. Growth, **137**, 3-4, 528, 1994

[A.5] L. B. Shaw and R. S. F. Chang, *Rare Earth Doped ULF Grown by Laser-Heated Pedestal Growth Technique*, J. Cryst. Growth, **112**, 4, 731, 1991

[A.6] Y. Ji, S. Zhao, Y. Hou, H. Zhang, M. Li and C. Huang, *Growth of Lithium Triborate (LBO) Single Crystal Fiber by Laser-Heated Pedestal Growth Method*, J. Cryst. Growth, **112**, 1, 283, 1991

[A.7] W. Jia, L. Lu, B. M. Tissue and W. M. Yen, *Valence and Site Occupation of Chromium Ions in Single-Crystal Forsterite Fibers*, J. Cryst. Growth, **109**, 1-4, 323, 1991

[A.8] M. Ferriol, A. Dakki, M. T. Cohen-Adad, G. Foulon, A. Brenier and G. Boulon, *Growth and Characterization of MgO-Doped Single-Crystal Fibers of Lithium Niobate in Relation to High Temperature Phase Equilibra in the Ternary System Li_2O-Nb_2O_5-MgO*, J. Cryst. Growth, **178**, 4, 529, 1997

[A.9] M. Ferriol, G. Foulon, A. Brenier, M. T. Cohen-Adad and G. Boulon, *Laser Heated Pedestal Growth of Pure and Nd^{3+}-Doped Potassium Lithium Niobate Single-Crystal Fibers*, **173**, 1-2, 226, 1997

Appendix B

Figure B1: Spec YAl 26 $Y_3Al_5O_{12}:Er^{3+}$ fluorescence decay at 1612nm at 293K

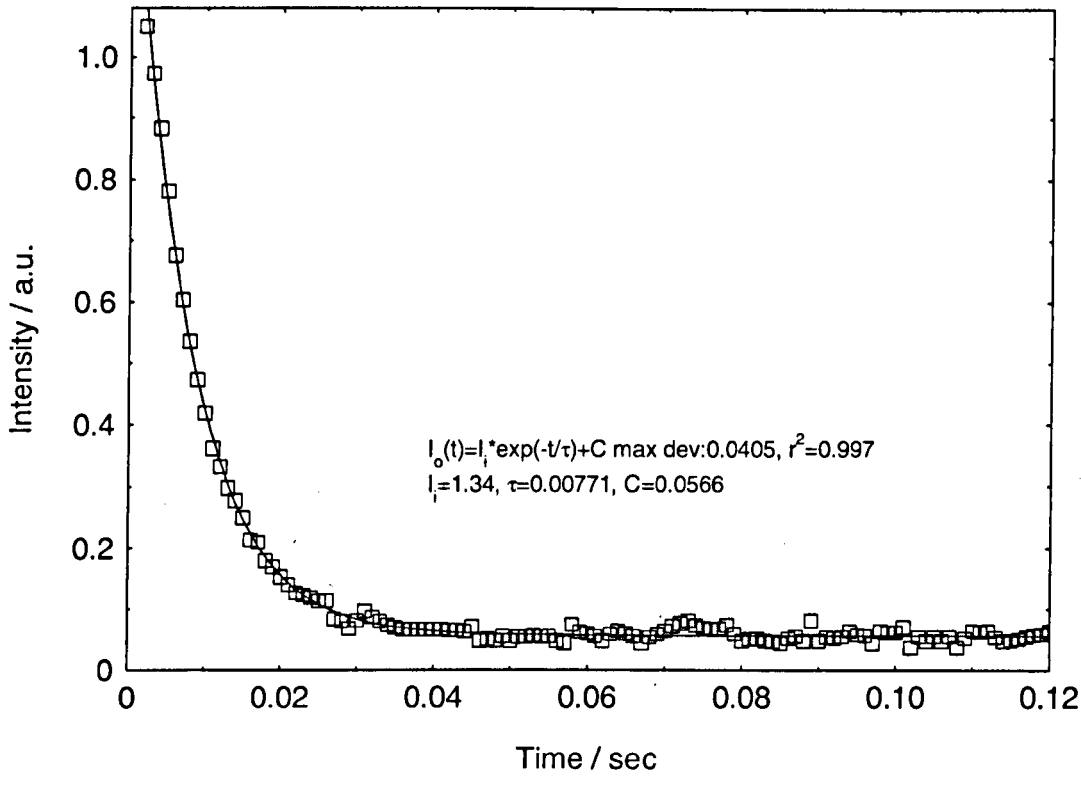

Figure B2: Spec YAl 26 $Y_3Al_5O_{12}:Er^{3+}$ fluorescence decay at 1612nm at 1473K

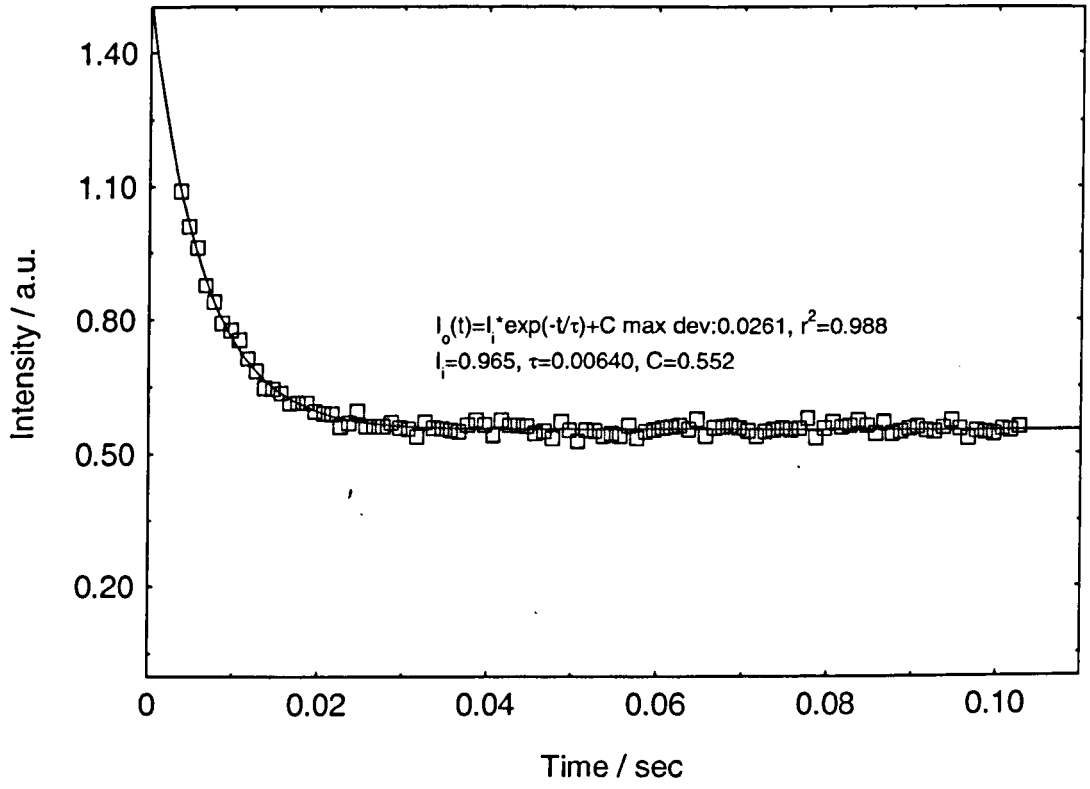

Figure B3: Spec YAl 32 $Y_3Al_5O_{12}:Er^{3+} + Yb^{3+}$ fluorescence decay at 1612nm at 293K

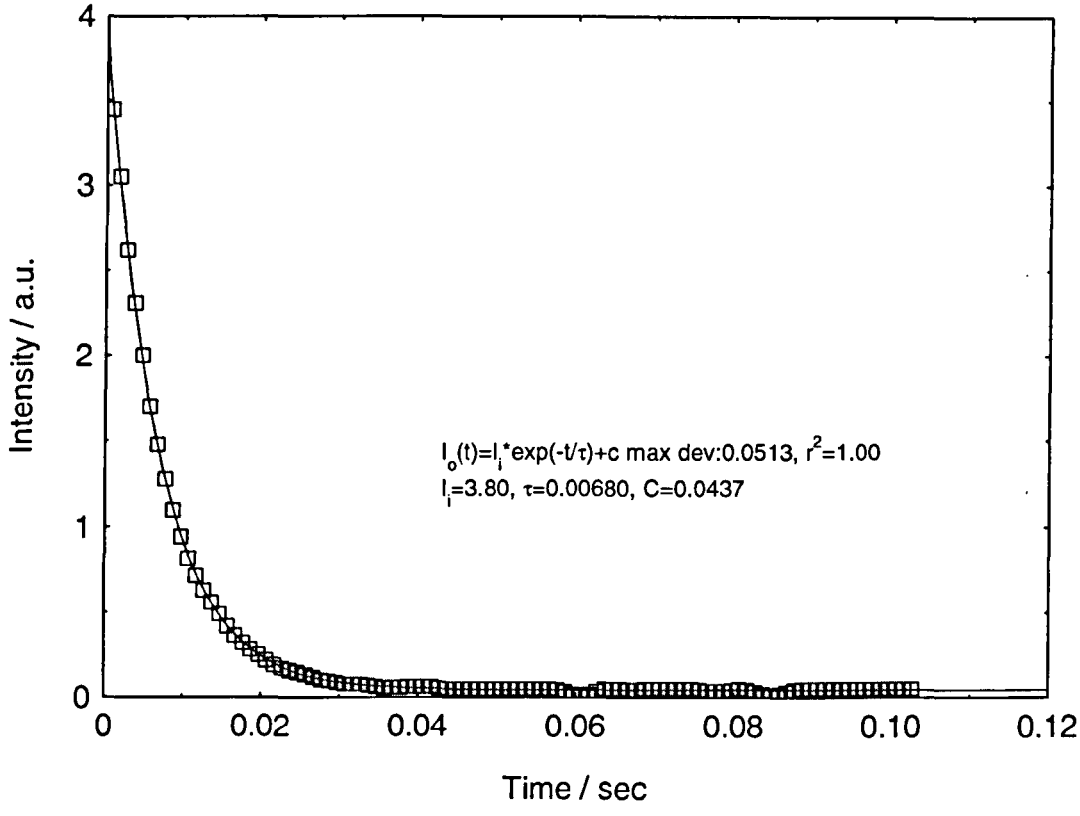

Figure B4: Spec YAl 32 $Y_3Al_5O_{12}:Er^{3+} + Yb^{3+}$ fluorescence decay at 1612nm at 1473K

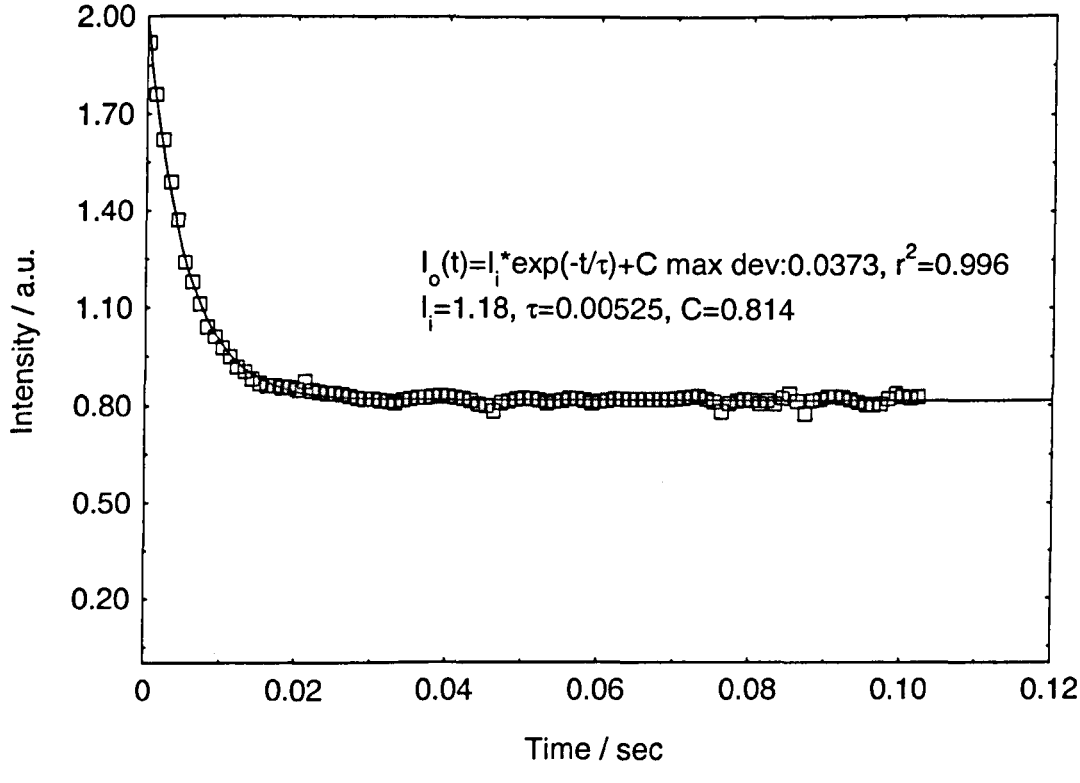

Figure B5: Spec 64 Y_2O_3:Er^{3+} fluorescence decay at 1530.5nm at 293K

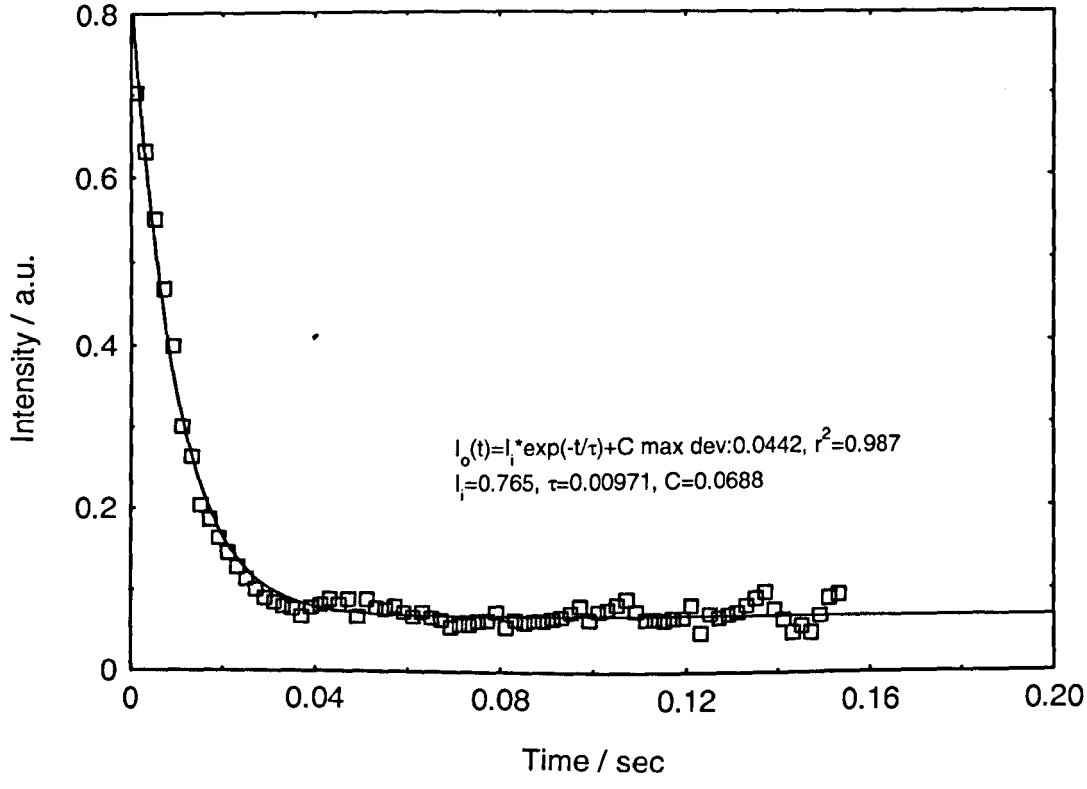

Figure B6: Spec 64 Y_2O_3:Er^{3+} fluorescence decay at 1530.5nm at 1473K